Pattern formation in thin liquid films: from coating-flow instabilities to microfluidic droplets

THÈSE N^{O} 8828 (2018)

PRÉSENTÉE LE 6 SEPTEMBRE 2018

À LA FACULTÉ DES SCIENCES ET TECHNIQUES DE L'INGÉNIEUR
LABORATOIRE DE MÉCANIQUE DES FLUIDES ET INSTABILITÉS
PROGRAMME DOCTORAL EN MÉCANIQUE

ÉCOLE POLYTECHNIQUE FÉDÉRALE DE LAUSANNE

POUR L'OBTENTION DU GRADE DE DOCTEUR ÈS SCIENCES

PAR

Gioele Mariano Nicolò BALESTRA

acceptée sur proposition du jury:

Prof. C. Ancey, président du jury
Prof. F. Gallaire, directeur de thèse
Prof. J. M. Gordillo Arias de Saavedra, rapporteur
Prof. B. Scheid, rapporteur
Prof. P. M. Reis, rapporteur

ÉCOLE POLYTECHNIQUE
FÉDÉRALE DE LAUSANNE
Suisse
2018

To my family

Le savant n'étudie pas la nature parce que cela est utile ; il l'étudie parce qu'il y prend plaisir et il y prend plaisir parce qu'elle est belle. Si la nature n'était pas belle, elle ne vaudrait pas la peine d'être connue, la vie ne vaudrait pas la peine d'être vécue. Je ne parle pas ici, bien entendu, de cette beauté qui frappe les sens, de la beauté des qualités et des apparences ; non que j'en fasse fi, loin de là, mais elle n'a rien à faire avec la science ; je veux parler de cette beauté plus intime qui vient de l'ordre harmonieux des parties, et qu'une intelligence pure peut saisir.

— Henri Poincaré *Science et Méthode*, 1908

Acknowledgements

I like to see this work as a puzzle-solving process, a puzzle of which you do not know the original image. I am extremely grateful to François for giving me this fantastic opportunity four years ago. Your guidance in this, for me, new world of low-Reynolds-number interfacial flows, your brilliant ideas that very often allowed me to put pieces of the puzzle together, your contagious passion for science and the endless time you dedicated to me, for which I feel particularly lucky, made the accomplishment of this puzzle possible.

I am very thankful to Prof. José Manuel Gordillo Arias de Saavedra, to Prof. Benoit Scheid and to Prof. Pedro Miguel Reis for having accepted to evaluate this work and for having read in great details this lengthy thesis. I deeply appreciated the constructive discussion during the thesis defense. My gratitude also goes to Prof. Christophe Ancey for kindly accepting to preside over the jury. Either through summer schools, lectures, conferences, or collaborations, I have been influenced by your work and you might notice this in the final image of this puzzle.

At the beginning of a PhD one has a large amount of obscure pieces of the puzzle in his own hand, but no clue on how to assemble them together. Luckily, I had the chance of having François as supervisor as well as fantastic colleagues at LFMI, who helped me in this process called scientific research. Step by step you progress in the solution of the puzzle and you start seeing the image on it. Eventually you dream of the missing parts and you do your best in order to connect them together. Special thanks go to Mathias N., my former bachelor's project supervisor, who has welcomed me back in Lausanne at the beginning of the PhD and strongly influenced my path. Thank you P.-T. for being a model in my first years of this adventure, I learned a lot from you. Thank you Nicolas for nicely introducing me to the experimental world and for being a really enjoyable officemate. Thank you Francesco for your precious theoretical support, you have been a wonderful predecessor for me. I will never forget listening Frank Sinatra in the car during our trip to Boston. Thank you Edouard for assisting me with the adjoint equations and for the nice moments in Bern. Thank you Giacomo for sharing this adventure called PhD together and the countless moments we spent together. Thank you Petra for taking care of us in such a lovely way. Thank you Lailai for your guidance in the numerical and scientific world and the swimming evenings on Tuesdays. Thank you Vlado for bringing some Spanish-Slovak-Cuban sun in the lab and the nice philosophical discussions. I will always remember the hike on Mont d'Or with you and Giacomo. Thank you Simon P. for your several precious tips. Thank you Andrea for the nice week we spent together at CISM. Thank you Laura for guiding me in the very first weeks on a bi-Poiseuille stability problem. Thank you Yoan for the nice ski days together. Thank you Marc-Antoine for having contributed

to my initial interest for fluid dynamics. Thank you also to Elise Lorenceau and Benjamin Dollet for their precious advices during their stay in the lab. Thank you Isha and Eunok for scaring me so often, for your contagious smile and for enjoying my cakes. Thank you Lorenzo S. for being such a nice person, I truly appreciate your presence in the lab. Thank you Mathias B. for the fruitful discussions on COMSOL. Thank you Gaétan for taking over the experimental labs and your beautiful experiments. Thank you Hervé for sharing the office during these last months. Thank you Ludovic for the stimulating conversations we had since the summer school at ULB. I wish a wonderful and successful PhD adventure to Shahab and Pier Giuseppe. During these years, I also had the chance of having excellent external collaborators who helped me putting the pieces of the puzzle together. Among them, and in addition to the previously mentioned people, I would like to express my special gratitude to Anna and Joël, who warmly welcomed me at MIT, to Pooria, Mohammad and Prof. Demetri Psaltis, and to Prof. Matthieu Wyart for embarking me in a beautiful speleological journey. Also, brilliant and faithful students crucially helped me in finishing the puzzle. Among them I would like to acknowledge Mohamed, Yves-Marie and David. I hope you can also enjoy the final result of this work. I would like to thank also Tobias and his ECPS lab, especially Simon S., Florian and Sajjad with whom I enjoyed very much doing the exercises of the doctoral school courses.
If I decided to start this adventure four years ago, it is also because of some people that I would like to deeply acknowledge. Nico, having you as a friend and classmate during all the university years has been wonderful. Many thanks for the countless stimulating discussions and for having forged my curiosity and interest in science. It meant a lot to me. Thank you Nemanja for the endless nice time we spent together at ETH. Thank you Michael for being an awesome supervisor. I would also like to acknowledge Prof. Leonhard Kleiser, Prof. Dominik Obrist and Prof. Patrick Jenny for having further increased my interest for fluid dynamics.
I have been pretty busy during the last years, but luckily I have some long lasting friends on whom I can rely. Thank you so much Fabio R., Beta and Laura for being always there. Many thanks also to Lorenzo R., Simone B., Fabio dell'A., Joël, Giulia G., Giorgio, Luisa S., Fernando, Matteo P., Simon G., Patrick, Federico, Colo, Cola, Giacomo C., Matteo L., Marco, Philo and Flavio for their friendship. A special thank to my flatmates, in particular to Luisa I., who often supported me in these four years during the dinners, when my state of mind was not the best. I would also like to express my deep gratitude to Mr. Henry Lambert and Mr. David Gay for their extremely precious help in the last year.
Thank you so much Karin, Jean-Marc and Fabien for having welcomed me in your family in such a lovely way. Anaëlle, I cannot thank you enough for your unconditional support and for having tolerated my difficult mood in several moments. The time with you is extremely precious to me. Merci infiniment!
Finally, from the bottom of my heart, I want to say that all this would not have been possible without a family who supported me, in the ups and downs, a family who has always believed in me and has been a source of energy and comfort for me. Grazie di cuore mami, papi, Gea e Benoît. Benvenuti Giulia e Massimiliano, grazie per i vostri magnifici sorrisi.

Lausanne, 5 July 2018 Gioele Balestra

Abstract

Nature and technical applications abound with thin viscous flows, ranging from the lava flow on volcanoes to the lubricating layer around confined bubbles in the microchannels of Lab-on-a-Chip devices. Countless are the examples where coating flows arise in industrial processes. We all have probably already observed that thin-film flows often form well-defined fascinating patterns, as the tears in a glass of wine, or the crystalline-like pattern of pendent droplets under the kitchen lid. Yet, the nonuniformity of the film thickness is not always desirable and calls for the development of flow-control strategies. Despite the fact that the mechanisms underpinning the pattern formation in thin liquid films are known for simple, often one-dimensional, geometries, little is known when thin films coat more geometrically complex two-dimensional surfaces.

The aim of this thesis is to investigate the pattern formation in thin-film flows for different configurations. The interface of a free-surface flow can deform as a result of hydrodynamic instabilities or due to boundary conditions. Here, we focus on both the gravity-induced destabilization of the liquid interface of thin films flowing on curved and inclined geometries and the pattern formation in thin films connected to thicker liquid regions via menisci.

We first consider the Rayleigh-Taylor instability when a fixed liquid quantity coats the underneath of a substrate as well as the fingering instability when the liquid flows onto the substrate. We show that both instabilities can be suppressed by carefully controlling the substrate geometry. A stable flow can be harnessed to produce thin hemispherical elastic shells in a very robust and versatile manner. Due to the intrinsic space and time dependence of these flows on curved geometries, classic hydrodynamic stability analyses are ruled out. Hence, we apply nonmodal optimal transient growth techniques, as recently used to develop understanding of the transition to turbulence in shear flows, for the study of the pattern formation in this entirely different class of flows. The substrate curvature is found to play a key role in the stabilization of the Rayleigh-Taylor instability through the gravity component parallel to the substrate. The resulting increased draining flow makes the film asymptotically stable with respect to infinitesimal perturbations. We demonstrate that the linearly most amplified pattern, in agreement with the performed experiments and nonlinear numerical simulations, differs from the classic one of a liquid coating the underneath of a planar horizontal substrate. Strikingly, we show that these Rayleigh-Taylor-instability patterns are very likely to be at the origin of the pattern selection in karst formations encountered in limestone caves.

In the last part of this thesis, we aim at providing a detailed theoretical and numerical characterization of the thin-film profiles around confined bubbles and droplets in microchannels in

order to better predict their dynamics, which is still an open question despite the dramatic increase in popularity of microfluidic devices.
In spite of the broad range of scales considered, all the thin-film flows can be described by similar lubrication equations. We show that the unidirectional dominant advection encountered in this work is responsible for breaking the symmetry of the problem and yielding anisotropic patterns.

Key words: thin-film flow, coating flow, hydrodynamic instability, Rayleigh-Taylor, lubrication equation, pattern formation, morphodynamics, interfacial flows, droplet dynamics, microfluidics.

Résumé

Les films liquides de fluides visqueux sont omniprésents dans la nature et les applications technologiques. Il suffit de penser aux coulées de lave des éruptions volcaniques ou aux films liquides entourant les bulles confinées dans les micro-canaux des dispositifs Lab-on-a-Chip. Nombreux sont les exemples de processus industriels qui impliquent des enductions liquides. Nous avons probablement tous déjà remarqué que ces films sont à l'origine de phénomènes fascinants comme les larmes du vin dans un verre ou les gouttes de condensation sous le couvercle d'une casserole. Malheureusement, les inhomogénéités qui en résultent ne sont pas toujours désirables et il est souvent nécessaire de recourir à des stratégies de contrôle. Les mécanismes à l'origine de la formation de ces motifs sont connus pour des films couvrant des géométries simples, souvent monodimentionnelles. En revanche, le comportement des films liquides sur des géométries plus complexes est peu connu.

La présente thèse a pour but d'étudier la formation des motifs de ces films dans le cadre de différentes configurations. Un écoulement à interface libre peut être déstabilisé par des instabilités hydrodynamiques ou par des conditions au bord. Dans ce travail, nous nous concentrerons sur la déstabilisation due à la force de gravité des écoulements minces sous et sur des surfaces courbes et inclinées. Nous étudierons également la formation des motifs lorsque ces films sont reliés à des régions liquides plus épaisses via des ménisques.

Nous nous concentrerons tout d'abord sur l'instabilité de Rayleigh-Taylor d'une quantité de liquide située au-dessous d'une surface ainsi que sur celle de 'fingering' d'un film qui s'écoule sur le dessus d'une surface. Nous démontrerons qu'il est possible de supprimer les deux instabilités susmentionnées en contrôlant attentivement la géométrie du substrat. Un écoulement stable peut être exploité pour produire des hémisphères élastiques minces de manière robuste et versatile. La théorie classique des instabilités hydrodynamiques ne peut pas être appliquée en raison de la dépendance spacio-temporelle de ces écoulements en géométrie courbe. Nous utiliserons par conséquent les techniques non modales de croissance transitoire optimale, récemment introduites dans l'étude de la transition vers la turbulence, pour expliquer la formation de motifs dans ce type d'écoulements complètement différents. Nous montrerons comment la courbure du substrat joue un rôle capital dans la suppression de l'instabilité de Rayleigh-Taylor grâce à la composante de la gravité parallèle à la surface. Une telle force induit en effet un écoulement inhomogène et rend le film asymptotiquement stable pour des perturbations infinitésimales. Par ailleurs, nous illustrerons le fait que le motif le plus amplifié linéairement, qui est en accord avec les expériences et les simulations numériques, diffère du motif classique d'un film fluide situé sous un substrat plan horizontal.

Nous montrerons ensuite que ces motifs instables sont probablement à l'origine des formes prises par certaines formations calcaires dans les grottes.
Enfin, nous caractériserons de manière théorique et numérique les films entourant les bulles ou les gouttes confinées dans les micro-canaux afin de prédire plus précisément leur dynamique. Il s'agit aujourd'hui encore d'une problématique ouverte malgré la popularité croissante de la microfluidique.
En dépit du vaste spectre des configurations étudiées, le comportement de ces films liquides minces peut être décrit par des équations de lubrification semblables les une aux autres. Nous démontrerons en particulier que l'advection dominante dans une direction préférentielle brise la symétrie du problème et régit la formation de motifs anisotropes.

Mots clés : écoulement de film mince, écoulement d'entraînement, instabilité hydrodynamique, Rayleigh-Taylor, équation de lubrification, formation de motifs, morphodynamique, écoulement à interface libre, dynamique des gouttes, microfluidique.

Zusammenfassung

Viskose Filme sind sowohl in der Natur als auch in technologischen Anwendungen allgegenwärtig: von Lavaströmen bis hin zu dünnen Schichten, die sich zwischen geometrisch eingeschränkten Tropfen oder Blasen und den Wänden von Mikrokanälen befinden. Es gibt unzählige Beispiele von viskosen Beschichtungen in industriellen Prozessen. Höchstwahrscheinlich haben wir alle schon beobachten können, wie diese Filme faszinierende Phänomene hervorrufen, wie zum Beispiel die Weinperlen am Glasrand oder die Wasserdampftropfen unter einem Kochtopfdeckel. Die Dicke dieser Schichten ist nicht immer gleichförmig, was leider nicht immer gewünscht wird und weshalb Kontrollmaßnahmen oft notwendig sind. Obwohl der Ursprung dieser Strukturen für einfache, meist eindimensionale Geometrien bekannt ist, weiß man wenig über das Verhalten von dünnen Beschichtungen von komplexen Geometrien.

Das Ziel dieser Arbeit ist die Erforschung der Musterbildung dieser Filmstrukturen in unterschiedlichen Konfigurationen. Die Grenzfläche einer Strömung mit freier Oberfläche kann sich aufgrund von hydrodynamischen Instabilitäten oder bestimmten Randbedingungen verändern. In dieser Arbeit wird die durch Schwerkraft induzierte Destabilisierung dünner viskoser Filme auf gekrümmten oder schrägen Oberflächen untersucht, sowie die Bildung von Strukturen, wenn diese Filme durch Menisken an dickere flüssige Regionen gebunden sind.

Zuerst werden wir uns auf die Rayleigh-Taylor Instabilität bei einer auf der Unterseite einer Fläche befindlichen, definierten Flüssigkeitsmenge konzentrieren. Anschließend wird auf die ‘fingering’ Instabilität bei einer Strömung auf der Oberseite eingegangen. Es wird gezeigt, dass beide Instabilitäten über geeignete Wahl der Oberflächengeometrie vermieden werden können. Eine stabile Strömung kann auf sehr robuste und vielseitige Weise zur Erzeugung dünner, elastischer Halbkugelschalen genutzt werden. Aufgrund der intrinsischen räumlichen und zeitlichen Abhängigkeit dieser Strömungen auf gekrümmten Geometrien kann die klassische hydrodynamische Stabilitätstheorie nicht angewandt werden. Deswegen wird eine nicht-modale Technik zur Bestimmung des größten transienten Störungswachstum verwendet, die kürzlich bei der Untersuchung des Übergangs zur Turbulenz in Scherströmungen angewandt wurde, um die Musterbildung bei diesen andersartigen Strömungen zu erklären. Die Krümmung des Substrats spielt, dank der zur Oberfläche parallel verlaufenden Schwerkraftkomponente, eine zentrale Rolle bei der Unterdrückung der Rayleigh-Taylor Instabilität. Durch die durch diese Kraft verursachte zunehmende Strömung wird der Film asymptotisch stabil gegenüber infinitesimalen Störungen. Es wird außerdem erläutert, dass die am schnellsten linear wachsende Filmstruktur, die ebenfalls mit Experimenten und nu-

merischen Simulationen übereinstimmt, sich von den klassischen Filmstrukturen auf der Unterseite von horizontalen Flächen unterscheidet. Anschließend wird gezeigt, dass diese Rayleigh-Taylor Instabilitätsmuster höchstwahrscheinlich die faszinierenden Karststrukturen in Kalksteingrotten verursachen.
Schlussendlich werden wir die Filmstrukturen um eingeschränkte Tropfen und Blasen in Mikrokanälen theoretisch und numerisch untersuchen, mit dem Ziel ihre Dynamik besser vorhersagen zu können, was trotz des stark wachsenden Interesses an Mikrofluidik noch immer eine offene Fragestellung ist.
Auch wenn die untersuchten Konfigurationen sehr unterschiedlich sind, kann das Verhalten der Filmströmungen mit ähnlichen Gleichungen beschrieben werden. Insbesondere wird gezeigt, dass die vorherrschend in eine Richtung orientierte Advektion zur Symmetriebrechung führt und dies die Ursache für die Bildung von anisotropischen Filmstrukturen darstellt.

Schlüsselwörter: Dünnschicht-Strömung, Beschichtungsströmung, hydrodynamische Instabilität, Rayleigh-Taylor, Gleichung der hydrodynamischen Schmierung, Musterbildung, Morphodynamik, Strömung mit freier Oberfläche, Tropfendynamik, Mikrofluidik.

Riassunto

Film liquidi di fluidi viscosi sono ampiamente presenti sia in natura che in applicazioni tecnologiche, dalle colate di lava sui vulcani ai film liquidi attorno alle bolle confinate nei microcanali dei dispositivi Lab-on-a-Chip. Innumerevoli sono gli esempi di processi industriali comprendenti rivestimenti liquidi. Abbiamo tutti probabilmente già osservato che questi film spesso danno origine a fenomeni affascinanti, come le lacrime di vino sul bordo di un bicchiere o le gocce di condensazione al di sotto di un coperchio da cucina. Purtroppo, la nonuniformità dello spessore di un film fluido non è sempre benvenuta e strategie di controllo sono spesso necessarie. Malgrado i meccanismi all'origine della formazione di questi motivi sono conosciuti per film che ricoprono geometrie semplici, spesso monodimensionali, poco si sa del comportamento di film liquidi in geometrie più complesse.

Lo scopo di questa tesi è lo studio della formazione di motivi in questi film in diverse configurazioni. Un flusso ad interfaccia libera può destabilizzarsi a causa d'instabilità idrodinamiche o a causa delle condizioni al contorno. In questo lavoro ci concentreremo sulla destabilizzazione indotta dalla forza di gravità dei flussi sottili sia al di sotto che al di sopra di superfici curve ed inclinate, come pure sulla formazione di motivi quando questi film sono connessi a regioni liquide più spesse attraverso dei menischi.

Ci focalizzeremo dapprima sull'instabilità di Rayleigh-Taylor di una quantità di liquido posta al di sotto di una superficie, così come sull'instabilità di 'fingering' di un film che scorre sulla parte superiore di una superficie. Dimostreremo che entrambe le instabilità possono essere soppresse controllando attentamente la geometria del sostrato. Un flusso stabile può essere sfruttato per produrre delle emisfere elastiche sottili in maniera robusta e versatile. A causa della dipendenza spazio-temporale di questi flussi in geometrie curve, la teoria classica delle instabilità idrodinamiche non può essere applicata. Utilizzeremo quindi delle tecniche non-modali di crescita transitoria ottimale, recentemente introdotte per studio della transizione alla turbolenza, per spiegare la formazione di motivi in questa classe di flussi completamente differenti. Verrà mostrato come la curvatura del sostrato sia cruciale per la soppressione dell'instabilità di Rayleigh-Taylor grazie alle componente della gravità parallela alla superficie. Tale forza induce infatti un crescente flusso e rende il film asintoticamente stabile per delle perturbazioni infinitesimali. Illustreremo inoltre che il motivo più amplificato linearmente, in accordo con gli esperimenti e le simulazioni numeriche, differisce da quello classico di un film fluido al di sotto di un sostrato piano orizzontale. Successivamente, mostreremo che questi motivi instabili sono molto probabilmente all'origine della forma assunta da alcune formazioni calcaree nelle grotte.

L'attenzione sarà infine rivolta alla caratterizzazione teorica e numerica dei film attorno a bolle o gocce confinate in microcanali, così da predire in maniera più accurata la loro dinamica che rimane ancora oggi una questione aperta nonostante la grande popolarità della microfluidica. Malgrado l'ampio spettro di configurazioni considerate, il comportamento di questi film può essere descritto da equazioni di lubrificazione analoghe. In particolare, verrà mostrato che l'avvezione dominante in una direzione preferenziale rompe la simmetria del problema ed è la causa della formazione di motivi anisotropici.

Parole chiave : flusso liquido sottile, flusso di rivestimento, instabilità idrodinamica, Rayleigh-Taylor, equazione di lubrificazione, formazione di motivi, morfodinamica, flusso ad interfaccia libera, dinamica di gocce, microfluidica.

Contents

Acknowledgements **vii**

Abstract (English/Français/Deutsch/Italiano) **ix**

1 Introduction **1**
1.1 Fluid dynamics of thin liquid films . . . 1
1.1.1 Motivation . . . 1
1.1.2 The lubrication equation . . . 5
1.1.3 Classical solutions of the lubrication equation . . . 9
1.2 Thin-film instabilities . . . 14
1.2.1 Instability analysis . . . 14
1.2.2 Rayleigh-Taylor . . . 16
1.2.3 Fingering . . . 18
1.2.4 Kapitza waves . . . 20
1.2.5 Rayleigh-Plateau . . . 21
1.2.6 Flow-driven morphodynamics . . . 22
1.2.7 In this thesis . . . 23
1.3 Thin films in confined bubbles and droplets in microchannels . . . 27
1.3.1 Analogy between coating flows and thin films in microchannels . . . 27
1.3.2 Microfluidic channels . . . 30
1.3.3 In this thesis . . . 31

I The effect of the substrate curvature on thin-film instabilities **33**

2 Fabrication of slender elastic shells by the coating of curved surfaces **35**
2.1 Introduction . . . 36
2.2 Results . . . 37
2.2.1 Elastic shells of uniform thickness from viscous coating . . . 37
2.2.2 The dynamics of coating . . . 38
2.2.3 Nonlinear drainage flow solution . . . 40
2.2.4 Including the effects of curing into the flow solution . . . 44
2.3 Discussion . . . 46
2.4 Methods . . . 50

2.4.1 Experiments . . . 50
2.4.2 Numerical simulations . . . 50

3 Rayleigh-Taylor instability under curved substrates: An optimal transient growth analysis 53
3.1 Introduction . . . 54
3.2 Governing equations and Methods . . . 54
3.2.1 Lubrication and linear perturbation equations . . . 54
3.2.2 Transient growth analysis . . . 57
3.2.3 Numerical methods . . . 59
3.3 Results . . . 60
3.3.1 Optimal perturbation regimes . . . 60
3.3.2 Influence of the Bond number . . . 61
3.3.3 Influence of the film aspect ratio . . . 62
3.4 Discussion . . . 63
3.4.1 Optimal transient growth analysis at $\theta = 0$ . . . 63
3.4.2 Transition to dripping droplets . . . 67
3.5 Conclusions . . . 69
3.6 Appendix . . . 71
3.6.1 Derivation of the lubrication equation . . . 71
3.6.2 Linear operator . . . 72
3.6.3 Derivation of the adjoint fields . . . 73
3.6.4 Numerical methods . . . 74

4 Three-dimensional Rayleigh-Taylor instability under a unidirectional curved substrate 77
4.1 Introduction . . . 78
4.2 Experimental results . . . 79
4.2.1 Relevant dimensionless parameters . . . 79
4.2.2 Experimental set-up . . . 79
4.2.3 Phase diagram: rivulets or dripping droplets? . . . 81
4.3 Linear optimal transient growth analysis . . . 83
4.3.1 Governing equation . . . 83
4.3.2 Linear disturbance solution . . . 84
4.3.3 Optimal growth . . . 86
4.3.4 Linear prediction . . . 88
4.4 Nonlinear two-dimensional simulations . . . 89
4.5 Characterization of the rivulets . . . 92
4.5.1 Nonlinear simulations at the top of the cylinder . . . 92
4.5.2 Experimental measurements . . . 95
4.5.3 Numerical experiment on the front propagation of rivulets . . . 97
4.6 Conclusions . . . 98
4.7 Appendix . . . 100

4.7.1 Derivation of the lubrication equation . . . 100
4.7.2 Lubrication equation for small angles . . . 103
4.7.3 Derivation of the drainage solution . . . 103
4.7.4 Numerical methods . . . 104
4.7.5 Confocal chromatic imaging technique . . . 104

5 Rayleigh-Taylor instability under a spherical substrate 107
5.1 Introduction . . . 107
5.2 Governing equation . . . 109
5.2.1 Entire upper hemisphere . . . 109
5.2.2 Limit for the vicinity of the north pole . . . 110
5.3 Linear optimal transient growth analysis at the north pole . . . 111
5.3.1 Linear disturbance solution . . . 111
5.3.2 Optimal growth . . . 113
5.4 Nonlinear evolution of the linear optimal initial conditions . . . 114
5.4.1 Spatio-temporal amplitude diagrams . . . 115
5.4.2 Effect of the initial azimuthal wavenumber . . . 121
5.4.3 Effect of the Bond number . . . 121
5.4.4 Pattern propagation velocity . . . 124
5.5 Random noise initial conditions . . . 126
5.6 Conclusions . . . 129
5.7 Appendix . . . 131
5.7.1 Derivation of the lubrication equation . . . 131
5.7.2 Derivation of the drainage solution . . . 133
5.7.3 Numerical methods . . . 134
5.7.4 Alternative representation of the thin-film evolution shown in Fig. 5.5 . 134

6 Fingering instability on curved substrates: optimal initial film and substrate perturbations 137
6.1 Introduction . . . 137
6.2 Problem formulation and governing equations . . . 140
6.3 Draining base flow . . . 142
6.3.1 Lubrication equation . . . 142
6.3.2 Drainage at the pole . . . 143
6.3.3 Spatial dependence of the outer region . . . 143
6.3.4 Front position . . . 144
6.3.5 Length of the inner region . . . 145
6.4 Optimal film thickness initial conditions over a smooth substrate . . . 147
6.4.1 Film-thickness decomposition . . . 147
6.4.2 Linear disturbance equation . . . 148
6.4.3 Optimization method . . . 149
6.4.4 Results . . . 151
6.5 Optimal substrate perturbations for an initially unperturbed film . . . 157

6.5.1 Free-surface-elevation decomposition . . . 157
6.5.2 Linear disturbance equation . . . 158
6.5.3 Optimization method . . . 158
6.5.4 Results . . . 160
6.6 Conclusions . . . 165
6.7 Appendix . . . 168
6.7.1 Linear operators . . . 168
6.7.2 Numerical methods . . . 169
6.7.3 Derivation of the adjoint fields for the optimal substrate algorithm . . . 169

II Precipitative pattern formation in limestone caves 171

7 Hydrodynamic-driven speleothem morphogenesis 173
7.1 Introduction . . . 173
7.2 Problem description and governing equations . . . 175
7.2.1 Hydrodynamics . . . 175
7.2.2 Morphogenesis . . . 178
7.3 Thin-film flow under an inclined plane coupled to the deposition process . . . 181
7.3.1 Linear stability analysis . . . 181
7.3.2 Spatio-temporal analysis . . . 185
7.3.3 Nonlinear selection of rivulets . . . 190
7.4 Hydrodynamics of the thin-film flow under a curved substrate followed by an inclined plane . . . 193
7.4.1 Base-flow solution under a curved substrate . . . 193
7.4.2 Linear stability analysis . . . 194
7.4.3 Nonlinear simulations . . . 198
7.5 Other possible mechanisms at the origin of the wavenumber selection . . . 203
7.5.1 Secondary instability of Kapitza waves . . . 204
7.5.2 Rayleigh-Plateau instability . . . 204
7.6 Conclusions and perspectives . . . 205

III Bubbles and droplets in microfluidic channels 209

8 Thin-film patterns induced by advancing and receding menisci 211
8.1 Introduction . . . 211
8.2 One-dimensional lubrication problem . . . 212
8.2.1 Linear solution of the lubrication equation . . . 214
8.2.2 Nonlinear solutions . . . 216
8.3 Two-dimensional lubrication problem . . . 219
8.3.1 Linear solution of the lubrication equation . . . 220
8.3.2 Nonlinear solutions . . . 227
8.4 Conclusions and perspectives . . . 231

8.5 Appendix . . . 233
8.5.1 Classical derivation of the linearized Landau-Levich-Derjaguin equation (Bretherton, 1961) . . . 233
8.5.2 Lubrication equation for a pressure-driven bubble in a curvilinear-coordinate system . . . 235

9 Viscous Taylor droplets in axisymmetric and planar tubes: from Bretherton's theory to empirical models 237
9.1 Introduction . . . 240
9.2 Governing equations and numerical methods . . . 242
9.2.1 Problem setup . . . 242
9.2.2 Governing equations . . . 243
9.2.3 Numerical methods and implementations . . . 244
9.2.4 Validation . . . 246
9.3 Flow field . . . 248
9.3.1 Velocity profiles in the thin-film region . . . 248
9.3.2 Recirculating flow patterns . . . 249
9.4 Film thickness . . . 252
9.4.1 Asymptotic result in the *low-Ca* limit . . . 252
9.4.2 Empirical model in the *low-Ca* limit . . . 255
9.4.3 Model for $10^{-3} \lessapprox Ca \lessapprox 1$ . . . 257
9.5 Droplet velocity . . . 258
9.6 Minimum film thickness . . . 260
9.7 Front and rear total stress jumps . . . 262
9.7.1 Front and rear plane curvatures . . . 263
9.7.2 Front and rear pressure jumps – classical model . . . 264
9.7.3 Front and rear normal viscous stress jumps . . . 264
9.7.4 Front and rear pressure jumps – improved model . . . 265
9.8 Stress distribution and total pressure drop . . . 265
9.8.1 Stress distribution along the channel centerline . . . 265
9.8.2 Pressure distribution along the channel wall . . . 267
9.8.3 Droplet-induced total pressure drop along a channel . . . 267
9.9 Conclusions . . . 268
9.10 Appendix . . . 270
9.10.1 Derivation of the flow profiles in the thin-film region for the planar configuration . . . 270
9.10.2 Derivation of the interface profile equation for the planar configuration 270
9.10.3 Derivation of the droplet velocity model for the planar configuration . . 271
9.10.4 Derivation of the critical uniform film thickness for the appearance of the recirculation regions . . . 272
9.10.5 Fitting laws for the model coefficients . . . 272
9.10.6 Additional results . . . 273

9.10.7 Pressure corrections due to nonparallel flow 273

10 Bubbles and droplets in polygonal microchannels **279**
10.1 Introduction 279
10.2 Confined droplets 280
10.3 Unconfined bubbles 282
10.4 Conclusions and perspectives 287

11 Conclusions and perspectives **289**

Bibliography **304**

Curriculum Vitae **333**

1 Introduction

1.1 Fluid dynamics of thin liquid films

1.1.1 Motivation

Thin-film flows are ubiquitous in nature as well as in everyday's life and are of undeniable interest to scientific and industrial communities. Geophysical examples are lava flows on volcanoes (see Fig. 1.1(b)), landslides and snow avalanches in the mountains (Ancey, 2001*a*,*b*), and water films on cave ceilings (Short, 2006). The deposits of lava flows are an indicator of the past activity of a volcano and provide clues to possible future eruptions (Huppert, Shepherd, Sigurdsson & Sparks, 1982; Takagi, 2010), whereas cave environments are a repository of climate records through the precipitation of calcium carbonate on the rock (Camporeale, 2015). In our body, the pulmonary airways are protected by a liquid lining (Grotberg, 1994) and so do our eyes, where the thin film is spread when we blink (Braun, Usha, McFadden, Driscoll, Cook & King-Smith, 2012; Bhamla, Giacomin, Balemans & Fuller, 2014). Unconsciously, we are often dealing with thin films in our daily lives. We are used to spread sauce on food (Stone, 2010), to wait some time for the last drop of oil to come out of the bottle (Takagi, 2010), to observe droplets of water vapor forming under the kitchen lid (see Fig. 1.1(a)) or on a car window when it rains (Wilczek, Tewes, Engelnkemper, Gurevich & Thiele, 2017), to spread paints on walls (Weidner, Schwartz & Eres, 2007), see Fig. 1.1(c), or sun cream on our body when the sun shines (Seiwert, 2010), to go ice-skating when water freezes (Kietzig, Hatzikiriakos & Englezos, 2010) and to blow soap bubbles when we were kids.

Furthermore, thin films are also widespread in many industrial applications, ranging from the fabrication of ductile iron pipes used for water distribution to the spin-coating process in soft-lithography microfabrication (Scriven, 1988). Several techniques have been developed in the coating industry, including dip, roll and slot coating, to modify the chemical, optical and mechanical properties of materials (Kistler, Schweizer et al., 1997). Coating processes arise in the production of packages, lithium batteries, solar cells, adhesive tapes, flexible circuits, e-papers, liquid-crystal displays, antibacterial surfaces and in the pharmaceutical industry. As for injection, rotational and blow molding, coating flows can also be used to manufacture

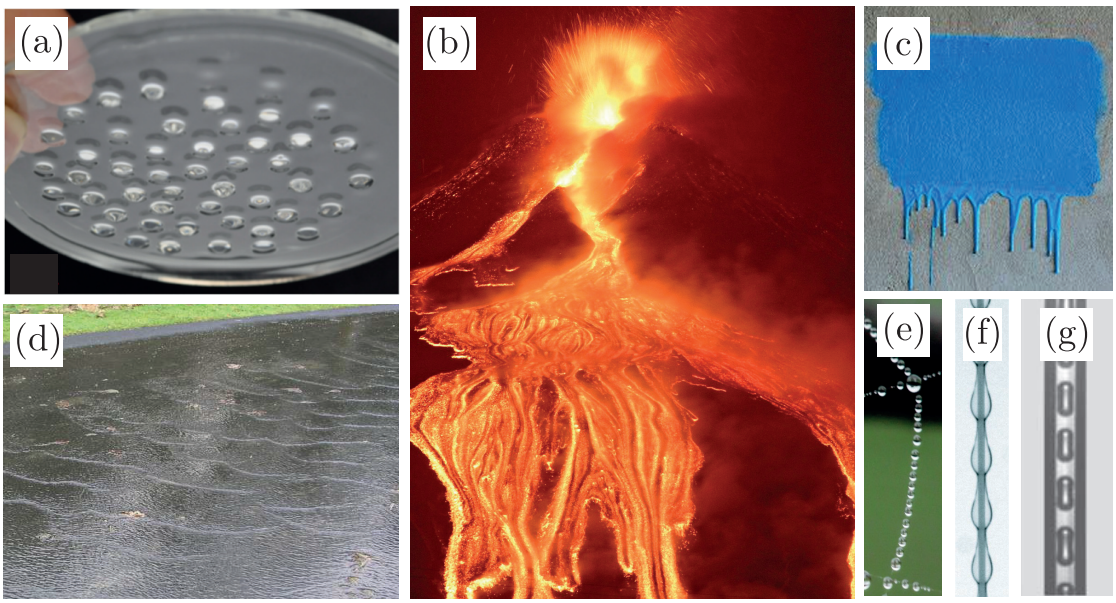

Figure 1.1 – Everyday's life patterns in thin-film flows: (a) regular pattern of droplets obtained by the Rayleigh-Taylor instability resulting in PDMS lenses (Brun, 2016), (b) lava fingers from Etna's eruption in 2012 (taken from http://dailymail.co.uk), (c) paint fingers on a wall, (d) Kapitza waves in the flow down an incline during a rainy day (taken from Andrew Fowler webpage http://people.maths.ox.ac.uk/fowler), (e) water droplets on a spider silk (taken from https://pxhere.com), (f) droplets on a fiber (taken from Duprat et al. (2007)) and (g) bubbles forming in the inner-side of a cylindrical tube resulting from a Rayleigh-Plateau instability (taken from Duclaux et al. (2006)).

thin materials, in a very similar way to the fabrication of hollow chocolate eggs (Lee, Brun, Marthelot, Balestra, Gallaire & Reis, 2016*a*).

Thin-film-coating flows present a fluid interface[1] which is free to deform. Surface-tension-induced forces become more and more crucial when the scale of the problem is decreased and volume forces, like gravity, become negligible compared to surface forces (Stone, 2010). This is precisely the case in microfluidic devices as the ones shown in Fig. 1.2, where the scale is less than a millimeter (Stone, Stroock & Ajdari, 2004). The interest of the scientific community in the study of fluid interfaces in viscous flows has considerably increased in the last two decades (Stone et al., 2004; Günther & Jensen, 2006), largely driven by the advent of Lab-on-a-Chip devices (Köhler & Cahill, 2014). The key for success of these microfluidic tools is the fluid compartmentalization, allowing the miniaturization and manipulation of small liquid portions at high-throughput rates with a limited number of necessary controls. Reduced liquid quantities of often expensive or dangerous substances, their ordered transport in a contamination-free environment and the reproducibility of experiments in individual reactors make them very suitable for biological and chemical applications. The capability of handling

[1] As *fluid interface* we denote an interface between a liquid and a gas or between two liquids.

controlled sub-microliter volumes of liquids is also relevant in other fields as material science, pharmaceutical and food industries (Baroud, Gallaire & Dangla, 2010; Rodríguez-Rodríguez, Sevilla, Martínez-Bazán & Gordillo, 2015), as well as in industrial processes (Abadie, Aubin, Legendre & Xuereb, 2012) and in micro-scale heat and mass transfer equipments (Leung, Gupta, Fletcher & Haynes, 2011; Warnier, De Croon, Rebrov & Schouten, 2010; Mikaelian, Haut & Scheid, 2015). Yet, the correct design of these microfluidic devices strongly relies on the

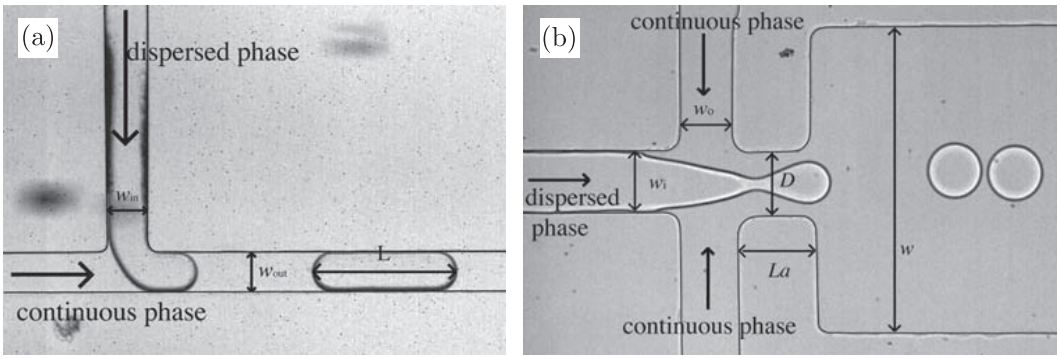

Figure 1.2 – Example of multiphase flows in a microfluidic device: (a) droplet production in a T-junction where the dispersed phase and the carrier phase meet at 90 degrees in a T-shaped junction, (b) droplet production in a flow-focusing device where the dispersed phase is squeezed by two counter-streaming flows of the carrier phase, forcing drops to detach. Images taken from Baroud et al. (2010).

correct modeling of the dynamics of droplets and bubbles in the microchannels. Unfortunately, a simple question as the velocity of a droplet in a straight channel is still an open challenge. When bubbles or droplets are confined by the walls of the microchannels, thin films similar to the ones of coating flows form between the fluid interface and the walls (see for example Fig. 1.2(a)). Despite the fact that these lubricating layers are not necessarily visible at the microscope, they play a crucial role in the dynamics of confined bubbles and droplets in microchannels.

As can be seen in Fig. 1.1, the thickness of thin viscous films is not always constant in space and well defined patterns occur. An array of droplets forms when the liquid film coats the underneath of a substrate (Fermigier, Limat, Wesfreid, Boudinet & Quilliet, 1992), see Fig. 1.1(a), as in a traditional Turkish bath or in limestone caves, where this pattern eventually results in the formation of stalactites (Short, Baygents, Beck, Stone, Toomey & Goldstein, 2005*a*). 'Finger'-like patterns occur when spreading a film on a vertical wall (Eres, Schwartz & Roy, 2000), see Fig. 1.1(c), when drinking a glass of wine (Thomson, 1855), or when wax flows on the candle sides. On rainy days, 'wave'-like patterns can be observed on the thin water flow on an inclined street (Kapitza & Kapitza, 1949), see Fig. 1.1(d), and isolated water droplets can be seen on spider silks (Carroll, 1976), similar to the droplets obtained when opening a faucet (Eggers & Villermaux, 2008), see Fig. 1.1(e-g). In Lab-on-a-Chip devices, the thin film separating confined bubbles and droplets from the microchannel walls is nonuniform in thickness as well (Burgess & Foster, 1990).

Patterns are ubiquitous in nature where they are found across length scales and material properties. Examples range from the columnar jointing in Giant's Causeway to the dendritic structure of snowflakes, suggesting the existence of robust mechanisms underpinning the genesis of such patterns. The question as to how patterns are formed is in fact at the crossroad of several fields, as recognized a century ago, when Thompson published the pioneering book *On growth and form* in 1917. He unravelled some of the generic principles at work in shaping living structures, *e.g.* the role played by surface tension in promoting area-minimizing surfaces and identified the link between growth and morphology, a process later formalized and coined *morphodynamics*.

In the context of thin-film flows, the above mentioned patterns mainly result from hydrodynamic instabilities driven by gravity, surface tension and inertia (Craster & Matar, 2009). Their correct understanding and prediction is of paramount importance for a wide range of technical applications. For instance, irregularities in the coating thickness could result in inadequate optical properties and in the buckling of a thin shell way below the critical load when the defective structure is obtained by the curing of a thin-film flow (Lee, Jiménez, Marthelot, Hutchinson & Reis, 2016*b*; Jiménez, Marthelot, Lee, Hutchinson & Reis, 2017). Nevertheless, when carefully controlled, these thin-film instabilities could also be harnessed to shape materials (Gallaire & Brun, 2017). As an example, soft lenses could be easily produced by the droplets forming under a planar substrate (see Fig. 1.1(a)) (Brun, 2016). Other kind of hydrodynamic instabilities have already been used successfully for different applications. For example, the instability of a thin gaseous ligament in a fluid has been employed to generate monodisperse bubbles in microchannels (Gañán-Calvo & Gordillo, 2001), whereas the coiling instability of a viscous thread (Brun, 2017) has been exploited to give the peculiar shape to the British ice-cream product 'Viennetta'. In the context of mechanical instabilities, the nonlinear behavior of slender structures in their postbuckling regime allows for the definition of novel functional mechanisms (Reis, 2015).

Desirable or not, the pattern formation in thin liquid films deserves deeper investigations. Despite the fact that these flows have already been the subject of several studies, the latter have been mainly focused on simple geometries. The aim of this thesis is to extend these analyses to flows on curved substrates and in three-dimensional geometries, where the dynamics is intrinsically time and space dependent and more sophisticated approaches have to be employed. Before describing the different hydrodynamic instabilities and the problems considered in the present work, we derive the general governing equation for the dynamics of thin-film flows.

1.1.2 The lubrication equation

All the liquid[2] films that we have seen in the previous examples are characterized by a small thickness[3] compared to the characteristic length of the streamwise, or spanwise, variations. Denoting by H_i^* the initial average film thickness and by λ^* the characteristic length of the streamwise, or spanwise, variations of the film thickness (see Fig. 1.3), the film aspect ratio can be defined as

$$\epsilon = \frac{H_i^*}{\lambda^*} \ll 1 \tag{1.1}$$

which is also referred to as the 'long-wavelength assumption' (Oron, Davis & Bankoff, 1997).

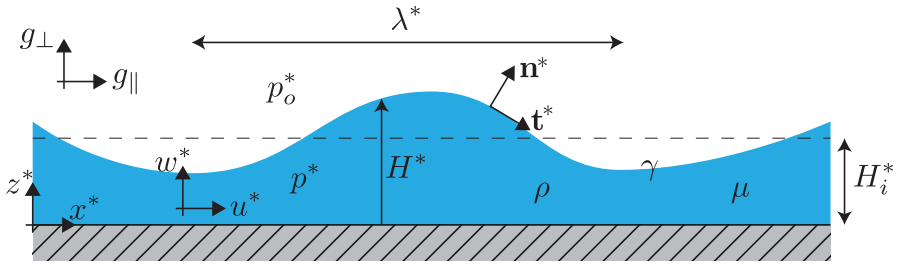

Figure 1.3 – Thin film of initial average thickness H_i^*, density ρ, dynamic viscosity μ and surface tension γ flowing in the two-dimensional plane (x^*, z^*) under the action of the gravitational field $\mathbf{g} = (g_\parallel, g_\perp)^T$. The velocity field is $\mathbf{u}^* = (u^*, w^*)^T$ and the pressure is p^*. p_o^* is the constant outer pressure. The interface profile is given by $z^* = H^*(x^*, t^*)$ and the characteristic length in the streamwise direction is λ^*. The unit normal pointing outward to the interface is $\mathbf{n}^*$ and the unit tangent is $\mathbf{t}^*$.

Given their small aspect ratio, the dynamics of thin liquid films is well described by a lubrication equation, which allows one to reduce the dimensionality of the problem by one unit. In the following, we present a general derivation of the lubrication equation for a two-dimensional thin-film flow, taking inspiration from Oron et al. (1997). For more details on the lubrication theory we refer to the exhaustive books by Leal (2007) and Ockendon & Ockendon (1995). A derivation of more elaborate models including inertial and thermal effects can be found in the comprehensive book by Kalliadasis, Ruyer-Quil, Scheid & Velarde (2011), whereas the extension to large interface slopes is described in Snoeijer (2006). Furthermore, non-Newtonian fluids can also be taken into account (Balmforth, Craster, Rust & Sassi, 2006; Ancey, 2007). In this thesis, we will only consider thin-film flows with one fluid interface, but lubrication flows also occur between two nondeformable solid substrates (Santos, 2011), as for the fluid bearings studied by Reynolds (1886), which reduce the friction between moving components.

Let us consider here a Newtonian incompressible fluid of density ρ, dynamic viscosity μ

[2] Since the focus of this thesis are *liquid* films, the adjective is often omitted.
[3] The thickness of the film is sufficiently large for the continuous approach to hold.

and constant surface tension γ under the action of the gravitational field $\mathbf{g}$ (see Fig. 1.3). We assume that the outer fluid has a negligible viscosity and density, and is at constant pressure p_o^*. The velocity field in the two-dimensional Cartesian coordinate system (x^*, z^*) is given by $\mathbf{u}^* = (u^*, w^*)^T$, where u^*, resp. w^*, is the velocity component parallel, resp. orthogonal, to the substrate and the pressure field is p^* [4].

The two-dimensional Navier-Stokes equations for an incompressible Newtonian fluid are

$$\rho\left(u^*_{t^*} + u^* u^*_{x^*} + w^* u^*_{z^*}\right) = -p^*_{x^*} + \mu\left(u^*_{x^*x^*} + u^*_{z^*z^*}\right) + \rho g_\parallel \tag{1.2}$$

$$\rho\left(w^*_{t^*} + u^* w^*_{x^*} + w^* w^*_{z^*}\right) = -p^*_{z^*} + \mu\left(w^*_{x^*x^*} + w^*_{z^*z^*}\right) + \rho g_\perp \tag{1.3}$$

where subscripts denote partial derivatives and $g_\parallel$, resp. $g_\perp$, are the parallel, resp. orthogonal, components of gravity with respect to the substrate. The gravitational body force can be seen as the gradient of the conservative potential $\Phi^* = -\rho(g_\parallel x^* + g_\perp z^*)$ (Oron et al., 1997). The continuity equation reads

$$u^*_{x^*} + w^*_{z^*} = 0. \tag{1.4}$$

The velocity at the wall has to satisfy the no-slip $u^* = 0$ and the no-penetration $w^* = 0$ conditions, whereas at the free surface $z^* = H^*(x^*, t^*)$ one has the kinematic boundary condition

$$w^* - u^* H^*_{x^*} = H^*_{t^*} \tag{1.5}$$

and the dynamic boundary condition

$$[[\sigma^* \mathbf{n}^*]] = -\gamma \kappa^* \mathbf{n}^*, \tag{1.6}$$

where $\sigma^* = -p^*\mathbf{I} + \mu\left[\nabla^*\mathbf{u}^* + (\nabla^*\mathbf{u}^*)^T\right]$ is the stress tensor and

$$\kappa^* = \nabla^* \cdot \mathbf{n}^* = -\frac{H^*_{x^*x^*}}{\left[1 + \left(H^*_{x^*}\right)^2\right]^{3/2}} \tag{1.7}$$

is the interface mean curvature with

$$\mathbf{n}^* = \frac{\left(-H^*_{x^*}, 1\right)^T}{\sqrt{1 + \left(H^*_{x^*}\right)^2}} \tag{1.8}$$

as unit normal outward to the interface. $[[\blacksquare]]$ denotes the difference between inner and outer quantities. Surface tension gradients resulting in Marangoni flows or other forcings at the interface are not considered here, see Oron et al. (1997) for a more general derivation.

[4] Throughout this thesis, dimensional variables are denoted by an asterisk, $\blacksquare^*$, to distinguish them from their dimensionless counterparts. The only dimensional quantities without an asterisk are the physical parameters ρ, μ, γ and g, as well as the characteristic times τ.

The governing equations can be adimensionalized using λ^*, resp. H_i^*, as characteristic length in the streamwise, resp. orthogonal, direction and U^*, resp. W^*, as characteristic velocities in these directions. From mass conservation (1.4) one has that the vertical velocity is much smaller than the horizontal one: $W^* \sim \epsilon U^*$. Furthermore, by balancing the pressure gradient, or the gravitational body force, and the viscous stresses in the streamwise direction, it can be shown that both the characteristic pressure and the gravitational potential scale as $\mu U^*/(\epsilon H_i^*)$. The dimensionless Navier-Stokes equations are

$$\epsilon Re\,(u_t + u u_x + w u_z) = -p_x + \mu\left(\epsilon^2 u_{xx} + u_{zz}\right) - \Phi_x \tag{1.9}$$

$$\epsilon^3 Re\,(w_t + u w_x + w w_z) = -p_z + \mu\left(\epsilon^4 w_{xx} + \epsilon^2 w_{zz}\right) - \Phi_z \tag{1.10}$$

where $Re = \rho H_i^* U^*/\mu$ is the Reynolds number prescribing the ratio between inertial and viscous forces. Note that the inertial term in the x-momentum equation scales as ϵRe, whereas it scales as $\epsilon^3 Re$ for the z-momentum equation. The inertial terms are thus one order ϵ higher than the dominant viscous terms. The dimensionless continuity equation reads

$$u_x + w_z = 0. \tag{1.11}$$

The boundary conditions at the wall are $u = w = 0$, whereas the kinematic boundary condition (1.5) at $z = H(x,t)$ becomes

$$w - u H_x = H_t. \tag{1.12}$$

The dynamic boundary condition (1.6) can be projected along the tangential vector $\mathbf{t}$ satisfying $\mathbf{n}\cdot\mathbf{t} = 1$, yielding, after adimensionalization and the use of the continuity equation (1.12):

$$\left(u_z + \epsilon^2 w_x\right)\left[1 - \epsilon^2 (H_x)^2\right] - 4\epsilon H_x u_x = 0. \tag{1.13}$$

The dimensionless projection of Eq. (1.6) on the normal vector reads:

$$-p\left[1 + \epsilon^2 (H_x)^2\right] + 2\epsilon^2\left\{u_x\left[\epsilon^2 (H_x)^2 - 1\right] - H_x\left(u_z + \epsilon^2 w_x\right)\right\} = \frac{\epsilon^3}{\hat{Ca}}\frac{H_{xx}}{\left[1 + \epsilon^2 (H_x)^2\right]^{3/2}} - p_o, \tag{1.14}$$

where $\hat{Ca} = \mu U^*/\gamma$ is the capillary number prescribing the ratio of viscous and surface-tension forces, and p_o is the dimensionless constant pressure of the surrounding gas. The velocity and pressure fields are expanded as perturbation series in the powers of the small film aspect ratio ϵ:

$$u = u_0 + \epsilon u_1 + \epsilon^2 u_2 + \cdots \tag{1.15}$$

$$w = w_0 + \epsilon w_1 + \epsilon^2 w_2 + \cdots \tag{1.16}$$

$$p = p_0 + \epsilon p_1 + \epsilon^2 p_2 + \cdots \tag{1.17}$$

If one takes the limit $\epsilon \to 0$, the surface-tension effects in the dynamic boundary condition (1.14) would disappear at first order. However, as we will see throughout this thesis, the

capillary pressure induced by surface tension effects is crucial and one should rather consider the capillary number $Ca = \hat{Ca}/\epsilon^3$ of order unity. This is agreement with the 'Least Degeneracy Principle' of Van Dyke (1975).

Eventually, the leading-order dimensionless momentum equations read, dropping the subscript 0:

$$0 = -p_x + \mu u_{zz} - \Phi_x \tag{1.18}$$

$$0 = -p_z - \Phi_z \tag{1.19}$$

and the continuity equation is

$$u_x + w_z = 0 \tag{1.20}$$

The boundary conditions at the wall are $u = w = 0$ and the ones at the free interface are

$$w - uH_x = H_t \tag{1.21}$$

$$u_z = 0 \tag{1.22}$$

$$-p = \frac{H_{xx}}{Ca} - p_o \tag{1.23}$$

where Eq. (1.22) is the free-shear condition and Eq. (1.23) is nothing else than Laplace law.

The pressure is given by integrating Eq. (1.19) and applying the boundary condition Eq. (1.23):

$$p(x,z) = p_o - \frac{H_{xx}}{Ca} + \underbrace{\Phi(x,H) - \Phi(x,z)}_{\Delta\Phi^H} \tag{1.24}$$

where $\Delta\Phi^H = \Phi(x,H) - \Phi(x,z)$ is the difference in the potential. Furthermore, the streamwise velocity is obtained by integrating Eq. (1.18) twice, resulting in the parabolic profile

$$u(x,z) = \left(p_x + \Phi_x\right)\left(\frac{z}{2} - H\right)z. \tag{1.25}$$

By integrating the continuity equation (1.20) and using the kinematic boundary condition (1.21), together with the Leibniz integral rule, one can write

$$H_t + Q_x = 0 \quad \text{with} \quad Q = \int_0^H u\,dz. \tag{1.26}$$

Given the velocity profile (1.25) one has $Q = -H^3(p_x + \Phi_x)/3$. Using the pressure given by Eq. (1.24), the lubrication equation eventually reads

$$H_t + \left\{ \frac{H^3}{3}\left[\frac{H_{xxx}}{Ca} - \left(\Delta\Phi^H\right)_x - \Phi_x \right] \right\}_x = 0. \tag{1.27}$$

As an example, let us consider the flow over a plane inclined with an angle θ with respect to the horizontal. In this case $g_{\parallel} = g\sin\theta$ and $g_{\perp} = -g\cos\theta$ so that the potential is $\Phi^* = -\rho g(\sin\theta x^* - \cos\theta z^*)$ and $\Delta\Phi^{*H} = \rho g\cos\theta(H^* - z^*)$. The dimensionless lubrication equation reads

$$H_t + \left[\frac{H^3}{3}\left(\underbrace{\frac{H_{xxx}}{Ca}}_{\text{I}} \underbrace{-\frac{Bo}{\epsilon^2 Ca}\cos\theta H_x}_{\text{II}} \underbrace{+\frac{Bo}{\epsilon^3 Ca}\sin\theta}_{\text{III}}\right)\right]_x = 0, \tag{1.28}$$

where $Bo = \rho g H_i^{*2}/\gamma$ is the Bond number prescribing the ratio between gravity and surface-tension forces. Term I represents the capillary pressure gradient, term II the variation of the hydrostatic pressure distribution and term III the gravity-induced drainage. Note that the relative importance of terms II and III depends on the inclination angle. For small inclinations $\theta \ll \epsilon$, the variation of the hydrostatic pressure is more important than the drainage, whereas the opposite is true when the inclination angle satisfies $\theta \gg \epsilon$. As mentioned in Sec. 1.1.1, the relative importance of gravitational and surface-tension forces depends also on the considered scale: surface-tension forces dominate at length scales below the capillary length $\ell_c^* = \sqrt{\gamma/(\rho g)}$ (de Gennes, Brochard-Wyart & Quéré, 2004).

1.1.3 Classical solutions of the lubrication equation

Using a very general formalism, we can rewrite the lubrication equation (1.28) as the following nonlinear partial differential equation

$$\boxed{H_t + \left[\frac{H^3}{3}\left(\mathscr{A} H_{xxx} - \mathscr{B} H_x + \mathscr{C}\right)\right]_x = 0} \tag{1.29}$$

with $\mathscr{A}$, $\mathscr{B}$ and $\mathscr{C}$ three coefficients which depend on the problem under consideration. Solving this type of equations has been the subject of active research in the applied mathematics community, see for instance Bertozzi (1996, 1998), Myers (1998), Bowen & Witelski (2006), Greer, Bertozzi & Sapiro (2006) and Dallaston, Tseluiko, Zheng, Fontelos & Kalliadasis (2017). In the following, we do not aim at describing this problem in an exhaustive way, but we would rather like to give a flavor of the main 'ingredients' of the lubrication equation considered in this thesis and their effects on the thin-film dynamics.

We consider a film whose initial thickness profile is described by the function

$$H(x,0) = H_0(x) = \frac{1+b}{2}\left[1 - \tanh(x\,s)\right] \quad \text{for} \quad -L/2 \le x \le L/2 \tag{1.30}$$

where b is the thickness of the thin region, s is the steepness of the profile and L is the domain length.

Capillary pressure gradient

$\mathscr{A} = 1$, $\mathscr{B} = 0$ **and** $\mathscr{C} = 0$**.** When only the capillary pressure gradient drives the flow, the lubrication equation reduces to

$$\boxed{H_t + \left(\frac{H^3}{3} H_{xxx}\right)_x = 0} \tag{1.31}$$

This equation has received great attention in the recent years with the development of miniaturization processes (see for example McGraw, Salez, Bäumchen, Raphaël & Dalnoki-Veress (2012)). It can be shown that equation (1.31) has a self-similar solution of the form H(ξ) with the self-similar variable being $\xi = x/t^{1/4}$ (Barenblatt, 1996) when the boundary conditions are $H_x(\pm L/2) = H_{xx}(\pm L/2) = 0$. As can be seen in Fig. 1.4, the film thickness relaxes to a smoother profile due to surface tension effects, which tend to minimize the curvature variations of the interface. The abrupt initial profile relaxes eventually to the one of a sessile drop on a prewetted substrate (Bergemann, Juel & Heil, 2018).

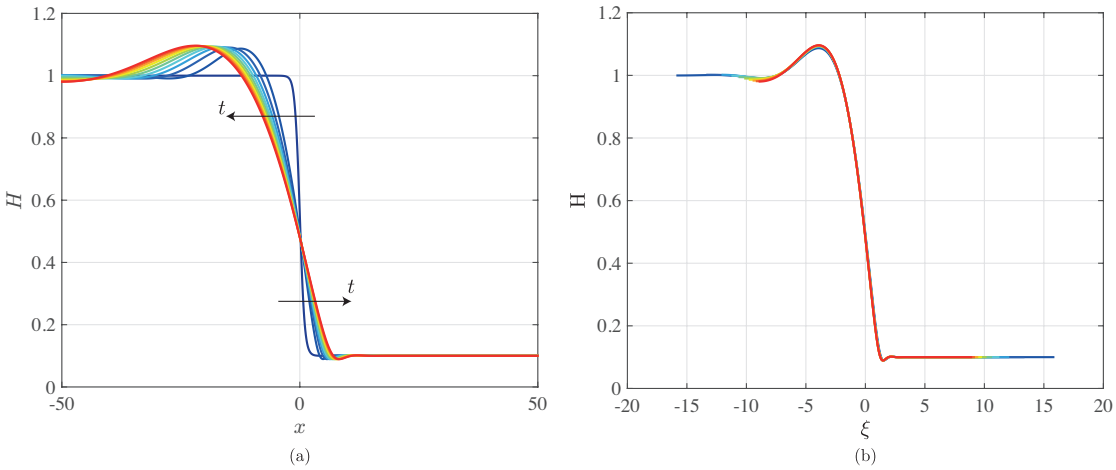

Figure 1.4 – Film thickness for a capillary relaxation in physical variables (a) and in self-similar variables (b). $b = 0.1$, $s = 1$ and $L = 100$. $t = 0$, 10^3, 2×10^3, ..., 10^4. $\mathscr{A} = 1$, $\mathscr{B} = 0$ and $\mathscr{C} = 0$. The temporal evolution for $\mathscr{A} = -1$ goes from the red to the blue line.

McGraw et al. (2012), Backholm, Benzaquen, Salez, Raphaël & Dalnoki-Veress (2014) and Rivetti, Salez, Benzaquen, Raphaël & Bäumchen (2015) have shown experimentally that this 'capillary leveling' occurs also in viscous films at the nanometer scale and impacts the apparent contact line at the moving boundary. Very interestingly, Benzaquen, Salez & Raphaël (2013) and Benzaquen, Fowler, Jubin, Salez, Dalnoki-Veress & Raphaël (2014) have demonstrated that the film profile tends to a universal self-similar attractor which is directly given by the Green's function of the linearized lubrication equation

$$H_t + \frac{1}{3} H_{xxxx} = 0. \tag{1.32}$$

$\mathscr{A} = -1$, $\mathscr{B} = 0$ **and** $\mathscr{C} = 0$**.** The problem with a negative coefficient for the capillary pressure gradient is equivalent to the previous one under the reflection of time $t \to -t$. Therefore, the film profile evolves in a way to increase the curvature variations (see Fig. 1.4(a), time evolves from the red to the blue line). Note that this problem might be relevant if one knows the final film-thickness profile and aims at knowing the original initial condition. In this case, the equation can be solved until the initial time, but integrating further the equation would result in the formation of singularities. As pointed out by Trefethen, negative diffusion problems are common in image enhancement where degraded images have to be made sharp.

Variation of hydrostatic pressure

$\mathscr{A} = 0$, $\mathscr{B} = 1$ **and** $\mathscr{C} = 0$**.** When the flow is driven by a variation of hydrostatic pressure, the lubrication equation becomes

$$\boxed{H_t - \left(\frac{H^3}{3} H_x\right)_x = 0} \tag{1.33}$$

Under the boundary conditions $H(x_N) = b$ and $\int_{-L/2}^{x_N} H dx = M$ with M a positive real constant

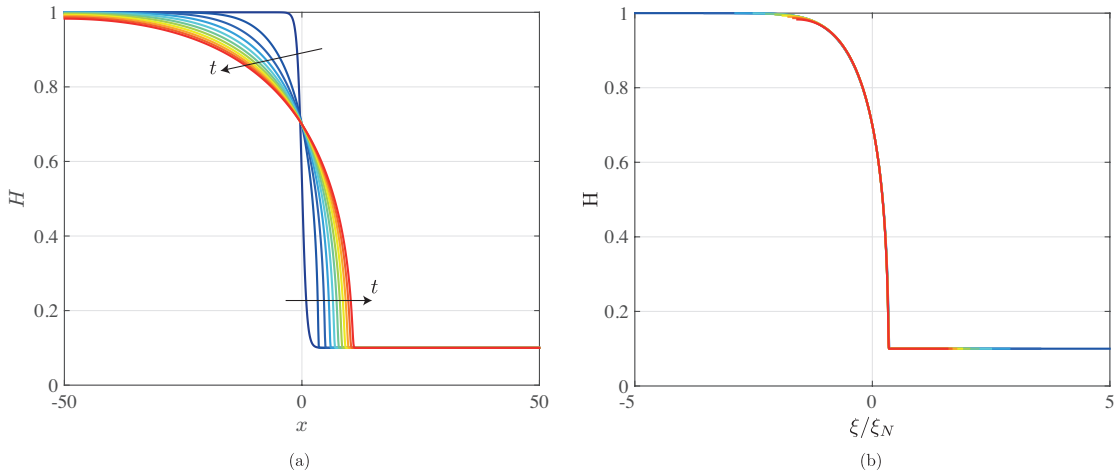

Figure 1.5 – Film thickness for a gravity current in physical variables (a) and in self-similar variables (b). $b = 0.1$, $s = 1$ and $L = 100$. $t = 0$, 10^2, 2×10^2, ..., 10^3. $\mathscr{A} = 0$, $\mathscr{B} = 1$ and $\mathscr{C} = 0$. The temporal evolution for $\mathscr{B} = -1$ goes from the red to the blue line.

and x_N the front location, it can be shown that the film thickness satisfies the self-similar solution $\mathrm{H}(\xi/\xi_N) = \xi_N^{-2/3} t^{1/5} H(x,t)$ where $\xi = x/t^{1/5}$ is the self-similar variable and $\xi_N = x_N/t^{1/5}$ (Huppert, 1982*b*). The front location x_N evolves as $x_N \sim t^{1/2}$. This flow, also known as 'gravity current' (Huppert, 1982*b*), is responsible for the spreading of fluids on horizontal substrates under the action of gravity (see Fig. 1.5).

$\mathscr{A} = 0$, $\mathscr{B} = -1$ and $\mathscr{C} = 0$. When the coefficient in front of the variation of hydrostatic pressure has an opposite sign the problem is unstable. The temporal evolution is the opposite of the one in Fig. 1.5. The variation of hydrostatic pressure acts as a negative diffusion and sharpens the film profile (Moffatt, 1998). If only the destabilizing variation of hydrostatic pressure is considered, an initially smooth profile eventually results in a singular behavior, as can be seen in Fig. 1.6. As we will see throughout this thesis, the destabilizing effect of the variation of hydrostatic pressure is the motor of the Rayleigh-Taylor instability.

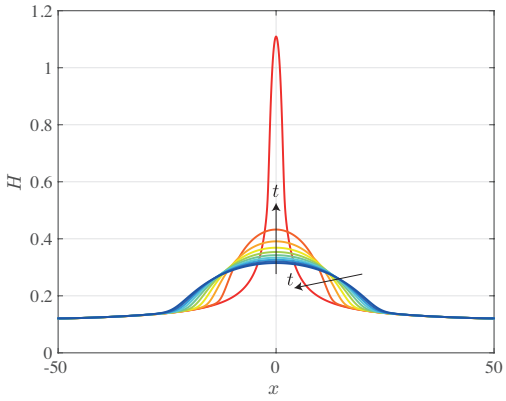

Figure 1.6 – Example of negative diffusion when only the destabilizing variation of hydrostatic pressure is considered, inspired by Moffatt (1998). $t = 0, 10^3, 2\times10^3, ..., 10^4$. $\mathscr{A} = 0$, $\mathscr{B} = -1$ and $\mathscr{C} = 0$. Note that in order to better highlight the singular behavior we considered a different initial condition than Eq. (1.30).

Advection

$\mathscr{A} = 0$, $\mathscr{B} = 0$ and $\mathscr{C} = -1$. When the film-thickness profile is advected by, for instance, the gravity component parallel to the substrate, the lubrication equation reads

$$\boxed{H_t - \left(\frac{H^3}{3}\right)_x = 0} \tag{1.34}$$

It is known that depending on the initial condition such an equation can result in either the formation of expansion or shock waves and special numerical techniques have to be employed (LeVeque, 1990). Yet, the solution is constant along the characteristics defined by $\xi = x - \mathscr{V} t$, where $\mathscr{V} = dQ/dH = -H^2$ is the characteristic's velocity. In Fig. 1.7 we illustrate the solution for an expansion wave. The coefficient $\mathscr{C} = -1$ can be seen as a gravity component parallel to the substrate pointing in the negative x-direction, which induces a drainage towards negative x values. Due to the dependence of the flux Q in $-H^3/3$, which is equivalent to the dependence of characteristic's velocity $\mathscr{V} = -H^2$, the thicker the film, the stronger the flux, explaining the formation of an expansion wave smoothening out the initially sharp profile.

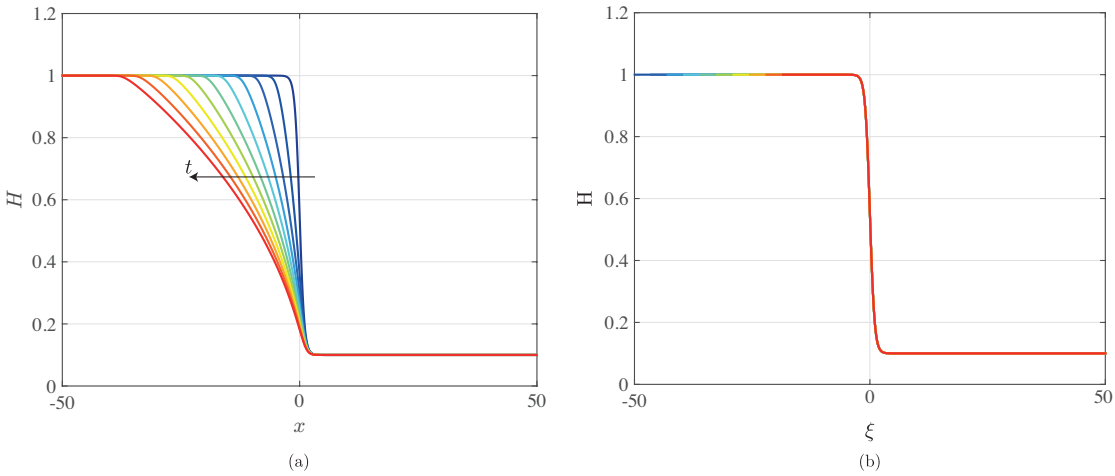

Figure 1.7 – Film thickness for an expansion wave in physical variables (a) and along the characteristic ξ (b). $b = 0.1$, $s = 1$ and $L = 100$. $t = 0, 3.5, 7, ..., 35$. $\mathscr{A} = 0$, $\mathscr{B} = 0$ and $\mathscr{C} = -1$. The temporal evolution for $\mathscr{C} = 1$ goes from the red to the blue line.

$\mathscr{A} = 0$, $\mathscr{B} = 0$ and $\mathscr{C} = 1$. On the other hand, when the gravity component points toward the positive x direction, which corresponds to a film-thickness evolution going from the red to the blue line in Fig. 1.7, a shock wave form. The thicker region for low x-values is advected faster than the thinner one at greater x-values, eventually resulting in a shock.

For the flows considered in this thesis, the regularizing capillary pressure gradient will be the key stabilizing term preventing the formation of singular behaviors like shocks. However, the drawback of considering at least two terms of the lubrication equation is the loss of self-similar solutions. Due to this reason, approximate asymptotic solutions or numerical solutions will be sought in the following chapters.

In the present section we only considered the one-dimensional lubrication equation for time-dependent thin-film flows for reasons of space. Nevertheless, in the thesis we will also employ two-dimensional lubrication equations to describe three-dimensional thin-film problems. We will consider both time-dependent problems where the dynamics depends on the initial condition and steady problems. The former are, for instance, obtained when pouring a fixed amount of fluid on a substrate and studying its evolution, whereas the latter occur when the thin-film flow is fed by a continuous constant flow rate. Note that, in some cases, time-dependent problems can be considered as quasi-steady when changing the reference frame, as we will see for the fingering instability in Sec. 1.2.2 or for the motion of bubbles in capillaries (see Sec. 1.3.1). For the steady problems, the film-thickness profile is solely dictated by the balance of the three terms of the stationary version of Eq. (1.28), namely the capillary pressure gradient, the variation of the hydrostatic pressure and the advection, subjected to the boundary conditions.

1.2 Thin-film instabilities

Gravity, surface tension and inertia lead to four major types of instabilities, depending on the geometry and the orientation of gravity with respect to the surface to be coated: Rayleigh-Taylor instabilities underneath surfaces, capillary-ridge instabilities in driven contact lines, inertia-driven Kapitza instabilities, and surface-tension-driven Rayleigh-Plateau instabilities.

1.2.1 Instability analysis

In many classic linear stability calculations for space- and time-independent base states one considers the Fourier decomposition of the disturbances, where each mode is $h = \exp[\mathrm{i}(kx - \omega t)] + c.c.$ with $k \in \mathbb{R}$ and $\omega \in \mathbb{C}$ for a temporal stability analysis. This so-called 'normal-mode ansatz' allows the transformation of the linear problem into an eigenvalue problem. The growth rate of the linear disturbances is directly given by $\omega_i = \Im(\omega)$. When $\omega_i > 0$ (resp. $\omega_i < 0$) the system is asymptotically unstable (resp. stable). We denote as *unconditional* an instability that does not present a critical threshold value in the governing parameters in order to appear, in contrast to *conditional* stabilities, which occur only if the critical parameter is overcome.

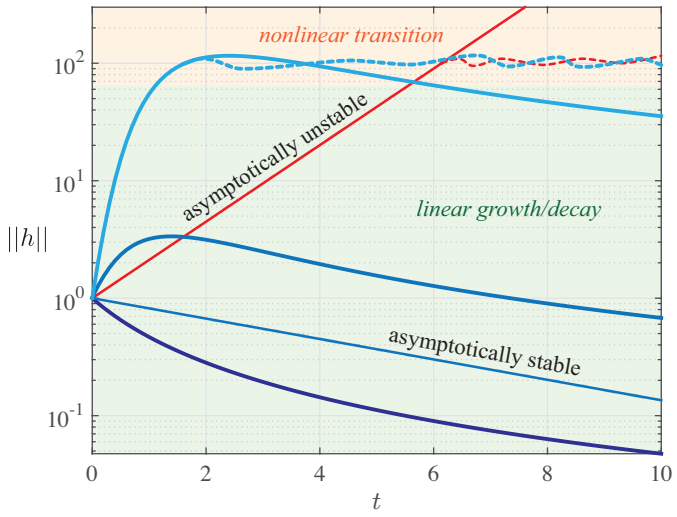

Figure 1.8 – Sketch of the possible disturbance norm evolutions: linearly asymptotically stable (blue lines), linearly asymptotically unstable (red line), transient growth (thick lines), exponential growth/decay (thin lines), linear growth/decay (solid lines) and nonlinear evolution (dashed lines). Three transient growth curves with different gains are shown as well as an exponentially growing and an exponentially decaying mode. The region where the dynamics is linear is highlighted by a green area, whereas the region where nonlinear effects matter is highlighted in orange.

However, this approach failed in providing the correct understanding of the mechanism yielding the transition to turbulence in several wall-bounded shear flows (Schmid, 2007). In fact, the spectrum of the linear problem only indicates on the long time fate of the disturbances in the limit $t \to \infty$ (see thin solid lines in Fig. 1.8). When the linear operator governing the

dynamics of the disturbances is non-normal, meaning that its eigenvectors are nonorthogonal, the system can achieve a transient growth of the initial condition, or the incoming noise, at short times, and this even if all eigenvalues are negative (see thick solid lines in Fig. 1.8). The disturbance gain will eventually tend to zero if the system is asymptotically stable, but the amplification attained at short time might be sufficiently large to trigger nonlinear effects (see dashed lines in Fig. 1.8), which results in the by-pass transition to turbulence in shear flows (Chomaz, 2005), or, in the present context, to the formation of thick droplets and fingers. A nonmodal transient growth analysis not only allows for the investigation of the perturbation evolutions at short times, but it also makes possible to consider time dependent flows, for which modal analyses cannot be readily employed (Schmid, 2007).

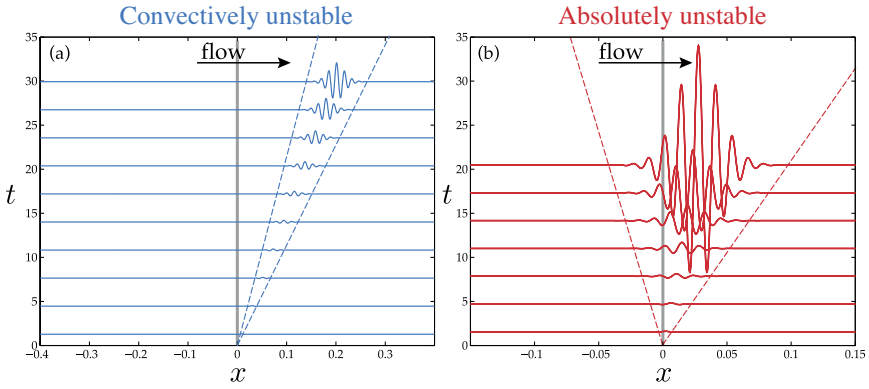

Figure 1.9 – Sketch of the impulse response for a convectively (a) and absolutely unstable (b) flow (taken from Brun et al. (2015)).

In this thesis, linear spatio-temporal analyses will also be undertaken to characterize the stability of thin-film flows. These approaches, originally coming from the study of plasma instabilities (Briggs, 1964; Bers, 1983) have been applied to fluid-dynamical instabilities of open flows since the work of Huerre & Monkewitz (1985). The nature of a given flow depends on the large-time asymptotic behavior of the linear impulse response. The flow is *convectively* unstable if the amplified disturbances move away from the source, conversely, the flow is *absolutely* unstable when amplified perturbations invade the entire flow domain[5]. Convectively unstable flows are denoted as *amplificators*, whereas absolutely unstable flows as *oscillators*. In contrast to the temporal stability problem, the absolute/convective nature of the instability is determined by applying the Briggs-Bers zero-group velocity criterion to the dispersion relation for fully complex (k,ω) pairs. In order to determine the transition from convective to absolute instability, it is sufficient to detect the occurrence of saddle points in the characteristics of spatio-temporal instability waves of zero group velocity. The absolute wavenumber is denoted as k_0 and the absolute growth rate is defined by $\omega_{0,i} = \omega_i(k_0)$. When $\omega_{0,i} < 0$, the flow is convectively unstable and conversely, it is absolutely unstable when $\omega_{0,i} > 0$. In spatially developing flows, if a sufficiently large pocket of absolutely instability is present close to the

[5]This description of absolute/convective flows has been largely inspired by the one of Brun et al. (2015).

inlet of the domain, the flow will be *globally* unstable and the frequency will correspond to the absolute one (Huerre & Monkewitz, 1990; Chomaz, 2005). The discrimination between absolutely and convectively unstable flows was shown to play a crucial role in accounting for the occurrence of synchronized self-sustained oscillations in a variety of spatially developing shear flows, such as single phase wakes, hot jets, and counter-flow mixing layers (Huerre & Monkewitz, 1990). But it also explains, for instance, the transition from dripping to jetting in two-phase immiscible microfluidic co-axial injectors (Gordillo, Gañán-Calvo & Pérez-Saborid, 2001; Guillot, Colin, Utada & Ajdari, 2007; Utada, Fernandez-Nieves, Gordillo & Weitz, 2008), as well as the different regimes occurring in the pearl-forming instability of a film flowing down a fiber (Kalliadasis & Chang, 1994; Duprat et al., 2007) and the formation of dripping droplets from a film flowing under an inclined plate (Brun et al., 2015; Scheid, Kofman & Rohlfs, 2016).

Throughout this work we will employ the modern hydrodynamic instability approaches, as recently used to develop understanding of the transition to turbulence in shear flows (Schmid & Henningson, 2001), to help explaining the transition to disorder in this, entirely different, flow category: coating flows of thin layers of liquid. As a successful example of these approaches coming from the context of liquid films we mention the work of Bertozzi & Brenner (1997), who showed that the transient growth is responsible for the initiation of the finger instability in an asymptotically linearly stable configuration. More recently, Gallino, Zhu & Gallaire (2016) found that an asymptotically stable rising droplet forms an instability at the tail for a lower perturbation amplitude when the initial shape is close to the one obtained by the optimal transient growth analysis. Not only these nonmodal approaches are suitable for problems governed by non-normal operators, but they can also be readily applied to space and time-dependent flows, as the one considered in this thesis. Here the temporal invariance is broken by considering the flow of fixed fluid quantity, whereas the space invariance is broken by the curved substrate geometry which induces nonuniform forces in space.

1.2.2 Rayleigh-Taylor

The interface separating two fluids of different densities is subjected to the Rayleigh-Taylor instability (RTI) when the heavier fluid accelerates towards the lighter one (Rayleigh, 1882; Taylor, 1950; Sharp, 1984). In the case of an unstable stratified fluid, the upper heavier fluid sinks whereas the lower lighter one rises due to buoyancy. The dynamics is solely stabilized by surface-tension forces and viscosity. A classical description of the RTI for two semi-infinite domains can be found in Chandrasekhar (1981, chap. X). In the present thesis, we will focus on the Rayleigh-Taylor instability when a thin viscous fluid coats the underside of a substrate orthogonal to gravity (see Fig. 1.10 and Fig. 1.3(a)), as it can be easily done in the laboratory by spreading a thin layer of oil underneath of a substrate.

The dispersion relation relating the growth rate ω_i^* to the wavenumber k^* for the classic

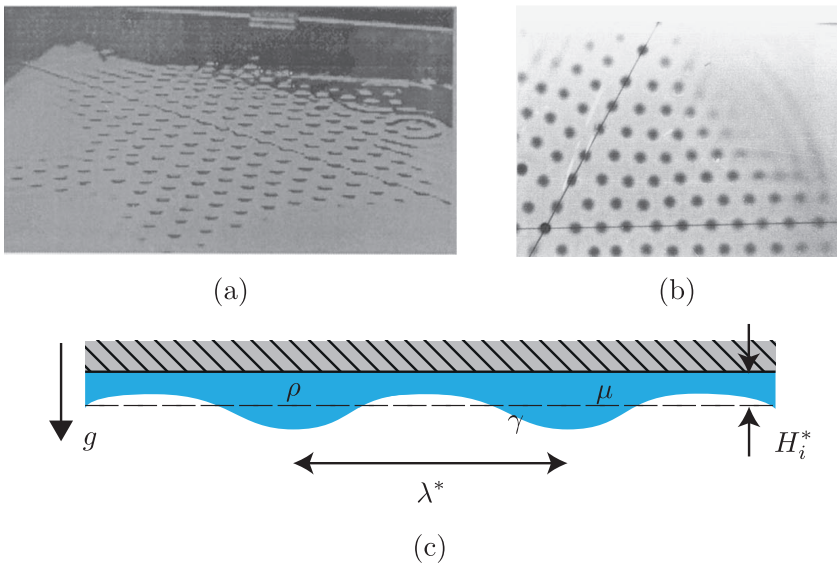

Figure 1.10 – (a,b) Rayleigh-Taylor instability pattern of a thin oil film under a planar substrate, taken from (a) Fermigier et al. (1992) and (b) Limat et al. (1992). (b) Sketch of the classical Rayleigh-Taylor problem with the relevant quantities.

two-dimensional problem is given by (Limat, 1993)

$$\omega_i^*(k^*) = \frac{\rho g H_i^{*3}}{3\mu}\left(k^{*2} - \frac{H_i^{*2}}{Bo}k^{*4}\right), \tag{1.35}$$

where H_i^* is the initial average film thickness (see Fig. 1.3), ρ is the density of the film, μ its dynamic viscosity, g the gravitational field and $Bo = \rho g H_i^{*2}/\gamma = H_i^{*2}/\ell_c^{*2}$ is the Bond number with γ being the surface tension and $\ell_c^* = \sqrt{\gamma/(\rho g)}$ the capillary length. The density and viscosity of the outer fluid are negligible (see Sec. 1.1.2). Perturbations with a wavelength $\lambda^* = 2\pi/k^*$ larger than $2\pi\ell_c^*$ are therefore unconditionally asymptotically unstable and the most amplified perturbation has a wavelength of $\lambda_0^* = 2\pi\sqrt{2}\ell_c^*$. Wavelengths smaller than $2\pi\ell_c^*$ would create too much surface energy and are therefore stable (Gallaire & Brun, 2017). Interface perturbations initially follow a linear growth, before saturating due to nonlinear effects. The liquid is eventually localized in pendent drops, which might drip if their volume is sufficiently large (Pitts, 1973; Yiantsios & Higgins, 1989).

In the three-dimensional configuration, droplets are found to arrange in well defined lattices and, in the absence of boundaries, the fastest-growing patterns have circular and hexagonal symmetries (see Fig. 1.10(a)). When the perturbations of the thin film are forced by the presence of contact lines at the boundaries, the interface first destabilizes into rolls, one-dimensional structures aligned with the boundaries and propagating into the domain (Limat et al., 1992); a two-dimensional pattern of droplet eventually results from the nonlinear interactions. Fermigier et al. (1992) have shown that the nonlinear interactions promote a hexagonal pattern while weakening the growth of rolls. Additional complexity arises as the

resulting pendent drops following the instability may pinch off or translate, collide and bounce (Limat et al., 1992; Lister, Rallison & Rees, 2010) depending on the film thickness and the initial conditions.

As discussed in Sec. 1.1.1, controlling the Rayleigh-Taylor instability is crucial for many technical applications. A variety of stabilizing techniques have been explored in recent years, including the use of heat, vibrating substrates and electrical current (e.g. Burgess, Juel, McCormick, Swift & Swinney, 2001; Lapuerta, Mancebo & Vega, 2001; Alexeev & Oron, 2007; Weidner et al., 2007; Weidner, 2012; Cimpeanu, Papageorgiou & Petropoulos, 2014). Babchin, Frenkel, Levich & Sivashinsky (1983) considered the RTI between two fluids in a Couette flow and showed that the instability saturates as a consequence of the combined effect of the convective and surface tension terms in the lubrication equation. A similar effect arises when the substrate is tilted (Oron & Rosenau, 1989; Abdelall, Abdel-Khalik, Sadowski, Shin & Yoda, 2006; Rohlfs, Pischke & Scheid, 2017). We have recently shown that dripping droplets can be avoided for sufficient inclinations, owing to the flow advection induced by the component of gravity parallel to the substrate (Brun et al., 2015). This stabilizing effect can be rationalized as a transition from an absolute to a convective instability (Brun et al., 2015; Scheid et al., 2016).

1.2.3 Fingering

When a thin film advances on a substrate driven by body or surface shear forces, such as gravity (Huppert, 1982*a*), centrifugal forces (Tanner, 1986; Melo, Joanny & Fauve, 1989; Fraysse & Homsy, 1994; Wang & Chou, 2001; Schwartz & Roy, 2004; Holloway, Habdas, Semsarillar, Burfitt & de Bruyn, 2007) or surface tension gradients (Cazabat, Heslot, Troian & Carles, 1990; Brzoska, Brochard-Wyart & Rondelez, 1992; Kataoka & Troian, 1997), the advancing front, which forms a capillary ridge in the vicinity of the moving contact line, often breaks into separate fingers (see Fig. 1.11 and Fig. 1.3(b,c)). Using energy calculations, Spaid & Homsy (1996) have shown that the fingering instability is mainly driven by how the perturbed free-surface base state responds to the body force: thicker regions travel faster than thin regions as they experience less viscous friction. As we have seen in Eq. (1.25), the film velocity scales with the square of its thickness. Therefore, spanwise film-thickness perturbations in the moving capillary ridge eventually result in the formation of fingers which advance faster and replenish from the thinner and slower regions separating them (Hocking & Miksis, 1993; Kondic, 2003).

The interest of the scientific community in driven thin-film flows has increased considerably in the last three decades, in particular after the seminal work of Huppert (1982*a*) on the viscous flow on an inclined plane. Newtonian and non-Newtonian fluids have both been considered in the literature (Fraysse & Homsy, 1994; Spaid & Homsy, 1996; de Bruyn, Habdas & Kim, 2002; Balmforth, Ghadge & Myers, 2007). The resulting nonlinear lubrication equation was first solved numerically by Schwartz (1989), showing the fingers' formation in a gravity-driven flow.

As can be seen in Fig. 1.11(b), the film thickness presents two regions. Far away from the moving front the film thickness is rather constant and its value is H_N^*, whereas a capillary ridge

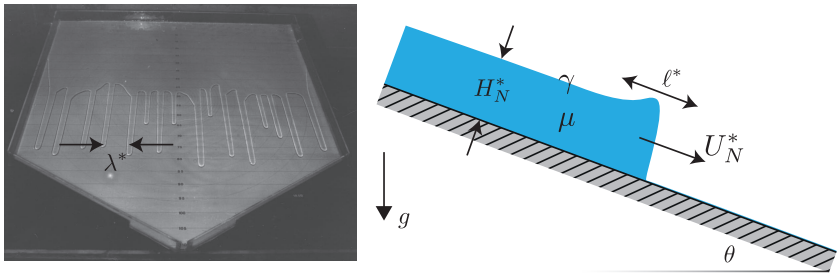

(a) (b)

Figure 1.11 – (a) Fingering instability of a thin film flowing on an inclined plane (taken from Huppert (1982*a*)). (b) Sketch of the classical fingering-instability problem with the relevant quantities.

forms close to the contact line. In the former region, also referred as *outer* region, body or surface-shear stresses balance viscous stresses, whereas in the latter region, also denoted as *inner* region, the capillary pressure gradient becomes important due to the large curvature variations in the film thickness, which goes from a small value close to the contact line[6] to the value H_N^* in the outer region.

Troian, Herbolzheimer, Safran & Joanny (1989) have shown that the linearly most amplified spanwise wavelength scales as $\lambda^* \simeq 2\pi 2\ell^*$, where $\ell^* = H_N^*(3Ca)^{-1/3}$ is the characteristic length of the ridge, with $Ca = \mu U_N^*/\gamma$ being the capillary number defined with the front advancing velocity U_N^* (Spaid & Homsy, 1996), which, for the flow over an inclined plane, varies with the inclination angle as $\sin\theta$. Brenner (1993), after a series of scaling arguments, has found that the approximated growth rate for the fingering instability can be written as

$$\omega_i^*(k^*) = c_1\left(c_2 k^{*2} - k^{*4}\right) \tag{1.36}$$

where the coefficients c_1 and c_2 depend on the capillary number Ca, on the thickness H_N^* and on the inclination angle θ for c_2 (Gallaire & Brun, 2017). In a similar way as for the Rayleigh-Taylor instability, the variations in the spanwise curvature of the free surface are responsible for the determination of the cutoff wavenumber (Spaid & Homsy, 1996). Following the linear stability analysis, fingers form only if the inclination angle θ is sufficiently large.

However, it is important to stress that a viscous flow over an inclined plane might form fingers at inclination angles θ which are smaller than the critical angle predicted by the modal linear stability theory. This is another example where the transition to a bifurcated state is not well captured by a modal linear stability approach. Bertozzi & Brenner (1997) have suggested that the transient growth induced by the microscopic scale perturbations at the contact line might be responsible for the formation fingers in asymptotically stable systems.

[6] A discussions on the contact line modeling can be found in Spaid & Homsy (1996), see also Chapter 6.

1.2.4 Kapitza waves

Thin liquid films flowing on inclines are prone to form another type of instability that, once saturated, results in the so-called Kapitza waves (Kapitza & Kapitza, 1949) (see Fig. 1.12 and Fig. 1.3(d)). However, despite the fact that this instability also relies on the higher flow velocity of the thick film regions, Kapitza waves form following an inertial mechanism and do not require a moving capillary ridge. Furthermore, although we often observe spanwise dependent secondary instabilities of these waves, the primary instability is purely in the streamwise direction. Note that the dispersion relation for this instability also follows the law $k^{*2} - k^{*4}$ (Charru, 2012).

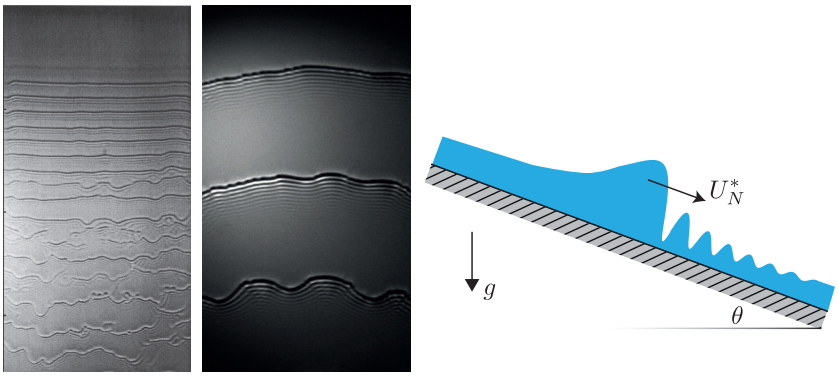

Figure 1.12 – (a,b) Secondary instabilities of Kapitza waves in a thin film flowing on an inclined plane, taken from (a) Park & Nosoko (2003) and (b) Kofman et al. (2014). (c) Sketch of the classical film-thickness profile.

In order to understand the mechanism at the origin of this instability, let us assume that the film thickness is perturbed in the streamwise direction on a wavelength much larger than its thickness, resulting in crests and troughs. When the perturbation travels downstream, the film thickness grows ahead of the crest and so does the velocity. At a more upstream location than the crest, the thickness and the velocity decrease when the crest moves away. However, inertia prevents from large accelerations and decelerations, that one would have if the velocity would solely be dictated by the film thickness in the absence of inertia (see Eq. (1.25)). Therefore, there is an accumulation of fluid at the crest, whose amplitude increases and the instability is set. Note that nonlinear effects are eventually crucial and yield the formation of solitary waves.

It has to be mentioned that the lubrication equation (1.27) is not capable of describing the formation of Kapitza waves due to the lack of inertial effects and more sophisticated models have to be considered. We refer to the book by Kalliadasis et al. (2011) for more details on the Kapitza instability and the suitable modeling equations.

1.2.5 Rayleigh-Plateau

A thin layer of fluid coating the exterior of a fiber or the interior of a tube is subjected to the Rayleigh-Plateau instability (Savart, 1833; Plateau, 1873; Rayleigh, 1878). This instability was first derived for a liquid thread that destabilizes into droplets (see Eggers & Villermaux (2008) for a review). As can be seen in Fig. 1.13 and in Fig. 1.3(e,f,g), the initially uniform film on a fiber or in a cylinder eventually destabilizes into a series of beads or drops.

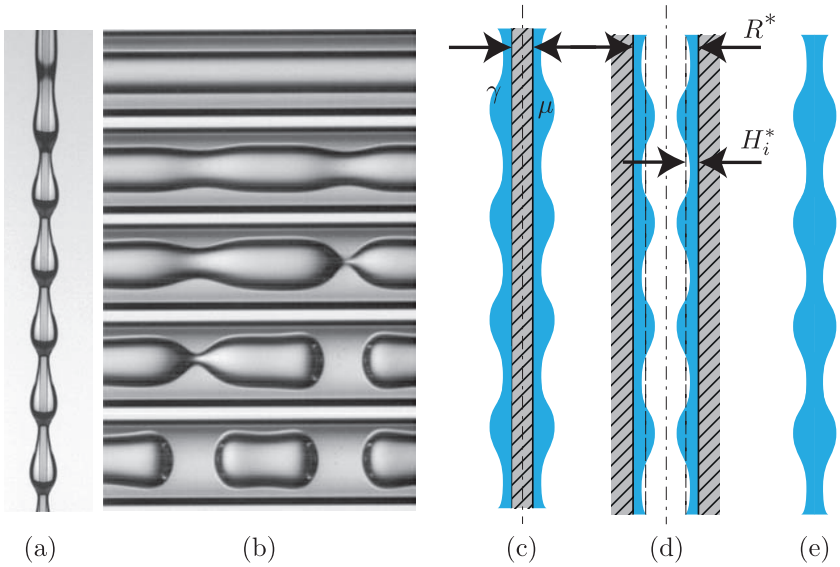

Figure 1.13 – (a) Rayleigh-Plateau instability of a thin film flowing on an fiber (taken from Duprat et al. (2009)) and (b) its dynamics in a hollow tube (taken from Duclaux et al. (2006)). (c,d) Sketches of the corresponding flow configurations with the relevant quantities. (e) Sketch of the classic Rayleigh-Plateau instability of a liquid jet.

Let us consider the classic problem of a liquid thread that is perturbed in the streamwise direction. Owing to the radial curvature, which scales as the inverse of the local diameter of the liquid thread, the Laplace law imposes a lower pressure in the thick regions compared to the thin regions. There is therefore an axial flow from the thin regions to the thicker ones and the liquid thread eventually breaks up following nonlinear effects (Eggers & Villermaux, 2008). Note that the axial curvature has a stabilizing effect, reason why a two-dimensional planar liquid sheet breaks up in a different way (Champougny, Rio, Restagno & Scheid, 2017).

The thin film on a fiber or in a hollow tube undergoes a similar surface-tension-driven transition as the liquid jet (Quéré, 1999). When the initial average thickness of the film H_i^* is much smaller than the radius R^* of the fiber or of the tube, one can derive the growth rate from a lubrication equation (Duclaux et al., 2006; Duprat et al., 2007):

$$\omega_i^*(k^*) = \frac{\gamma H_i^{*3}}{3\mu R^{*2}}\left(k^{*2} - R^{*2}k^{*4}\right). \tag{1.37}$$

We recover again a dispersion relation of the form $k^{*2} - k^{*4}$ which yields a most amplified wavelength of $\lambda_0^* = 2\pi\sqrt{2}R^*$. Perturbations with a wavelength smaller than $2\pi R^*$ are asymptotically stable. It is worth noting that the most amplified wavelength is selected by the geometry of the experiment and not by the properties of the fluid and gravity like for the Rayleigh-Taylor instability (see Sec. 1.2.2).

In the case of a thin film in a tube, if the film thickness is sufficiently large compared to the radius R^*, one eventually obtains a train of lubricated bubbles separated by liquid regions, called *plugs*. Otherwise, *lobes* and *collars* form (Hammond, 1983; Lister, Rallison, King, Cummings & Jensen, 2006).

The Rayleigh-Plateau instability of a liquid thread is the fundamental mechanism at the origin of the bubbles or droplets formations in several microfluidic devices (Rodríguez-Rodríguez et al., 2015).

1.2.6 Flow-driven morphodynamics

Fluid flows not only form beautiful patterns when flowing (see for instance Fig. 1.3), but they sometimes also leave even more fascinating patterns on their way. For example, terraces often form in fluvial systems and geothermal hot springs (see Fig. 1.14(a)), where the precipitation of calcium carbonate is enhanced at the pool dam, which represents an obstruction and yields higher fluid velocity in the thin liquid film overflowing the pool (Hammer, Dysthe, Lelu, Lund, Meakin & Jamtveit, 2008; Chan & Goldenfeld, 2007). A similar pattern occurs in rimstone dams of calcite in caves (Goldenfeld, Chan & Veysey II, 2006). Interestingly, small and large ponds and terraces do not grow equally, so that small ones are eventually inundated by the larger one and a well defined large-scale pattern forms. The characteristic length of the latter is found to depend on the initial slope of the terrain (Veysey II & Goldenfeld, 2008).

Another remarkable pattern driven by a fluid flow is the scallop pattern found on rocks, icebergs and ice cave ceilings (see Fig. 1.14(b)). Claudin, Durán & Andreotti (2017) have shown that these patterns result from a different coupling between the dissolution of the substrate under laminar or turbulent flow conditions. When the pattern reaches a sufficiently large amplitude, the mechanism reverts so that a specific pattern amplitude is selected.

Ristroph (2018) suggests that the stereotyped forms often encountered in nature may be interpreted as stable attractors of the shape dynamics. As an example, Short et al. (2005*a*) have shown that stalactites form in limestone cave following a self-similar shape, so as do icicles (see Fig. 1.14(c,d)). More precisely, Short, Baygents & Goldstein (2005*b*) have shown that stalactites result from the coupling of the thin-film flow and the deposition of the calcium carbonate, which is found to be proportional to the thickness of the film at low Reynolds numbers and explains their long and slender, often roughly conical, shape.

There are several other astonishing patterns in nature that are driven by a fluid flow and we refer to Meakin & Jamtveit (2009) for a review. If one would like to reproduce some of these

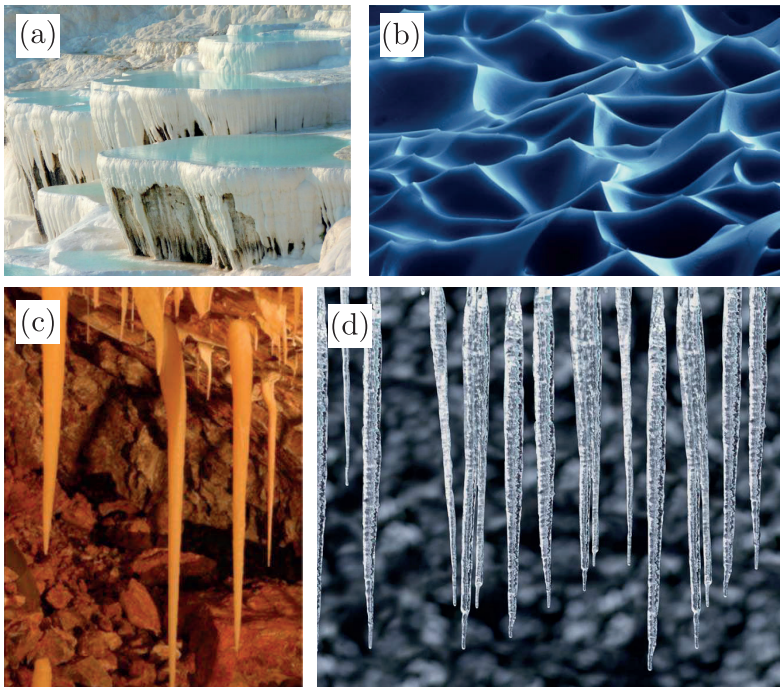

Figure 1.14 – (a) Travertine – a form of limestone deposited by mineral springs – terraces, Pamukkale, Turkey (taken from http://www.geologypage.com), (b) roof of an ice cave, Bavaria (Karsten Peters, *National Geographic*, 1999), (c) stalactites and (d) icicles (taken from (Short et al., 2006)).

precipitative patterns in the laboratory, we suggest the articles by Schmidkonz (1998) and Schmidkonz & Wittke (2006).

In order to model the morphodynamics of the patterns driven by a thin-film flow one has to derive a deposition law for the substrate growth and to modify the lubrication equation derived in Sec. 1.1.2 to account for topographical modifications of the substrate resulting from the deposition process. In the hydrodynamic literature, the effect of the substrate topography on the thin-film flow has been already investigated in the past since the work of Stillwagon & Larson (1988) (see for instance Bielarz & Kalliadasis (2003), Saprykin, Koopmans & Kalliadasis (2007), Veremieiev, Thompson, Lee & Gaskell (2011) and Slade, Veremieiev, Lee & Gaskell (2013)), but few studies have taken into account the substrate growth (Myers, Charpin & Chapman, 2002; Bertagni & Camporeale, 2017).

1.2.7 In this thesis

Part I: The effect of the substrate curvature on thin-film instabilities

Surprisingly, although the governing equations for thin films in curved geometries have been derived (Roy, Roberts & Simpson, 2002; Howell, 2003), there is very little knowledge about the effect of curvature onto the aforementioned instabilities (Krechetnikov, 2009). Yet, in many

technical applications, a thin film is flowing on a substrate with one or two nonvanishing principal curvatures.

As an example, in toroidal nuclear fusion reactors, liquid metals coating the inside are used to protect the tokamak walls from the high-temperature plasma (Kaita, Berzak, Boyle, Gray, Granstedt, Hammett, Jacobson, Jones, Kozub, Kugel et al., 2010; Majeski, Kugel, Kaita, Avasarala, Bell, Bell, Berzak, Beiersdorfer, Gerhardt, Granstedt et al., 2010). A droplet detaching and falling into the plasma could quench the process, with severe consequences. In oil-recovery applications, maximizing oil extraction is of paramount economic importance. In this context, the Rayleigh-Taylor instability in tubes might be a desirable feature, since it affects the drainage of the film, as we shall discover in this thesis. Furthermore, the growing interest in bottom up fabrication techniques, like additive manufacturing, requires an accurate control of the instability of thin films also on curved substrates. For instance, when coating a spherical object, the fingering instability has to be prevented in order to obtain a complete coverage.

For what concerns the Rayleigh-Taylor instability, we have seen in Sec. 1.2.2 that the substrate inclination has a stabilizing effect. Trinh, Kim, Hammoud, Howell, Chapman & Stone (2014) found that when the inclination of the substrate varies uniformly, *i.e.*, the solid surface has a finite curvature – such as that of a cylinder – the Rayleigh-Taylor instability is suppressed if surface-tension forces are sufficiently large. Similarly to the tilted case, gravity acts not only as the destabilizing force at the origin of the instability (through its component perpendicular to the substrate), but also as a stabilizing force originating in the progressive drainage of the film (through its component parallel to the substrate). The gravity components vary along the substrate, making the search for a transition criteria delicate.

The stabilizing effect of the substrate curvature on the Rayleigh-Taylor instability was already empirically known by the Romans, who designed calidariums with curved vaults. The latter were designed in a way to channel away the condensed water vapour and to prevent it from dripping on the backs of the bathers (Delaine, 1983).

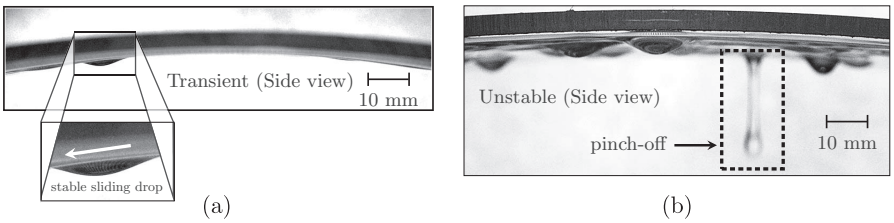

Figure 1.15 – Transient (a) and dripping (b) droplets under a curved substrate investigated by Trinh et al. (2014).

Trinh et al. (2014) performed a linear stability analysis for an axially invariant film coated on the inside of a horizontal cylinder, restricting their work to the most unstable region near the top of the cylinder. There, they showed that the only significant parameter was a modified Bond number prescribing the ratio between gravitational and surface-tension forces in this geometry. They found a critical value of order 10 for this dimensionless number. Above this

threshold, perturbations display an initial transient growth, and, below this critical value, all perturbations decay monotonically. Their experiments confirmed this trend for sufficiently small Bond numbers. For higher values the physical picture is more complex. In particular, the transition between droplets that form but do not detach from the substrate and droplets that form and pinch off (see Fig. 1.15) takes place at a significantly higher Bond numbers (of order 100), which is not accounted for by theory.

Regarding the fingering instability, Takagi & Huppert (2010) have shown experimentally that fingers also occur when the thin-film flows on the exterior of a cylinder or a sphere. However, a predictive theory for the most amplified wavelength is still lacking.

Common to all thin-film flows of fixed volume on curved substrates is their spatial and temporal dependences, which rule out any classic hydrodynamic instability theory using a normal-mode expansion. On the contrary, the nonmodal transient growth approaches with global modes used in this thesis best fit these situations, which also have the salutary feature of being capable of describing the transition scenario when the operator is non-normal and does not commute with its adjoint.

The aim of the first part of this thesis is to investigate the Rayleigh-Taylor and the fingering instabilities for the thin-film flow in cylindrical and spherical geometries (see Fig. 1.16). In particular, we shall shed light on the onset of these instabilities and their most amplified patterns. What is the precise thickness profile of the stable draining flow? When does the thin film become unstable? Is the most amplified pattern affected by the substrate geometry? What is the dominant wavelength? To answer these questions, nonmodal linear stability analyses will be complemented by nonlinear numerical simulations and experiments.

Prior to any stability analysis, one has to determine the base flow which is eventually perturbed. In **Chapter 2** we investigate the drainage of a thin film over a spherical substrate (see Fig. 1.16(a)). In the absence of a capillary ridge, no fingers occur and the flow is stable. We show that this gravity-driven flow can be employed to produce thin elastic shells upon curing of the polymer solution. The draining flow outside of the sphere is identical to the one inside provided that the Bond number is sufficiently small and no Rayleigh-Taylor instability occurs.

To better understand the stabilizing effect of the substrate curvature on the onset of the Rayleigh-Taylor instability, we extend in **Chapter 3** the study of Trinh et al. (2014) for the flow in a horizontal cylinder by performing an optimal transient growth analysis over the entire cross-section. We consider also nonlinear effects for the transition from transient to dripping droplets at larger Bond numbers. The study of the most amplified Rayleigh-Taylor instability pattern of a thin film inside a horizontal cylinder is the subject of **Chapter 4**, see Fig. 1.16(b).

With the knowledge gained by the study of the Rayleigh-Taylor instability in a cylindrical geometry, we go back to the spherical geometry and show in **Chapter 5** why a thin film coating the interior of a sphere (see Fig. 1.16(c)) is more stable than the one in a cylinder of same radius, allowing for the robust fabrication of elastic shells discussed in **Chapter 2**. The most

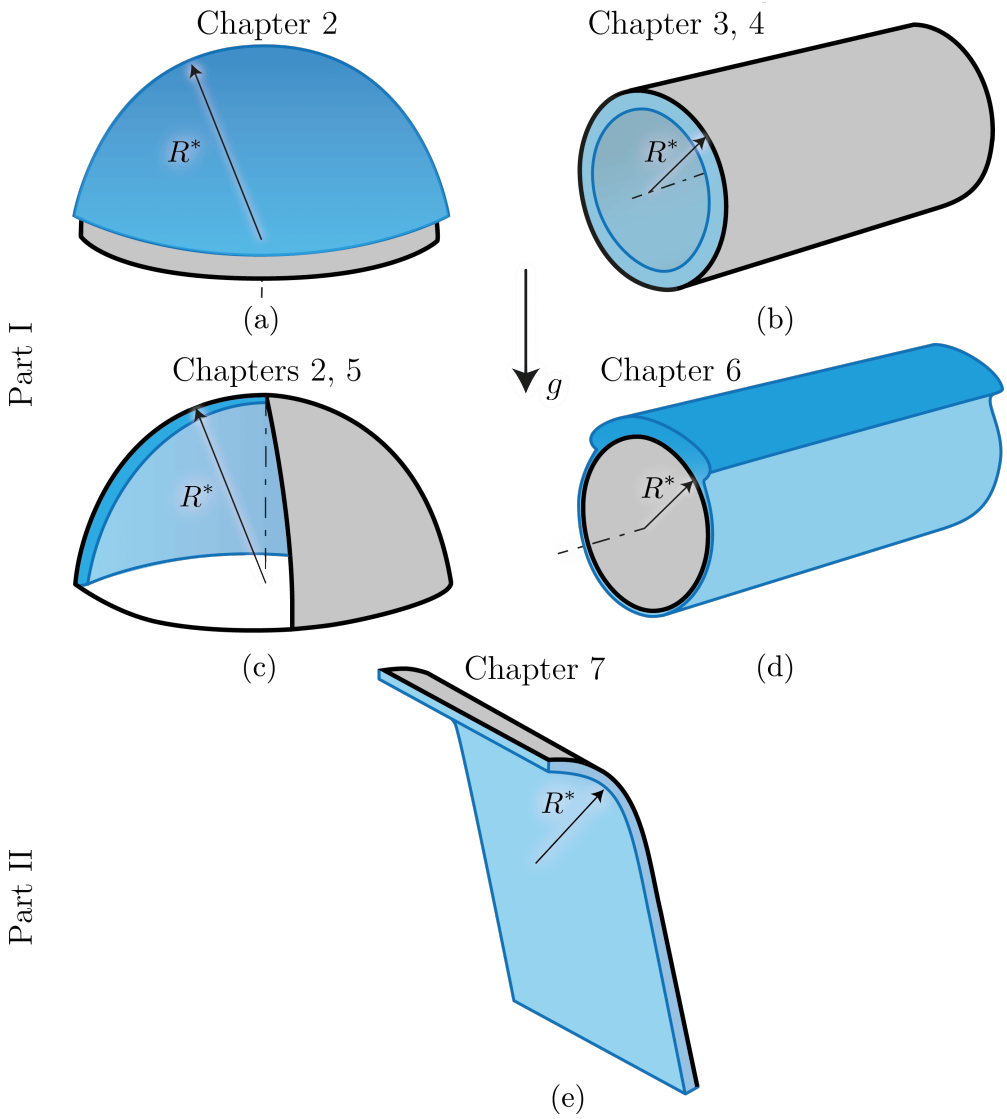

Figure 1.16 – Gravity-driven thin-film flows on the geometries considered in Parts I and II: (a) flow outside of a sphere, (b) inside of a cylinder, (c) inside of a sphere, (d) outside of a cylinder with a capillary ridge and (e) under a curved, then inclined, substrate. The principal radius of curvature of the curved substate is R^*.

amplified pattern in the spherical geometry is also investigated and contrasted to the one in a cylindrical substrate.

Finally, we perform in **Chapter 6** an optimal transient growth analysis for the flow on the exterior of a horizontal cylinder in the presence of a capillary ridge (see Fig. 1.16(d)). We do not only consider the optimal initial film perturbations, but also the optimal substrate topography yielding the formation of fingers.

Part II: Precipitative pattern formation in limestone caves

The fascinating beauty of structures found in limestone caves, from stalactites to stalagmites and draperies contrasts with the incomplete understanding of their morphodynamics, and in particular with the conditions which govern the pattern formation.

The aim of Part II is the investigation of the role played by hydrodynamic instabilities in the formation of karst structures in limestone caves.

In **Chapter 7** we consider the flow of a thin liquid film with constant flux under a curved and planar substrate, as shown in Fig. 1.16(e), coupled with the deposition of calcium carbonate. We perform a spatio-temporal stability analysis for the flow under an inclined plane to investigate the effect of the deposition as well as the effect of the nonlinearities in the governing equations. The dependence of the most amplified Rayleigh-Taylor instability wavelength on the substate-inclination angle is also sought. Furthermore, we propose a possible explanation based on the Rayleigh-Taylor instability for the morphogenesis of two typical karst formations encountered on the inclined ceilings of limestone caves: flutings and draperies. Flutings are also visible on the exterior of the terraces shown in Fig. 1.14(a).

1.3 Thin films in confined bubbles and droplets in microchannels

1.3.1 Analogy between coating flows and thin films in microchannels

In Parts I and II we focus on coating flows on substrates. The probably most classic coating problem is the plate withdraw from a liquid bath treated by Landau & Levich (1942) and Derjaguin (1943). As can be seen in Fig. 1.17(c), when withdrawing a plate from a liquid bath at velocity U_p^*, a thin liquid layer of thickness H_∞^* coats the substrate by viscous entrainment. This is the key mechanism of dip coating processes (Wilson, 1982). Furthermore, as shown by Maleki, Reyssat, Restagno, Quéré & Clanet (2011), when a prewetted substrate is immersed in a bath of the same liquid, the film-thickness profile is nonmonotonous and a minimum film thickness H_{min}^* is obtained close to the meniscus (see Fig. 1.17(a)). Hence, despite the fact that these flows are stable, the thin film presents again a well defined pattern which depends on the flow conditions.

Remarkably, the thickness profile of the liquid film surrounding a confined bubble in a microchannel displays exactly the same patterns. The receding meniscus at the front of a bubble deposits a layer of uniform film thickness H_∞^*, before a minimum film thickness H_{min}^* is reached close to the advancing meniscus at the rear of the bubble (see Fig. 1.17(b)). However, and in contrast to the thin-film patterns discussed in Parts I and II of this thesis, here, the nonuniformity of the film thickness does not result from an instability, but is the natural solution of the governing equations with the corresponding boundary conditions.

Bretherton (1961) has shown in his seminal work that the lubrication equation governing

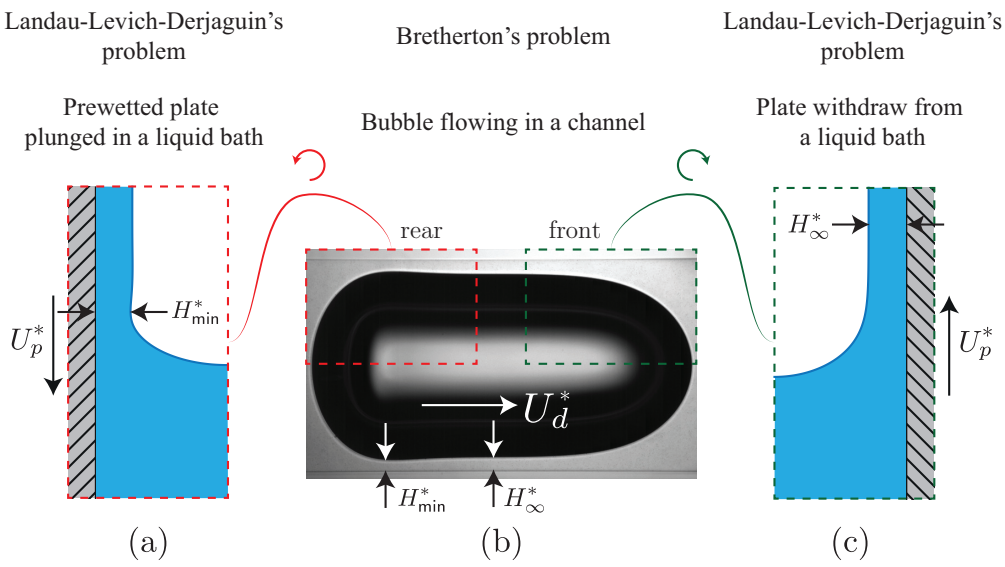

Figure 1.17 – Analogy between the dip coating problem of a plate studied by Landau-Levich-Derjaguin (a,c) and the one of a bubble flowing in a channel studied by Bretherton (1961) (b). The image of the bubble is taken from Khodaparast (2014).

the thickness of the film separating a bubble from the channel walls is identical to the one governing the thickness in the coating problem of Landau-Levich-Derjaguin. Both problems are governed by the same nondimensional parameter: the capillary number $Ca = \mu_o U^*/\gamma$, where U^* is the velocity of the plate U^*_p or the one of the bubble U^*_d, μ_o is the dynamic viscosity of the liquid and γ is the surface tension. At low velocities and small scales, capillary effects dominate inertia and gravity, which can be both neglected (Stone, 2010).

A more detailed sketch of the film-thickness profile surrounding a confined bubble in a microchannel is shown in Fig. 1.18. Three different regions can be distinguished depending

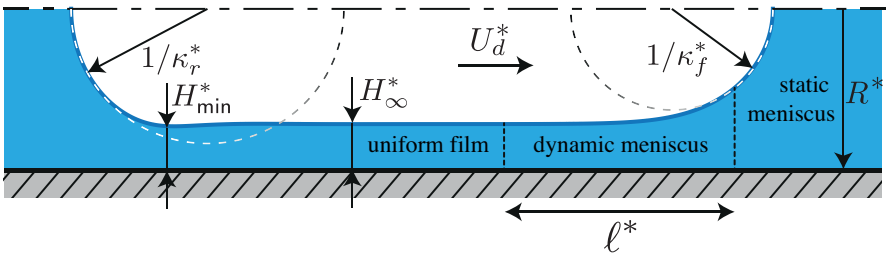

Figure 1.18 – Sketch of film-thickness profile for a bubble advancing at velocity U^*_d in a capillary of radius R^* with indication of the uniform thin-film region of thickness H^*_∞, the dynamic meniscus region and the static meniscus region. The minimum film thickness $H^*_{\min}$ and the plane curvatures $\kappa^*_{f,r}$ of the front and rear static caps in the are also highlighted. The same regions are found for the Landau-Levich-Derjaguin's problem of Fig. 1.17.

on the dominant forces at play. The uniform thin-film region of constant thickness H^*_∞, where viscous effects dominate, is matched in the dynamic meniscus region to a static meniscus

with constant curvature $\kappa^*_{f,r} = 1/R^*$ (at low Ca), where surface-tension forces prevail. These regions can be also identified in the meniscus of the Landau-Levich-Derjaguin's problem with the only difference that the curvature of the static cap is $\sqrt{2}/\ell^*_c$ at small Ca [7].

The uniform film thickness and the length of the dynamic meniscus region can be found by order-of-magnitude arguments (Aussillous & Quéré, 2000; Stone, 2010). In the dynamic meniscus region of characteristic length ℓ^* surface tension stresses balance viscous stresses. The typical curvature is of the order H^*_∞/ℓ^{*2} so that the pressure difference induced by Laplace law with respect to the ambient pressure scales like $-\gamma H^*_\infty/\ell^{*2}$. Assuming the velocity in the flow being of the same order as the bubble velocity U^*_d, we can balance the viscous force with the pressure gradient along the dynamic meniscus to obtain a scaling for the capillary number

$$\frac{\mu_o U^*_d}{H^{*2}_\infty} \approx \frac{1}{\ell^*}\frac{\gamma H^*_\infty}{\ell^{*2}} \Leftrightarrow Ca \sim \left(\frac{H^*_\infty}{\ell^*}\right)^3. \tag{1.38}$$

The length ℓ^* of the dynamic meniscus region is obtained by matching the orders of magnitude of the curvatures at the dynamic and static menisci:

$$\frac{H^*_\infty}{\ell^{2*}} \approx \frac{1}{R^*} \Leftrightarrow \ell^* \sim (H^*_\infty R^*)^{1/2}. \tag{1.39}$$

The famous scalings for the uniform film thickness $H^*_\infty/R^* \sim Ca^{2/3}$ and for the length of the dynamic meniscus region $\ell^*/R^* \sim Ca^{1/3}$ are therefore obtained. The same scalings are obtained for the Landau-Levich-Derjaguin's problem where R^* is replaced by $\ell^*_c/\sqrt{2}$.

The exact factors of these physically explained scalings have been found by Bretherton (1961) using a one-dimensional lubrication equation for the thin film. Roughly at the same time, Taylor (1961) measured the film thickness remaining on the inner wall of a tube filled by a viscous fluid after blowing air into the tube, which corresponds to Bretherton's problem with a bubble of infinite length. As an historical note, this problem was already considered by Fairbrother & Stubbs (1935), who where interested in the bubble velocity compared to the mean flow velocity. Unfortunately, the asymptotic results of Bretherton (1961) fit to the experimental results only at low capillary numbers, typically $Ca < 10^{-3}$. Park & Homsy (1984); Reinelt (1987) extended the asymptotic expansion to the next order for the similar problem of the motion of an air finger in a Hele-Shaw cell [8] (Saffman & Taylor, 1958; Taylor & Saffman, 1959), but, still, the validity range of the asymptotic result is rather small. Aussillous & Quéré (2000) proposed an *ad-hoc* rational function for the thickness of the uniform film, using a single fitting parameter, which is in very good agreement with the results of Taylor (1961). Note that the numerical results of Reinelt & Saffman (1985), Martinez & Udell (1990) and

[7] Landau & Levich (1942) have shown that the static cap curvature corresponds to the curvature given by the balance of capillary and gravity forces at the location where the film thickness is almost parallel to the plate (see Probstein (1989) for more details).

[8] A Hele-Shaw cell, named after Henry Selby Hele-Shaw (1854–1941), is composed by two flat plates separated by a very thin gap. It can be seen as a rectangular channel with a very large width-to-height aspect ratio so that the effect of the lateral walls can be neglected.

Giavedoni & Saita (1997, 1999), among others, confirm the rational behavior of the uniform film thickness with respect to the capillary number. More recently, Klaseboer, Gupta & Manica (2014) and Cherukumudi, Klaseboer, Khan & Manica (2015) proposed a possible explanation for the rational function.

1.3.2 Microfluidic channels

Thanks to tools for bubble and droplet [9] forming, coalescence, sorting, mixing and other operations, the flow of bubbles and droplets in low-cost microfabricated channels can operate in a passive way. In most of the cases, bubbles and droplets flow in microchannels with round or polygonal cross-sections (Kreutzer, Kapteijn, Moulijn, Kleijn & Heiszwolf, 2005; Khodaparast, Magnini, Borhani & Thome, 2015; Mikaelian et al., 2015). The geometry of microchannels strongly depends on their purpose and fabrication technique. Round capillaries are often made out of glass, whereas polygonal microchannels are fabricated using soft-lithography techniques.

Compared to the square and round capillaries, where the motion of bubbles and droplets is rather one-dimensional, rectangular microchannels with a large width-to-height aspect ratio allow for the manipulation of bubbles and droplets in two-dimensions, which reduces the complexity of the channels network in the device. When bubbles and droplets are not confined laterally, but only by the upper and lower plates, as in a Hele-Shaw cell, they assume a 'pancake'-like shape. The motion of pancakes in the channel can be controlled by surface tension gradients (Boos & Thess, 1997; Bush, 1997; Verneuil, Cordero, Gallaire & Baroud, 2009; Selva, Cantat & Jullien, 2011; Gallaire, Meliga, Laure & Baroud, 2014) as well as by confinement gradients (Dangla, Gallaire & Baroud, 2010; Abbyad, Dangla, Alexandrou & Baroud, 2011; Nagel, Brun & Gallaire, 2014; Nagel, 2014; Reyssat, 2014).

A critical ingredient for the correct design of Lab-on-a-Chip devices is the accurate prediction of the bubble and droplet velocity. Despite the fact that the velocity of a bubble in a round capillary in the limit of small capillary numbers is known since the work of Bretherton (1961), a satisfying theory for the velocity of droplets with a non-negligible inner viscosity in round and polygonal channels is still missing. As an example, Jakiela, Makulska, Korczyk & Garstecki (2011) have shown, by performing an extensive set of experiments, that the velocity of a droplet in a square microchannel depends in a complex way on the capillary number, on the viscosity ratio between the inner and outer fluids and on the length of the droplet. Regarding pancake bubbles in Hele-Shaw cells, actual models fail at predicting their correct velocity (Kopf-Sill & Homsy, 1988; Saffman & Tanveer, 1989; Meiburg, 1989).

[9] In this thesis, *bubbles* have a zero inner viscosity, whereas *droplets* have a nonvanishing inner viscosity.

1.3.3 In this thesis

The main aim of Part III of this thesis is to investigate the patterns arising in the thin-film flows separating bubbles, droplets and liquid bridges [10] from the walls of microchannels of different geometries. Furthermore, we will model the relevant quantities describing the dynamics of these multiphase flows.

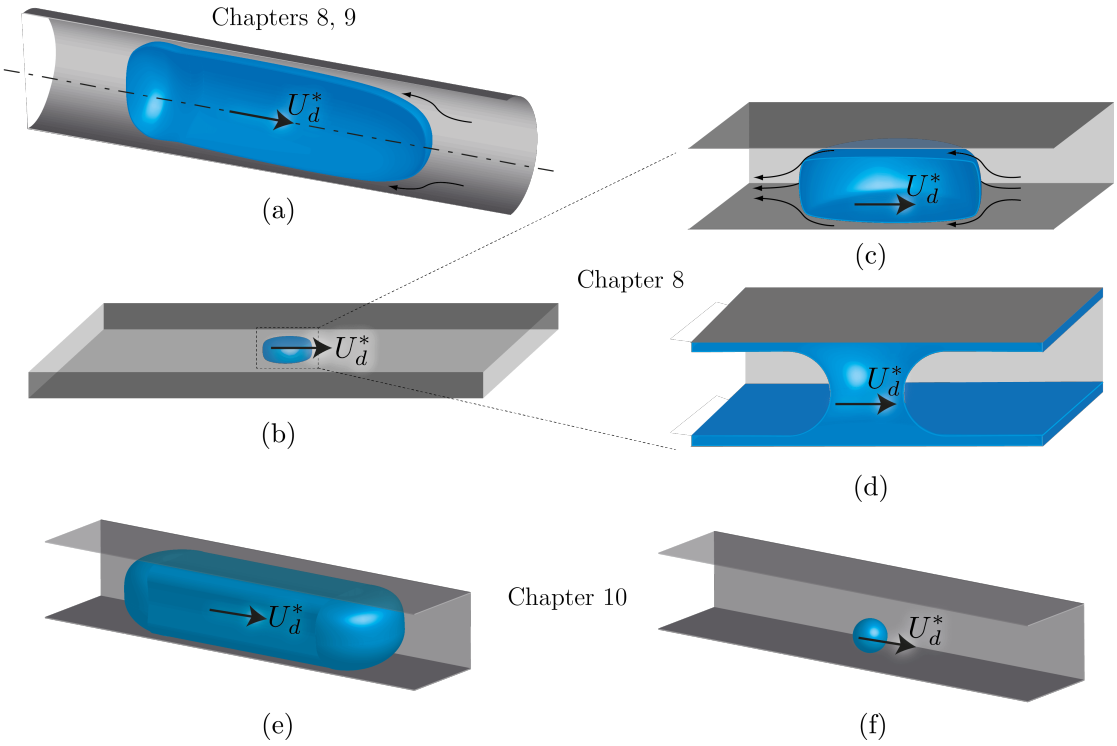

Figure 1.19 – Geometries of the problems considered in Part III: (a) confined bubble or droplet in a round capillary; (b) pancake bubble in a large width-to-height aspect ratio rectangular channel, (c) zoom on the pancake bubble and (d) on the liquid bridge in this rectangular channel; (e) confined and (f) unconfined bubble in a polygonal channel with width-to-heigh aspect ratio of order 1. All bubbles or droplets move at velocity U_d^* with respect to the channel walls.

In **Chapter 8** we describe the thin-film patterns induced by the advancing and receding menisci of bubbles and liquid bridges (see Fig. 1.19(a,b,c,d)), in both two and three-dimensions. The two-dimensional problem corresponds to the bubble motion in a planar channel studied by Bretherton (1961). Here, however, we use a different approach, which is readily extendible to the three-dimensional problem of a pancake bubble or liquid bridge in a Hele-Shaw cell. We highlight the similarities and differences between the patterns in the thin film of a pancake bubble and the ones surrounding a liquid bridge. The latter is compared to the pattern induced

[10] Liquid bridges are nothing else than the complementary of bubbles when inverting front and rear menisci (see Fig. 1.19(d)).

by a substrate-topography perturbation on a thin-film flow. In this study, we consider both linear and nonlinear solutions of the lubrication equation. The nonlinear lubrication results are compared to the results of 2D or 3D Stokes numerical simulations.

The classic problem of a bubble flowing in a two-dimensional planar or axisymmetric channel (see Fig. 1.19(a)) is generalized to droplets of nonvanishing inner viscosity and to higher capillary numbers in **Chapter 9**. To do so, we combine asymptotic results based on the lubrication equation considering the inner phase viscosity, inspired by the work of Schwartz, Princen & Kiss (1986), to numerical simulations of the full Stokes equations. Empirical models for the relevant quantities characterizing the dynamics of droplets as the uniform film thickness, the minimum film thickness, the front and rear cap curvatures and the viscous normal stress jumps at the droplet extremities are derived. The droplet velocity is directly obtained once the uniform film thickness is known. The total pressure drop induced by the presence of the droplet can eventually be modeled as well, which is of great help for the practical design of microfluidic devices. Also, we describe the flow patterns depending on the viscosity ratio and on the capillary number.

After having discussed bubbles and droplets in Hele-Shaw cells and in round capillaries in the two previous chapters, we consider in **Chapter 10** the motion of confined and unconfined bubbles in polygonal capillaries with a width-to-height aspect ratio of order 1 (see Fig. 1.19(e,f)). In contrast to the pancake bubbles in Hele-Shaw cells, the confined bubbles in these polygonal capillaries are also confined laterally, so that thicker film regions, called *gutters*, appear in the corners of the channels. On the other hand, when the bubble is no longer confined, it can move in the cross-stream direction. We show that the equilibrium position of the unconfined bubble depends on the size of the bubble, on the channel aspect ratio, on the deformability of the bubble and on inertial effects, which have been neglected, so far, in this thesis.

Part I

The effect of the substrate curvature on thin-film instabilities

2 Fabrication of slender elastic shells by the coating of curved surfaces

Remark This chapter is largely inspired by the publication of the same name

A. Lee[1], P.-T. Brun[2], J. Marthelot[3], G. Balestra[4], F. Gallaire[4] and P.M. Reis[1,3]

[1]Department of Mechanical Engineering, Massachusetts Institute of Technology, Cambridge, Massachusetts 02139, USA
[2]Department of Mathematics, Massachusetts Institute of Technology, Cambridge, Massachusetts 02139, USA
[3]Department of Civil and Environmental Engineering, Massachusetts Institute of Technology, Cambridge, Massachusetts 02139, USA
[4]Laboratory of Fluid Mechanics and Instabilities, EPFL, CH1015 Lausanne, Switzerland

Nature Communications **7**, 11155 (2016)

Author contributions P.M.R. and F.G. conceived project. A.L., P.-T.B., J.M. performed experiments and analyzed data. G.B. and F.G., performed simulations and analyzed data. F.G., G.B. and P.-T.B. developed theoretical model. F.G. and P.M.R. supervised the research. A.L., P.-T.B., J.M., G.B., F.G. and P.M.R. wrote paper.

Various manufacturing techniques exist to produce double-curvature shells, including: injection, rotational and blow molding, as well as dip coating. However, these industrial processes are typically geared for mass production and are not directly applicable to laboratory research settings, where adaptable, inexpensive and predictable prototyping tools are desirable. Here, we study the rapid fabrication of hemispherical elastic shells by coating a curved surface with a polymer solution that yields a nearly uniform shell, upon polymerization of the resulting thin film. First, we experimentally characterize how the curing of the polymer affects its drainage dynamics and eventually selects the shell thickness. The coating process is then rationalized through a theoretical analysis that predicts the final thickness, in quantitative agreement with

experiments and numerical simulations of the lubrication flow field. This robust fabrication framework should be invaluable for future studies on the mechanics of thin elastic shells and their intrinsic geometric nonlinearities.

2.1 Introduction

Hollow chocolate eggs, rabbits and bonbons have been fabricated since the 1600s by pouring molten chocolate into a mold and draining the excess. Solidification upon cooling ceases the flow and results in a solid shell of nearly constant thickness (Crawford & Kearns, 2012). Beyond chocolatiers, the polymer industry abounds with needs to fabricate thin-shell structures, and a plethora of manufacturing processes have been developed for this purpose, including: injection (Rees & Catoen, 2006), rotational (Crawford & Kearns, 2012) and blow molding (Lee, 2006), as well as dip coating (Scriven, 1988). Common to all of the above techniques are limitations in the thickness of the shells (*e.g.*, ~0.5 mm for injection molding) and its uniformity (typically ~20% for rotational molding (Beall, 1998)), as well as a striking lack of predictive theoretical models due to the multi-physics complexity of the processes. Rotational molding, for example, involves coating the inner surface of a hollow mold with a polymer melt, which is then rotated biaxially while applying a decreasing heating profile until a solid shell is formed (Crawford & Kearns, 2012). As another example, injection molding, is geared for mass-production manufacturing and requires costly precision-machined molds that are inflexible to variations in the geometry of the part (Rees & Catoen, 2006). In these processes, the optimization of the control parameters is largely tuned empirically, with compromises on versatility, predictability and reproducibility (Beall, 1998). As such, these techniques are not directly applicable to laboratory settings, where adaptable, inexpensive and predictable rapid-prototyping tools are more desirable. This is particularly the case for the fabrication of thin, smooth and flexible three dimensional structures.

For flat and cylindrical surfaces, a variety of thin-film coating techniques are well established (Weinstein & Ruschak, 2004). A significant advantage for these geometries is that, when compared to their double-curved counterparts, they are more amenable to theoretical modeling to predict how the final film thickness depends on the control parameters (Landau & Levich, 1942; Derjaguin, 1943; Bretherton, 1961). In these cases, the flow driven by viscous stresses and held by capillary forces is 'frozen' as the media cools, cures or dries, yielding a defect-free and uniform finish. As a result, these robust coating techniques have matured to be ubiquitous in industry. To generate (ultra-) thin sheets, spin-coating is now widespread (*e.g.*, in microfluidics) to attain constant and tunable film thicknesses (Emslie, Bonner & Peck, 1958; Meyerhofer, 1978). Similarly, spin-casting exploits centrifugal forces on a rotating cylindrical surface to evenly distribute a polymer solution and fabricate nearly constant thickness shells in a highly controllable manner (Kalpakjian & Schmid, 2014). This technique was instrumental in identifying the role of imperfections on the critical buckling conditions of cylindrical shells in the 1960s (Tennyson, 1968; Elishakoff, 2014). For double-curved surfaces, there is a need for simple and versatile fabrication methods that are analogous to the coating of fibers, plates

and cylinders and able to yield uniform, controllable and predictable results.

Here, we introduce a simple and robust mechanism to fabricate hemispherical thin elastic shells by the coating, drainage and subsequent curing of polymer solutions on curved molds. Our process is analogous to spin-coating (itself not applicable on curved surfaces), albeit with a gravity-driven flow in lieu of centrifugal forces. Through a systematic series of experiments using elastomers, we show that drainage can lead to coatings that are 'frozen' in time as the polymer cures, thereby leading to a nearly uniform thin elastic shell. A theoretical analysis of the underlying lubrication flow during drainage, which includes the evolution of the rheological properties of the polymer as it cures, is able to accurately predict the final thickness of the shell as a function of the material properties of the polymer and the geometry of the substrate. Importantly, the final shell thickness is found to be independent of the initial conditions such as the height of pouring and the volume of poured fluid, as well as the initial thickness profile. Moreover, we find that the shell thickness can be tuned over one order of magnitude by changing the waiting time between the preparation of the polymer solution and the moment of pouring onto the mold. Our analysis demonstrates that the robustness and flexibility of this mechanism are inherent consequences of the loss of memory in the flow field. Our approach provides a fast, robust and predictable mechanism to fabricate thin shells with flexibility in their material and geometric properties by tuning the control parameters.

2.2 Results

2.2.1 Elastic shells of uniform thickness from viscous coating

In Fig. 2.1(a), we present a series of photographs that illustrate our coating process. A silicone-based liquid polymer solution is poured onto a rigid sphere (mold), drains under the effect of gravity and eventually covers the surface. We used both VPS and PDMS, at different mixing and curing conditions (see Sec. 2.4.1 for details), to achieve a variety of rheological properties. With time, cross-linking of the polymer film that emerges from the drainage process yields a thin elastic shell that can be readily peeled from the mold. The final thickness of these elastic shells, H_f^*, is found to be uniform (to within 6.6% (VPS) and 8.7% (PDMS) over the hemisphere).

The above procedure was repeated with molds in a range of radii ($1 \leq R^*$ [mm] ≤ 375, see Fig. 2.1b), and we found that $H_f^* \sim \sqrt{R^*}$, as shown in Fig. 2.1(c). This result is robust and independent of either the details of the polymer or the curing temperature. The square-root dependence of H_f^* on R^* can be rationalized by balancing the characteristic curing time, τ_c, of the polymer solution and the characteristic drainage time, $\mu_0 R^*/(\rho g H_f^{*2})$, that is obtained when balancing the viscous stresses and gravity in the lubrication layer, such that

$$H_f^* \sim \sqrt{\frac{\mu_0 R^*}{\rho g \tau_c}}, \tag{2.1}$$

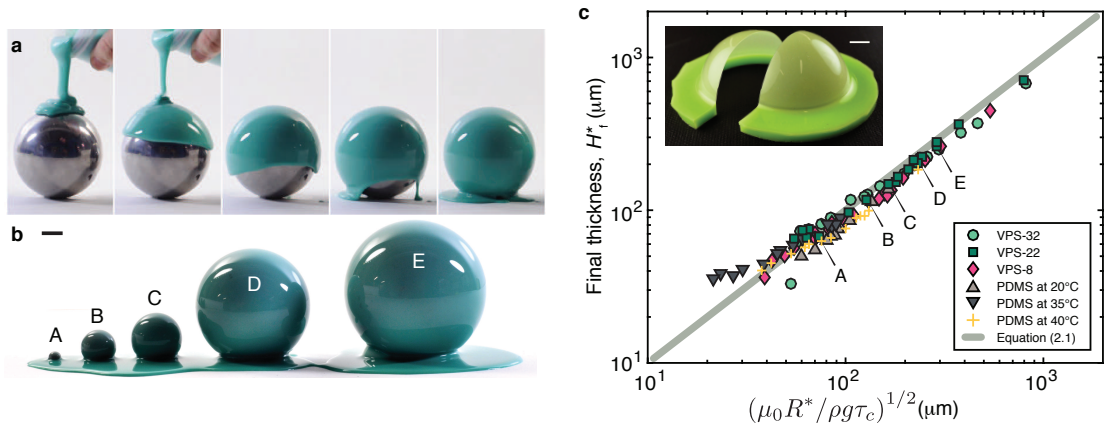

Figure 2.1 – Coating process and resulting thickness of elastic shells. (a) Liquid VPS-22 (see Sec. 2.4.1) is poured onto a sphere ($R^* = 38$ mm), then drains under gravity and eventually cures to produce an elastic shell (see Supplementary Movie 1). Time interval between each frame is 2 s. (b) Similar procedure to that of (a) for spheres in a range of radii, $1 \leq R^*$ [mm] ≤ 375. (c) Thickness of the elastic shells, H_f^*, as a function of $\sqrt{\mu_0 R^*/(\rho g \tau_c)}$, for various polymer solutions (VPS and PDMS) and temperatures (for PDMS). See Sec. 2.4.1 for details. The solid line corresponds to equation (2.1). Inset: An elastic shell is cut along a meridian for the thickness measurements. Scale bars, 10 mm.

where μ_0 is a characteristic viscosity of the polymer (*e.g.*, its initial value), ρ its density, and g is the acceleration of gravity. The fact that all the data in Fig. 2.1(c) collapses onto a master curve (irrespective of the polymer and curing temperature, over a wide range of R^*) supports this scaling analysis. Below, we shall develop a theoretical description that more formally recovers this scaling, both analytically and numerically.

2.2.2 The dynamics of coating

We proceed by experimentally characterizing the coating dynamics that, upon curing of the polymer, results in a thin elastic shell (Fig. 2.1a). As a representative case, we focus on VPS Elite 32 (hereafter referred to as VPS-32, see Sec. 2.4.1) poured onto a sphere with $R^* = 38$ mm. A broader exploration with other silicone-based polymers is provided in the Supplementary Table 1, as well as Supplementary Figs. 1 and 5, nonetheless, yielding similar results.

A schematic diagram of our system is presented in Fig. 2.2a, for a hemispherical mold, aligned such that gravity is parallel to the axis that connects its center to the pole; $\mathbf{g} = -g\,\mathbf{e}_z$. Both the local thickness, $H^*(\theta, t^*)$, and the free surface velocity, $U^*(\theta, t^*)$, of the draining film are assumed axisymmetric and vary in both time, t^*, and space (*i.e.*, polar angle, θ). At the pole ($\theta = 0$), the fluid flow vanishes due to symmetry. Elsewhere, the velocity is predominantly in the polar direction, $\mathbf{e}_\theta$. This is supported by the representative velocity field shown in Fig. 2.2(b), obtained through PIV (see Sec. 2.4.1), at $t^* = 60$ s in a 1×1 cm^2 region of the film

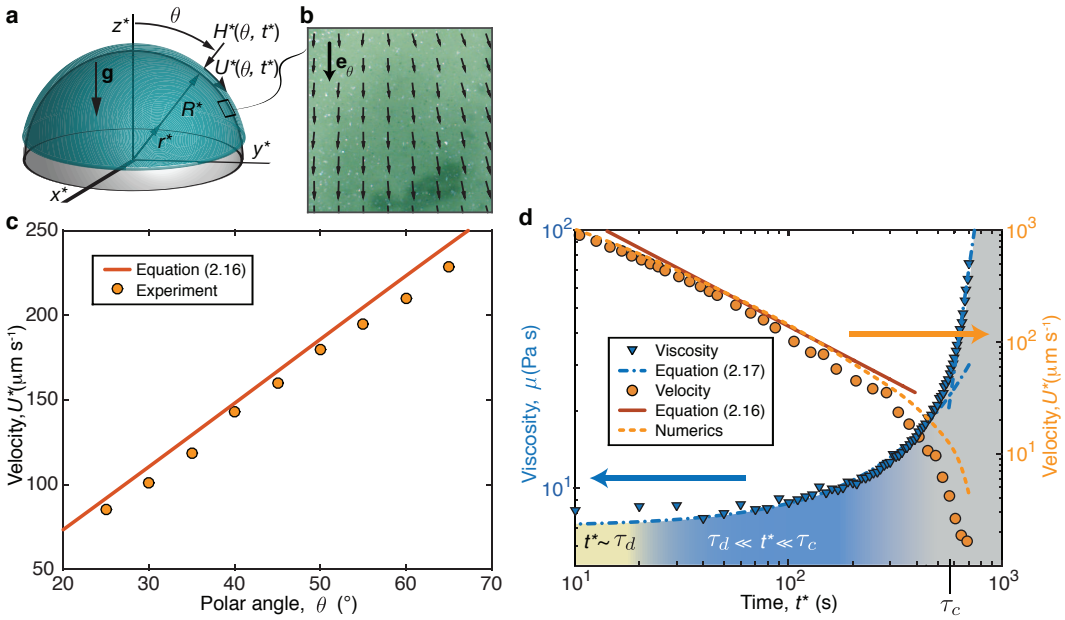

Figure 2.2 – Spatial and temporal variation of the flow velocity. (a) Schematic diagram of the coating problem; $H^*(\theta, t^*)$ is the thickness of the viscous film and $U^*(\theta, t^*)$ is the flow velocity during drainage. (b-d) All data is for VPS-32 at 20°C. (b) Instantaneous velocity field at $t^* = 60\,\mathrm{s}$ in a $1\times1\,\mathrm{cm}^2$ region of the film located at $\theta = 60°$ of a sphere ($R^* = 38\,\mathrm{mm}$), obtained through PIV. (c) Dependence of the instantaneous local velocity (at $t^* = 60\,\mathrm{s}$) on θ. (d) Time variation of the velocity, $U^*(\theta = 60°, t^*)$ orange circles, and the viscosity, $\mu(t^*)$ blue triangles, of the polymer. The characteristic curing time, τ_c, separates the drainage and curing regimes for both $U^*(\theta, t^*)$ and $\mu(t^*)$. The dash-dot line is the best fit for the viscosity: equation (2.17) with $\mu_0 = 7.1 \pm 0.2\,\mathrm{Pa\,s}$, $\alpha = 5.3 \pm 0.7$, $\beta = (2.06 \pm 0.09) \times 10^{-3}$, and $\tau_c = 574 \pm 11\,\mathrm{s}$. The solid and dashed lines are the predictions from our model for the velocity field using equation (2.16) and direct numerical simulations, respectively.

located at $\theta = 60°$. Moreover, the instantaneous local velocity is found to increase with θ (Fig. 2.2(c)).

In Fig. 2.2(d), we plot the time-series of the free surface velocity at the specific polar location $U^*(\theta = 60°, t^*)$; the flow progressively slows down and eventually comes to a halt in finite time. This leaves a coating of the final thickness, H_f^*, on the mold. The velocity profile and its arrest are found to correlate directly to the change in the viscosity, μ, as the polymer cures (Fig. 2.2(d)), which was determined through the rheometry at the appropriate shear rate (see Sec. 2.4.1). Note that the initial drainage and subsequent curing regimes are separated by the characteristic curing time, τ_c, which is significantly larger than the initial drainage time, $\tau_d = \mu_0 R^*/(\rho g H_i^{*2})$, where H_i^* is the initial average coating thickness. For example, in the representative case above for VPS-32, we find $\tau_d = 5.9\,\mathrm{s} \simeq 0.01\,\tau_c$ (using $H_i^* = 2\,\mathrm{mm}$, $R^* = 38\,\mathrm{mm}$, $\rho = 1160\,\mathrm{kg\,m^{-3}}$, $\mu_0 = 7.1\,\mathrm{Pa\,s}$ and $\tau_c = 574\,\mathrm{s}$). A direct consequence of this

separation of timescales is that there is loss of memory in the process, such that H_f^* should be independent of H_i^*. This prediction will be thoroughly examined in Sec. 2.3. Returning to the time evolution of U^* and μ (Fig. 2.2(d)), at early times ($t^* < \tau_d$) there are some disturbances due to initial conditions and we do not attempt to describe this regime. During intermediates times ($\tau_d \ll t^* \ll \tau_c$), μ is approximately constant, and the velocity is set by viscous drainage with $U^* \sim 1/t^*$ (Takagi & Huppert, 2010). For $t^* > \tau_c$, as the curing of the polymer accelerates, μ increases sharply with time, and consequently, the flow velocity slows down dramatically.

The separation of the drainage and curing timescales can be leveraged to further tune the final thickness of the shell. Since H_f^* is dictated by the interplay between the drainage timescale and polymerization timescale, τ_c, the final thickness can be increased by accelerating the curing process. One strategy to achieve this would be to alter τ_c by modifying the kinetics of cross-linking (*e.g.*, through additives or temperature), which would also modify the viscosity of the thin film or the elastic modulus of the final shell. An alternative is to shift the origin of the process by waiting for a time, τ_w, between the preparation of the polymer and the instant when the mixture is poured onto the mold. This waiting procedure offers an additional lever in tuning the properties of the fabricated shells.

Having presented our robust and versatile mechanism to fabricate thin elastic shells by the coating and subsequent curing of a polymer film, we proceed by rationalizing this process through a theoretical framework that is able to predict H_f^*.

2.2.3 Nonlinear drainage flow solution

We assume a thin liquid film of initial characteristic thickness H_i^* flowing on a sphere of radius R^*, resulting in a film aspect ratio $\delta = H_i^*/R^*$. Taking advantage of the azimuthal symmetry, our model is derived in a polar coordinate system (see schematic in Fig. 2.2(a)). Considering the small aspect ratio δ of the film and mass conservation, the flow velocity $\mathbf{u}^* = (u^*, v^*)$ can be regarded to be essentially one-dimensional and predominantly tangential to the surface of the sphere in the θ direction (the characteristic velocity normal to the substrate is $V^* \sim U^* H^*/R^* \ll U^*$, where U^* is the one tangential to the substrate, see Chapter 1). Furthermore, the low Reynolds number for this flow allows for the use of the Stokes equations. The equation for the momentum balance in the radial direction is (Leal, 2007)

$$0 = -\frac{1}{\rho}\frac{\partial p^*}{\partial r^*} - g\cos\theta, \tag{2.2}$$

where subscripts denote partial derivatives. The boundary condition for the pressure at the free surface is $p^*(R^* + H^*, \theta, t^*) = p_0^* - \gamma\kappa^*$ (p_0^* is the external pressure, γ is the surface tension of the fluid, and κ^* is the curvature of the interface). Integrating Eq. (2.2) along the radial direction and using the above boundary condition yields the pressure distribution, $p^*(r^*, \theta, t^*) = p_0^* - \gamma\kappa^* + \rho g\cos\theta(R^* + H^* - r^*)$. By integrating twice, the θ component of the

momentum equation

$$0 = \frac{1}{\rho r^*}\frac{\partial p^*}{\partial \theta} + \nu \frac{1}{r^{*2}}\frac{\partial}{\partial r^*}\left(r^{*2}\frac{\partial u^*}{\partial r^*}\right) + g\sin\theta \tag{2.3}$$

and considering the no-slip boundary condition at the sphere surface, $u^*(R^*,\theta,t^*) = 0$, as well as the zero-shear stress interface, $\partial u^*(R^*+H^*,\theta,t^*)/\partial r^* = 0$, we obtain the tangential velocity component:

$$u^*(r^*,\theta,t) = \left(\frac{\gamma\kappa_\theta^*}{\mu R^*} - \frac{\rho g\cos\theta H_\theta^*}{\mu R^*} + \frac{\rho g\sin\theta}{\mu}\right)\left(H^* - \frac{r^*-R^*}{2}\right)(r^*-R^*). \tag{2.4}$$

The depth-integrated velocity is given by $Q^*(\theta,t^*) = \int_{R^*}^{R^*+H^*} u^*\left(r',\theta,t^*\right)dr'$. Using the local mass conservation in spherical coordinates, namely $\partial H^*/\partial t^* + (R^*\sin\theta)^{-1}\partial(\sin\theta Q^*)/\partial\theta = 0$, we eventually obtain the lubrication equation:

$$H_t^* + \frac{1}{3\sin\theta\mu R^*}\left[H^{*3}\sin\theta\left(\underbrace{\frac{\gamma\kappa_\theta^*}{R^*}}_{\mathbf{I}} - \underbrace{\frac{\rho g\cos\theta H_\theta^*}{R^*}}_{\mathbf{II}} + \underbrace{\rho g\sin\theta}_{\mathbf{III}}\right)\right]_\theta = 0, \tag{2.5}$$

where the leading order curvature derivative is $\kappa_\theta^* = R^{-*2}(H_{\theta\theta\theta}^* + 2H_\theta^* + H_{\theta\theta}^*\cot\theta - H_\theta^*\csc^2\theta)$. The term **I** in the spatial variation of the flux corresponds to the capillary pressure gradient, term **II** represents the variation of the hydrostatic pressure distribution and term **III** accounts for the drainage. In the case of a liquid film on the underside of a sphere, the hydrostatic pressure variation term would have an opposite sign, but the rationale would otherwise be identical.

Note that the free-surface velocity can be easily computed as:

$$U^*(\theta,t^*) = \frac{3}{2} < u^*(r^*,\theta,t) >= \frac{3}{2}\frac{Q^*(\theta,t^*)}{H^*(\theta,t^*)} \tag{2.6}$$

The film thickness and time can be nondimensionalized by H_i^* and the initial drainage time, $\tau_d = \mu R^*/(\rho g H_i^{*2})$, respectively, such that the lubrication equation expressed with nondimensional quantities is written as

$$H_t + \frac{1}{3\sin\theta}\left\{H^3\sin\theta\left[\frac{\delta^2}{Bo}\left(H_{\theta\theta\theta} + 2H_\theta + H_{\theta\theta}\cot\theta - H_\theta\csc^2\theta\right) - \delta H_\theta\cos\theta + \sin\theta\right]\right\}_\theta = 0, \tag{2.7}$$

where $Bo = \rho g R^* H_i^*/\gamma$ is the modified Bond number, prescribing the ratio between gravitational and surface-tension forces [1]. As we have seen in the introductory Chapter 1, the

[1] Note that the Bond number considered in the chapters of Part I is a modified Bond number which contains both effects of the film thickness and of the substrate curvature. As will become clear in Chapter 3, this definition of Bond number, which can be seen as the ratio between the drainage and the instability times, suffices to describe the flow dynamics.

capillary pressure term is two orders smaller than the drainage term [2], but is the key ingredient for the stability of these flows.

Assuming that the depth of the fluid varies slowly along the substrate and that the effect of surface tension is negligible, which are both valid assumptions except close to the moving front at short times (see Chapter 6), we obtain the simplified version of the lubrication equation (2.7):

$$H_t + \frac{1}{3\sin\theta}(H^3\sin^2\theta)_\theta = 0. \tag{2.8}$$

This equation confirms that, under the aforementioned assumptions, the dynamics of the thin film does not depend on whether it is formed on the underside or outside of the substrate. The free-surface velocity field is given by $U(\theta,t) = H(\theta,t)^2\sin\theta/2\delta$, or in dimensional form:

$$U^*(\theta,t^*) = \frac{\rho g H^*(\theta,t^*)^2}{2\mu}\sin\theta. \tag{2.9}$$

We now seek to find the temporal and spatial variation (in θ) of the film thickness H. We shall first consider a Newtonian fluid and, once the nonlinear drainage flow solution is obtained, then include curing effects (*i.e.*, the time dependence of $\mu(t^*)$ shown in Fig. 2.2(d)).

To do so, we postulate an expansion solution of the form $H(\theta,t) = H_0(t) + \theta^2 H_2(t) + \theta^4 H_4(t) + O(\theta^6)$, where odd terms vanish due to symmetry reasons. It is well known that the thickness at the pole of a thin viscous film draining on a spherical surface is given by $H_0(t) = (1+4t/3)^{-1/2}$ (Takagi & Huppert, 2010; Trinh et al., 2014) and corresponds to the exact solution of Eq. (2.8) at the pole (*i.e.*, $\theta = 0$). By substituting the expansion for H into Eq. (2.8) and further developing $\cos\theta \sim 1-\theta^2/2+\theta^4/24+O\left(\theta^6\right)$ and $\sin\theta \sim \theta-\theta^3/6+O\left(\theta^5\right)$, we obtain a differential equation for each order. The equation for H_2 is:

$$\frac{dH_2}{dt} + 4H_0^2 H_2 = \frac{1}{3}H_0^3. \tag{2.10}$$

The particular solution is assumed to be of the form $H_2^P(t) = a(1+4t/3)^{-1/2}$. Substituting this form into Eq. (2.10) results in an equation for the parameter a, yielding $a = 1/10$. On the other hand, the homogeneous solution of the equation is $H_2^H(t) = b(1+4t/3)^{-3}$. The second order solution of Eq. (2.8), $H(\theta,t) \approx H_0(t) + \theta^2\left[H_2^P(t) + H_2^H(t)\right]$, can be eventually shown to read

$$H(\theta,t) \approx \frac{1}{\sqrt{1+\frac{4}{3}t}}\left[1+\frac{\theta^2}{10}\left(1+c\left(1+\frac{4}{3}t\right)^{-5/2}\right)\right], \tag{2.11}$$

where the parameter c depends on the initial condition.

[2] In Eq. (1.28), the capillary pressure term was three orders smaller than the drainage term due to the different definition of the Bond number for the flow on a planar substrate.

Note that the homogeneous solution only influences the transient regime; for large times the solution decreases as $(4t/3)^{-1/2}$ and is independent of the initial condition. In dimensional form, the asymptotic solution for the film thickness is given by:

$$H^*(\theta,t^*) \approx \frac{H_i^*}{\sqrt{1+\frac{4}{3}\frac{t^*}{\tau_d}}}\left[1+\frac{\theta^2}{10}\left(1+c\left(1+\frac{4}{3}\frac{t^*}{\tau_d}\right)^{-5/2}\right)\right], \tag{2.12}$$

A more accurate solution is obtained when considering the fourth-order term in the expansion. The equation for H_4 is:

$$\frac{dH_4}{dt}+6H_0^2H_4=\frac{4}{3}H_0^2H_2-6H_0H_2^2-\frac{1}{36}H_0^3. \tag{2.13}$$

Proceeding in a similar way as for the second-order problem, the fourth-order solution reads:

$$H_4(t)=\frac{41/4800}{\sqrt{1+\frac{4}{3}t}}\left[1+\frac{216c^2}{41}\left(1+\frac{4}{3}t\right)^{-5}+\frac{32c}{41}\left(1+\frac{4}{3}t\right)^{-5/2}+d\left(1+\frac{4}{3}t\right)^{-4}\right], \tag{2.14}$$

where the parameter d depends on the initial condition. At late times, the spatial variation of the film thickness is therefore of the form $1+(1/10)\theta^2+(41/4800)\theta^4+O\left(\theta^6\right)$.

In the limit of $t^* \gg \tau_\mathrm{d}$, equation (2.12) simplifies to

$$H^*(\theta,t^*) \approx \sqrt{\frac{3\mu_0 R^*}{4\rho g t^*}}\left(1+\frac{\theta^2}{10}\right). \tag{2.15}$$

The memory loss of the flow mentioned earlier arising from the separation of the drainage and curing timescales is well captured by this description given that H_i^* is absent from equation (2.15). Moreover, there is a weak dependence on θ (7.0% standard deviation); a general result that has also been observed in the thinning of an air bubble formed in a fluid bath (Lhuissier & Villermaux, 2012), as well as in the thin air layer that supports a drop bouncing on a fluid interface (Couder, Fort, Gautier & Boudaoud, 2005).

As an indirect validation of equation (2.15), we substitute it into the free surface velocity equation describing the parabolic flow profile on a sphere, Eq. (2.16), to obtain

$$U^*(\theta,t^*) \approx \frac{3}{8}\frac{R^*}{t^*}\left(1+\frac{\theta^2}{10}\right)^2\sin\theta. \tag{2.16}$$

This prediction for the variation of U^* on both θ (at fixed t^*) and t^* (at fixed θ) is in agreement with the experimental velocity profiles shown in Fig. 2.2(c-d) for $\tau_\mathrm{d} \ll t^* \ll \tau_\mathrm{c}$ (*i.e.*, in the regime after the initial drainage, when the polymer viscosity is approximately constant, and prior to curing). In particular U^* is found to be almost linear in θ as the cubic term of the Taylor expansion is $\theta^3/30$ in lieu of the conventional $\theta^3/6$ of the sine. Strikingly, the velocity field in this regime is independent of both gravity and viscosity and is solely set by the geometry of

the problem, so that no material parameters enter the prediction.

2.2.4 Including the effects of curing into the flow solution

The curing of the polymer has not yet been taken into account in our model, which, as is, yields a vanishing coating thickness since equation (2.15) states that $H^* \sim 1/\sqrt{t^*}$. To do so, the above framework is modified by considering a time-varying viscosity (Roller, 1986) using a piecewise function of the form

$$\mu(t^*) = \begin{cases} \mu_0 \exp(\beta t^*), & \text{if } t^* \leq \tau_c, \\ \mu_1 t^{*\alpha}, & \text{if } t^* > \tau_c, \end{cases} \tag{2.17}$$

with $\mu_1 = \mu_0 \exp(\beta\tau_c)\tau_c^{-\alpha}$ chosen to ensure continuity at τ_c and where β and α are fitting parameters (see Supplementary Table 1 for the numerical values for the polymers used in our experiments). Equation (2.17) is fitted to the experimental data and found to accurately describe the viscosity evolution (Fig. 2.2(d)). Note that because of the small value of the parameter β , the viscosity can be initially assumed as constant (see Sec. 2.2.2). The asymptotic estimates for the film thickness and for the film surface velocity resulting from this viscosity model and Eqs. (2.12) and (2.16) are now derived.

During the curing regime, $\tau_c \ll t^*$, the film thickness is written as

$$H^*(\theta, t^*) \approx \frac{H_i^*}{\sqrt{1 + \frac{4}{3}\frac{\rho g H_i^{*2}}{R^*}\int_0^{t^*} \frac{1}{\mu(t')}dt'}}\left(1 + \frac{\theta^2}{10}\right), \tag{2.18}$$

or

$$H^*(\theta, t^*) \approx \frac{H_i^*\left(1 + \frac{\theta^2}{10}\right)}{\sqrt{1 + \underbrace{\frac{4}{3}\frac{\rho g H_i^{*2}}{R^*}\frac{(\alpha-1)(e^{\beta\tau_c}-1)+\tau_c\beta}{\beta\mu_0 e^{\beta\tau_c}(\alpha-1)}}_{\mathbf{I}} - \underbrace{\frac{4}{3}\frac{\rho g H_i^{*2}}{R^*}\frac{\tau_c^\alpha}{\mu_0 e^{\beta\tau_c}(\alpha-1)}t^{*1-\alpha}}_{\mathbf{II}}}} \tag{2.19}$$

If the curing time τ_c is large enough so that the term **I** is much larger than unity and if the final time t^* is larger than τ_c so that term **II** becomes negligible, then the asymptotic solution for the film thickness is given by

$$H_f^*(\theta) \approx \sqrt{\frac{3\mu_0 R^*}{4\rho g}\frac{\beta e^{\beta\tau_c}(\alpha-1)}{(\alpha-1)(e^{\beta\tau_c}-1)+\tau_c\beta}}\left(1 + \frac{\theta^2}{10}\right) = \sqrt{\frac{3\mu_0 R^*}{4\rho g}\frac{1}{K}}\left(1 + \frac{\theta^2}{10}\right), \tag{2.20}$$

that is consistent with equation (2.15) but with $K = \{(k - e^{-\beta\tau_c})/\beta\} + \{\tau_c e^{-\beta\tau_c}/(\alpha-1)\}$ (instead of $K = t^*$), where $k = 1$ when there is no delay between the preparation and the coating with the polymer solution.

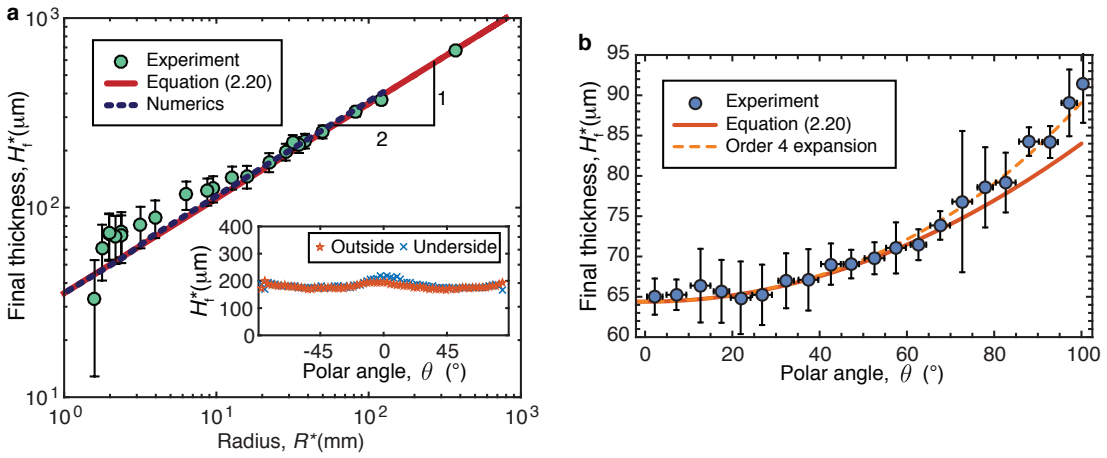

Figure 2.3 – Influence of the geometry on the final shell thickness. (a) Comparison between theory, numerics and experiments for the dependence of H_f^* on R^*, for the representative case of VPS-32. The results are consistent with the power law $H_f^* \sim \sqrt{R^*}$ and in agreement with equations (1) and (6). Inset: Final thickness of shells obtained by pouring VPS-32 on the outside or the underside of a hemisphere with $R^* = 25\,\text{mm}$. The error bars of the data correspond to the standard deviation of three thickness measurements performed at three different locations of the shell. (b) Final thickness of a shell fabricated by pouring PDMS on the outside of a hemisphere with $R^* = 38\,\text{mm}$ compared to equation (2.20); solid line. The dashed line is the prediction obtained by refining the expansion to the next order, $O(\theta^4)$, which adds $\frac{41}{4800}\theta^4$ to the term the parentheses of equation (2.20); see Eq. (2.14) in Sec. 2.2.3 for details. The error bars of the data for H_f^* (y-axis) correspond to the standard deviation on multiple measurements. The error bars for of the data for θ (x-axis) correspond to the size of the angular range used to bin the data.

In Fig. 2.3(a), we compare experimental results (circles) for H_f^* of the shells fabricated with VPS-32 to the prediction (solid line) from equation (2.20) and find good agreement between the two. It is important to note that our model has no adjustable parameters; all numerical coefficients (α, β and τ_c) are independently determined once and for all from the viscosity profile and then used in the theory. Note that the profiles obtained when coating either the outside or the underside of complementary spherical molds are nearly identical (Fig. 2.3(a), inset).

In Fig. 2.3(b), we test the shell thickness profile, $H_f^*(\theta)$, and find that the experimental results (circles) are in excellent agreement with equation (2.20).

Our theoretical framework is now further validated through numerical simulations (see Sec. 2.4.2). The fully nonlinear governing equation Eq. (2.7) is integrated directly, with the appropriate initial conditions and the desired viscosity profile, either constant or time-varying according to equation (2.17). The results from these numerical simulations are in agreement with both the experimental data and the theoretical predictions for the surface velocity over

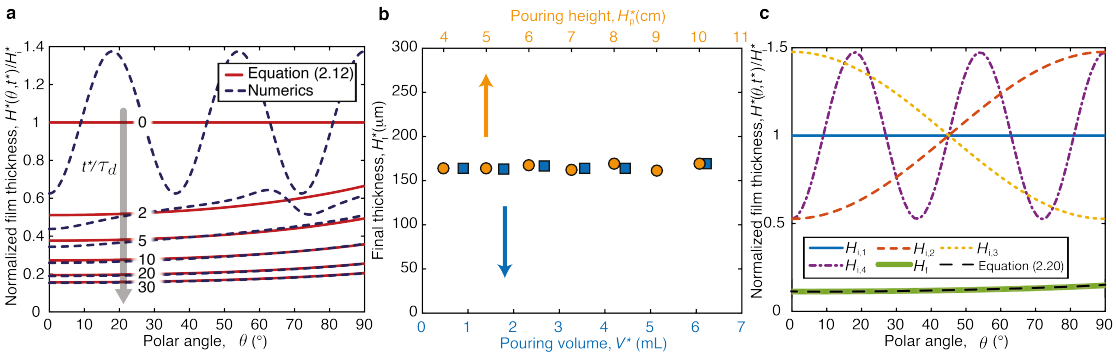

Figure 2.4 – Insensitivity of the coating mechanism to the initial conditions. (a) Time-series of the normalized film thickness, $H^*(\theta,t^*)/H_i^*$, with a constant viscosity, at $t^*/\tau_d = 0,2,5,10,20,$ and 30. Dashed lines correspond to the numerically computed evolution of an initially sinusoidal thickness profile of the form $H^*(\theta,t^*=0)/H_i^* = 1+0.375\cos(10\theta)$ (see Sec. 2.4.2 and Fig. 2.7). Solid lines are the theoretical prediction, equation (2.12), with uniform initial thickness profile, $H^*(\theta,t^*=0)/H_i^*=1$. The various parameters are: average initial film thickness $H_i^*=0.2\,$mm, sphere radius $R^*=20\,$mm, and material properties for VPS-32. (b) Shell thickness, H_f^*, obtained for different pouring conditions: pouring height, H_p^*, and volume poured volume, V^*, onto a spherical mold with $R^*=20\,$mm using VPS-32. (c) Four different initial conditions used in the numerics converge to the same final thickness, H_f^*, and agree well with equation (2.20) (black dashed line). The simulation parameters are: $H_i^*=2\,$mm, $R^*=38\,$mm, $H_{i,1}=1$, $H_{i,2}=1-0.475\cos(2\theta)$, $H_{i,3}=1+0.475\cos(2\theta)$, $H_{i,4}=1-0.475\cos(10\theta)$, all with the material properties of VPS-32.

time and final shell thickness (dashed lines in Fig. 2.2(d) and Fig. 2.3(a), respectively). In particular, we have computed the time evolution for a coating film that has an initial sinusoidal thickness profile (dashed line in Fig. 2.4(a)), which rapidly converges to the analytically derived equation (2.12), plotted in Fig. 2.4(a) as solid lines for different times.

2.3 Discussion

Our above results establish the basis for the rapid and robust coating process to fabricate spherical elastic shells of nearly uniform thickness, and with radii spanning over two orders of magnitudes ($1 \le R^*$ [mm]≤ 375). As the radius of the sphere is decreased below $R^* < 10$ mm, the agreement between our model and the experiments deteriorates due to the influence of the meniscus that connects the flow on the hemisphere to the puddle that forms as the fluid drains. This effect is not accounted for in our model, but we expect it to be negligible when $R^* \gg \ell_c^*$, where $\ell_c^* = \sqrt{\gamma/(\rho g)}$ is the capillary length that prescribes the relative magnitude of capillary and gravitational forces. Since $\ell_c^* \simeq 1.3$ mm and $\ell_c^* \simeq 1.4$ mm for VPS and PDMS, respectively, the deviations of the theory from the data for small R^* are consistent with the onset of these surface tension effects (see Fig. 2.1(c) and Fig. 2.3(a)).

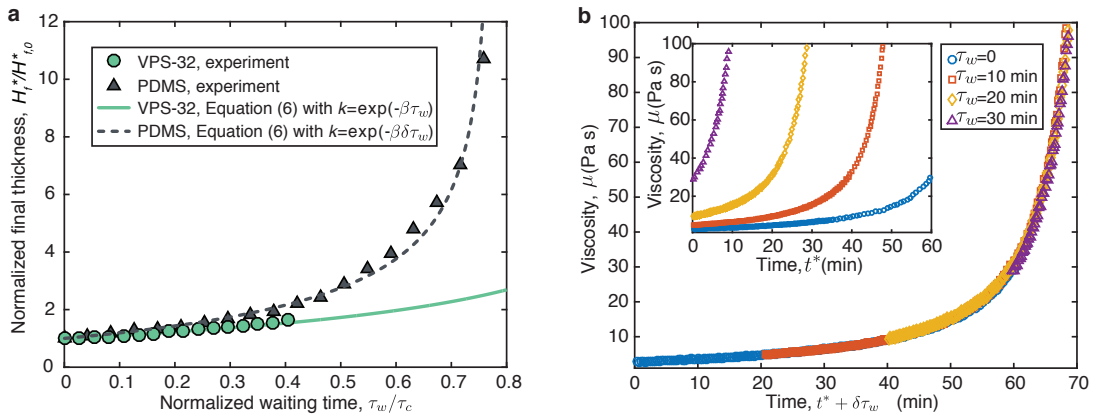

Figure 2.5 – Varying the shell thickness by delaying pouring. (a) The shell thickness (normalized by its value $H^*_{f,0}$ when $\tau_w = 0$) can be tuned by delaying the pouring time by τ_w from the moment of preparation of the polymer solution. Results for both VPS-32 and PDMS are shown. (b) Viscosity of PDMS versus the sum of the measuring time, t^*, and the effective waiting time, $\delta\tau_w$ ($\delta = 2.02 \pm 0.02$ from fitting all the curves to the master curve obtained for $\tau_w = 0$). Inset: Viscosity as measured after holding the mixture for a time τ_w in a quiescent state prior to testing in the rheometer.

Our model, *e.g.* equation (2.20), uses the physical parameters for the rheology of the polymer. PDMS was found to behave as a Newtonian fluid for small shear rates (but the viscosity varies with time; see Fig. 2.5(b)) whereas VPS exhibited shear thinning (see Supplementary Figs. 3 and 4). An estimate of the relevant shear rate is therefore needed. We used the value $\dot{\gamma}^* = 0.1$ s^{-1}, assuming a uniform shear rate across the sample. In reality, $\dot{\gamma}^*$ varies from zero at the apex to its peak value at the equator (and also depends on R^*). However, our choice for $\dot{\gamma}^*$ is representative of the applied shear rates over the hemisphere and leads to good agreement between theory and experiments for most values of R^* and θ. We have analyzed the sensitivity of the predictions for H_f^* with respect to $\dot{\gamma}^*$ and found that it is small (see Supplementary Note 1).

The variation of the thickness from the pole to the equator of the hemispherical shells was found to be, at most, 6.6% (VPS) and 8.7% (PDMS) from the experiments, 8.7% in the theoretical model, and 8.4% in the numerical analysis (using standard deviations). For PDMS, the thickness profile follows equation (2.20) without any adjustable parameters. This agreement validates our model for the case of time varying viscosities (Fig. 2.3(b)). For VPS, shear thinning effects lead to an increase of the thickness at the apex (see Fig. 2.3(a)); where the viscosity is largest. These effects are not captured by our model, yet they do not prevent the shell from being uniform within 6.6% variations. We argue that these same effects are the source of the difference between the numerics and the measured free surface velocity for large times (see Fig. 2.2(c)).

When the polymer is poured on the underside of a mold, curvature can suppress the Rayleigh-

Taylor instability and thereby prevent the formation of dripping droplets (Trinh et al., 2014). Therefore, the uniformity bounds of the shell that were just stated are ensured, as long as the modified Bond number $Bo = \rho g R^* H_i^* / \gamma$ remains smaller than the critical value, $Bo < 24$ (see Chapter 5). On the other hand, when the outside of a mold is used, fingering instabilities can occur at the advancing front of the flow, but this can be precluded by pouring a sufficiently large volume of liquid over the surface (Takagi & Huppert, 2010), see also Chapter 6. A critical volume may be derived following Takagi & Huppert (2010) and we estimated it be of the order of 1 mL for an hemisphere of radius $R^* = 20$ mm, in agreement with what was observed experimentally for the sensitivity analysis in Fig. 2.4(b). Under these conditions, pouring on the underside or the outside of complementary molds yields identical shells of the same uniform thickness, H_f^*. Note that during this process an $\approx 90\%$ of the volume drains out of the hemisphere. Even if this technique is an excellent rapid-prototyping method, it may not be suitable for large scale industrial applications. Similar limitations are found for spin-coating.

The physical principles that underlay the dynamics of the coating process are rationalized by our analytical model above, to which the separation between the initial drainage and curing timescales is key. Drainage occurs significantly faster than the polymer curing, such that the memory of the flow vanishes before it is arrested by cross-linking to yield the final elastic shell. Consequently, geometry prevails, and the curvature of the mold together with the rheology of the polymer set both the dynamics of the flow and the final thickness of the shell ($H_f^* \sim \sqrt{R^*}$). The robustness of this mechanism and its insensitivity to the initial conditions are now corroborated by both experiments and simulations. We measured the thickness of shells obtained for different values of the height from which the polymer is poured onto the mold ($4 \leq H_p^*$ [cm] ≤ 10), as well as the volume poured ($0.9 \leq V^*$ [mL] ≤ 6.3), and find that H_f^* is constant to within 5.6% across these various conditions (Fig. 2.4(b)). Furthermore, simulations that were initiated with four significantly different initial fluid distributions – uniform, sinusoidal, as well as tapered profiles towards the pole and the equator – all converge to the same final shell thickness, which agrees well with the prediction from equation (2.20), as shown in Fig. 2.4(c).

Since the final shell thickness is directly connected to the curing time, H_f^* can be continuously tuned by waiting a time τ_w between the preparation of the polymer mixture and the instant when it is poured onto the mold. In Fig. 2.5(a), H_f^* is plotted versus τ_w, for the representative experiments with both VPS-32 and PDMS. We find that H_f^* can be increased by as much as 60% for VPS-32 and elevenfold for PDMS. The tuned final thickness by delayed pouring can be obtained by changing the bounds of the integral $\int_0^{t^*} \frac{1}{\mu(t')} dt'$ to $\int_{\tau_w}^{t^*} \frac{1}{\mu(t')} dt'$ in Eq. (2.18), which results in $k = e^{-\beta \tau_w}$. The velocity estimate then becomes

$$U^*(\theta, t^*) \approx \frac{3}{8} \frac{\beta(\alpha-1)\tau_c^\alpha}{(\alpha-1)(e^{\beta\tau_c}-1)+\tau_c\beta} \frac{R^*}{t^{*\alpha}} \left(1+\frac{\theta^2}{10}\right)^2 \sin\theta = \frac{3}{8} \frac{\tau_c^\alpha}{e^{\beta\tau_c} K} \frac{R^*}{t^{*\alpha}} \left(1+\frac{\theta^2}{10}\right)^2, \quad (2.21)$$

where we highlight the fast temporal decrease of the velocity $U^* \sim t^{*-\alpha}$ and its independence on the viscosity, density and gravity. Substituting $e^{-\beta\tau_\mathrm{w}}$ for k in equation (2.20) allows for a

direct comparison to the experimental result, with favorable agreement in the case of VPS-32 (solid curve in Fig. 2.5(a)). For the PDMS, however, an additional adjustment to our framework is required since we found that its rheology differs if the curing occurred in a quiescent state (*e.g.*, when waiting in bulk for τ_w before pouring) versus when sheared (*e.g.*, during coating). Rheometry measurements were performed where the values of τ_w were systematically varied (inset of Fig. 2.5(b)). If the time axis for each of these tests is shifted by $\delta\tau_w$ (the constant factor $\delta = 2.02 \pm 0.02$ was determined by fitting), all of the data collapses onto the master curve obtained for $\tau_w = 0$. We have therefore concluded empirically that PDMS cures δ times faster when quiescent compared to under shear, but we have not been able to find this specific result in the literature. We speculate that the shifting factor required for collapse will likely depend on the shear rate and the specifics of the polymer. With this additional information at hand, substituting $e^{-\beta\delta\tau_w}$ for k in equation (2.20) accounts for the effective waiting time, and yields a prediction for H_f^* (dashed line in Fig. 2.5(a)) that is in agreement with the experimental data for PDMS. Our model is therefore able to accurately capture the elevenfold continuous variation of the shell thickness obtained when pouring partially cured polymer solutions. As explained in the Supplementary Note 2, we did not have to consider δ for VPS-32 because the entire bulk of this more viscous polymer solution is experiencing sustained shear while it was sequentially poured onto a series of identical molds. It is important to note that our theoretical description is only applicable if $\tau_w < \tau_c$.

In summary, we have shown that coating hemispherical molds with a polymer solution yields thin uniform shells whose thickness can be accurately predicted. Moreover, the final shell thickness can be tuned by modifying the time between polymer preparation and the moment of pouring. The resulting shells are a realization of the drainage dynamics, driven by gravity, slowed down by viscous stresses and eventually arrested by the curing of the polymer. The robustness and flexibility of this mechanism are inherent consequences of the loss of memory in the flow field. The generality of this framework should open the door for future studies to fabricate slender solid structures in a variety of other geometries. A particularly interesting case outside the scope of the current study is the coating of ellipsoidal molds (Ebrahimi, Ajdari, Vella, Boudaoud & Vaziri, 2014), with two distinct principal curvatures, where the difference between the pouring direction and the orientation of the surface could also play a role. Furthermore, our fabrication technique could be important in the ongoing revival of the mechanics of thin elastic shells, in particularly since it enables fully elastic structures that can reversibly explore strong geometric nonlinearities in their post-buckling regime (Audoly & Pomeau, 2010; Vaziri & Mahadevan, 2008; Katifori, Alben, Cerda, Nelson & Dumais, 2010; Lazarus, Florijn & Reis, 2012; Terwagne, Brojan & Reis, 2014; Stoop, Lagrange, Terwagne, Reis & Dunkel, 2015; Nasto & Reis, 2014; Vella, Huang, Menon, Russell & Davidovitch, 2015; Bende, Evans, Innes-Gold, Marin, Cohen, Hayward & Santangelo, 2015; Reis, 2015).

2.4 Methods

2.4.1 Experiments

Curing of the PDMS (Sylgard 184, Dow Corning) was performed in a convection oven at 20, 35 and 40°C. The base and curing agent were mixed in a 10:1 weight ratio using a centrifugal mixer for 30 s at 2000 rpm (clockwise), and then for 30 s at 2200 rpm (counterclockwise). We sped up the curing process using a cure accelerator (3-6559 Cure Accelerator, Dow Corning) that was mixed to the PDMS elastomer in the weight proportion 5:1 (PDMS-base:Cure-accelerator). VPS (Elite Double 8, 22 and 32, Zhermack, referenced throughout the text as VPS-8, VPS-22 and VPS-32, respectively) was mixed at room temperature (20°C) with a base/cure ratio 1:1 in weight for 10 s at 2000 rpm (clockwise), and then 10 s at 2200 rpm (counterclockwise).

The various polymer solutions (VPS and PDMS) were characterized with a rheometer (AR-G2, TA Instruments) as a function of time and at a constant temperature. The shear rate was fixed at $\dot{\gamma}^* \approx U^*/H^* \approx 0.1\ \mathrm{s}^{-1}$, consistently with the characteristic drainage velocity and film thickness (see Supplementary Note 1 and Supplementary Fig. 2). The data for the measured viscosity was then fitted with the piecewise model $\mu(t^* \le \tau_c) = \mu_0 \exp(\beta t^*)$ and $\mu(t^* > \tau_c) = \mu_1 t^{*\alpha}$ (see Fig. 2.2(d) and Supplementary Fig. 1).

The velocity field of the draining polymer was measured using an open-source package for particle imaging velocimetry (PIVlab (Thielicke & Stamhuis, 2014)). A powder spray (Sparkler, Body Shop) was sputtered onto the surface of the flow and imaged using a digital microscope camera (Discovery VMS-004, Veho).

Upon curing, the final thickness, H_f^*, of the hemispherical elastic shells was measured with an optical microscope after cutting the shell along a meridian using a scalpel (insets of Fig. 2.1(c) and 2.3(a)).

2.4.2 Numerical simulations

A numerical procedure was developed to solve equation (2.7). The polar angle is discretized uniformly, and we exploit the periodic domain and employ the Fourier spectral method (Weideman & Reddy, 2000) to compute spatial derivatives with a high degree of accuracy. The effect of numerical diffusion is minimized by performing the time integration with the second-order Crank-Nicolson MATLAB routine `ode23t.m`. The computational time to derive a solution for a set of geometric and physical parameters is of the order of a few minutes.

To verify the numerics, we compare the numerical solution for an initially uniform film with the analytical solution obtained in the limit $\delta = H_i^*/R^* \to 0$ and $\theta = 0$, namely $H(0,t) = (1+4t/3)^{-1/2}$. Figure 2.6 shows good agreement between the analytical and the numerical solutions, using $N = 256$ discretization points.

To complement the comparison between the numerics and the 2nd-order asymptotic solution

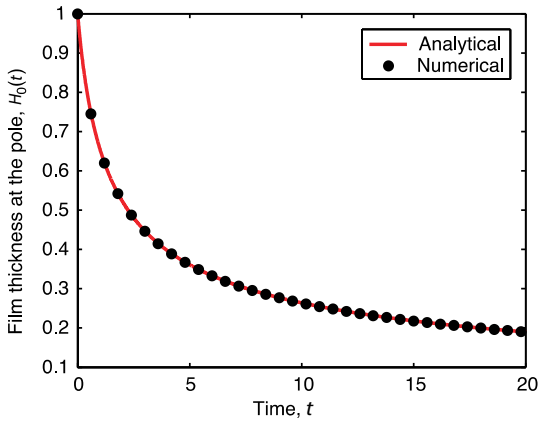

Figure 2.6 – Time evolution of the dimensionless thickness of the film at the pole. Comparison between analytical and numerical solutions for the film-thickness evolution at $\theta = 0$ with $N = 256$, $Bo = 2.3$ and $\delta = 0.01$ (N is the number of discretization nodes, Bo is the modified Bond number defined in the main text, $\delta = H_i^* / R^*$ is the aspect ratio of the film). These results act as a verification of the simulations with the theoretical model, both of which are validated with experiments in the main text.

shown in Fig. 2.4(a), we have obtained results with both methods for sinusoidal initial thickness profiles of the form $H(\theta,0) = 1 + A\cos\theta$ with $A = \{-0.5, 0, 0.5\}$. These results are plotted in Fig. 2.7 and confirm that our asymptotic solution is indeed able to predict the correct dynamics for moderate nonuniform film distributions.

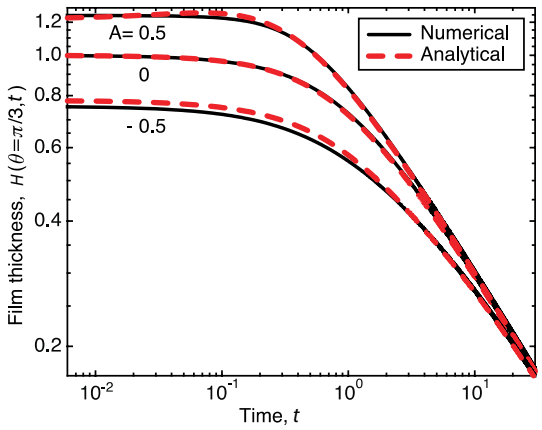

Figure 2.7 – Time evolution of the dimensionless thickness of the film for initially sinusoidal thickness profiles. Comparison between the film-thickness evolution computed numerically and the 2nd-order asymptotic solution, both of which for initially sinusoidal thickness profiles, $H(\theta,0) = 1 + A\cos(\theta)$ with $A = \{-0.5, 0, 0.5\}$. The dimensionless governing parameters for Eq. (2.7) are $\delta = 0.01$ and $Bo = 2.3$.

Acknowledgments This work was supported by the National Science Foundation, CAREER CMMI-1351449 (A.L. and P.M.R.), and by the European Research Council, ERC-2011-StG, PE8 SIMCOMICS (G.B. and F.G.).

Supplementary Information The Supplementary Information can be found at https://www.nature.com/articles/ncomms11155#supplementary-information.

3 Rayleigh-Taylor instability under curved substrates: An optimal transient growth analysis

Remark This chapter is largely inspired by the publication of the same name

G. Balestra[1], P.-T. Brun[2] and F. Gallaire[1]

[1]Laboratory of Fluid Mechanics and Instabilities, EPFL, CH1015 Lausanne, Switzerland
[2]Department of Mathematics, Massachusetts Institute of Technology, Cambridge, Massachusetts 02139, USA

Physical Review Fluids **1**, 083902 (2016)

We investigate the stability of thin viscous films coated on the inside of a horizontal cylindrical substrate. In such a case, gravity acts both as a stabilizing force through the progressive drainage of the film and as a destabilizing force prone to form droplets via the Rayleigh-Taylor instability. The drainage solution, derived from lubrication equations, is found asymptotically stable with respect to infinitesimally small perturbations, although in reality, droplets often form. To resolve this paradox, we perform an optimal transient growth analysis for the first-order perturbations of the liquid's interface, generalizing the results of Trinh *et al.* [Phys. Fluids **26**, 051704 (2014)]. We find that the system displays a linear transient growth potential that gives rise to two different scenarios depending on the value of the Bond number (prescribing the relative importance of gravity and surface-tension forces). At low Bond numbers, the optimal perturbation of the interface does not generate droplets. In contrast, for higher Bond numbers, perturbations on the upper hemicircle yield gains large enough to potentially form droplets. The gain increases exponentially with the Bond number. In particular, depending on the amplitude of the initial perturbation, we find a critical Bond number above which the short-time linear growth is sufficient to trigger the nonlinear effects required to form dripping droplets. We conclude that the transition to droplets detaching from the substrate is noise and perturbation dependent.

3.1 Introduction

We refer to Sec. 1.2 for a general introduction on the Rayleigh-Taylor instability.

In this chapter we apply a nonmodal transient growth analysis to the RTI under a curved substrate (Schmid, 2007). In contrast to the classical studies (see Sec. 1.2.2), the base flow is time-dependent, which rules out any classical eigenvalue calculation. The optimal initial conditions maximizing the gain are computed on the entire physical space for several time horizons, Bond numbers and finite film thicknesses. These calculations allow for a better understanding of the most amplified perturbations yielding the droplet formation. Two regimes are evidenced. For surface-tension-dominated flows, the optimal perturbations are fronts and their maximal gain is achieved when located at the equator. When gravity dominates surface tension, optimal perturbations correspond to oscillations at the north pole, possibly resulting in droplets. Indeed, large-Bond-number regimes display a strong transient growth of perturbations which, in turn, might trigger the nonlinear effects at the origin of the droplet formation and dripping observed in experiments. Using nonlinear simulations, we show that depending on the initial perturbation amplitude, there indeed exists a critical Bond number above which dripping droplets start to occur.

The chapter is structured as follows. Section 3.2.1 presents the governing equations of the problem, the transient growth analysis is explained in Sec. 3.2.2 and the employed numerical methods are shown in Sec. 3.2.3. The results are presented in Sec. 3.3. The two regimes are introduced in Sec. 3.3.1, and their dependence on the Bond number and on the film aspect ratio are described in in Secs. 3.3.2 and Sec. 3.3.3, respectively. The transient growth analysis over the entire geometry is discussed and compared to the one at the north pole in Sec. 3.4.1. Nonlinear simulations are discussed in Sec. 3.4.2. Conclusions are drawn in Sec. 3.5.

3.2 Governing equations and Methods

3.2.1 Lubrication and linear perturbation equations

The inside of a cylindrical substrate of inner radius R^* is coated with a viscous film of dimensionless thickness $\bar{H}(\theta,t)$ (using the initial average film thickness H_i^* as a gauge), as depicted in Fig. 3.1(a). The drainage of this film occurs over a typical time $\tau_d = \mu R^*/(\rho g H_i^{*2})$, where μ is the dynamic viscosity, ρ is the density and g is the gravitational field.

Owing to the small aspect ratio, and the typically large viscosity of the fluid used in such coatings, we model the flow using lubrication equations (Oron et al., 1997). From the continuity equation one may show that the flow velocity is essentially one-dimensional (in the polar direction θ, tangent to the substrate). Integrating the Stokes equations along the radial direction with the proper set of boundary conditions and considering mass conservation, the

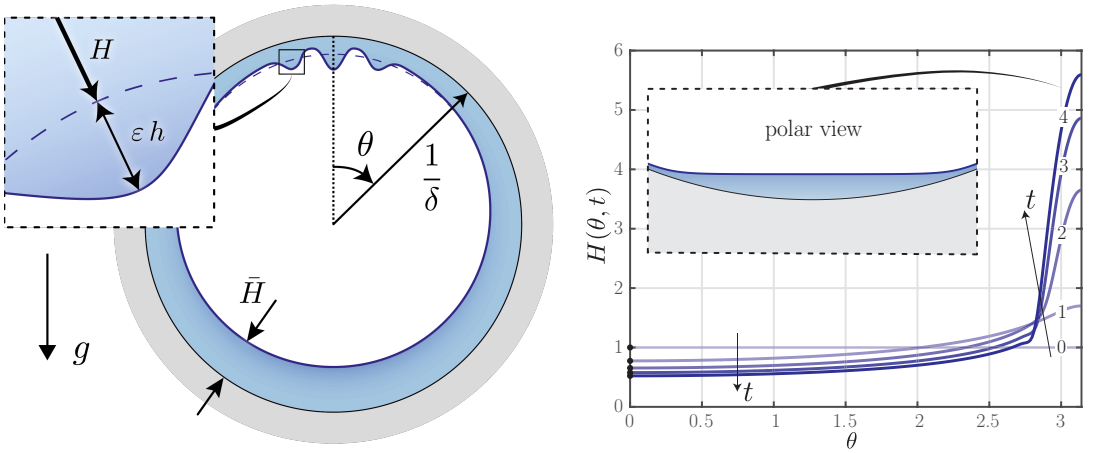

Figure 3.1 – (a) Sketch of the two-dimensional problem geometry. Inset: decomposition of film thickness $\bar{H}$ into draining solution H and first order perturbations εh. (b) Evolution of the drainage solution H at several times. The black bullets on the left represent the analytical solution at $\theta = 0$, $H(0,t) = (1+2t/3)^{-1/2}$. $Bo = 20$ and $\delta = 10^{-2}$. Inset: fluid profile at the bottom of the cylinder for $t = 4$.

following lubrication equation is obtained (see Appendix 3.6.1 for the complete derivation):

$$\bar{H}_t + \frac{1}{3}\left\{\bar{H}^3\left[\frac{\delta^2}{Bo}(\bar{H}_{\theta\theta\theta} + \bar{H}_\theta) + \delta\bar{H}_\theta\cos\theta + \sin\theta\right]\right\}_\theta = 0, \tag{3.1}$$

where indices represent partial derivatives. The modified Bond number representing the ratio between gravitational and surface-tension forces, incorporating also geometric parameters, is given by $Bo = \rho g H_i^* R^*/\gamma$, where γ is the surface tension. The second dimensionless parameter of the problem is the aspect ratio of the film, defined as $\delta = H_i^*/R^*$. Note that only the leading order terms of the curvature are kept.

The film-thickness evolution has to be computed numerically (see Sec. 3.2.3 for details) since there is no analytical solution of Eq. (3.1) for finite aspect ratios δ and Bond numbers Bo. The solution resulting from an initially uniform film profile is shown in Fig. 3.1(b). As will become clear later, this solution is asymptotically linearly stable and we will refer to it as *drainage solution* $H(\theta,t)$. In the limit of vanishing aspect ratios, $\delta \ll 1$, and negligible surface tension effects, $Bo \gg \delta^2$, we can show that equation (3.1) has an approximate solution of the form $(1+\theta^2/16)/\sqrt{1+2\,t/3}$ (see Chapters 2 and 4) close to the north pole (Takagi & Huppert, 2010) and a similarity solution for the upper hemicircle, following Couder et al. (2005). As seen in Fig. 3.1(b), the analytical solution for $\theta = 0$ is in good agreement with the numerical one also for finite δ- and Bo-values.

In order to obtain the linear perturbation equation necessary for the transient growth analysis,

we decompose the film thickness as (see inset of Fig. 3.1(a)):

$$\bar{H}(\theta,t) = \underbrace{H(\theta,t)}_{\text{drainage solution}} + \varepsilon \underbrace{h(\theta,t)}_{\text{perturbation}}, \quad \varepsilon \ll 1. \tag{3.2}$$

The *perturbation* εh corresponds to the difference between the perturbed film dimensionless thickness $\bar{H}$ and the smooth draining solution H. Note that the same lubrication equation (3.1) and nondimensional parameters have been used by Trinh et al. (2014). However, the decomposition into drainage solution and perturbation is slightly different; in our case, the entire temporal dependence of the perturbation is contained in $h(\theta,t)$. The implications of the different definitions are discussed in Sec. 3.4.1.

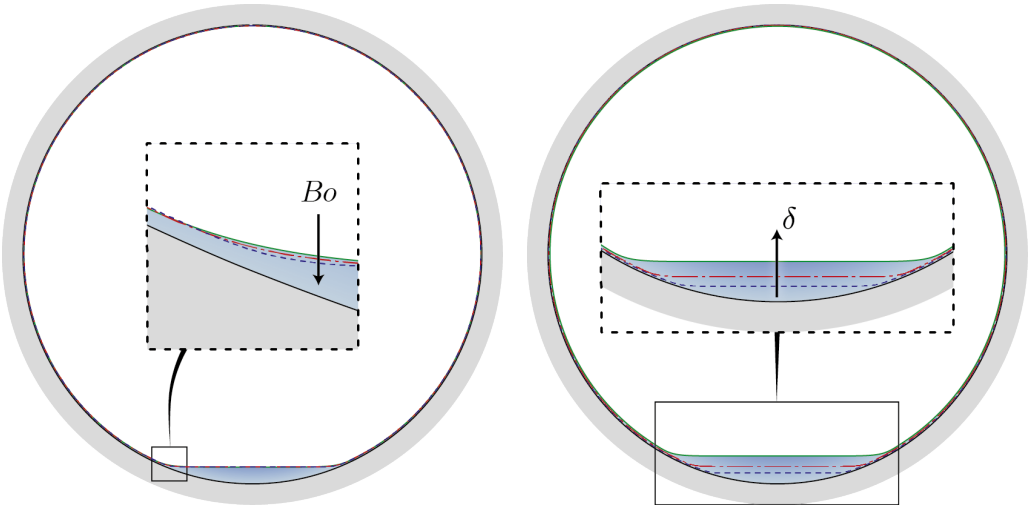

Figure 3.2 – Effect of the Bond number (a) and of the film aspect ratio (b) on the draining solution H at the time $t = 10$. (a) $Bo = 5$, 10 and 50 for $\delta = 10^{-2}$, (b) $\delta = 5\cdot10^{-3}$, 10^{-2} and $2\cdot10^{-2}$ for $Bo = 20$.

The structure of the flow is reported in Fig. 3.2. The thin film occupies the most part of the domain and connects to a small pool, which forms at the bottom of the cylinder. The Bond number affects the curvature of the meniscus bridging the pool and the film (see inset of Fig. 3.2(a)). Increasing the Bond number leads to an increase of the curvature of this meniscus, while no significant changes of the film thickness could be registered at the north pole. In contrast, changing δ directly affects the volume of fluid in the cylinder relative to its size, thereby impacting all quantities as anticipated by dimensional analysis.

We now proceed to derive the linear perturbation equations of the system. We substitute the decomposition (3.2) into the nonlinear film-thickness evolution (3.1) and consider first order terms in ε only to obtain:

$$\mathbf{h}_t + \mathbf{L}(H, Bo, \delta)\,\mathbf{h} = \mathbf{0}, \tag{3.3}$$

where $\mathbf{L} = \mathbf{L}(H, Bo, \delta)$ is the linear operator which depends on the drainage solution, the Bond number and the aspect ratio. The detailed expression of $\mathbf{L}$ is given in Appendix 3.6.2.

3.2.2 Transient growth analysis

The drainage solution being space and time dependent, the linear operator in Eq. (3.3) is a function of the polar angle θ and is not autonomous. As a consequence, we cannot use a normal mode ansatz for the perturbation and we therefore proceed to a nonmodal analysis. With this method, we seek for the amplification of the perturbation at finite times.

We start by defining the gain function that we will be using to find optimal initial conditions. In our study we consider the ratio of the square of the actual perturbation norm to the initial value. A L_2 norm is chosen since both variations in potential energy and in surface energy are proportional to $\langle \mathbf{h}|\mathbf{h}\rangle$ (Olsson & Henningson, 1995). Thereby, the gain at the temporal horizon T reads:

$$G(T) = \frac{\langle \mathbf{h}(T)|\mathbf{h}(T)\rangle}{\langle \mathbf{h}_0|\mathbf{h}_0\rangle}, \tag{3.4}$$

where the Hermitian scalar product for real quantities on the geometry $\Omega = \{\theta \,|\, \theta \in [0, 2\pi]\}$ is defined by

$$\langle \mathbf{a}|\mathbf{b}\rangle = \int_\Omega \mathbf{a}^T \mathbf{b}\, \mathrm{d}\theta = \mathbf{a}^T \mathbf{M} \mathbf{b}. \tag{3.5}$$

In order not to favor perturbations at a specific location, a mass matrix with uniform weights is employed:

$$\mathbf{M} = \frac{2\pi}{N}\mathbf{I}, \tag{3.6}$$

with N being the number of discretization points and $\mathbf{I}$ being the identity matrix. The initial condition is given by $\mathbf{h}_0 = \mathbf{h}(0)$.

For time-independent operators, the perturbation's evolution can be computed using the propagator operator. The optimal initial condition is directly obtained by the singular value decomposition of the propagator operator (Schmid & Henningson, 2001). While such eigenvalue methods can also be generalized for time-dependent operators (Barkley, Blackburn & Sherwin, 2008; Mao, Blackburn & Sherwin, 2013), the optimal growth can also be conveniently obtained with a variational formulation and adjoints fields (Schmid, 2007). A comparison between the two methods has been pursued by Mao et al. (2013), showing that eigenvalue approaches are preferable when dealing with large-dimensional problems.

Here, the constraints resulting from the governing equation and the initial condition are enforced via the Lagrange multipliers $\mathbf{h}^\dagger$ and $\mathbf{h}_0^\dagger$, respectively. Since these constrains have to be fulfilled locally, the Lagrange multipliers are space (and time, for $\mathbf{h}^\dagger$) dependent. They are

governed by the so called adjoint equations. The augmented Lagrangian consisting of the objective function to be optimized and the constraints reads:

$$\mathscr{L}\left(\mathbf{h},\mathbf{h}^\dagger,\mathbf{h}_0,\mathbf{h}_0^\dagger;T\right)=\underbrace{G(T)}_{\text{gain}}-\underbrace{\int_0^T\langle\mathbf{h}^\dagger\left|\mathbf{h}_t+\mathbf{L}\mathbf{h}\right\rangle\mathrm{d}t}_{\text{enforcing governing equation}}-\underbrace{\langle\mathbf{h}_0^\dagger\left|\mathbf{h}(0)-\mathbf{h}_0\right\rangle}_{\text{enforcing initial condition}}\quad. \tag{3.7}$$

The last two terms of Eq. (3.7) penalize the Lagrangian if the fields $\mathbf{h}$ and $\mathbf{h}_0$ do not satisfy the governing equation (3.3) and the initial condition.

The adjoint fields equations are obtained by setting to zero the first variations of $\mathscr{L}$ with respect to any variation $\delta\mathbf{h}$ (see derivation in the Appendix 3.6.3):

$$\langle\frac{\partial\mathscr{L}}{\partial\mathbf{h}}\Big|\delta\mathbf{h}\rangle=0\,,\ \forall\,\delta\mathbf{h}\Leftrightarrow\mathbf{h}^\dagger(T)=2\frac{\mathbf{h}(T)}{\langle\mathbf{h}_0|\mathbf{h}_0\rangle}\,, \tag{3.8}$$

$$\mathbf{h}_t^\dagger-\mathbf{L}^\dagger\mathbf{h}^\dagger=\mathbf{0}\quad t\in[0,T]\,, \tag{3.9}$$

$$\mathbf{h}_0^\dagger=\mathbf{h}^\dagger(0)\,, \tag{3.10}$$

where $\mathbf{L}^\dagger$ is the adjoint operator, defined as $\langle\mathbf{a}|\mathbf{L}\mathbf{b}\rangle=\langle\mathbf{L}^\dagger\mathbf{a}|\mathbf{b}\rangle$. Instead of analytically finding the continuous adjoint of the direct operator, we follow Schmid & Henningson (2001) and use the discrete adjoint, which for an identity weight matrix, see Eq. (3.6), reduces to the transpose: $\mathbf{L}^\dagger=\mathbf{L}^T$. The adjoint equation (3.9) has to be integrated backward in time with the terminal condition given by Eq. (3.8). The Lagrange multiplier $\mathbf{h}_0^\dagger$ turns out to be the final value of the adjoint field $\mathbf{h}^\dagger$. Additionally, the stationarity condition with respect to the control variable $\mathbf{h}_0$ yields the optimality condition:

$$\langle\frac{\partial\mathscr{L}}{\partial\mathbf{h}_0}\Big|\delta\mathbf{h}_0\rangle=0\,,\ \forall\,\delta\mathbf{h}_0\ \Leftrightarrow\ \mathbf{h}_0=\mathbf{h}_0^\dagger\frac{\langle\mathbf{h}_0|\mathbf{h}_0\rangle^2}{2\,\langle\mathbf{h}(T)|\mathbf{h}(T)\rangle}\,. \tag{3.11}$$

By deriving the augmented Lagrangian by their multipliers one retrieves the constraints.

In order to compute the optimal initial conditions, the algorithmic approach schematized in Fig. 3.3 is employed. The linear equation Eq. (3.3) is integrated forward in time from $t=0$ to

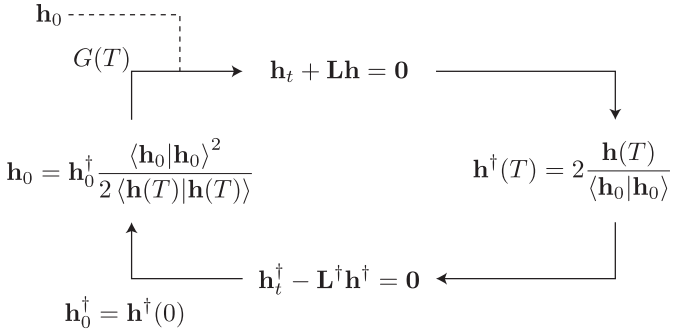

Figure 3.3 – Sketch of the iterative procedure to find the optimal gain and initial condition for a given time horizon T, Bond number Bo and film aspect ratio δ.

the chosen time horizon $t = T$, using an arbitrary initial condition $\mathbf{h}_0$. The initial condition for the adjoint equation is then computed from Eq. (3.8) and the adjoint equation (3.9) is integrated backward in time from $t = T$ to $t = 0$. Using Eq. (3.10), the new guess of the optimal initial condition is then given by Eq. (3.11). The forward and backward integrations have to be continued until convergence of the gain $G(T)$ introduced in Eq. (3.4). Since the direct and adjoint linear operators are not mass preserving, the mass of the initial condition is subtracted at every iteration to find zero-mass optimal perturbations. If this step is omitted, the optimality condition would be biased by initial perturbations adding mass to the system. Note that this constraint could also have been included as a constraint in the augmented Lagrangian (3.7). However, for the imposition of such a single scalar constraint, the use of a projection method is equivalent from a computational-cost point of view. At first order, the zero-mass condition for the perturbations is:

$$m = \int_\Omega h_0(\theta) \left[\frac{1}{\delta} - H(\theta, 0) \right] \mathrm{d}\theta = \left(\frac{1}{\delta} - 1 \right) \int_\Omega h_0(\theta) \mathrm{d}\theta = 0 \,,$$

where the uniform initial drainage profile $H(\theta, 0) = 1$ has been used. The resulting gain $G(T)$ and the initial condition $\mathbf{h}_0$ are the optimal for the time horizon T. By repeating the algorithm for several time horizons, all other things being equal, one obtains the envelope of the optimal amplifications for a given Bond number and film aspect ratio δ. For each increment of horizon time T, the optimal initial condition of the previous time horizon is used as the initial guess. Examples of such quantities are given in Fig. 3.4 and are discussed in section 3.3.1.

The final step of our method consist in identifying the maximum $G_{\max}$ of $G(T)$ for each couple (Bo, δ), which is associated to an optimal growth and initial condition. Examples are shown in Fig. 3.5 and are discussed in section 3.3.1. Prior to commenting on the obtained results, we briefly evoke our numerical methods.

3.2.3 Numerical methods

A numerical procedure was developed to solve the highly nonlinear Eq. (3.1) as well for the transient growth study. The polar angle $\theta \in [0, 2\pi]$ is uniformly discretized with N collocation points. We exploit the periodicity of the domain and use Fourier spectral methods (Weideman & Reddy, 2000) to compute spatial derivatives with a high degree of accuracy (Trefethen, 2000). The effect of numerical diffusion is minimized by performing the time integration with the second-order Crank-Nicolson MATLAB routine `ode23t.m`.

It is important to state that the discretization scheme is accurate enough to avoid the amplification of numerical errors up to $Bo \approx 350$. The base flow solution is therefore exempt of transient waves and can be used for the stability analysis for the considered Bond number range.

First, the drainage solution for a given set of physical and geometrical parameters is calculated with a computation time of the order of a few minutes on a single Intel Core at 2.6 GHz.

Second, the iterative scheme giving the optimal condition is ran. In order to reduce the memory-storage requirement, the direct and adjoint linear operators are built at several time steps and not computed a priori for the entire time interval. Yet, due to the repeated forward and backward integrations, the computation of the optimality conditions and the evaluation of the largest gain are computationally more expensive than the first step. The computation of the optimal conditions for the entire Bond number and aspect ratios range is of the order of few days, depending on the number of time horizons considered. For more details and a series of validation tests see the Appendix 3.6.4.

To complement these tools we used the open source two-phase 2D Stokes solver Ulambator (Nagel & Gallaire, 2015) (see Sec. 3.4.2).

3.3 Results

3.3.1 Optimal perturbation regimes

The results of the optimal transient growth analysis are presented hereafter; a deeper discussion follows in Sec. 3.4. The dependence of the optimal gains as a function of the time horizon, as well as some corresponding initial perturbations and resulting responses, are presented in Fig. 3.4 for two different Bond numbers, $Bo = 10$ and $Bo = 50$. Common to all

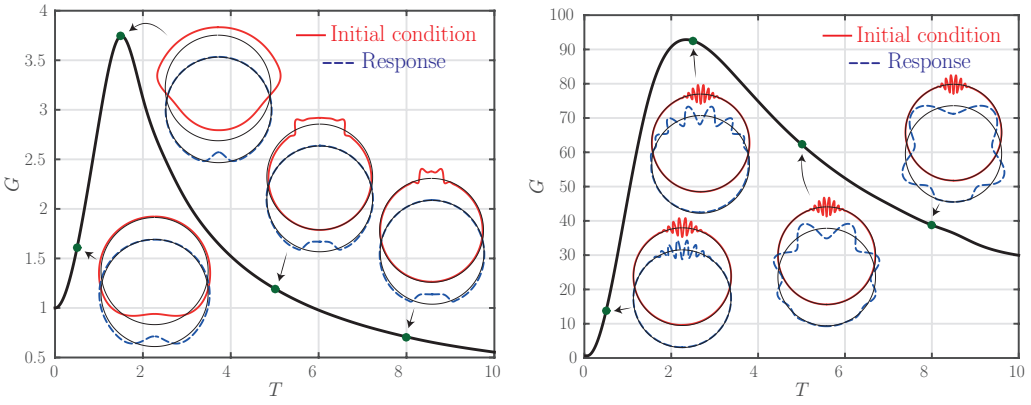

(a) (b)

Figure 3.4 – Optimal gains as a function of the time horizon for two Bond numbers: (a) $Bo = 10$ and (b) $Bo = 50$. $\delta = 10^{-2}$. For visualization purposes the initial conditions (solid red) and responses (dashed blue) are normalized by their respective largest value and magnified by 20.

explored cases is the shape of $G(T)$, where the gain tends to zero for large enough values of T, revealing the asymptotic stability of the film. As a consequence, we focus our attention on the amplifications over a short, yet finite, time period.

Although the system is asymptotically stable independently of the parameters, the respective values of $G_{\max}$ depend significantly on the Bond number, ranging from less than 4 for $Bo = 10$

in Fig. 3.4(a) to more than 90 for $Bo = 50$ in Fig. 3.4(b). In addition to this quantitative difference, the two cases also differ qualitatively. The optimal initial conditions for $Bo = 10$ correspond to perturbations with a front whose location gets closer to the north pole as the time horizon increases. In fact, these fronts are solely convected downstream by the draining flow until the final time T. Their maximal gain is achieved when the front is close to the equator, here for $T \approx 1.5$. On the other hand, for $Bo = 50$, the optimal initial conditions are oscillations of the interface at the top of the geometry. They are largely amplified (not visible on the responses of Fig. 3.4 because of normalization) and travel downstream.

3.3.2 Influence of the Bond number

When increasing the Bond number for a given film aspect ratio δ, the optimal perturbation switches from a front to oscillations at the top as shown in Fig. 3.5(a) along with the values of the largest obtainable gain (and the corresponding optimal time in Fig. 3.5(b)). The transition

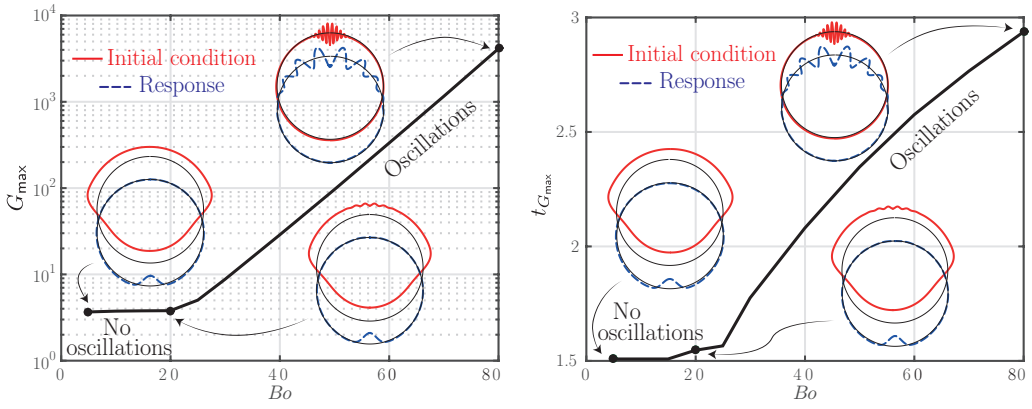

Figure 3.5 – Largest optimal gains $G_{\max}$ (a) and time horizons $t_{G_{\max}}$ (b) as a function of the Bond number. $\delta = 10^{-2}$. For visualization purposes the initial conditions (solid red) and responses (dashed blue) are normalized by their respective largest value and magnified by 20. The two regimes are highlighted.

between these two type of instabilities is identified. For $\delta = 10^{-2}$, the critical Bond number corresponding to the transition from nonoscillating to oscillating perturbations is around 20. Nonoscillating perturbations display a constant maximal optimal gain $G_{\max}$ which is reached at the same time horizon of $T \approx 1.5$. At $Bo = 20$, the optimal initial condition corresponds to a mix of front and oscillating perturbations and is obtained at a slightly later time. The draining front is still present, but oscillations start to appear at the north pole. For higher Bond numbers, the oscillating perturbations are characterized by a largest optimal gain whose value increases exponentially with the Bond number. Although the draining flow makes the system asymptotically stable, the potential amplification due to the Rayleigh-Taylor instability at short times is unbounded as the Bond number increases. The system behaves as a (very

effective) noise amplifier. The corresponding optimal time as a function of Bo is found to follow a power law with exponent of ~ 0.2. Broadly speaking, as the higher the Bond number increases, the Rayleigh-Taylor instability has more time to grow to larger gains before being dampened by the thinning of the film.

3.3.3 Influence of the film aspect ratio

The problem's aspect ratio, δ, impacts the low Bond number regime (see Fig. 3.6). The gains of the front-like perturbations are larger as the film aspect ratio decreases, and those values are attained at slightly larger times. Similarly, δ has an effect on the transition between the two type of instabilities. In Fig. 3.6(b) one observes that for $Bo = 20$ a thin film gives rise to a front perturbation, whereas for a thick film, the perturbation is oscillatory. In contrast, δ has very

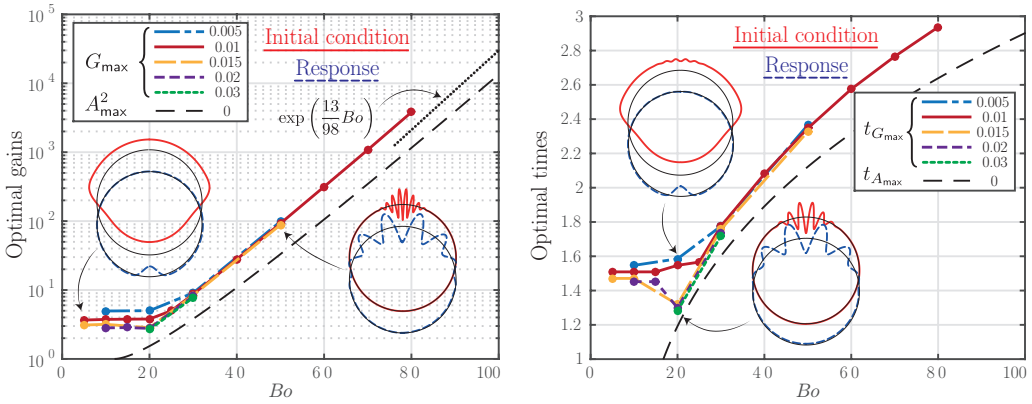

(a) (b)

Figure 3.6 – Largest optimal gains $G_{\max}$ (a) and time horizons $t_{G_{\max}}$ (b) as a function of the Bond number for several film aspect ratios δ (see legend). For visualization purposes the initial conditions (solid red) and responses (dashed blue) are normalized by their respective largest value and magnified by 20. Long dashed black lines correspond to the square of the optimal amplifications at the top, $A^2_{\max}$, and the corresponding optimal times, $t_{A_{\max}}$; see Sec. 3.4.1. Black dotted line in panel (a) corresponds to the optimal gain evolution limit for large Bond numbers, see Sec. 3.4.1.

little effect on the high Bond number regime. This means that the geometrical parameters of the problem are solely captured by the Bond number defined by the combination of R^* and H_i^*. This fact is confirmed by the collapse of curves in Figs. 3.6(a) and 3.6(b). In particular, this master curve displays the earlier evoked exponential dependance of $G_{\max}$ on the Bond number (Fig. 3.6(a)), which is discussed next.

3.4 Discussion

3.4.1 Optimal transient growth analysis at $\theta = 0$

The perturbations giving rise to significant optimal gains $G_{\max}$ have been found to be oscillations of the film interface around the north pole. It is therefore natural to consider the top region, in agreement with the work of Trinh et al. (2014). In the following, we will use and extend their linear stability analysis to rationalize our results.

If one focuses only on the region at the north pole ($\theta = \delta^{1/2}x$ for $\delta \to 0$), the lubrication equation (3.1) can be greatly simplified in the asymptotic limit of small aspect ratios. For an initial harmonic perturbation of wave number k, $h(x,1) = \exp(\mathrm{i}kx)$, the resulting linear perturbation equation has the following analytical solution

$$h(x,\tilde{t}) = A(k,\tilde{t}) \exp\left[\mathrm{i}\left(k\frac{x}{\tilde{t}^{3/2}}\right)\right], \tag{3.12}$$

with the amplitude being a function of the wave number k and the rescaled time $\tilde{t} = 1 + 2\,t/3$[1]:

$$A(k,\tilde{t}) = \underbrace{\frac{1}{\tilde{t}^{3/2}}}_{\mathrm{I}} \underbrace{\exp\left[\underbrace{\left(1-\tilde{t}^{-7/2}\right)\frac{k^2}{7}}_{\mathrm{a}} - \underbrace{\frac{1}{Bo}\left(1-\tilde{t}^{-13/2}\right)\frac{k^4}{13}}_{\mathrm{b}}\right]}_{\mathrm{II}}. \tag{3.13}$$

In this case, the amplitude squared $A(k,\tilde{t})^2$ corresponds to our definition of the perturbation's gain (see Eq. (3.4)) for $\theta = 0$.

The $-3/2$ power-law dependence of the amplitude on the rescaled time in term I differs from the value of -1 obtained by Trinh et al. (2014). The reason is the different film-thickness decomposition. We consider $\bar{H}(x,\tilde{t}) = H(\tilde{t}) + \varepsilon h(x,\tilde{t})$, whereas in Trinh et al. (2014) the decomposition is $\bar{H}(x,\tilde{t}) = H(\tilde{t})[1+\varepsilon\eta(x,\tilde{t})]$. Since $H(\tilde{t})$ decreases monotonically in time at $\theta = 0$ (see Fig. 3.1(b)), the perturbation $h(x,\tilde{t}) = H(\tilde{t})\eta(x,\tilde{t})$ increases in time only if the growth of $\eta(x,\tilde{t})$ overcomes the decay in $H(\tilde{t})$; a growth in $\eta(x,\tilde{t})$ does not imply a growth in $h(x,\tilde{t})$. Trinh et al. (2014) find that $\eta(x,\tilde{t})$ grows for Bond numbers larger than 8. With our definition, the necessary value for initial growth of $h(x,\tilde{t})$ becomes 12.

By definition, the dimensionless drainage time is of order 1 for all Bond numbers. On the contrary, the time scale associated with the growth of the Rayleigh-Taylor instability varies with Bo, it is typically of the order of $1/Bo$ (Fermigier et al., 1992). The difference in the time scales may lead to transient growths for sufficiently large Bond numbers. The threshold may be obtained comparing the initial temporal dependence of the contributions I and II in Eq. (3.13). At first order for $\tilde{t} \to 1$, the thinning term I evolves as $1 - 3(\tilde{t}-1)/2$, whereas the largest value of the Rayleigh-Taylor term II is found for $k_0 = \sqrt{Bo/2}$ and increases as $1 + Bo\,(\tilde{t}-1)/8$.

[1] Note that $\tilde{t}$ has been used instead of T as in Chapters 4 and 5 to avoid confusion with the time horizon.

Initial growth of perturbations at the top only occurs if the instability grows faster than the thinning of the film, which is indeed the case for $Bo > 12$.

The analytical expression (3.13) is now employed to elucidate the reasons of the algebraic growth at finite transient times. The evolution of the gain A as a function of the rescaled time $\tilde{t}$ is shown in Fig. 3.7 for $Bo = 100$. At short times, an exponential growth of the gravitational instability is observed (as $Bo > 12$). The Rayleigh-Taylor contribution II of Eq. (3.13) dominates the flow; the thinning term I is close to unity. Term II incorporates the destabilizing and stabilizing components of the Rayleigh-Taylor instability, namely IIa and IIb. As a result of the thinning of the film with time, the instability saturates to a plateau (see curve II in Fig. 3.7), thereby increasing the relative importance of part I which scales as $\tilde{t}^{-3/2}$ (see curve I in Fig. 3.7). This stabilizing effect therefore dominates the saturated exponential growth of the instability at large times (see curve A in Fig. 3.7), so that only a transient growth scenario may effectively destabilize the fluid's interface.

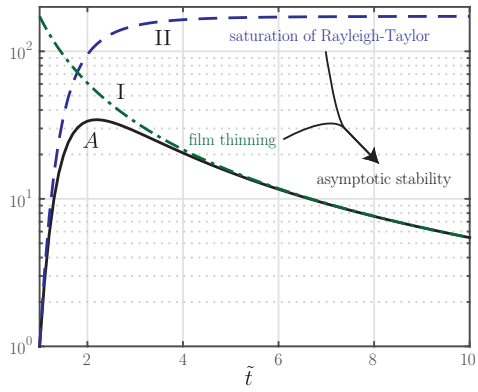

Figure 3.7 – Temporal evolution of the gain at $\theta = 0$ given by Eq. (3.13), A, for $Bo = 100$ and $k = 7$ (solid line), Rayleigh-Taylor exponential contribution II (dashed line) and pure film-thinning contribution I (dash-dotted line) of Eq. (3.13). Term I is rescaled by the final value of II, namely $\exp(13Bo/196)$, see text. Note that A is the product of terms I and II.

The analytical solution (3.13) for the gain A is now optimized in the wave number-time space to find the optimal transient growth. The optimization procedure reduces to finding a maximum of the two arguments function $A(k,\tilde{t})$ (the Bond number is here a parameter). The optimal wave number is obtained by solving $\partial A/\partial k = 0$:

$$k_{\max}(\tilde{t}) = \sqrt{\frac{13}{14}\frac{\left(1-\tilde{t}^{-7/2}\right)}{\left(1-\tilde{t}^{-13/2}\right)}Bo}. \tag{3.14}$$

In the short time limit, $\tilde{t} \to 1$, we recover $k_{\max} = k_0 = \sqrt{Bo/2}$ classically obtained for the Rayleigh-Taylor instability under a horizontal plane and in Trinh et al. (2014). For large optimal times, $\tilde{t} \gg 1$, $k_{\max}$ converges to $\sqrt{13Bo/14}$, so that the relative change in the optimal wave number is weak. Note that $k_{\max}(\tilde{t})$ is not the evolution of the perturbation wave number,

but is the initial wave number giving rise to the largest amplitude $A_{k_{\max}}$ at time $\tilde{t}$. $A_{k_{\max}}$ can be found by substituting the expression of $k_{\max}(\tilde{t})$ in Eq. (3.13):

$$A_{k_{\max}}(\tilde{t}) = \frac{1}{\tilde{t}^{3/2}} \exp\left[\frac{13}{196}\frac{\left(1-\tilde{t}^{-7/2}\right)^2}{\left(1-\tilde{t}^{-13/2}\right)} Bo\right]. \tag{3.15}$$

The optimal wave number as well as the resulting gain obtained for different Bond numbers are presented in Fig. 3.8. The fast convergence of $k_{\max}$ to the large time limit $\sqrt{13Bo/14}$ is shown in inset.

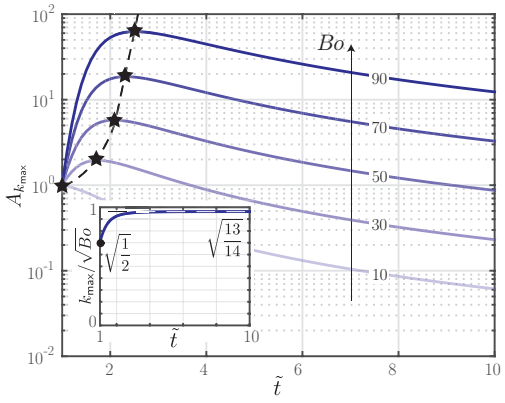

Figure 3.8 – Gain $A_{k_{\max}} = A(k_{\max}, \tilde{t})$ as a function of time for different Bond numbers. Inset: normalized optimal wave number $k_{\max}/\sqrt{Bo}$. Stars and dashed line indicate the largest transient growth and the corresponding times. Full circle (dashed line) corresponds to the short (long) time limit of the normalized optimal wave number.

The optimal times and gains, highlighted by stars and the dashed line in Fig. 3.8, are found by solving $\partial A_{k_{\max}}/\partial\tilde{t} = 0$. No analytical expression was found and a numerical resolution had to be performed. The optimal times and the corresponding optimal gains at the top are reported in Fig. 3.6.

We now compare these results of the optimization of the transient growth at $\theta = 0$ for $\delta \to 0$ to the ones presented in Sec. 3.3 for the optimization over all angles and finite aspect ratios. The optimal gain $A^2_{\max}$ obtained semianalytically at the top follows the same exponential dependence in Bond number as the one of $G_{\max}$ earlier obtained by the optimal transient growth analysis on the entire geometry (see Fig. 3.6(a)). The difference in their exact values is imputable to a difference in the norm used to evaluate each case. $A^2_{\max}$ accounts only for the perturbation value at $\theta = 0$ by contrast with $G_{\max}$ which covers the entire domain (see Eq. (3.4)).

We note that the variation of the algebraic growth with the Bond number tends to $\exp(13Bo/98)$ for $Bo \gg 1$. This is intrinsically related to the wave number stretching effect. In fact, the drainage stretches the perturbations as the effective wave number in Eq. (3.12) is $k/\tilde{t}^{3/2}$ (see

the plots in Fig. 3.4(b) for an illustration). As a result, the stabilizing term IIb of Eq. (3.13) evolves faster than its destabilizing counterpart, IIa. If the perturbations were not stretched, i.e., the destabilizing and stabilizing terms IIa and IIb of Eq. (3.13) would have the same temporal dependence, the exponential increase of the gain would tend to $\exp(Bo/2)$; the algebraic growth would solely be dictated by the thinning contribution of the draining flow. The mismatch between the two components of term II adds to this effect reducing the prefactor from 1/2 to 13/98. In the context of viscous filaments, the wave number stretching has also been shown to be stabilizing (Villermaux, 2012).

Regarding the optimal times shown in Fig. 3.6(b), both $t_{G_{\max}}$ and $t_{A_{\max}}$ follow a similar power-law with an exponent smaller than unity, typically ~ 0.2. The shape of the optimal perturbations can be compared as well. In both cases, the optimal perturbations are oscillations of the interface close to the top. This is a result for the optimal transient growth analysis on the entire circle and an assumption for the analysis at the pole. However, for the analysis over all θ, their wave number and amplitude decrease in space as the distance from $\theta = 0$ increases (see Fig. 3.4(b) for example). Thus, only the first and second apparent wave numbers, which are close to the pole, will be considered for the comparison. A very good correspondence of the wave numbers of the optimal initial conditions as obtained in the two approaches is shown in Fig. 3.9. In conclusion, the optimal perturbations found by the analysis at the top, slightly modulated in space, are optimal for the problem on the entire geometry for $Bo \gtrapprox 20$. Note that the analysis at $\theta = 0$ holds in the limit of a vanishing film aspect ratio, which turns out to be a valid assumption since the oscillating regime has been found not to directly dependent on δ (see Sec. 3.3.3).

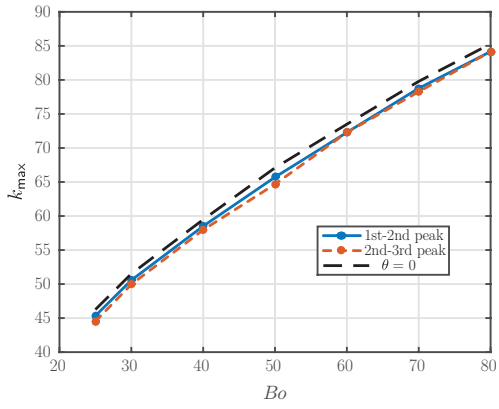

Figure 3.9 – Wave numbers corresponding to the optimal initial condition obtained from the transient growth analysis on the entire geometry for $\delta = 10^{-2}$ (solid and dotted lines) and at the top, Eq. (3.14) multiplied by $\delta^{-1/2}$ to convert from x- to θ-space (dashed line), with $\tilde{t}$ maximizing $A_{k_{\max}}$. The $k_{\max}$ of the transient growth analysis over all θ are the wave numbers corresponding to the distance between the first and second or second and third peak of the oscillations, respectively.

3.4.2 Transition to dripping droplets

The initial growth analysis at the top tells us that below $Bo = 12$ no droplets can be formed, whereas from the transient growth analysis on the entire geometry we know that below $Bo \approx 20$ the optimal perturbations do not correspond to oscillations of the film at the top. We classify droplets in two categories : *Transient* droplets grow for a certain time before being reabsorbed by the film whereas *dripping* droplets pinch off from the substrate (see Figs. 3.11 and 3.12). We now turn to the question of dripping droplets.

In view of the exponentially increasing algebraic gain with the Bond number in the oscillating regime, we argue that the system acts as an effective amplifier. Initial perturbations are crucial. They project onto the most unstable perturbation which will emerge in the growth at finite times. The linear evolution initially dictates the growth of the perturbations, but as they reach a certain amplitude, nonlinear effects enter in consideration (see Fig. 3.10). In particular, the linear dynamics initially presents a faster increase of the disturbance amplitudes as well as a slightly larger sliding velocity of the droplets (see Fig. 3.10(b)). The peculiar shape of the front and rear menisci of the sliding droplets on a thin wetting precursor film (see Fig. 3.10(c,d)), and the eventual pinch off, are purely nonlinear effects (Eggers & Villermaux, 2008).

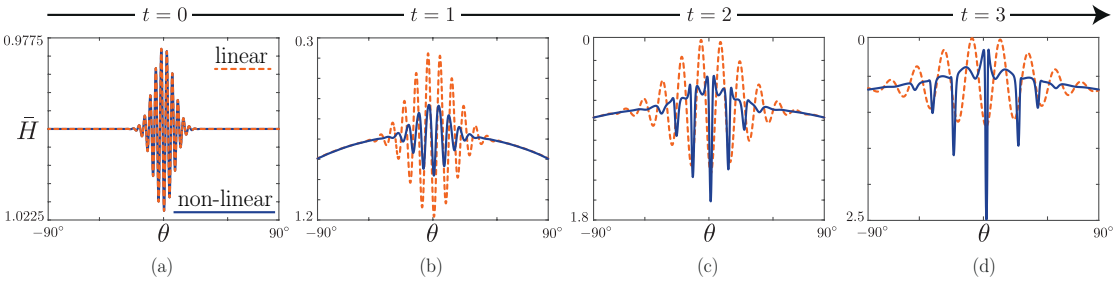

Figure 3.10 – Linear (dashed) and nonlinear (solid) evolutions of the interface initially perturbed by the optimal initial condition $h_0^{\max}$ obtained by the linear stability for the specific Bond number. The initial condition reads $\bar{H}(\theta,0) = 1 + a\, h_0^{\max}/||h_0^{\max}||_\infty$ with $a = 2.25 \cdot 10^{-2}$. The film aspect ratio is $\delta = 10^{-2}$ and the Bond numbers is $Bo = 80$. Dripping will occur at $t = 3.65$. The linear evolution is obtained by the resolution of the linearized lubrication equation (3.3) for the disturbances h on a draining flow H given by Eq. (3.1), whereas the nonlinear evolution is obtained by the resolution of the two-phase 2D Stokes equations. Note that the scale of the y-axis changes.

We expect that the transition from transient droplets to dripping droplets is dependent on the initial perturbations intensity. For large initial perturbations, the necessary amplification in order to trigger the formation of droplets is smaller, i.e., the transition to dripping droplets will occur already for smaller Bond numbers. On the other hand, when the film is only weakly disturbed, a larger Bond number is necessary to create dripping droplets before drainage makes the film too thin. Given a perturbation amplitude, there exists therefore a critical Bo above which the linear growth results in the formation of droplets which pinch off. Conversely, given a Bond number, there likely exists a critical initial disturbance amplitude for the transition to

dripping droplets.

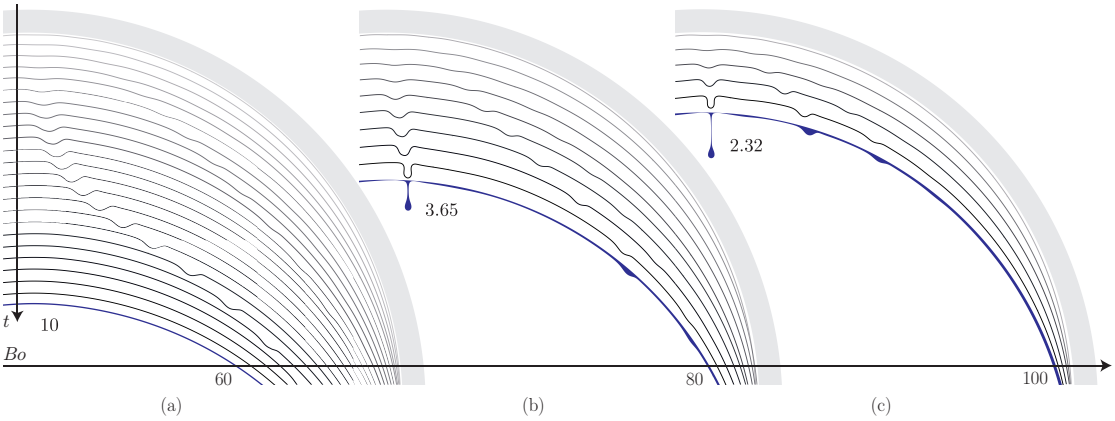

Figure 3.11 – Nonlinear evolution of the interface initially perturbed by the optimal initial condition h_0^{max} obtained by the linear stability for the specific Bond number. The initial condition reads $\bar{H}(\theta,0) = 1 + a\, h_0^{max}/||h_0^{max}||_\infty$ with $a = 2.25 \cdot 10^{-2}$. The film aspect ratio is $\delta = 10^{-2}$ and the Bond numbers are (a) $Bo = 60$, (b) $Bo = 80$ and (c) $Bo = 100$. Grey lines correspond to the interface shapes at successive time instants; the time step is 0.4. The filled profiles correspond to the liquid films at the indicated final time when the droplet is reabsorbed (a) or when pinching off occurs (b)-(c). No dripping occurs even at larger times for the case (a).

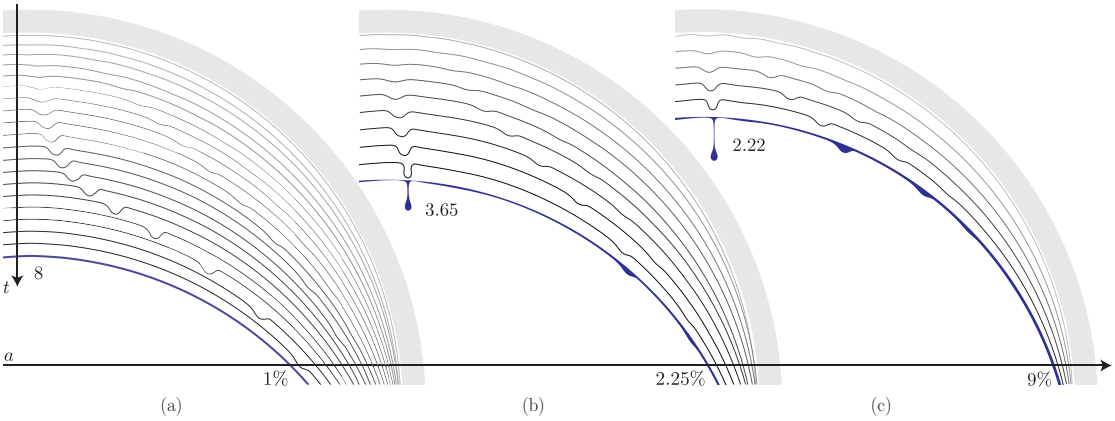

Figure 3.12 – Nonlinear evolution of the interface initially perturbed by the optimal initial condition h_0^{max} obtained by the linear stability for $Bo = 80$. The initial condition reads $\bar{H}(\theta,0) = 1 + a\, h_0^{max}/||h_0^{max}||_\infty$ with (a) $a = 10^{-2}$, (b) $a = 2.25 \cdot 10^{-2}$ and (c) $a = 9 \cdot 10^{-2}$. The film aspect ratio is $\delta = 10^{-2}$. Grey lines correspond to the interface shapes at successive time instants; the time step is 0.4. The filled profiles correspond to the liquid films at the indicated final time when the droplet is reabsorbed (a) or when pinching off occurs (b)-(c). No dripping occurs even at larger times for the case (a).

To support our argument, we performed nonlinear numerical simulations using the two-phase 2D Stokes solver Ulambator (Nagel & Gallaire, 2015) for different Bond numbers and perturbation amplitudes. The resulting film profiles for $Bo = 60$, 80, and 100, perturbed at

$t = 0$ by the optimal initial condition found by the linear analysis at the given Bond number, with an amplitude of 2.25% the average initial thickness are shown in Fig. 3.11. Different sort of droplets form, depending on the value of the Bond number. In all three cases, droplets are created close to the north pole. For $Bo = 60$, after an initial growth, they decay and are reabsorbed by the liquid film, thereby behaving as transient droplets. For $Bo = 80$ and 100, the linear amplification is strong enough for the nonlinear effects to lead to pinch off (keeping in mind the limitation of the two-dimensional geometry). We furthermore investigated the effect of the initial disturbance amplitude on the transition. The nonlinear evolutions for $Bo = 80$ and optimal initial conditions with amplitudes $a = 1\%$, 2.25%, and 9% are shown in Fig. 3.12. The linear gain for $Bo = 80$ is not large enough to yield dripping droplets when the perturbation amplitude is reduced to 1% the average initial thickness. We verified that for $Bo = 100$ an amplitude of 1% is sufficient for dripping droplets to form whereas for $Bo = 60$ an amplitude of 9% is not sufficient for droplets to pinch off. Increasing the Bond number or the initial disturbance amplitude have therefore similar effects. In addition, as the Bond number (or initial amplitude) is larger, the pinch off does occur earlier. Note that for illustration purposes only a fourth of the circle is shown in Figs. 3.11 and 3.12; on the rest of the geometry transient droplets occur, but they do not detach from the substrate, and the perturbations are not symmetric.

We now briefly comment on the limitations of our method. First and foremost, our calculation is 2D although droplet pinch off is a 3D mechanism. We therefore anticipate that the precise value of the critical dripping Bond number will differ if using 3D computations in this section. Nevertheless, we anticipate that a similar scenario will occur. Similarly we note that the present theoretical approach accounts for an initial perturbation only. We speculate that a coupling between the microscopic scale and the macroscopic scale similar to the one described by Bertozzi & Brenner (1997) is at the origin of the film perturbations necessary for the droplet formation. The sensitivity of the system to perturbations persisting in time goes beyond the aim of this work and is the subject of a separate study.

3.5 Conclusions

In this study, the Rayleigh-Taylor instability of a thin viscous film coating the interior of a cylindrical substrate has been investigated by performing a linear optimal transient growth analysis. For such a geometry, gravity has a twofold effect. On the one hand, it creates a draining flow that stabilizes the interface. On the other hand the gravitational field destabilizes the free surface and is at the origin of dripping droplets. The exponential growth of perturbations dominates at early times, saturates and is stabilized by the algebraic dampening of the draining flow at larger times. In the asymptotic limit of large times, the liquid interface is stable with respect to infinitesimal perturbations; and this is for all Bond numbers and all initial film thickness to cylinder radius ratios, δ. Nonetheless, it has been found that droplets may drip from the cylindrical substrate (Trinh et al., 2014). We therefore performed an optimal transient growth analysis considering the entire geometry at finite times.

By analyzing the influence of the Bond number on the optimal conditions, we have been able to distinguish between two types of optimal perturbations. For surface tension dominated flows, the optimal gains are independent of the Bond number and increase for a decreasing film aspect ratio. The corresponding initial conditions display a front, which is solely drained downstream by the gravitational field and does not present any oscillations at the top ($\theta = 0$). Such instability could not be found by a stability analysis at the north pole, but is not at the origin of droplets. When the Bond number is increased, typically above 20, a second regime has been observed. The optimal conditions correspond to interface oscillations on the upper hemicircle. The optimal algebraic gains $G_{\max}$ increase exponentially with the Bond number. The influence of the film thickness versus the curvature of the cylinder is solely contained in the modified Bond number. It is the only relevant nondimensional parameter for the oscillating regime. In effect, the Bond number may be interpreted as the ratio between the drainage time scale and the Rayleigh-Taylor instability time scale, which are the two competing mechanisms at play.

The oscillating perturbations found by adjoint-based optimization agree very well with the ones recovered semianalytically at $\theta = 0$. The optimal conditions, namely the gain $G_{\max}$, the wave number $k_{\max}$, and the time to attain the largest growth are in excellent agreement. More precisely, the same exponential dependence of the maximal optimal gain and the power-law increase of the corresponding time on the Bond number have been observed. The optimal perturbations found at the top, slightly modulated in space, become optimal over the entire geometry. The upper bound of the exponential increase of the optimal gain as a function of Bo, $G_{\max} \sim \exp(13Bo/98)$, is related to the stretching effect of the flow. Using substrates with an increasing curvature might therefore stabilize thin liquid films at even higher Bond numbers.

For $Bo \gtrapprox 20$, the initial linear growth of perturbations triggers nonlinear effects eventually resulting in the formation of droplets. The practically relevant transition between transient and dripping droplets is a function of the perturbation amplitude. Given that the algebraic gain increases exponentially with the Bond number, a threshold will always exist, no matter how small the perturbations are. We illustrated this point using full two-dimensional nonlinear simulations. The experimentally observed threshold reported in Trinh et al. (2014) is not universal and is experiment dependent.

The novelty of our work lies in the investigation of an interfacial instability using an optimal transient growth analysis with an evolving base state (here the draining solution). Such an approach based on the forward and backward integration of the direct and adjoint system opens the door to the stability analysis of other unsteady free-surface flows, ranging from thin films to deforming drops and bubbles. Another natural extension of our work is concerned with the determination of a nonlinear optimal transient growth analysis, as reviewed by Luchini & Bottaro (2014) and Kerswell, Pringle & Willis (2014).

In Chapter 4 we will consider the full three-dimensional geometry, enabling the exploration

of the two-dimensional pattern formation, generalizing the work of Fermigier et al. (1992) to curved substrates.

Acknowledgments We would like to thank Edouard Boujo and Francesco Viola for helpful discussions on the subject of adjoint-based optimization techniques as well as Mathias Nagel for the two-phase 2D Stokes solver Ulambator. This work was funded by ERC Grant No. SIMCOMICS 280117.

3.6 Appendix

3.6.1 Derivation of the lubrication equation

The derivation of the model equation presented in Sec. 3.2.1 is briefly outlined hereafter. Assume a thin film coating the interior of a cylinder of radius R^* as shown in Fig. 3.1(a). The initial average thickness is H_i^* and the resulting film aspect ratio reads $\delta = H_i^*/R^*$. The characteristic lengths in the radial and polar directions are H_i^* and R^*, respectively. Exploiting the small aspect ratio of the film, $\delta \ll 1$, we can use a lubrication approach (Oron et al., 1997). Mass conservation indicates that the characteristic velocity normal to the substrate is much smaller than the tangential component, $V^* \sim \delta U^* \ll U^*$. The low Reynolds number for this flow allows the use of the Stokes equations. The momentum equation in the radial direction is therefore

$$0 = -\frac{1}{\rho}\frac{\partial p^*}{\partial r^*} - g\cos\theta, \tag{3.16}$$

and the boundary condition for the pressure is given by $p^*(R^* - \bar{H}^*) = p_0^* - \gamma\bar{\kappa}^*$ (p_0^* is the external pressure, γ is the surface tension and $\bar{\kappa}^*$ is the curvature of the interface). By integrating Eq. (3.16) along the radial direction and using the boundary condition, one obtains the pressure distribution $p^*(r^*,\theta) = p_0^* - \gamma\bar{\kappa}^* + \rho g\cos\theta(R^* - \bar{H}^* - r^*)$. The θ component of the momentum equation reads

$$0 = -\frac{1}{\rho r}\frac{\partial p^*}{\partial \theta} + \nu\left[\frac{\partial}{\partial r^*}\left(\frac{1}{r^*}\frac{\partial}{\partial r^*}\left(r^* u^*\right)\right) + \frac{1}{r^{*2}}\frac{\partial^2 u^*}{\partial \theta^2}\right] + g\sin\theta\,. \tag{3.17}$$

By performing the change of variable $r^* = R^* - y^*$, where $0 \le y^* \le \bar{H}^* \ll R^*$, the viscous term reduces to $\nu\partial^2 u^*/\partial y^{*2}$ plus terms at least an order δ smaller. Keeping the dominant order of the viscous term, as well as the surface tension and gravitational terms, Eq. (3.17) with the expression for p^* becomes:

$$0 = \frac{\gamma\bar{\kappa}_\theta^*}{\rho R^*} + \frac{g\cos\theta\bar{H}_\theta^*}{R^*} + \nu\frac{\partial^2 u^*}{\partial y^{*2}} + g\sin\theta\,. \tag{3.18}$$

Equation (3.18) can be integrated twice and considering the zero-slip boundary condition at the cylinder surface, $u^*(0,\theta)=0$, as well as the zero-shear stress interface, $\partial u^*(\bar{H}^*,\theta)/\partial y^*=0$, yields the tangential velocity component:

$$u^*(y^*,\theta)=\left(\frac{\gamma\bar{\kappa}_\theta^*}{\mu R^*}+\frac{\rho g\cos\theta\bar{H}_\theta^*}{\mu R^*}+\frac{\rho g\sin\theta}{\mu}\right)\left(\bar{H}^*-\frac{y^*}{2}\right)y^*. \tag{3.19}$$

The flow-rate is given by $Q^*(\theta)=\int_0^{\bar{H}^*}u^*(y^*,\theta)\mathrm{d}y^*$. By using the local mass conservation in cylindrical coordinates $\partial\bar{H}^*/\partial t+R^{*-1}\partial Q^*/\partial\theta=0$ we eventually obtain the lubrication equation:

$$\bar{H}_t^*+\frac{1}{3\mu R^*}\left[\bar{H}^{*3}\left(\underbrace{\frac{\gamma\bar{\kappa}_\theta^*}{R^*}}_{\mathbf{I}}+\underbrace{\frac{\rho g\cos\theta\bar{H}_\theta^*}{R^*}}_{\mathbf{II}}+\underbrace{\rho g\sin\theta}_{\mathbf{III}}\right)\right]_\theta=0, \tag{3.20}$$

where the leading order curvature derivative is $\bar{\kappa}_\theta^*=R^{*-2}(\bar{H}_{\theta\theta\theta}^*+\bar{H}_\theta^*)$. The term **I** in the spatial variation of the flux corresponds to the surface tension effects, term **II** corresponds to the variation of the hydrostatic pressure distribution and term **III** corresponds to the drainage. A more sophisticated model could be employed to consider higher order curvature terms and larger film aspect ratios, as done by Weidner, Schwartz & Eres (1997).

The film height can be nondimensionalized by the initial average film thickness H_i^* and the time by the gravitational relaxation scale $\mu R^*/(\rho g H_i^{*2})$ so that the lubrication equation expressed with nondimensional quantities finally reads:

$$\bar{H}_t+\frac{1}{3}\left\{\bar{H}^3\left[\frac{\delta^2}{Bo}\left(\bar{H}_{\theta\theta\theta}+\bar{H}_\theta\right)+\delta\bar{H}_\theta\cos\theta+\sin\theta\right]\right\}_\theta=0. \tag{3.21}$$

where $Bo=\rho g H_i^* R^*/\gamma$ is the modified Bond number.

3.6.2 Linear operator

The linear operator for the perturbation equation (3.3) in matrix form is given by:

$$\begin{aligned}\mathbf{L}=-\frac{1}{3}[&-\frac{\delta^2H^3}{Bo}(\mathbf{D}_2+\mathbf{D}_4)-\frac{\delta^2H^2H_\theta}{Bo}(6\mathbf{D}_1+3\mathbf{D}_3)-\frac{3\delta^2H^2H_{\theta\theta}}{Bo}\mathbf{I}\\&-\frac{3\delta^2H^2H_{\theta\theta\theta}}{Bo}\mathbf{D}_1-\frac{3\delta^2H^2H_{\theta\theta\theta\theta}}{Bo}\mathbf{I}-\frac{6\delta^2HH_\theta^2}{Bo}\mathbf{I}-\frac{6\delta^2HH_\theta H_{\theta\theta\theta}}{Bo}\mathbf{I}\\&+\delta H^3\sin\theta\mathbf{D}_1-\delta H^3\cos\theta\mathbf{D}_3+3\delta H^2H_\theta\sin\theta\mathbf{I}-6\delta H^2H_\theta\cos\theta\mathbf{D}_1\\&-3\delta H^2H_{\theta\theta}\cos\theta\mathbf{I}-6\delta HH_\theta^2\cos\theta\mathbf{I}-3H^2\cos\theta\mathbf{I}-3H^2\sin\theta\mathbf{D}_1\\&-6HH_\theta\sin\theta\mathbf{I}],\end{aligned} \tag{3.22}$$

where $\mathbf{I}$ is the identity operator and $\mathbf{D}_i$ with $i=1,...,4$ are the differential operators, constructed in our study using Fourier spectral methods (Weideman & Reddy, 2000). Subscripts with θ

correspond to spatial derivatives of the drainage solution H.

3.6.3 Derivation of the adjoint fields

We provide here the extended derivation of the adjoint fields. See the introductory paper by Cossu (2014) for more details on the use of variational techniques for solving constrained optimization problems.

The augmented Lagrangian of our concern, consisting of the objective function $G(T)$ to be optimized and the constraints given by the evolution equation and the initial condition, reads:

$$\mathscr{L}\left(\mathbf{h},\mathbf{h}^\dagger,\mathbf{h}_0,\mathbf{h}_0^\dagger;T\right)=\frac{\langle\mathbf{h}(T)|\mathbf{h}(T)\rangle}{\langle\mathbf{h}_0|\mathbf{h}_0\rangle}-\int_0^T\langle\mathbf{h}^\dagger\Big|\mathbf{h}_t+\mathbf{L}\mathbf{h}\rangle\,\mathrm{d}t-\langle\mathbf{h}_0^\dagger\Big|\mathbf{h}(0)-\mathbf{h}_0\rangle\,. \tag{3.23}$$

$\langle\mathbf{a}|\mathbf{b}\rangle=\int_\Omega\mathbf{a}^T\mathbf{b}\,\mathrm{d}\theta=\mathbf{a}^T\mathbf{M}\mathbf{b}$ is the Hermitian scalar product for real quantities on the geometry $\Omega=\{\theta\,|\,\theta\in[0,2\pi]\}$, defined via a weight matrix $\mathbf{M}=\frac{2\pi}{N}\mathbf{I}\in\mathbb{R}^{N\times N}$.

By setting to zero the variations of $\mathscr{L}$ with respect to both $\mathbf{h}$ and $\mathbf{h}_0$, one obtains the equations for the Lagrange multipliers $\mathbf{h}^\dagger$ and $\mathbf{h}_0^\dagger$. For the derivation, we will make use of Frechét derivatives, which for an operator $\mathbf{A}(\mathbf{s})$ are defined by (see Cossu (2014)):

$$\langle\frac{\partial\mathbf{A}}{\partial\mathbf{s}}\Big|\delta\mathbf{s}\rangle=\lim_{\epsilon\to0}\frac{\mathbf{A}(\mathbf{s}+\epsilon\delta\mathbf{s})-\mathbf{A}(\mathbf{s})}{\epsilon}\,. \tag{3.24}$$

The variation of $\mathscr{L}$ with respect to $\delta\mathbf{h}$ results in

$$\langle\frac{\partial\mathscr{L}}{\partial\mathbf{h}}\Big|\delta\mathbf{h}\rangle=2\frac{\langle\mathbf{h}(T)|\delta\mathbf{h}(T)\rangle}{\langle\mathbf{h}_0|\mathbf{h}_0\rangle}-\int_0^T\langle\mathbf{h}^\dagger\Big|\delta\mathbf{h}_t+\mathbf{L}\delta\mathbf{h}\rangle\,\mathrm{d}t-\langle\mathbf{h}_0^\dagger\Big|\delta\mathbf{h}(0)\rangle \tag{3.25}$$

$$=2\frac{\langle\mathbf{h}(T)|\delta\mathbf{h}(T)\rangle}{\langle\mathbf{h}_0|\mathbf{h}_0\rangle}-\int_0^T\langle\mathbf{h}^\dagger\Big|\delta\mathbf{h}_t\rangle\,\mathrm{d}t-\int_0^T\langle\mathbf{h}^\dagger\Big|\mathbf{L}\delta\mathbf{h}\rangle\,\mathrm{d}t-\langle\mathbf{h}_0^\dagger\Big|\delta\mathbf{h}(0)\rangle \tag{3.26}$$

$$=2\frac{\langle\mathbf{h}(T)|\delta\mathbf{h}(T)\rangle}{\langle\mathbf{h}_0|\mathbf{h}_0\rangle}-\langle\mathbf{h}^\dagger(T)\Big|\delta\mathbf{h}(T)\rangle+\langle\mathbf{h}^\dagger(0)\Big|\delta\mathbf{h}(0)\rangle+\int_0^T\langle\mathbf{h}_t^\dagger\Big|\delta\mathbf{h}\rangle\,\mathrm{d}t \tag{3.27}$$

$$-\int_0^T\langle\mathbf{L}^\dagger\mathbf{h}^\dagger\Big|\delta\mathbf{h}\rangle\,\mathrm{d}t-\langle\mathbf{h}_0^\dagger\Big|\delta\mathbf{h}(0)\rangle \tag{3.28}$$

$$=\langle2\frac{\mathbf{h}(T)}{\langle\mathbf{h}_0|\mathbf{h}_0\rangle}-\mathbf{h}^\dagger(T)\Big|\delta\mathbf{h}(T)\rangle+\int_0^T\langle\mathbf{h}_t^\dagger-\mathbf{L}^\dagger\mathbf{h}^\dagger\Big|\delta\mathbf{h}\rangle\,\mathrm{d}t+\langle\mathbf{h}^\dagger(0)-\mathbf{h}_0^\dagger\Big|\delta\mathbf{h}(0)\rangle\,. \tag{3.29}$$

The distributive property of the scalar product has been used in (3.26), integration by part in (3.27) and the definition of the adjoint operator, namely $\langle\mathbf{a}|\mathbf{L}\mathbf{b}\rangle=\langle\mathbf{L}^\dagger\mathbf{a}|\mathbf{b}\rangle$, in (3.28). Since the Hermitian scalar product is defined with an identity (up to a factor) matrix $\mathbf{M}$, the discrete adjoint corresponds to the transpose of the direct one: $\mathbf{L}^\dagger=\mathbf{L}^T$, where $\mathbf{L}$ is defined by Eq.

(3.22). The analytical calculation of the continuous adjoint operator can therefore be avoided (Schmid & Henningson, 2001). Similarly, by imposing a vanishing variation of $\mathscr{L}$ to any $\delta\mathbf{h}$, one eventually obtains:

$$\langle\frac{\partial\mathscr{L}}{\partial\mathbf{h}}\Big|\delta\mathbf{h}\rangle = 0\,,\ \forall\,\delta\mathbf{h} \Leftrightarrow \mathbf{h}^\dagger(T) = 2\frac{\mathbf{h}(T)}{\langle\mathbf{h}_0|\mathbf{h}_0\rangle}\,, \tag{3.30}$$

$$\mathbf{h}_t^\dagger - \mathbf{L}^\dagger\mathbf{h}^\dagger = \mathbf{0} \quad t\in[0,T]\,, \tag{3.31}$$

$$\mathbf{h}_0^\dagger = \mathbf{h}^\dagger(0)\,. \tag{3.32}$$

These are the terminal condition for the adjoint field, Eq. (3.8), the adjoint equation (3.9) and the definition of the second adjoint variable, Eq. (3.10), respectively. The variation of the augmented Lagrangian with respect to $\mathbf{h}_0$ reads:

$$\begin{aligned}\langle\frac{\partial\mathscr{L}}{\partial\mathbf{h}_0}\Big|\delta\mathbf{h}_0\rangle &= \langle -2\mathbf{h}_0\frac{\langle\mathbf{h}(T)|\mathbf{h}(T)\rangle}{\langle\mathbf{h}_0|\mathbf{h}_0\rangle^2}\Big|\delta\mathbf{h}_0\rangle \\ &\quad -\int_0^T\langle\mathbf{h}^\dagger\Big|\mathbf{0}\rangle\,\mathrm{d}\,t - \langle\mathbf{h}_0^\dagger\Big| - \delta\mathbf{h}_0\rangle \\ &= \langle -2\mathbf{h}_0\frac{\langle\mathbf{h}(T)|\mathbf{h}(T)\rangle}{\langle\mathbf{h}_0|\mathbf{h}_0\rangle^2} + \mathbf{h}_0^\dagger\Big|\delta\mathbf{h}_0\rangle\,.\end{aligned} \tag{3.33}$$

The stationarity condition with respect to any $\delta\mathbf{h}_0$ yields the optimality condition, Eq. (3.11):

$$\langle\frac{\partial\mathscr{L}}{\partial\mathbf{h}_0}\Big|\delta\mathbf{h}_0\rangle = 0\,,\ \forall\,\delta\mathbf{h}_0 \Leftrightarrow \mathbf{h}_0 = \mathbf{h}_0^\dagger\frac{\langle\mathbf{h}_0|\mathbf{h}_0\rangle^2}{2\,\langle\mathbf{h}(T)|\mathbf{h}(T)\rangle}\,. \tag{3.34}$$

3.6.4 Numerical methods

The developed numerical schemes are validated hereafter. For an initially uniform film, the analytical solution of the lubrication equation (3.1) at $\theta = 0$ is given by $(1+2\,t/3)^{-1/2}$, see for example Trinh et al. (2014) and Takagi & Huppert (2010), as well as Chapter 2. The numerical solution of Eq. (3.1) with $N = 256$ collocation points nicely agrees with the analytical one (see Fig. 3.13(a)). The comparison of the numerical solution of the lubrication equation to the analytical solution allows us to verify the absence of transient waves in the base state (draining) solution. Also, as discussed in Sec. 3.2.1, the effect of the Bond number on the base state solution is only visible in the meniscus connecting the draining film to the liquid pool al the bottom of the cylinder. When $Bo \gtrapprox 350$, the amplification of numerical errors results in the formation of droplets at the top of the geometry, which allows us to clearly distinguish between a correct base state and a base state containing transient waves. For $\theta > 0$, the numerical result is compared to the two-phase 2D Stokes simulation result obtained with Ulambator (Nagel & Gallaire, 2015). The good correspondence is visible in Fig. 3.13(b).

A convergence study for the drainage solution and for the transient growth gain is presented in Fig. 3.14. Convergence is attained already for $N = 256$ collocation points for $Bo = 5$. Note

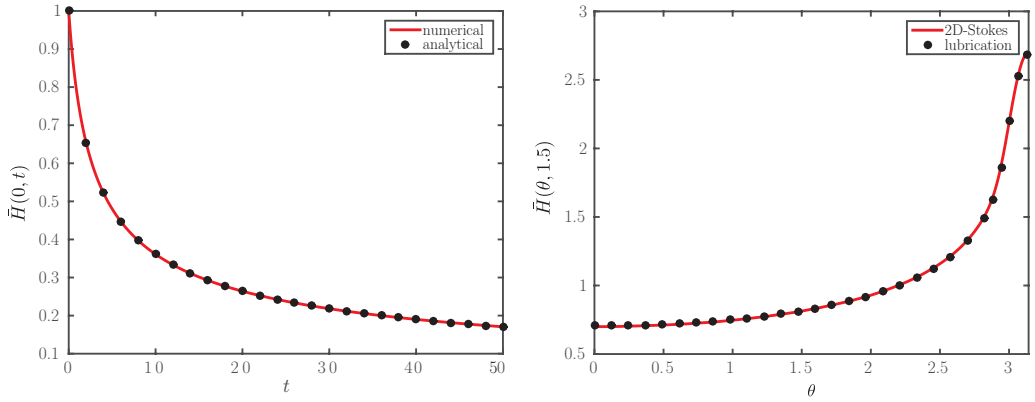

(a) (b)

Figure 3.13 – (a) Comparison between the numerical (solid line) and analytical (bullets) solutions of the lubrication equation (3.1) for the film thickness at the north pole, $\theta = 0$. (b) Comparison between the film-thickness profile obtained by the resolution of the lubrication equation (3.1) (bullets) and using the two-phase 2D Stokes solver Ulambator (solid line) at $t = 1.5$. $Bo = 20$, $\delta = 10^{-2}$ and $N = 256$.

that the capillary length, expressed with nondimensional quantities as $\ell_c = 1/(Bo\delta)$, has to be resolved. The condition $\ell_c > \Delta x = 2\pi/(N\delta)$ imposes a large number of discretization points N for large Bond numbers, the reason why our numerical study is restricted to $Bo \leq 80$.

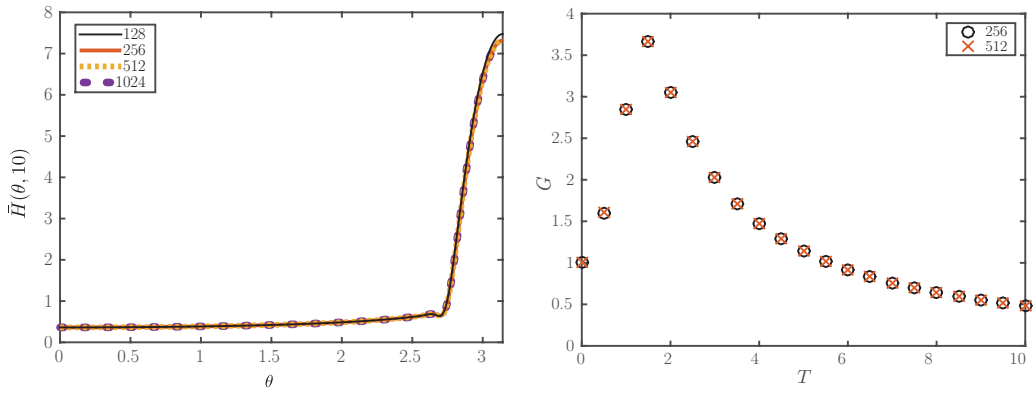

(a) (b)

Figure 3.14 – Convergence study for the resolution of (a) the lubrication equation (3.1) for the film-thickness profile at $t = 10$ and (b) the transient growth gain for $Bo = 5$ and $\delta = 10^{-2}$. Legend: number of grid points N.

4 Three-dimensional Rayleigh-Taylor instability under a unidirectional curved substrate

Remark This chapter is largely inspired by the publication of the same name

G. Balestra[1], N. Kofman[1], P.-T. Brun[2,3], B. Scheid[4] and F. Gallaire[1]

[1]Laboratory of Fluid Mechanics and Instabilities, EPFL, CH1015 Lausanne, Switzerland
[2]Department of Mathematics, Massachusetts Institute of Technology, Cambridge, Massachusetts 02139, USA
[3]Department of Chemical and Biological Engineering, Princeton University, Princeton, NJ 08544, USA
[4]TIPs Laboratory, Université Libre de Bruxelles, Code Postal 165/67, Avenue Franklin Roosevelt 50, 1050 Bruxelles, Belgium

Journal of Fluid Mechanics **837** (2017): 19 – 47

We investigate the Rayleigh-Taylor instability of a thin liquid film coated on the inside of a cylinder whose axis is orthogonal to gravity. We are interested in the effects of geometry on the instability, and contrast our results with the classical case of a thin film coated under a flat substrate. In our problem, gravity is the destabilizing force at the origin of the instability, but also yields the progressive drainage and stretching of the coating along the cylinder's wall. We find that this flow stabilizes the film, which is asymptotically stable to infinitesimal perturbations. However, the short-time algebraic growth that these perturbations can achieve promotes the formation of different patterns, whose nature depends on the Bond number that prescribes the relative magnitude of gravity and capillary forces. Our experiments indicate that a transverse instability arises and persists over time for moderate Bond numbers. The liquid accumulates in equally spaced rivulets whose dominant wavelength corresponds to the most amplified mode of the classical Rayleigh-Taylor instability. The formation of rivulets allows for a faster drainage of the liquid from top to bottom when compared to a uniform drainage. For higher Bond numbers, a two-dimensional stretched lattice of droplets is found to form on the

top part of the cylinder. Rivulets and the lattice of droplets are inherently three-dimensional phenomena and therefore require a careful three-dimensional analysis. We found that the transition between the two types of pattern may be rationalized by a linear optimal transient growth analysis and nonlinear numerical simulations.

4.1 Introduction

We refer to Sec. 1.2 for a general introduction on the Rayleigh-Taylor instability.

In spite of the stabilizing effect of curvature on the Rayleigh-Taylor instability, we have shown in Chapter 3 that such curved systems are still able to greatly amplify initial noise at short times. Depending on the initial magnitude of the perturbation, the initial transient growth might be sufficiently large to trigger nonlinear effects resulting in three different regimes when solely considering a two-dimensional circular section of the cylinder: (i) no droplets, (ii) transient droplets eventually reabsorbed by the film and (iii) dripping droplets. Contrasting with the RTI under a horizontal substrate, where there is no preferential direction for the instability (if boundaries are neglected) and a one-dimensional stability analysis suffices, the cylindrical substrate requires in principle a more intricate theoretical treatment. The dynamics in the polar and axial directions are different and a two-dimensional analysis has to be undertaken to consider the three-dimensionality of the problem (recall that the wall-normal direction has been averaged out into the lubrication approximation). Yet, as pointed out by Trinh et al. (2014), the dynamics of the RTI can be investigated by considering only the uppermost sector of the cylinder, which simplifies the theoretical treatment.

Here we undertake the analysis of a thin liquid film of initial average thickness H_i^* coating the inner side of a horizontal cylinder of radius R^*, extending the one-dimensional analysis of Trinh et al. (2014) and the one of Chapter 3 to the remaining axial dimension. We show that allowing film perturbations along the axial direction can trigger various instability patterns including drops and rivulets, which we explore experimentally, theoretically and numerically. The results of the linear optimal transient growth analysis, together with nonlinear numerical simulations, allow us to rationalize our experimental results. For moderate Bond numbers, $Bo = \rho g H_i^* R^* / \gamma$, a purely axial instability – yielding *rivulets* – arises. The liquid accumulates in equally spaced rivulets, similar to the rolls of Fermigier et al. (1992), yet with the significant difference that they persist over time as they drain out the film. For large Bond numbers, the instability pattern consists of *droplets*. These droplets form on a two-dimensional array similar to the one observed for the planar geometry (Fermigier et al., 1992), although the pattern in the curved geometry is stretched in the polar direction because of the draining flow.

The chapter is structured as follows. The relevant dimensionless quantities are introduced in Sec. 4.2.1. The experimental set-up is presented in Sec. 4.2.2, followed by the description of the phase diagram in Sec. 4.2.3. The linear optimal transient growth analysis is detailed in Sec. 4.3. In particular, the governing equations are presented in section 4.3.1, linearized and solved analytically in Sec. 4.3.2 and the results of the optimal transient growth analysis, described

in Sec. 4.3.3, are elucidated in section 4.3.4. Nonlinear effects on the pattern selection are investigated by performing two-dimensional simulations, which are presented in Sec. 4.4. The draining rivulets are described in greater detail in Sec. 4.5. The influence of the nonlinear interactions are discussed in Sec. 4.5.1, whereas the experimental characterization of the rivulets dynamics is presented in Sec. 4.5.2, followed by a numerical experiment of rivulet drainage in Sec. 4.5.3.

4.2 Experimental results

4.2.1 Relevant dimensionless parameters

A thin viscous film of initial average thickness H_i^* coats the inside of a cylinder of inner radius R^* whose axis is orthogonal to gravity (Fig. 4.1). The film aspect ratio $\delta = H_i^*/R^*$ is small,

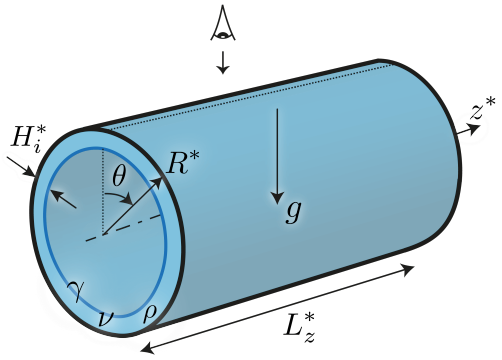

Figure 4.1 – Sketch of the three-dimensional problem geometry.

$\delta \ll 1$. Defining μ as the dynamic viscosity, ρ the density and g the gravitational field, the drainage time is given by the gravitational relaxation scale $\tau_d = \mu R^*/(\rho g H_i^{*2})$ (Trinh et al., 2014). The other relevant time scale of the problem is that of the classic Rayleigh-Taylor instability τ_{RT}, which is proportional to $\mu\gamma/(\rho^2 g^2 H_i^{*3})$ (Fermigier et al., 1992), where γ is the fluid's surface tension. Taking the ratio between these two times we define the Bond number: $Bo = \rho g H_i^* R^*/\gamma$ therefore accounting for the relative magnitude of gravitational and surface-tension forces.

4.2.2 Experimental set-up

Experiments are performed with two types of silicone oil (Carl Roth GmbH) with kinematic viscosity $\nu = 1000$ cSt, density $\rho = 970$ kg/m^3, surface tension $\gamma = 21.2$ mN/m and $\nu = 5000$ cSt, $\rho = 973$ kg/m^3, $\gamma = 21.4$ mN/m, respectively. Two different techniques are adopted to obtain the initial uniform coating (see Fig. 4.2). The first one consists in using a poly(methyl methacrylate) (PMMA) cylinder partially filled with silicone oil and spinning it around its axis (see Fig. 4.2(a)). Following Melo (1993), the critical rotation velocity Ω_c above which

a homogeneous film can be obtained is: $\Omega_c = (A^*/4.428R^*)^2 g/\nu R^*$, where A^* is the cross-section of the cylinder occupied by the fluid. For $\Omega \gg \Omega_c$ the film thickness is expected to be uniform, so that the liquid is in solid-body rotation with the cylinder, whereas for $\Omega < \Omega_c$, different kinds of undesired instabilities can be observed (Thoroddsen & Mahadevan, 1997; Hosoi & Mahadevan, 1999; Seiden & Thomas, 2011; Pougatch & Frigaard, 2011). For the range of parameters under study, the threshold Ω_c is always less than 100 rpm, the speed at which we operate. Furthermore, for this speed, inertial instabilities such as the ones studied by Benilov & Lapin (2013) do not form in our experiments. The relative nonuniformity of the film thickness is within 2%. After the uniform film is obtained, the rotation is suddenly stopped so that the coating stops too with time scale $\tau = H_i^{*2}/\nu$. Owing to the small film thickness and large viscosity, the time τ is small compared to the gravitational drainage time τ_d. More precisely, we get 0.4 ms $< \tau <$ 16 ms and 0.55 s $< \tau_d <$ 20.1 s, confirming $\tau \ll \tau_d$. We can therefore assume that the gravity-induced drainage starts from a uniform stationary condition.

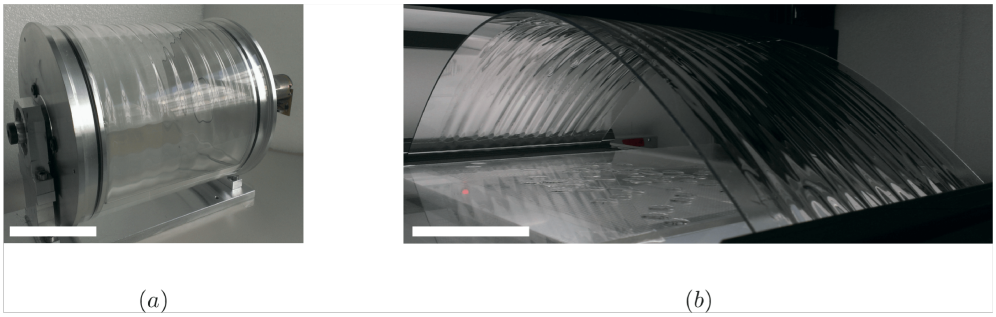

(*a*) (*b*)

Figure 4.2 – (*a*) Cylindrical substrate formed by a PMMA cylinder of radius $R^* = 8.6$ cm and length $L_z^* = 15$ cm partially filled with silicone oil. The axis of the cylinder is mounted on a motor which can reach 100 rpm for coating purpose. (*b*) Curved PMMA plate of 500x200x4 mm clamped at its extremities to prescribe the desired substrate curvature. The thin film of silicone oil is applied with a film applicator prior to deforming the plate. Scale bars correspond to 10 cm. Rivulets are visible on both figures.

For the second technique (see Fig. 4.2(b)), a uniform film of silicone oil is coated onto a planar PMMA plate with dimensions 500x200x4 mm using a film applicator (Film Casting Knife 15cm, BYK GmbH), whose gap clearance can be tuned. The actual film thickness as well as its uniformity, which is within 4%, are verified before proceeding. The film thickness is measured with a Confocal Chromatic Sensing technique (STIL CL2-MG140 and CL4-MG20 with CCS PRIMA), which allows measurements between 20 and 4000 μm, with an accuracy of 250 nm (see Appendix 4.7.5 for further details on the measurement technique). After coating, the plate is then turned upside down and bent by clamping its extremities. As a result, the upper part of the substrate – expected to be the key region – has a circular cross-section.

The achievable parameter range for each method is reported in Tab. 4.1. As evident from the table, the rotating cylinder is suitable for intermediate Bond numbers and relatively large film aspect ratios, whereas the curved plate allows for a slightly wider range of Bond numbers and

	Rotating cylinder	Curved plate
H_i^*	0.9 – 7.7 mm	0.11 – 2.04 mm
R^*	0.086 m	0.18 – 0.98 m
δ	$1.1\times10^{-2} - 9.3\times10^{-2}$	$1.1\times10^{-4} - 9.8\times10^{-3}$
Bo	35 – 308	37 – 349
τ_d	0.55 – 20.1 s	5.4 s – 2 h 10 min

Table 4.1 – Values of relevant quantities for the experimentally explored parameter range.

smaller aspect ratios owing to its flexibility in tuning the plate curvature.

A Basler camera (acA1300 – 60gm) with a long-focus zoom lens 18-108mm f/2.5 (LMZ 45C5, Japan Lens Inc.) is employed to record the experiment. For the cylindrical set-up, we measured the temporal evolution of the film thickness at $\theta = 0$ along the cylinder length of $L_z^* = 15\,\text{cm}$ (see Fig. 4.1). The optical pen, measuring the film thickness at 200 Hz, is mounted on a linear motor stage (Aerotech PRO165LM), which performs oscillatory motions at 0.4 Hz. Given the slow dynamics induced by the high viscosity of the fluid, a sufficient temporal and spatial resolution (0.6 mm) is thus achieved.

4.2.3 Phase diagram: rivulets or dripping droplets?

In the classical Rayleigh-Taylor instability for horizontal substrates, thin films eventually destabilize into droplets, either directly or following the formation of rolls and axisymmetric structures caused by the presence of the contact line at the boundaries or local perturbations (Fermigier et al., 1992). The orientation of these structures is dictated only by the boundaries of the geometry or initial conditions. The fate of thin films coating the concave side of a cylindrical substrate is qualitatively different, as patterns such as rivulets may persist over time, i.e. drops do not necessarily form. Aiming to classify the patterns observed in our experiments, we have built a phase diagram that we report in Fig. 4.3. As evident from the figure, the diagram divides into three main regions, which we now describe.

Dripping droplets arise in the limit of very large Bond numbers ($Bo \gtrsim 200$) and vanishing film aspect ratios ($\delta < 10^{-2}$), that is when the substrate may be seen as nearly horizontal on the scale of the film (see Supplementary Movie 1). Often, droplets arrange themselves on a hexagonal structure, as shown in the inset of Fig. 4.3. However, the initially formed two-dimensional array of droplets deforms over time following the drainage flow. Droplets were found to pinch off or slide along the substrate.

Rivulets are found for smaller Bond numbers, $Bo \lesssim 100$ (see Fig. 4.2 and Supplementary Movie 2), yet larger than the critical value, $Bo > 12$ (Trinh et al., 2014), see Chapter 3. Unlike the rolls forming under a horizontal substrate, rivulets persist over time and do *not* further destabilize into droplets. These rivulets have a clear orientation dictated by the geometric anisotropy of the substrate curvature and are always orthogonal to the axis of the cylinder.

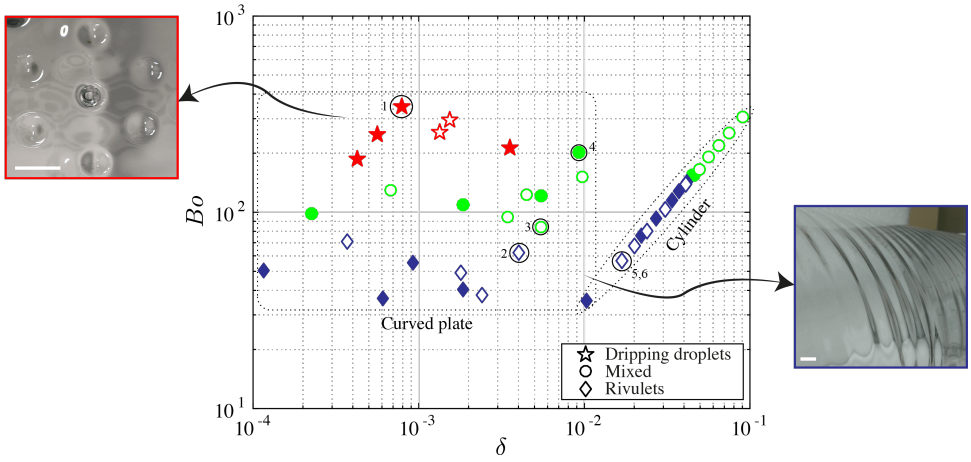

Figure 4.3 – Phase diagram as a function of the film aspect ratio δ and Bond number Bo. Full symbols correspond to $\nu = 1000\,$cSt and empty symbols to $\nu = 5000\,$cSt. Numbers correspond to supplementary movies. The uncertainty on the film aspect ratio is of the order of 4% (resp. 2%) for the curved plate (resp. cylinder) set-up and the uncertainty on the Bond number is of the order of 5%. Insets: top-view of the two-dimensional hexagonal pattern of droplets (left) and side-view of rivulets (right). Scale bars correspond to 10 mm.

Dripping droplets and rivulets are separated by a *mixed* regime for Bond numbers of the order of 100, where both patterns coexist on the substrate: rivulets are typically found at the boundaries and droplets in the center (see Supplementary Movie 3). For film aspect ratios $\delta > 7 \times 10^{-3}$, rivulets are found to experience a secondary instability at later times and destabilize into several aligned droplets which pinch off, similar to the pinch-off studied by Indeikina, Veretennikov & Chang (1997) and Alekseenko, Aktershev, Bobylev, Kharlamov & Markovich (2015) (see Supplementary Movie 4).

Experiments performed with the cylinder display a larger critical Bond number for the transition from rivulets to the mixed regime. The main reason is the smoother initial film thickness in this configuration compared to curved plate set-up. As will become clear in Sec. 4.4, the system is very sensitive to ambient noise and particular care has to be taken when performing the experiments. The thin film evolutions in a cylinder for two different experiments with the same parameters are shown in Supplementary Movies 5 and 6, illustrating the reproducibility of the results.

In the phase diagram of Fig. 4.3 experiments with similar values of (Bo, δ) and different viscosities collapse to the same region. This is an indication that viscosity does not seem to play a major role in the pattern selection, while it modifies the time scale for the appearance of such a pattern. Note that in our problem the typical time scale of the Rayleigh-Plateau instability (Hammond, 1983; Lister et al., 2006; Duclaux et al., 2006) is several orders of magnitude larger than the characteristic time of the classical Rayleigh-Taylor instability. In fact we have $\tau_{\mathrm{RP}} \sim \mu(R^* - H_i^*)^4/(\gamma H_i^{*3}) \sim \mu R^*/(\gamma\delta^3)$ for the Rayleigh-Plateau instability and $\tau_{\mathrm{RT}} \sim \mu\ell_c^{*4}/(\gamma H_i^{*3})$ for the RTI, so that $\tau_{\mathrm{RP}}/\tau_{\mathrm{RT}} = \left(R^*/\ell_c^*\right)^4 \gg 1$. Furthermore, the dominant wavelength (see Fig.

4.2 or the inset of Fig. 4.3) is found to be proportional to the capillary length in our experiments as another indication of the relevance of the Rayleigh-Taylor instability. Recall that for the Rayleigh-Plateau instability the wavelength is proportional to the cylinder radius (see Sec. 1.2). We thus argue that rivulets form following the gravitational Rayleigh-Taylor instability.

Note finally that perturbations invariant in the axial direction, or *waves*, as studied in Trinh et al. (2014) and in Chapter 3, are not observed in our experiments. In Sec. 4.3 we propose a two-dimensional linear optimal transient growth analysis, for small aspect ratios, where we expect to identify the transition between rivulets and dripping droplets. Given the phase diagram in Fig. 4.3, we expect the value of the critical Bo to be independent of δ for $\delta \lesssim 10^{-2}$.

4.3 Linear optimal transient growth analysis

4.3.1 Governing equation

Owing to the small aspect ratio of the problem, $\delta \ll 1$, we use a lubrication approach to model the evolution of the film thickness (Oron et al., 1997). Inertial effects are neglected due to the large viscosity of the fluid (the Reynolds number is of the order of 10^{-3}). The flow is driven by the gravitational field and by the capillary pressure gradient. By using the local mass conservation in cylindrical coordinates as well as H_i^* and τ_d as length and time gauges of the problem, the governing equation for the dimensionless film thickness $\bar{H}$ for small aspect ratios reduces to (see Appendix 4.7.1 for more details on the derivation)

$$\bar{H}_t + \frac{1}{3}\left[\underbrace{\bar{H}^3}_{\text{IV}}\left(\underbrace{\frac{1}{Bo}\bar{\kappa}_\theta}_{\text{I}} + \underbrace{\delta\bar{H}_\theta\cos\theta}_{\text{II}} + \underbrace{\sin\theta}_{\text{III}}\right)\right]_\theta + \frac{1}{3\delta^2}\left[\underbrace{\bar{H}^3}_{\text{IV}}\left(\underbrace{\frac{1}{Bo}\bar{\kappa}_z}_{\text{I}} + \underbrace{\delta\bar{H}_z\cos\theta}_{\text{II}}\right)\right]_z = 0, \quad (4.1)$$

where indices represent partial derivatives and $\bar{\kappa}$ is the curvature of the film interface. Terms I represent surface tension effects, terms II the variation of the hydrostatic pressure distribution, term III accounts for the gravity-induced drainage and term IV is the mobility of the liquid. The curvature up to the second order in δ is

$$\begin{aligned}\bar{\kappa} = &\frac{\bar{H}_{zz}}{\left(\bar{H}_z^2+1\right)^{3/2}} + \frac{\delta}{\left(\bar{H}_z^2+1\right)^{1/2}} \\ &-\delta^2\left[\frac{\bar{H}_{zz}\bar{H}_\theta^2}{2\left(\bar{H}_z^2+1\right)^{3/2}} - \frac{3\bar{H}_z^2\bar{H}_{zz}\bar{H}_\theta^2}{2\left(\bar{H}_z^2+1\right)^{5/2}} + \frac{2\bar{H}_z\bar{H}_{\theta z}\bar{H}_\theta}{\left(\bar{H}_z^2+1\right)^{3/2}} - \frac{\bar{H}_{\theta\theta}}{\left(\bar{H}_z^2+1\right)^{1/2}} - \frac{\bar{H}}{\left(\bar{H}_z^2+1\right)^{1/2}}\right] + O\left(\delta^3\right).\end{aligned} \quad (4.2)$$

Inspired by the good agreement between the linear optimal transient growth analysis of the top region of the cylinder (Trinh et al., 2014) with that of the entire circular geometry (see Chapter 3), we concentrate on the cylinder's most unstable region close to $\theta = 0$. For $\delta \ll 1$, the change of variable $\theta = \delta^{1/2}x$ and $z = \delta^{-1/2}y$ is suitable. At leading order, the curvature

reduces to $\bar{\kappa} = \delta(1 + \bar{H}_{xx} + \bar{H}_{yy})$. In the limit $x \ll 1$, the lubrication equation (4.1) becomes (see Appendix 4.7.2)

$$\bar{H}_t + \nabla \cdot \left[\frac{\bar{H}^3}{3} \nabla \left(\frac{1}{Bo} \nabla^2 \bar{H} + \bar{H} + \underbrace{\frac{x^2}{2}}_{\text{III}} \right) \right] = 0, \tag{4.3}$$

where $\nabla = [\partial_x, \partial_y]^T$ is the gradient operator. Equation (4.3) differs from the classical lubrication equation employed for the horizontal substrate (Fermigier et al., 1992) only by the presence of the drainage term III. This term breaks the symmetry of the problem and is the key to the following analysis.

4.3.2 Linear disturbance solution

For a uniform film thickness, $\bar{H}(x, y, t) = H(t)$, equation (4.3) has an analytical solution of the form (see Chapter 2, Takagi & Huppert (2010) and Trinh et al. (2014))

$$H(T) = \frac{1}{\sqrt{T}}, \tag{4.4}$$

with $T = 1 + \frac{2}{3} t$ [1] (see Appendix 4.7.3 for the derivation). This solution will be shown to be asymptotically stable and we will refer to it as the *drainage solution*.

The film thickness is decomposed into this spatially uniform drainage solution $H(T)$ and small space-dependent disturbances $\varepsilon h(x, y, T)$:

$$\bar{H}(x, y, T) = H(T) + \varepsilon h(x, y, T) \quad , \quad \varepsilon \ll 1. \tag{4.5}$$

Entering the decomposition (4.5) into the lubrication equation (4.3) and considering first-order terms, we obtain the linear disturbance equation for the perturbations:

$$h_T + \frac{1}{2T^{3/2}} \left(\frac{\nabla^4 h}{Bo} + \nabla^2 h \right) + \frac{3}{2T} (x h_x + h) = 0. \tag{4.6}$$

In this expression, the base flow H is explicitly accounted for by the powers of T. For an initially harmonic disturbance $h(x, y, 1) = h_0(x, y) = \exp[\mathrm{i}(\alpha x + \beta y)] + c.c.$ with wavenumber α in the polar direction and β in the axial direction, the solution is

$$h(x, y, T) = A(\alpha, \beta, T) \exp\left[\mathrm{i} \left(\alpha \frac{x}{T^{3/2}} + \beta y \right) \right] + c.c., \tag{4.7}$$

where A satisfies

$$A_T + \frac{1}{2} \left[\frac{1}{Bo} \left(\frac{\alpha^4}{T^{15/2}} + \frac{\beta^4}{T^{3/2}} + 2 \frac{\alpha^2 \beta^2}{T^{9/2}} \right) - \left(\frac{\alpha^2}{T^{9/2}} + \frac{\beta^2}{T^{3/2}} \right) + \frac{3}{T} \right] A = 0. \tag{4.8}$$

[1] Note that T has been used instead of $\tilde{t}$ (used in Chapters 3) to denote the rescaled time.

The temporal dependence of the apparent wavenumber in the polar direction, $x/T^{3/2}$, is chosen so as to annihilate the stretching term xh_x in Eq. (4.6). The solution

$$A(\alpha,\beta,T) = \frac{1}{T^{3/2}}\exp\left[\left(1-\frac{1}{T^{7/2}}\right)\frac{\alpha^2}{7} - \frac{1}{Bo}\left(1-\frac{1}{T^{13/2}}\right)\frac{\alpha^4}{13} + \left(1-\frac{1}{T^{1/2}}\right)\beta^2 - \frac{1}{Bo}\left(1-\frac{1}{T^{1/2}}\right)\beta^4 + - \frac{1}{Bo}\left(1-\frac{1}{T^{7/2}}\right)\frac{2\alpha^2\beta^2}{7}\right] \tag{4.9}$$

is composed of two parts. On the one hand, the exponential term results from the Rayleigh-Taylor instability, with both destabilizing terms in α^2 or β^2 and stabilizing terms in α^4, β^4 or $\alpha^2\beta^2$. This exponential term saturates to a maximal amplitude due to the thinning of the film, accounted for by the powers of T. The largest amplitude depends only on the wavenumbers and on the Bond number. On the other hand, the gravity-induced drainage also enters through the algebraic term $1/T^{3/2}$, which eventually makes the amplitude vanish for large times, $\lim_{T\to\infty} A(\alpha,\beta,T) = 0$. In view of Eq. (4.9), it is therefore clear that the system is linearly asymptotically stable and only a transient growth can be achieved.

The initial amplitude evolution is given by

$$A(\alpha,\beta,T\to 1) \sim 1 + \frac{(\alpha^2+\beta^2-3)Bo-(\alpha^2+\beta^2)^2}{2Bo}(T-1) + O[T-1]^2. \tag{4.10}$$

Introducing the oblique mode $\mathbf{k} = \alpha\,\mathbf{e}_x + \beta\,\mathbf{e}_y$, with norm $k = \sqrt{\alpha^2+\beta^2}$, initial grow occurs only if $k^2 - 3 - k^4/Bo > 0$. This condition is best met for

$$k_0 = \sqrt{\frac{Bo}{2}}, \tag{4.11}$$

which is the initially most amplified wavenumber. In agreement with Trinh et al. (2014) and Chapter 3 we thus recover the condition $Bo > 12$. We conclude that the threshold of the initial growth is not dependent on perturbation direction and the wavenumber k_0 corresponds to the wavenumber with the largest linear growth in the planar Rayleigh-Taylor instability (Fermigier et al., 1992).

In our formalism, *waves* and *rivulets* correspond to modes with $\mathbf{k} = \alpha\,\mathbf{e}_x$ and $\mathbf{k} = \beta\,\mathbf{e}_y$, respectively. The time evolution of the amplitude of waves and rivulets for the initial wavenumber of norm k_0 are shown in Fig. 4.4 for different Bond numbers. The growth of *rivulets* is much stronger than that of *waves*, and they persist longer, thereby rationalizing why *waves* are never seen in experiments. Note that *waves* and *rivulets* are the two limiting cases, as more generic perturbations can be expressed as a linear combination of α and β such that $\mathbf{k} = \alpha\,\mathbf{e}_x + \beta\,\mathbf{e}_y$.

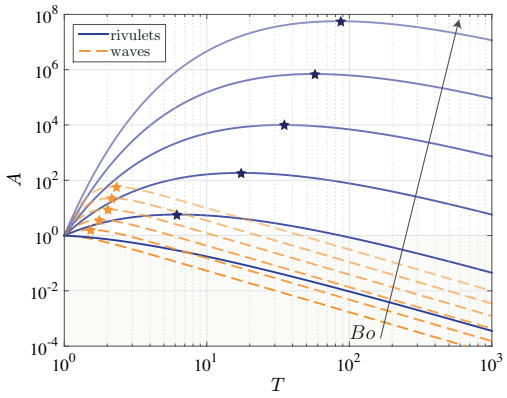

Figure 4.4 – Linear perturbative results. The amplitude A is shown for waves ($\beta = 0$) and rivulets ($\alpha = 0$). They correspond to an initial perturbation with $k = k_0$ (see Eq. (4.11)) for Bond numbers, $Bo = 10, 30, 50, 70, 90$ and 110. Stars denote the largest amplitudes.

4.3.3 Optimal growth

The optimization of the perturbations modes is performed for pure α and pure β modes separately. The optimal wavenumbers and the optimal times correspond to the wavenumbers and times for which the amplitude is the largest.

Following Eq. (4.9) we find that optimal wavenumber for the waves is

$$\left.\frac{\partial A}{\partial \alpha}\right|_{\beta=0} = 0 \quad \Leftrightarrow \quad \alpha_{\max}(T) = \sqrt{\frac{13}{14}\frac{(1-T^{-7/2})}{(1-T^{-13/2})}Bo}, \tag{4.12}$$

whereas for the rivulets it is

$$\left.\frac{\partial A}{\partial \beta}\right|_{\alpha=0} = 0 \quad \Leftrightarrow \quad \beta_{\max} = \sqrt{\frac{Bo}{2}}. \tag{4.13}$$

Hence, the wavenumber for the *rivulets* to reach the largest growth at any time always corresponds to the classical RTI most amplified wavenumber k_0. The optimal wavenumber for *waves* has a weak dependence on the optimization time and tends to $k_0\sqrt{13/7}$ for large time horizons (see inset in Fig. 4.5(a)). The largest growths reached by *waves* and *rivulets* as a function of time are therefore

$$A_{\alpha_{\max}}(T) = A(\alpha_{\max}, 0, T) = \frac{1}{T^{3/2}}\exp\left[\frac{13}{196}\frac{\left(1-T^{-7/2}\right)^2}{\left(1-T^{-13/2}\right)}Bo\right], \tag{4.14}$$

$$A_{\beta_{\max}}(T) = A(0, \beta_{\max}, T) = \frac{1}{T^{3/2}}\exp\left[\frac{1}{4}\left(1-T^{-1/2}\right)Bo\right]. \tag{4.15}$$

Solving $\partial A_{\alpha_{\max}}/\partial T = 0$ and $\partial A_{\beta_{\max}}/\partial T = 0$ yields the times at which the amplitude is the largest. For rivulets, one finds $T_{A^{\beta}_{\max}} = (Bo/12)^2$ and the largest linear transient growth of

rivulets is thus

$$A^{\beta}_{\mathsf{max}} = \left(\frac{12}{Bo}\right)^3 \exp\left(\frac{1}{4}Bo - 3\right). \tag{4.16}$$

The time optimization for waves yields an irreducible polynomial of degree 25 that does not have an algebraic solution. The numerical solution shows that $T_{A^{\alpha}_{\mathsf{max}}}$ follows a power law with exponent close to 0.2 for the considered Bond-number range. The largest linear transient growth that the waves can achieve for large Bond numbers scales as

$$A^{\alpha}_{\mathsf{max}} \sim \exp\left(\frac{13}{196}Bo\right) \quad \text{for} \quad Bo \gg 12. \tag{4.17}$$

The optimal times, as well as the corresponding largest amplitudes, are reported in Fig. 4.5. This optimization procedure confirms what has been observed in Fig. 4.4. The optimal times and amplitudes of the rivulets are much greater than those of the waves. *Waves* are stretched by the draining flow, see Eq. (4.7), reducing the time available for the instability to grow. The stretching effect is evidenced by the different temporal evolutions of the stabilizing and destabilizing RTI terms in Eq. (4.9). In contrast, *rivulets* only experience the thinning of the film, without being stretched along their characteristic direction. They grow for longer times and therefore reach larger amplitudes.

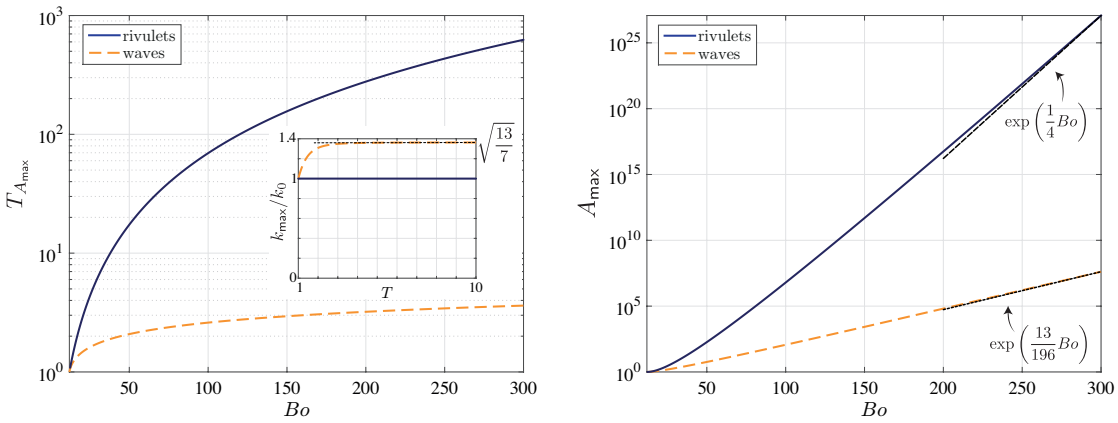

(*a*) (*b*)

Figure 4.5 – (*a*) Times $T_{A_{\mathsf{max}}} = \{T_{A^{\alpha}_{\mathsf{max}}}, T_{A^{\beta}_{\mathsf{max}}}\}$ corresponding to the largest amplitude $A_{\mathsf{max}} = \{A^{\alpha}_{\mathsf{max}}, A^{\beta}_{\mathsf{max}}\}$ obtained by perturbing with the optimal wavenumbers $k_{\mathsf{max}} = \{\alpha_{\mathsf{max}}, \beta_{\mathsf{max}}\}$ as a function of the Bond number. Inset: optimal wavenumbers rescaled by the horizontal RTI wavenumber k_0 as a function of time. (*b*) Largest achievable amplitudes A_{max} as a function of the Bond number. Black dashed lines correspond to the high-Bond number limit evolutions. Note that the disturbance amplitude εA needs to be smaller than the base flow of order unity for the linear theory to hold.

4.3.4 Linear prediction

	Optimal wavenumber	Optimal time	Optimal gain ($Bo \gg 12$)
waves	$\alpha_{\max}(T) = \sqrt{\frac{13}{14}\frac{(1-T^{-7/2})}{(1-T^{-13/2})}Bo}$	$T_{A^{\alpha}_{\max}} \sim Bo^{0.2}$	$A^{\alpha}_{\max} \sim \exp\left(\frac{13}{196}Bo\right)$
	$\alpha_{\max}(T \to 1) = \sqrt{\frac{Bo}{2}}$		
	$\alpha_{\max}(T \to \infty) = \sqrt{\frac{13Bo}{14}}$		
rivulets	$\beta_{\max} = \sqrt{\frac{Bo}{2}}$	$T_{A^{\beta}_{\max}} = \left(\frac{Bo}{12}\right)^2$	$A^{\beta}_{\max} \sim \exp\left(\frac{1}{4}Bo\right)$

Table 4.2 – Summary of main results of the linear optimal transient growth analysis.

Equipped with the results of the linear optimal transient growth (summarized in Tab. 4.2), we aim to better understand our experimental results. In particular, we consider the linear evolution of *rivulets*, $h_0(x,y) = \exp\left(\mathrm{i}k_0 y\right) + c.c.$, *waves*, $h_0(x,y) = \exp\left(\mathrm{i}k_0 x\right) + c.c.$, and *hexagons* having one vector aligned with the axis of the cylinder,

$$h_0(x,y) = \frac{1}{3}\left\{\exp\left(\mathrm{i}k_0 y\right) + \exp\left[\mathrm{i}\left(\frac{\sqrt{3}}{2}k_0 x - \frac{1}{2}k_0 y\right)\right] + \exp\left[\mathrm{i}\left(-\frac{\sqrt{3}}{2}k_0 x - \frac{1}{2}k_0 y\right)\right]\right\} + c.c., \quad (4.18)$$

with $\alpha = \beta = k_0$ the initially most amplified wavenumber, and we choose an initial perturbation with amplitude $\varepsilon = 10^{-3}$. The linear theory holds as long as the magnitude of the disturbances εA is smaller than the base flow, which is of order unity; see Eq. (4.5).

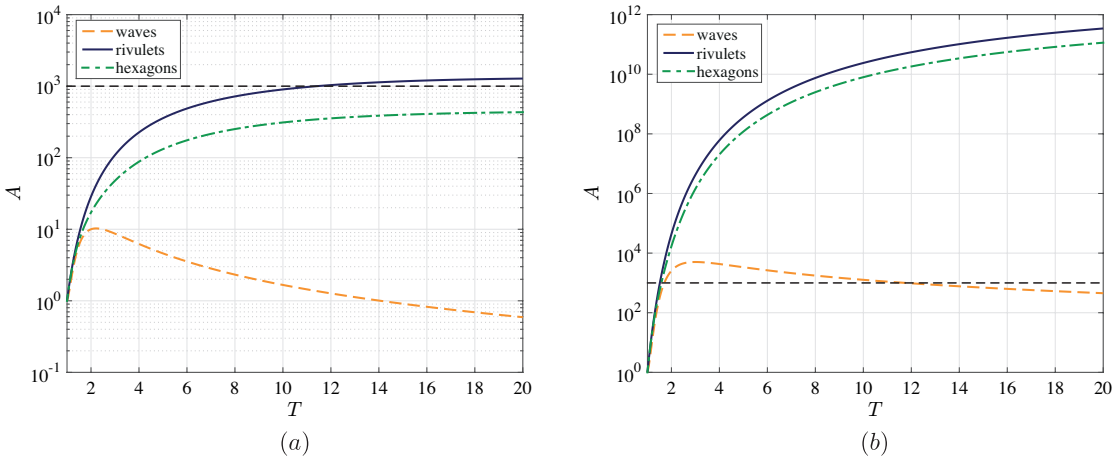

Figure 4.6 – Amplitude evolution of rivulets, waves and hexagons for (*a*) $Bo = 60$ and (*b*) $Bo = 160$. Thin dashed lines indicate necessary amplification of disturbances to become of order one when $\varepsilon = 10^{-3}$. Given the asymptotic stability of the system, the amplitude of all initial conditions saturates and tends to zero for large times, reason why only the evolution for $T \leq 20$ is presented here.

We find that, for low Bond numbers, $Bo \simeq 60$, *rivulets* experience a linear growth strong enough for the perturbation to become of the order of the base flow (see Fig. 4.6(a)), while the *waves* remain much smaller. The *hexagons* experience a large linear growth since they contain a rivulet mode. However, their amplitude remains smaller than one-third of that of the *rivulets*. For larger Bond numbers, e.g. $Bo = 160$ in Fig. 4.6(b), *rivulets, hexagons* as well as *waves* experience a similar linear growth up to the amplitude where nonlinear effects become relevant. Thereby, for sufficiently large Bond numbers, the instability pattern is selected only by the nonlinear effects. Conversely, linear growth selects the pattern for low Bond numbers. Note that the critical Bond number at which nonlinear effects enter into play before the linear growth has promoted a specific pattern is dependent on perturbation amplitude. The experimental threshold of $Bo \sim 100$, corresponding to the mixed regime of Fig. 4.3, is related to our experimental settings.

4.4 Nonlinear two-dimensional simulations

We have seen in Sec. 4.3.4 that the linear stability analysis is sufficient to predict the occurrence of *rivulets* in some cases (low Bond numbers), but does not allow us to conclude anything about the fate of perturbations in other cases (large Bond numbers). Fermigier et al. (1992) performed a weakly nonlinear analysis for the horizontal Rayleigh-Taylor instability. In particular, they showed that the fundamental mode of rolls, which correspond to rivulets for the planar geometry, is stabilized by the nonlinear interaction with the first harmonic of the perturbations. This interaction modifies the amplitude of the rolls only at order ε^3. Furthermore, they have also shown that a two-dimensional pattern of hexagons is amplified at second order through the interactions between fundamental modes oriented at 120° to each other, like the one of Eq. (4.19). This pattern typically appears when the instability's vertical symmetry is broken (Lister et al., 2010; Fauve, 2005), meaning that the equations are not invariant under a change of sign for h. In our context, these nonlinear effects could explain the predominance of a two-dimensional array of droplets instead of rivulets for large Bo. However, although the weakly nonlinear expansion of Fermigier et al. (1992) suggests the right stabilizing/destabilizing nonlinear effects, the expansion is not convergent and can be used only for $t \to 0$ when ε gets larger.

Here, such a truncated weakly nonlinear expansion is even more delicate in view of the draining flow in the polar direction, which stretches the wavenumbers. As a consequence, we instead propose to use two-dimensional numerical simulations of equation (4.1) so as to investigate nonlinear effects in two-dimensional initial disturbances (see Appendix 4.7.4 for details on the numerical methods). The computational domain is $\theta \in [-\pi, \pi]$ and $z \in [-4\pi/b_0, 4\pi/b_0]$. We consider the most amplified pattern for the classic Rayleigh-Taylor instability with wavenumbers in the (θ, z)-space $a_0 = k_0\delta^{-1/2} = \sqrt{Bo/2\delta}$ and $b_0 = k_0\delta^{1/2} = \sqrt{Bo\delta/2}$, and set the initial

condition to be

$$\bar{H}_0 = 1+\varepsilon\left[\cos(b_0 z)+\cos\left(-\frac{1}{2}b_0 z+\frac{\sqrt{3}}{2}a_0(\theta+\phi)\right)+\cos\left(-\frac{1}{2}b_0 z-\frac{\sqrt{3}}{2}a_0(\theta+\phi)\right)\right], \quad (4.19)$$

The initial condition is chosen to be aligned with z and shifted by ϕ along the polar direction to avoid symmetry at $\theta = 0$.

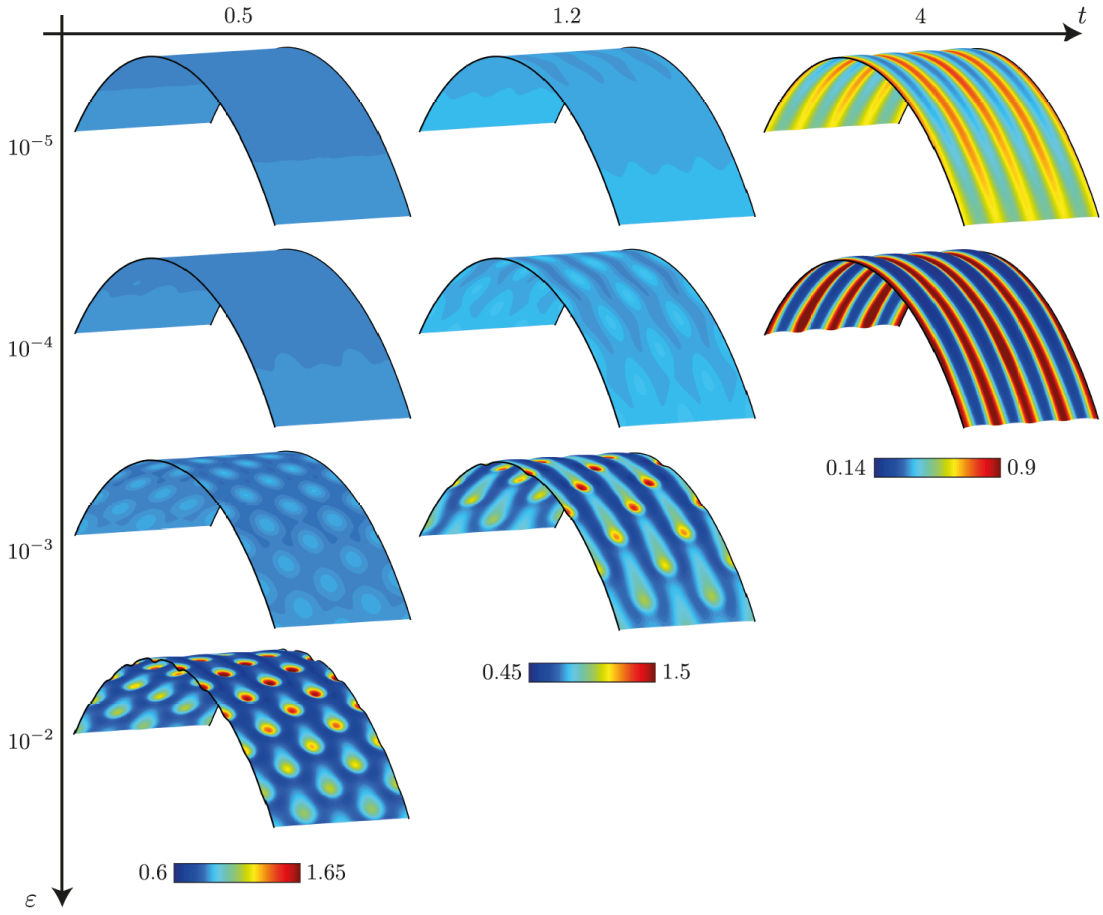

Figure 4.7 – Numerical results of nonlinear two-dimensional simulation. Evolution of the film thickness for a similar initial hexagonal condition (Eq. (4.19)) with amplitude $\varepsilon = 10^{-5}$, 10^{-4}, 10^{-3} and 10^{-2} at times $t = 0.5$, 1.2 and 4 for $Bo = 100$ and $\delta = 0.01$. The angular shift is $\phi = 0.02$. Only the uppermost area in the sector $z \in [-4\pi/b_0, 4\pi/b_0]$ and $\theta \in [-\pi/4, \pi/4]$ is shown.

The results for several values of ε and $\phi = 0.02$ are shown in Fig. 4.7. They correspond to the same Bond number, $Bo = 100$. As evident from the figure, different patterns arise depending on the initial perturbation amplitude. Rivulets are found to form for small ε, despite the imposed hexagonal initial condition. However, when the perturbation is large, the two-dimensional pattern of hexagons grows and dominates the dynamics. Note an intrinsic limitation of our model: owing to the use of the lubrication equation, we do not account for pinching-off drops, which may arise at longer times.

Given the amplifying nature of this system (see Table 4.2), the same result is obtained by fixing the disturbance amplitude and varying the Bond number (see Fig. 4.8).

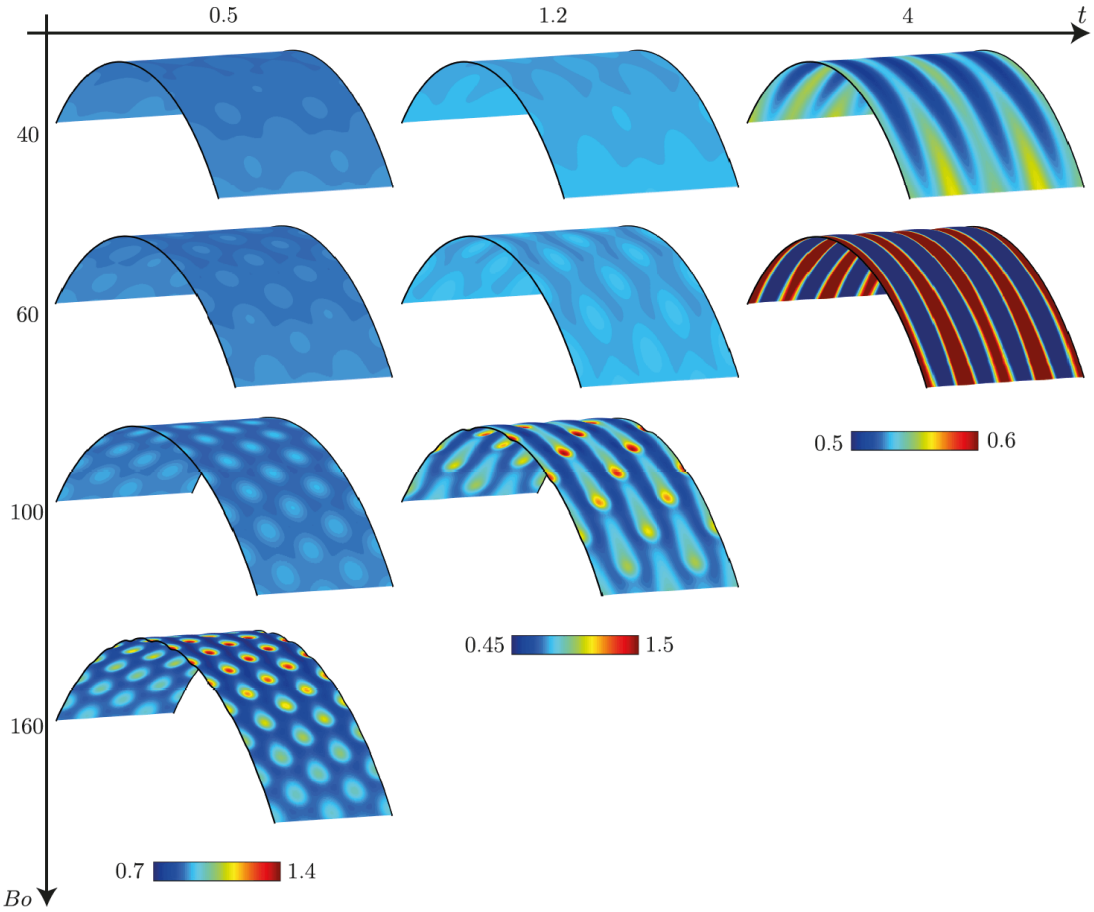

Figure 4.8 – Numerical results of nonlinear two-dimensional simulation. Evolution of the film thickness for a similar initial hexagonal condition (Eq. (4.19)) with amplitude $\varepsilon = 10^{-3}$ at times $t = 0.5$, 1.2 and 4 for $Bo = 40$, 60, 100, 160 and $\delta = 0.01$. The angular shift is $\phi = 0.02$. Only the uppermost area in the sector $z \in [-4\pi/b_0, 4\pi/b_0]$ and $\theta \in [-\pi/4, \pi/4]$ is shown. If one fixes the initial film thickness and the cylinder radius, increasing Bo reduces to increasing the most amplified wavenumber in the axial direction $b_0 = \sqrt{Bo\delta/2}$, i.e. to decreasing the capillary length.

It has to be stressed that the finally observed pattern is not dependent on the structure of the initial condition. If random noise is imposed as initial condition, rivulets will still appear at low Bond numbers and a two-dimensional pattern of isolated droplets will form at large Bond numbers (see Fig. 4.9). The randomness of the initial condition limits the nonlinear interactions and pushes the critical Bo as well as the pattern-formation time to larger values.

The transition from rivulets to a two-dimensional pattern is in agreement with what has been obtained experimentally and presented in Sec. 4.2.3. Rivulets dominate at low Bond numbers whereas nonlinear interactions select the pattern from linearly equally growing modes at

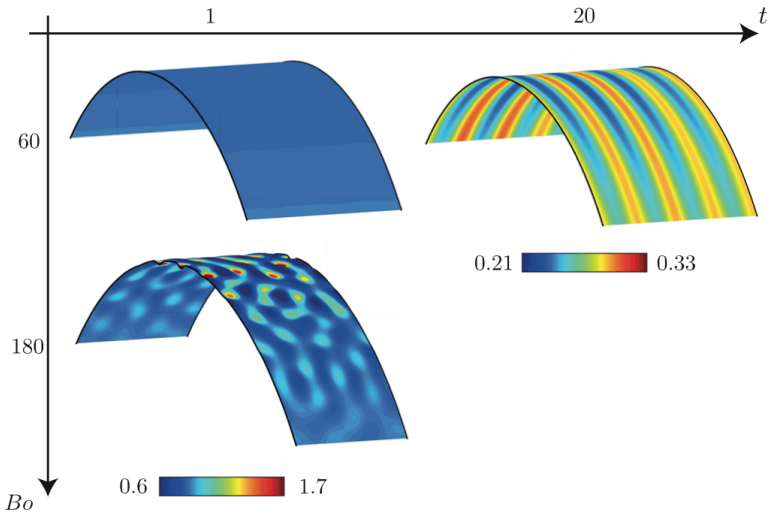

Figure 4.9 – Numerical results of nonlinear two-dimensional simulation. Evolution of the film thickness for a random-noise initial condition with maximal amplitude $\varepsilon = 5 \times 10^{-4}$ at times $t = 1$ and 20 for $Bo = 60$ and 180 and $\delta = 0.01$. Only the uppermost area in the sector $z \in [-4\pi/b_0, 4\pi/b_0]$ and $\theta \in [-\pi/4, \pi/4]$ is shown, with $b_0 = \sqrt{Bo\delta/2}$.

larger Bond numbers. Numerical results show that this transition can be triggered similarly by varying disturbance amplitudes, which is difficult to check experimentally. Nonlinear two-dimensional simulations complete the analysis of the pattern selection for the three-dimensional Rayleigh-Taylor instability under a curved substrate. While rivulets are mainly selected by linear effects along the axial direction, the two-dimensional pattern of droplets relies solely on nonlinear interactions.

4.5 Characterization of the rivulets

4.5.1 Nonlinear simulations at the top of the cylinder

In order to gain more insight into the dynamics of the rivulets, numerical simulations of the one-dimensional lubrication equation for the film thickness at the top of the cylinder are carried out ($\theta = 0$). The lubrication equation (4.1) at $\theta = 0$ with vanishing polar derivatives reads

$$\bar{H}_t + \underbrace{\frac{1}{3}\bar{H}^3}_{\text{I}} + \underbrace{\frac{1}{3\delta^2}\left[\bar{H}^3\left(\frac{1}{Bo}\bar{\kappa}_z + \delta\bar{H}_z\right)\right]_z}_{\text{II}} = 0. \tag{4.20}$$

The term labeled I results from the drainage term in Eq. (4.1) and is responsible for the thinning of the film over time. The terms labeled II match the classical terms of the equation describing the classical horizontal Rayleigh-Taylor instability (Fermigier et al., 1992). Equation (4.20) can be resolved numerically (see Appendix 4.7.4 for details) and its solution is validated by

comparison with a two-dimensional nonlinear numerical simulation in Fig. 4.10(b). The domain size is $L_z = 2 \times 2\pi/b_0$, with $b_0 = k_0\delta^{1/2} = \sqrt{Bo\delta/2}$ the linear optimal wavenumber in the physical z-space and the initial condition is $\bar{H}_0 = 1 + \varepsilon\cos(b_0 z)$. Periodic boundary conditions are used. An example of nonlinear evolution given by Eq. (4.20) is presented in Fig. 4.10. The narrow rivulets, whose peaks grow initially in time, are separated by a rather flat thin-film region (see Fig. 4.10(b)).

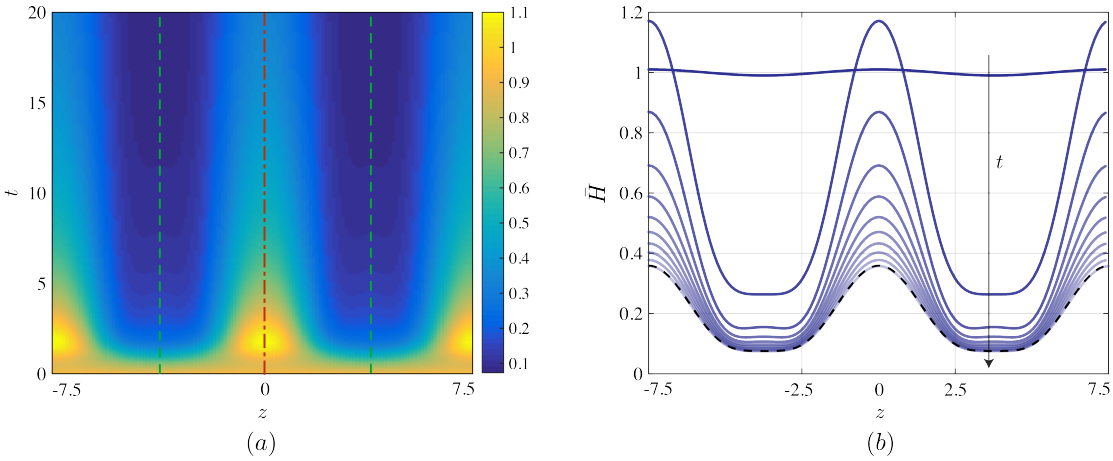

Figure 4.10 – Nonlinear simulations at $\theta = 0$, i.e. using Eq. (4.20). Film thickness as a function of time for rivulets with optimal initial disturbance $\bar{H}_0 = 1 + 0.01\cos(b_0 z)$ with $b_0 = \sqrt{Bo\delta/2}$. (*a*) Spatio-temporal map of the film thickness $\bar{H}$. Dash-dotted and dashed lines correspond to the locations of the peaks and valleys, respectively, whose thickness evolution is shown in Fig. 4.12(a). (*b*) $\bar{H}$-profiles at successive times $t = 0, 2, ..., 20$. Black dashed line corresponds to the nonlinear solution at $\theta = 0$ and $t = 20$ obtained when considering the entire circular geometry $-\pi < \theta < \pi$, Eq. (4.1). $Bo = 70$ and $\delta = 0.02$.

The nonlinear perturbation solution is given by $h(z,t) = [\bar{H}(z,t) - H(t)]/\varepsilon$, where $H(t) = (1 + 2t/3)^{-1/2}$ is the drainage solution at $\theta = 0$ introduced in Eq. (4.4) and $\bar{H}(z,t)$ is obtained by the numerical resolution of Eq. (4.20). The amplitudes of the different harmonics can be found by the Fourier series decomposition of the perturbation h

$$h(z,t) = \sum_{n\in\mathbb{N}} A_n(t)\exp(\mathrm{i}nb_0 z) + c.c.. \tag{4.21}$$

Results are presented in Fig. 4.11(a). The fundamental mode, A_1, obtained via nonlinear simulations agrees well with our linear prediction for small values of ε. Nonetheless, for larger initial perturbations, A_1 is found to saturate and to subsequently decrease well before the linear prediction A does. Albeit $||A||_2$ and A_1 mostly agree, that is A_0 and higher harmonics do not contribute significantly to the energy as evident from Fig. 4.11(b), we argue that their interaction with A_1 generates the observed saturation and therefore cannot be neglected. This type of stabilizing effect is in agreement with the aforementioned analysis of Fermigier et al. (1992) for rolls. Note that the larger the initial disturbance amplitude is, the earlier the higher harmonics will influence the dynamics of the fundamental mode. Yet, if the amplitude

is sufficiently small, the transient growth nature of the instability guarantees that the linear prediction holds for all times (not shown in Fig. 4.11(a), the linear evolution remains superimposed on the nonlinear evolution for $\varepsilon = 10^{-5}$ and $T > 10$). The perturbation amplitude saturates and eventually vanishes due to the asymptotic stability of the system.

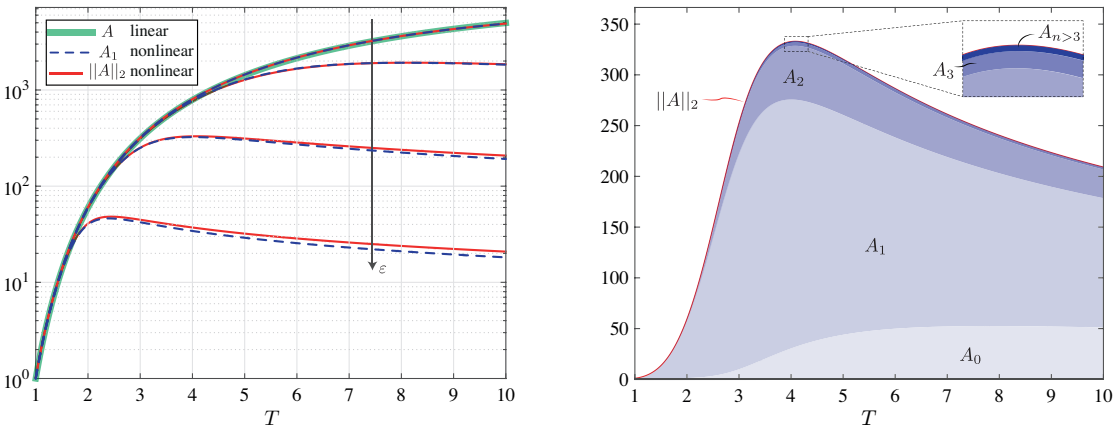

Figure 4.11 – (*a*) Linear (green solid line) and nonlinear (blue dashed lines) amplitudes of the fundamental, together with the total nonlinear amplitude (red solid lines) for the optimal initial disturbance $\bar{H}_0 = 1 + \varepsilon \cos(b_0 z)$ with $b_0 = \sqrt{Bo\delta/2}$ and different initial disturbance amplitudes $\varepsilon = 10^{-5}$, 10^{-4}, 10^{-3} and 10^{-2}. $Bo = 70$ and $\delta = 0.02$. (*b*) Evolution of the total nonlinear disturbance energy $||A||_2$ together with the relative amplitude of the different harmonics A_n of Eq. (4.21). $\varepsilon = 10^{-3}$, $Bo = 70$ and $\delta = 0.02$.

Despite their small contribution to $||A||_2$, the higher-order harmonics are visible in our system. In Fig. 4.10(b). one can see that the flat regions between two fundamentals are subject to an instability too. This phenomenon is akin to the cascade of structures observed by Boos & Thess (1999) for the Marangoni instability in a thin film.

Our nonlinear analysis also indicates a modification in the base flow. We found that the mean film thickness of the perturbed film is smaller than the one of the draining solution $H(t) = 1/\sqrt{1+2\,t/3}$ (Takagi & Huppert, 2010; Trinh et al., 2014) (see Fig. 4.12(a)). The development of rivulets hastens the drainage, which results from the coupling between the shape of the rivulets and the strong variation in the mobility of the liquid that scales as the cube of the local thickness, see Eq. (4.1). Initially, the different components of the thickness follow the linear evolution. There is no correction of the drainage solution due to the rivulets at early times. Nonetheless, when the higher harmonics come into play, A_0 is no longer vanishing (see Fig. 4.11(b)). Building upon this observation, forcing the formation of rivulets is advantageous if one wishes to accelerate the drainage. Similar effects exist when waves run down at the surface of a liquid film flowing down an inclined plane (Kofman, Ruyer-Quil & Mergui, 2016). Such a modification of the mean flow is also a key to the saturation of hydrodynamic instabilities like the vortex shedding in the wake flow behind a cylinder (Maurel, Pagneux & Wesfreid, 1995; Mantič-Lugo, Arratia & Gallaire, 2014).

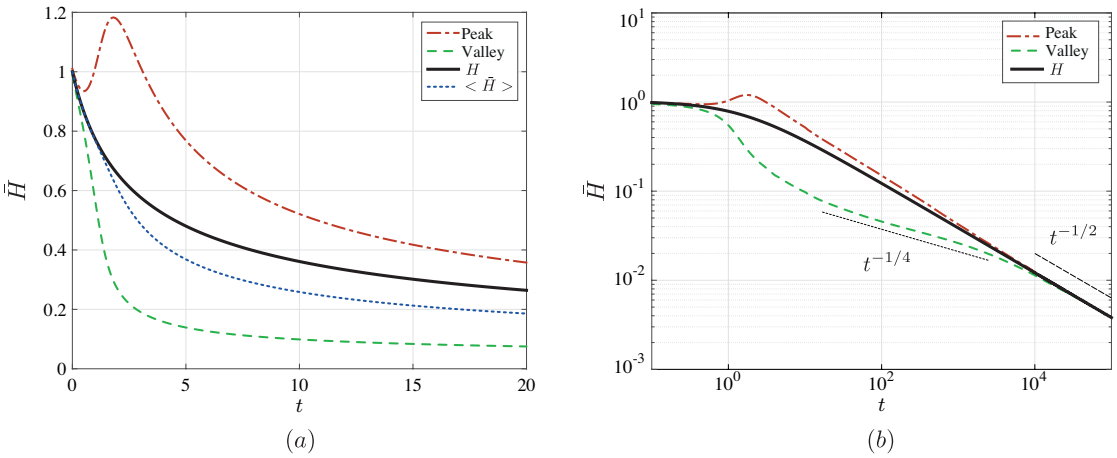

Figure 4.12 – (*a*) Film-thickness evolutions at the peaks (red dash-dotted line) and valleys (green dashed line) of the rivulets shown in Fig. 4.10. The thick black solid line corresponds to the pure drainage solution H and the blue dotted line to the mean film thickness $< \bar{H} >$. (*b*) Long-time evolutions for peaks, valleys and the pure drainage solution. $Bo = 70$, $\delta = 0.02$ and $\varepsilon = 10^{-2}$.

Moving away from the mean value of the film thickness, we now describe the evolution of the film-thickness evolution in the peaks and valleys shown in Fig. 4.12. The growth of the peaks is fed by liquid extracted from the valleys. This mechanism is similar to the rolls in the planar RTI (Fermigier et al., 1992; Lister et al., 2010; Weidner et al., 1997) or to the collars in the instability of a thin annular film coating the inside or outside of a cylinder in the absence of gravity (Hammond, 1983; Lister et al., 2006). However, due to the thinning of the film in time, rivulets can only grow at short times. At later stages, the film thins and thus limits the liquid that a rivulet can pull from its vicinity. We find that before the film becomes uniform again, the thickness in the valleys follow the scaling $t^{-1/4}$ (see Fig. 4.12(b)). The same scaling was found by Lister et al. (2010) for thin regions between pendent drops below planar substrates and for the lobes inside a cylinder studied by Hammond (1983). At these intermediate times, the drainage of the rivulet valleys is driven by the classical RTI term II in Eq. (4.20) yielding $\bar{H} \sim t^{-1/4}$, as the effect of the term I is negligible. For peaks, the term I of Eq. (4.20) is not negligible, as the film thicknesses $\bar{H}$ is relatively larger. Eventually, the film thickness becomes uniform again due to the drainage in the rivulets and the drainage scales like the base flow, $\bar{H} \sim t^{-1/2}$.

4.5.2 Experimental measurements

Rivulets are characterized experimentally by measuring the film thickness at the top of the cylinder. The spatio-temporal film-thickness map is shown in Fig. 4.13(a). *Rivulets* first form at the boundaries of the cylinder where the film is perturbed by the existence of a meniscus. They then progressively invade the entire domain (see Fig. 4.13(b)). As time evolves, the thickness of the rivulets eventually decreases, but their structure does not destabilize and we do not see

any drops forming.

The rivulets were found to be almost equally spaced in experiments, with wavelength $\lambda^* = 14 \pm 1$mm. The linearly most amplified wavelength is $\lambda^{*\beta}_{\max} = \lambda^*_0 = 2\pi/\sqrt{Bo\delta/2}H^*_i = 13.5$mm (see Sec. 4.3.3). Keeping in mind that the calculation leading to this value is idealized – infinite domain approximation – we find that the agreement is satisfactory. In reality, rivulets grow in a finite domain whose width is not an integer multiple of the most amplified wavelength, which they progressively invade starting from the boundaries. The profiles in Fig. 4.13(b) are qualitatively similar to their numerical counterpart. In particular the aforementioned higher harmonics are evident in the valleys between the rivulets. The detailed evolution of

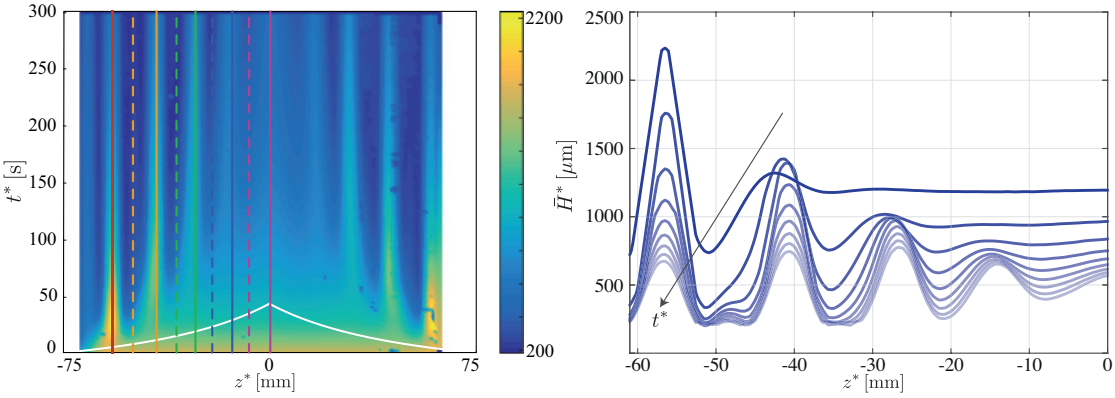

(a) (b)

Figure 4.13 – (a) Spatio-temporal diagram of the film thickness $\bar{H}^*$ measured experimentally along the cylinder generatrix at $\theta = 0$. Solid and dashed lines correspond to the locations of the peaks and valleys, respectively, whose thickness evolutions are shown in Fig. 4.14(b). The white line corresponds to the invading front location z^*_f predicted by the linear theory. The film thickness close to the extremities of the cylinder is not shown in the spatio-temporal diagram due to measurement uncertainties induced by the large thickness gradients. (b) $\bar{H}^*$-profiles at successive times $t^* = 30, 60, ..., 270$ s for a range of dimensional axial locations $z^* \in [-61, 0]$ mm. The Bond number is approximatively 67 and the film aspect ratio 0.02.

film thickness along the peaks and valleys is shown in Fig. 4.14(b). The trend of these curves is similar to that found numerically (see Fig. 4.12(a)). Rivulets undergo a transient growth, whose magnitude decreases as we move towards the center of the sample. The Rayleigh-Taylor instability propagates from the boundaries, where it is forced by a meniscus or a contact line. Limat et al. (1992) have shown that the front velocity of rolls predicted by the linear marginal stability criterion is given by $v_f = 0.54\, H^{*3}(\rho g)^{3/2}/(\mu\gamma^{1/2})$, corresponding to the pulled fronts of Van Saarloos (2003). Such a front velocity model would predict a linear propagation of the front position in time. In experiments the front velocity reduces with time – the white lines from linear theory as reported in Fig. 4.13(a) are concave up. We hypothesize that this effect is caused by drainage, which effectively lowers H^* as time goes by: $H^*(t^*) = H^*_i/\sqrt{1+2\,t^*/3}$. We have successfully reproduced the effect of the lateral boundaries on the inward propagation of rivulets using a periodic but inhomogeneous initial condition, as described in section 4.5.3.

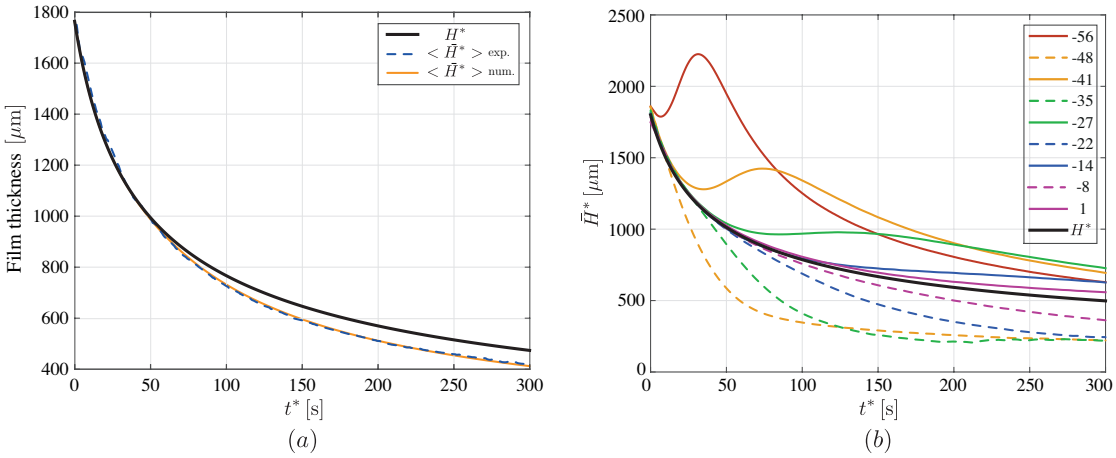

Figure 4.14 – (*a*) Evolution of the mean film thickness $< \bar{H}^* >$ obtained experimentally (blue dashed line) and numerically (orange thin line) compared to the uniform pure draining solution $H^*(t^*) = H_i^*/\sqrt{1+2\,t^*/3}$ (thick black solid line). (*b*) Film-thickness evolutions at the peaks (solid lines) and valleys (dashed lines) of the rivulets shown in Fig. 4.13(a). The location in mm is shown in the legend. The thick black solid line corresponds to the pure drainage solution H^*. $Bo = 67$, $\delta = 0.02$; $\varepsilon = 0.01$ and $\sigma = 2$ (for numerical results, see Sec. 4.5.3).

4.5.3 Numerical experiment on the front propagation of rivulets

The experimentally observed drainage characteristics of rivulets presented in Sec. 4.5.2 can be reproduced by resolving the lubrication equation (4.20) with particular boundary conditions. In order to avoid dealing with the difficult problem of a moving contact line at the boundaries, we consider periodic boundary conditions with a symmetric initial perturbation of the form: $\bar{H}_0 = 1 + \varepsilon\left\{\exp[-(z+L_z/2)^2/(2\sigma^2)] + \exp[-(z-L_z/2)^2/(2\sigma^2)]\right\}$, with $\sigma = 2$ for example.

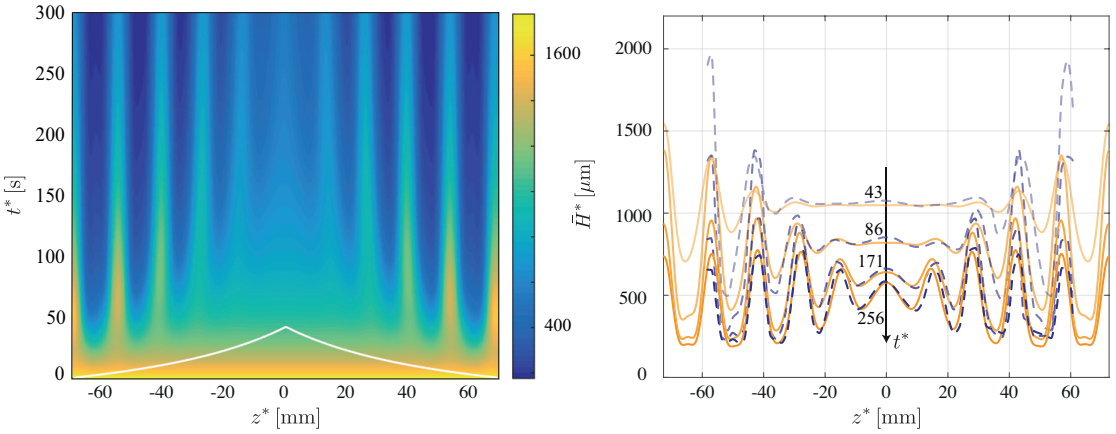

Figure 4.15 – (a) Spatio-temporal diagram of the film thickness $\bar{H}^*$ obtained numerically using the initial and boundary conditions described in Sec. 4.5.3. The white line corresponds to the invading front location z_f^* predicted by the linear theory. (b) Comparison between experimental (blue dashed line) and numerical (orange solid line) film thicknesses at different times. $Bo = 67$, $\delta = 0.02$, $\varepsilon = 0.01$ and $\sigma = 2$.

The spatio-temporal evolution of the film thickness for such an initial condition is displayed in Fig. 4.15(a). Similarly to Fig. 4.13(a), the rivulets first form close to the boundary and then propagate into the domain. Again, the front velocity reduces as the film becomes thinner. The linearly most amplified wavelength $\lambda_{\mathsf{max}}^{*\beta}$ is also selected. This *ad hoc* model for the boundary conditions is able to capture the dynamics of the rivulets invading the domain (see Fig. 4.15(b)) and thus the faster drainage of the rivulets (see Fig. 4.14(a)). The initial differences, imputable to the *ad hoc* boundary conditions, do not affect the later stage of rivulet formation and invasion, making this model satisfactory.

4.6 Conclusions

We have investigated the Rayleigh-Taylor instability of thin viscous films coating the interior of a cylinder. Unlike the classic RTI under a horizontal substrate, where the most amplified pattern has a circular or hexagonal symmetry, here, the geometry of the substrate breaks the symmetry of the problem and gives rise to different patterns depending on the Bond number and the perturbations amplitude. For moderate Bond numbers ($12 < Bo \lesssim 100$) and small film aspect ratios, the thin film results into *rivulets*, i.e. equally spaced axial perturbations that initially grow and eventually decay due to the drainage. For $Bo \gtrsim 100$, the initially uniform film quickly destabilizes into a two-dimensional pattern of *droplets*, which might drip for thick coatings or, are convected to the bottom of the cylinder for thinner films. We showed numerically that this transition is dependent on the amplitude of the perturbation, which precludes the determination of universal thresholds. We have rationalized our experimental phase diagram using a linear optimal transient growth analysis and nonlinear numerical simulations. The linear optimal transient growth analysis at the top of the cylinder predicts the faster growth of rivulets for moderate Bond numbers (or small perturbations) as well as the eventual asymptotic stability of the coating. The linearly most amplified wavenumber along the axial direction corresponds to the classical wavenumber $1/(\sqrt{2}\ell_c^*)$ of the horizontal RTI. Yet, the linear amplification does not coincide with the classical theory (Fermigier et al., 1992) because of the film drainage in the polar direction. For larger Bond numbers (or large perturbations), all modes experience the same linear growth so that the resulting pattern is solely selected by their nonlinear interactions. In particular, the thin film may destabilize into a two-dimensional array of droplets rather than into rivulets, as seen in our numerical simulations of the nonlinear lubrication equation. The novelty of our work lies in the proof that rivulets are the prevailing pattern at moderate Bond numbers ($12 < Bo \lesssim 100$) for thin films in cylindrical substrates. Recall that they are not dominant for the horizontal RTI. Such rivulets may induce a faster drainage (up to 20% faster in the case under study). We have shown that this effect relies on the nonlinear interactions between the fundamental and higher-order harmonics. The more the film is perturbed, the earlier the nonlinear terms will become relevant and the faster the mean film thickness on the upper part of the cylinder will decrease. When the film aspect ratio is larger, the transition to a two-dimensional array of droplets shifts to larger Bond numbers, as found experimentally. Rivulets first form and

destabilize into aligned droplets due to a secondary instability.

It should be mentioned that rivulets, defined here as structures aligned in the direction of the flow, are not intrinsic to the cylindrical geometry. Similar structures arise when totally different forces are at play. For example, Scheid, Kalliadasis, Ruyer-Quil & Colinet (2008) observed the formation of equally spaced rivulets aligned with the direction of the flow for thin films on a vertical heated wall when inertia effects are negligible. They also appear for a thin film above (Troian et al., 1989) and below (Lin, Kondic & Filippov, 2012) an inclined plane or a cylinder (Takagi & Huppert, 2010) in the presence of a moving contact line (see Chapter 6), or on a film falling along the outside wall of a vertical spinning cylinder (Rietz, Scheid, Gallaire, Kofman, Kneer & Rohlfs, 2017) (see Chapter 7).

As a possible follow-up to this work, it would be interesting to consider a thin liquid film coating the outside of horizontal or inclined cylinders of moderate diameter. For this configuration, the drainage solution is not asymptotically stable. Reisfeld & Bankoff (1992), Weidner et al. (1997), de Bruyn (1997) and Lenschen, Calvo & Cachile (2010), who considered thin films on the exterior of a horizontal cylinder, showed that the fluid accumulates at the lower external part of the cylinder and forms droplets, which grow in size and eventually pinch off. However, the diameter of the cylinder in all these studies was too small to observe the transition from rivulets to a two-dimensional array of droplets. Mainly single droplets aligned along the axial direction were observed. For even smaller radii, the Rayleigh-Plateau instability would appear (Duclaux et al., 2006). Concerning the limitations of our work, the pinching off of droplets (Eggers & Villermaux, 2008) as well as the later stages of the dynamics are not considered in this study. After the rivulets have drained out and the droplets have dripped, the liquid will be mainly collected at the bottom of the cylinder and only a thin layer will remain on the upper part of the cylinder. When the corresponding Bond number becomes of the order of the film aspect ratio we expect lobes, collars and dry spots to form, as discussed by King, Cummings, Naire & Jensen (2007) and Jensen (1997) for inclined and curved cylinders. Finally, we expect that a spherical substrate would annihilate the formation of rivulets (see Chapter 5). This is probably the key to the success of chocolatiers, who easily coat spherically shaped moulds in a uniform way, as we have seen in Chapter 2.

Acknowledgments We would like to acknowledge Laurent Limat for delightful discussions about the nonlinear analysis of the Rayleigh-Taylor instability. Also, we would like to thank Lailai Zhu for nicely introducing us to COMSOL Multiphysics. This work was funded by ERC Grant No. SIMCOMICS 280117. B.S. thanks the FRS-FNRS and the IAP-7/38 MicroMAST project for financial support.

Supplementary Material The Supplementary movies can be found at https://doi.org/10.1017/jfm.2017.817.

4.7 Appendix

4.7.1 Derivation of the lubrication equation

The derivation of the model equation presented in Sec. 4.3.1 is briefly outlined hereafter, extending to the axial direction the derivation of Chapter 3. Consider a thin film coating the interior of a cylinder of radius R^* and length L_z^* as shown in Fig. 4.1. Given an initial average thickness of H_i^*, the resulting film aspect ratio reads $\delta = H_i^*/R^*$. The characteristic length in the radial direction is H_i^*, whereas the characteristic length in the polar and axial directions is R^*. The long-wavelength approximation is employed since $\delta \ll 1$ (Oron et al., 1997). Mass conservation indicates that the characteristic velocity normal to the substrate is much smaller than the polar and axial components, $V^* \sim \delta U^* \ll U^*$ and $V^* \sim \delta W^* \ll W^*$, respectively. The Stokes equations are used as the Reynolds number is low and inertial effects can be neglected. The momentum equation in the radial direction is

$$0 = -\frac{1}{\rho}\frac{\partial p^*}{\partial r^*} - g\cos\theta, \tag{4.22}$$

and the boundary condition for the pressure is given by $p^*(R^* - \bar{H}^*, \theta, z^*) = p_0^* - \gamma\bar{\kappa}^*$, where p_0^* is the external pressure, γ the surface tension and $\bar{\kappa}^*$ the curvature of the interface. Equation (4.22) can be integrated along the radial direction, and, using the aforementioned boundary condition, one obtains the pressure distribution $p^*(r^*, \theta, z^*) = p_0^* - \gamma\bar{\kappa}^* + \rho g\cos\theta(R^* - \bar{H}^* - r^*)$. The θ and z^* components of the momentum equation read

$$0 = -\frac{1}{\rho r^*}\frac{\partial p^*}{\partial \theta} + \nu\left[\frac{\partial}{\partial r^*}\left(\frac{1}{r^*}\frac{\partial}{\partial r^*}\left(r^* u^*\right)\right) + \frac{1}{r^{*2}}\frac{\partial^2 u^*}{\partial \theta^2} + \frac{\partial^2 u^*}{\partial z^{*2}}\right] + g\sin\theta, \tag{4.23}$$

$$0 = -\frac{1}{\rho}\frac{\partial p^*}{\partial z^*} + \nu\left[\frac{1}{r^*}\frac{\partial}{\partial r^*}\left(r^*\frac{\partial w^*}{\partial r^*}\right) + \frac{1}{r^{*2}}\frac{\partial^2 w^*}{\partial \theta^2} + \frac{\partial^2 w^*}{\partial z^{*2}}\right]. \tag{4.24}$$

With the change of variable $r^* = R^* - s^*$, where $0 \le s^* \le \bar{H}^* \ll R^*$, the viscous terms in Eq. (4.23) and Eq. (4.24) reduce to $\nu\partial^2 u^*/\partial s^{*2}$ and $\nu\partial^2 w^*/\partial s^{*2}$, respectively, plus terms at least an order δ smaller. Keeping the dominant order of the viscous term, as well as the surface tension and gravitational terms, Eq. (4.23) and Eq. (4.24) with the expression for p^* become:

$$0 = \frac{\gamma\bar{\kappa}_\theta^*}{\rho R^*} + \frac{g\cos\theta\bar{H}_\theta^*}{R^*} + \nu\frac{\partial^2 u^*}{\partial s^{*2}} + g\sin\theta, \tag{4.25}$$

$$0 = \frac{\gamma\bar{\kappa}_{z^*}^*}{\rho} + g\cos\theta\bar{H}_{z^*}^* + \nu\frac{\partial^2 w^*}{\partial s^{*2}}. \tag{4.26}$$

Equations (4.25) and (4.26) can be integrated twice, and considering the zero-slip boundary condition at the cylinder surface, $u^*(0,\theta,z^*) = 0$ and $w^*(0,\theta,z^*) = 0$, as well as the zero-shear-stress interface, $\partial u^*(\bar{H}^*,\theta,z^*)/\partial s^* = 0$ and $\partial w^*(\bar{H}^*,\theta,z^*)/\partial s^* = 0$, yields the velocity

components:

$$u^*(s^*,\theta,z^*) = \left(\frac{\gamma\bar{\kappa}^*_\theta}{\mu R^*} + \frac{\rho g\cos\theta\bar{H}^*_\theta}{\mu R^*} + \frac{\rho g\sin\theta}{\mu}\right)\left(\bar{H}^* - \frac{s^*}{2}\right)s^*, \tag{4.27}$$

$$w^*(s^*,\theta,z^*) = \left(\frac{\gamma\bar{\kappa}^*_{z^*}}{\mu} + \frac{\rho g\cos\theta\bar{H}^*_{z^*}}{\mu}\right)\left(\bar{H}^* - \frac{s^*}{2}\right)s^*. \tag{4.28}$$

The flow rate in the polar direction is given by $Q^{*\theta}(\theta,z^*) = \int_0^{\bar{H}^*} u^*(s^*,\theta,z^*)\mathrm{d}s^*$ and in the axial direction by $Q^{*z}(\theta,z^*) = \int_0^{\bar{H}^*} w^*(s^*,\theta,z^*)\mathrm{d}s^*$. Mass conservation in cylindrical coordinates $\partial\bar{H}^*/\partial t^* + R^{*-1}\partial Q^{*\theta}/\partial\theta + \partial Q^{*z}/\partial z^* = 0$ yields the lubrication equation:

$$\bar{H}^*_{t^*} + \frac{1}{3\mu R^*}\left[\bar{H}^{*3}\left(\underbrace{\frac{\gamma\bar{\kappa}^*_\theta}{R^*}}_{\mathbf{I}} + \underbrace{\frac{\rho g\cos\theta\bar{H}^*_\theta}{R^*}}_{\mathbf{II}} + \underbrace{\rho g\sin\theta}_{\mathbf{III}}\right)\right]_\theta + \frac{1}{3\mu}\left[\bar{H}^{*3}\left(\underbrace{\gamma\bar{\kappa}^*_{z^*}}_{\mathbf{I}} + \underbrace{\rho g\cos\theta\bar{H}^*_{z^*}}_{\mathbf{II}}\right)\right]_{z^*} = 0, \tag{4.29}$$

The term **I** in the spatial variation of the flux corresponds to the surface tension effects, term **II** to the variation of the hydrostatic pressure distribution and term **III** to the drainage.

The free surface of the viscous film is defined by

$$F^*(r^*,\theta,z^*,t^*) = r^* - \left[R^* - \bar{H}^*(\theta,z^*,t^*)\right] = 0, \tag{4.30}$$

and its normal vector $\mathbf{n}^*$ is given by

$$\mathbf{n}^* = \frac{\nabla^* F^*}{||\nabla^* F^*||} = \frac{\left[1, \frac{\bar{H}^*_\theta}{r^*}, \bar{H}^*_{z^*}\right]^T}{\sqrt{1 + \left(\frac{\bar{H}^*_\theta}{r^*}\right)^2 + \left(\bar{H}^*_{z^*}\right)^2}} \tag{4.31}$$

at $r^* = R^* - \bar{H}^*$.

The interfacial curvature therefore reads

$$\begin{aligned}\bar{\kappa}^* =& \nabla^* \cdot \mathbf{n}^* \\ =& -\frac{\bar{H}^*_{z^*z^*}\bar{H}^{*2}_{z^*}}{\left(\frac{\bar{H}^{*2}_{\theta}}{r^{*2}}+\bar{H}^{*2}_{z^*}+1\right)^{3/2}} - \frac{2\bar{H}^*_{\theta}\bar{H}^*_{\theta z^*}\bar{H}^*_{z^*}}{r^{*2}\left(\frac{\bar{H}^{*2}_{\theta}}{r^{*2}}+\bar{H}^{*2}_{z^*}+1\right)^{3/2}} \\ &+\frac{\bar{H}^*_{\theta\theta}}{r^{*2}\sqrt{\frac{\bar{H}^{*2}_{\theta}}{r^{*2}}+\bar{H}^{*2}_{z^*}+1}} + \frac{\bar{H}^*_{z^*z^*}}{\sqrt{\frac{\bar{H}^{*2}_{\theta}}{r^{*2}}+\bar{H}^{*2}_{z^*}+1}} \\ &+\frac{1}{r^*\sqrt{\frac{\bar{H}^{*2}_{\theta}}{r^{*2}}+\bar{H}^{*2}_{z^*}+1}} - \frac{\bar{H}^{*2}_{\theta}\bar{H}^*_{\theta\theta}}{r^{*4}\left(\frac{\bar{H}^{*2}_{\theta}}{r^{*2}}+\bar{H}^{*2}_{z^*}+1\right)^{3/2}} \\ &+\frac{\bar{H}^{*2}_{\theta}}{r^{*3}\left(\frac{\bar{H}^{*2}_{\theta}}{r^{*2}}+\bar{H}^{*2}_{z^*}+1\right)^{3/2}}\end{aligned} \tag{4.32}$$

at $r^* = R^* - \bar{H}^*$.

Lengths can be nondimensionalized by the initial average film thickness H_i^* and the time by the gravitational relaxation scale $\mu R^*/(\rho g H_i^{*2})$, so that the lubrication equation expressed with nondimensional quantities finally reads

$$\bar{H}_t + \frac{1}{3}\left[\bar{H}^3\left(\underbrace{\frac{1}{Bo}\bar{\kappa}_\theta}_{\text{I}} + \underbrace{\delta\bar{H}_\theta\cos\theta}_{\text{II}} + \underbrace{\sin\theta}_{\text{III}}\right)\right]_\theta + \frac{1}{3\delta^2}\left[\bar{H}^3\left(\underbrace{\frac{1}{Bo}\bar{\kappa}_z}_{\text{I}} + \underbrace{\delta\bar{H}_z\cos\theta}_{\text{II}}\right)\right]_z = 0, \tag{4.33}$$

where $Bo = \rho g H_i^* R^*/\gamma$ is the modified Bond number.

The curvature up to the second order in δ is

$$\begin{aligned}\bar{\kappa} =& \frac{\bar{H}_{zz}}{\left(\bar{H}_z^2+1\right)^{3/2}} + \frac{\delta}{\left(\bar{H}_z^2+1\right)^{1/2}} \\ &-\delta^2\left[\frac{\bar{H}_{zz}\bar{H}_\theta^2}{2\left(\bar{H}_z^2+1\right)^{3/2}} - \frac{3\bar{H}_z^2\bar{H}_{zz}\bar{H}_\theta^2}{2\left(\bar{H}_z^2+1\right)^{5/2}} + \frac{2\bar{H}_z\bar{H}_{\theta z}\bar{H}_\theta}{\left(\bar{H}_z^2+1\right)^{3/2}} - \frac{\bar{H}_{\theta\theta}}{\left(\bar{H}_z^2+1\right)^{1/2}} - \frac{\bar{H}}{\left(\bar{H}_z^2+1\right)^{1/2}}\right] + O\left(\delta^3\right).\end{aligned} \tag{4.34}$$

A more sophisticated model could be employed to consider higher-order curvature terms and larger film aspect ratios, as done by Weidner et al. (1997).

4.7.2 Lubrication equation for small angles

The lubrication equation (4.33) can be further simplified if one considers the limit of small angles θ. Following Trinh et al. (2014), the change of variable $\theta = \delta^{1/2}x$ and $z = \delta^{-1/2}y$ can employed when $\delta \ll 1$. The curvature becomes $\bar{\kappa} = \delta(1 + \bar{H}_{xx} + \bar{H}_{yy}) + O(\delta^2)$ so that Eq. (4.33) reads, using $\cos\theta \approx 1$ and $\sin\theta \approx \theta = \delta^{1/2}x$:

$$\bar{H}_t + \frac{\delta^{-1/2}}{3}\left[\bar{H}^3\left(\frac{\delta\delta^{-1/2}}{Bo}\left(\bar{H}_{xxx} + \bar{H}_{yyx}\right) + \delta\delta^{-1/2}\bar{H}_x + \delta^{1/2}x\right)\right]_x + \frac{\delta^{1/2}}{3\delta^2}\left[\bar{H}^3\left(\frac{\delta\delta^{1/2}}{Bo}\left(\bar{H}_{xxy} + \bar{H}_{yyy}\right) + \delta\delta^{1/2}\bar{H}_y\right)\right]_y = 0. \tag{4.35}$$

The resulting equation, which can be rewritten as

$$\bar{H}_t + \nabla\cdot\left[\frac{\bar{H}^3}{3}\nabla\left(\frac{1}{Bo}\nabla^2\bar{H} + \bar{H} + \frac{x^2}{2}\right)\right] = 0, \tag{4.36}$$

with $\nabla = [\partial_x, \partial_y]^T$ as the gradient operator, is independent of the aspect ratio and the Bond number is the only remaining parameter. Equation (4.36) is the planar thin-film equation of Fermigier et al. (1992) with an additional polar flux term proportional to the distance from the uppermost generatrix.

4.7.3 Derivation of the drainage solution

For an initial uniform profile $H(x, y, 0) = 1$, the film thickness will remain uniform close to the top of the cylinder. Equation (4.36) becomes

$$H_t + \frac{H^3}{3} = 0, \tag{4.37}$$

whose solution with the unitary initial profile is the drainage solution (Takagi & Huppert, 2010; Trinh et al., 2014)

$$H(t) = \frac{1}{\sqrt{1 + \frac{2}{3}t}}. \tag{4.38}$$

It has to be pointed out that by employing the full lubrication equation (4.33) and under the assumption of small deformations, i.e. neglecting surface tension and hydrostatic pressure effects, the lubrication equation would be

$$H_t + \frac{1}{3}\left(H^3\sin\theta\right)_\theta = 0. \tag{4.39}$$

Equation (4.39) can be resolved analytically by a regular perturbation expansion around $\theta = 0$ as explained in Chapter 2 for the drainage on a sphere. The same cannot be done starting

from Eq. (4.36), as it requires terms in θ^2 to be kept in the equation. Eventually, the first spatial correction to the drainage solution from a uniform initial condition reads

$$H(t,\theta) = \frac{1}{\sqrt{1+\frac{2}{3}t}}\left[1+\frac{\theta^2}{16}\left(1-\frac{1}{(1+\frac{2}{3}t)^4}\right)\right]+O(\theta^4). \tag{4.40}$$

We have found that this solution is accurate at least up to $\pi/6$ and the largest error with respect to the numerical resolution of the full lubrication equation (4.33) is within 2.5% at $\pi/2$. Finally, as the first correction is at second order in space, θ^2, considering a uniform drainage solution is a valid assumption for the region close to the top of the cylinder (see Fig. 4.16(a)).

4.7.4 Numerical methods

Two-dimensional simulations

For the numerical resolution of the two-dimensional lubrication equation (4.1) we employed COMSOL Multiphysics, which uses a finite element method. Cubic elements with Lagrangian shape functions are employed on a free triangular grid with characteristic size of 0.8. The film thickness $\bar{H}$ as well as the curvature $\bar{\kappa}$ are the two resolved variables.

The obtained film thickness at $\theta = 0$ and at $z = 0$ for an initially uniform profile are compared to the analytical result H and to an in-house one-dimensional spectral code (see Chapter 3) in Fig. 4.16. The comparison for initially forced rivulets is shown in Fig. 4.10(b). In view of the very good agreement, the choice for the use of COMSOL Multiphysics to solve for the lubrication equation in two dimensions follows naturally. Other options would be the implementation of an ADI method (Witelski & Bowen, 2003) such as the one employed by Lister et al. (2010) or Weidner et al. (1997).

One-dimensional simulations

The lubrication equation (4.20) is discretized with a central finite difference scheme and evolved in time with the second-order Crank-Nicolson MATLAB routine `ode23t.m` to avoid numerical diffusion. The axial range is uniformly discretized with N collocation points, giving a grid spacing typically of approximately 0.03 for $N = 500$. The convergence study for a typical parameter set is shown in Fig. 4.17.

4.7.5 Confocal chromatic imaging technique

The principle of the Confocal chromatic Imaging technique is the following. An achromatic lens decomposes the incident white light into a continuum of monochromatic images which constitutes the measurement range. The light reflected by a sample surface put inside this range is collected by a beam splitter. A pinhole then allows one to block the defocused light that

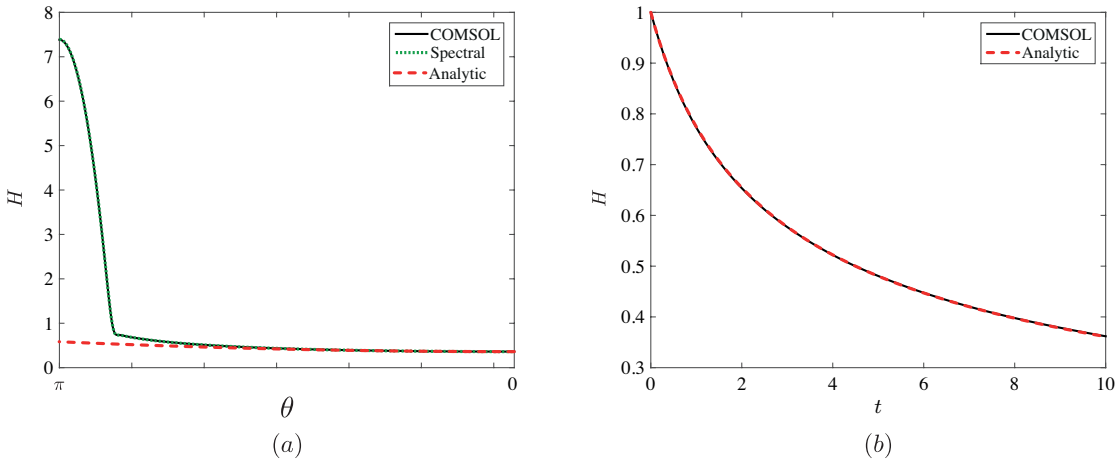

Figure 4.16 – (*a*) Polar dependence of the film-thickness profile at $z = 0$ for $t = 10$ obtained by the two-dimensional numerical resolution with COMSOL Multiphysics (solid line) and by the numerical resolution of the one-dimensional lubrication equation in θ with a spectral code (dotted green line) of Chapter 3. Dashed red line corresponds to spatial variation of drainage solution given by Eq. (4.40). (*b*) Film-thickness evolution at $\theta = 0$ obtained by the two-dimensional numerical resolution with COMSOL Multiphysics (solid line) and analytical prediction H given by Eq. (4.4) (dashed line). $Bo = 100$ and $\delta = 0.01$.

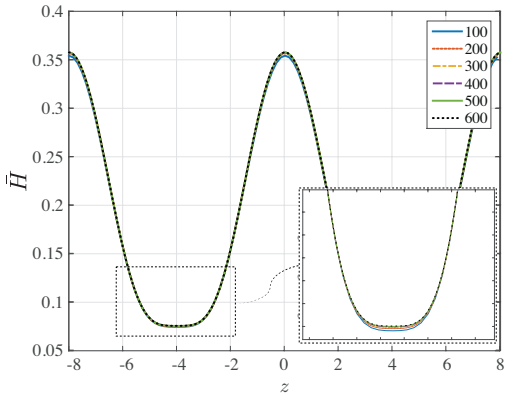

Figure 4.17 – Convergence study for the nonlinear evolution of rivulets initially perturbed with b_0 for $Bo = 70$, $\delta = 0.02$, $\varepsilon = 10^{-2}$ and $t = 20$. The number of collocation points N is shown in the legend.

does not come from the sample surface. Eventually, the spectral repartition of the collected light is analyzed by a spectrometer. The wavelength of maximum intensity is detected and the distance value is deduced from a calibration curve. Several reflecting interfaces can be detected at the same time, allowing thickness measurement of thin transparent layers. When mounted onto a linear translation stage, the spatial resolution depends on the measurement frequency and speed of the translation stage.

5 Rayleigh-Taylor instability under a spherical substrate

Remark This chapter is largely inspired by the publication of the same name

G. Balestra[1], D. M.-P. Nguyen[1] and F. Gallaire[1]

[1]Laboratory of Fluid Mechanics and Instabilities, EPFL, CH1015 Lausanne, Switzerland

Submitted to Physical Review Fluids

We investigate the Rayleigh-Taylor instability of a thin viscous film coating the inside of a spherical substrate. The aim of this work is to find and characterize the instability pattern in this spherical geometry. In contrast to the Rayleigh-Taylor instability under a planar substrate, where the interface is asymptotically unstable with respect to infinitesimal perturbations, the drainage induced by the component of gravity tangent to a curved substrate stabilizes the liquid interface, making the system linearly asymptotically stable. By performing a linear optimal transient growth analysis we show that the double curvature of a spherical substrate yields a critical Bond number – prescribing the ratio between gravitational and capillary forces – before an initial growth of perturbations is possible two-times larger than for a circular cylindrical substrate. This linear transient growth analysis however does not yield any selection principle for an optimal azimuthal wavenumber and we have to resort to a fully nonlinear analysis. By numerically solving the nonlinear lubrication equation we find that the most amplified azimuthal wavenumber increases with the Bond number. Nonlinear interactions are responsible for the transfer of energy to higher-order harmonics. The larger the Bond number and the farther away from the apex of the sphere, the richer the wavenumber spectrum.

5.1 Introduction

We refer to Sec. 1.2 for a general introduction on the Rayleigh-Taylor instability.

In Chapter 3 we have shown that the stabilization induced by the curvature has a twofold

reason. First, the gravity has not only a component orthogonal to the interface, promoting the instability, but also a component tangent to the interface, which is responsible for the drainage of the film. The film becomes thinner and thinner as time evolves, leaving only a short time for the instability to be effective. Second, the gravity-induced drainage stretches the perturbations which form at the top of the cylinder, further stabilizing their growth. Depending on the Bond number and the initial disturbance amplitude, the transient growth might be sufficiently large to trigger nonlinear effects resulting in the formation of droplets sliding along the cylinder walls or even droplets pinching-off from the substrate.

In Chapter 4 we have seen that the cylindrical geometry of the substrate breaks the symmetry of the problem and the anisotropy of the forces acting on the thin film modifies the most amplified pattern. At moderate Bond numbers, rivulets form rather than droplets. The thin film destabilizes into structures whose wavevector is aligned with the axis of the cylinder while its wavelength corresponds to the one of the classical RTI, $\lambda_0^* = 2\pi\sqrt{2}\ell_c^*$ with $\ell_c^* = \sqrt{\gamma/(\rho g)}$, where γ is the surface tension, ρ is the density and g is the gravitational acceleration. Such axial disturbances dominate over perturbations with a component in the polar direction as they experience only the thinning of the film, but are not further stabilized by the drainage-induced stretching. The flow-anisotropy is the key to the stronger linear growth of rivulets. The latter resemble to the rolls of the classical RTI, yet with the difference that they persist over the whole time of the instability. The transition to a two-dimensional pattern of droplets relies solely on nonlinear interactions and occurs only for large Bond numbers (see Chapter 4). Therefore, for a cylindrical substrate, the liquid film can either drain smoothly for Bond numbers smaller than the critical value $Bo = 12$, or it can destabilize into rivulets or a two-dimensional pattern of dripping droplets for moderate and large Bond numbers, respectively.

With the knowledge gained by the analysis of the RTI for a unidirectionally curved substrate, it can be already guessed that the key to the success of chocolatier in fabricating nearly uniform eggs results from the stabilizing effect induced by the substrate curvature on the RTI and the small Bond number value, i.e. the small radii. However, what would be the disturbance pattern at large Bo for a thin film underneath a spherical substrate where the curvature is again isotropic?

Here we undertake the stability analysis of the RTI of a thin film coating the interior of a sphere of radius R^*. Albeit the employed technique is similar to the one for a cylindrical substrate of Chapter 4, we contrast our results with the ones of the cylindrical case. The linear stability analysis proves that the spherical geometry has a stabilizing effect which is twice as strong as the one for a cylindrical substrate. Furthermore, we show that given the spherical symmetry of the system, the linear optimal transient growth analysis does not select any particular azimuthal mode. Nonlinear numerical simulations of the governing equations allow us to show that there is an optimal azimuthal mode depending on the Bond number and on the disturbance amplitude. The nonlinear interactions are responsible for the transfer of energy from one mode to the other, creating an energy cascade in space and time, which is much richer than for the cylindrical substrate. In particular, the spherical geometry results in the

widening of the perturbation spectrum as the distance from the pole increases, similarly as what is observed for an initially punctual perturbation for the classical RTI (Fermigier et al., 1992). Nonetheless, the arising perturbation structures are intrinsically related to the spherical geometry. The nonlinear dynamics is characterized by introducing spatio-temporal diagrams for the disturbance norm along the azimuthal direction as well as for the azimuthal mode with the largest amplitude.

The governing equations are given in Sec. 5.2.1 and specified for the region close to the north pole in Sec. 5.2.2. The linear optimal transient growth analysis is presented in Sec. 5.3. In particular, the linear disturbance solution at the north pole is given in Sec. 5.3.1, followed by the optimal growth analysis in Sec. 5.3.2. The nonlinear results for the linear optimal initial conditions are described in Sec. 5.4, where the spatio-temporal diagrams are introduced in Sec. 5.4.1. The effects of the initial azimuthal wavenumber and the Bond number are presented in Sec. 5.4.2 and Sec. 5.4.3, respectively, whereas the sliding-droplet velocity is discussed in Sec. 5.4.4. Finally, the results for the nonlinear evolutions of random noise initial conditions are discussed in Sec. 5.5. Conclusions are drawn in Sec. 5.6.

5.2 Governing equation

5.2.1 Entire upper hemisphere

A film of initial average thickness H_i^* coats the inside of a spherical substrate of inner radius R^*. Since the focus of this work is the destabilization of the interface under the action of the gravitational forces, only the upper hemisphere is relevant (see Fig. 5.1). The lower hemisphere would be relevant if one would investigate the destabilization of a thin film coating the outside of a spherical substrate. Given the small film thickness H_i^* compared to the sphere radius R^*,

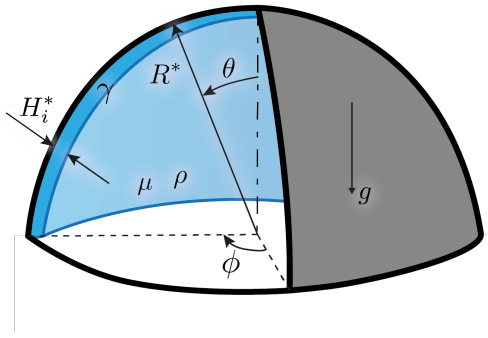

Figure 5.1 – Sketch of the problem geometry.

the aspect ratio is small, $\delta = H_i^*/R^* \ll 1$. Furthermore, we assume that inertial effects can be neglected, i.e. $Re\delta \ll 1$, where $Re = g\rho^2 H_i^{*3}/(3\mu^2)$ is the Reynolds number. A lubrication approach (Oron et al., 1997) can be employed to derive the governing equation for the film

thickness. The characteristic time is the drainage time τ_d, which is given by the ratio of the viscous over the gravitational stresses, $\tau_d = \mu R^*/(\rho g H_i^{*2})$, where μ is the dynamic viscosity, ρ is the density, and g is the gravitational field. By using the local mass conservation in spherical coordinates as well as H_i^* and τ_d as length and time gauges of the problem, the evolution equation of the film thickness $\bar{H}(\theta,\phi,t)$ is (see Appendix 5.7.1 for the detailed derivation)

$$\bar{H}_t + \frac{1}{3\sin\theta}\left[\bar{H}^3\sin\theta\left(\underbrace{\frac{1}{Bo}\bar{\kappa}_\theta}_{\text{I}} + \underbrace{\delta\bar{H}_\theta\cos\theta}_{\text{II}} + \underbrace{\sin\theta}_{\text{III}}\right)\right]_\theta + \frac{1}{3\sin\theta}\left[\frac{\bar{H}^3}{\sin\theta}\left(\underbrace{\frac{1}{Bo}\bar{\kappa}_\phi}_{\text{I}} + \underbrace{\delta\bar{H}_\phi\cos\theta}_{\text{II}}\right)\right]_\phi = 0, \tag{5.1}$$

where the capillary pressure gradient corresponds to the terms **I**, the variation of the hydrostatic to the terms **II** and the drainage to the term **III**; indices represent partial derivatives. The modified Bond number, prescribing the ratio between gravitational and capillary forces, is given by $Bo = \rho g H_i^* R^*/\gamma$, where γ is the surface tension. The curvature $\bar{\kappa}$ up to the second order in δ is :

$$\bar{\kappa} = 2\delta + \delta^2\left(\bar{H}_{\theta\theta} + \cot\theta\,\bar{H}_\theta + \csc^2\theta\,\bar{H}_{\phi\phi} + 2\bar{H}\right) + O(\delta^3). \tag{5.2}$$

5.2.2 Limit for the vicinity of the north pole

Following Chapter 3 and Trinh et al. (2014), the stability properties of the system are well captured by the analysis at the north pole. The lubrication equation (5.1) can be simplified when considering the region close to the north pole, i.e. $\theta \ll 1$. The change of variables $\theta = \delta^{1/2} r$ can be employed(Trinh et al., 2014) when $\delta \ll 1$. The curvature becomes

$$\bar{\kappa} = \delta\left[2 + \frac{1}{r}\frac{\partial}{\partial r}(r\bar{H}_r) + \frac{1}{r^2}\bar{H}_{\phi\phi}\right] + O(\delta^2) = \delta\left[2 + \nabla^2\bar{H}\right] + O(\delta^2) = \delta\bar{\bar{\kappa}} + O(\delta^2), \tag{5.3}$$

where ∇^2 is the Laplace operator in polar coordinates and $\bar{\bar{\kappa}} = 2 + \nabla^2\bar{H}$ is the rescaled curvature. The mean curvature is indeed the double of the one of a cylinder. Using $\cos\theta \approx 1$ and $\sin\theta \approx \theta = \delta^{1/2} r$, equation (5.1) eventually reads:

$$\bar{H}_t + \frac{1}{3r}\left[\bar{H}^3 r\left(\frac{1}{Bo}\bar{\bar{\kappa}}_r + \bar{H}_r + r\right)\right]_r + \frac{1}{3r}\left[\frac{\bar{H}^3}{r}\left(\frac{1}{Bo}\bar{\bar{\kappa}}_\phi + \bar{H}_\phi\right)\right]_\phi = 0. \tag{5.4}$$

The resulting equation is aspect-ratio independent and the Bond number is the only remaining parameter. Using the above mentioned change of variable and the small aspect ratio limit allows to transform the lubrication equation from a spherical coordinate system to a polar coordinate system in the vicinity of the north pole.

5.3 Linear optimal transient growth analysis at the north pole

5.3.1 Linear disturbance solution

Assuming an initial film thickness uniform in space, $\bar{H}(r,\phi,t)=1$, the lubrication equation in the vicinity of the north pole, Eq. (5.4), has an analytical solution, called *drainage solution*, given by

$$H(T)=\frac{1}{\sqrt{T}}, \tag{5.5}$$

with $T=1+(4/3)t$ the rescaled time (see Chapter 2 and Appendix 5.7.2 for the derivation).

The film thickness is decomposed into this spatially uniform drainage solution H and small space-dependent *disturbances* $\varepsilon h(r,\phi,T)$:

$$\bar{H}(r,\phi,T)=H(T)+\varepsilon h(r,\phi,T) \quad , \quad \varepsilon \ll 1. \tag{5.6}$$

The linear equation is obtained by entering the decomposition (5.6) into the lubrication equation (5.4) and collecting the terms at order ε:

$$h_T+\frac{1}{4T^{3/2}}\left(\frac{\nabla^4 h}{Bo}+\nabla^2 h\right)+\frac{3}{4T}\left(rh_r+2h\right)=0, \tag{5.7}$$

where ∇^2 and ∇^4 are the Laplacian and bi-Laplacian in polar coordinates, respectively. The base flow H is explicitly accounted for by the powers of T.

The solution of equation (5.7) can be expressed in the eigenfunction basis of the Laplace operator in polar coordinates. Only the Bessel functions of the first kind, J_{m_0}, are not diverging neither at the origin nor at $r\to\infty$. Given the orthogonality of the eigenfunctions J_{m_0} and following Parseval's theorem, we can consider mode per mode separately. For an initial condition of the form $h(r,\phi,1)=h_0(r,\phi)=J_{m_0}(kr)\exp(\mathrm{i}m_0\phi)+c.c.$, the solution is given by

$$h(r,\phi,T)=A(k,m_0,T)J_{m_0}\left(k\frac{r}{T^{3/4}}\right)\exp(\mathrm{i}m_0\phi)+c.c., \tag{5.8}$$

where the apparent radial wavenumber $k/T^{3/4}$ is time-dependent as for the flow inside a cylinder (see Chapter 4). The amplitude A satisfies:

$$A_T+\frac{1}{4}\left(\frac{1}{Bo}\frac{k^4}{T^{9/2}}-\frac{k^2}{T^3}+\frac{6}{T}\right)A=0, \tag{5.9}$$

which is obtained by entering Eq. (5.8) into the linear disturbance equation (5.7). The solution of (5.9) reads

$$A(k,m_0,T)=A(k,T)=\frac{1}{T^{3/2}}\exp\left[\left(1-\frac{1}{T^2}\right)\frac{k^2}{8}-\frac{1}{Bo}\left(1-\frac{1}{T^{7/2}}\right)\frac{k^4}{14}\right]. \tag{5.10}$$

It has to be observed that the amplitude (5.10) does not depend on the azimuthal number m_0.

The exponential term in Eq. (5.10) results from the Rayleigh-Taylor instability, where both the destabilizing term in k^2 and the stabilizing term in k^4 can be evidenced. The time-dependent coefficients of the destabilizing and stabilizing terms saturate for large times due to the thinning of the film. Thus, the largest value of the exponential term only depends on the wavenumber k and on the Bond number. Furthermore, the gravity-induced drainage also enters through the algebraic term $T^{-3/2}$, which, together with the saturated exponential term, is responsible for the linear asymptotic stability of the system, $\lim_{T\to\infty} A(k,T,Bo) = 0$. Hence, the disturbances can grow only over a finite, transient time.

The initial amplitude evolution is given by

$$A(k, T \to 1) \sim 1 + \frac{(k^2-6)Bo - k^4}{4Bo}(T-1) + O[T-1]^2. \tag{5.11}$$

Initial growth only occurs if $k^2 - 6 - k^4/Bo > 0$. This condition is best met for

$$k_0 = \sqrt{\frac{Bo}{2}}, \tag{5.12}$$

which is the initially most amplified wavenumber, corresponding to the wavenumber with the largest linear growth in the planar Rayleigh-Taylor instability (Fermigier et al., 1992). Initial growth is only possible for $Bo > 24$, which is the double of the critical Bond number for a cylindrical geometry (see Chapter 3 and Trinh et al. (2014)). This result is imputable to the fact that the drainage occurs over the two principal radii of curvature of the sphere and not only the unique one of the cylinder. As observable in Eq. (5.5), the film thins two times as fast as for a cylinder (Takagi & Huppert, 2010). This result has been found before discovering the work of Hammoud (2016), who arrived at the same conclusion.

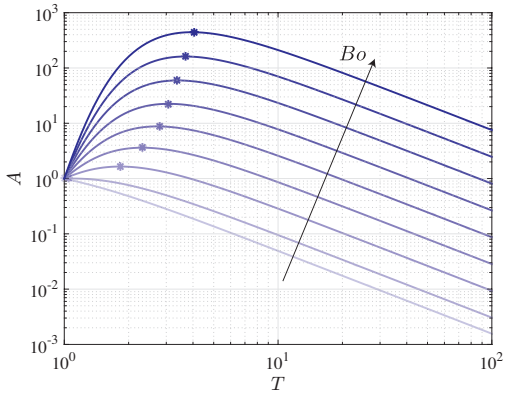

Figure 5.2 – Temporal evolution of the linear amplitude A for different Bond numbers, Bo = 10, 25, 50, 75, 100, 125, 150, 175 and 200, with the initial optimal wavenumber k_0. Asterisks denote the largest amplitudes.

5.3.2 Optimal growth

As visible in Fig. 5.2, the amplitude of the disturbances for a specified initial wavenumber presents a maximum at a given time; both amplitude and time increase with the value of the Bond number.

The amplitude A of the disturbances can be optimized as a function of the wavenumber k and time T, which will become functions of the Bond number. The optimal wavenumber $k_{\max}$ is given by

$$\frac{\partial A}{\partial k} = 0 \quad \Leftrightarrow \quad k_{\max}(T) = \sqrt{\frac{7}{8}\frac{(1+T+T^{7/2}+T^{9/2})T^{3/2}}{(1+T+T^2+T^3+T^4+T^5+T^6)}Bo}, \tag{5.13}$$

whose limits are $\lim_{T\to 1} k_{\max}(T) = \sqrt{Bo/2}$ and $\lim_{T\to\infty} k_{\max}(T) = \sqrt{7Bo/8}$ (see inset of Fig. 5.3(a)). The largest growth reached with $k_{\max}(T)$ is thus given by

$$A_{k_{\max}}(T) = A(k_{\max}, T) = \frac{1}{T^{3/2}} \exp\left[\frac{7(T^{1/2}-1)(T^{1/2}+1)^2(T+1)^2 Bo}{128(T^{1/2}+T+T^{3/2}+T^2+T^{5/2}+T^3+T^{7/2})}\right]. \tag{5.14}$$

Solving $\partial A_{k_{\max}}/\partial T = 0$, the optimal time $T_{A_{\max}}$ is found to be a monotonic function of the Bond number, approximated by the empirical fitting law $T_{A_{\max}} = 0.8363 Bo^{0.4} - 1.846$, which holds for $24 < Bo \lesssim 300$ (see Fig. 5.3(a)).

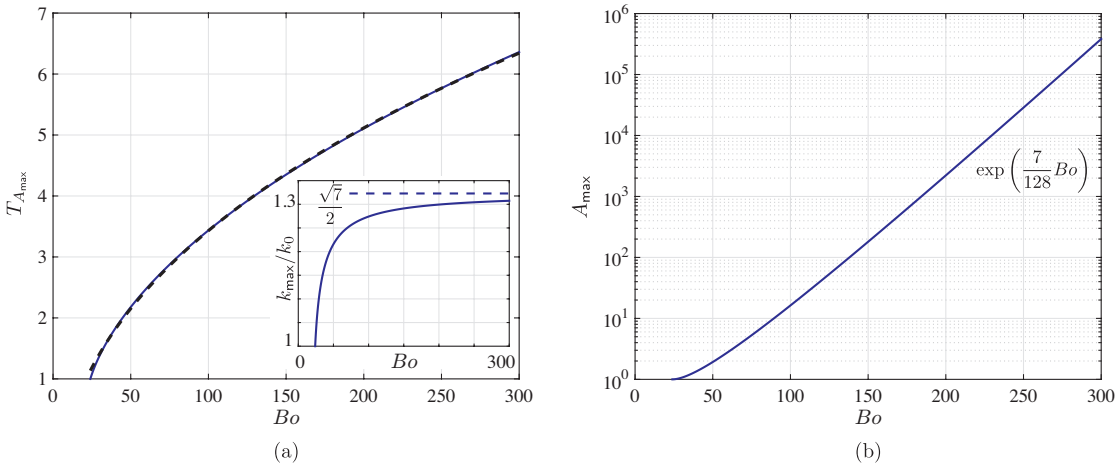

Figure 5.3 – (a) Optimal time $T_{A_{\max}}$ (blue solid line), with its approximation (black dashed line), and wavenumber $k_{\max}$ (inset) giving the largest amplitude $A_{\max}$ (b) as a function of the Bond number.

With the optimal wavenumber $k_{\max}$ and the optimal time $T_{A_{\max}}$, one obtains the largest possible amplitude $A_{\max}$ (see Fig. 5.3(b)). For $Bo \gg 24$, the largest optimal amplitude is found to be an exponential function of the Bond number, $A_{\max} \sim \exp(7Bo/128)$.

By performing the linear optimal transient growth analysis we have found the optimal wavenum-

ber in the radial direction and the optimal time, but we cannot conclude on the optimal azimuthal wavenumber, reason why a nonlinear study is undertaken next.

5.4 Nonlinear evolution of the linear optimal initial conditions

Equipped with the insights of the linear optimal transient growth analysis in the vicinity of the north pole, we investigate hereafter the nonlinear evolution of the perturbations over the entire geometry. The nonlinear lubrication equation (5.1) for the total thickness $\bar{H}$ is solved numerically for $\theta \in [0,\pi]$ and $\phi \in [0,2\pi]$ (see Appendix 5.7.3 for details on the numerical method). Periodic boundary conditions are used for the azimuthal direction ϕ and no flux is imposed at the poles $\theta = 0$ and $\theta = \pi$. Since we are interested in the unstable region of the film coated under the spherical geometry, only the dynamics for the upper hemisphere is presented. In the lower hemisphere the liquid accumulates in a way similar to what was found for a circular geometry (see Chapter 3). The initial condition for the film thickness is given by

$$\bar{H}_0(\theta,\phi) = 1 + \varepsilon J_{m_0}(k_{\mathsf{max}}\theta)\cos(m_0\phi), \tag{5.15}$$

where k_{max} is the optimal wavenumber given by equation (5.13) and m_0 is the azimuthal wavenumber. To avoid the formation of a singular droplet at the pole, the axisymmetric perturbation $m_0 = 0$ is not considered. Due to the lubrication approach pursued in this study, droplets pinching off from the substrate(Eggers & Villermaux, 2008; Indeikina et al., 1997) cannot be taken into account.

The linear film-thickness evolution predicted by the analytical solution (5.8), together with its amplitude, Eq. (5.10), can be compared to the film thickness given by the nonlinear evolution of the fundamental mode over the entire geometry. As visible in Fig. 5.4, the analytical and numerical solutions are in very good agreement. Hence, the initial evolution is linear and the analytical solution for the region close to the north pole is correct also for finite, yet small, polar angles. The larger the Bond number, the earlier the nonlinear evolution will differ from the linear prediction due to the nonlinear interactions, as we will discuss in the following.

To illustrate the typical nonlinear dynamics of the RTI, the total film thickness over the upper hemisphere at successive time instants is shown in Fig. 5.5 for $Bo = 150$, $\varepsilon = 10^{-2}$ and $m_0 = 6$ (see also Supplementary Movie 1). The six largest initial perturbation peaks rapidly grow into droplets ($t = 1$, location 1). This first generation of droplets, denoted as $G^1_{m_0}$, quickly slides along the spherical substrate, catching up the second largest initial perturbations, denoted as $G^1_{2m_0}$ ($t = 2$). Subsequently, a second generation of six droplets, $G^2_{m_0}$, forms close to the pole ($t = 3$). The droplets $G^2_{m_0}$ translate more easily due to the thicker film left by the former generation of droplets $G^1_{m_0}$ along their trajectory, which reduces the viscous drag ($t = 4$, location 2), thereby flowing in the wakes of their predecessor. The droplet velocity will be quantified later in Sec. 5.4.3. In the mean time, the nonlinear interactions promote the formation of additional droplets, $G^1_{4m_0}$ ($t = 4$, location 3). When draining between the wakes of previous droplets, these additional perturbations form an inverted-U shape perturbation,

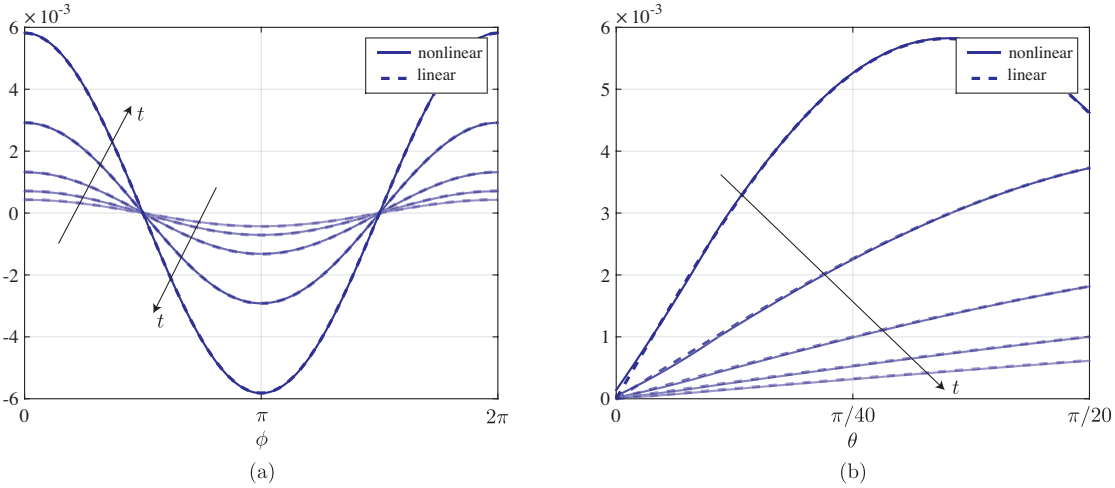

Figure 5.4 – Comparison between the linear evolution of the film thickness given by equation (5.8) (dashed line) and the one of the fundamental (solid line) obtained by the nonlinear evolution of the initial condition (5.15) with $Bo = 25$, $m_0 = 1$ and $\varepsilon = A(T = 1) = 10^{-2}$ at the times $t = 0$, 1, 2, 3 and 4. (a) Film thickness along the polar direction at $\theta = \pi/30$ for $\phi \in [0, 2\pi]$ and (b) along the azimuthal direction for $\theta \in [0, \pi/20]$ and $\phi = 0$. The agreement remains good also for later times.

whose uppermost peak ($t = 6$, location 4) is followed by a second generation of droplets $G^2_{2m_0}$, as well as by a third generation $G^3_{m_0}$. This peculiar inverted-U shaped structure is swept away by the draining flow ($t = 10$, location 5), leaving only the wakes of the fundamental droplets $G^{1,2,3}_{m_0}$ and the secondary droplets $G^{1,2}_{2m_0}$. As time increases, a single droplet G^1_0 forms at the north pole ($t = 10$, location 0). Eventually, after the three generations of fundamental droplets and the two of secondary droplets are swept away, the thin film is only perturbed along their wakes ($t = 14$, locations 6) as well as along additional regions between the wakes for large polar angles (see location 7) and at the pole. The wake perturbations at late times are extended over a large range of polar angles, excluding the pole, and correspond to rivulets rather than to localized droplets.

Hereafter, the different stages of the nonlinear evolution of the RTI under a spherical substrate are discussed and characterized in more detail.

5.4.1 Spatio-temporal amplitude diagrams

The nonlinear film-thickness perturbation is given by

$$\varepsilon h(\theta, \phi, t) = \bar{H}(\theta, \phi, t) - H(\theta, \phi, t). \tag{5.16}$$

The drainage solution over the entire geometry $H(\theta, \phi, t)$ is obtained numerically by solving equation (5.1) with a smooth initial condition $H_0(\theta, \phi) = 1$, similarly to what done in Chapter 3. Although the Bond number might be larger than the critical value for transient growth, the

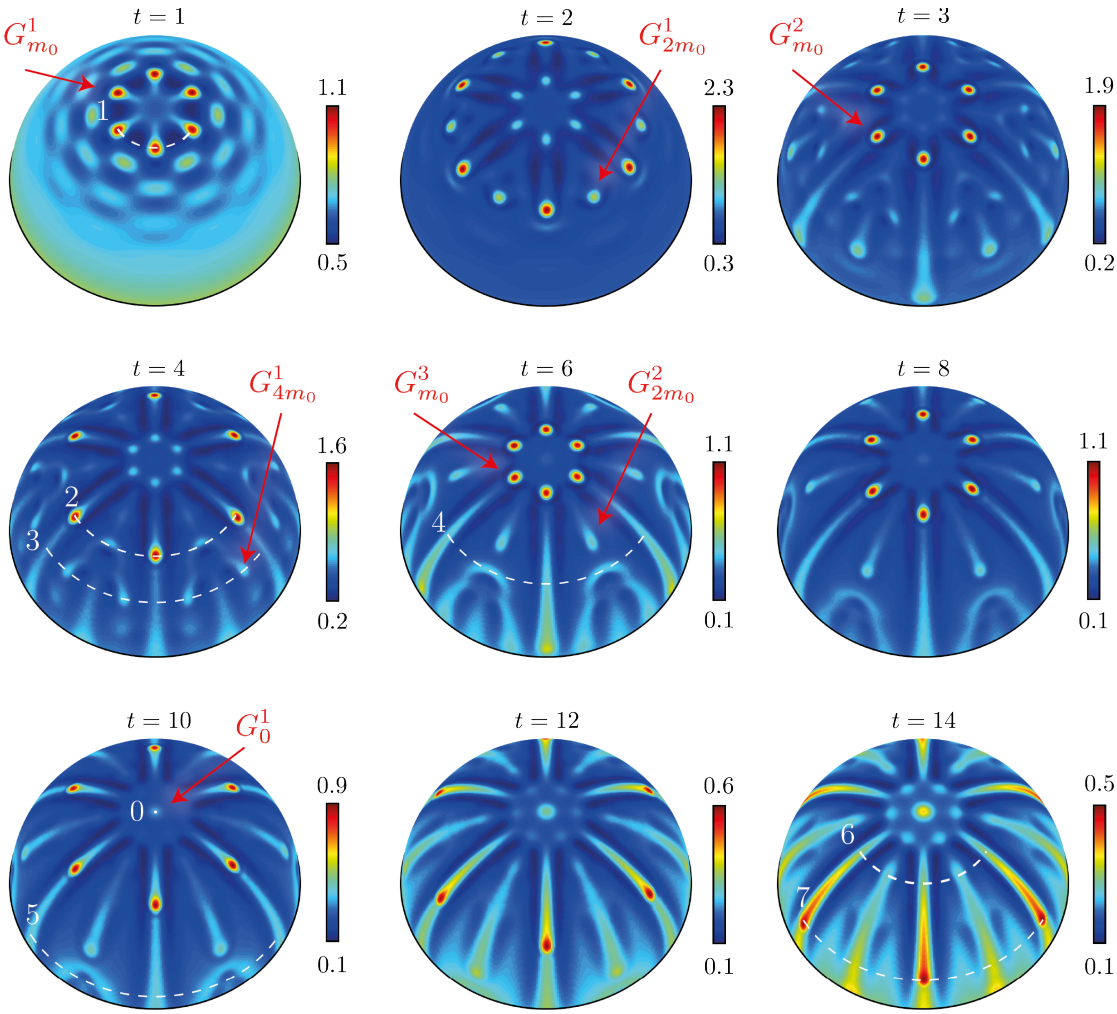

Figure 5.5 – Nonlinear evolution of the film thickness for the initial condition given by equation (5.15) for $Bo = 150$, $m_0 = 6$ and $\varepsilon = 10^{-2}$ at the times $t = 1$, 2, 3, 4, 6, 8, 10, 12 and 14. The film thickness is indicated by the colorbar, which changes scaled nonmonotonically with time. The evolution with a constant colorbar is shown in Fig. 5.22 in the Appendix 5.7.4. Particular spatial locations are indicated by a white dashed line; the numbers are used also in the following figures. The droplet generations G_{m_0}, G_{2m_0}, G_{2m_0} and G_0 are also highlighted. See Supplementary Movie 1 for the entire evolution.

accuracy of the numerical scheme is good enough to avoid numerical errors to be amplified. The obtained solution remains smooth and can be considered as the drainage solution (see Appendix 5.7.3 for further details).

Given the periodicity of the disturbances in the azimuthal direction, it is natural to define a disturbance norm over the azimuthal direction

$$\mathscr{H}(\theta,t) = \left(\int_0^{2\pi} |\varepsilon h(\theta,\phi,t)|^2 d\phi \right)^{1/2} \tag{5.17}$$

and to study its spatio-temporal dynamics. The result for the evolution presented in Fig. 5.5

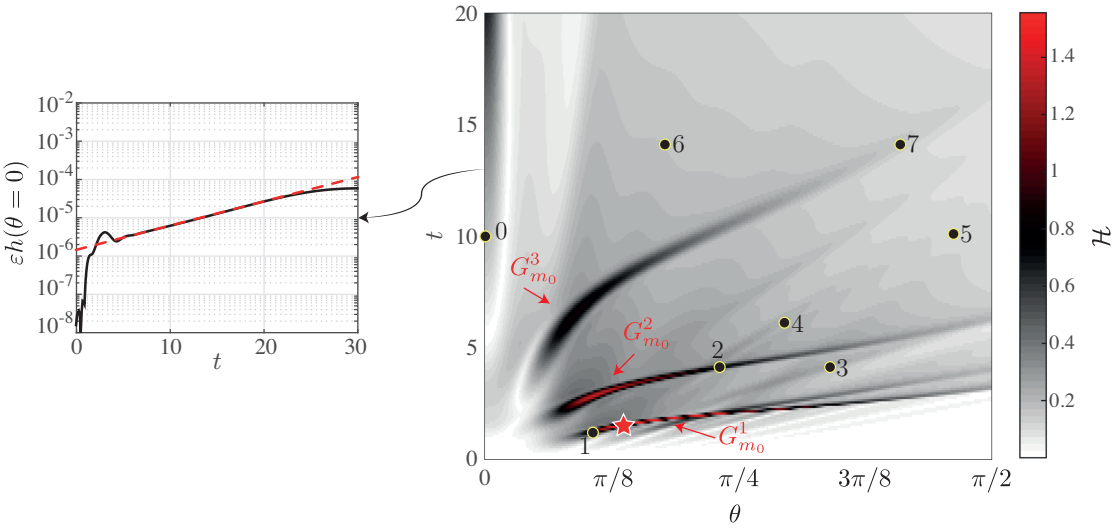

Figure 5.6 – Azimuthal disturbance norm $\mathscr{H}$ for the evolution shown in Fig. 5.5, namely for $Bo = 150$, $m_0 = 6$ and $\varepsilon = 10^{-2}$ with a linear optimal initial condition. The numbered points correspond to the locations specified in Fig. 5.5 and the red star highlights the instant of largest amplitude. The amplitude ridges of the droplets generations $G^{1,2,3}_{m_0}$ are also indicated. The discontinuous appearance of the amplitude is due to the limited temporal sampling. The film-thickness disturbance amplitude at the pole, $\varepsilon h(\theta = 0)$, is shown in the inset on the left (black solid line), together with the growth predicted by the linear theory (red dashed line).

is shown in the diagram of Fig. 5.6. The main stages of the previous qualitative description of the perturbation dynamics can be highlighted in the spatio-temporal diagram. The fast motion of the first generation $G^1_{m_0}$ of droplets can be seen by the largest-amplitude ridge (location 1), along which the largest disturbance amplitude is found (red star). The droplets of the first generation catch up the other smaller perturbations, represented by the thin rays at short times. The successive droplet generations $G^2_{m_0}$ and $G^3_{m_0}$ correspond to the other large-amplitude ridges (on which points 2 and 7 are located). It can observed that the sliding velocity of the successive droplet generations is slower and slower, as the film becomes thinner due to the drainage. Finally, the amplitude close to $\theta = 0$ increases with time due to the droplet formation at the north pole.

The evolution of the disturbance amplitude at the pole is shown in the inset of Fig. 5.6. The disturbance is initially vanishing, since for $m_0 = 6$ there is no initial perturbation at $\theta = 0$. However, due to nonlinear interactions, a droplet forms at the pole and its initial growth is exponential with the Rayleigh-Taylor growth rate $H_f^3(k_f^2 - k_f^4/Bo)/3$ (Fermigier et al., 1992), where the film thickness H_f corresponds to the mean film thickness at the instant of formation, here $t_f \simeq 8$, and k_f is the optimal wavenumber given by Eq. (5.13) evaluated at t_f. Note that after $t > 20$ the growth is no longer exponential due to nonlinear effects.

To further unravel the mechanisms at play in the nonlinear evolution of the perturbations it is

useful to study the amplitude of the azimuthal modes obtained by Fourier transform of the perturbations along ϕ. The thickness perturbation can be decomposed into the Fourier series

$$\varepsilon h(\theta,\phi,t) = \sum_{m\in\mathbb{N}} A_m(\theta,t)\exp(\mathrm{i}m\phi) + c.c., \tag{5.18}$$

where $A_m(\theta,t)$ is the space and time dependent amplitude of the azimuthal modes m. The spatio-temporal diagrams for the amplitudes of the fundamental A_{m_0} and the harmonics A_{2m_0}, A_{4m_0} and A_0 are presented in Fig. 5.7. The modes with the largest amplitude are the

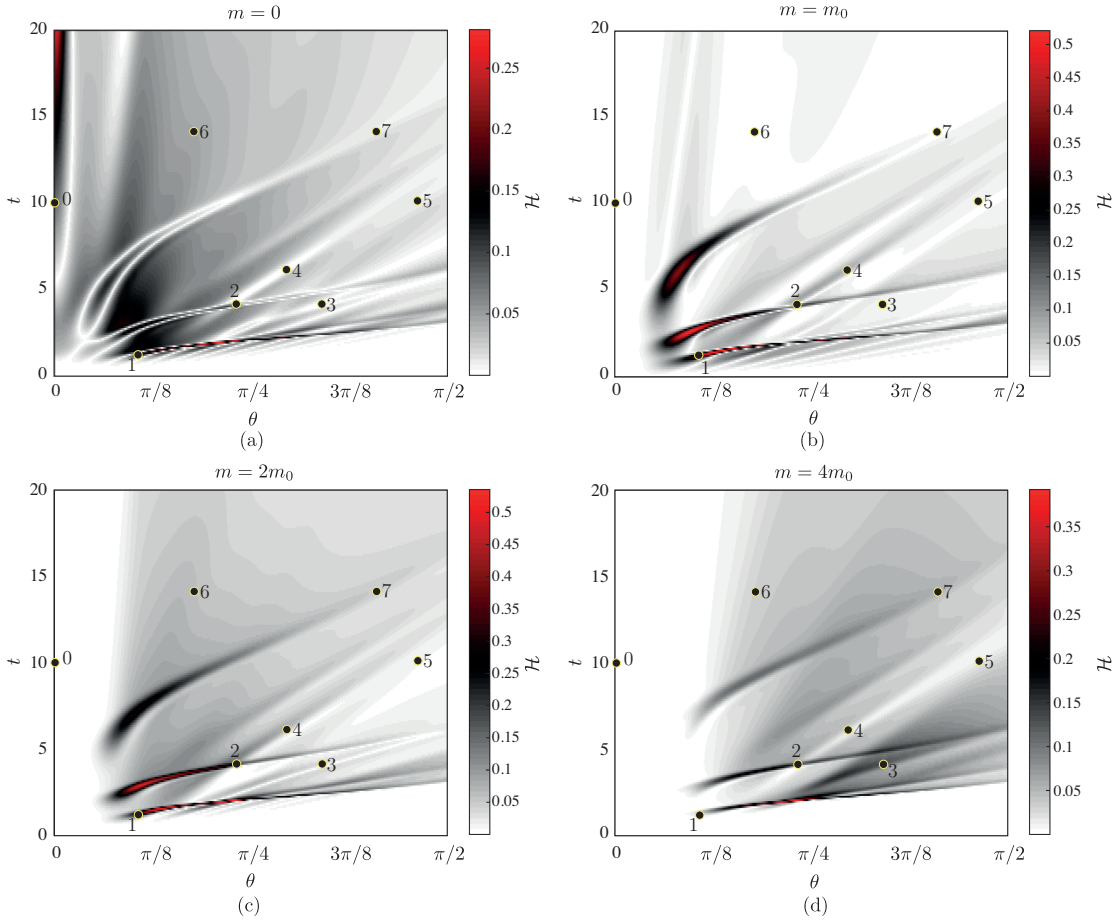

Figure 5.7 – Amplitude of the azimuthal modes $m = 0$ (a), $m = m_0$ (b), $m = 2m_0$ (c) and $m = 4m_0$ (d) for $Bo = 150$, $m_0 = 6$ and $\varepsilon = 10^{-2}$ with a linear optimal initial condition. The numbered points correspond to the locations specified in Fig. 5.5.

fundamental m_0 and the first harmonic $2m_0$, as already observed in the snapshot for $t = 14$ in Fig. 5.5. All the modes have a similar spatio-temporal dynamics, with a finite number of ridges corresponding to the number of droplet generations. However, the higher the harmonics, the larger the polar angle θ where they appear (see also Fig. 5.5, $t = 14$). The axisymmetric perturbation $m = 0$ clearly dominates at very small angles, close to the north pole, where a stationary droplet forms. It has to be stressed that the mode $m = 0$ does not only correspond to

a droplet at the pole, but also to any axisymmetric perturbation resulting from a modification of the mean film thickness through nonlinear interactions compared to the drainage solution. A similar effect has been found for the flow inside a cylinder (see Chapter 4). Therefore, away from the pole, the mode $m = 0$ indicating a mean flow modification is not relevant for the prediction of the instability pattern.

With the use of Fig. 5.7 we infer that location 3 corresponds to the second harmonics $4m_0$, whereas the location 4 is mainly composed by the first harmonic $2m_0$, together with the fundamental m_0. The mode with the largest amplitude at the location 6 is $2m_0$, whereas at location 7 it is $4m_0$.

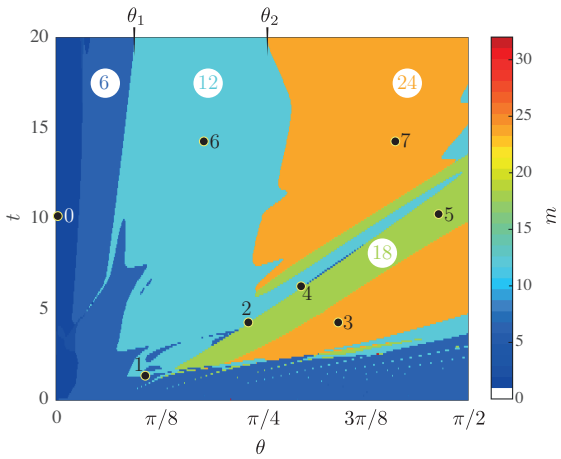

Figure 5.8 – Azimuthal mode m with the largest amplitude for $Bo = 150$, $m_0 = 6$ and $\varepsilon = 10^{-2}$ with a linear optimal initial condition. The colorbar indicates the m-values. Numbered points correspond to the locations in Fig. 5.5 and numbers on a white background correspond to the m-value. θ_1 and θ_2 indicate the polar angle at $t = 20$ where the largest mode switches to the higher harmonics.

The perturbation can be characterized by the azimuthal mode with the largest amplitude at each time t and polar angle θ, excluding the mode $m = 0$ in light of the previous remark. The observations of Fig. 5.7 are confirmed by the spatio-temporal diagram of Fig. 5.8. Starting with $m_0 = 6$, the nonlinear interactions excite the modes $2m_0 = 12$, $3m_0 = 18$ and $4m_0 = 24$. At late times, the harmonics $2m_0$ and $4m_0$ are dominant for angles greater than θ_1 and θ_2, respectively (see Fig. 5.8).

Furthermore, with the help of the schematic of Fig. 5.9(a), it can be also inferred that the perturbation at location 5 corresponds to a mode with $m = 3m_0$. The ray in Fig. 5.8 where locations 4 and 5 are situated corresponds to the drainage of the inverted-U shape perturbations. These perturbations disappear for $t \gtrapprox 14$, leaving only the first and second harmonics of the perturbations, locations 6 and 7, depending on the polar angle (see Fig. 5.9(b)).

In order to highlight the nonlinear transfer of energy from one azimuthal mode to the higher harmonics, we define the disturbance-energy norm over the entire upper hemisphere for the

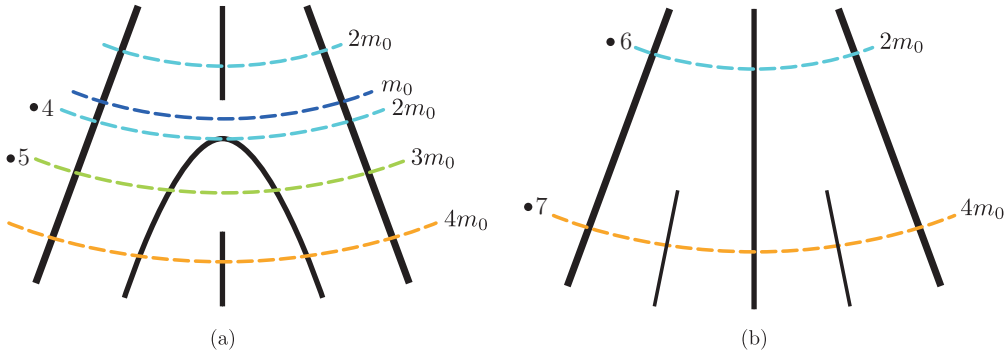

Figure 5.9 – Schematic representation of (a) the inverted-U pattern and (b) the late time pattern, with the corresponding locations in Fig. 5.8 (left) and the wavenumbers (right).

azimuthal mode m as

$$\mathscr{E}_m(t) = \left(\int_0^{\pi/2} |A_m(\theta, t)|^2 d\theta \right)^{1/2}. \tag{5.19}$$

The evolution of $\mathscr{E}_m$ for the considered case is presented in Fig. 5.10. The azimuthal mode

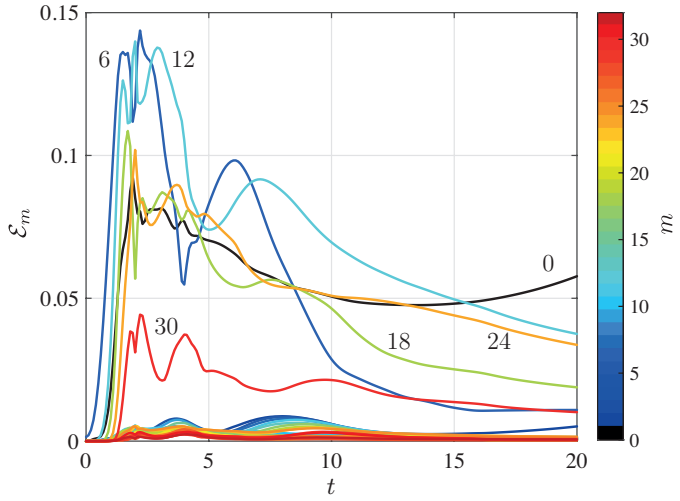

Figure 5.10 – Evolution of the energy norm $\mathscr{E}_m$ of the different modes over the upper hemisphere for $Bo = 150$, $m_0 = 6$ and $\varepsilon = 10^{-2}$ with a linear optimal initial condition. The colorbar indicates the m-values, also highlighted on the plot for the dominant modes.

with the largest amplitude is the fundamental $m = 6$, followed by the harmonics $m = 12$, $m = 18$ and $m = 24$. The mode $m = 30$ reaches also a relatively large amplitude. Therefore, the nonlinear interactions are responsible for the transfer of energy from one harmonics to the higher ones. Furthermore, the number of peaks in the disturbance energy for a given azimuthal mode corresponds to the number of droplet generations formed. For instance, for $m = 6$ one observes three peaks corresponding to the three droplet generations of Fig. 5.5. Note also that the mode $m = 0$ grows at large times due to the droplet at the pole, whereas all

the other modes decay in time.

Thus far the analysis has hinged on the particular case $Bo = 150$, $m_0 = 6$ and $\varepsilon = 10^{-2}$, which allowed us to introduce the different quantities necessary to quantify the nonlinear dynamics. In the following sections, the effects of the fundamental azimuthal wavenumber and of the Bond number are investigated.

5.4.2 Effect of the initial azimuthal wavenumber

The film-thickness maps at $t = 4$ for the initial azimuthal wavenumbers $m_0 = 1$, 6 and 12 are shown in Fig. 5.11. Focusing for now on the second row for $Bo = 150$, we see that for $m_0 = 1$, when initially only one peak is present in the disturbance field, the resulting droplet generates a cascade of several droplets when sliding on the substrate. The pattern is symmetric with respect to the wake of the first droplet, but the appearance of a dominating azimuthal wavelength is less clear. For $m_0 = 12$, instead, the pattern of equally spaced wake-rivulets is already well established.

The perturbation dynamics for the different fundamental wavenumbers m_0 can be inferred by the spatio-temporal diagrams of the azimuthal disturbance norm $\mathscr{H}$ of Fig. 5.12 for $Bo = 150$. The most amplified azimuthal wavenumbers are shown in Fig. 5.13 and the evolution of the energy norm in Fig. 5.14. When $m_0 = 1$, the first droplet forms close to the north pole, but translates very fast along the substrate. While sliding, successive droplets form through the nonlinear interactions, as can be visible by the different ridges on Fig. 5.12. All successive harmonics $m = 2,3,...$ are formed (see Fig. 5.13). The energy is transferred from one harmonic to the successive one, while decreasing in amplitude (see Fig. 5.14). On the other hand, for $m_0 = 12$, the nonlinear dynamics is less rich. The first 12 perturbation peaks drain with an almost constant velocity, generating the harmonics $m = 24$ (see Fig. 5.13) and modifying the mean film thickness (see Fig. 5.14). However, already for $t = 20$, the disturbance amplitude is very small over the entire upper hemisphere. Higher order harmonics cannot be formed as they would correspond to too small wavelengths, which are stabilized by capillary forces.

5.4.3 Effect of the Bond number

The film-thickness maps at $t = 4$ for $Bo = 100$, 150 and 175 and the three azimuthal wavenumbers $m_0 = 1$, 6 and 12 have been presented in Fig. 5.11. The spatio-temporal diagrams for the azimuthal disturbance norm $\mathscr{H}$ for $Bo = 150$ is shown in Figs. 5.6; qualitatively similar results have been obtained for $Bo = 175$. The spatio-temporal diagram of the disturbances for $Bo = 100$ can be inferred from Fig. 5.16(a). In agreement with the observations of the linear optimal growth study of Sec. 5.3.2, the disturbance amplitude increases with the Bond number. Due to the amplifying nature of the system, for a given initial disturbance amplitude ε, the linear growth might be sufficiently large, or not, for nonlinear effects to be relevant.

For $Bo = 100$, the linear growth is found to be insufficient to trigger strong nonlinear effects.

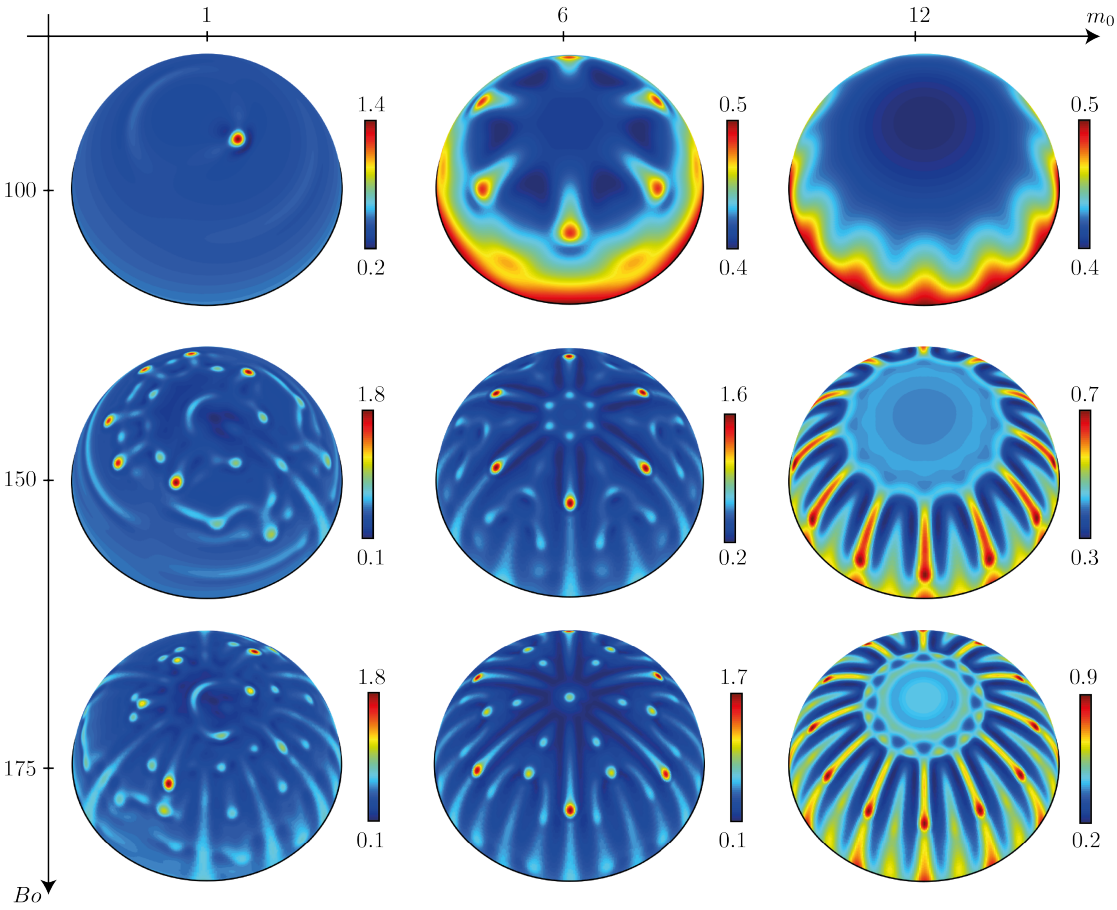

Figure 5.11 – Effect of the azimuthal wavenumber m_0 and of the Bond number Bo for the initial condition given by equation (5.15). $\varepsilon = 10^{-2}$; $m_0 = 1$, 6 and 12; $Bo = 100$, 150 and 175; $t = 4$.

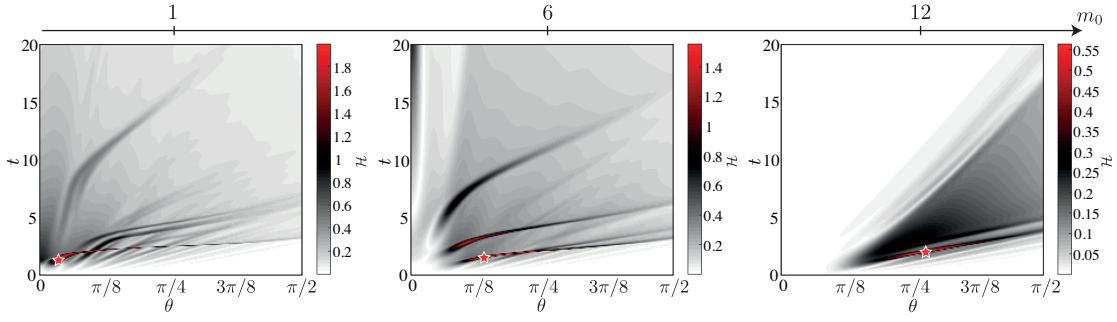

Figure 5.12 – Effect of the azimuthal wavenumber on the azimuthal disturbance norm $\mathscr{H}$ for $Bo = 150$, $\varepsilon = 10^{-2}$ and $m_0 = 1$, 6 and 12 with a linear optimal initial condition. The red star highlights the instant of largest amplitude.

The disturbance amplitude along the meridian $\phi = 0$, where the thickest perturbation is located, presents ridges with almost a linear slope, evidencing the linearity of the dynamics, as will become clear in Sec. 5.4.4 (see Fig. 5.16(a)). Due to the absence of strong nonlinear

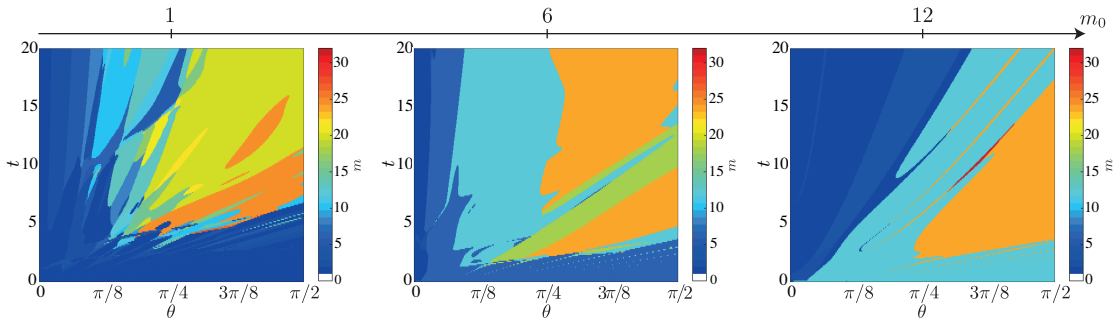

Figure 5.13 – Effect of the azimuthal wavenumber on the azimuthal mode m with the largest amplitude for $Bo = 150$, $\varepsilon = 10^{-2}$ and $m_0 = 1$, 6 and 12 with a linear optimal initial condition. The colorbar indicates the m-values.

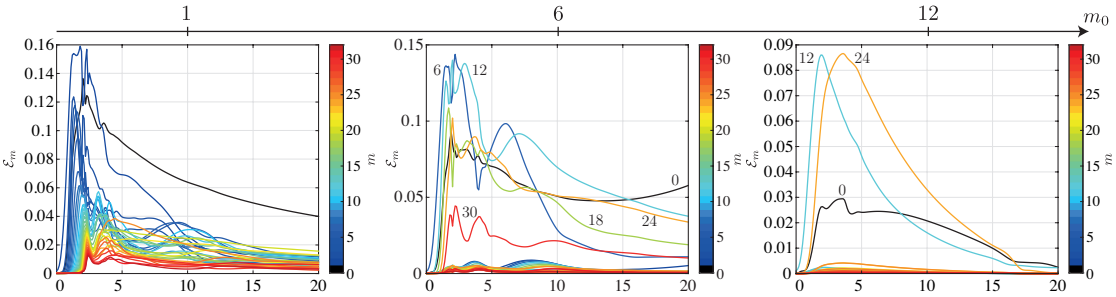

Figure 5.14 – Effect of the azimuthal wavenumber on the evolution of the energy norm $\mathscr{E}_m$ for $Bo = 150$, $\varepsilon = 10^{-2}$ and $m_0 = 1$, 6 and 12 with a linear optimal initial condition. The colorbar indicates the m-values.

interactions, the dominant azimuthal mode remains the fundamental one.

However, for $Bo = 150$ and $Bo = 175$, the linear growth is sufficiently large for the nonlinear effects to be relevant. The nonlinear interactions for $Bo = 175$ are stronger than for $Bo = 150$, resulting in an increased number of droplet generations (see Fig. 5.11). The nonlinear interactions at the pole are also stronger, resulting in a thicker droplet at $\theta = 0$. As can be seen in Fig. 5.11 and in Fig. 5.15(a), the larger the Bond number, the smaller the polar angle where the most amplified azimuthal wavenumber changes from m_0 to $2m_0$ and from $2m_0$ to $4m_0$.

By comparing the largest azimuthal disturbance norm $\mathscr{H}$ in time and space as a function of the fundamental wavenumber m_0 and the Bond number Bo we have found that for each Bond number there is an optimal m_0 for which the perturbation is the largest (see Fig. 5.15(b)). For $Bo = 100$ the largest azimuthal disturbance norm is reached for $m_0 = 1$ and monotonically decreases for greater m_0 values. For $Bo = 125$, the largest azimuthal disturbance norm is reached for $m_0 = 2$, whereas the optimal azimuthal wavenumber is $m_0 = 3$ or 4 for $Bo = 150$ and 175. When the optimal azimuthal wavenumber is larger than 1, the most amplified pattern consists in a thick droplet at the pole formed through nonlinear interactions of the fundamentals, requiring the simulations to be interrupted once the droplet is too thick. Hence, the higher the Bond number, the larger the most amplified azimuthal wavenumber. The same

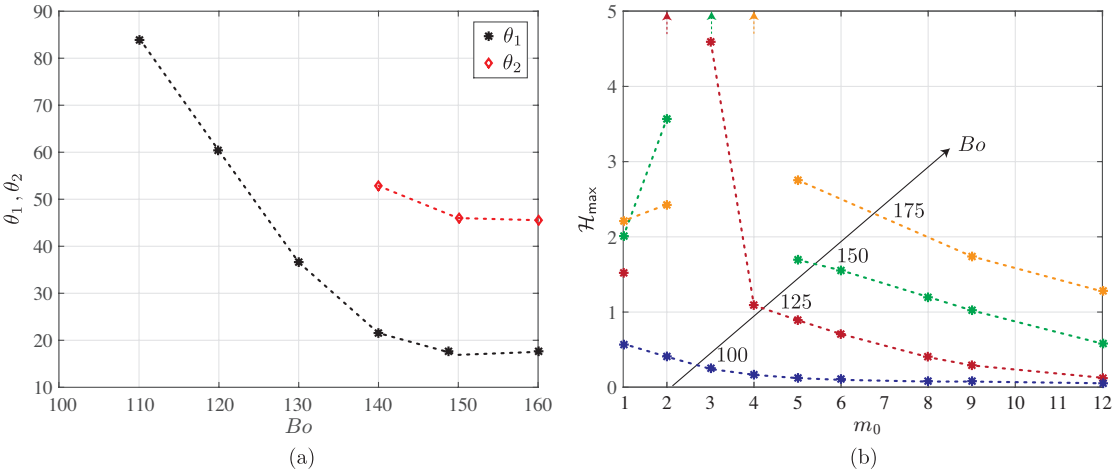

Figure 5.15 – (a) Effect of the Bond number on the angles θ_1 and θ_2 for the transition of the azimuthal mode with the largest amplitude from m_0 to $2m_0$ and from $2m_0$ to $4m_0$, respectively, at $t = 20$ (see Fig. 5.8). (b) Maximal azimuthal energy $\mathscr{H}_{\max} = \max_{(t,\theta)} \mathscr{H}$ as a function of the initial azimuthal wavenumber m_0 for $\varepsilon = 10^{-2}$; $Bo = 100$, 125, 150 and 175 with a linear optimal initial condition. Arrows for $m_0 = 2$, 3 and 4 indicate that the largest azimuthal energy for $Bo = 125$, 150 and 175 is larger than 5, but cannot be computed as a thick droplet forms at the north pole and the simulations have to be interrupted. $\varepsilon = 10^{-2}$, $m_0 = 6$ and $Bo = 100$, 110, 120,..., 160 with a linear optimal initial condition. Dashed lines are added for visualization purposes.

conclusion was drawn for the polar wavenumber in Sec. 5.3.2.

The rationale for this result is that increasing the Bond number corresponds to decreasing the capillary length for a fixed initial film thickness H_i^* and sphere radius R^*, or to increasing $H_i^* R^*$ for a fixed capillary length. As the most amplified wavelength of the classical RTI decreases with the capillary length (Fermigier et al., 1992), it is not surprising that the typical spacing between the droplets is smaller when the Bond number increases. Consequently, more droplets can be located under a sphere of increased radius R^*.

5.4.4 Pattern propagation velocity

We have seen that the dynamics of the perturbations can be either linear or nonlinear. In the latter case the perturbations result in the formation of droplets which slide on the substrate. The advection velocity of the perturbation in the linear regime can be assumed to correspond to the free-surface velocity (Brun et al., 2015; Scheid et al., 2016). For a spherical substrate, the free-surface velocity of the smooth draining film H is given by (see Chapter 2)

$$U = \frac{3}{2\delta}\frac{Q}{H} = \frac{1}{2}\frac{1}{\delta}H^2 \sin\theta, \tag{5.20}$$

where Q is the flux, given only by the gravity-induced drainage term $H^3 \sin\theta/3$. If one further assumes small angles θ, the analytical solution of the draining flow $H(t) = 1/\sqrt{1+4/3t}$ can be employed. The interfacial velocity for $t \gg 3/4$ becomes

$$U \sim \frac{3}{8\delta}\frac{\theta}{t}. \tag{5.21}$$

Thus, the velocity of the free-surface is constant along the ray defined by $\theta/t = \text{const}$. The exact free-surface velocity, Eq. (5.20), as well as the approximation for small angles, Eq. (5.21), are represented on the spatio-temporal diagram for $Bo = 100$ in Fig. 5.16(a). The isocontours of constant velocity are in good agreement with the ridges of the perturbations $\varepsilon h(\theta, \phi = 0, t)$, confirming that small perturbations are advected by the free-surface velocity. For small θ, the exact and asymptotic free-surface velocities are in good agreement. The asymptotic estimation (5.21) always underestimates the draining velocity (5.20) due to the assumption of small angles θ, which results in a weaker tangential component of gravity.

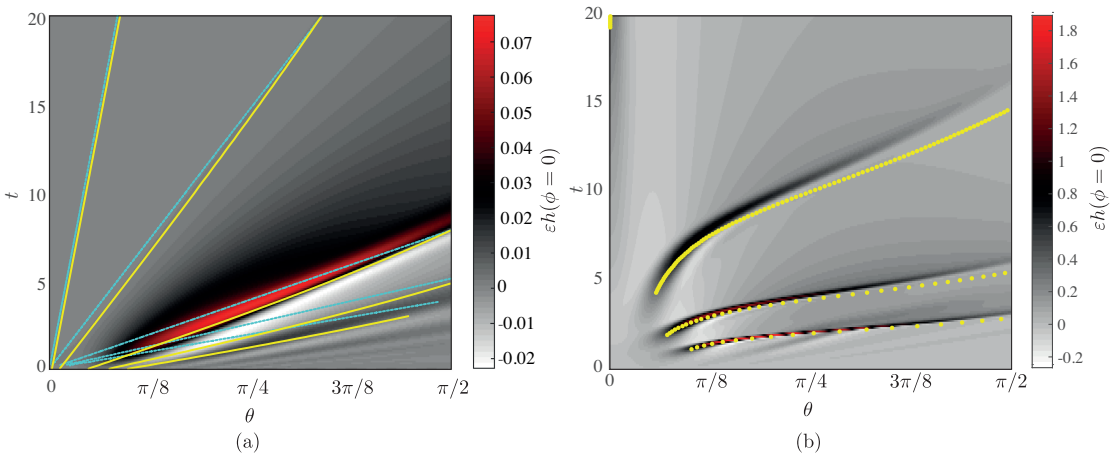

Figure 5.16 – (a) Spatio-temporal diagram of the film-thickness disturbance $\varepsilon h = \bar{H} - H$ at $\phi = 0$ together with the isocontours of the free-surface velocity $U = 0.1$, 0.4, 1.5, 2.3 and 3 for the asymptotic solution (5.21) (turquoise dashed line) and for Eq. (5.20) with the numerical solution of the draining film (yellow solid line), respectively, for $Bo = 100$. (b) Spatio-temporal diagram of the film-thickness disturbance $\varepsilon h = \bar{H} - H$ at $\phi = 0$ with the sliding-droplet trajectories obtained by the integration of the shock speed predicted by Eq. (5.22) (yellow circles) for the three droplet generations at $\phi = 0$ for $Bo = 150$. For both panels, $m_0 = 6$ and $\varepsilon = 10^{-2}$ with a linear optimal initial condition.

For larger Bond numbers, the perturbations have larger amplitudes, the dynamics is nonlinear and the velocity of the formed droplets no longer corresponds to the free-surface velocity of the film. The thickness of the droplets is larger than the surrounding film, which increases their mobility and results in a larger sliding velocity. In order to quantify the velocity of thick droplets, it is instructive to consider them as one-dimensional shocks, for which the velocity

is given by the Rankine-Hugoniot jump condition (LeVeque, 1990)

$$s = \frac{\bar{Q}(\bar{H}_L) - \bar{Q}(\bar{H}_r)}{\bar{H}_L - \bar{H}_R}. \tag{5.22}$$

As a shock we consider the downstream side of the sliding droplets, so that $\bar{H}_L$ is the largest thickness of the droplet and $\bar{H}_R$ is the smallest thickness just ahead of the droplet. The polar flux is (see also Eq. (5.1))

$$\bar{Q} = \frac{1}{3}\left[\bar{H}^3\left(\frac{1}{Bo}\bar{\kappa}_\theta + \delta\bar{H}_\theta\cos\theta + \sin\theta\right)\right], \tag{5.23}$$

where the curvature is given by Eq. (5.2). Note that since the dynamics is nonlinear, the total film thickness $\bar{H}$ has to be considered. Although the sliding droplets are not discontinuous due to the surface-tension term in the flux and the fact that the problem is two-dimensional, the droplet velocity is well predicted by Eq. (5.22), in particular for the first generation of droplets, which are the thickest. To illustrate the good agreement we superpose the droplet trajectory obtained by integrating Eq. (5.22) in time on the spatio-temporal map of the film-thickness disturbances $\varepsilon h(\theta, \phi = 0, t)$ in Fig. 5.16(b). The velocity of thick droplets is therefore given by the ratio of the difference in fluxes and in film thicknesses at the droplet center and front. We have found that the velocity is not monotonous and is strongly affected by the transient nature of this flow. Furthermore, successive droplet generations have a sliding velocity larger than if they were flowing on a film thickness given by the draining solution, since previous drops have deposited a certain amount of fluid and have therefore increased the value of $\bar{H}_R$ (see Fig. 5.16(b)), resulting in an increased mobility. For the considered parameters of Fig. 5.16(b), the relative difference in velocities can go up to 20% for the second generation of droplets and up to 30% for the third generation.

5.5 Random noise initial conditions

To get closer to the experimental reality, a random white noise initial condition with uniform distribution is now considered. The same distribution of mean value 0 and range 2ε is employed for all Bond numbers. As observable in the film-thickness maps of Fig. 5.17, where the same maximal initial disturbance amplitude ε as in Fig. 5.11 is employed, no droplet forms for $Bo = 100$. The rationale for the different behaviour with respect to Fig. 5.11 is the nonoptimality of the random noise initial condition, which limits the nonlinear interactions. For the same reason, we observe only a thick droplet at $t = 4$ for $Bo = 125$ and $Bo = 150$, whereas we have found in Sec. 5.4.3 that the most amplified mode for $Bo = 125$ should have an azimuthal wavenumber of 2 and 3 or 4 for $Bo = 150$, meaning that several droplets should form at short times. A single thick droplet would be the most amplified perturbation for $Bo = 100$ when the optimal initial condition (5.15) is considered. Therefore, the randomness of the initial condition shifts the value of Bond number for a given most amplified perturbation to larger values. For $Bo = 175$, the random initial condition gives rise to several droplets at short times,

as one would expect for $Bo = 150$ when an optimal initial condition is considered.

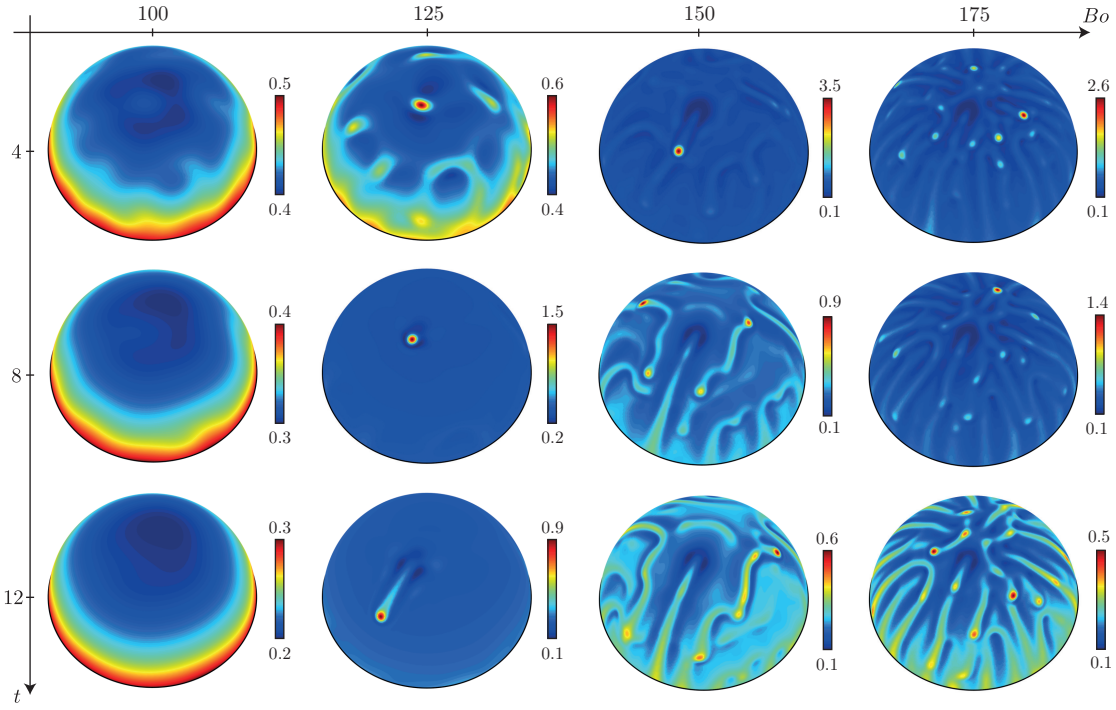

Figure 5.17 – Effect of the Bond number for a random noise initial condition with maximal amplitude $\varepsilon = 10^{-2}$, $Bo = 100$, 125, 150 and 175 and $t = 4$, 8 and 12. See Supplementary Movie 2 for the entire evolution for $Bo = 175$.

Nonetheless, what we have learned from the nonlinear evolutions of the optimal initial conditions of Sec. 5.4 also holds for the dynamics of a random noise initial condition. For example, the larger the Bond number, the faster the dynamics and the smaller the spacing between the droplets, as we have seen in Fig. 5.11 and Fig. 5.15. Furthermore, the quantities $\mathscr{H}$, A_m and $\mathscr{E}_m$ can be employed to understand the dynamics. For $Bo = 100$, one recognizes the almost linear ridges in the spatio-temporal diagrams of Figs. 5.18 and 5.19, evidencing the linear dynamics as discussed for Fig. 5.16(a). From the evolution of the energy norm $\mathscr{E}_m$ it can be concluded that the initial energy, distributed over all modes because of the randomness of the spatial distribution, experiences only a weak transient growth for $Bo = 100$, where low-order modes reach the largest growths. For $Bo = 125$ and $Bo = 175$, the spatio-temporal diagrams of Fig. 5.18 highlight the formation of one and several droplets at short times, respectively. The larger the Bond number, the more the formed droplets, as found for the optimal initial conditions in Sec. 5.4.3. The subsequent droplets generations are also visible. In particular, when a single drop is formed at short times, a cascade of droplets of the successive harmonics is generated as time increases, transferring energy from low to high azimuthal modes m (see Fig. 5.20). By comparing the azimuthal modes with the largest amplitude (see Fig. 5.19), one confirms that the larger the Bond number, the wider the spectrum of the azimuthal wavenumbers m of the perturbation.

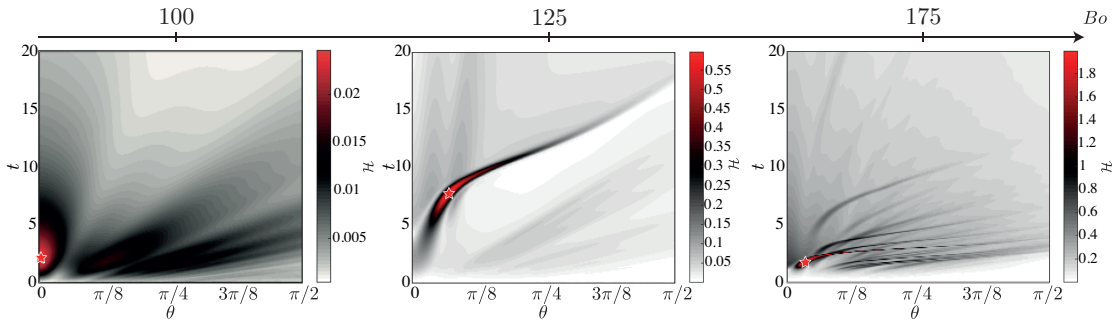

Figure 5.18 – Azimuthal disturbance norm $\mathscr{H}$ for a random noise initial condition with maximal amplitude $\varepsilon = 10^{-2}$ and $Bo = 100$, 125 and 175. The red star highlights the instant of largest amplitude.

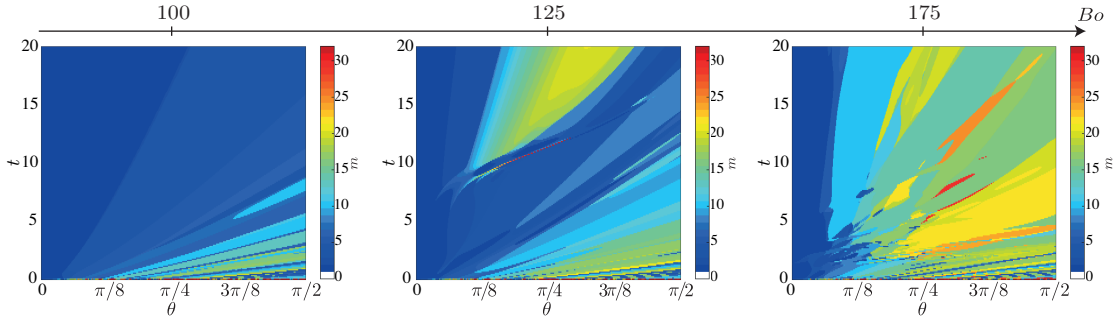

Figure 5.19 – Azimuthal mode m with the largest amplitude for a random noise initial condition with maximal amplitude $\varepsilon = 10^{-2}$ and $Bo = 100$, 125 and 175. The colorbar indicates the m-values.

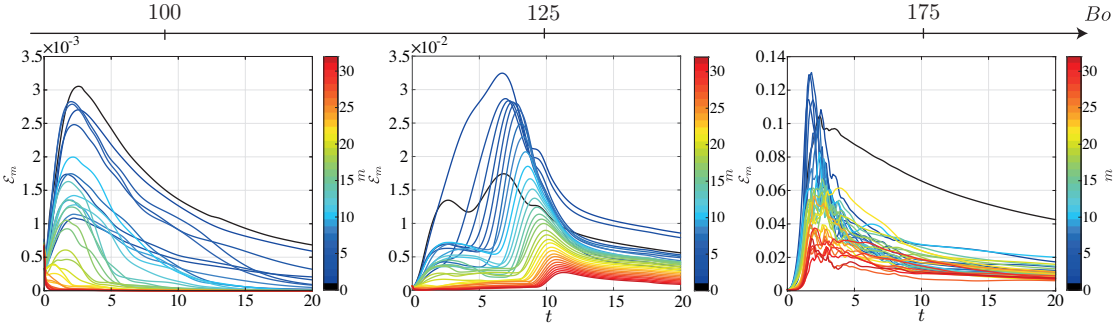

Figure 5.20 – Evolution of the energy norm $\mathscr{E}_m$ for for a random noise initial condition with maximal amplitude $\varepsilon = 10^{-2}$ and $Bo = 100$, 125 and 175. The colorbar indicates the m-values.

Finally, the peculiar inverted-U shape perturbation is observed also for random initial conditions (see for instance Fig. 5.17 for $Bo = 175$). We believe that the reason for the formation of this general pattern is twofold. First, such perturbation structures form due to the drainage of two initially close perturbations which get apart while draining on the spherical geometry. Secondly, the trajectory of successive droplets strongly depends on the precise film-thickness perturbations surrounding them. As can be seen in Figs. 5.5 and 5.17, as well as in the Sup-

plementary Movies 1 and 2, a sliding drop leaves a wake behind, which is characterized by a reduced film thickness at its sides. Furthermore, it is also possible that a localized region of reduced film thickness exists due to the initial condition. Lister et al. (2010) have shown that the anisotropic perturbation field induced by the motion of one droplet interacts with other perturbations and affects the droplet dynamics. In particular, a droplet is repelled by a region of reduced film thickness. Therefore, the thick film regions upstream of previously generated wakes or of zones of reduced film thickness drain in a way to minimize these repulsive forces. We conjecture that this is very likely to be at the origin of the inverted-U shape pattern. Only a droplet which is exactly aligned with the center of a previous wake can benefit from the thicker region at the center of the wake and follow the trajectory of previous droplets.

5.6 Conclusions

The stability of a thin viscous film coating the interior of a sphere has been investigated. For a curved substrate, gravity has a twofold effect. On the one hand, it is the origin of the destabilization of the interface, through the component normal to it. On the other hand, the gravity component tangent to the substrate induces a flow which stabilizes the Rayleigh-Taylor instability (RTI). The rationale for this stabilization mechanism is the thinning of the film and the stretching of the interface perturbations due to the drainage flow. The system is asymptotically stable and only a short-time algebraic growth can be achieved, when gravitational forces overcome the capillary forces by a given value (see Chapter 3). By performing a linear stability analysis for the critical region close to the north pole we have found that the Bond number for an initial growth of the perturbations is $Bo = 24$, the double of what was found for a cylindrical substrate in Chapter 3. The corresponding optimal wavenumber is identical to the classical RTI for a horizontal substrate, $k_0 = \sqrt{Bo/2}$ (Fermigier et al., 1992). The stabilizing effect of the curvature, firstly noted by Trinh et al. (2014) for a cylinder, is doubled as the mean curvature of a sphere is the double of the mean curvature of a cylinder. Physically speaking, the fluid drains over two main directions, rather than only along the polar direction of a cylinder. As a result, the thickness of the film close to the north pole decreases twice as fast as for a cylinder. The enhanced stabilization of the curvature explains why thin films do not destabilize under spherical substrates of radii larger than for cylinders, making it possible to fabricate large hollow chocolate eggs or elastic hemispherical shells of nearly uniform thickness, as we have seen in Chapter 2.

The linear optimal transient growth analysis yields an optimal polar wavenumber, but does not provide any optimal azimuthal wavenumber. The largest optimal disturbance amplitude increases exponentially with the Bond number, as for a cylindrical geometry, but has a smaller value. The exponential dependence with Bo confirms the amplifying nature of the system. Initial disturbances are amplified over a short time, by a Bond-number-dependent factor. When the disturbance magnitude is of the order of the base flow, nonlinear effects become relevant. The critical Bond number for the transition to the nonlinear formation of droplets is found to be initial-disturbance amplitude dependent.

The nonlinear dynamics have been investigated by resolving the fully nonlinear lubrication equation over the entire geometry. The optimal initial conditions found by the linear analysis with a particular azimuthal wavenumber have been considered at first. We have found that there is an energy cascade from the fundamental azimuthal mode to the successive higher harmonics, until the azimuthal wavelength is too small and capillary forces stabilize the perturbation. At every polar location there is a dominant azimuthal wavenumber, increasing as the distance from the north pole, or the Bond number, increases. Furthermore, we have found that for each Bond number there is an optimal initial azimuthal wavenumber giving the largest nonlinear growth. The optimal initial azimuthal wavenumber is found to increase with the Bond number. Small-amplitude perturbations move with the free-surface velocity, whereas the velocity of thick droplets is well described by the one-dimensional shock theory.

Qualitatively similar results are found by resolving the nonlinear dynamics starting from an arbitrary random white noise initial condition. Depending on the Bond number, the following scenarios occur. For $Bo < 24$, the thin film drains smoothly and no droplet forms. For moderate Bond numbers, yet sufficiently large for nonlinear effects to be important, a single droplet will form close to the pole. When sliding along the substrate, all successive harmonics will be excited and several droplets will appear at later times if the Bond number is sufficiently large. Instead, for very large Bond numbers, several droplets form close to the north pole already at short times. Nonlinear interactions will then promote the formation of their harmonics. The higher the Bond number, the larger the number of droplets generations, the closer they are to the pole and the faster the dynamics. Droplets form in the largest available space left by the previous ones, similarly to the formation of primordia in Phyllotaxic patterns (Douady & Couder, 1996). At late times, the film thickness will present thicker regions, surrounded by narrow thin regions, corresponding to the wakes of the droplets (see Chapter 8). These structures resemble to the rivulets found for a cylindrical substrate (see Chapter 4 and Rietz et al. (2017)), yet with the significant difference that the rivulets in a sphere only form as a result of the droplet motion and are not an intrinsic instability pattern of the system.

If a thin film coats the outside of a spherical substrate, the interface is subjected to the Rayleigh-Taylor instability when it flows on the lower hemisphere. In this case the system is asymptotically unstable and no stable regime exists. The gravity-induced drainage is responsible for destabilizing the interface by focusing the flow at the south pole. At low Bond numbers a single droplet will form at the south pole, whereas a pattern of several droplets will form at high Bond numbers. Furthermore, we conjecture that rivulets will form at moderate Bond numbers.

It has to be stressed that the considered thin film is initially smooth. Otherwise, the moving capillary ridge close to the contact line would be unstable with respect to spanwise perturbations and would eventually result in the formation of fingers (Fraysse & Homsy, 1994; Lin et al., 2012), as investigated by Takagi & Huppert (2010) and Hammoud (2016), see Chapter 6. Thin liquid films coating spherical substrates can undergo also other types of instabilities when other forces are at play. For instance, if the liquid layer is submitted to an oscillating ac-

celeration field, the liquid interface might become unstable to the Faraday instability (Falcon, Falcon, Bortolozzo & Fauve, 2009; Adou & Tuckerman, 2016).

Acknowledgments The authors would like to acknowledge the valuable comments from the anonymous referees that helped to improve the manuscript. This work was funded by the ERC Grant No. SIMCOMICS 280117 and by the Swiss National Science Foundation Grant No. 200021_178971.

5.7 Appendix

5.7.1 Derivation of the lubrication equation

The following description of the derivation of the equation is widely inspired by the one for the cylindrical geometry of Chapter 4. For a general derivation of the lubrication equation on curved substates see Schwartz & Weidner (1995), Roy et al. (2002) and Howell (2003). A thin film coating the interior of a sphere of radius R^* is considered. The initial average thickness is $H_i^* \ll R^*$, yielding a small film aspect ratio $\delta = H_i^*/R^* \ll 1$. Using H_i^* as characteristic length in the radial direction and R^* as the characteristic length in the polar and azimuthal directions, the long wavelength approximation can be employed as $\delta \ll 1$ (Oron et al., 1997). Mass conservation indicates that the velocity normal to the interface is much smaller than the polar and azimuthal components, $V^* \sim \delta U^* \ll U^*$ and $V^* \sim \delta W^* \ll W^*$, respectively (see Chapter 1). Furthermore, the small Reynolds number for this flow allows the use of the Stokes equations and inertial effects can be neglected. The momentum equation in the radial direction is

$$0 = -\frac{1}{\rho}\frac{\partial p^*}{\partial r^*} - g\cos\theta, \tag{5.24}$$

and the boundary condition for the pressure is given by $p^*(R^* - \bar{H}^*, \theta, \phi) = p_0^* - \gamma\bar{\kappa}^*$, where p_0^* is the external pressure, γ the surface tension and $\bar{\kappa}^*$ the curvature of the interface. Equation (5.24) can be integrated along the radial direction and using the boundary condition for the pressure, the pressure distribution $p^*(r^*, \theta, \phi) = p_0^* - \gamma\bar{\kappa}^* + \rho g\cos\theta(R^* - \bar{H}^* - r^*)$ is obtained. The polar and azimuthal components of the momentum equation read

$$\begin{aligned} 0 = &-\frac{1}{\rho r^*}\frac{\partial p^*}{\partial \theta} + \nu\left[\frac{1}{r^{*2}}\frac{\partial}{\partial r^*}\left(r^{*2}\frac{\partial u^*}{\partial r^*}\right)+\right. \\ &\left.+\frac{1}{r^{*2}}\frac{\partial}{\partial\theta}\left(\frac{1}{\sin\theta}\frac{\partial}{\partial\theta}\left(u^*\sin\theta\right)\right)+\frac{1}{r^{*2}\sin^2\theta}\frac{\partial^2 u^*}{\partial\phi^{*2}}-\frac{2\cot\theta}{r^{*2}\sin\theta}\frac{\partial w^*}{\partial\phi}\right]+g\sin\theta, \end{aligned} \tag{5.25}$$

$$\begin{aligned} 0 = &-\frac{1}{\rho r^*\sin\theta}\frac{\partial p^*}{\partial\phi} + \nu\left[\frac{1}{r^{*2}}\frac{\partial}{\partial r^*}\left(r^{*2}\frac{\partial w^*}{\partial r^*}\right)+\frac{1}{r^{*2}}\frac{\partial}{\partial\theta}\left(\frac{1}{\sin\theta}\frac{\partial}{\partial\theta}\left(w^*\sin\theta\right)\right)+\right. \\ &\left.+\frac{1}{r^{*2}\sin^2\theta}\frac{\partial^2 w^*}{\partial\phi^2}+\frac{2\cot\theta}{r^{*2}\sin\theta}\frac{\partial u^*}{\partial\phi}\right]. \end{aligned} \tag{5.26}$$

With the change of variable $r^* = R^* - s^*$, where $0 \leq s^* \leq \bar{H}^* \ll R^*$, the viscous terms in Eq. (5.25) and Eq. (5.26) reduce to $\nu\partial^2 u^*/\partial s^{*2}$ and $\nu\partial^2 w^*/\partial s^{*2}$, respectively, plus terms at least an order δ smaller. Considering only the dominant order of the viscous term, as well as the surface tension and gravitational terms, Eq. (5.25) and Eq. (5.26) with the expression for p^* become:

$$0 = \frac{\gamma\bar{\kappa}^*_\theta}{\rho R^*} + \frac{g\cos\theta\bar{H}^*_\theta}{R^*} + \nu\frac{\partial^2 u^*}{\partial s^{*2}} + g\sin\theta\,, \tag{5.27}$$

$$0 = \frac{\gamma\bar{\kappa}^*_\phi}{\rho R^*\sin\theta} + \frac{g\cos\theta\bar{H}^*_\phi}{R^*\sin\theta} + \nu\frac{\partial^2 w^*}{\partial s^{*2}}\,. \tag{5.28}$$

Equations (5.27) and (5.28) can be integrated twice and considering the zero-slip boundary condition at the sphere surface, $u^*(0,\theta,\phi) = 0$ and $w^*(0,\theta,\phi) = 0$, as well as the zero-shear stress interface, $\partial u^*(\bar{H}^*,\theta,\phi)/\partial s^* = 0$ and $\partial w^*(\bar{H}^*,\theta,\phi)/\partial s^* = 0$, the velocity components are found to be

$$u^*(s^*,\theta,\phi) = \left(\frac{\gamma\bar{\kappa}^*_\theta}{\mu R^*} + \frac{\rho g\cos\theta\bar{H}^*_\theta}{\mu R^*} + \frac{\rho g\sin\theta}{\mu}\right)\left(\bar{H}^* - \frac{s^*}{2}\right)s^*\,, \tag{5.29}$$

$$w^*(s^*,\theta,\phi) = \left(\frac{\gamma\bar{\kappa}^*_\phi}{\mu R^*\sin\theta} + \frac{\rho g\cos\theta\bar{H}^*_\phi}{\mu R^*\sin\theta}\right)\left(\bar{H}^* - \frac{s^*}{2}\right)s^*\,. \tag{5.30}$$

The flow-rate in the polar direction is $Q^{*\theta}(\theta,\phi) = \int_0^{\bar{H}^*} u^*(s^*,\theta,\phi)\mathrm{d}s^*$ and in the azimuthal direction is $Q^{*\phi}(\theta,\phi) = \int_0^{\bar{H}^*} w^*(s^*,\theta,\phi)\mathrm{d}s^*$.

Mass conservation in spherical coordinates $\partial\bar{H}^*/\partial t^* + (R^*\sin\theta)^{-1}\partial(\sin\theta\,Q^{*\theta})/\partial\theta + (R^*\sin\theta)^{-1}\partial Q^{*\phi}/\partial\phi = 0$ yields the lubrication equation:

$$\bar{H}^*_{t^*} + \frac{1}{3\mu R^*\sin\theta}\left[\bar{H}^{*3}\sin\theta\left(\underbrace{\frac{\gamma\bar{\kappa}^*_\theta}{R^*}}_{\mathbf{I}} + \underbrace{\frac{\rho g\cos\theta\bar{H}^*_\theta}{R^*}}_{\mathbf{II}} + \underbrace{\rho g\sin\theta}_{\mathbf{III}}\right)\right]_\theta + \\ + \frac{1}{3\mu R^*\sin\theta}\left[\frac{\bar{H}^{*3}}{\sin\theta}\left(\underbrace{\frac{\gamma\bar{\kappa}^*_\phi}{R^*}}_{\mathbf{I}} + \underbrace{\frac{\rho g\cos\theta\bar{H}^*_\phi}{R^*}}_{\mathbf{II}}\right)\right]_\phi = 0\,, \tag{5.31}$$

The term **I** in the spatial variation of the flux corresponds to the surface tension effects, term **II** to the variation of the hydrostatic pressure distribution and term **III** to the drainage.

The free surface of the viscous film is defined by

$$F^*(r^*,\theta,\phi,t^*) = r^* - \left[R^* - \bar{H}^*(\theta,\phi,t^*)\right] = 0, \tag{5.32}$$

its normal vector $\mathbf{n}^*$ is given by

$$\mathbf{n}^* = \frac{\nabla^* F^*}{||\nabla^* F^*||} = \frac{\left[1, \frac{\bar{H}^*_\theta}{r^*}, \frac{\csc\theta \bar{H}^*_\phi}{r^*}\right]^T}{\sqrt{1+\left(\frac{\bar{H}^*_\theta}{r^*}\right)^2 + \left(\frac{\csc\theta \bar{H}^*_\phi}{r^*}\right)^2}} \tag{5.33}$$

at $r^* = R^* - \bar{H}^*$, and the interfacial curvature is $\bar{\kappa}^* = \nabla^* \cdot \mathbf{n}^*$.

Lengths can be nondimensionalized by the initial average film thickness H_i^* and the time by the gravitational relaxation scale $\mu R^*/(\rho g H_i^{*2})$ so that the lubrication equation expressed with nondimensional quantities finally reads:

$$\bar{H}_t + \frac{1}{3\sin\theta}\left[\bar{H}^3 \sin\theta \left(\underbrace{\frac{1}{Bo}\bar{\kappa}_\theta}_{\text{I}} + \underbrace{\delta \bar{H}_\theta \cos\theta}_{\text{II}} + \underbrace{\sin\theta}_{\text{III}}\right)\right]_\theta + \frac{1}{3\sin\theta}\left[\frac{\bar{H}^3}{\sin\theta}\left(\underbrace{\frac{1}{Bo}\bar{\kappa}_\phi}_{\text{I}} + \underbrace{\delta \bar{H}_\phi \cos\theta}_{\text{II}}\right)\right]_\phi = 0, \tag{5.34}$$

where $Bo = \rho g H_i^* R^*/\gamma$ is the modified Bond number.

The curvature up to the second order in δ is :

$$\bar{\kappa} = 2\delta + \delta^2\left(\bar{H}_{\theta\theta} + \cot\theta \bar{H}_\theta + \csc^2\theta \bar{H}_{\phi\phi} + 2\bar{H}\right) + O(\delta^3). \tag{5.35}$$

5.7.2 Derivation of the drainage solution

If a uniform initial film thickness is assumed, $H(r,\phi,t=0)=1$, the lubrication equation at the pole (5.4) becomes

$$\frac{\partial H}{\partial t} + \frac{1}{3r}\frac{\partial}{\partial r}\left(H^3 r^2\right) = 0 \Leftrightarrow \frac{\partial H}{\partial t} + \frac{2}{3}H^3 = 0 \tag{5.36}$$

and the first order temporal solution, uniform in space, is $H(t) = \sqrt{1+4t/3}$ (Takagi & Huppert, 2010). It can be noted that the thinning of the film is twice as fast as for a cylindrical substrate discussed in Chapter 4.

The higher order solution for the drainage flow can be computed by considering a regular perturbation expansion of the film thickness starting from the equation (5.1) simplified for a uniform initial condition and under the assumption of small interface deformations

$$\frac{\partial H}{\partial t} + \frac{1}{3\sin\theta}\frac{\partial}{\partial\theta}\left(H^3 \sin^2\theta\right) = 0. \tag{5.37}$$

As detailed in Chapter 2, the asymptotic solution up to the fourth order is

$$H(\theta,t) \approx \frac{1}{\sqrt{1+\frac{4}{3}t}}\left[1+\frac{\theta^2}{10}\left(1-\frac{1}{(1+\frac{4}{3}t)^{5/2}}\right)\right.$$
$$\left.+\theta^4\left(\frac{41}{4800}+\frac{9}{200(1+\frac{4}{3}t)^5}-\frac{1}{150(1+\frac{4}{3}t)^{5/2}}+\frac{135}{16(1+\frac{4}{3}t)^4}\right)\right]. \tag{5.38}$$

5.7.3 Numerical methods

The two-dimensional nonlinear lubrication equation (5.1) is solved numerically using the finite element method of COMSOL Multiphysics. The total film thickness $\bar{H}$ as well as the total film curvature $\bar{\kappa}$ are the two variables. Quadratic elements with Lagrangian shape functions are employed on a free triangular grid of characteristic size 0.8, which allows the consideration of azimuthal wavenumbers up to 78. The relative tolerance for the time-stepping algorithm is set to 10^{-3}. The numerical procedure is validated with the analytical solution for the evolution of the draining thickness at the pole (see Fig. 5.21(a)) as well with the asymptotic solution for the spatial evolution of the drainage solution along the polar angle (see Fig. 5.21(b)). The largest relative error between the numerical and the analytical solution for the drainage at the pole is below 10^{-3}.

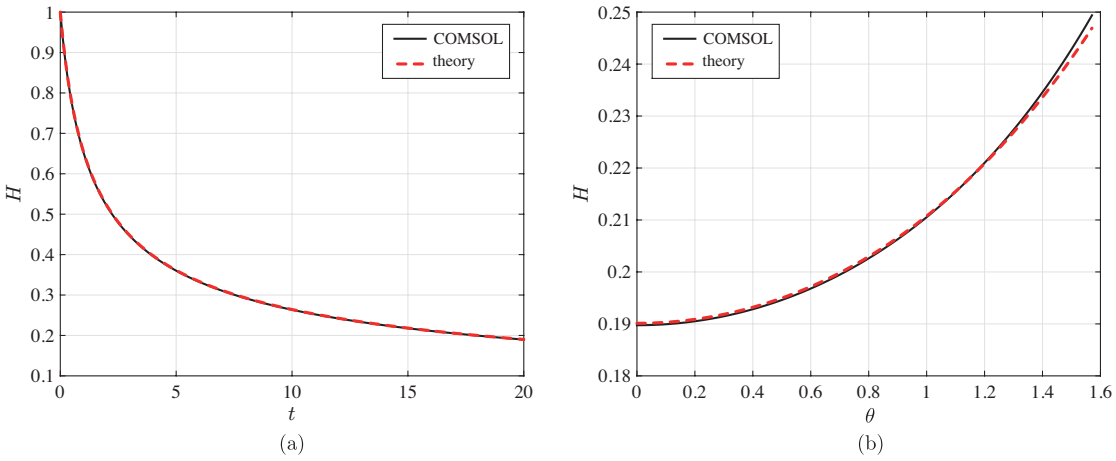

Figure 5.21 – Validation of the numerical scheme against the theoretical predictions. (a) Drainage at the pole, Eq. (5.36), (b) drainage over the polar angle for $t = 20$, Eq. (5.38). $Bo = 25$.

5.7.4 Alternative representation of the thin-film evolution shown in Fig. 5.5

For the sake of clarity, we show in Fig. 5.22 the corresponding the film-thickness evolution shown in Fig. 5.5 using a constant colorbar range. One can clearly observe how the film thickness is reduced during time and how the successive droplet generations have a smaller

amplitude, highlighting the transient nature of this flow.

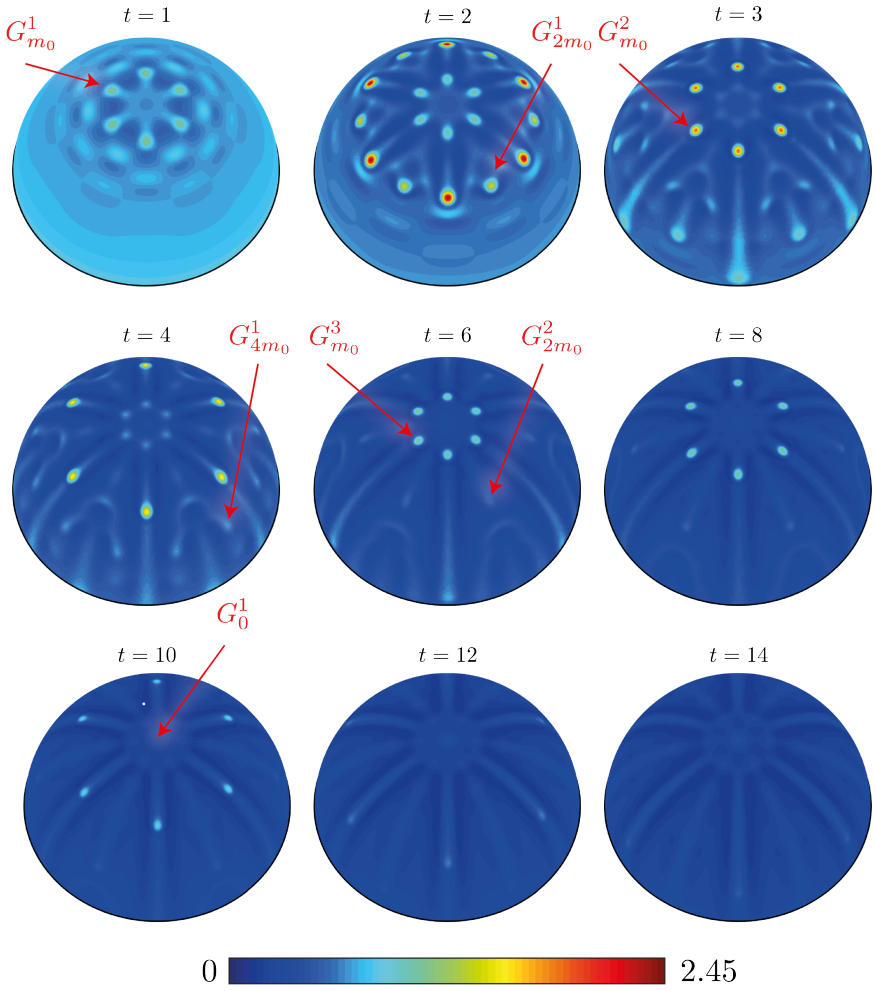

Figure 5.22 – Corresponding of Fig. 5.5 with a constant colorbar for the film thickness. Nonlinear evolution of the film thickness for the initial condition given by equation (5.15) for $Bo = 150$, $m_0 = 6$ and $\varepsilon = 10^{-2}$ at the times $t = 1$, 2, 3, 4, 6, 8, 10, 12 and 14. The droplet generations G_{m_0}, G_{2m_0}, G_{2m_0} and G_0 are also highlighted.

6 Fingering instability on curved substrates: optimal initial film and substrate perturbations

Remark This chapter is largely inspired by the publication of the same name

G. Balestra[1], M. Badaoui[1], Y.-M. Ducimetière[1] and F. Gallaire[1]

[1]Laboratory of Fluid Mechanics and Instabilities, EPFL, CH1015 Lausanne, Switzerland

Submitted to the Journal of Fluid Mechanics

We investigate the stability of a thin viscous Newtonian fluid spreading on a horizontal cylinder under the action of gravity. The capillary ridge forming at the advancing front is known to be unstable with respect to spanwise perturbations, resulting in the formation of fingers. In contrast to the classic case of a flow over an inclined plane, the gravity components along a cylindrical substrate vary in space and the draining flow is time-dependent, making a modal stability analysis inappropriate. A linear optimal transient growth analysis is instead performed to find the optimal spanwise wavenumber. We do not only consider the optimal perturbations of the initial film thickness, as commonly done in the literature, but also the optimal topographical perturbations of the substrate, which are of significant practical relevance. We found that the optimal gains are obtained when the perturbation structures are the least affected by the optimization time. The optimal spanwise wavenumber of the initial film-thickness perturbations is found to be dependent on the front location, due to the dependence of the characteristic length of the capillary ridge on its polar location. On the other hand, the optimal spanwise wavenumber for the substrate perturbations tends to a constant value, meaning that a time-horizon-independent optimal substrate promoting the fingers' formation exists.

6.1 Introduction

We refer to Sec. 1.2 for a general introduction on the fingering instability.

A thin film flowing under the action of body or surface shear forces presents two distinct regions. The draining film far upstream from the ridge is almost flat with thickness H_N^* and the capillary pressure can be neglected. This region is usually called the *outer region*. The body force, or the surface shear force, balances the viscous stresses and the film profile is given by a self-similar solution for a fixed fluid quantity (Huppert, 1982*a*), which finishes abruptly at the front location. There, in reality, the film profile is regularized by surface tension. In this *inner region* close to the contact line, surface tension effects have to be considered together with the body force, or surface-shear stresses, and with the viscous stresses. The upstream boundary condition for the inner solution is found by matching its film thickness to the one of the outer solution, H_N^*, whereas the boundary condition at the downstream region requires the modeling of the contact line. Spaid & Homsy (1996) have shown that a precursor film model or a slip model can both be used without impacting the value of the most amplified wavelength. The detailed flow field in the vicinity of the contact line has been computed by Goodwin & Homsy (1991). Brenner (1993) first pointed out that the instability mechanism is driven by the macroscopic feature of the capillary ridge profile and is not significantly influenced by the contact-line dynamics. A composite solution (Van Dyke, 1975) valid over the entire domain has been proposed by Moriarty, Schwartz & Tuck (1991).

The first precise description of the inner solution for the gravity driven flow of Huppert (1982*a*) has been given by Troian et al. (1989) and Hocking (1990). In contrast to the solution in the outer region, which follows a self-similar solution (Huppert, 1982*a*), the solution in the inner region can be assumed as quasi-static and corresponds to a traveling wave solution (Bertozzi & Brenner, 1997). Due to the stationarity of the base state solution in the inner region, a classical modal stability analysis can be performed. The linearly most amplified spanwise wavelength scales as $\lambda^* \sim \ell^*$, where $\ell^* = H_N^*(3Ca)^{-1/3}$ is the characteristic length of the ridge, with Ca being the capillary number defined with the front advancing velocity (Spaid & Homsy, 1996).

Furthermore, it has been shown that the microscopic scale perturbation at the contact line might experience a transient growth sufficiently large to modify the macroscopic structure of the ridge and thus affect the fingers' formation (Bertozzi & Brenner, 1997). The reason is the singular dependence of the base state on the microscopic length scale at the contact line. This mechanism might explain the irregularity of the observed patterns in experiments, which are very sensitive to the substrate inhomogeneities.

In contrast to the commonly considered case of a fixed fluid quantity spreading over a substrate, for which the outer solution is time-dependent, when the flow is continuously fed, the outer solution is stationary (Tuck & Schwartz, 1990). This configuration has been investigated in great detail by Eres et al. (2000) and Kondic & Diez (2001).

However, there are also flow configurations where not only the outer solution is time dependent, but also the inner solution cannot be considered as quasi-static. This is for example the case of the flow over a curved substrate (Takagi & Huppert, 2010), where the forces acting on the advancing ridge vary depending on its location. The same is true for the spin-coating

problem, where the centrifugal forces are space dependent. Therefore, in these cases, the stability analysis is more complex and a classical normal mode decomposition leading to an eigenvalue problem cannot be performed. The physical reason is that the most unstable mode cannot grow exponentially in time as an eigenmode since the base flow on which it evolves is modified in time, and is not a traveling wave solution. Hence, the most amplified perturbation at one time instant will not be effective at the following time, when the forces at play will be different. So far, the stability properties of these complex configurations have been investigated mostly either by experiments (Wang & Chou, 2001; Takagi & Huppert, 2010) or numerical simulations (Schwartz & Roy, 2004), but a complete stability analysis for these time and space dependent flows is still lacking. Fraysse & Homsy (1994) successfully compared the linear growth predicted by the linear theory for a quasi-steady base state (Troian et al., 1989) with their experimental results of a film spreading under centrifugal forces. Nevertheless, they had to provide the critical radius where the fingers form, *i.e.* the critical time for the onset of the instability, as an input parameter.

Inspired by the work of Takagi & Huppert (2010), we investigate here the fingering instability on a cylindrical substrate by performing a linear optimal transient growth analysis. Given the spatial variations of the forces at play, the characteristics of the draining flow, as the length of the capillary ridge, vary in space and time. Nonmodal approaches have been proven to be effective in predicting stability properties of time-evolving flows (Schmid, 2007), also in the context of thin films (see Chapter 3). In the present work, we consider two distinct optimization problems. First, we look for the optimal initial condition of the film-thickness perturbations for a flow draining on a smooth cylindrical substrate. Secondly, we aim at finding the optimal perturbations of the substrate topography. The gain function to be optimized at finite times corresponds to the energy of the film-thickness perturbations, normalized by the initial thickness or substrate-perturbation energy, for the first and second problem, respectively. Substrate and film-thickness perturbations are assumed to be of the same order. We show that, for both problems, the optimal perturbations correspond to the perturbations which are the least affected by the optimization time, and are thus the most universal. Furthermore, the shape of optimal substrate perturbations is less dependent on the spanwise wavenumber and results therefore in the selection of a constant optimal spanwise wavenumber for sufficiently large times. A correct prediction of the most amplified pattern is only possible by considering the transient dynamics of the flow, which underlines the importance of these nonmodal approaches in the study of time-dependent flows.

The chapter is structured as follows. The considered problem and the governing equations are presented in Sec. 6.2. In Section 6.3, we describe the axially invariant draining flow. More precisely, the lubrication equation and the initial condition are specified in Sec. 6.3.1, followed by the description of the drainage at the pole (Sec. 6.3.2), the asymptotic solution for the outer region (Sec. 6.3.3), the spatio-temporal dependence of the front location (Sec. 6.3.4) and the evolution of the capillary ridge length (Sec. 6.3.5). The optimal transient growth analysis for the initial film-thickness perturbations is presented in Sec. 6.4, starting with the decomposition into base state and perturbations in Sec. 6.4.1, the linear disturbance equation in Sec. 6.4.2

and the optimization method in Sec. 6.4.3. The results follows in Sec. 6.4.4, where the effect of the optimization time is given in Sec. 6.4.4 and the one of the spanwise wavenumber in Sec. 6.4.4. The same structure is employed for the description of the optimal transient growth for the substrate perturbations in Sec. 6.5. Conclusions are drawn in Sec. 6.6.

6.2 Problem formulation and governing equations

Consider the instantaneous release of a Newtonian fluid of dynamic viscosity μ and density ρ spreading on the outside of a smooth cylindrical substrate of radius R^* whose axis is orthogonal to gravity (see Fig. 6.1). The fluid is pulled by the gravitational field g and slowed down by viscous friction. The fluid thickness profile is initially invariant in the axial direction and the cross-sectional area is A^*. We assume a small film aspect ratio, $\delta = \sqrt{A^*}/R^* \ll 1$. The characteristic time can be defined by the ratio of the viscous over the gravitational stresses, $\tau_d = \mu R^*/(\rho g A^*)$ (Takagi & Huppert, 2010; Trinh et al., 2014). The ratio between the gravitational and the capillary forces defines the Bond number $Bo = \rho g A^{*3/2}/(\gamma R^*)$. The considered Bond number and film aspect ratio are chosen such as to correspond to the experiment of Takagi & Huppert (2010); their values are $Bo = 15$ and $\delta = 0.15$.

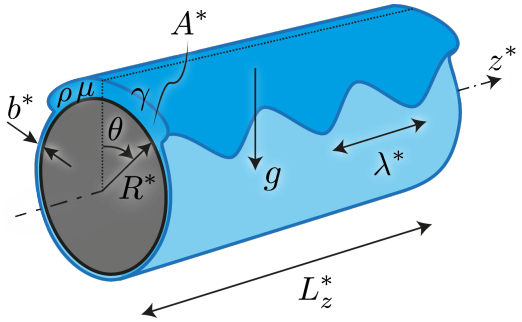

Figure 6.1 – Sketch of the considered problem geometry.

Given the small Reynolds number $Re = g\rho^2 A^{*3/2}/(3\mu^2)$ for this flow, inertial effects can be neglected. Under the long-wavelength approximation (Oron et al., 1997), the Stokes equations in polar coordinates (r^*, θ, z^*) can be integrated over the small characteristic radial direction to obtain, using mass conservation, the lubrication equation for the film thickness $\bar{H}^*(\theta, z^*, t^*)$ (see Chapter 4 for a detailed derivation)

$$\bar{H}^*_{t^*} + \frac{1}{3\mu R^*}\left[\bar{H}^{*3}\left(\underbrace{\frac{\gamma\bar{\kappa}^*_\theta}{R^*}}_{\mathbf{I}} - \underbrace{\frac{\rho g\cos\theta\bar{H}^*_\theta}{R^*}}_{\mathbf{II}} + \underbrace{\rho g\sin\theta}_{\mathbf{III}}\right)\right]_\theta + \frac{1}{3\mu}\left[\bar{H}^{*3}\left(\underbrace{\gamma\bar{\kappa}^*_{z^*}}_{\mathbf{I}} - \underbrace{\rho g\cos\theta\bar{H}^*_{z^*}}_{\mathbf{II}}\right)\right]_{z^*} = 0, \tag{6.1}$$

where γ is the surface tension and $\bar{\kappa}^* = \nabla^*\cdot\mathbf{n}^*$ is the curvature of the interface with normal vector $\mathbf{n}^* = \nabla^* F^*/||\nabla^* F^*||$ and $F^* = r^* - (R^* + \bar{H}^*) = 0$ defines the free surface; subscripts

correspond to partial derivatives. Term **I** corresponds to the capillary pressure gradient, term **II** to the variation of the hydrostatic pressure and term **III** to the drainage. The term $\bar{H}^{*3}$ is the mobility of the liquid and results from the integration of the half-Poiseuille velocity profile in the thin film. The only difference with the lubrication equation for a thin film flowing inside of a cylindrical substrate used in Chapter 4 is the sign of the hydrostatic pressure variation. In the present geometry, the variation of the hydrostatic pressure is stabilizing for $\theta \in [0, \pi/2[$ and destabilizing for $\theta \in]\pi/2, \pi]$. Herein, we focus on the thin film on the upper part of the cylinder, $\theta \in [0, \pi/2]$, where the liquid-air interface is stable with respect to the Rayleigh-Taylor instability. On the lower part of the cylinder, the liquid will accumulate in rivulets, eventually forming dripping droplets (Duffy & Moffatt, 1995; Indeikina et al., 1997; Takagi & Huppert, 2010; Lin et al., 2012; Leslie, Wilson & Duffy, 2013; Paterson, Wilson & Duffy, 2014). The problem being symmetric with respect to $\theta = 0$, only half of the upper part of the cylinder is considered.

If one allows for substrate perturbations $\bar{H}^{o*}$, the free surface is defined by $F^* = r^* - (R^* + \bar{H}^* + \bar{H}^{o*}) = 0$ and the lubrication equation (6.1) can be modified accordingly. As will become clear in Sec. 6.5, we assume small substrate perturbations of order $\varepsilon \ll 1$, $\bar{H}^{o*} = \varepsilon \hat{h}^{o*}$, *i.e.* substrate perturbations much smaller than the draining-film thickness. Within this assumption, the polar component of the drainage term **III** reads, at leading order in δ

$$\rho g \sin\theta - \frac{\rho g \cos\theta \bar{H}^{o*}_{\theta}}{R^*}, \tag{6.2}$$

whereas the drainage in the axial direction is no longer zero, but reads $-\rho g \cos\theta \bar{H}^{o*}_{z^*}$. Also the variation of the hydrostatic pressure in the axial direction is modified by to the substrate topography and the term

$$-\frac{\rho g \sin\theta \bar{H}^* \bar{H}^{o*}_{\theta z^*}}{R^*} \tag{6.3}$$

has to be added. Eventually, the lubrication equation for the film thickness $\bar{H}^*$ over a substrate with small topography perturbations $\bar{H}^{o*}$ reads

$$\begin{aligned} \bar{H}^*_{t^*} + \frac{1}{3\mu R^*}\left\{ \bar{H}^{*3}\left[\frac{\gamma \bar{\kappa}^*_{\theta}}{R^*} - \frac{\rho g \cos\theta (\bar{H}^*_{\theta} + \bar{H}^{o*}_{\theta})}{R^*} + \rho g \sin\theta \right] \right\}_{\theta} \\ + \frac{1}{3\mu}\left\{ \bar{H}^{*3}\left[\gamma \bar{\kappa}^*_{z^*} - \rho g \cos\theta (\bar{H}^*_{z^*} + \bar{H}^{o*}_{z^*}) - \frac{\rho g \sin\theta \bar{H}^* \bar{H}^{o*}_{\theta z^*}}{R^*} \right] \right\}_{z^*} = 0. \end{aligned} \tag{6.4}$$

The capillary pressure gradient term is modified as the curvature depends also on $\bar{H}^{o*}$. Using $L^* = \sqrt{A^*}$ as characteristic length and the drainage time $\tau_d = \mu R^*/(\rho g A^*)$ as characteristic time (Takagi & Huppert, 2010), the lubrication equation can be written in the following

dimensionless form

$$\bar{H}_t+\frac{1}{3}\left\{\bar{H}^3\left[\frac{\delta^2}{Bo}\bar{\kappa}_\theta-\delta\cos\theta(\bar{H}_\theta+\bar{H}^o_\theta)+\sin\theta\right]\right\}_\theta \\ +\frac{1}{3\delta^2}\left\{\bar{H}^3\left[\frac{\delta^2}{Bo}\bar{\kappa}_z-\delta\cos\theta(\bar{H}_z+\bar{H}^o_z)-\delta^2\sin\theta\bar{H}\bar{H}^o_{\theta z}\right]\right\}_z=0. \tag{6.5}$$

The curvature up to the second order in δ is

$$\bar{\kappa}=-\frac{\delta}{\left(\bar{H}_z^2+1\right)^{1/2}}+\frac{\bar{H}_{zz}+\bar{H}^o_{zz}-\bar{H}_z\bar{H}^o_z\bar{H}_{zz}+\bar{H}_z^2\bar{H}^o_{zz}}{\left(\bar{H}_z^2+1\right)^{3/2}} \\ -\delta^2\left[-\frac{\bar{H}+\bar{H}^o}{\left(\bar{H}_z^2+1\right)^{1/2}}-\frac{\bar{H}_{\theta\theta}+\bar{H}^o_{\theta\theta}}{\left(\bar{H}_z^2+1\right)^{1/2}}\right. \\ \left.\frac{(\bar{H}_{zz}+\bar{H}^o_{zz})\bar{H}_\theta^2}{2\left(\bar{H}_z^2+1\right)^{3/2}}-\frac{3\bar{H}_z(\bar{H}_z+\bar{H}^o_z)\bar{H}_{zz}\bar{H}_\theta^2}{2\left(\bar{H}_z^2+1\right)^{5/2}}+\frac{(2\bar{H}_z\bar{H}_\theta+\bar{H}^o_z\bar{H}_\theta+\bar{H}_z\bar{H}^o_\theta)\bar{H}_{\theta z}}{\left(\bar{H}_z^2+1\right)^{3/2}}\right]+O\left(\delta^3\right). \tag{6.6}$$

6.3 Draining base flow

6.3.1 Lubrication equation

The draining base flow H on a smooth cylindrical substrate is assumed to be invariant along the axial direction, which simplifies the lubrication equation (6.5) to

$$H_t+\frac{1}{3}\left\{H^3\left[\underbrace{\frac{\delta^4}{Bo}(H_\theta+H_{\theta\theta\theta})}_{\mathbf{I}}-\underbrace{\delta\cos\theta H_\theta}_{\mathbf{II}}+\underbrace{\sin\theta}_{\mathbf{III}}\right]\right\}_\theta=0. \tag{6.7}$$

The considered initial condition is

$$H_0(\theta)=c_1\{1-\tanh[c_2(\theta-\phi)]\}+b, \tag{6.8}$$

where c_1 is the dimensionless amplitude such that the dimensionless fluid area is unity, $\int_0^{\pi/2}[H_0(\theta)-b]d\theta/\delta=1$, $c_2=15$ sets the initial slope of the front, located for $t=0$ at $\theta=\phi=19°$ and b is the precursor film thickness. As will become clear in Sec. 6.3.4, the base-flow solution at late times does not depend on the initial condition. Note that the fluid in the precursor film is removed in the measure of the volume.

A typical evolution of the base flow in shown in Fig. 6.2 (see Appendix 6.7.2 for details on the numerical method).

The drainage solution given by Eq. (6.7) can be decomposed into an *outer region* where the drainage term **III** dominates and an *inner region* close to the front where the surface tension

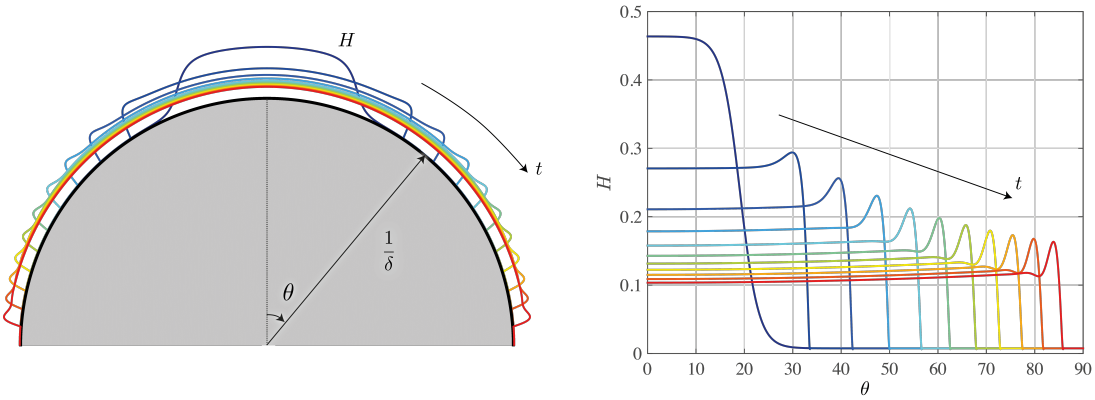

(a) (b)

Figure 6.2 – Base flow temporal evolution for $Bo = 15$ and $\delta = 0.15$. The parameters are taken such as to have the same dimensionless numbers of the experiment of Takagi & Huppert (2010). The film thickness on panel (a) has been magnified by a factor 3 for visualization purposes.

and variation of hydrostatic pressure terms **I** and **II**, respectively, are no longer negligible (Takagi & Huppert, 2010).

6.3.2 Drainage at the pole

Following Takagi & Huppert (2010), the film thickness at the pole $\theta = 0$ evolves as

$$H(\theta = 0, t) = \frac{1}{\sqrt{\frac{1}{e^2} + \frac{2}{3}t}}, \tag{6.9}$$

where $e = H_0(\theta = 0)$ is the initial thickness at the pole. The drainage becomes initial condition independent and follows the universal law $H \sim (2t/3)^{-1/2}$ for large times $t \gg \tau_i = 3/(2e^2)$, as visible in Fig. 6.3(a).

6.3.3 Spatial dependence of the outer region

The spatial variation of the film thickness in the outer region can be found by a regular perturbation expansion as described in Chapter 4. Under the assumption of negligible capillary pressure and hydrostatic pressure contributions, the asymptotic solution for the film thickness up to the fourth order in θ reads

$$\begin{aligned} H(\theta, t) = &\frac{1}{\sqrt{\frac{1}{e^2} + \frac{2}{3}t}} \left\{ 1 + \frac{\theta^2}{16} \left[1 - \frac{1}{\left(\frac{1}{e^2} + \frac{2}{3}t\right)^4} \right] \right. \\ &\left. + \frac{43\theta^4}{10752} \left[1 + \frac{315}{43\left(\frac{1}{e^2} + \frac{2}{3}t\right)^8} - \frac{288}{43\left(\frac{1}{e^2} + \frac{2}{3}t\right)^7} - \frac{70}{43\left(\frac{1}{e^2} + \frac{2}{3}t\right)^4} \right] \right\} + O(\theta^6). \end{aligned} \tag{6.10}$$

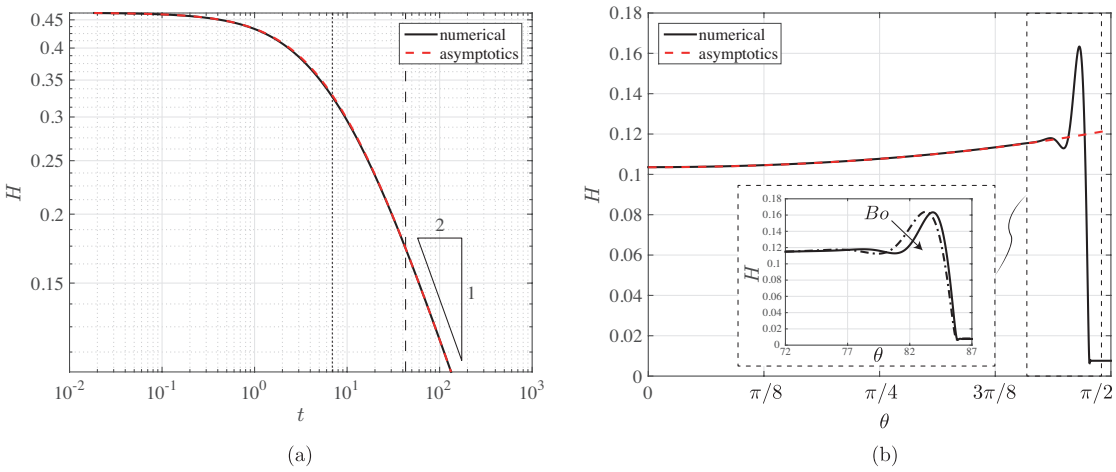

Figure 6.3 – (a) Comparison between the temporal film thickness evolution at the pole $\theta = 0$ obtained numerically (black solid line) and the asymptotic prediction (6.9) (red dashed line). The dotted line indicates the critical initial time $\tau_i = 3/(2e^2)$ and the dashed line the crossover time at which $\ell_c = \ell$. (b) Comparison between the film thickness profile at $t = 133$ obtained numerically (black solid line) and the asymptotic prediction (6.10) (red dashed line). Inset: zoom in the inner region. $Bo = 15$ (and $Bo = 8$ for the dot-dashed line in the inset of panel (b)) and $\delta = 0.15$.

Note that the equivalent expression for the draining flow on a spherical substrate has been proven to be in excellent agreement with experimental measurements by Lee et al. (2016*a*), see Chapter 2. The very good agreement between the numerical solution of the full lubrication equation (6.7) and the asymptotic prediction (6.10) (see Fig. 6.3(b)) clearly indicates that the capillary pressure term and the variation of hydrostatic pressure are negligible in the outer region.

6.3.4 Front position

The viscous liquid spreads on the cylinder as time evolves, following the expression (6.10) in the outer region. Mass conservation imposes

$$\int_0^{\theta_N} [H(\theta, t) - b] d\theta/\delta = 1, \tag{6.11}$$

where the precursor film thickness is removed to avoid an increase in fluid when the ridge advances. Equation (6.11), together with the asymptotic expression for the draining flow H, Eq. (6.10), can be solved to yield an implicit solution for the front position over time $\theta_N(t)$ (see Fig. 6.4). An explicit expression can be found if one assumes that the film has constant thickness $H_N = (2t/3)^{-1/2} \gg b$. Mass conservation yields (Takagi & Huppert, 2010):

$$\theta_N(t) = \frac{\delta}{H_N} \sim \delta\sqrt{\frac{2t}{3}}, \tag{6.12}$$

which is valid for $3/(2e^2) \ll t \ll 3/(2b^2)$. Equation (6.12), which agrees well with the implicit solution obtained by combining Eq. (6.11) together with the spatial dependence of H given by Eq. (6.10) (see Fig. 6.4), evidences the square-root dependence of the front position with time.

Within this limit, the velocity of the front is given by $U_N = d\theta_N/dt/\delta \sim (6t)^{-1/2}$. The drainage slows down, despite the fact it is located on a substrate whose local inclination increases as the ridge travels. This is due to the fact that although the average velocity of the film increases with θ_N as $U_N = Q_N/H_N = \sin\theta_N H_N^2/(3\delta) \approx \theta_N/(2\delta t)$, where Q_N is the drainage flux of Eq. (6.7), the front location varies as $\theta_N \sim t^{1/2}$ so that the film velocity at the front varies as $t^{-1/2}$.

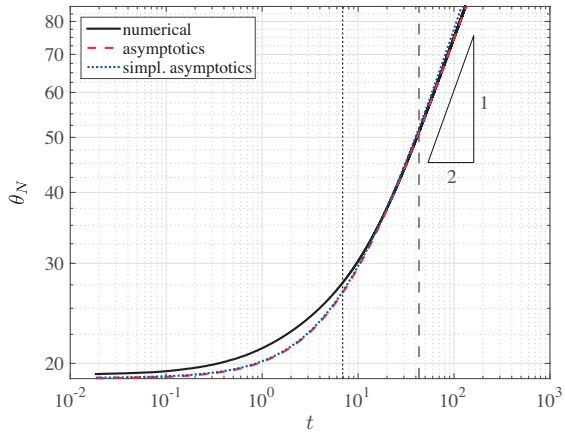

Figure 6.4 – Comparison between the evolution of the front position θ_N obtained numerically (black solid line), asymptotically (red dashed line) and with the explicit asymptotic expression (6.12) (blue dotted line). $Bo = 15$ and $\delta = 0.15$. The black dotted line indicates the critical initial time $\tau_i = 3/(2e^2)$ and the black dashed line the crossover time at which $\ell_c = \ell$.

The implicit and explicit asymptotic estimates for the spreading length θ_N compare well with the result of the numerical solution of Eq. (6.7) (see Fig. 6.4). Note that the front location deduced from the numerical results is arbitrarily chosen to correspond to the location where the film thickness is $H_N = [H(\theta = 0, t) + b]/2$. Furthermore, it has to be stressed that the asymptotic estimates rely only on the conservation of mass for the outer region, neglecting the precise profile in the inner region close to the front. For $t \gg \tau_i$, the initial condition is forgotten and the numerical front position correspond to the asymptotic ones. The late-time dynamics are therefore insensitive to the choice of the initial condition.

6.3.5 Length of the inner region

Surface tension is only relevant in the vicinity of the ridge, where the outer film thickness has to be connected to the precursor film, inducing strong film-thickness variations. In the inner region, the film profile presents a shape very similar to the one found for the other driven films, like the ones on an inclined plane (Spaid & Homsy, 1996) (see inset of Fig. 6.3(b)).

The characteristic length of the ridge is found by balancing the dominant terms in Eq. (6.7). At small angles θ, the drainage term **III** is weak compared to terms **I** and **II** due to the large film-thickness gradients at the front. Hence, the capillary pressure term **I** has to balance the variation of the hydrostatic pressure term **II** and the characteristic length of the inner region is

$$\ell_c = \left(\frac{\delta}{Bo\cos\theta_N}\right)^{1/2}, \tag{6.13}$$

where θ_N is the front location. Note that this is nothing else that the capillary length with the gravity projected on the radial direction. Written in dimensional quantities, it reads $\ell_c^* = \sqrt{\gamma/(\rho g\cos\theta_N)}$ (Bertozzi & Brenner, 1997). ℓ_c is a monotonic increasing function of θ_N, and thus increases with time. For sufficiently large angles, the drainage term **III** overcomes the variation of the hydrostatic pressure term **II** and the film thickness variations at the ridge occurs on a length scale found by balancing the drainage term and the surface tension term, yielding

$$\ell = \left(\frac{\delta H_N}{Bo\sin\theta_N}\right)^{1/3} = \left(\frac{\delta^2}{Bo\theta_N\sin\theta_N}\right)^{1/3}, \tag{6.14}$$

where conservation of mass $H_N\theta_N = \delta$ has been used. For $3/(2e^2) \ll t \ll 3/(2b^2)$, with the use of Eq. (6.12), one obtains $\ell \sim (2Bo\,t/3)^{-1/3}$, indicating that ℓ decreases with time. Equation (6.14) is equivalent to the length of the capillary ridge for a film flowing on an inclined plane, $\ell = H_N/(3Ca)^{1/3}$, when using $Ca = Bo/\delta U_N$ as capillary number, with U_N the velocity at the front, given by $U_N = \sin\theta_N H_N^2/(3\delta)$.

For the parameters considered in the present study, the crossover between the two regimes is found to be at $t \simeq 44$. The first regime corresponds to the relaxation of the film thickness from the initial profile over a relatively flat substrate, whereas the second regime is the well developed gravity-driven ridge regularized by surface tension, where the initial condition is lost and the solution follows the scaling $H_N \sim (2t/3)^{-1/2}$.

The two regimes have been identified also for the flow over an inclined plane depending on the inclination angle (Bertozzi & Brenner, 1997). Bertozzi & Brenner (1997) showed that the bump of the ridge vanishes for small inclination angles due to the component of gravity orthogonal to the substrate. This is also true for the flow over a cylinder, where the bump gains in thickness as the flow evolves downstream. It can be concluded that the length of the ridge always decreases with the Bond number, whereas it increases or decreases with the polar angle, and thus with time, for the first and second regime, respectively, as already observed in Figs. 6.2 and 6.3.

The most important scalings are summarized in Table 6.1. The good agreement between the asymptotic estimate for the film thickness H given by Eq. (6.10), which is independent on the Bond number, is only valid for the weak surface tension limit, when the Bond number is

	General $\forall\, t$	Approximated for $3/(2e^2) \ll t \ll 3/(2b^2)$
H	$\left(\frac{1}{e}+\frac{2}{3}t\right)^{-1/2}$	$\left(\frac{2}{3}t\right)^{-1/2}$
ℓ	$\left(\frac{Bo\,\theta_N \sin\theta_N}{\delta^2}\right)^{-1/3}$	$\left(\frac{2}{3}Bo\,t\right)^{-1/3}$
θ_N	$\int_0^{\theta_N}(H-b)d\theta=\delta$	$\delta\left(\frac{2}{3}t\right)^{1/2}$
U_N	$\frac{1}{3\delta}H_N^2\sin\theta_N$	$(6t)^{-1/2}$

Table 6.1 – Summary of main scalings for the film thickness at the pole H, the capillary ridge length ℓ, the front location θ_N and its velocity U_N; the general expressions valid for any time and their simplified forms for $3/(2e^2) \ll t \ll 3/(2b^2)$ are specified.

sufficiently large. For very large Bond numbers, Ancey, Cochard & Andreini (2009) showed that if surface tension is negligible everywhere, a very steep nose forms at the front. Otherwise, the capillary forces will impact also the film thickness far from the ridge and the outer solution is no longer valid. Following Takagi & Huppert (2010), the present theory holds as long as $\theta_N \gg Bo^{-1/5}\delta$, which is the case for the considered parameters.

Furthermore, the precursor film thickness has to be $b \ll e$ to avoid a non-negligible addition of mass when the ridge advances on the precursor film. In this work, we have set $b = 8\times10^{-3}$, two orders of magnitude smaller than e. With this value of b, the upper time limit for the theory to hold is $3/(2b^2) \gg t_f$, where $t_f = 133$ is the time at which the ridge reaches $\theta = \pi/2$ with the considered parameters. It has to be pointed out, however, that the precise film thickness profile of the inner region is dependent on the exact value of the precursor film (Bertozzi & Brenner, 1997). The height of the ridge is a weak (logarithmic) function of b (Troian et al., 1989; Tuck & Schwartz, 1990). The smaller the precursor film thickness, the higher the bump and thus the stronger the growth of the perturbations. Yet, the selection of the most unstable spanwise wavenumber is not affected (Spaid & Homsy, 1996).

6.4 Optimal film thickness initial conditions over a smooth substrate

An optimal transient growth analysis is employed hereafter to find the optimal initial conditions for the film-thickness perturbations over a smooth substrate, $\bar{H}^o = 0$.

6.4.1 Film-thickness decomposition

The numerically obtained one-dimensional draining flow discussed in Sec. 6.3 is asymptotically linearly stable for $\theta \in [0, \pi/2]$ and can be considered as the base state for the linear

stability analysis. The film thickness is decomposed into this *drainage solution* $H(\theta,t)$ and small *perturbations* $\varepsilon\hat{h}(\theta,t)$, with $\varepsilon \ll 1$ (see Fig. 6.5):

$$\bar{H}(\theta,z,t) = \underbrace{H(\theta,t)}_{\text{drainage solution}} + \underbrace{\varepsilon\hat{h}(\theta,z,t)}_{\text{perturbation}}, \quad \varepsilon \ll 1 \tag{6.15}$$

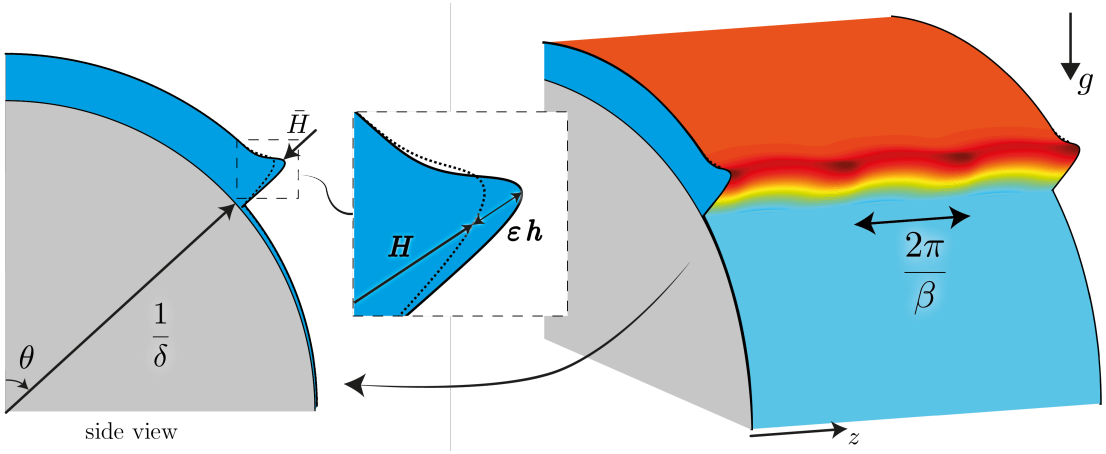

Figure 6.5 – Decomposition of the total film thickness $\bar{H}$ (solid line) into draining solution H (dotted line) and first-order perturbations $\varepsilon h\cos(\beta z)$ for the optimal transient growth of initial conditions h_0 over a smooth substrate. The spanwise perturbations with wavenumber β are shown in the three-dimensional sketch. $\theta \in [0,\pi/2]$ and $z \in [0, 3\times 2\pi/\beta]$.

Furthermore, we assume the perturbations to be periodic in the transverse direction so that the we can proceed to a normal mode expansion in the z-direction

$$\hat{h}(\theta,z,t) = h(\theta,t)\exp(\mathrm{i}\beta z) + c.c., \tag{6.16}$$

where $\beta \in \mathbb{R}$ is the spanwise wavenumber. The one-dimensional perturbations $h(\theta,t)$ have to be optimized for a given spanwise wavenumber β.

6.4.2 Linear disturbance equation

The linear disturbance equation governing the dynamics of the first order perturbations $h(\theta,t)$ is found by entering the decomposition (6.15) together with Eq. (6.16) into the nonlinear lubrication equation (6.5), assuming $\bar{H}^o = 0$, and considering terms of order ε:

$$\mathbf{h}_t + \mathbf{L}(H,\beta,Bo,\delta)\mathbf{h} = \mathbf{0}, \tag{6.17}$$

where the linear operator $\mathbf{L}(H,\beta,Bo,\delta)$ is a function of the drainage solution, the spanwise wavenumber, the Bond number and the film aspect ratio (see Appendix 6.7.1 for its expression).

6.4.3 Optimization method

Due to the polar and temporal dependences in the linear operator through the base state H, the classical normal mode ansatz for h cannot be employed and a nonmodal analysis is necessary (Schmid, 2007). Given the transient dynamics of the draining flow, a nonmodal transient growth approach is natural as one seeks the largest amplification of perturbations at finite times T, and not in the limit $t \to \infty$. Furthermore, Bertozzi & Brenner (1997) have shown that in spite of the linear stability of a flow over an inclined plane at low inclination angles, a transient growth can always occur. Given the base flow drainage on a substrate whose inclination increases in space, the employed procedure is therefore suitable.

The algorithm for the optimal transient growth for the optimal initial conditions is based on the one described in Chapter 3, and only the main steps are presented hereafter.

The energy of the film-thickness perturbations can be defined as (Spaid & Homsy, 1996; Olsson & Henningson, 1995)

$$E(t) = \frac{1}{2}\int_\Omega \mathbf{h}(t)^T \mathbf{h}(t) d\theta = \frac{1}{2}\langle \mathbf{h}(t)|\mathbf{h}(t)\rangle, \tag{6.18}$$

where the scalar product for real quantities $\mathbf{a}$ and $\mathbf{b}$ on the geometry $\Omega = \{\theta \,|\, \theta \in [0, \pi/2]\}$ is given by

$$\langle \mathbf{a}|\mathbf{b}\rangle = \int_\Omega \mathbf{a}^T \mathbf{b}\, d\theta = \mathbf{a}^T \mathbf{M}\mathbf{b}. \tag{6.19}$$

The mass matrix with uniform weights is defined as

$$\mathbf{M} = \frac{\pi}{2N}\mathbf{I}, \tag{6.20}$$

where N is the number of discretization points and $\mathbf{I}$ is the identity matrix.

The gain of the film-thickness perturbations to be optimized for a given time horizon T is defined by the ratio of the actual disturbance energy $E(T)$ and its initial value $E(0) = \langle \mathbf{h}_0|\mathbf{h}_0\rangle/2$, where $\mathbf{h}_0 = \mathbf{h}(0)$ is the initial condition of the perturbation:

$$G(T) = \frac{E(T)}{E(0)} = \frac{\langle \mathbf{h}(T)|\mathbf{h}(T)\rangle}{\langle \mathbf{h}_0|\mathbf{h}_0\rangle}. \tag{6.21}$$

The optimal growth analysis is based on the augmented Lagrangian, consisting of the objective function to be optimized, *i.e.* the gain, and the constraints, namely the governing equation (6.17) and the initial condition. The constraints are enforced via the Lagrange multipliers $\mathbf{h}^\dagger$ and $\mathbf{h}_0^\dagger$, respectively.

$$\mathscr{L}\left(\mathbf{h}, \mathbf{h}^\dagger, \mathbf{h}_0, \mathbf{h}_0^\dagger; T\right) = \underbrace{G(T)}_{\text{gain}} - \underbrace{\int_0^T \langle \mathbf{h}^\dagger \left| \mathbf{h}_t + \mathbf{L}\mathbf{h}\right\rangle \mathrm{d}t}_{\text{enforcing governing equation}} - \underbrace{\langle \mathbf{h}_0^\dagger \left| \mathbf{h}(0) - \mathbf{h}_0\right\rangle}_{\text{enforcing initial condition}}. \tag{6.22}$$

The Lagrange multipliers $\mathbf{h}^\dagger$ and $\mathbf{h}_0^\dagger$ depend on space and on time, for $\mathbf{h}^\dagger$. They are given by the adjoint equations, which are obtained by taking the Fréchet derivatives of the augmented Lagrangian with respect to $\mathbf{h}$ and $\mathbf{h}_0$, respectively (Cossu, 2014) (see Chapter 3 for a detailed derivation):

$$\langle \frac{\partial \mathscr{L}}{\partial \mathbf{h}} \Big| \delta\mathbf{h} \rangle = 0\,,\ \forall\, \delta\mathbf{h} \Leftrightarrow \mathbf{h}^\dagger(T) = 2\frac{\mathbf{h}(T)}{\langle \mathbf{h}_0 | \mathbf{h}_0 \rangle}\,, \tag{6.23}$$

$$\mathbf{h}_t^\dagger - \mathbf{L}^\dagger \mathbf{h}^\dagger = \mathbf{0} \quad t \in [0, T]\,, \tag{6.24}$$

$$\mathbf{h}_0^\dagger = \mathbf{h}^\dagger(0)\,, \tag{6.25}$$

and

$$\langle \frac{\partial \mathscr{L}}{\partial \mathbf{h}_0} \Big| \delta\mathbf{h}_0 \rangle = 0\,,\ \forall\, \delta\mathbf{h}_0 \Leftrightarrow \mathbf{h}_0 = \mathbf{h}_0^\dagger \frac{\langle \mathbf{h}_0 | \mathbf{h}_0 \rangle^2}{2\,\langle \mathbf{h}(T) | \mathbf{h}(T) \rangle}\,. \tag{6.26}$$

In order to find the optimal initial condition, one starts with an arbitrary initial condition $\mathbf{h}_0$ and integrates the direct problem (6.17) forward in time from $t = 0$ to the chose time horizon $t = T$ (see Appendix 6.7.2 for details on the numerical method). The adjoint equation (6.24) is then integrated backward in time, starting from the condition (6.23) at $t = T$ and using the adjoint operator $\mathbf{L}^\dagger = \mathbf{L}^T$. The latter satisfies the property $\langle \mathbf{a} | \mathbf{L}\mathbf{b} \rangle = \langle \mathbf{L}^\dagger \mathbf{a} | \mathbf{b} \rangle$. The Lagrange multiplier $\mathbf{h}_0^\dagger$ is given by Eq. (6.25), and the new guess for the optimal initial condition is given by Eq. (6.26). This algorithm (see Fig. 6.6) is repeated until the gain $G(T)$ converges, eventually yielding the optimal initial condition and the optimal gain for a particular time horizon T, spanwise wavenumber β, Bond number Bo and film aspect ratio δ. By repeating the same

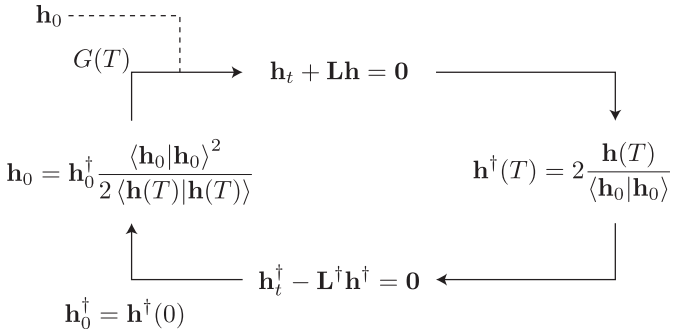

Figure 6.6 – Sketch of the iterative procedure to find the optimal gain and initial condition for a given time horizon T, spanwise wavenumber β, Bond number Bo and film aspect ratio δ.

procedure for successive time horizons T, the envelope of the optimal gains for the selected parameters can be found.

6.4.4 Results

Influence of the time horizon

As can be seen in Fig. 6.7(a), we have found that the optimal initial film perturbation profile at short time horizons mainly consists in a localized perturbation close to the region reached by the ridge of the draining flow at $t = T$, whereas it presents a significant wide-bump perturbation over the entire region swept by the draining-flow ridge for large time horizons. In

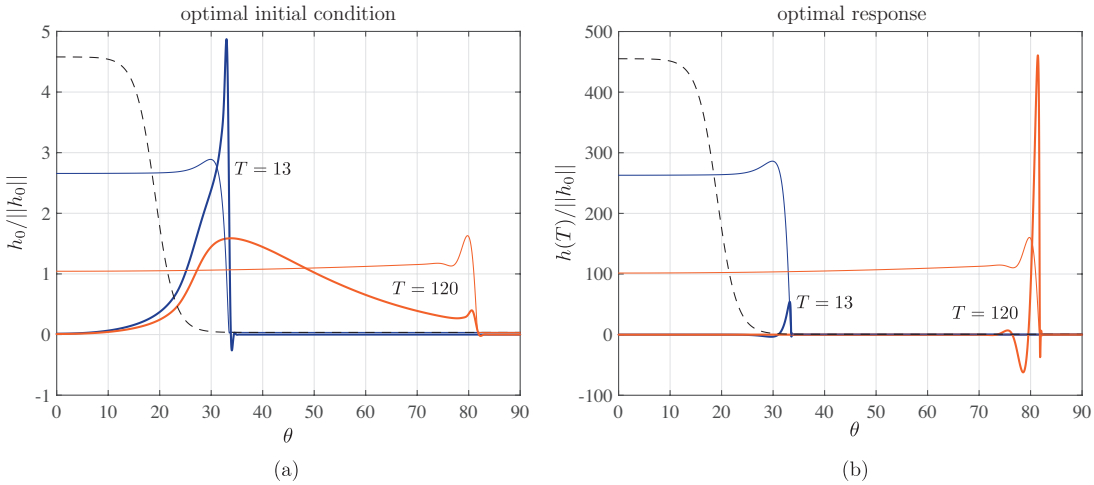

Figure 6.7 – Optimal initial conditions h_0 (a) and optimal responses $h(T)$ (b) for the time horizons $T = 13$ and 120 (thick solid lines), normalized by the initial L_2-norm of the perturbation $||h_0||$. The thin solid lines indicate the base flow profile H at the times T and the black dashed line are the base flow at $t = 0$ (in arbitrary units). $\beta = 2$.

agreement with the sensitivity of the instability on the detail of the ridge, and thus on the details of the perturbations at the virtual contact line (Bertozzi & Brenner, 1997), the optimal perturbations are found to be mainly located in the precursor-film region and not in the thick outer region of the draining flow (see Sec. 6.3). Note that given the very small thickness of the precursor film, the mobility of the perturbations, given by the term $\bar{H}^3$ in Eq. (6.5), is almost none. The perturbations become mobile only when the base flow front reaches their location.

The optimal responses are, on the other hand, located in the inner region of the draining flow (see Fig. 6.7(b)). Despite the fact that their structure is very similar to the dominant eigenfunction for the flow over an inclined plane (Spaid & Homsy, 1996), the precise profile of the response changes with time due to the space-dependent forces at play.

For the sake of clarity, we present in Fig. 6.8 the evolution of the total film thickness, *i.e.* the base draining flow H plus the disturbance field h given by the optimal initial condition h_0 scaled by an arbitrary $\varepsilon = 10^{-3}$. The perturbations induce an increase/decrease in film thickness at the front (see for instance the total profile at $t = 66$), sinusoidally modulated in the spanwise direction with a wavenumber β, see Eq. (6.16). If nonlinear effects were considered, thicker regions would eventually flow faster than the thinner ones and fingers would form.

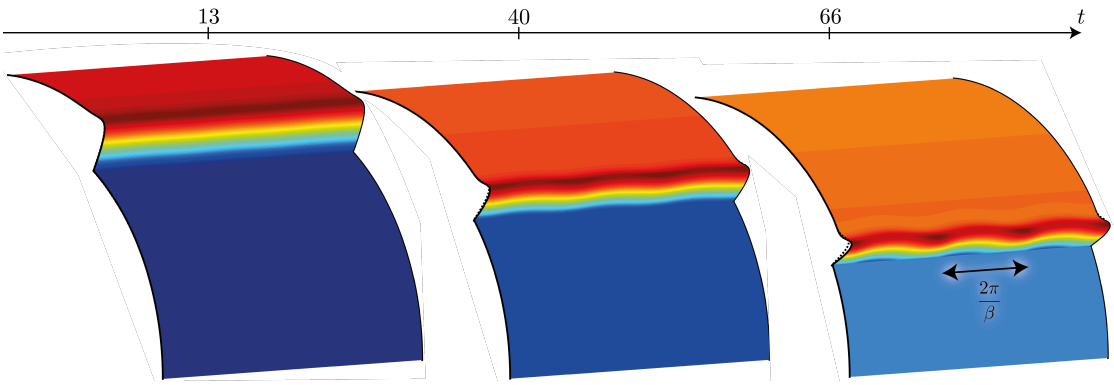

Figure 6.8 – Evolution of the total film thickness $\bar{H} = H + \varepsilon h$ starting from the optimal initial condition h_0 for $T = 120$ at the times $t = 13$, 40 and 66. The dashed lines indicate the base flow profile H at the selected times. $\beta = 2$. The perturbations are rescaled by the maximum of the initial condition h_0 for visualization purposes and $\varepsilon = 10^{-3}$.

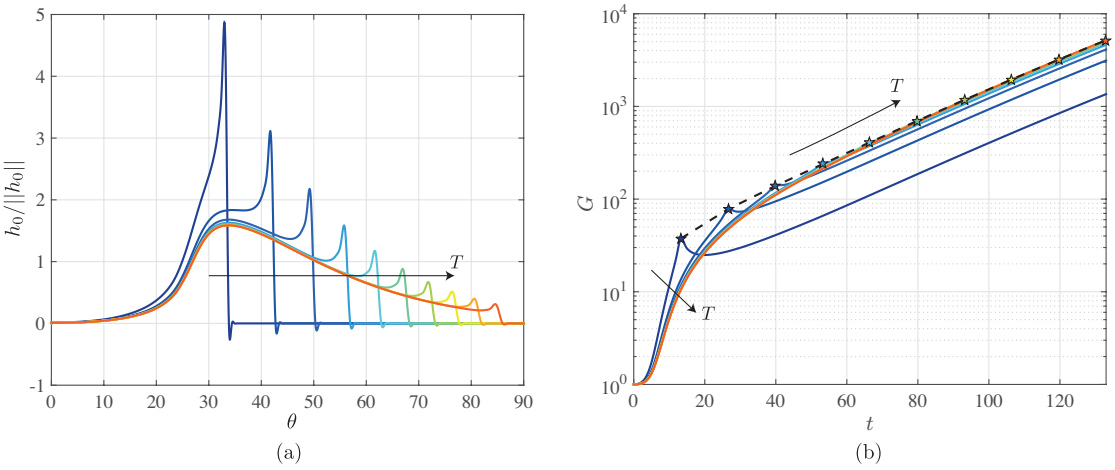

Figure 6.9 – Optimal initial conditions h_0, normalized by the initial L_2-norm of the perturbation $||h_0||$ (a) and gain G (b) for the time horizons $T = 13$, 27, 40, 53, 66, 80, 93, 106, 120 and 133. The stars indicate the optimal gains $G_{\max} = G(T)$. The black dashed line corresponds to the envelope of the gains $G_{\max}$. $\beta = 2$.

When looking at the gain evolutions for several optimal initial conditions, it can be observed that the gain increases with time also after the time horizon T (see Fig. 6.9). The rationale for this is the fact that the ridge continues advancing and remains locally unstable (Huerre & Rossi, 1998) for the considered wavenumber. Furthermore, the time dependent slope of the gain evolution, which would correspond to an instantaneous growth rate, indicates that the problem is not stationary and an eigenvalue decomposition cannot be employed. A flow on an inclined plane would develop an exponentially growing instability at the front (Spaid & Homsy, 1996).

The structure of the optimal initial conditions progressively changes from a localized per-

turbation at the front for small T to a wide-bump perturbation for large T (see Fig. 6.9(a)). In contrast to the optimal initial perturbations at short times, the wide-bump structure of the optimal perturbations for large time horizons induces a large gain over a longer time interval. In fact, the ridge of the draining flow is continuously perturbed by the initial optimal disturbance located in the precursor film over a wide polar range. Thereby, the optimal perturbation for large time horizons is less specific to a precise time. Furthermore, the optimal initial conditions for large time horizons become more and more similar, sharing the same wide-bump structure, with the thickest region at the same polar angle.

By interpolating the optimal gains $G_{\max} = G(T)$ one can define the envelope of the optimal gains. Due to the previous observation, the envelope coincides with the evolutions of the gains for the late times horizons.

Optimal spanwise wavenumber

Thus far the spanwise wavenumber $\beta = 2$ has been considered. As seen in Fig. 6.10, most of the optimal initial conditions for different spanwise wavenumber β however also present a localized perturbation for small T and a wide-bump perturbation for large time horizons.

The maximum of the wide-bump perturbation is located at a polar location which increases with β (see stars in Fig. 6.10). This dependence can be understood by recalling that the characteristic length of the ridge, ℓ, given by Eq. (6.14), decreases as θ_N increases (see Table 6.1). Furthermore, the linear stability analysis for the flow over an inclined plane (Troian et al., 1989; Spaid & Homsy, 1996) shows that the most amplified wavenumber is inversely proportional to ℓ. Therefore, larger wavenumbers β require larger inclinations θ_N to be effective. When the wavenumber is large, a localized perturbation at the front location is optimal for small time horizons T, *i.e.* for small polar angles. There, perturbing a larger region, which penalizes the gain, is not effective.

In view of the dependence of the wide-bump location as a function of the spanwise wavenumber and the different gain evolution induced by the localized and wide-bump perturbations (see Fig. 6.9), the achievable gain also depends on the spanwise wavenumber β (see Fig. 6.11). We have found that for small and large β, typically $\beta < 2$ and $\beta > 7$, for which the wide-bump perturbation is never optimal in the range $\theta \in [0, \pi/2]$ and the localized initial condition dominates, the gain evolutions present a clear peak for times close to the time horizons. Conversely, when the optimal initial conditions present a similar wide-bump structure, their gain evolutions are closer, and reach much larger values.

The spanwise-wavenumber dependence of the gain is clearly visible in Fig. 6.12, where all the computed gain envelopes are shown. The gain at the smallest considered time horizon increases monotonically with β for $0 < \beta \leq 10$, but its value remains small. On the contrary, the gain for large time horizons is not monotonic with β, indicating that an optimal β exists. Strikingly, we have found that the optimal initial condition which is the least affected by the

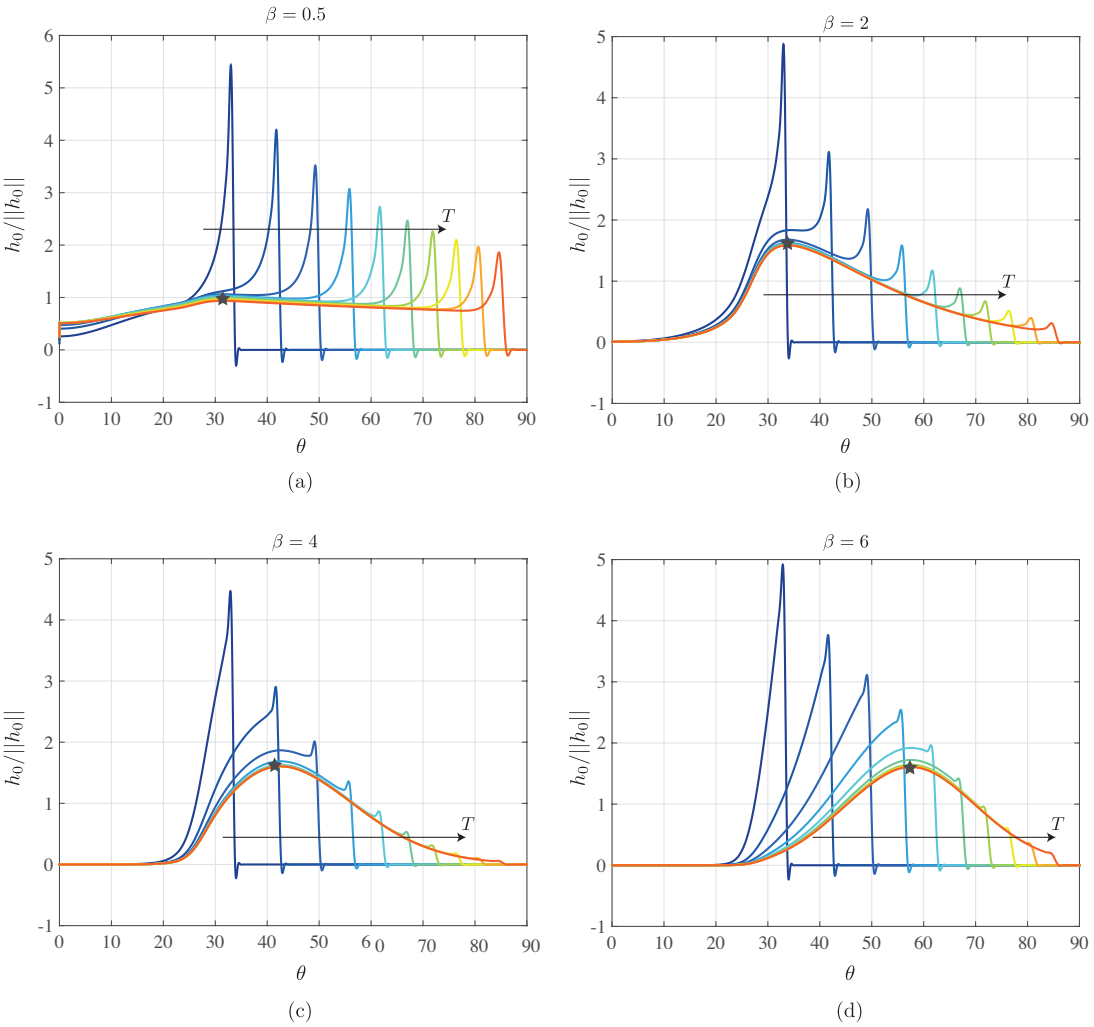

Figure 6.10 – Optimal initial conditions h_0, normalized by the initial L_2-norm of the perturbation $||h_0||$, for the time horizons $T = 13$, 27, 40, 53, 66, 80, 93, 106, 120 and 133 for $\beta = 0.5$, 2, 4 and 6. The stars indicate the thickest location of the wide-bump perturbation.

time horizon, and thus is the most universal (see for example Fig. 6.10(c) and Fig. 6.11(c)), yields the largest gain at large times.

The different behaviors of the optimal spanwise wavenumber with respect to time (see symbols in Fig. 6.12) can be qualitatively rationalized using again the dependence of the optimal wavenumber on the characteristic size of the ridge, $\beta = c/\ell$, obtained by the linear stability analysis for the flow over an inclined plane. The precise value of the proportionality coefficient c depends on the model for the moving contact line (Spaid & Homsy, 1996). However, its value is found to be always around 0.5 (Troian et al., 1989; Spaid & Homsy, 1996). At short times, typically $t \lesssim 40$, the optimal wavenumber found by the optimal transient growth analysis decreases with time, from $\beta = 10$ to 3.5. During this time, the base flow strongly evolves from the particular initial condition to the well developed draining flow (see for

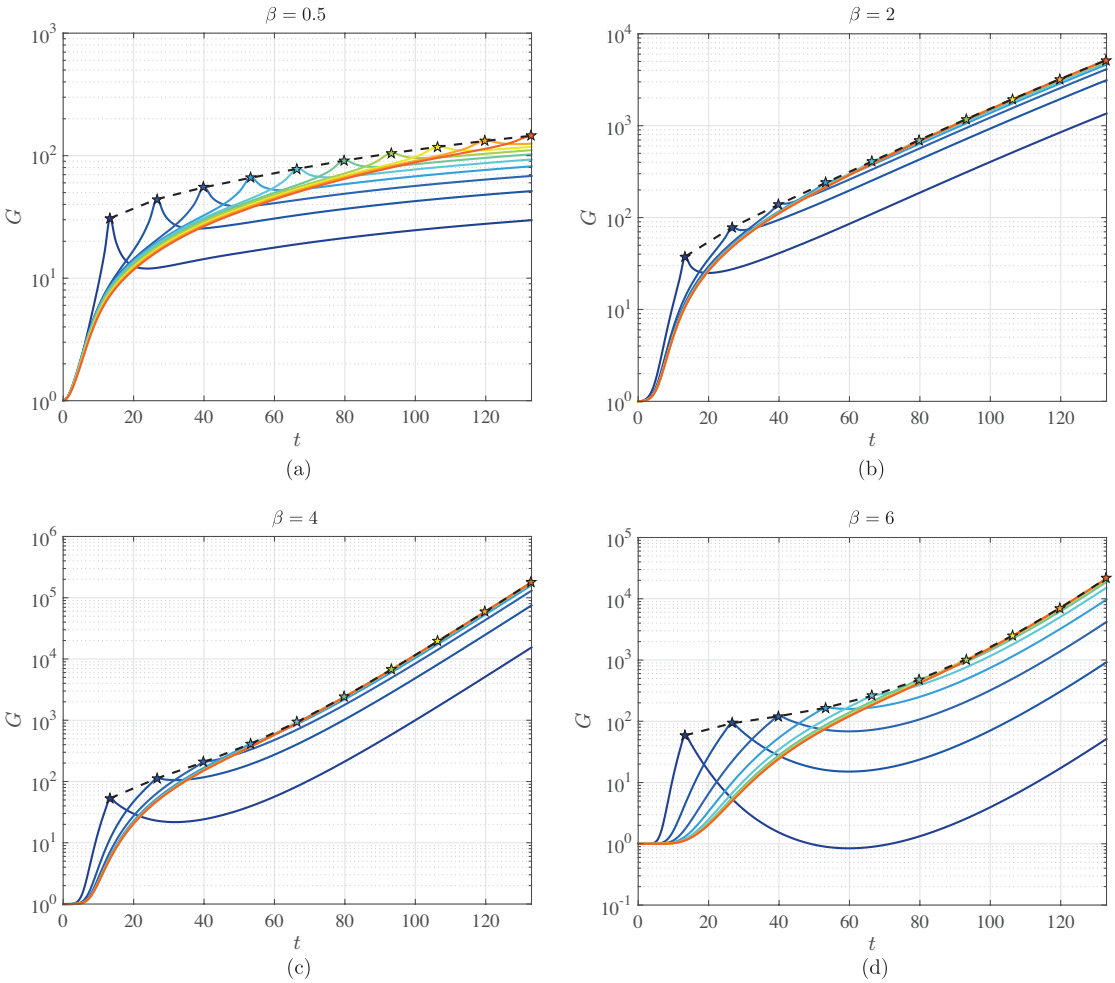

Figure 6.11 – Gain G for the time horizons $T = 13$, 27, 40, 53, 66, 80, 93, 106, 120 and 133 for $\beta = 0.5$, 2, 4 and 6. The stars indicate the optimal gains $G_{\max} = G(T)$. The black dashed lines correspond to the envelope of the gains $G_{\max}$.

instance Fig. 6.4), and the characteristic length of the ridge is ℓ_c, given by Eq. (6.13). Since ℓ_c increases with time, the optimal wavenumber $\beta = 0.5/\ell_c$ decreases (see dashed line in Fig. 6.12). However, for $t \gtrsim 40$, the base drainage solution reaches the well developed state where the characteristic length of the ridge is given by ℓ, Eq. (6.14). The optimal wavenumber $\beta = 0.5/\ell$ increases with time since ℓ decreases (see solid line in Fig. 6.12). For the late time limit, $t \gg \tau_i$, $\beta \sim 0.5(2Bo\,t/3)^{1/3}$ (see Table 6.1). The crossover time for the ridge length from ℓ_c to ℓ was found to be 44, in agreement with the change in regime for the optimal wavenumber β.

However, the precise value for the optimal wavenumber found by the optimal transient growth for large times is smaller than the one predicted by the local inclined-plane theory (see solid line in Fig. 6.12). The reason is the transient behavior of the draining flow. In fact, the instability inherits from the past history, and thus from the growth in a region with a smaller

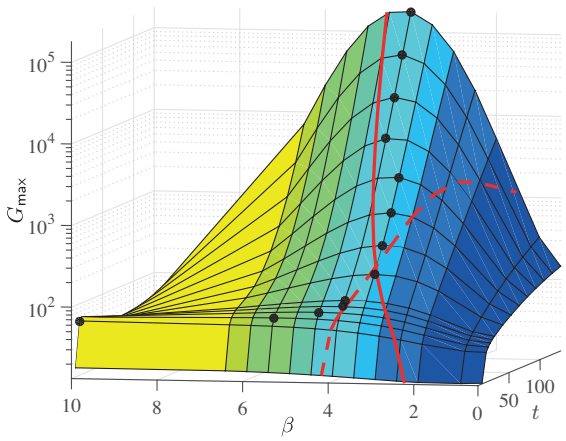

Figure 6.12 – Envelopes $G_{max}(\beta, t)$ for the gain evolutions for $\beta = 0.5$, 1, 2, 2.5, 3, 3.5, 4, 4.5, 5, 5.5, 6, 6.5 and 10. The largest optimal gains obtained by the transient growth analysis, and the corresponding optimal wavenumbers β, at every considered time, are indicated by the black symbols. The optimal wavenumber given by inclined-plane theory with $\beta = 0.5/\ell_c$ (red dashed line) and $\beta = 0.5/\ell$ (red solid line) are also represented.

inclination, promoting smaller wavenumbers. Hence, the linear stability analysis of the flow over an inclined plane cannot be used to quantitatively predict the most amplified wavelength. Furthermore, the latter theory fails at quantitatively predicting the optimal wavelength at very short times, where the transient dynamics is essential. Thus, a transient growth analysis as the one performed in this work is crucial to predict the optimal spanwise wavenumber for all times as well as the optimal gains.

In their experiment, Takagi & Huppert (2010) observed the formation of fingers between $t^* = 0.7\,\mathrm{s}$ and $t^* = 1.5\,\mathrm{s}$ with a wavelength of about 5 cm. Given their cross-sectional area of fluid $A^* = 5.2\,\mathrm{cm}^2$, kinematic viscosity $\nu = 5.1\,\mathrm{cm}^2\mathrm{s}^{-1}$ and cylinder of radius $R^* = 15\,\mathrm{cm}$, the characteristic length is $L^* = \sqrt{A^*} = 2.3\,\mathrm{cm}$ and the characteristic time is $\tau_d = 0.015\,\mathrm{s}$. The dimensionless fingers-formation time is between $t = 47 - 100$, which corresponds to an optimal wavenumber between $\beta = 3.5 - 4$ (see Fig. 6.12). Thus, our analysis predicts a fingering wavelength in the range $3.6 - 4.1\,\mathrm{cm}$. Considering the different initial conditions and the finite length of the cylinder used in their experiment, which imposes a strong lateral confinement and results in the formation of two fingers only, the agreement is satisfactory.

The physical outcome of this section is that, depending on the amplitude of the film perturbations, a different spanwise wavenumber will be selected. If the perturbations are strong, a small gain will be sufficient and fingers with a large wavenumber will form at short times. Nevertheless, since the differences in gains at short times are not significant, the distribution of promoted wavelengths is larger, as already observed by Silvi & Dussan V (1985) for low plate-inclination angles. On the other hand, if the perturbation amplitude is small, a large amplification will be necessary and fingers will only form at late times with a smaller wavenumber.

To conclude, from the optimization of the initial conditions over a smooth surface we have learned that an optimal wavenumber exists and that, for late times, it corresponds to the least time-dependent optimal initial conditions, allowing for an optimal growth over a longer time. Note that at later times, $t > t_f = 133$, the ridge is on the lower part of the cylinder and is asymptotically unstable to the Rayleigh-Taylor instability (Indeikina et al., 1997; Takagi & Huppert, 2010).

The perturbation in the thin-film region being stationary, one is tempted to ask the question whether or not the perturbation of the precursor film thickness can be also attributed to a perturbation in the substrate. This is the subject of Sec. 6.5.

6.5 Optimal substrate perturbations for an initially unperturbed film

6.5.1 Free-surface-elevation decomposition

When the substrate is perturbed, *i.e.* $\bar{H}^o \neq 0$, the free surface of the film is located at a distance $\bar{H}+\bar{H}^o$ from the originally smooth cylindrical substrate. As announced in Sec. 6.2, we consider only small substrate perturbations of order $\varepsilon \ll 1$: $\bar{H}^o = \varepsilon \hat{h}^o$, so that the base state drainage solution H discussed in Sec. 6.3 remains unaffected. The substrate perturbations are assumed to be time independent. Hence, the elevation of the film free surface can be decomposed as (see Fig. 6.13)

$$\bar{H}(\theta,z,t)+\bar{H}^o(\theta,z) = \underbrace{H(\theta,t)}_{\text{drainage solution}} + \varepsilon \left[\underbrace{\hat{h}(\theta,z,t)}_{\text{film perturbation}} + \underbrace{\hat{h}^o(\theta,z)}_{\text{substrate perturbation}} \right] , \quad \varepsilon \ll 1. \quad (6.27)$$

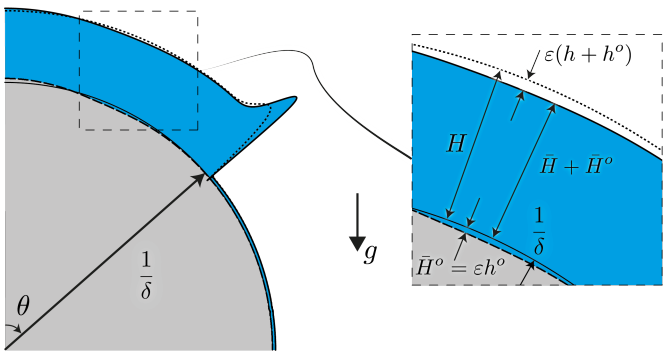

Figure 6.13 – Decomposition of the free-surface elevation $\bar{H}+\bar{H}^o$ starting from the smooth cylindrical substrate into draining solution H and first-order perturbations $\varepsilon(h+h^o)$ for the optimal transient growth over a perturbed substrate with an initially uniform film. It is important to stress that the liquid thickness is only $\bar{H} = H+\varepsilon h$, whereas $\bar{H}^o = \varepsilon h^o$ is the substrate-topography perturbation. The axial dependence as in Fig. 6.5 is not repeated here.

As for the study of the optimal initial conditions of Sec. 6.4, given the invariance of the base state in the z-direction, we consider periodic perturbations in the transverse direction:

$$\hat{h}(\theta, z, t) = h(\theta, t)\exp(\mathrm{i}\beta z) + c.c., \tag{6.28}$$

$$\hat{h}^o(\theta, z) = h^o(\theta)\exp(\mathrm{i}\beta z) + c.c., \tag{6.29}$$

where $\beta \in \mathbb{R}$ is the spanwise wavenumber. Please do not confuse h_0, the initial condition of the perturbation, with h^o the substrate profile. The one-dimensional perturbations $h^o(\theta)$ have to be optimized for a given spanwise wavenumber β.

6.5.2 Linear disturbance equation

The governing equation for the first order disturbances is obtained by entering the film-thickness decomposition (6.27) together with Eqs. (6.28) and (6.29) into the nonlinear lubrication equation (6.5) and considering terms at order ε:

$$\mathbf{h}_t + \mathbf{L}(H, \beta, Bo, \delta)\mathbf{h} = -\mathbf{L}^o(H, \beta, Bo, \delta)\mathbf{h}^o. \tag{6.30}$$

The linear operators $\mathbf{L}(H, \beta, Bo, \delta)$, which is the same as in Sec. 6.4, and $\mathbf{L}^o(H, \beta, Bo, \delta)$ are a function of the drainage solution, the spanwise wavenumber, the Bond number and the film aspect ratio (see Appendix 6.7.1 for their expressions). Thus, the linear operators are space dependent and not autonomous.

As expected, the perturbation of the substrate results in the apparition of a time-dependent – through $H(\theta, t)$ – forcing term: $\mathbf{L}^o(H, \beta, Bo, \delta)\mathbf{h}^o$. Note that a change of variable in order to homogenize equation (6.30), making the optimal substrate and the optimal initial condition problems mathematically similar (the state variable being only the difference $\mathbf{h} - \mathbf{h}^o$) was found not to be possible due to the time dependency of the forcing term.

6.5.3 Optimization method

We will now derive the equations leading to the optimization algorithm for the substrate-topography perturbations. The gain to be optimized at a time horizon T is defined as the ratio of the film disturbance energy $E(T)$ and the substrate disturbance energy $E^o = \langle \mathbf{h}^o | \mathbf{h}^o \rangle / 2$:

$$G(T) = \frac{E(T)}{E^o} = \frac{\langle \mathbf{h}(T) | \mathbf{h}(T) \rangle}{\langle \mathbf{h}^o | \mathbf{h}^o \rangle}. \tag{6.31}$$

In order to guarantee the convergence of the optimization algorithm with the cost function chosen as (6.31), it is primordial to have $\langle \mathbf{h}(T) | \mathbf{h}(T) \rangle = 0$ if $\langle \mathbf{h}^o | \mathbf{h}^o \rangle = 0$, resulting in $G(0) = 0$. Otherwise, the algorithm will bring $\mathbf{h}^o$ to zero naturally, leading to an infinite gain as soon as $\mathbf{h}(T)$ is a nonzero number (which is the case if $\mathbf{h}_0 \neq \mathbf{0}$). A pragmatic way to satisfy this condition is to set the initial condition on the perturbation to zero: $\mathbf{h}_0 = \mathbf{0}$, so that perturbing

the substrate – the forcing term in the state equation (6.30) – is the only way to perturb the base flow. This choice also has a practical relevance since it is sufficient to let the base flow evolve on the substrate, without having to experimentally impose an initial condition for the perturbation.

The augmented Lagrangian reads

$$\mathscr{L}\left(\mathbf{h},\mathbf{h}^\dagger,\mathbf{h}^o;T\right)=\underbrace{G(T)}_{\text{gain}}-\underbrace{\int_0^T\langle\mathbf{h}^\dagger\left|\mathbf{h}_t+\mathbf{L}\mathbf{h}+\mathbf{L}^o\mathbf{h}^o\right\rangle\mathrm{d}t}_{\text{enforcing governing equation}}. \tag{6.32}$$

By proceeding in the same manner as for the derivation of the algorithm for the optimal initial condition of Sec. 6.4.3, the adjoint equations for the Lagrange multiplier $\mathbf{h}^\dagger$ are given by setting to zero the first variations of $\mathscr{L}$ with respect to any variation $\delta\mathbf{h}$:

$$\langle\frac{\partial\mathscr{L}}{\partial\mathbf{h}}\Big|\delta\mathbf{h}\rangle=0\,,\ \forall\,\delta\mathbf{h}\Leftrightarrow\mathbf{h}^\dagger(T)=2\frac{\mathbf{h}(T)}{\langle\mathbf{h}^o|\mathbf{h}^o\rangle}\,, \tag{6.33}$$

$$\mathbf{h}_t^\dagger-\mathbf{L}^\dagger\mathbf{h}^\dagger=\mathbf{0}\quad t\in[0,T]\,. \tag{6.34}$$

The optimality condition for the substrate perturbation is obtained by imposing a zero Fréchet derivative of $\mathscr{L}$ with respect to $\mathbf{h}^o$ (see derivation in Appendix 6.7.3):

$$\langle\frac{\partial\mathscr{L}}{\partial\mathbf{h}^o}\Big|\delta\mathbf{h}^o\rangle=0\,,\ \forall\,\delta\mathbf{h}^o\ \Leftrightarrow\ \frac{\mathbf{h}^o}{\langle\mathbf{h}^o|\mathbf{h}^o\rangle^2}=\frac{1}{-2\,\langle\mathbf{h}(T)|\mathbf{h}(T)\rangle}\int_0^T\mathbf{L}^{o\dagger}\mathbf{h}^\dagger\mathrm{d}t\,. \tag{6.35}$$

By deriving the augmented Lagrangian by the multiplier one retrieves the constraint.

Hence, in order to find the optimal substrate, one starts with an arbitrary substrate profile $\mathbf{h}^o$ and integrates the direct problem (6.30) from $t=0$, with $\mathbf{h}_0=\mathbf{0}$, to the chosen time horizon $t=T$ (see Appendix 6.7.2 for details on the numerical method). Equation (6.33) gives the initial condition for the adjoint field, which is then integrated backward in time using the adjoint equation (6.34) from $t=T$ to $t=0$. The new guess for the optimal substrate can be found with the help of Eq. (6.35). First, the new guess is approximated by

$$\tilde{\mathbf{h}}^o=\frac{1}{-2\,\langle\mathbf{h}(T)|\mathbf{h}(T)\rangle}\int_0^T\mathbf{L}^{o\dagger}\mathbf{h}^\dagger\mathrm{d}t, \tag{6.36}$$

which is then normalized by $\langle\tilde{\mathbf{h}}^o|\tilde{\mathbf{h}}^o\rangle^2$ according to Eq. (6.35) to get $\mathbf{h}^o$. Secondly, a low-pass filter is applied to $\mathbf{h}^o$, whose meaning is explained in the following. The algorithm (see Fig. 6.14) is repeated until the gain $G(T)$ converges. The optimal substrate as well as the optimal gain for the time horizon T, the wavenumber β, Bond number Bo and film aspect ratio δ are obtained. The envelope of the optimal gains for the selected parameters can be found by repeating the procedure for different time horizons T.

The necessity of a low-pass filter for the optimal substrate perturbation can be argued with both numerical and physical reasons. In fact, we have found that the optimal substrate

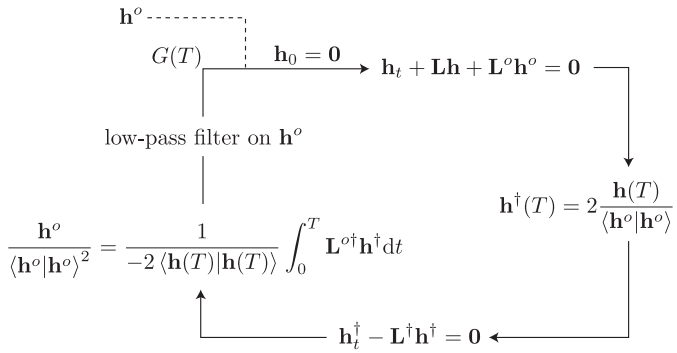

Figure 6.14 – Sketch of the iterative procedure to find the optimal gain and substrate perturbation for a given time horizon T, spanwise wavenumber β, Bond number Bo and film aspect ratio δ.

after an iteration, before filtering, presents high-frequency perturbations. The latter would result in very large oscillating derivatives in the linear operators $\mathbf{L}$ and $\mathbf{L}^o$, compromising therefore the numerical stability. This point is even more dramatic since derivatives up to the fourth-order have to be computed. The high-frequency perturbations of the optimal substrate perturbations for a given time horizon T are situated in the region close to the front location reached by the draining flow at $t = T$. In fact, as already demonstrated by Bertozzi & Brenner (1997), the roughness of the substrate at the contact line is a very effective amplifier of film perturbations. It is therefore not surprising that the optimal substrate found by the algorithm presents such a rough pattern. However, our numerical discretization does not allow for describing a realistic random roughness distribution. Therefore, a low-pass filter is applied to smoothen out these perturbations and only consider low-frequency perturbations, which can be resolved accurately. The filter can also be very pragmatically justified by noting that, in practice, one can only fabricate an optimal perturbed substrate for experiments with a relatively large characteristic size. The smoothed-out high-frequency perturbations would naturally correspond to the intrinsic roughness of the material.

6.5.4 Results

Influence of the time horizon

Similarly to the shape of the optimal initial conditions of Sec. 6.4.4, the optimal substrate topography is composed by two parts: a wide-bump perturbation and a localized perturbation at the location reached by the draining flow at time $t = T$ (see Fig. 6.15(a)). The latter is particularly evident in the optimal substrate profiles for short time horizons, whereas the former mainly composes the optimal substrates for late time horizons. In contrast to the optimal initial conditions (see for instance Fig. 6.7), the wide-bump perturbation has an opposite amplitude with respect to the film thickness response (see Fig. 6.15(b)).

Film-thickness perturbations grow, from an initially zero profile, following a two-step process

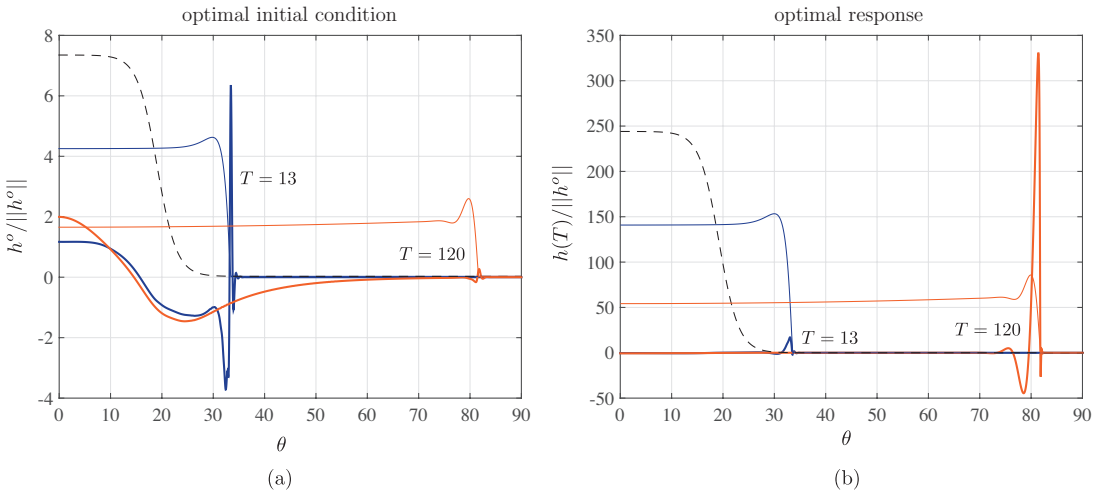

Figure 6.15 – Optimal substrate h^o (a) and optimal responses $h(T)$ (b) for the time horizons $T =$ 13 and 120 (thick solid lines), normalized by the initial L_2-norm of the substrate perturbation $||h^o||$. The thin solid lines indicate the base flow profile H at the times T and the black dashed line are the base flow at $t = 0$ (in arbitrary units). $\beta = 2$.

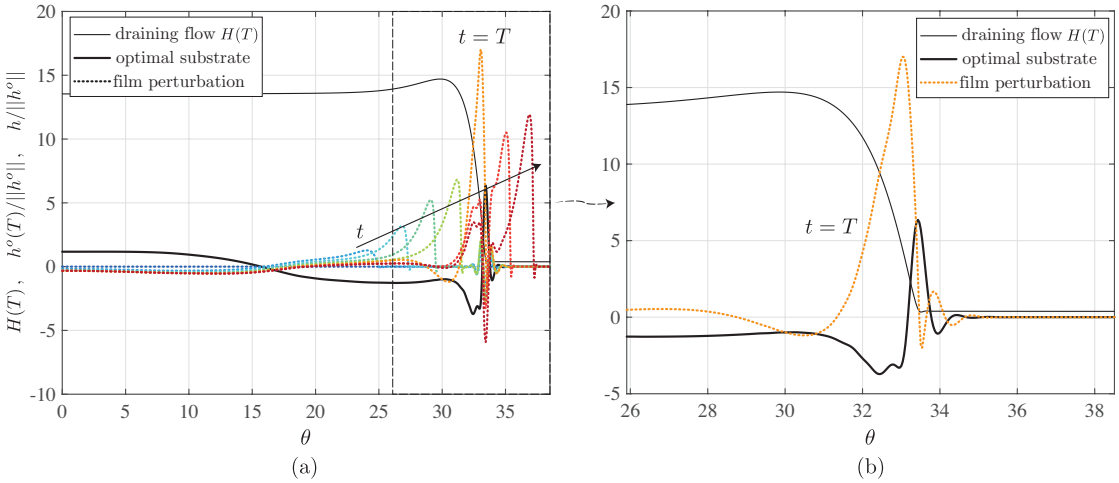

Figure 6.16 – (a) Evolution of the film perturbations h (dotted lines) over the optimal substrate $h^o(T)$ for $T = 13$ (thick solid line), both normalized by the initial L_2-norm of the substrate perturbation $||h^o||$, for the times $t = 0$, 2.6, 5.3, 8.0, 10.6, 13, 15.9 and 18.6. (b) Zoom on the optimal response $h(T)$. The thin solid line indicates the base flow profile $H(T)$ (in arbitrary units). $\beta = 2$.

(see Fig. 6.16(a)). First, when the fluid flows over the wide-bump of the substrate, a perturbation ridge forms under the effect of the capillary pressure gradient due to the wide-bump curvature. Kalliadasis, Bielarz & Homsy (2000) also observed the formation of a large asymmetric capillary ridge right before a step down in the substrate. The formed perturbation ridge grows as time runs, replenished from the base flow. Secondly, when the perturbation ridge reaches the localized substrate perturbation, it experiences a very fast growth (see orange

dotted curve in Fig. 6.16). The second step can be understood with the help of Fig. 6.16(b). The optimal substrate presents a trough in the base-flow inner region, followed by a steep front at the virtual contact line. Therefore, the fluid perturbation reaching this location suddenly increases in amplitude while meeting the localized substrate obstacle. Note that the peak in the film perturbation is always located upstream with respect to the peak in the optimal substrate. Once the perturbation has passed the localized substrate peak, the perturbation decays, before increasing again due to the instability of the three-dimensional advancing perturbed ridge. In the outer region, where the base flow reaches a uniform (but thinning) profile, the perturbation relaxes to the reversed shape as the one of the substrate, in particular over the highly oscillating region of the substrate, due to surface tension effects.

In a similar way as for the gain evolutions of the optimal initial conditions of Fig. 6.9, the larger the time horizon, the larger and more similar the gain evolutions induced by the optimal substrate perturbations due to their weak dependence on T (see Fig. 6.17).

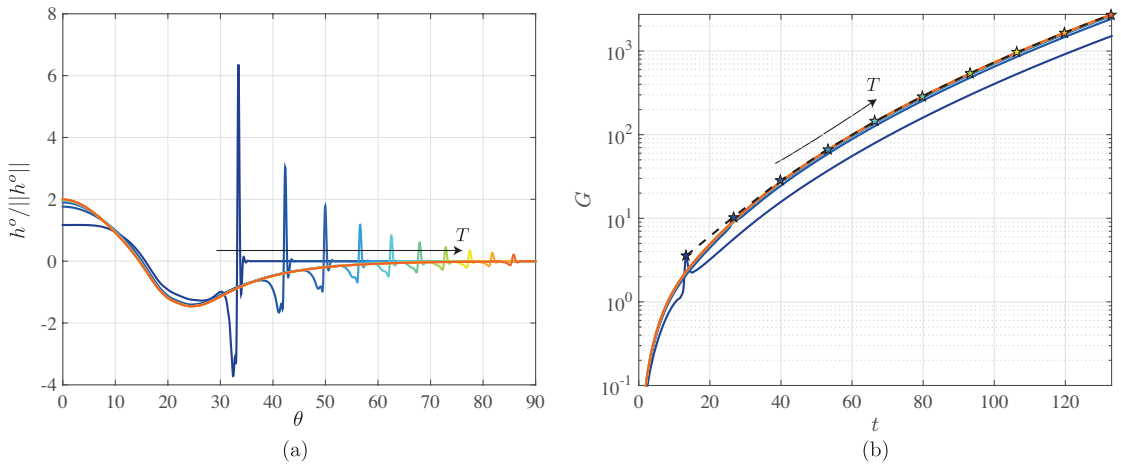

Figure 6.17 – Optimal substrate $h^o(T)$, normalized by the initial L_2-norm of the substrate perturbation $||h^o||$ (a) and gain G (b) for the time horizons T = 13, 27, 40, 53, 66, 80, 93, 106, 120 and 133. The stars indicate the optimal gains $G_{\max} = G(T)$. The black dashed line corresponds to the envelope of the gains $G_{\max}$. $\beta = 2$.

Optimal spanwise wavenumber

The importance of the wide-bump substrate perturbation with respect to the localized substrate perturbation is found to be again dependent on the spanwise wavenumber (see Fig. 6.18 and Fig. 6.19). In particular, one can observe that the optimal substrate for $\beta = 6$ is almost uniquely composed by a wide-bump perturbation, the localized perturbations remaining only for the shortest time horizons.

However, the location where the wide-bump substrate perturbation has the largest amplitude is only weakly dependent on β. Its value is approximatively constant, $\theta \simeq 26°$, which is close

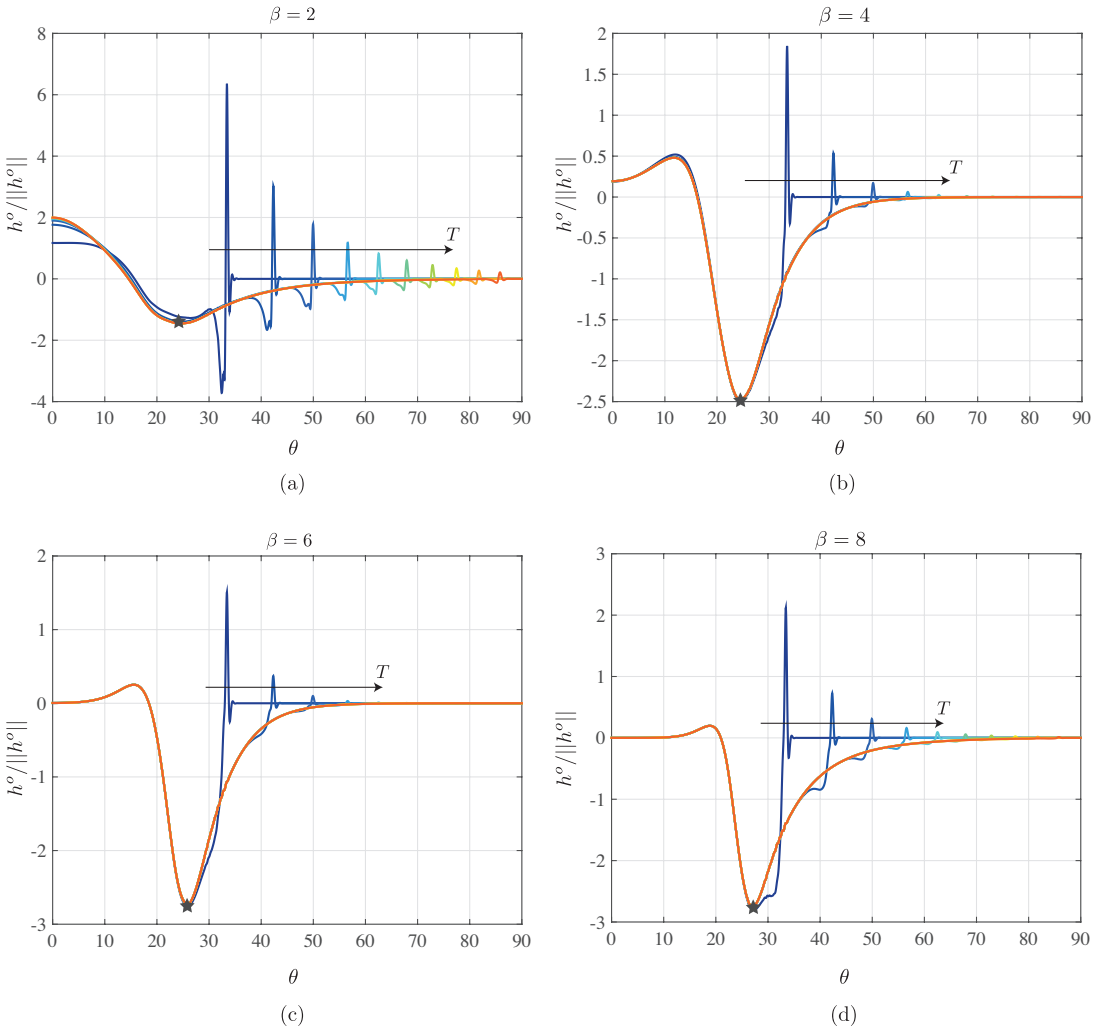

Figure 6.18 – Optimal substrate $h^o(T)$, normalized by the initial L_2-norm of the substrate perturbation $||h^o||$ for the time horizons T = 13, 27, 40, 53, 66, 80, 93, 106, 120 and 133 for β = 0.5, 2, 4 and 6. The stars indicate the thickest location of the wide-bump perturbation.

to the front location of the base-flow initial condition given by Eq. (6.8). This is in contrast to what we have found for the optimal initial conditions (see Fig. 6.10), where the polar location of the bump was increasing significantly with β. A possible rationale for the difference is that the wide-bump in the initial film thickness profile corresponds to an increase in fluid at a particular location, which is indeed sensitive to the spanwise wavenumber. The optimal initial perturbation eventually becomes mobile and is swept away with the draining flow. On the other hand, the wide-bump in the substrate perturbation only modifies the geometry profile on which the base flow is evolving, impacting the growth of the perturbations during the entire evolution. Its optimal location is likely to be only dependent on the initial front location, but not on the successive locations reached by the front during drainage.

The universality of the optimal substrate with respect to the time horizon for β = 6 results again

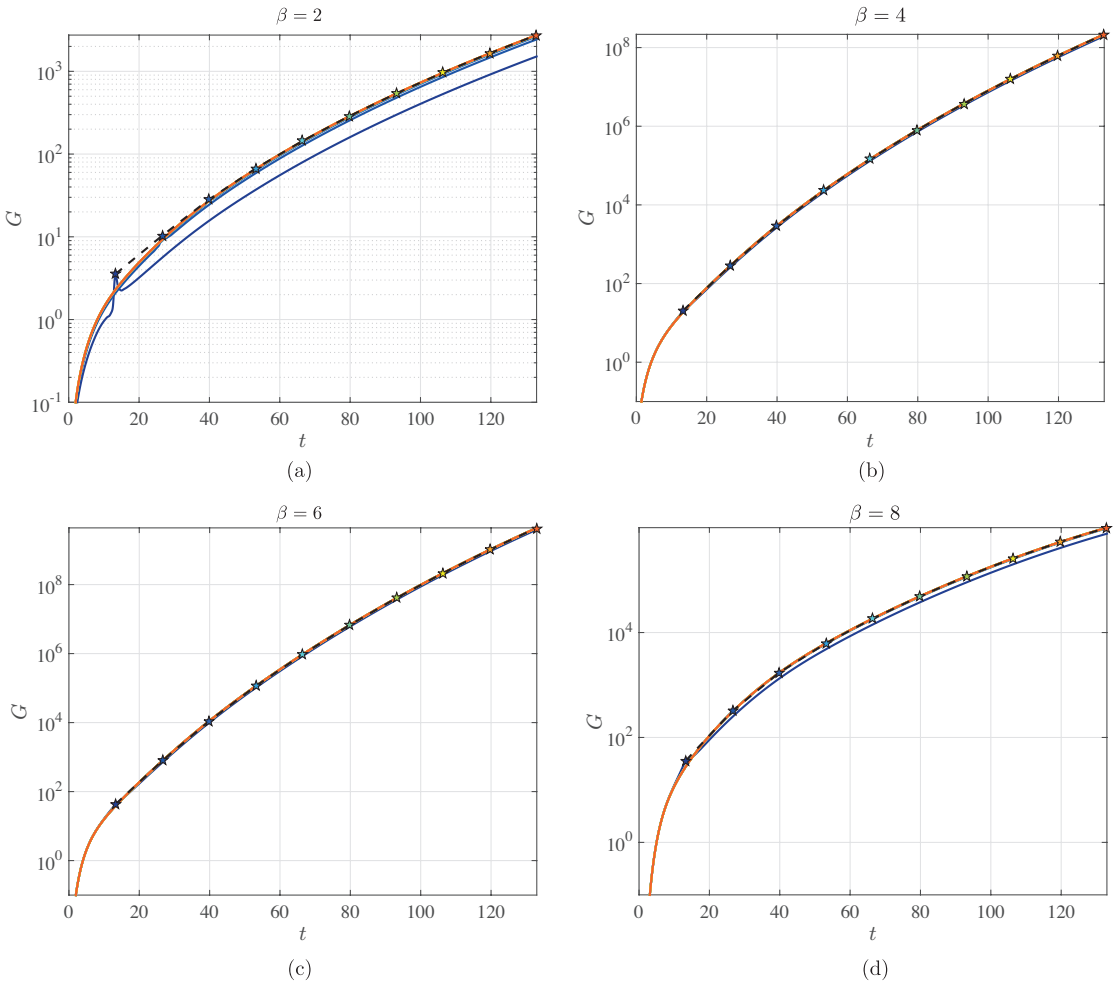

Figure 6.19 – Gain G for the time horizons $T = 13$, 27, 40, 53, 66, 80, 93, 106, 120 and 133 for $\beta = 0.5$, 2, 4 and 6. The stars indicate the optimal gains $G_{\max} = G(T)$. The black dashed lines correspond to the envelope of the gains $G_{\max}$.

in gain evolutions which are extremely similar (see Fig. 6.19(c)). Note that the achieved optimal gains are much larger than the ones for the optimal initial film-thickness perturbations (see Fig. 6.11).

Furthermore, the weak dependence of the optimal substrate shape for large T on the spanwise wavenumber β has important consequences on the selection of the optimal β as a function of time. One can again distinguish a short and a late time regime, but the variations of the optimal β are much smaller (see Fig. 6.20) than for the optimal spanwise wavenumber of the initial film-thickness perturbations seen in Fig. 6.12. At short times, the optimal spanwise wavenumber decreases from $\beta = 8$ to $\beta = 6$, whereas its value is constant $\beta \simeq 5.5$ for $t \gtrsim 30$. Therefore, a time-independent optimal substrate-topography perturbation exists, and its spanwise wavenumber is $\beta \simeq 5.5$.

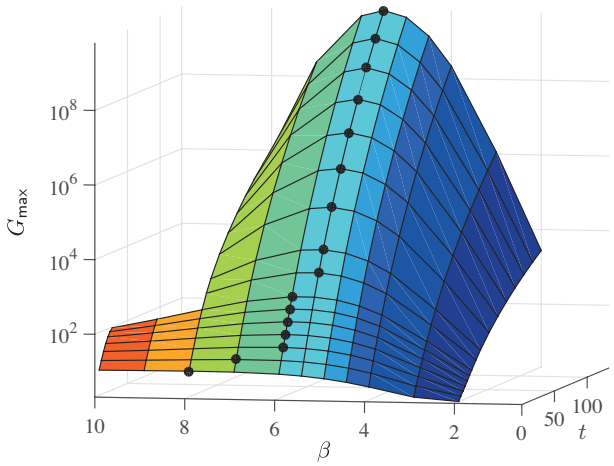

Figure 6.20 – Envelopes $G_{max}(\beta, t)$ for the gain evolutions for $\beta = 2, 3, 4, 4.5, 5, 5.5, 6, 7, 8, 9$ and 10. The largest optimal gains obtained by the transient growth analysis, and the corresponding optimal wavenumbers β, at every considered time, are indicated by the black symbols.

Note that the found optimal wavenumber $\beta \simeq 5.5$ is only an approximation and a finer discretization of the spanwise wavenumbers would give a more precise value. However, the general result will be unaffected, reason why this is not performed here.

6.6 Conclusions

The fingering instability of a Newtonian thin viscous film flowing on a horizontal cylindrical substrate has been investigated. In contrast to the classic fingering instability on an inclined plane, where the advancing capillary ridge can be considered as quasi-static and its stability is well captured by a modal linear stability analysis, the flow on a cylinder is intrinsically unsteady and a nonmodal transient growth analysis has to be undertaken. The novelty of our work lies in the generalization of the fingering instability to curved substrates, including the optimization of substrate-topography perturbations, which have been scarcely investigated in the literature despite their practical interest.

First, we have characterized the axially invariant draining flow. We assume total wetting, *i.e.* the absence of a contact line, by imposing a precursor film downstream of the advancing ridge (Troian et al., 1989; Bertozzi & Brenner, 1997; Spaid & Homsy, 1996). As for the flow over an inclined plane, the draining solution is composed by an outer solution, where the film is smooth, and an inner solution close to capillary ridge, where the film thickness experiences large variations to match the precursor film thickness (Troian et al., 1989). Since the dynamics in the outer region is governed only by the balance of gravity and viscous stresses, we have been able to derive an asymptotic solution for the film thickness in this region. Excellent agreement is found for the temporal and spatial variations of the film thickness, as well as for the front position. Both the film thickness and the front velocity decrease in time as $t^{-1/2}$. We

have shown that the cylindrical geometry of the substrate induces a nonmonotonic temporal variation of the characteristic length of the capillary ridge, where the capillary pressure term and the variation of the hydrostatic pressure have to be considered as well. At short times, when the capillary ridge is on a rather horizontal substrate, the length of the inner region is given by the capillary length, obtained by balancing the capillary pressure to the variation of the hydrostatic pressure. However, at large times, when the capillary ridge is on a rather inclined substrate, its characteristic length is given by balancing the capillary pressure with the drainage, and it decreases in time as $t^{-1/3}$.

Secondly, the instability of the advancing ridge has been investigated by performing an optimal transient growth analysis. We have found that an optimal spanwise wavenumber β exists at every time: it decreases at short times and increases at large ones. The crossover between the two behaviors is in good agreement with the crossover between the two characteristic lengths of the capillary ridge, assuming that the modal linear stability analysis of the flow over an inclined plane would predict an optimal spanwise wavenumber $\beta = 0.5/\ell$ (Troian et al., 1989; Spaid & Homsy, 1996). However, the optimal β found by the optimal transient growth analysis at short times is much larger. The draining flow experiences very large variations and the capillary ridge is far from a traveling-wave solution; the classic modal stability analysis fails. At large times, the optimal spanwise wavenumber predicted by our analysis is closer to the one of the modal analysis since the variations in the draining flow are slower. Yet, the optimal spanwise wavenumber is always smaller than the one predicted by the modal analysis due to the time-dependent history of the flow. The most amplified mode from a modal analysis at one time instant will be inefficient for later times as the linear operator has changed.

Strikingly, we have been able to show that the optimal spanwise wavenumber corresponds to the optimal initial perturbations of the film thickness which is the least time dependent. These universal optimal initial conditions correspond to a wide-bump perturbation of the precursor film thickness and are therefore efficient over the entire time the capillary ridge takes to travel along them. Furthermore, we have observed that the location where the wide-bump perturbations are the largest increases with β. This is very likely to be related to the result of the modal linear stability analysis for the flow over an inclined plane, where large spanwise wavenumbers are found to be more effective at large inclination angles. The finding of optimal perturbations located in the precursor film region is in agreement with the sensitivity of the instability growth on the detail of the perturbations at the moving virtual contact line (Bertozzi & Brenner, 1997).

Finally, we have answered the question of the optimal substrate-topography perturbations. The latter are in fact more relevant in practice as imposing an initial disturbance of the film thickness is not an easy task. In this work, we considered only substrate perturbations whose characteristic length can be well resolved numerically or manufactured. Smaller scales perturbations are in fact intrinsic to the material and only result in a slightly larger growth. By performing an optimal transient growth analysis with an additional forcing term due to the substrate perturbations, we have shown that the optimal substrate-topography perturbations

are composed by the same structures as the optimal initial film-thickness disturbances, yet of opposite sign. However, in contrast to fluid perturbations, the wide-bump location of the solid perturbations is only weakly dependent on the spanwise wavenumber. Hence, the optimal spanwise wavenumber only weakly depends on time, and its value for late times is constant: $\beta \simeq 5.5$. Given a draining flow resulting from a precise initial condition, there is an optimal substrate profile which is the most suitable to excite the perturbations, which only results from the substrate topography.

To conclude, the appearing fingering wavelength depends, on the one hand, on the disturbance amplitude if the film thickness is initially perturbed. For low disturbance amplitude, a large growth will be necessary and thus a large wavelength will appear, while for a large disturbance amplitude, a small growth suffices for the fingers' formation at short times with a small wavelength. On the other hand, the fingering wavelength for a substrate perturbation is not dependent on the disturbance amplitude if the latter is sufficiently small.

Our current efforts are directed towards considering the robust control of this problem (Bewley, Temam & Ziane, 2000), *i.e.* finding the optimal substrate to *stabilize* the most dangerous perturbation in order to suppress the fingering formation, a problem of critical practical importance. Furthermore, it would be very interesting to generalize the present work for the case of a spherical substrate treated by Takagi & Huppert (2010), where the perimeter of the advancing ridge increases in time and the fingering wavenumber can take only discrete values, as we have seen for the Rayleigh-Taylor instability in Chapter 5. The problem in spherical coordinates shares some analogies with the splashing of a droplet on a rigid substrate, where a radially expanding lamella, similar to an advancing ridge, also forms. The lamella might eventually dewet the substrate and eject smaller droplets following a capillary instability of the rim (Riboux & Gordillo, 2014, 2015). However, inertial effects have to be considered for the splashing of a drop.

Acknowledgments We would like to acknowledge P.-T. Brun for motivating us in this project. This work was funded by the ERC Grant No. SIMCOMICS 280117 and by the Swiss National Science Foundation Grant No. 200021_178971.

6.7 Appendix

6.7.1 Linear operators

The linear operator for the film perturbation $\mathbf{h}$ in equations (6.17) and (6.30) in matrix form is given by:

$$\begin{aligned}\mathbf{L} = &\frac{\beta^4 H^3}{3Bo}\mathbf{I} - \frac{\beta^2\delta^4 H^5}{3Bo}\mathbf{D}_2 - \frac{5\beta^2\delta^4 H^4 H_\theta}{3Bo}\mathbf{D}_1 + \frac{\beta^2\delta^3 H^4}{3Bo}\mathbf{D}_2 + \frac{4\beta^2\delta^3 H^3 H_\theta}{3Bo}\mathbf{D}_1 \\ &- \frac{2\beta^2\delta^2 H^3}{3Bo}\mathbf{D}_2 - \frac{\beta^2\delta^2 H^2 H_\theta}{Bo}\mathbf{D}_1 - \frac{\beta^2\delta^2 H^3}{3Bo}\mathbf{I} + \frac{\delta^4 H^3}{3Bo}\mathbf{D}_4 + \frac{\delta^4 H^2 H_{\theta\theta\theta}}{Bo}\mathbf{I} \\ &+ \frac{\delta^4 H^2 H_{\theta\theta\theta}}{Bo}\mathbf{D}_1 + \frac{\delta^4 H^2 H_\theta}{Bo}\mathbf{D}_3 + \frac{2\delta^4 H H_\theta H_{\theta\theta\theta}}{Bo}\mathbf{I} + \frac{\delta^4 H^3}{3Bo}\mathbf{D}_2 + \frac{\delta^4 H^2 H_{\theta\theta}}{Bo}\mathbf{I} + \\ &\frac{2\delta^4 H^2 H_\theta}{Bo}\mathbf{D}_1 + \frac{2\delta^4 H H_\theta^2}{Bo}\mathbf{I} - \frac{1}{3}\delta H^3\cos\theta\mathbf{D}_2 - \delta H^2\cos\theta H_{\theta\theta}\mathbf{I} + \\ &\frac{1}{3}\delta H^3\sin\theta\mathbf{D}_1 + \delta H^2\sin\theta H_\theta\mathbf{I} - 2\delta H^2\cos\theta H_\theta\mathbf{D}_1 - 2\delta H\cos\theta H_\theta^2\mathbf{I} + \\ &H^2\cos\theta\mathbf{I} + H^2\sin\theta\mathbf{D}_1 + 2H\sin\theta H_\theta\mathbf{I} - \frac{\beta^4\delta^2 H^3 H_\theta^2}{6Bo}\mathbf{I} \\ &+ \frac{\beta^2\delta^4 H^3 H_\theta H_{\theta\theta\theta}}{3Bo}\mathbf{I} + \frac{2\beta^2\delta^4 H^3 H_\theta H_{\theta\theta}}{3Bo}\mathbf{D}_1 + \frac{\beta^2\delta^4 H^3 H_\theta^2}{6Bo}\mathbf{D}_2 \\ &+ \frac{\beta^2\delta^4 H^3 H_{\theta\theta}^2}{3Bo}\mathbf{I} + \frac{\beta^2\delta^4 H^2 H_\theta^2 H_{\theta\theta}}{Bo}\mathbf{I} + \frac{\beta^2\delta^4 H^2 H_\theta^3}{2Bo}\mathbf{D}_1\end{aligned} \tag{6.37}$$

where $\mathbf{I}$ is the identity operator and $\mathbf{D}_i$ with $i = 1, ..., 4$ are the differential operators, constructed in our study using a fourth-order finite-difference scheme. Subscripts with θ correspond to spatial derivatives of the drainage solution H.

The linear operator for the substrate perturbation $\mathbf{h}^o$ in equation (6.30) in matrix form is given by:

$$\begin{aligned}\mathbf{L}^o = &\frac{\beta^4 H^3}{3Bo}\mathbf{I} - \frac{\beta^2\delta^4 H^5}{3Bo}\mathbf{D}_2 - \frac{5\beta^2\delta^4 H_\theta H^4}{3Bo}\mathbf{D}_1 + \frac{\beta^2\delta^3 H^4}{3Bo}\mathbf{D}_2 + \frac{4\beta^2\delta^3 H_\theta H^3}{3Bo}\mathbf{D}_1 \\ &- \frac{2\beta^2\delta^2 H^3}{3Bo}\mathbf{D}_2 - \frac{\beta^2\delta^2 H_\theta H^2}{Bo}\mathbf{D}_1 - \frac{\beta^2\delta^2 H^3}{3Bo}\mathbf{I} + \frac{\delta^4 H^3}{3Bo}\mathbf{D}_4 + \frac{\delta^4 H_\theta H^2}{Bo}\mathbf{D}_3 \\ &+ \frac{\delta^4 H^3}{3Bo}\mathbf{D}_2 + \frac{\delta^4 H_\theta H^2}{Bo}\mathbf{D}_1 + \frac{1}{3}\delta^2\sin\theta H^4\mathbf{D}_1 - \frac{1}{3}\delta\cos\theta H^3\mathbf{D}_2 \\ &- \delta\cos\theta H_\theta H^2\mathbf{D}_1 + \frac{1}{3}\beta^2\sin\theta H^4\mathbf{D}_1 - \frac{\beta^4\delta^2 H_\theta^2 H^3}{6Bo}\mathbf{I} \\ &+ \frac{\beta^2\delta^4 H_\theta H_{\theta\theta\theta} H^3}{3Bo}\mathbf{I} + \frac{2\beta^2\delta^4 H_\theta H_{\theta\theta} H^3}{3Bo}\mathbf{D}_1 + \frac{\beta^2\delta^4 H_\theta^2 H^3}{6Bo}\mathbf{D}_2 \\ &+ \frac{\beta^2\delta^4 H_{\theta\theta}^2 H^3}{3Bo}\mathbf{I} + \frac{\beta^2\delta^4 H_\theta^2 H_{\theta\theta} H^2}{Bo}\mathbf{I} + \frac{\beta^2\delta^4 H_\theta^3 H^2}{2Bo}\mathbf{D}_1\end{aligned} \tag{6.38}$$

6.7.2 Numerical methods

The draining base flow is obtained by resolving the nonlinear lubrication equation (6.7) with the finite element method of COMSOL Multiphysics. Cubic elements with Lagrangian shape functions have been used on a regular grid of characteristic size 8×10^{-4}. The film thickness and curvature are the two resolved variables. The ability of this method to correctly resolve the film thickness profile is proven by the excellent comparison with respect to the analytical solutions (see Sec. 6.3 and Chapter 4). Half of a cylinder is considered, $\theta \in [0, \pi]$, and no-flux conditions are imposed at $\theta = 0$ and $\theta = \pi$. To avoid dripping phenomena in the lower part of the cylinder, we stop the simulations once the ridge arrives at $\theta = \pi/2$. Only the upper quarter of the cylinder is considered for the optimal transient growth analysis.

In order to have a correct evolution of the disturbances on the draining flow, it is necessary to have a sufficiently fine temporal representation of the draining flow. This is achieved by interpolating the computed draining flow profiles. Due to the hyperbolic character of the equation, the following approach is employed. During the time interval $\Delta t = t^{i+1} - t^i$, the front has travel by a distance $\Delta\theta_N = \theta_N^{i+1} - \theta_N^i$. The interpolated film thickness is given by

$$H(\theta, t + \Delta t/2) = \frac{H(\theta, t) + H(\theta + \Delta\theta_N, t + \Delta t)}{2}. \tag{6.39}$$

Note that for $t \lessapprox \tau_i$, the front position is almost not changing, meaning that the interpolation results in the arithmetic mean of H at the successive times.

For the optimal transient growth analysis, the linear operators $\mathbf{L}$ and $\mathbf{L}^o$ are constructed with the obtained draining flow and the linear disturbance equations are integrated in time using a Crank-Nicolson method to minimize numerical diffusion. The disturbances satisfy symmetric boundary conditions at $\theta = 0$ and $h(\pi/2) = h_\theta(\pi/2) = h_{\theta\theta}(\phi/2) = 0$.

In the optimal transient growth algorithm of the substrate-topography perturbations described in Sec. 6.5.3 we have employed the low-pass filter `fir1.m` of Matlab with order 60 and a cutoff length of $0.0084\,\mathrm{rad}^{-1}$, together with a Chebyshev window with 100 dB of attenuation.

6.7.3 Derivation of the adjoint fields for the optimal substrate algorithm

The optimality condition for the augmented Lagrangian (6.32) with respect to $\delta\mathbf{h}$ is found in a very similar way to the derivation for the algorithm giving the optimal initial condition of Sec. 6.4.3, which is described in great details in Chapter 3. The only difference is that the initial condition for the film thickness is no longer the variable to be optimized and therefore the augmented Lagrangian does not need to enforce this condition. Note however that, if one would have enforced also the initial condition, the optimality condition with respect to $\delta\mathbf{h}_0$ would have indeed given $\delta\mathbf{h}^\dagger = \mathbf{0}$.

More interestingly is the optimality condition with respect to the substrate perturbation. For

the derivation, we will make use of Fréchet derivatives, which for an operator $\mathbf{A}(\mathbf{s})$ are defined by (see Cossu (2014)):

$$\langle \frac{\partial \mathbf{A}}{\partial \mathbf{s}} \Big| \delta \mathbf{s} \rangle = \lim_{\epsilon \to 0} \frac{\mathbf{A}(\mathbf{s} + \epsilon \delta \mathbf{s}) - \mathbf{A}(\mathbf{s})}{\epsilon} . \tag{6.40}$$

The variation of $\mathscr{L}$ with respect to $\delta \mathbf{h}^o$ results in

$$\langle \frac{\partial \mathscr{L}}{\partial \mathbf{h}^o} \Big| \delta \mathbf{h}^o \rangle = \langle -2\mathbf{h}^o \frac{\langle \mathbf{h}(T) | \mathbf{h}(T) \rangle}{\langle \mathbf{h}^o | \mathbf{h}^o \rangle^2} \Big| \delta \mathbf{h}^o \rangle - \int_0^T \langle \mathbf{h}^\dagger \Big| \mathbf{L}^o \, \delta \mathbf{h}^o \rangle \, \mathrm{d}t \tag{6.41}$$

$$= \langle -2\mathbf{h}^o \frac{\langle \mathbf{h}(T) | \mathbf{h}(T) \rangle}{\langle \mathbf{h}^o | \mathbf{h}^o \rangle^2} \Big| \delta \mathbf{h}^o \rangle - \int_0^T \langle \mathbf{L}^{o\dagger} \mathbf{h}^\dagger \Big| \delta \mathbf{h}^o \rangle \, \mathrm{d}t \tag{6.42}$$

$$= \langle -2\mathbf{h}^o \frac{\langle \mathbf{h}(T) | \mathbf{h}(T) \rangle}{\langle \mathbf{h}^o | \mathbf{h}^o \rangle^2} \Big| \delta \mathbf{h}^o \rangle - \langle \int_0^T \mathbf{L}^{o\dagger} \mathbf{h}^\dagger \, \mathrm{d}t \Big| \delta \mathbf{h}^o \rangle \tag{6.43}$$

$$= \langle -2\mathbf{h}^o \frac{\langle \mathbf{h}(T) | \mathbf{h}(T) \rangle}{\langle \mathbf{h}^o | \mathbf{h}^o \rangle^2} - \int_0^T \mathbf{L}^{o\dagger} \mathbf{h}^\dagger \, \mathrm{d}t \Big| \delta \mathbf{h}^o \rangle \, . \tag{6.44}$$

Where the definition of the adjoint operator, namely $\langle \mathbf{a} | \mathbf{L}^o \mathbf{b} \rangle = \langle \mathbf{L}^{o\dagger} \mathbf{a} | \mathbf{b} \rangle$, has been used in (6.42). Since the optimal substrate perturbation $\mathbf{h}^o$ is time independent, we can commute temporal integration and spatial integration (through the scalar product) in Eq. (6.43). By imposing a vanishing variation of $\mathscr{L}$ to any $\delta \mathbf{h}^o$, one eventually obtains:

$$\langle \frac{\partial \mathscr{L}}{\partial \mathbf{h}^o} \Big| \delta \mathbf{h}^o \rangle = 0 \, , \, \forall \, \delta \mathbf{h}^o \Leftrightarrow \frac{\mathbf{h}^o}{\langle \mathbf{h}^o | \mathbf{h}^o \rangle^2} = \frac{1}{-2 \langle \mathbf{h}(T) | \mathbf{h}(T) \rangle} \int_0^T \mathbf{L}^{o\dagger} \mathbf{h}^\dagger \, \mathrm{d}t \, . \tag{6.45}$$

Part II

Precipitative pattern formation in limestone caves

7 Hydrodynamic-driven speleothem morphogenesis

This work has been done in collaboration with M. Wyart[1] and B. Scheid[2]

[1]Physics of complex systems laboratory, EPFL, CH1015 Lausanne, Switzerland
[2]TIPs Laboratory, Université Libre de Bruxelles, Code Postal 165/67, Avenue Franklin Roosevelt 50, 1050 Bruxelles, Belgium

7.1 Introduction

We investigate the role of hydrodynamic instabilities in the morphogenesis of some typical structures encountered in limestone caves, known as *speleothems*. The most common speleothems are stalactites, stalagmites, draperies, flowstones, soda straws, and helicites, to name a few (see Fig. 7.1). Due to their astonishing beauty, these fascinating structures have been the object of human wonder for hundreds of years, as recorded by the writings of the Elder Pliny in the first century A.D. (Hill & Forti, 1997). However, the physicochemical mechanisms at the origin of their growth have been unravelled only in the 19th century. Water percolating through the soil becomes enriched in carbon dioxide due to the higher partial pressure of CO_2 in the soil compared to the atmospheric conditions, slightly lowering the pH of the water. As a result, a higher concentration of calcium carbonate can be dissolved in the water (Short, 2006). Eventually, water rich in dissolved carbon dioxide and calcium ions enters the cave through openings in the rock. There, the partial pressure of CO_2 is lower and carbon dioxide outgases from the solution (Buhmann & Dreybrodt, 1985). Hence, the calcium carbonate becomes supersaturated and precipitates on the underlying rock. Strikingly, and for the delight of fluid dynamicists, the speleothem morphogenesis is mainly dictated by the hydrodynamics (Hill & Forti, 1997).

This subject has experienced an increased interest in the scientific community only in the last one or two decades. Short et al. (2005*a*) have demonstrated that stalactites grow following a self-similar shape resulting from the coupling of the hydrodynamic thin-film flow and the

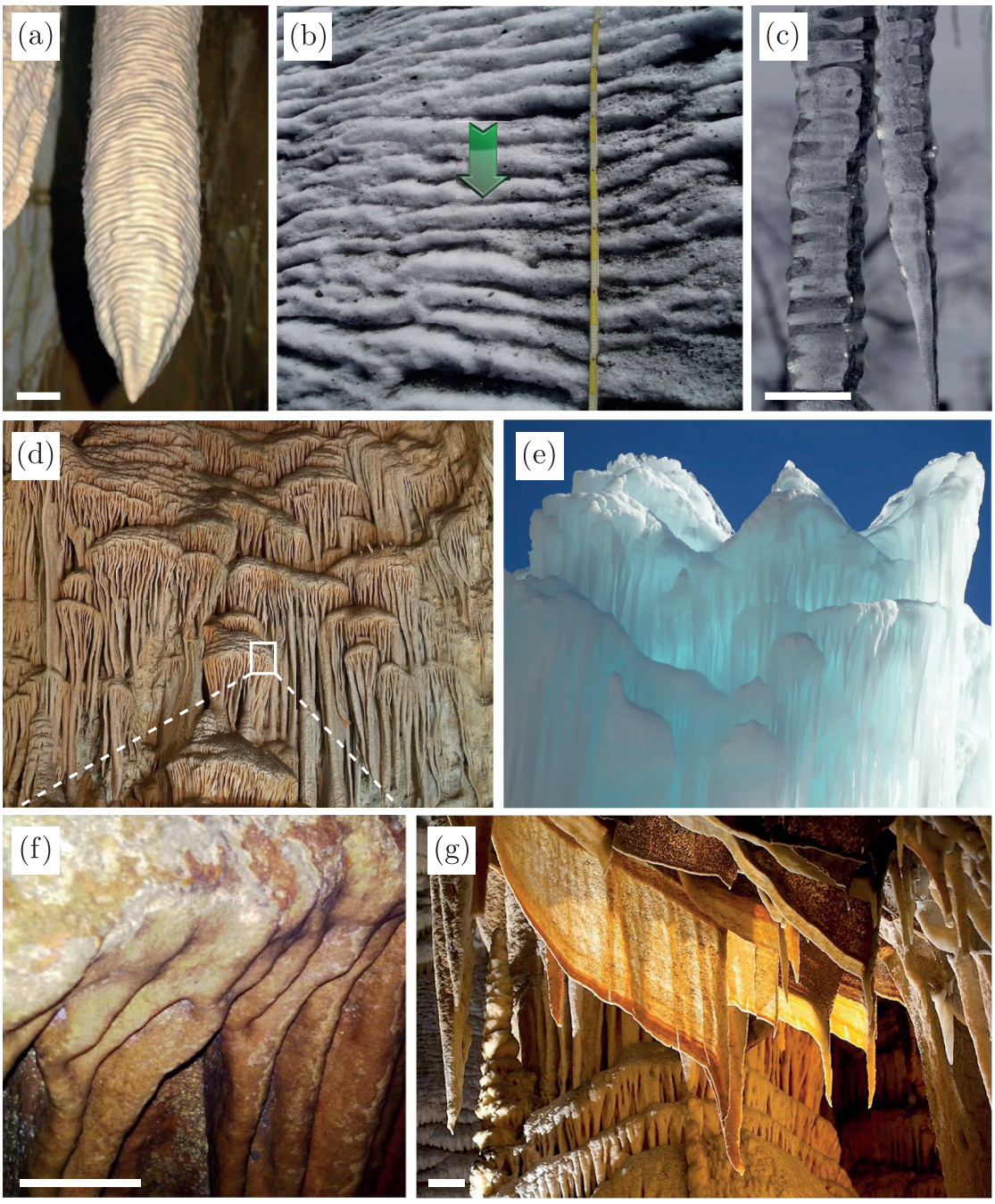

Figure 7.1 – Typical hydrodynamically-locked karst and ice structures. Figures (a-f) are taken from Camporeale (2015) and Bertagni & Camporeale (2017). (a) stalactite in the Lehman caves, Nevada, USA, with crenulations; (b) ice ripples on the surface of the Ciardoney glacier, Italy; (c) icicles with crenulations; (d,e) karst and ice flutings; (f) zoom on a fluting head; (g) drapery (http://www.geologyfortoday.com). White bar indicates 10 cm.

physiochemical mechanism at the origin of the calcium deposition. In particular, they showed that the latter is directly proportional to the liquid film thickness, thus explaining the elongated

structure of stalactites. The mystery of the ripple-like structures at the surface of stalactites, called crenulations (see Fig. 7.1(a-c)), has been successfully solved by Camporeale & Ridolfi (2012*a*), indicating that this morphological pattern is dictated by a hydrodynamic instability (Vesipa, Camporeale & Ridolfi, 2015; Camporeale, 2017). More recently, it has been suggested that the formation of other speleothems, like flutings in flowstones or draperies (see Fig. 7.1(d-g)), are also driven by a hydrodynamic instability (Camporeale, 2015; Bertagni & Camporeale, 2017). They have shown that the characteristic spacing between these structures is related to the most amplified wavelength of the fluid perturbations.

Remarkably, speleothems have frozen-fluid counterparts: icicles (see Fig. 7.1(c)), also presenting ripples (Chen & Morris, 2011, 2013), are the corresponding of stalactites and ice flutings can be observed in icefalls (see Fig. 7.1(e)). Flowstone formations are indeed often called 'frozen waterfalls' due to the resemblance to their frozen-fluid counterparts. Despite the different physical mechanism at the origin of their growth, their shape is intrinsically related to the hydrodynamics (Short, 2006). Camporeale & Ridolfi (2012*b*) have shown that ice ripples (see Fig. 7.1(b)) on glaciers are also hydrodynamically driven.

Here, we study the morphogenesis of cave flutings, longitudinally oriented organ-pipe-like structures and draperies, by combining linear stability analyses and nonlinear numerical simulations of the governing equations. More precisely, we propose a possible explanation for the patterns typically observed in flowstones (see Fig. 7.1(f)) and draperies (see Fig. 7.1(g)), and we show how the selected wavelength depends on the hydrodynamic stability properties.

7.2 Problem description and governing equations

We consider a liquid film of characteristic thickness H_i^*, density ρ and dynamic viscosity μ flowing under an plane inclined with an angle ϕ with respect to the vertical (see Fig. 7.2(a)). The substrate upstream to the inclined plane might be convex or concave (see Fig. 7.2(b),(c), respectively), with a radius of curvature R^*. The substrate deformations, denoted by $\bar{H}^{o*}$, arising due to the calcium carbonate deposit, are assumed to be much smaller than the liquid film thickness $\bar{H}^*$.

7.2.1 Hydrodynamics

The thickness of the liquid film observed in caves is of about $10\,\mu$m, much smaller than the characteristic length of the spatial variations, which is of the order of few centimeters (see Fig. 7.1(f)). One can therefore use a long-wavelength approximation and, under the assumption of negligible inertial effects due to the small Reynolds number of the flow, the Stokes equations can be integrated to give the following lubrication equations.

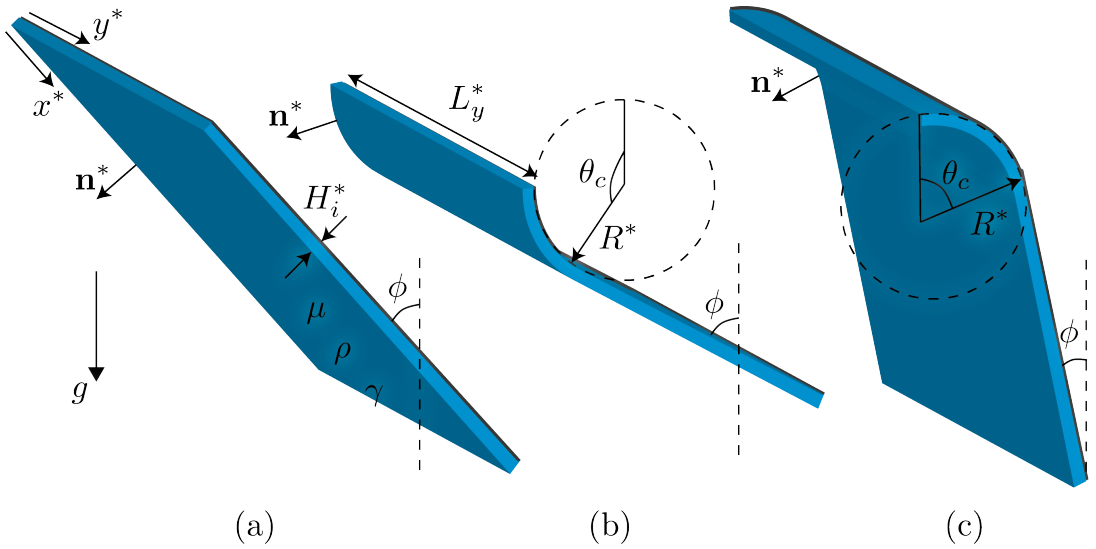

Figure 7.2 – Sketch of the considered problem geometries. Thin film under an inclined plane (a), under a convex substrate followed by an inclined plane (b) and under a concave substrate followed by an inclined plane (c). The fluid (blue) is always under the substrate (black).

Inclined substrate

The film thickness under the inclined plane is governed by

$$\frac{\partial \bar{H}^*}{\partial t^*} + \frac{\rho g}{3\mu}\nabla^* \cdot \Bigg\{ \underbrace{\bar{H}^{*3}\ell_c^{*2}\begin{bmatrix}\bar{\kappa}^*_{x^*}\\ \bar{\kappa}^*_{y^*}\end{bmatrix}}_{\text{I}} + \underbrace{\bar{H}^{*3}\begin{bmatrix}-\cos\phi\,(\bar{H}^{o*}_{x^*}\bar{H}^*_{x^*} + \bar{H}^{o*}_{x^*x^*}\bar{H}^*) + \sin\phi\,\bar{H}^*_{x^*}\\ -\cos\phi\,(\bar{H}^{o*}_{x^*}\bar{H}^*_{y^*} + \bar{H}^{o*}_{x^*y^*}\bar{H}^*) + \sin\phi\,\bar{H}^*_{y^*}\end{bmatrix}}_{\text{II}} + \underbrace{\bar{H}^{*3}\begin{bmatrix}\cos\phi\\ 0\end{bmatrix} + \bar{H}^{*3}\begin{bmatrix}-\cos\phi\bar{H}^{o*2}_{x^*} + \sin\phi\,\bar{H}^{o*}_{x^*}\\ -\cos\phi\,\bar{H}^{o*}_{x^*}\bar{H}^{o*}_{y^*} + \sin\phi\,\bar{H}^{o*}_{y^*}\end{bmatrix}}_{\text{III}} \Bigg\} = 0, \tag{7.1}$$

where $\ell_c^* = \sqrt{\gamma/(\rho g)}$ is the capillary length built with the surface tension γ and gravity g and $\bar{\kappa}^* = \nabla^* \cdot \mathbf{n}^*$ is the curvature computed as the divergence of the normal to the fluid interface $\mathbf{n}^*$. Indices correspond to partial derivatives and ∇^* is the divergence operator in Cartesian coordinates. Term I corresponds to surface-tension effects, term II contains the effect of the variation of the hydrostatic pressure distribution due to both the variation of the film thickness and of the substrate profile, while term III corresponds to the drainage, either directly induced by the unperturbed inclination ϕ, or by the slope of the substrate $\bar{H}^{o*}$. Note that this equation is derived under the assumption that the normal vector is given by $\mathbf{n}^* = (-\bar{H}^*_x - \bar{H}^{o*}_x, -\bar{H}^*_y - \bar{H}^{o*}_y, 1)^T$, *i.e.* under the assumptions $\bar{H}^{*2}_x \ll 1$, $\bar{H}^{o*2}_x \ll 1$, $\bar{H}^{*2}_y \ll 1$ and $\bar{H}^{o*2}_y \ll 1$.

Equation (7.1) can be made dimensionless using the following characteristic scales: $L_z^* = H_i^*$ is the average initial film thickness, $L_x^* = L_y^* = \ell_c^*/\sqrt{\sin\phi}$ is the capillary length built with the gravity component normal to the unperturbed substrate and $\tau = \mu\ell_c^{*4}/(\gamma H_i^{*3}\sin^2\phi)$ is the characteristic time of the Rayleigh-Taylor instability under the inclined plane. The dimensionless lubrication equation is

$$\frac{\partial \bar{H}}{\partial t} + \frac{1}{3}\nabla\cdot\Bigg\{\underbrace{\bar{H}^3\begin{bmatrix}\bar{\kappa}_x\\ \bar{\kappa}_x\end{bmatrix}}_{\text{I}} + \underbrace{\bar{H}^3\begin{bmatrix}-\cot\phi\,\frac{1}{\tilde{\ell}_c}(\bar{H}_x^o\bar{H}_x + \bar{H}_{xx}^o\bar{H}) + \bar{H}_x\\ -\cot\phi\,\frac{1}{\tilde{\ell}_c}(\bar{H}_x^o\bar{H}_y + \bar{H}_{xy}^o\bar{H}) + \bar{H}_y\end{bmatrix}}_{\text{II}} + \underbrace{\bar{H}^3\begin{bmatrix}\cot\phi\tilde{\ell}_c\\ 0\end{bmatrix} + \bar{H}^3\begin{bmatrix}-\cot\phi\,\frac{1}{\tilde{\ell}_c}\bar{H}_x^{o2} + \bar{H}_x^o\\ -\cot\phi\,\frac{1}{\tilde{\ell}_c}\bar{H}_x^o\bar{H}_y^o + \bar{H}_y^o\end{bmatrix}}_{\text{III}}\Bigg\} = 0, \tag{7.2}$$

where $\tilde{\ell}_c = \ell_c^*/(\sqrt{\sin\phi}H_i^*)$ is the dimensionless capillary length built with the gravity component normal to the plane.

Curved substrate

The lubrication equation for a thin liquid film inside or outside of a cylindrical substrate is [1]:

$$\frac{\partial \bar{H}^*}{\partial t^*} + \frac{\rho g}{3\mu}\nabla^*\cdot\Bigg\{\underbrace{\bar{H}^{*3}\ell_c^{*2}\begin{bmatrix}\frac{\bar{\kappa}_\theta^*}{R^*}\\ \bar{\kappa}_{y^*}^*\end{bmatrix}}_{\text{I}} + \underbrace{\chi\bar{H}^{*3}\begin{bmatrix}-\frac{\sin\theta}{R^{*2}}(\bar{H}_\theta^{o*}\bar{H}_\theta^* + \bar{H}_{\theta\theta}^{o*}\bar{H}^*) + \frac{\cos\theta}{R^*}\bar{H}_\theta^*\\ -\frac{\sin\theta}{R^*}(\bar{H}_\theta^{o*}\bar{H}_{y^*}^* + \bar{H}_{\theta y^*}^{o*}\bar{H}^*) + \cos\theta\,\bar{H}_{y^*}^*\end{bmatrix}}_{\text{II}} + \underbrace{\bar{H}^{*3}\begin{bmatrix}\sin\theta\\ 0\end{bmatrix} + \chi\bar{H}^{*3}\begin{bmatrix}-\frac{\sin\theta}{R^{*2}}\bar{H}_\theta^{o*2} + \frac{\cos\theta}{R^*}\bar{H}_\theta^{o*}\\ -\frac{\sin\theta}{R^*}\bar{H}_\theta^{o*}\bar{H}_{y^*}^{o*} + \cos\theta\,\bar{H}_{y^*}^{o*}\end{bmatrix}}_{\text{III}}\Bigg\} = 0, \tag{7.3}$$

where ∇^* is the divergence operator in cylindrical coordinates and χ is a coefficient whose value is 1 when the curved substrate is concave (see Fig. 7.2(c)), and -1 when it is convex (see Fig. 7.2(b)). $\bar{\kappa}^* = \nabla^*\cdot\mathbf{n}^*$ is the curvature computed as the divergence of the normal $\mathbf{n}^*$ to the fluid interface. The lubrication equation can be rewritten using the curvilinear coordinate $x^* = \theta R^*$. Considering the same characteristic quantities as for the inclined plane, but evaluated at $\phi = \pi/2$, namely $L_r^* = H_i^*$, $L_x^* = L_y^* = \ell_c^*$ and $\tau' = \mu\ell_c^{*4}/(\gamma H_i^{*3})$, we get the

[1] Note that in order to be consistent with the notation employed for the inclined substrate, the spanwise direction for the curved substrate is denoted by y^* and not by z^* as in Chapters 4 and 6.

dimensionless lubrication equation:

$$\frac{\partial \bar{H}}{\partial t}+\frac{\rho g}{3\mu}\nabla\cdot\Bigg\{\underbrace{\bar{H}^3\begin{bmatrix}\bar{\kappa}_x\\ \bar{\kappa}_y\end{bmatrix}}_{\text{I}}+\underbrace{\chi\bar{H}^3\begin{bmatrix}-\frac{\sin(x\ell_c\delta)}{\ell_c}\left(\bar{H}^o_x\bar{H}_x+\bar{H}^o_{xx}\bar{H}\right)+\cos(x\ell_c\delta)\,\bar{H}_x\\ -\frac{\sin(x\ell_c\delta)}{\ell_c}\left(\bar{H}^o_x\bar{H}_y+\bar{H}^o_{xy}\bar{H}\right)+\cos(x\ell_c\delta)\,\bar{H}_y\end{bmatrix}}_{\text{II}} \tag{7.4}$$

$$+\underbrace{\bar{H}^3\begin{bmatrix}\ell_c\sin(x\ell_c\delta)\\ 0\end{bmatrix}+\chi\bar{H}^3\begin{bmatrix}-\frac{\sin(x\ell_c\delta)}{\ell_c}\bar{H}^{o2}_x+\cos(x\ell_c\delta)\,\bar{H}^o_x\\ -\frac{\sin(x\ell_c\delta)}{\ell_c}\bar{H}^o_x\bar{H}^o_y+\cos(x\ell_c\delta)\,\bar{H}^o_y\end{bmatrix}}_{\text{III}}\Bigg\}=0,$$

where $\delta=H_i^*/R^*$ is the film aspect ratio, $\ell_c=\ell_c^*/H_i^*$ the dimensionless capillary length and ∇ is the divergence operator in the Cartesian coordinate system (x,y).

7.2.2 Morphogenesis

As introduced in Sec. 7.1, speleothems grow by the precipitation of calcium carbonate on the cave walls due to its decreased solubility when carbon dioxide outgases from the solution. The typical growth is of 1 cm/century, even if significant fluctuations can occur during the decades as a result of different water fluxes, carbon dioxide and calcium levels (Short et al., 2005*b*). During the water journey along a speleothem, the depletion of calcium is so small that its concentration can be assumed constant. In this section, we present the derivation of the deposition law nicely described by Short et al. (2005*b*). The chemical reactions can be stoichiometrically summarized as (Romanov, Kaufmann & Dreybrodt, 2008)

$$CaCO_3+CO_2+H_2O\rightleftharpoons Ca^{2+}+2HCO_3{}^-. \tag{7.5}$$

Therefore, for each molecule of $CaCO_3$ depositing on the cave wall, one molecule of CO_2 has to diffuse to the atmosphere (Bertagni & Camporeale, 2017). The most important chemical reactions occurring in the fluid layer are (Dreybrodt, 1999; Kaufmann, 2003; Kaufmann & Dreybrodt, 2007):

$$CO_2+H_2O\overset{k_{\pm1}}{\rightleftharpoons}H^++HCO_3{}^- \tag{7.6}$$

$$CO_2+OH^-\overset{k_{\pm2}}{\rightleftharpoons}HCO_3{}^- \tag{7.7}$$

$$Ca^{2+}+HCO_3{}^-+OH^-\rightleftharpoons CaCO_3+H_2O \tag{7.8}$$

$$H^++CO_3{}^{2-}\rightleftharpoons HCO_3{}^-. \tag{7.9}$$

Reactions (7.6) and (7.7), coupling the carbon dioxide to the bicarbonate, are the slowest chemical reactions, setting the limiting deposition rate of calcium carbonate (Buhmann & Dreybrodt, 1985). The production rate of CO_2 is given by $R_{CO_2}=k_-[HCO_3{}^-]-k_+[CO_2]$, where $k_-\equiv k_{-1}[H^+]+k_{-2}$ and $k_+\equiv k_{+1}+k_{+2}[OH^-]$, with $k_{\pm1}$ and $k_{\pm2}$ being the reaction-

rate constants of the reactions (7.6) and (7.7), respectively [2]. For typical pH values of cave environments (~ 9), which sets the concentrations $[H^+]$ and $[OH^-]$, $k_+ \sim 0.1 s^{-1}$ and k_- is much smaller. Thus, the reaction time is of the order of 10 s, much greater than the diffusional time $\tau_d = H_i^{*2}/D \sim 0.1$ s, where $D \approx 10^{-9} m^2 s^{-1}$ is the diffusion constant for small aqueous solutes (Short et al., 2005*b*). The concentrations of the chemical species can therefore be assumed constant along the direction normal to the substrate. To investigate the effect of the film thickness on the evolution of the concentration of CO_2, which determines the amount of calcium carbonate that precipitates, Short et al. (2005*b*,*a*) thoroughly studied the reaction-diffusion equation for the concentration of carbon dioxide. Their analysis eventually shows that the flux of CO_2 outgassing from the fluid to the atmosphere, and thus the flux of $CaCO_3$ depositing on the wall, reads

$$\mathscr{F}^* = \hat{\rho} \frac{\partial \bar{H}^{o*}}{\partial t^*} = \bar{H}^* \left(k_- [HCO_3^-] - k_+ \mathscr{H} [CO_2]_\infty \right), \tag{7.10}$$

where $\hat{\rho}$ is the ratio of molar mass to density of calcite and $\mathscr{H} = 0.01$ (Short et al., 2005*b*) is a constant relating the concentration of carbon dioxide in the atmosphere, $[CO_2]_\infty$, to its concentration in the fluid at the free surface. From Eq. (7.10) it is therefore clear that the deposition-rate of calcium carbonate is linearly proportional to the liquid film thickness, with a proportionality coefficient which depends on the chemical concentrations.

Equation (7.10) can be rewritten in a more intuitive fashion using the concentration of $[Ca^{2+}]$. Following Short et al. (2005*b*), one first has to impose the electroneutrality condition which holds at any point in the fluid:

$$2[Ca^{2+}] + [H^+] = 2[CO_3^{2-}] + [HCO_3^-] + [OH^-]. \tag{7.11}$$

Furthermore, $[OH^-]$ and $[H^+]$ are related via the equilibrium constant of water $K_w = [H^+][OH^-]$ and $[CO_3^{2-}]$, $[H^+]$ and $[HCO_3^-]$ through the equilibrium constant

$$K = \frac{[H^+][CO_3^{2-}]}{[HCO_3^-]}, \tag{7.12}$$

so that one can express

$$[HCO_3^-] = \frac{2[Ca^{2+}] + \left(1 - \frac{K_w}{[H^+]^2}\right)[H^+]}{1 + \frac{2K}{[H^+]}}. \tag{7.13}$$

Finally, entering Eq. (7.13) into Eq. (7.10), one obtains

$$\mathscr{F}^* = \hat{\rho} \frac{\partial \bar{H}^{o*}}{\partial t^*} = \bar{H}^* \left(k'_- [Ca^{2+}] + k_0 [H^+] - k_+ \mathscr{H} [CO_2]_\infty \right), \tag{7.14}$$

where $k'_- = 2k_-/(1 + 2K/[H^+])$ and $k_0 = (1 - K_w/[H^+]^2) k_-/(1 + 2K/[H^+])$. Equation (7.14) can

[2] The concentrations of chemical species, [■], are for instance given in mol/m^3.

be rewritten in the more intuitive form

$$\mathscr{F}^* = \hat{\rho}\frac{\partial \bar{H}^{o*}}{\partial t^*} = \bar{H}^* k'_- \left([\mathrm{Ca}^{2+}] - [\mathrm{Ca}^{2+}]_{\mathrm{sat}}\right), \tag{7.15}$$

where $[\mathrm{Ca}^{2+}]_{\mathrm{sat}} = \frac{k_+}{k'_-}\mathscr{H}[\mathrm{CO}_2]_\infty - \frac{k_0}{k'_-}[\mathrm{H}^+]$ is the concentration at saturation (Short et al., 2005*b*). The constants k_+, k'_- and k_0 depend on the concentrations $[\mathrm{H}^+]$ and $[\mathrm{OH}^-]$ and thus on the pH of the solution. However, it can be assumed that these concentrations do not vary significantly during the water journey along a cave (Short et al., 2005*b*). Therefore, the deposition only depends on the difference between the amount of calcium dissolved in the water when flowing in the soil and the saturation concentration $[\mathrm{Ca}^{2+}]_{\mathrm{sat}}$, which depends also on the partial pressure of CO_2 in the cave. The larger the difference of the concentration $[\mathrm{Ca}^{2+}]$ to the saturation value and the thicker the liquid film, the larger the deposition rate.

The law for the deposition can therefore be written as

$$\frac{\partial \bar{H}^{o*}}{\partial t^*} = \bar{H}^* C^*, \tag{7.16}$$

where $C^* = k'_- \left([\mathrm{Ca}^{2+}] - [\mathrm{Ca}^{2+}]_{\mathrm{sat}}\right)/\hat{\rho}$ is the chemistry-dependent constant, of the order of 10^{-7} s^{-1} for typical karst environments (Short et al., 2005*b*; Camporeale, 2015). Using H_i^* as characteristic length and the Rayleigh-Taylor instability time $\tau' = \mu\ell_c^{*4}/(\gamma H_i^{*3})$ of the order of 10^3 s as characteristic time, the dimensionless deposition constant C is typically 10^{-4} and the deposition law reads

$$\frac{\partial \bar{H}^o}{\partial t'} = \bar{H}C. \tag{7.17}$$

Note that since the characteristic time used for the adimensionalization of the lubrication equation for the thin-film flow under an inclined plane is $\tau = \mu\ell_c^{*4}/(\gamma H_i^{*3}\sin^2\phi)$ and depends therefore on the inclination angle ϕ, the dimensionless deposition law with this characteristic time becomes

$$\frac{\partial \bar{H}^o}{\partial t} = \bar{H}\tilde{C} \tag{7.18}$$

where the deposition constant in the dimensionless time scale of the flow under an inclined plane is

$$\tilde{C} = \frac{C}{\sin^2\phi}. \tag{7.19}$$

Finally, it has to be mentioned that a law similar to Eq. (7.18) can be derived for the ice growth in the context of ice formations; the constant $\tilde{C}$ will then depend on thermal properties and on the ambient conditions (Short et al., 2006).

7.3 Thin-film flow under an inclined plane coupled to the deposition process

7.3.1 Linear stability analysis

The liquid film thickness is decomposed as

$$\bar{H}(x,y,t) = H + \varepsilon h(x,y,t) \quad , \quad \varepsilon \ll 1 \tag{7.20}$$

where the base-state solution H is unity due to adimensionalization and the perturbations are small, $\varepsilon h \ll 1$. On the other hand, the substrate thickness is decomposed as

$$\bar{H}^o(x,y,t) = H^o + \varepsilon h^o(x,y,t) = \varepsilon h^o(x,y,t) \quad , \quad \varepsilon \ll 1 \tag{7.21}$$

since the base-state solution for the substrate thickness is zero, $H^o = 0$ (see Fig. 7.3).

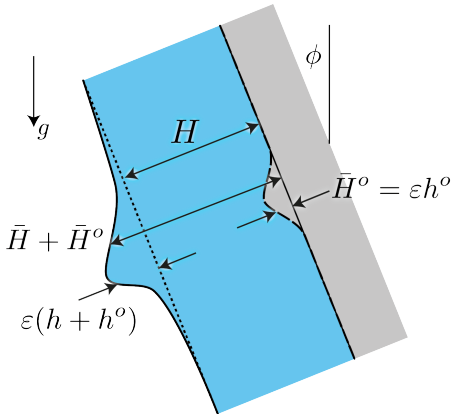

Figure 7.3 – Sketch of the decomposition of the liquid film thickness $\bar{H}$ and the substrate perturbations $\bar{H}^o$.

The disturbance equations for the first order perturbations h and h^o are obtained by linearizing the lubrication equation (7.2) and the deposition law (7.18):

$$\frac{\partial h}{\partial t} + \frac{1}{3}\nabla\cdot\left\{ \begin{bmatrix} h_{xxx} + h^o_{xxx} + h_{xyy} + h^o_{xyy} \\ h_{xxy} + h^o_{xxy} + h_{yyy} + h^o_{yyy} \end{bmatrix} + \begin{bmatrix} -\cot\phi\,\frac{1}{\tilde{\ell}_c} h^o_{xx} + h_x \\ -\cot\phi\,\frac{1}{\tilde{\ell}_c} h^o_{xy} + h_y \end{bmatrix} + 3h \begin{bmatrix} \cot\phi\,\tilde{\ell}_c \\ 0 \end{bmatrix} + \begin{bmatrix} h^o_x \\ h^o_y \end{bmatrix} \right\} = 0, \tag{7.22}$$

$$\frac{\partial h^o}{\partial t} = h\tilde{C}. \tag{7.23}$$

Furthermore, we assume harmonic perturbations of wavenumber $\alpha \in \mathbb{R}$ and $\beta \in \mathbb{R}$ in the streamwise and spanwise directions, respectively, in a periodic domain. The normal mode ansatz reads:

$$\begin{bmatrix} h \\ h^o \end{bmatrix}(x,y,t) = \begin{bmatrix} \hat{h} \\ \hat{h^o} \end{bmatrix} \exp\left[\mathrm{i}(\alpha x + \beta y - \omega t)\right] + c.c., \tag{7.24}$$

where $\omega \in \mathbb{C}$ is the eigenvalue of the coupled problem, whose imaginary part ω_i is the growth rate and ω_r is the angular frequency of the mode $\mathbf{k} = \alpha \mathbf{e}_x + \beta \mathbf{e}_y$.

The dispersion relation relating ω to the wavenumbers α and β for the coupled hydrodynamic-deposition problem is obtained by entering the normal mode ansatz (7.24) into the linear disturbance equations (7.22) and (7.23):

$$\omega^C(\alpha,\beta,\tilde{\ell}_c,\phi,\tilde{C}) = \frac{\omega^H}{2} \pm \sqrt{\left(\frac{\omega^H}{2}\right)^2 + 12\tilde{C}\left[-(\alpha^2+\beta^2)(1-\alpha^2-\beta^2) + \frac{\mathrm{i}}{\tilde{\ell}_c}(\alpha^2+\beta^2)\alpha\cot\phi\right]}, \tag{7.25}$$

where $\omega^H = \omega^H(\alpha,\beta,\tilde{\ell}_c,\phi)$ is the dispersion relation for the pure hydrodynamic problem without deposition (Brun et al., 2015; Scheid et al., 2016):

$$\omega^H(\alpha,\beta,\tilde{\ell}_c,\phi) = \tilde{\ell}_c \alpha \cot\phi + \frac{\mathrm{i}}{3}(\alpha^2+\beta^2)(1-\alpha^2-\beta^2). \tag{7.26}$$

Note that the dispersion relation (7.26) presents an isotropic growth rate, meaning that there is no preferential direction for the growth of linear perturbations of the pure hydrodynamic problem. The real angular frequency is a direct result of the flow advection in the x direction.

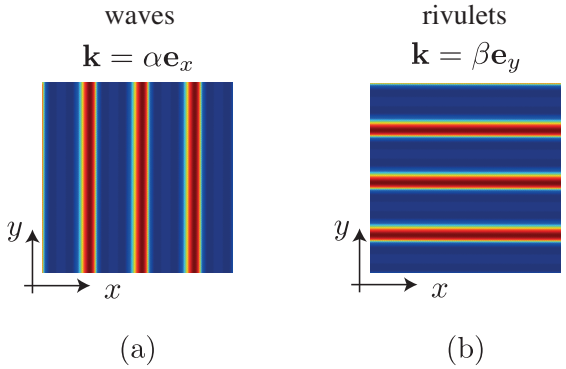

Figure 7.4 – Sketch of waves (a) and rivulets (b).

The isotropic growth rate is broken as soon as the flow advection is coupled to the deposition process. The growth rate ω_i^C for typical cave conditions is shown in Fig. 7.5. The spanwise perturbations, denoted hereafter as *rivulets* (see Fig. 7.4(b)), experience a larger growth than the streamwise perturbations, called *waves* (see Fig. 7.4(a)), due to the calcium carbonate

deposition. This can be understood by keeping in mind that the deposition is proportional to the film thickness. On the one hand, the stationary rivulets experience a positive coupling with the substrate, deposing always at the same location. On the other hand, liquid waves are advected by the draining flow, depositing calcium carbonate along their trajectory, resulting in a less favorable fluid-solid coupling, at least for these parameters. However, as we will discover in the following, there are also parameter ranges for which rivulets are not the most amplified pattern. The small deposition constant $C \sim 10^{-4}$ results in a small difference in the growth

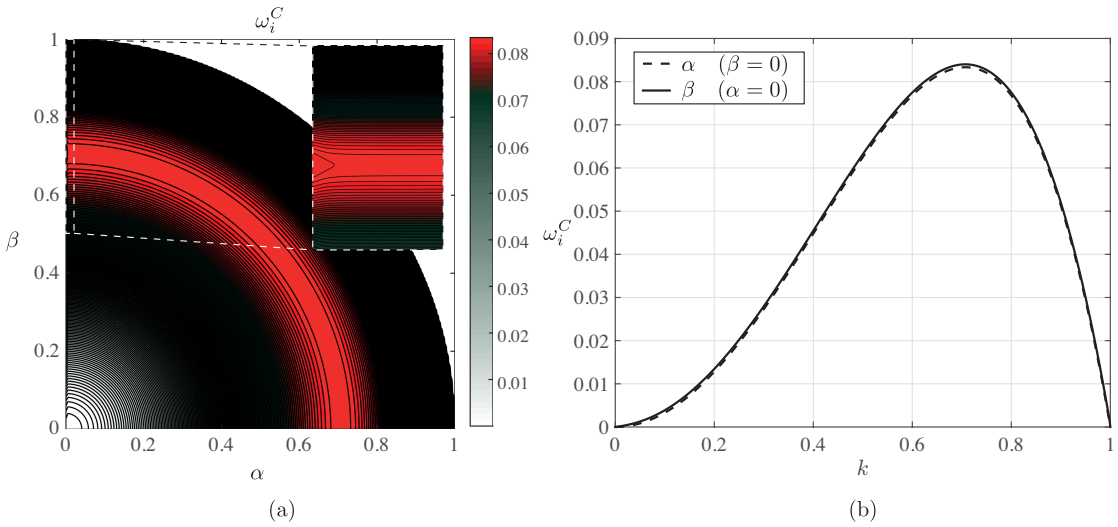

Figure 7.5 – (a) Growth rate as a function of the wavenumbers for typical cave conditions. (b) Growth rate for pure waves $\mathbf{k} = \alpha \mathbf{e}_x$ ($\beta = 0$) and rivulets $\mathbf{k} = \beta \mathbf{e}_y$ ($\alpha = 0$). $\ell_c = 270$, $C = 10^{-4}$ and $\phi = \pi/8$.

rates of these two structures, yet it is essential to the dominance of one pattern over the other. If no deposition is assumed, perturbations grow isotropically in all directions, see Eq. (7.26).

Increasing the deposition constant, or reducing the inclination angle ϕ, as can be deduced from Eq. (7.19), enhances the linear growth of rivulets (see Fig. 7.6(a)), whereas reducing the dimensionless capillary length to values smaller than the film thickness promotes the formation of waves rather than rivulets (see Fig. 7.6(b)). Note that the deposition modifies the dominant wavelength and the cutoff wavelength of waves, shifting it to smaller values, whereas it does not affect the one of rivulets.

The present model is therefore able to predict the dominance of rivulets or waves depending on the chosen parameters (see Fig. 7.7). Rivulets are responsible for the morphogenesis of the longitudinal flute and drapery structures, whereas waves result in ripples, also called crenulations by speleologists (see Fig. 7.1). However, waves occur only for small capillary length over film thickness ratios, when the theory of Sec. 7.2.2 should be corrected to account for the nonuniform diffusion of carbon dioxide in the thicker film (Camporeale, 2017). In the literature, the predominance of waves on rivulets is attributed to inertial effects (Bertagni & Camporeale, 2017). Note that for large deposition constants, a mixed mode $\mathbf{k} = \alpha \mathbf{e}_x + \beta \mathbf{e}_y$ is

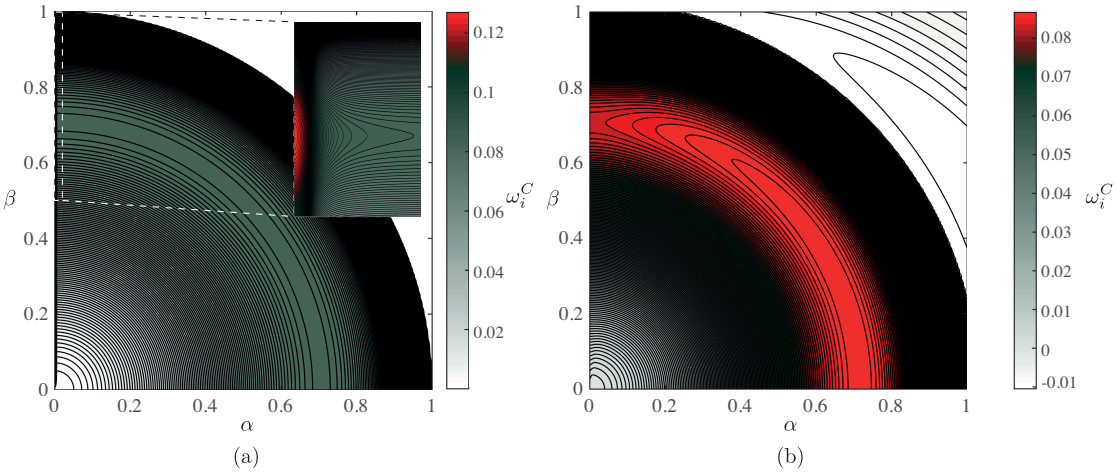

Figure 7.6 – Effect of the deposition constant (a) and dimensionless capillary length (b) on the growth rate as a function of the wavenumbers. (a) $\ell_c = 270$, $C = 10^{-2}$ and $\phi = \pi/8$; (b) $\ell_c = 0.1$, $C = 10^{-4}$ and $\phi = \pi/8$.

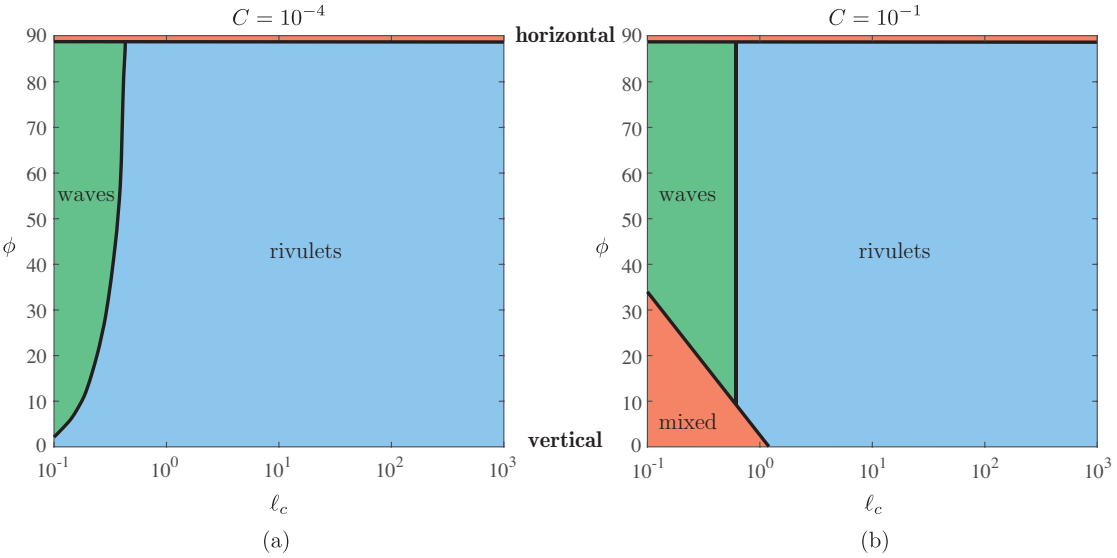

Figure 7.7 – Phase diagram indicating the most amplified pattern as a function of the dimensionless capillary length $\ell_c = \ell_c^* / H_i^*$ and inclination angle ϕ for a deposition constant $C = 10^{-4}$ (a) and $C = 10^{-1}$ (b). Rivulets form in the blue region, waves in the green one and a mixed mode in the red one. The phase diagrams have been obtained by performing a parametric study for several ℓ_c and ϕ values and looking at the wavenumber $\mathbf{k} = \alpha \mathbf{e}_x + \beta \mathbf{e}_y$ with the largest growth rate. The boundaries between the domains have been obtained by linear interpolation. Waves correspond to a larger growth of a mode with $\beta = 0$, rivulets to a mode with $\alpha = 0$ and the mixed regime to a most amplified mode with $\alpha \neq 0$ and $\beta \neq 0$. Physically relevant values of ℓ_c observed in caves are between 10^2 and 10^3.

found to be the most amplified at small capillary lengths ℓ_c and small inclination angles ϕ (see Fig. 7.7(b)). The wavenumber of these mixed mode is found to increase with decreasing

angle ϕ. Furthermore, it has to be mentioned that an isotropic mixed mode arises for $\phi = \pi/2$ and any deposition constant C when the plane is horizontal and there is no advection.

For physically relevant parameters observed in cave environments, rivulets dominate as they experience a stronger linear growth. The thin film flowing under the inclined plane is modulated in the spanwise direction and, following the deposition law (7.18), parallel karst structures aligned with the flow form. The dimensional spacing between these structures predicted by the present linear stability theory reads

$$\lambda^*_{\beta_{\max}} = \frac{2\pi\sqrt{2}\ell_c^*}{\sqrt{\sin\phi}}, \tag{7.27}$$

ranging from the classical Rayleigh-Taylor spacing $2\pi\sqrt{2}\ell_c^*$ (Fermigier et al., 1992) to infinity when the inclination of the plate is increased from $\phi = \pi/2$ to $\phi = 0$. We will discuss the limitation of this prediction in Sec. 7.5.1.

In the literature, a more involved analysis has been performed to essentially obtain the same result (Camporeale, 2015; Bertagni & Camporeale, 2017). Equation (7.27) can be used to explain the typical spacing observed in karst structures formed along a cave wall. However, as visible in Fig. 7.1, the spacing between the flutes is not constant in space. The reason for this nonparallelism will be explained in Sec. 7.4.

7.3.2 Spatio-temporal analysis

Before turning our attention to the morphogenesis of some typical speleothems, we undertake here a spatio-temporal analysis of the flow under an inclined plane. We believe that such an analysis is able to shed light on the key mechanisms at the origin of these structures and the pattern selection, as it has already been the case for the pure hydrodynamic problem, where an absolute instability has been shown to be related to the dripping phenomena under an inclined plane (Brun et al., 2015; Scheid et al., 2016).

The spatio-temporal properties are given by the impulse response, which can be computed either analytically or numerically (Huerre, 2000). The second approach is employed hereafter. The uniform draining flow $H = 1$ and the substrate $H^o = 0$ are initially perturbed by a Gaussian-shaped disturbance:

$$\varepsilon h(x,y,0) = \varepsilon h^o(x,y,0) = \varepsilon \exp\left[-\frac{(x-x_0)^2}{2}\right] \exp\left[-\frac{(y-y_0)^2}{2}\right] \tag{7.28}$$

of amplitude $\varepsilon = 10^{-3}$. The linear evolution of the perturbations is given by Eqs. (7.22) and (7.23), whereas the nonlinear one by Eqs. (7.2) and (7.18). Both the cases without and with deposition are considered. In the former case, no substrate perturbations are considered: $\varepsilon h^o(x,y,0) = 0$.

Linear impulse response without deposition

The linear impulse response without deposition for two inclination angles in the laboratory frame is shown in Fig. 7.8. For small inclination angles ϕ, when the advection is strong, the

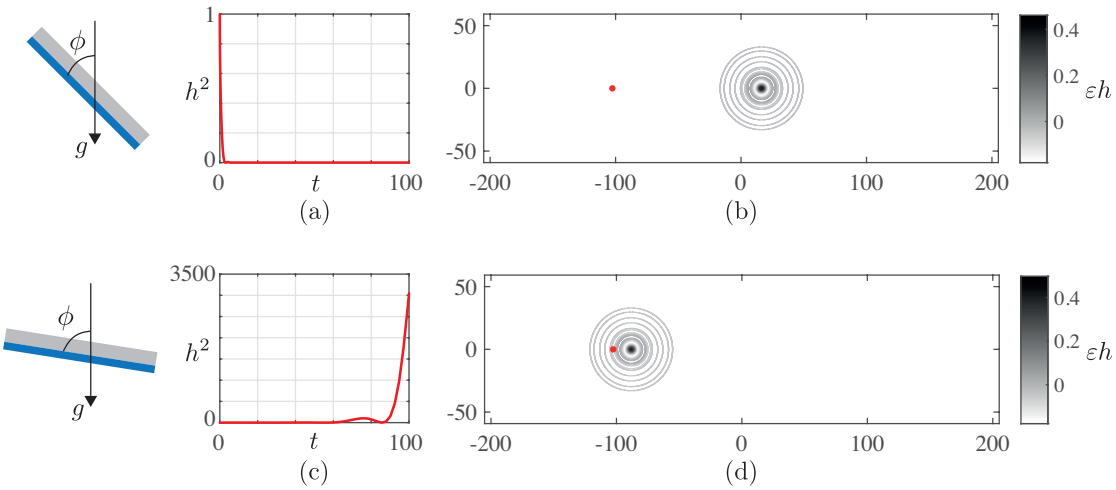

Figure 7.8 – Linear impulse response without deposition for the film thickness h at $t = 100$. (a,b) $\phi = \pi/4$, $\ell_c = 1$; (c,d) $\phi = \pi/2.2$, $\ell_c = 1$. Red point in panels (b,c) indicates the initial perturbation, of amplitude $\varepsilon = 10^{-3}$, whose temporal evolution is shown in panels (a) and (c). $C = 0$. Note that the same dimensionless time corresponds to different dimensional times.

growing impulse response travels downstream faster than it spreads across the flow and the most upstream location of the perturbed wavepacket has a positive front velocity (see Fig. 7.8(b)). As a consequence, the perturbation at the source point decreases with time (see Fig. 7.8(a)), and it eventually does so at any point in space. This type of instability is named *convective* (Huerre & Monkewitz, 1985).
Conversely, the wavepacket grows exponentially at the source point for large inclination angles ϕ, when the advection is weak. The upstream and downstream front velocities have opposite signs and the instability contaminates the entire domain. This type of instability is called *absolute* (Huerre & Monkewitz, 1985).
Absolute and convective instabilities can be distinguished by the absolute growth rate $\omega_{0,i} = \omega_i(k_0)$ of the mode with zero group velocity k_0 that corresponds to a saddle point of the dispersion relation in the complex-wavenumber plane (see Chapter 1)

$$\frac{\partial \omega_i}{\partial k_i} = \frac{\partial \omega_i}{\partial k_r} = 0. \tag{7.29}$$

If $\omega_{0,i} < 0$ the instability is convective, whereas if $\omega_{0,i} > 0$ the instability is absolute.

Another important result evidenced in Fig. 7.8 is the isotropy of the impulse response. In the frame of reference moving with the wavepacket, perturbations in the streamwise and spanwise directions grow equally. This is in agreement with the fact that the growth rate of α and β disturbances without deposition, and in absence of inertial or extensional viscous stresses

(Scheid et al., 2016), is identical, see Eq. (7.26). A one-dimensional spatio-temporal analysis is therefore sufficient to find the absolute/convective transition $\omega_{0,i} = 0$ and the resulting wavenumber $k_0 = \alpha_0$ will set the spanwise wavenumber β_0.

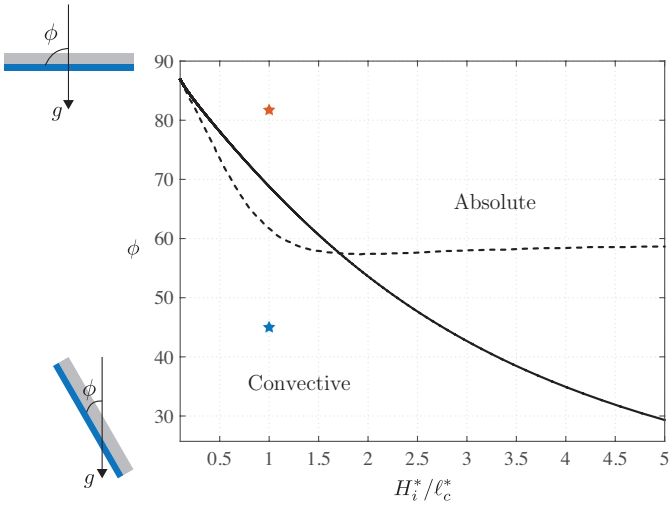

Figure 7.9 – Absolute marginal instability curve of the flow under an inclined plane. The solid line corresponds to the critical conditions for the transition form a convective to an absolute instability using the theory of this chapter, whereas the dashed line corresponds to the transition obtained by including extensional viscous stresses (Scheid et al., 2016). Symbols correspond to the parameters of Fig. 7.8. $C = 0$.

The state diagram for the flow under the inclined plane as a function of the ratio H_i^*/ℓ_c^* and the inclination angle ϕ is shown in Fig. 7.9 (Brun et al., 2015). The flow is absolutely unstable for large angles ϕ and thick films, whereas it is convectively unstable when the plane is close to the vertical and the film is thin. Scheid et al. (2016) considered also the extensional viscous stresses, which have to be taken into account at the successive order of the lubrication approach, and extended this analysis to the inertial regime, showing that a critical inclination angle exists below which the flow is always convectively unstable (see dashed line in Fig. 7.9).

Linear impulse response with deposition

The linear impulse response for a deposition-rate constant of $C = 0.01$ and the same inclination angles as in Fig. 7.8 is shown in Fig. 7.10. Strikingly, the results are very different than the ones without deposition. The linearly growing film-thickness perturbations are 'engraved' on the substrate while traveling downstream. For the convectively unstable case of Fig. 7.10(a,b), the perturbed wedge is clearly visible on the substrate perturbations εh^o. As a result, the film-thickness wavepacket is no longer isotropic, but rivulets are clearly visible at its rear half. Interestingly, the wavelength of these rivulets is found to be set by the one of the streamwise perturbations, since the front half of the wavepacket remains isotropic. On the other hand, for the absolutely unstable case of Fig. 7.10(c,d), the wavepacket grows almost in situ due to the small advection, limiting the formation of rivulets and resulting in a rather isotropic response.

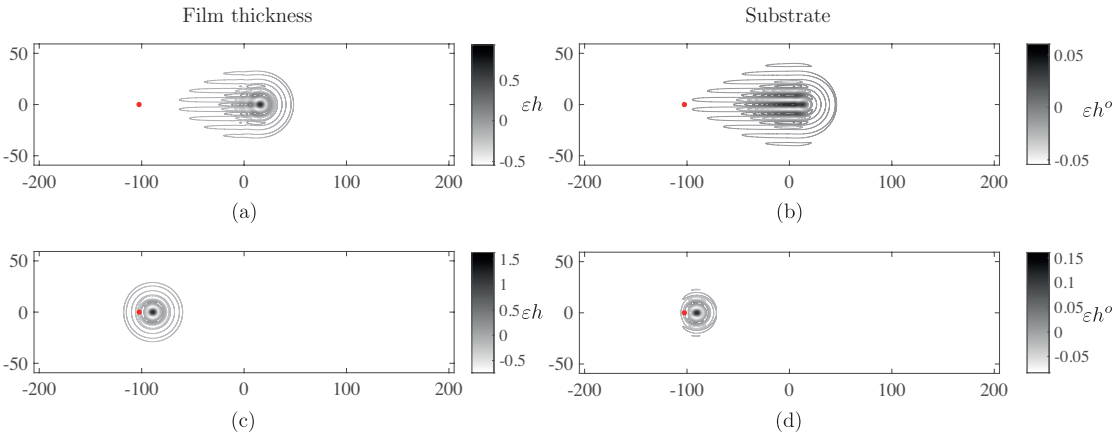

Figure 7.10 – Linear impulse response with deposition for the film thickness h (a,c) and substrate thickness h^o (b,d). (a,b) $\phi = \pi/4$, $\ell_c = 1$; (c,d) $\phi = \pi/2.2$, $\ell_c = 1$. Red point indicates the initial perturbation, of amplitude $\varepsilon = 10^{-3}$. $C = 0.01$, $t = 100$.

Based on this very simple result, one can understand why draperies form on the inclined parts of cave ceilings, whereas stalactites are more abundant where the ceiling is rather horizontal.

Nonlinear impulse response without deposition

The analysis has been, so far, based on the linear dynamics of the perturbations. However, as soon as the perturbation amplitude becomes of the order of the base flow – and thus of order 1 – nonlinear effects have to be taken into account.

The nonlinear impulse response for the pure hydrodynamic problem at the same time as for the linear one of Fig. 7.8 is shown in Fig. 7.11(a,c). In contrast to the linear impulse response without deposition, the nonlinear one is anisotropic. More precisely, the anisotropy becomes more and more significant as the advection is increased (compare Figs. 7.11(c,d) to Figs. 7.11(a,b)), or as the time passes, when the largest film thickness corresponding to the rivulets or sliding droplets increases (see Fig. 7.11(b,d)). The rationale for the anisotropic dynamics is the nonuniform advection of the perturbations if nonlinear effects are considered. As visible in Eq. (7.2), the mobility of the perturbations is $\bar{H}^3$ (see also Chapters 5 and 6): thick single droplets, or rivulets, travel faster and overtake the linearly isotropically growing smaller amplitude perturbations surrounding them, resulting in a 'lyre'-shaped pattern (see Fig. 7.11(b)). Hence, the nonlinear effects of the pure hydrodynamic problem promote a pattern $\mathbf{k} = \beta \mathbf{e}_y$, similarly to the most amplified pattern found for the linear coupled hydrodynamic-deposition problem (see Fig. 7.5). A detailed description of the hydrodynamic nonlinear mechanism at the origin of this pattern selection follows in Sec. 7.3.3.

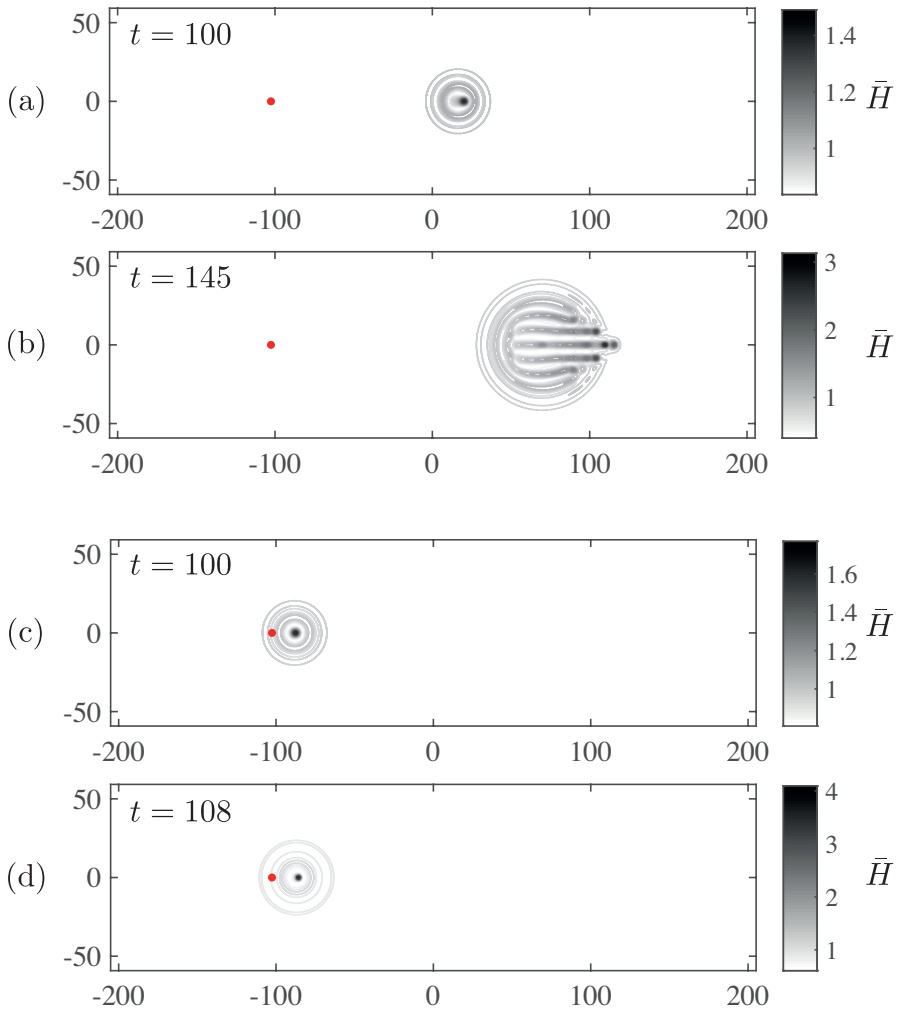

Figure 7.11 – Nonlinear impulse response without deposition for the film thickness $\bar{H}$. (a,b) $\phi = \pi/4$, $\ell_c = 1$; (c,d) $\phi = \pi/2.2$, $\ell_c = 1$. Red point indicates the initial perturbation, of amplitude $\varepsilon = 10^{-3}$. $C = 0$.

Nonlinear impulse response with deposition

To complete the present spatio-temporal analysis, the impulse response considering nonlinear effects as well as deposition is shown in Fig. 7.12. As already observed in Fig. 7.10, deposition is responsible for the rivulets' formation at the rear half of the impulse response, whereas nonlinear effects result in a faster advection of the thicker region and modify thus the front half, as evidenced in Fig. 7.11. When the plane is close to the vertical, the substrate perturbations clearly assume a longitudinal structure, whereas when the plane is close to the horizontal, the perturbation is rather isotropic and localized close to the perturbation point.

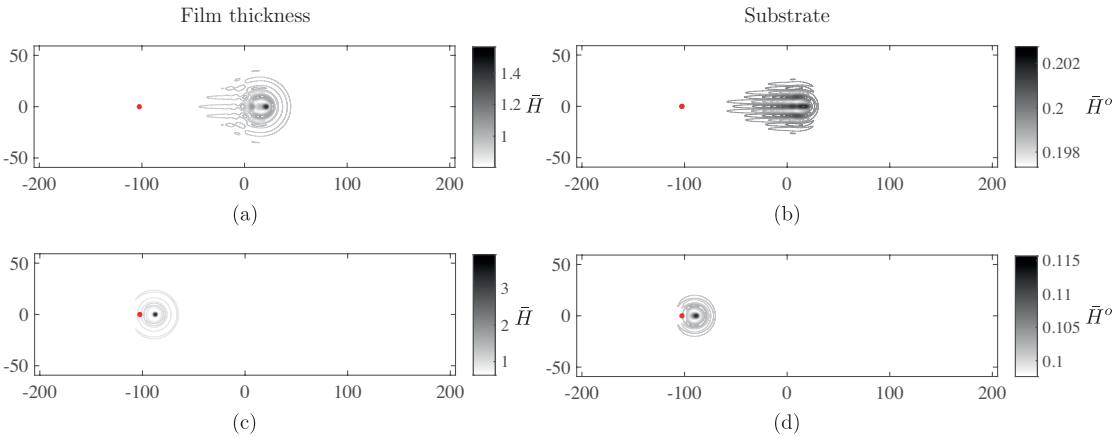

Figure 7.12 – Nonlinear impulse response with deposition for the film thickness $\bar{H}$ (a,c) and substrate thickness $\bar{H}^o$ (b,d). (a,b) $\phi = \pi/4$, $\ell_c = 1$; (c,d) $\phi = \pi/2.2$, $\ell_c = 1$. Red point indicates the initial perturbation, of amplitude $\varepsilon = 10^{-3}$. $C = 0.001$, $t = 100$.

7.3.3 Nonlinear selection of rivulets

We have seen in Fig. 7.11 that nonlinear effects promote the formation of an anisotropic pattern composed by rivulets. Together with Gaétan Lerisson, we have recently verified experimentally that rivulets are indeed the arising pattern for this flow when inertia is negligible (see Fig. 7.13). This complements the findings of Rietz et al. (2017) and Charogiannis, Denner, van Wachem, Kalliadasis, Scheid & Markides (2018), who showed experimentally that rivulets occur following a destabilization of inertia-induced waves, firstly formed due to the Kapitza instability.

The aim of this section is to propose a nonlinear mechanism which explains the dominance of rivulets over waves. For the sake of simplicity, we consider one-dimensional waves ($\mathbf{k} = \alpha \mathbf{e}_x$) or one-dimensional rivulets ($\mathbf{k} = \beta \mathbf{e}_y$), invariant in the spanwise or streamwise direction, respectively (see Fig. 7.4). The nonlinear lubrication equation (7.2) simplifies to

$$\frac{\partial \bar{H}}{\partial t} + \frac{1}{3}\frac{\partial}{\partial x}\left[\bar{H}^3\left(\bar{\kappa}_x + \bar{H}_x + \cot\phi\tilde{\ell}_c\right)\right] = 0 \tag{7.30}$$

for waves and to

$$\frac{\partial \bar{H}}{\partial t} + \frac{1}{3}\frac{\partial}{\partial y}\left[\bar{H}^3\left(\bar{\kappa}_y + \bar{H}_y\right)\right] = 0 \tag{7.31}$$

for rivulets. One can observe that the only difference between the governing equation for waves and rivulets is the advection term $\bar{H}^3 \cot\phi\tilde{\ell}_c$ in the flux of Eq. (7.30). Let us consider the evolution of these one-dimensional perturbations subjected to the same initial condition, where the most amplified wavenumber $1/\sqrt{2}$ of the dispersion relation (7.26) is employed. As can be seen in Fig. 7.14, waves and rivulets initially experience the same Rayleigh-Taylor-induced growth since the dynamics for small disturbance amplitudes is linear and the linear

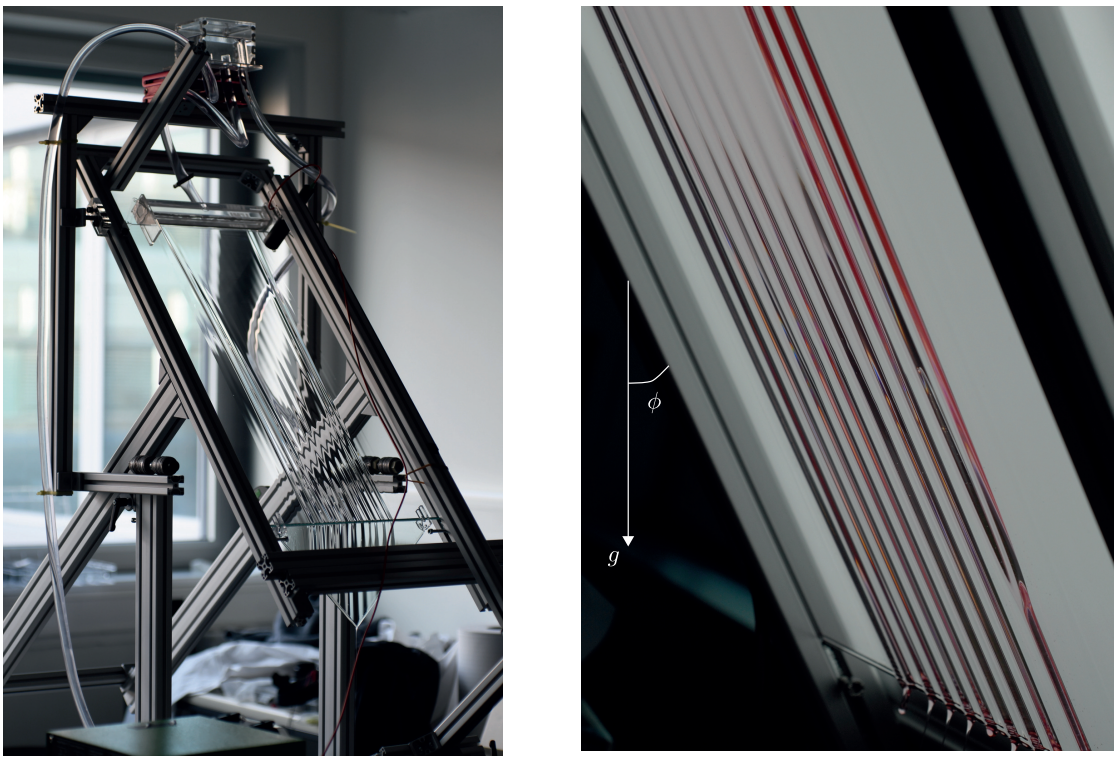

Figure 7.13 – (a) Experimental setup and (b) experimentally observed rivulets. Credits: Gaétan Lerisson, LFMI.

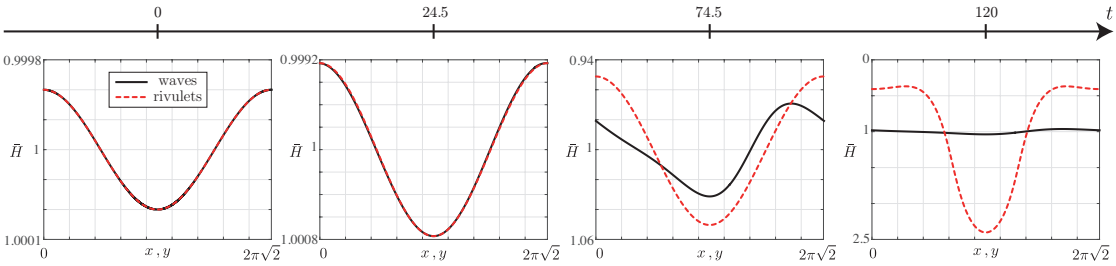

Figure 7.14 – Nonlinear evolution of the film thickness of one-dimensional waves (black solid line) or one-dimensional rivulets (red dashed line) for an initial disturbance amplitude $\varepsilon = 10^{-4}$ and an optimal wavelength of $2\pi\sqrt{2}$. Waves are followed in their moving reference frame for ease of comparison. $\phi = \pi/8$, $\tilde{\ell}_c = 4.4$ and $C = 0$. Important note: the scale of the ordinates changes in time for visualization purposes.

growth rate is isotropic, see Eq. (7.26). The linearized advection term for waves is responsible for the transport of the growing wavepacket with the flow, but it does not impact the growth rate (see Fig. 7.8). However, as soon as the disturbance amplitude is sufficiently large, nonlinear effects are relevant. The nonlinear advection term $\bar{H}^3 \cot\phi \tilde{\ell}_c$ is of hyperbolic nature and causes the steepening of the front profile of waves (see Sec. 1.1.3), as visible for $t = 74.5$ in

Fig. 7.14. As a result, the wave profile presents stronger curvature gradients, which induce an additional capillary flow in order to reduce the interface deformations and eventually yield the saturation of the waves' amplitude. If the amplitude of waves would further increase due to the Rayleigh-Taylor instability, the advection term would steepen their profile, and the resulting capillary flow would again smooth it out, preventing from a further increase of their amplitude.

This saturation mechanism, first employed by Babchin et al. (1983) to explain the saturation of the Rayleigh-Taylor instability in the presence of flow shear, is the result of a nonlinear equilibrium between the variation of the hydrostatic pressure term, the advection term and the capillary pressure term. It combines the effect of the contraction of the x scale induced by the advection term, which increases with increasing disturbance amplitude, to the effect of the surface-tension term, which strongly increases since it contains the highest-order x derivative. The stronger the advection, the smaller the saturation amplitude, which is therefore a function of both the inclination angle ϕ and the dimensionless capillary length $\tilde{\ell}_c$.

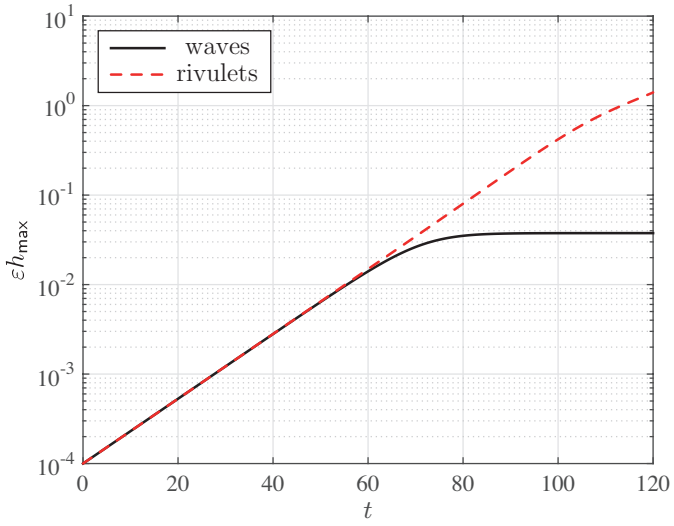

Figure 7.15 – Largest disturbance amplitude of the nonlinear evolution shown in Fig. 7.14 of the film thickness of one-dimensional waves (black solid line) or one-dimensional rivulets (red dashed line) for an initial disturbance amplitude $\varepsilon = 10^{-4}$ and an optimal wavelength of $2\pi\sqrt{2}$. $\phi = \pi/8$, $\tilde{\ell}_c = 4.4$ and $C = 0$.

Rivulets, which are not stabilized by this nonlinear mechanism, reach much larger amplitudes than waves (see Fig. 7.15). Hence, they are the dominant pattern when nonlinear effects are considered, also in the absence of deposition. The pattern anisotropy is therefore an heritage of the anisotropy of the equations. This is an additional reason explaining the dominance of longitudinal structures on inclined cave ceilings. A similar result has been found by Rost & Krug (1995) in the study of the anisotropic Kuramoto-Sivashinsky equation for surface growth and erosion.

7.4 Hydrodynamics of the thin-film flow under a curved substrate followed by an inclined plane

The shape of cave ceilings or walls is in reality more complex than an inclined plane. In particular, the local inclination angle can vary in space. In the following, we consider two types of model geometries: a concave wall followed by an inclined plane and a convex wall followed by an inclined plane (see Fig. 7.2). In the first case water flows on a substrate whose local inclination increases (ϕ decreases), while in the second case the substrate inclination decreases (ϕ increases).

Here, we are only concerned with the initial stages of the speleothem growth, when the substrate deformations are negligible and the hydrodynamics alone dictates the film-thickness profile. Due to the small value of the deposition constant C^* for typical cave environments, resulting in a separation of time scales between the hydrodynamic instability time τ and the deposition time $1/C^*$, we can assume that the deposition is solely dictated by the hydrodynamics and that there is no feedback from the substrate deformation on the hydrodynamic instability. In other words, we consider that the substrate growth would only enhance the formation of rivulets (see Sec. 7.3). However, when the substrate-topography deformations become important, typically of the order of the film thickness, the picture is different and the hydrodynamics follows the substrate perturbations. During these later stages, the liquid will mainly flow along the lowermost extremities of these structures, enhancing their growth. Since the liquid flow rate is likely to vary during the years and decades, the selected speleothem structure is an indicator of the initial stages of the flow. At a later stage, the small-topography-variation lubrication equation breaks down and one should derive new equations for a general substrate topography in a curvilinear coordinate system following the substrate deformations.

7.4.1 Base-flow solution under a curved substrate

In contrast to the uniform base flow under the inclined plane of Sec. 7.3.1, the draining base flow under a curved substrate is not constant in the streamwise direction, while it is still assumed invariant along the spanwise direction, and stationary: $H^* = H^*(\theta)$. Simplifying Eq. (7.3), the governing equation for the base flow H^* reads:

$$\frac{d}{d\theta}\left[H^{*3}\left(\ell_c^{*2}\frac{\kappa_\theta^*}{R^*}+\chi\frac{\cos\theta}{R^*}H_\theta^*+\sin\theta\right)\right]=0. \tag{7.32}$$

In the limit of small film aspect ratios $\delta = H_i^*/R^* \ll 1$ and neglecting surface-tension effects, Eq. (7.32) becomes

$$\frac{d}{d\theta}\left(H^{*3}\sin\theta\right)=0, \tag{7.33}$$

whose solution is

$$H^*(\theta) = H_m^* \left(\frac{\sin\theta_m}{\sin\theta} \right)^{1/3}. \tag{7.34}$$

The equation (7.34) diverges at $\theta = 0$ and π, where the solution should be regularized by surface-tension effects, and is therefore bounded to $\theta \in [\theta_m, \pi/2]$ or $\theta \in [\pi/2, \pi - \theta_m]$, for the concave or convex substrate, respectively, with $\theta_m > 0$ a small angle. The largest thickness is H_m^*. The base-flow solution (7.34), shown in Fig. 7.16, is in excellent agreement with the numerical resolution of the full equation (7.32) for small δ, typically of the order of 10^{-3}, except very close to θ_m.

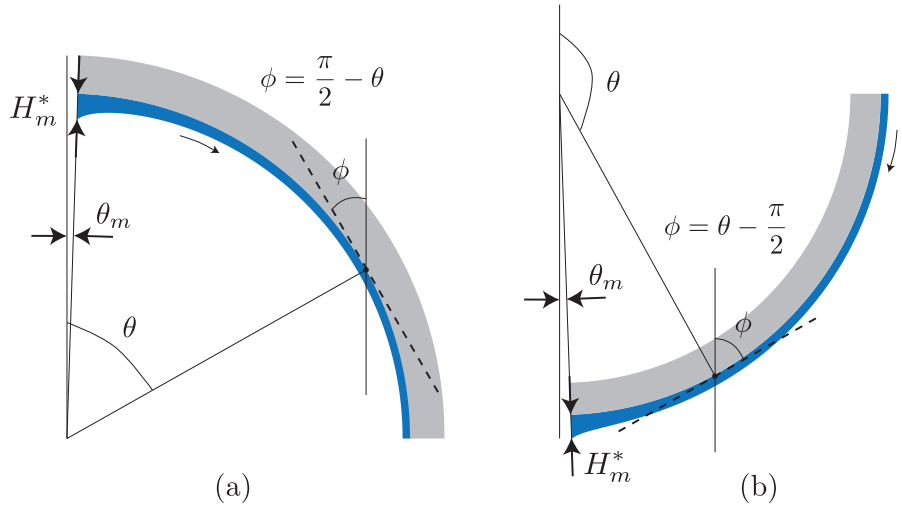

Figure 7.16 – Stationary base flow (blue) under a curved concave (a) and convex (b) substrate (grey). Magnification of film thickness 100x for visualization purposes, $\delta = 0.002$.

Note that this base-flow solution for a thin film flowing under a curved substate differs from the one used in Chapters 3 and 4, where the flow resulted from an initial release of fluid on a substrate and was therefore unstationary.

7.4.2 Linear stability analysis

Equipped with the stability analysis results for the flow under an inclined plane and the base flow profile under a curved substrate, we can perform a stability analysis for the latter flow at successive polar locations, considering the curved substrate as a collection of successive inclined planes. Such a procedure is commonly employed in hydrodynamic stability problems of spatially developing flows (Huerre & Monkewitz, 1990). The key ingredient for this analysis is the weakly nonparallel flow assumption, which implies variations of the base flow over a characteristic length much larger than the typical wavelength of the instability. In the present context, this assumption is satisfied by the small film aspect ratio δ.

The base-flow parameters are the largest film thickness H_m^* and the angle θ_m. In the following, we fix $\theta_m = 1°$ and modify the ratio H_m^*/ℓ_c^*. Given a value of H_m^*/ℓ_c^*, one can compute for each angle θ, and thus for each inclination angle ϕ, the ratio $H^*(\theta)/\ell_c^*$ (see Fig. 7.16). Following the spatio-temporal analysis of Sec. 7.3.2 (see Brun et al. (2015) for more details), the absolute or convective nature of the flow instability at the chosen angle and for the local film thickness over capillary length ratio can be determined. The loci satisfied by the base flow for different H_m^*/ℓ_c^* values are shown in the state diagram of Fig. 7.17, where the color code indicates whether the instability is absolute or convective. For a concave substrate, the film thickness is

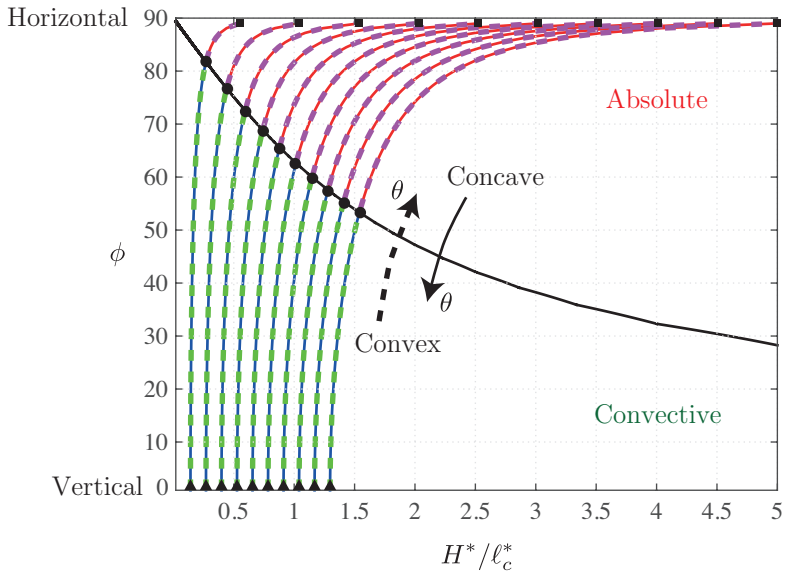

Figure 7.17 – Absolute marginal instability curve of the flow under an inclined plane with the loci satisfied by the base flow for $H_m^*/\ell_c^* = 0.55$, 1.04, 1.55, 2.03, 2.53, 3.02, 3.52, 4.01, 4.51, and 5 and $\theta_m = 1°$. Squares indicate the initial/final locus for the flow under a concave/convex substrate, whereas triangles indicate the final/initial locus for the flow under a concave/convex substrate. Full circles indicate the absolute marginal stability: for larger ϕ the flow is absolutely unstable, whereas it is convectively unstable below. If the film thickness was constant in space, as for an inclined plane, the loci $H^*(\theta)/\ell_c^*$ would be vertical lines.

initially the largest, $H^* = H_m^*$ and the angle is also the largest, $\phi = \pi/2 - \theta_m$ (see squares in Fig. 7.17). The instability is therefore absolute. For successive polar angles θ, the inclination angle ϕ decreases, and so does the film thickness (see Fig. 7.16(a)). On the other hand, the initial film thickness for a convex substrate is the smallest, and so is the inclination angle ϕ (see triangles in Fig. 7.17). The instability is therefore convective. When the polar angle is increased, the film thickness becomes thicker and thicker, and the inclination angle ϕ larger and larger (see Fig. 7.16(b)). For each value H_m^*/ℓ_c^*, which corresponds to the normalized initial or final film thickness under a concave or convex substrate, respectively, there exists therefore a critical inclination angle ϕ for the absolute/convective transition. It can be clearly seen that due to the rapid thinning of the film in the vicinity of the thickest region, the absolutely unstable domain is bounded to larger inclination angles ϕ. Since the base-flow thickness profile (7.34)

for a concave and convex substrate is the same up to a reflection of ϕ, the loci of $H^*(\phi)$ in the $(H^*/\ell_c^*, \phi)$-plane are identical, but swept in the opposite direction.

The critical inclination angles for the absolute/convective transition define the absolute marginal instability curve as a function of the ratio H_m^*/ℓ_c^*, which is shown in Fig. 7.18. For the sake of clarity, we present the phase diagrams for a concave and convex substrate separately, even if the absolute marginal curves could be plotted on the same diagram using the inclination angle ϕ rather than the polar angle θ. Compared to the absolute marginal instability

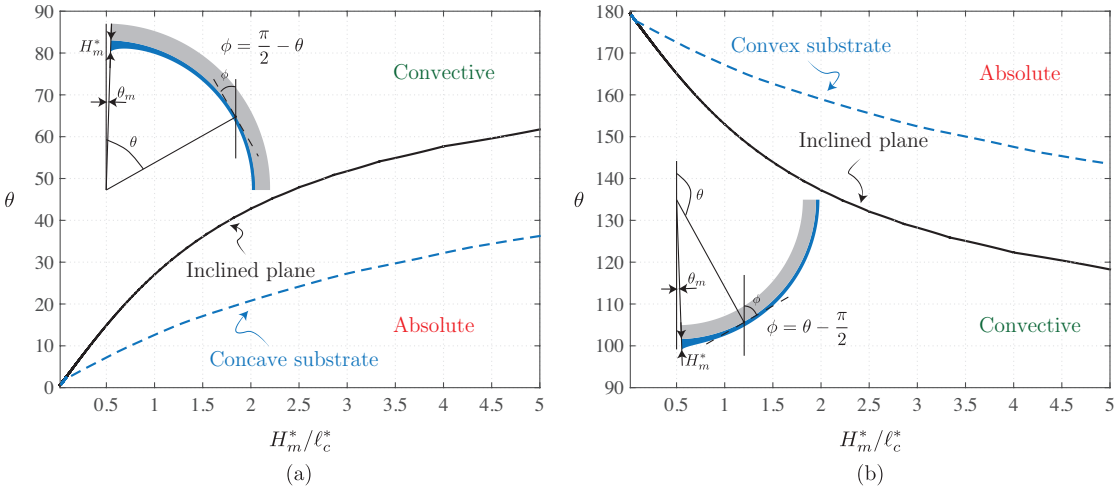

Figure 7.18 – Absolute marginal instability curve of the flow under an inclined plane (solid line) and under a curved concave (a) and convex (b) substrate with a space-dependent base flow (dashed line). H_m^* is the largest film thickness under a curved substrate and the uniform film thickness for an inclined plane. $\theta_m = 1°$. The dashed line is the collection of the circles of Fig. 7.17. For $\theta \to 0°$ or $180°$, the flow is absolutely unstable, whereas it is convectively unstable for $\theta \to 90°$.

curve for a flow under an inclined plane, the absolute marginal instability curve of the flow under a curved substrate, being it concave or convex, is bounded to a smaller sector of the curved substrate. Due to the thinning of the film in the regions where the local inclination ϕ is the smallest, which follows from mass conservation, the absolutely unstable region is also bounded to larger maximal film thickness over capillary length ratios.

Let consider now the specific case of $H_m^*/\ell_c^* = 0.37$, which corresponds to plausible cave conditions with $\ell_c^* = 2.7\,\text{mm}$ and $H_m^* = 1\,\text{mm}$. The spatial evolutions of the absolute growth rate $\omega_{0,i}$ and largest temporal growth rate $\omega_{i,\text{max}}$ are shown in Fig. 7.19(a). These quantities have been made dimensionless using the characteristic time of the Rayleigh-Taylor instability under a horizontal plane, $\tau' = \mu\ell_c^{*4}/(\gamma H_i^{*3})$. For a concave substrate, the flow is initially absolutely unstable, but it becomes convectively unstable already for $\phi < 84°$. On the other hand, for a convex substrate, the flow is initially convectively unstable and becomes absolutely unstable only for $\phi > 84°$. The largest temporal growth rate is always positive, or zero for $\phi = 0$, indicating that the flow is unstable for $\phi > 0$.

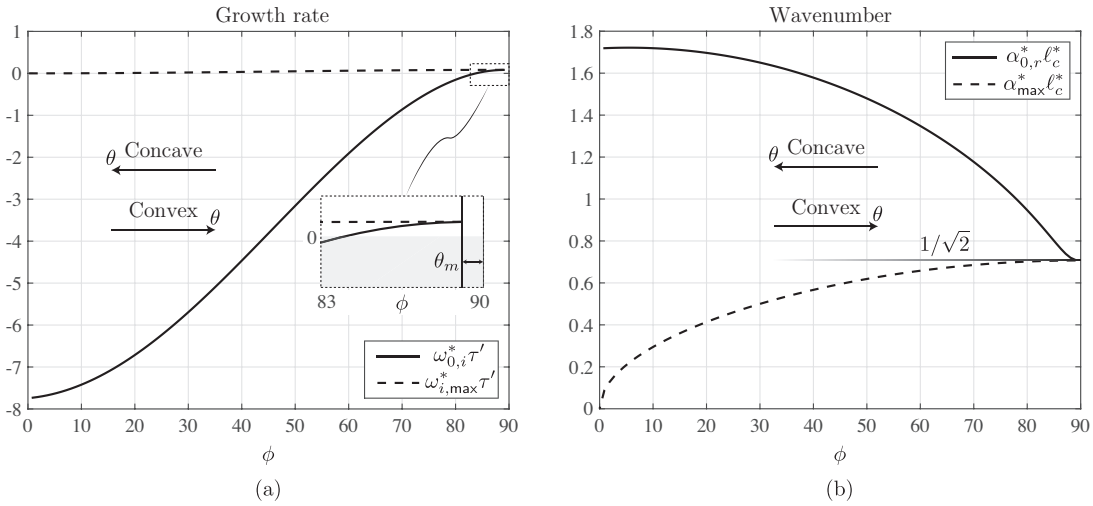

Figure 7.19 – (a) Absolute growth rate $\omega^*_{0,i}\tau'$ and largest temporal growth rate $\omega^*_{i,\max}\tau'$ and (b) corresponding absolute wavenumber $\alpha^*_{0,r}\ell^*_c$ and most amplified wavenumber $\alpha^*_{\max}\ell^*_c$ as a function of the inclination angle ϕ. $\theta_m = 1°$ and $H^*_m/\ell^*_c = 0.37$. The spatial evolution for the flow under a concave/convex substrate has to be read from right/left to left/right.

Furthermore, one can also look at the dimensionless wavenumber corresponding to the mode of zero group velocity, $\alpha_{0,r}$, as well as the wavenumber giving the largest growth, $\alpha_{\max}$ (see Fig. 7.19(b)). When the substrate is locally horizontal, $\phi = 90°$, the two wavenumbers are identical and correspond to the most amplified ones of the classical Rayleigh-Taylor instability (Fermigier et al., 1992): $\alpha_{0,r} = \alpha_{\max} = 1/\sqrt{2}$. However, the wavenumber of the mode with zero group velocity, which becomes strongly convectively unstable, increases as the inclination angle ϕ decreases, in contrast to the wavenumber giving the largest growth. The latter is known to decrease as the local inclination gets closer to the verticality, see also Eq. (7.27).

It has to be remembered that the present spatio-temporal analysis only considers the one-dimensional problem in the streamwise direction. Yet, we have seen in Sec. 7.3.2 that the linear impulse response without deposition is isotropic in space and, if deposition is considered, the wavelength of the pattern in the spanwise direction is also dictated by the wavelength in the streamwise direction. Therefore, the present results for the one-dimensional problem in the streamwise direction are assumed to describe spanwise perturbations as well. In particular, the streamwise wavenumbers $\alpha_{0,r}$ and $\alpha_{\max}$ are assumed to select the spanwise wavenumbers $\beta_{0,r}$ and $\beta_{\max}$.

At this point, one is naturally tempted to predict the global stability properties of this flow using the formalism described in Huerre & Monkewitz (1990). In fact, when a pocket of absolute instability is present at the inlet of the flow domain, which is the case for a concave substrate (see Fig. 7.19), the flow acts as an *oscillator* (Huerre & Monkewitz, 1990): it can sustain self-excited oscillations without external forcing. If the absolutely unstable region is sufficiently large, the flow is globally unstable. The global mode frequency is found to be the one of the absolute region at the inlet (Monkewitz, Huerre & Chomaz, 1993). On the other

hand, when the flow is initially convectively unstable and then absolutely unstable, which is the case for a convex substrate, the global mode frequency corresponds to the absolute frequency at the complex saddle point $\partial\omega_0/\partial X(X_s) = 0$, where X is the complex slow spatial scale (see Chomaz, Huerre & Redekopp (1991) for more details).
Following this theory, the spacing of the rivulets should therefore be dictated by the absolute wavenumber $\beta_{0,r}$ at the inlet or at the convective/absolute transition, for a concave or convex substrate, respectively.

If the angle θ_m is increased, typically above 10° for $H_m^*/\ell_c^* = 0.37$, the flow under the curved substrate is convectively unstable for all angles and no absolute unstable region is present. Convectively unstable flows act as *noise amplifiers* (Huerre & Monkewitz, 1990), so that the stability of the flow depends on the growth or decay of external perturbations.

As a follow-up work, it would be enlightening to perform such a WKBJ analysis (Bender & Orszag, 2013) for this flow, including also the effects of the substrate curvature to the local stability properties. Due to time constraints, we have rather performed numerical simulations of the nonlinear lubrication equations to unravel some typical speleothem-morphogenesis mechanisms.

7.4.3 Nonlinear simulations

As we have seen in Chapter 4, the nonlinear lubrication equation successfully predicts the thin-film dynamics and the pattern selection. Hereafter, we present numerical results obtained by solving the lubrication equation (7.3) for the flow under the curved substrate, followed by equation (7.1) for the inclined plane part, without considering the deposition of calcium carbonate at the wall.

We have found that considering the absolutely unstable region poses numerical difficulties since, as explained in Sec. 7.4.2, the flow would grow exponentially in that region, resulting in the formation of dripping droplets. The latter cannot be taken into account by the considered lubrication approach and blow up the numerical solution. Therefore, we limit the domain to the convectively unstable region and force the flow at the inlet by random noise perturbations, in order to mimic the inhomogeneous flow conditions in caves. Close to the outlet, a linear damping term $-A(x)[\bar{H}(x,y,t) - \bar{H}_0]$ as in Chomaz (2003) is added to the right hand side of the lubrication equation (7.1) to smoothen out the perturbations and apply the Dirichlet boundary condition $\bar{H}_0$ at the downstream boundary. The damping function $A(x)$ is given by (Högberg & Henningson, 1998)

$$x < x_s: \quad A(x) = 0 \tag{7.35}$$

$$x_s < x < x_x + d_r: \quad A(x) = \frac{\mathscr{A}}{1 + \exp\left(\frac{d_r}{x - x_s} + \frac{d_r}{x - x_s - d_r}\right)} \tag{7.36}$$

$$x > x_s + d_r: \quad A(x) = \mathscr{A} \tag{7.37}$$

where x_s is the starting location of the sponge, d_r the width of the ramp and $\mathscr{A}$ the damping intensity. Periodic boundary conditions are imposed in the spanwise direction.

The angle θ_c where the substrate changes from being curved to inclined (see Fig. 7.2) is chosen such that the spanwise instability wavelength at the inlet is a multiple of the one at θ_c. We consider here the rivulet wavelength predicted by the linearly most amplified mode, $\lambda^*_{\beta_{\max}}$, given by Eq. (7.27), since the flow is convectively unstable. As seen in Fig. 7.19, this wavelength would be close to the absolute one at the most unstable region.

Increasing substrate inclination

Flowstones are usually composed by an upper and a lower part (see Fig. 7.1(d,f)), connected by a rim. The flow over the upper part of a flowstone is smooth since gravity is stabilizing and the gravitational Rayleigh-Taylor instability is absent. Inertial instabilities resulting in Kapitza waves, like for the flow over an inclined plane (Kalliadasis et al., 2011; Rohlfs et al., 2017), could arise, but they can be neglected for the small observed film thicknesses and associated Reynolds number. Deposition is therefore homogeneous and the upper part of the flowstone remains smooth. In the lower part, however, water initially flows on a substrate whose inclination increases (see Fig. 7.2(c) and Fig. 1.14(a) on page 23). There, longitudinal flutes form, often coalescing together, reducing in number as the distance from the rim increases (see Fig. 7.1(f) and Fig. 7.20(a)). In the following, we will show that this pattern can be nicely reproduced and interpreted by our model.

A typical film-thickness map obtained by the numerical resolution of the lubrication equations for this geometry is shown in Fig. 7.20(b). First, it can be observed that rivulets, rather than waves, form, as discussed for Fig. 7.11. Furthermore, the present model is clearly able to reproduce the flute patterns observed in caves. Remember that the deposition would 'engrave' the hydrodynamic pattern on the substrate proportionally to the film thickness and give rise to the karst structures. Since the liquid film thickness is the largest where the substrate is the closest to the horizontal, flutes grow downwards rather than outwards, similarly to what is found for the morphogenesis of stalactites (Short et al., 2005*a*).

The norm of the film-thickness disturbances $\varepsilon h^* = \bar{H}^* - H^*$, where the base flow H^*, approximated by Eq. (7.34), is computed imposing a spanwise uniform flow and no inlet disturbances, is shown in Fig. 7.21(a). Starting from the random noise perturbations at the inlet, the perturbations rapidly grow, reaching the largest intensity in the curved substrate region. A large number of rivulets initially form. However, as shown in Fig. 7.21(b), the dominant initial wavenumber is slightly smaller than the most amplified one expected at the inlet, $\beta^*_{\text{inlet}} = \sqrt{\sin\phi_0/2}$, where the local inclination is $\phi_0 = \pi/2 - \theta_0$. The reason is the finite length necessary for the rivulets to form. Rivulets appear at a smaller inclination angle ϕ, resulting in a smaller local most amplified wavenumber (see Fig. 7.19(b)). For the same reason, the formed rivulets do not correspond to the most amplified wavelength at larger streamwise locations, reason why their amplitude decreases. We have found that the nonlinear interactions between the formed

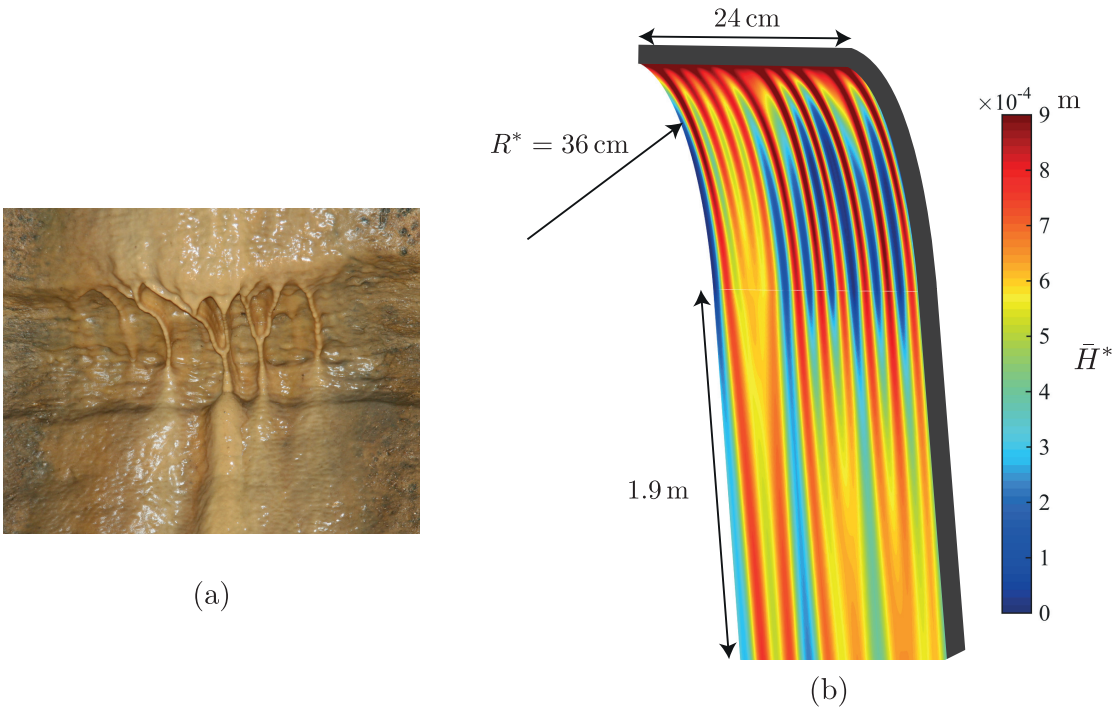

Figure 7.20 – (a) Coalescence of flutes observed in the Mystery Cave Minnesota State Park (https://en.wikipedia.org/wiki/Flowstone). The scale can be guessed considering that the thickness of a rivulet is approximatively 1 cm. (b) Film-thickness map obtained by the numerical solution of the lubrication equations. Initial angle: $\theta_0 = 10°$, inlet film thickness $H_i^* = 1$ mm, inlet random noise maximal amplitude $0.1\,H_i^*$, capillary length $\ell_c^* = 2.7$ mm, transition angle $\theta_c = 76°$, film aspect ratio $\delta = 2.8 \times 10^{-3}$, sponge parameters $\mathscr{A} = 10^3$ and $d_r = 0.3$ m. The flow can be considered as stationary since it is fed by a constant flow rate. Colorbar indicates the film thickness $\bar{H}^*$. Note that the streamwise direction of the inclined plane is rescaled by a factor 4 for visualization purposes. The film thickness in the sponge region is not shown.

rivulets and the other perturbations present in the flow result in the coalescence of the rivulets to form new structures, whose characteristic wavelength is closer to the most unstable one. When these rivulets are located on the inclined plane part, they start growing again, as visible in Fig. 7.21(a), since the inclination angle ϕ remains constant. For the case shown in Fig. 7.21, the most amplified wavenumber for the inclined plane region is one third of the one at the inlet. If only a curved substrate was considered, rivulets would continue merging, as their spacing would not be the most unstable one at further downstream locations. This coalescence cascade would probably stop once the rivulets amplitude is too weak for the nonlinear interactions to be effective. Note that the periodic boundary conditions imposed at the lateral boundaries might also affect the wavenumber selection.

To summarize, we have found that the varying local inclination of the substrate, which modifies

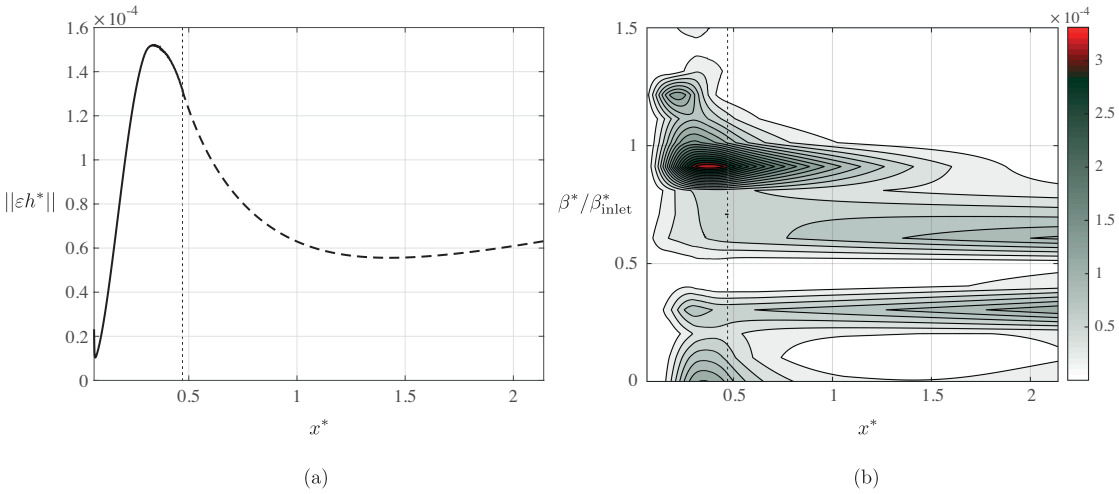

Figure 7.21 – (a) Streamwise evolution of the disturbance norm $||\varepsilon h^*||$ and (b) the most amplified spanwise wavenumber β^* with respect to the linearly most amplified one at the inlet, β^*_{inlet}, for the nonlinearly obtained flow shown in Fig. 7.20. Solid/dashed line in panel (a) corresponds to the curved/inclined part of the substrate. The transition location θ_c is indicated by a vertical dotted line.

the most amplified spanwise wavenumber as (see Secs. 7.3.1 and 7.4.2)

$$\beta^*_{\text{max}}(\phi) = \frac{\sqrt{\sin\phi}}{\sqrt{2}\ell^*_c}, \tag{7.38}$$

is at the origin of the coalescence of rivulets at successive downstream locations through nonlinear interactions. Furthermore, since the flow is the most unstable close to the inlet (see Fig. 7.19(a)), rivulets rapidly grow. Qualitatively similar results are obtained for different curvature radii R^*, disturbance amplitudes or angles θ_0 and θ_c.

Decreasing substrate inclination

Another fascinating speleothem, closely related to the previous one, are draperies (see Fig. 7.1(g)). Draperies form practically in every cave in the world (Hill & Forti, 1997) on gently sloped ceilings. Here, we consider the morphogenesis of parallel draperies, forming on a substrate whose local inclination angle ϕ increases with increasing downstream locations. As it is visible in Fig. 7.22(a), these draperies do not all form at the same location: few form more upstream while others more downstream.

An example of film-thickness map obtained by the resolution of the nonlinear lubrication equations for this geometry is shown in Fig. 7.22(b). Again, one can observe the appearance of rivulets rather than waves. However, they do not form close to the inlet, but further downstream. This is in agreement with the linear stability result of Fig. 7.19, where we have seen that the growth rate of the flow under a convex substrate is initially small. Furthermore,

since the flow is initially convectively unstable, it acts as a noise amplifier, meaning that the location where rivulets form depends on the disturbance amplitude at the inlet. The selected wavenumber corresponds to the one of the Rayleigh-Taylor instability under an inclined plane, Eq. (7.38). Only few widely spaced rivulets form first, as expected due to the small local inclination angle ϕ. However, as the inclination angle ϕ increases downstream, the most amplified wavelength of rivulets decreases and additional rivulets form due to nonlinear interactions, similarly to what is observed in Section 4.5.1. Once the region of constant inclination is reached, rivulets grow in amplitude (see Fig. 7.23(a)), but remain parallel, as observed in Fig. 7.22(a). This explains why draperies do not form at the same location and increase in number as the substrate is closer to the horizontal. The angle θ_c is chosen such that the most amplified wavenumber on the inclined plane is 1.5 times the one at the inlet, β^*_{inlet}. However, since rivulets do not form exactly at the inlet, but at a later downstream location, the initially observed most amplified wavenumber is larger and the observed wavenumber on the inclined

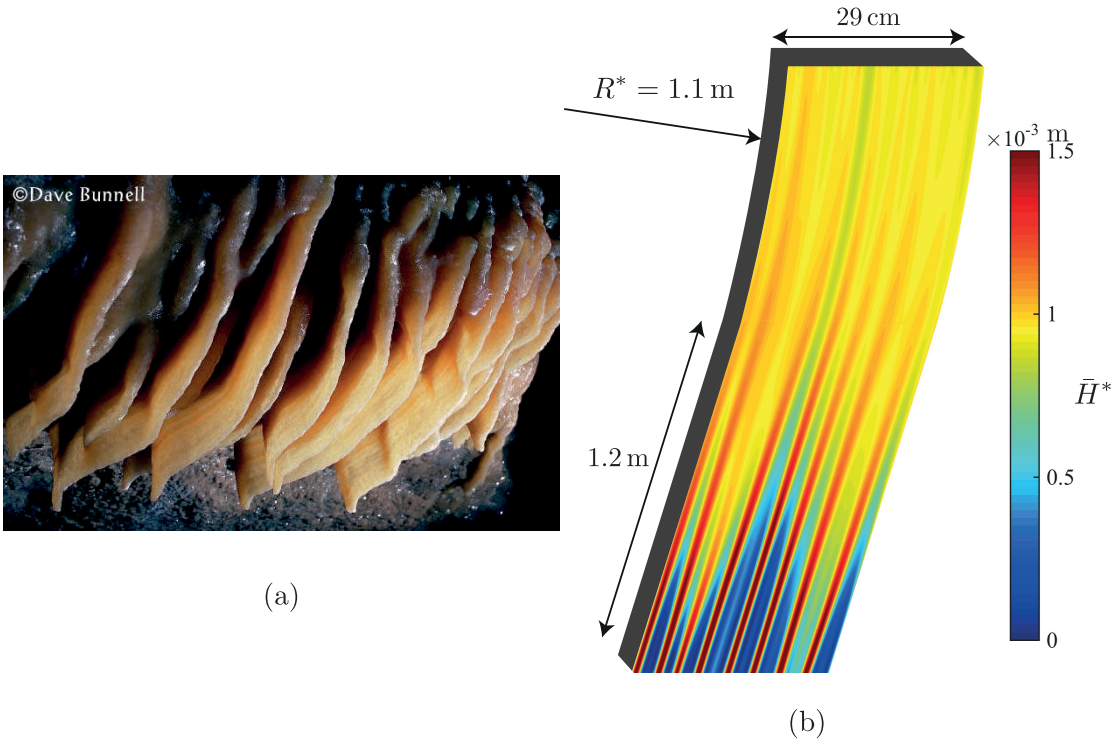

Figure 7.22 – (a) Parallel draperies (photo credits: Dave Bunnell http://www.goodearthgraphics.com/virtcave/drapery/drapery.html). The scale can be guessed considering that the thickness of a rivulet is approximatively 1 cm. (b) Film-thickness map obtained by the numerical solution of the lubrication equations. Initial angle: $\theta_0 = 104°$, inlet film thickness $H_i^* = 0.9$ mm, inlet random noise maximal amplitude $0.1H_i^*$, capillary length $\ell_c^* = 2.7$ mm, transition angle $\theta_c = 123°$, film aspect ratio $\delta = 9 \times 10^{-4}$, sponge parameters $\mathscr{A} = 10^3$ and $d_r = 0.2$ m. The flow can be considered as stationary since it is fed by a constant flow rate. Colorbar indicates the film thickness $\bar{H}^*$. Note that the streamwise direction of the inclined plane is rescaled by a factor 2 for visualization purposes. The film thickness in the sponge region is not shown.

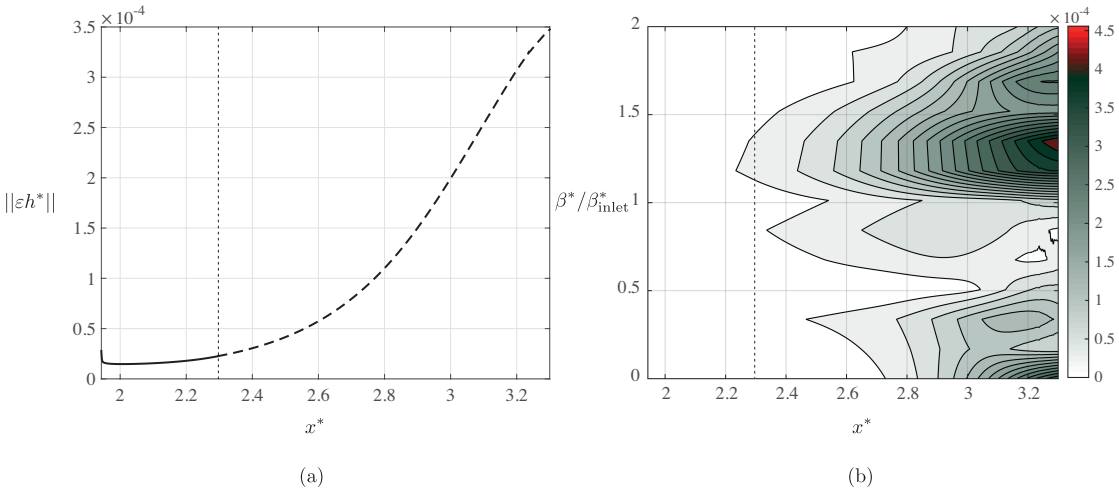

Figure 7.23 – (a) Streamwise evolution of the disturbance norm $||\varepsilon h^*||$ and (b) the most amplified spanwise wavenumber β^* with respect to the linearly most amplified one at the inlet, β^*_{inlet}, for the nonlinearly obtained flow shown in Fig. 7.22. Solid/dashed line in panel (a) corresponds to the curved/inclined part of the substrate. The transition location θ_c is indicated by a vertical dotted line.

plane is of about 1.35 times the theoretically most amplified wavenumber at the inlet β^*_{inlet} (see Fig. 7.23(b)).

It is important to stress that rivulets do not saturate in amplitude, as often assumed in the literature (Bertagni & Camporeale, 2017). As it is clearly visible in Fig. 7.23(a) as well as in Fig. 7.15, the amplitude of rivulets increases in space or time, respectively. In fact, rivulets thicken by pulling liquid from the valleys separating them (see Sec. 4.5.1), similarly to what is found for pendent drops under a horizontal ceiling (Lister et al., 2010) or collars inside a cylinder (Hammond, 1983).

Finally, it has to be stressed that parallel draperies also form under constant inclination ceilings. The effect of the curved substrate is only to modify the number of the formed rivulets, and their thickness, as a function of the streamwise location.

7.5 Other possible mechanisms at the origin of the wavenumber selection

We have seen in Sec. 7.4 that a substrate with varying inclination is at the origin of the selection of particular wavelengths. When the substrate is almost horizontal at the inlet, this most unstable region selects the first rivulet wavelength, whereas when the substrate is initially close to the vertical, the spacing between the rivulets is set by the location where their growth is sufficiently large.

However, there are other mechanisms in caves which are responsible for the determination of the spacings between the rivulets. Hereafter we consider two of them, which are again related to hydrodynamic instabilities.

7.5.1 Secondary instability of Kapitza waves

As we have seen in Sec. 7.3.1, the most amplified wavelength of rivulets diverges as the plate approaches the vertical, $\phi \to 0$, and its growth rate tends to zero. Therefore, and in the absence of inertia, such a film should remain uniform in thickness. However, if inertia effects are considered, a thicker liquid film flowing along a vertical plate forms Kapitza waves, see Sec. 1.2.4, Kalliadasis et al. (2011) and Rohlfs et al. (2017). The latter can experience a secondary instability and form rivulets (Rietz et al., 2017), whose spacing is given by the most amplified mode of the Rayleigh-Taylor instability under a horizontal substrate. In fact, waves can be seen as horizontal ridges, which are destabilized by gravity, that is orthogonal to them. Hence, as recently suggested by Charogiannis et al. (2018), the spacing between rivulets seems to follow the most amplified wavelength predicted by the inertialess linear stability analysis, Eq. (7.27), when the substrate is not too far from the horizontal, but it switches again to the wavelength of the horizontal Rayleigh-Taylor instability $\lambda_0^* = 2\pi\sqrt{2}\ell_c^*$ when the substrate gets closer to the verticality. The rivulets wavelength as a function of the inclination angle ϕ is therefore not monotonous.

As a result, water flowing on vertical cave walls can destabilize into rivulets if inertia is considered. Successively, if the local inclination of the cave wall changes, these rivulets can coalesce, or additional rivulets can form, as discussed in Sec. 7.4.3, starting from the wavelength selected by the secondary instability of waves on the vertical wall.

The formation of rivulets on vertical walls also explains the morphogenesis of draperies on these substrates, often observed in caves.

7.5.2 Rayleigh-Plateau instability

Another possible mechanism at the origin of the rivulet-wavelength selection is given by the Rayleigh-Plateau instability of a liquid film flowing on a strongly curved rock, like water overflowing a fountain's rim. In this case, the fluid interface is destabilized by capillary pressure gradients. The most amplified wavelength is $2\pi\sqrt{2}R^*$, where R^* is the curvature radius of the substrate, and the characteristic time of the Rayleigh-Plateau instability is $\tau_{RP} = \mu R^{*4}/\gamma H_i^{*3}$ (see Sec. 1.2.5) . However, as soon as the liquid flows along the underside of the rim, it is also destabilized by gravity and is subjected to the Rayleigh-Taylor instability. The ratio of characteristic times of the Rayleigh-Plateau and the Rayleigh-Taylor instability is $\tau_{RP}/\tau' = (R^*/\ell_c^*)^4$, meaning that the Rayleigh-Plateau instability is relevant only for substrate-curvature radii R^* of the order of the capillary length ℓ_c^*. Yet, when this is the case, the strong curvature of the rim can dictate the initial spacing of the formed rivulets. Note that when $R^* \sim \ell_c^*$,

the most amplified wavelength of the Rayleigh-Plateau instability coincides with the one of the horizontal Rayleigh-Taylor instability. A nonparallel stability analysis of the flow along a curved rim has been performed by Camporeale (2015), showing that a finite wavelength is selected even close to the verticality due to the substrate curvature.

7.6 Conclusions and perspectives

In this chapter we have seen that the morphogenesis of typical speleothems encountered in caves, as well as the formation of equally fascinating ice structures, are intrinsically related to the hydrodynamic instabilities of thin liquid films studied in Part I of this thesis. To shed light on the pattern formation, we have performed linear and nonlinear analyses of the flow under inclined or curved substrates. In particular, we have shown that longitudinal structures, called *rivulets*, are the dominant pattern when the deposition of calcium carbonate on the substrate is considered. Structures transversal to the flow, denoted as *waves*, as well as oblique modes, can also occur, but in a restricted parameter space. Furthermore, we have found that rivulets are selected by nonlinear effects, also in the absence of deposition. Waves are stabilized by a coupled effect of the flow advection and and the capillary flow, which bounds their amplitude. A crucial result of the linear stability analysis is the wavenumber selection: the spacing between rivulets is shown to vary as a function of the local inclination angle of the substrate.

We argue that although the deposition creates an anisotropy in the problem, the latter is eventually too small to originate in the pattern selection. Furthermore, given the large separation of time scales between the hydrodynamic instability and the deposition, we can state that it is rather the nonlinear hydrodynamic instability that determines the pattern selection and that the deposition 'solely engraves' the history of the flow on the substrate. Under this assumption, we have investigated the pure hydrodynamic problem by performing a spatio-temporal analysis for the flow under a curved substrate. We have shown that the flow under a concave substrate is initially absolutely unstable, up to an inclination angle after which it becomes convectively unstable, whereas the opposite is true when liquid flows under a convex substrate. Due to mass conservation, the thickness of the film under a curved substrate varies in space, reducing the parameter space where an absolute instability occurs, compared to the case of the flow under an inclined substrate.

To complement the linear analyses, we have performed nonlinear numerical simulations of the lubrication equation for the flow under an initially curved, then inclined, substrate. We have been able to show that an initially concave substrate promotes the formation of closely spaced rivulets, which grow close to the inlet, before coalescing at more downstream locations due to nonlinear interactions and the modification of the most amplified wavelength. We hypothesize that this hydrodynamic pattern is at the origin of the morphogenesis of *flutes*. In fact, flutes form at the underside of flowstones, where the local inclination of the substrate increases from being almost horizontal to vertical. The coalescence of rivulets forms a pattern

which is very similar to the wrinkles observed in curtains, which exists over a broad range of scales (Vandeparre, Piñeirua, Brau, Roman, Bico, Gay, Bao, Lau, Reis & Damman, 2011). On the other hand, when the curved substrate is convex, the Rayleigh-Taylor instability is initially weak and only few rivulets form, until a location where the inclination is sufficiently large (from the vertical) for the grow to be effective and to yield the formation of additional rivulets. Once the deposition taken into account, this hydrodynamic pattern should give rise to the formation of parallel *draperies*, which are often observed on gently sloped substrates.

Of course the shape of cave walls and ceilings is much more complex than a curved substrate followed by an inclined wall. Yet, we believe that the mechanisms presented in this chapter are relevant for the speleothems morphogenesis. In particular, the dependence of the linearly most amplified wavelength as a function of the local inclination and the possibility of coalescence phenomena or the formation of higher harmonics through nonlinear interactions are key ingredients.

We have seen in Chapters 3 and 4 that the most amplified wavelength of the Rayleigh-Taylor instability of a thin film in a cylinder corresponds to the one at the pole. This is in agreement with the result of the present spatio-temporal analysis, since the pole corresponds to a region of absolute instability, which selects the global frequency of the perturbation.

The present chapter has to be considered as a first attempt in the description of these speleothems formations, leaving plenty of exciting possibilities for future research. For example, it would be very enlightening performing a theoretical two-dimensional spatio-temporal analysis, as it has been done for the Rayleigh-Benard-Poiseuille convection problem (Carriere & Monkewitz, 1999; Mutabazi, Wesfreid & Guyon, 2010). Furthermore, linear analyses have to be followed by nonlinear studies, as the nonlinear response of spatially developing flows often differs from the linear one (Chomaz, 2005). The spatio-temporal analysis could also be extended to the nonlinear regime, as explained in Couairon & Chomaz (1997) and Delbende & Chomaz (1998). A detailed WKBJ analysis for the flow under a curved substrate will be relevant to assess the effect of the substrate curvature on the global stability properties (Huerre & Monkewitz, 1990).

Finally, there are still many wonderful speleothems whose morphogenesis remains mysterious. One of them are the oscillation of draperies, which have received several names by cavers: curtains, scarf, bacon strip, angel wings, flags, tobacco leaves, ruffled ribbons, cornices and elephant ears (Hill & Forti, 1997), see Fig. 7.24 for a visual explanation. We believe that the formation of these folded structures results from a meandering instability of the liquid film at the tip of the drapery. Curtains form only when the drapery has grown already and the liquid flows at its tip, similarly to what studied by Wilson & Duffy (1998). We performed a hydrodynamic linear stability analysis for the pendent rivulet underneath of such a drapery (see Fig. 7.24(b)), but we found that only symmetric modes with respect to the vertical are unstable. All the anti-symmetric varicose modes are found to be stable. Therefore, and in view of the larger thickness of these flows due to the accumulation of the liquid in a narrow region,

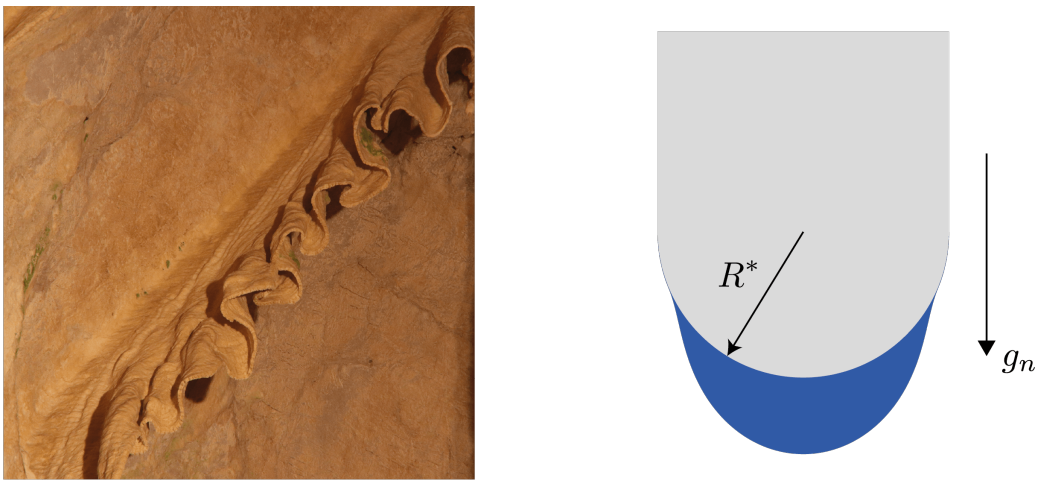

Figure 7.24 – (a) Curtain drapery observed in the Grottes de Vallorbe, Switzerland. (b) Model of the liquid flow at the tip of a drapery, where R^* is the radius of curvature of the tip and g_n the component of gravity normal to it.

we hypothesize that one has to consider the inertia of the flow for the meandering instability to occur. Note that the mechanisms at the origin of meandering instabilities, possibly related to the wetting properties and the contact line dynamics, are still a subject of debates (Kim, Kim & Kang, 2004; Le Grand-Piteira, Daerr & Limat, 2006; Daerr, Eggers, Limat & Valade, 2011; Couvreur & Daerr, 2012). Furthermore, it cannot be excluded that this pattern results from a coupling between the hydrodynamics and the deposition mechanism. The latter might need to be corrected to account for the strong variations in the film thickness (see Fig. 7.24(b)), which might affect the carbon dioxide diffusion through the liquid (Vesipa et al., 2015). As we have seen in Fig. 7.7, a strong coupling with the deposition can promote the formation of mixed modes, which in the present context would probably result in a meandering instability.

Part III
Bubbles and droplets in microfluidic channels

8 Thin-film patterns induced by advancing and receding menisci

8.1 Introduction

In the previous two parts of this thesis we have seen how a thin liquid film destabilizes under the action of the gravitational field and we have found the arising dominant 'global' patterns. The aim of this chapter is to investigate the details of the patterns observed when a thin liquid film is locally destabilized, or more precisely perturbed, by the presence of an advancing or a receding meniscus. This is, for instance, the case when a Rayleigh-Taylor-induced droplet slides on a thin film (see Chapters 3, 4 and 5), or when a thick liquid finger advances on a thin precursor film (see Chapter 6). More classically, receding and advancing menisci naturally arise when coating a plate by withdrawing it from a liquid bath (Landau & Levich, 1942; Derjaguin, 1943; Snoeijer, Ziegler, Andreotti, Fermigier & Eggers, 2008; Delon, Fermigier, Snoeijer & Andreotti, 2008) or when entering a prewetted plate in a liquid bath (Maleki et al., 2011); see Rio & Boulogne (2017) for a review. Very interestingly, the exact same 'local' patterns arise for a thin film separating a confined Taylor bubble from the channel walls (Bretherton, 1961), see Chapter 1, as well as for a pancake-shaped bubble or droplet confined in a Hele-Shaw cell (Burgess & Foster, 1990; Huerre, Theodoly, Leshansky, Valignat, Cantat & Jullien, 2015; Ling, Fullana, Popinet & Josserand, 2016; Zhu & Gallaire, 2016). Furthermore, by inverting the receding and the advancing menisci, one can extend the results for Taylor bubbles and pancakes to liquid bridges between two prewetted parallel plates, corresponding to the slugs investigated by Bico & Quéré (2002) or to the drops in Hele-Shaw cells investigated by Reyssat (2014).

All the above mentioned problems share the same lubrication equation, composed by a capillary-gradient-induced flux and a flux induced by the motion of the meniscus. In the literature, most of the studies considered the one-dimensional lubrication equation, either for the Landau-Levich-Derjaguin coating problem or for the motion of a bubble in a capillary studied by Bretherton (1961). However, the three-dimensional problem, which can be investigated by a two-dimensional lubrication equation, has received much less attention. Yet, the anisotropic flux induced by the motion of the meniscus relative to the wall induces additional

fascinating patterns in the thin film. As an example, recent experiments (Huerre et al., 2015) and numerical simulations (Ling et al., 2016; Zhu & Gallaire, 2016) for pancake bubbles and droplets in Hele-Shaw cells have confirmed the very peculiar catamaran-like structure of the lubricating film predicted by Burgess & Foster (1990).

The aim of this chapter is therefore to present, in a unified way, the film-thickness profiles obtained by perturbing a thin film by an advancing or a receding meniscus for both two and three-dimensional problems. In order to highlight the similarities and differences, we do not only consider confined bubbles in capillaries or Hele-Shaw cells, but also liquid bridges between two prewetted plates. As introduced in Sec. 1.3.1 (see also Chapter 9), a moving meniscus is composed by a dynamic region and a static region. Here, we will mainly focus on the dynamic meniscus region and the thin film region surrounding it; the static meniscus will only be considered in some particular cases. For the sake of simplicity, we neglect the viscosity of one phase, which corresponds to considering an inviscid bubble in a much more viscous fluid or a liquid bridge of a very viscous fluid into a much less viscous fluid. However, and as will become clear in Chapter 9, the results of the one-dimensional lubrication problem can be generalized to any viscosity ratio between the two fluids. In the present chapter, the motion is either induced by a pressure gradient or by buoyancy, but we do not aim here at finding the relation between the forces at play and the observed velocity. This will be discussed in Chapters 9 and 10, see also Sec. 5.4.4.

The chapter is structured as follows. The two-dimensional problem, governed by a one-dimensional lubrication equation, is described in Sec. 8.2. The linear solution of the lubrication equation is derived in Sec. 8.2.1, followed by the nonlinear solution in Sec. 8.2.2. The three-dimensional problem, governed by a two-dimensional lubrication equation, is presented in Sec. 8.3, starting again with the linear solution in Sec. 8.3.1, where we also propose a similarity with the linear response of a liquid film over a localized perturbation in the substrate topography. The nonlinear lubrication solution is compared to the one of the three-dimensional Stokes equations in Sec. 8.3.2. Conclusions and perspectives follows in Sec. 8.4.

8.2 One-dimensional lubrication problem

We consider a bubble of dynamic viscosity $\mu_i = 0$, density ρ_i and length L^* moving with constant velocity U_d^* in a planar two-dimensional channel of height $2R^*$ filled with a liquid of dynamic viscosity μ_o and density ρ_o (see Fig. 8.1(a)). The interfacial tension between the two fluids is γ. The motion is either driven by an outer pressure gradient or by buoyancy. This problem is similar to the motion of a liquid bridge in a prewetted tube filled with a fluid of negligible viscosity (see Fig. 8.1(b)). More generally, both problems present a receding and an advancing meniscus, corresponding to the front/rear and rear/front of the bubble/bridge, respectively. By considering the two menisci separately, one recovers the well know Landau-

Levich-Derjaguin problem of the plate withdraw from a liquid bath of the same fluid (Landau & Levich, 1942; Derjaguin, 1943) (see Fig. 8.1(c)) or the problem of the penetration of a prewetted plate in a liquid bath (Maleki et al., 2011) (see Fig. 8.1(d)). The thickness of the uniform film in the bubble or the precursor film on the plates are assumed to be all equal to H^*_∞.

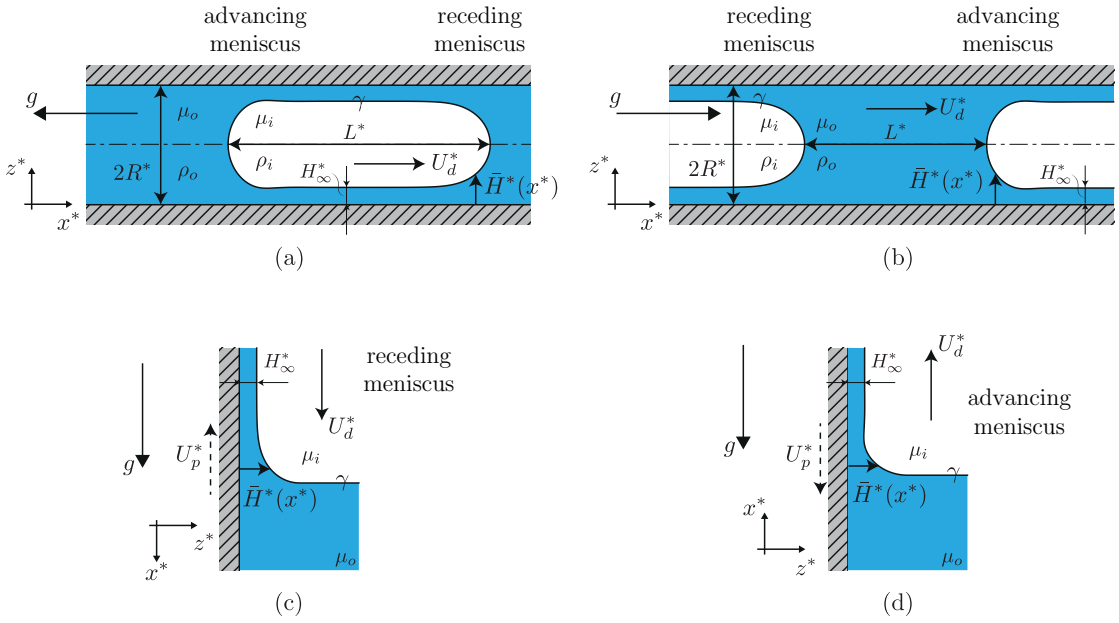

Figure 8.1 – Sketch of the considered problem geometries: (a) bubble moving at velocity U^*_d in a channel of height $2R^*$, (b) liquid bridge moving at velocity U^*_d in a channel of height $2R^*$, (c) withdraw of a plate from a liquid bath with velocity U^*_p and (d) penetration of a prewetted plate into a liquid bath with velocity U^*_p. The velocity of the meniscus with respect to the walls is U^*_d. $\rho_o \gg \rho_i$, $\mu_o \gg \mu_i$. H^*_∞ is the thickness of the uniform thin film and the x^*-axis is oriented in the direction of motion of the meniscus with respect to the wall.

Under the assumption of negligible inertia and a long-wavelength approach, the one-dimensional lubrication equation for the film thickness $\bar{H}^*$ separating the interface from the wall reads, in the frame of reference moving at velocity U^*_d (see Chapter 9 for more details):

$$\frac{\partial \bar{H}^*}{\partial t^*} + \frac{\partial}{\partial x^*}\left[\frac{\bar{H}^{*3}}{3\mu_o}\left(\gamma \bar{\kappa}^*_{x^*} - \Delta\rho g\right) - U^*_d \bar{H}^*\right] = 0, \tag{8.1}$$

where $\Delta\rho = \rho_o - \rho_i$ is the density difference between the two fluids and $\bar{\kappa}^*$ the curvature of the interface. Using the half-channel height R^* as characteristic length and R^*/U^*_d as characteristic time, the dimensionless lubrication equation is

$$\frac{\partial \bar{H}}{\partial t} + \frac{\partial}{\partial x}\left[\bar{H}^3\left(\frac{1}{3Ca}\bar{\kappa}_x - \frac{Bo}{3Ca}\right) - \bar{H}\right] = 0, \tag{8.2}$$

where $Ca = \mu_o U^*_d/\gamma$ is the capillary number and $Bo = \Delta\rho g R^{*2}/\gamma$ is the Bond number. Fur-

thermore, we assume here a steady film profile, so that Eq. (8.2) becomes

$$\frac{d}{dx}\left[\bar{H}^3\left(\frac{1}{3Ca}\bar{\kappa}_x - \frac{Bo}{3Ca}\right) - \bar{H}\right] = 0. \tag{8.3}$$

It is important to stress that we use the lubrication equation to describe the film-thickness profile over the entire domain, also in the static meniscus region, where, strictly speaking, such an approach no longer holds due to the nonconstant pressure in the z^*-direction and the non-negligible z^*-velocity component. However, as we will see in this chapter, considering the ad-hoc lubrication equation also in these regions yields satisfactory results. A possible reason for the success of the lubrication approach in describing problems where its underlying assumption no longer holds has been given by Krechetnikov (2010).

8.2.1 Linear solution of the lubrication equation

One can decompose the film thickness as $\bar{H} = H_\infty + \varepsilon h$, where h is the deviation from the uniform film thickness H_∞. Entering this decomposition into Eq. (8.3) and considering terms in ε yields:

$$\frac{H_\infty^3}{3Ca}h_{xxxx} - \left(1 + \frac{H_\infty^2 Bo}{Ca}\right)h_x = 0. \tag{8.4}$$

Equation (8.4) can be integrated once to obtain

$$\frac{H_\infty^3}{3Ca}h_{xxx} - \left(1 + \frac{H_\infty^2 Bo}{Ca}\right)h = 0, \tag{8.5}$$

where the integration constant is zero since the perturbations vanishes in the region of uniform thickness H_∞ (see also Appendix 8.5.1). The linear disturbance equation can be therefore rewritten as

$$h_{xxx} = Kh \tag{8.6}$$

with

$$K = \frac{3Ca}{H_\infty^3} + \frac{3Bo}{H_\infty}. \tag{8.7}$$

Equation (8.6) is the linearized version of the classical Landau-Levich-Derjaguin equation that we will retrieve in Chapter 9 (see also Appendix 8.5.1), with the addition of the gravity force. In Appendix 8.5.1 we present the derivation of Bretherton (1961), who started from the nonlinear Eq. (8.3) and considered different changes of variables for the pressure-driven and gravity-driven problems, that, once linearized, result in Eq. (8.6). The general solution of

Eq. (8.6) reads

$$h(x) = \alpha \exp(K^{1/3}x) + \beta \exp\left(-\frac{K^{1/3}x}{2}\right)\cos\left(\frac{\sqrt{3}K^{1/3}x}{2} + \phi\right) \tag{8.8}$$

where α and β are real coefficients and ϕ a parameter taken such that the curvatures of the advancing and receding menisci are equal (Cantat, 2013). Bretherton (1961) found that, in the limit $Ca \ll 1$, the leading order curvatures of the front and rear static caps coincide and are equal to half the channel height. For the case of the Landau-Levich-Derjaguin problem, the curvature radius of the static cap for $Ca \ll 1$ is proportional to the capillary length (Maleki et al., 2011) (see Chapter 1). The solution (8.8) is monotonically increasing for $x \to \infty$, whereas it is oscillating for $x \to -\infty$.

The wavelength of the oscillations for the advancing meniscus is given by $\lambda = 2\pi/K^{1/3}$. For the case of a receding meniscus with $Bo = 0$ it is known that $H_\infty \sim Ca^{2/3}$ (see Sec. 1.3.1 of the introductory Chapter 1) so that the wavelength scales as $\lambda \sim Ca^{1/3}$. For the advancing meniscus of a liquid bridge moving on a precursor film of thickness H_∞ there is no relation between Ca and H_∞ so that the wavelength for $Bo = 0$ scales as $H_\infty/(Ca^{1/3})$. Furthermore, the linear growth rate of the oscillations varies as $K^{1/3}$.

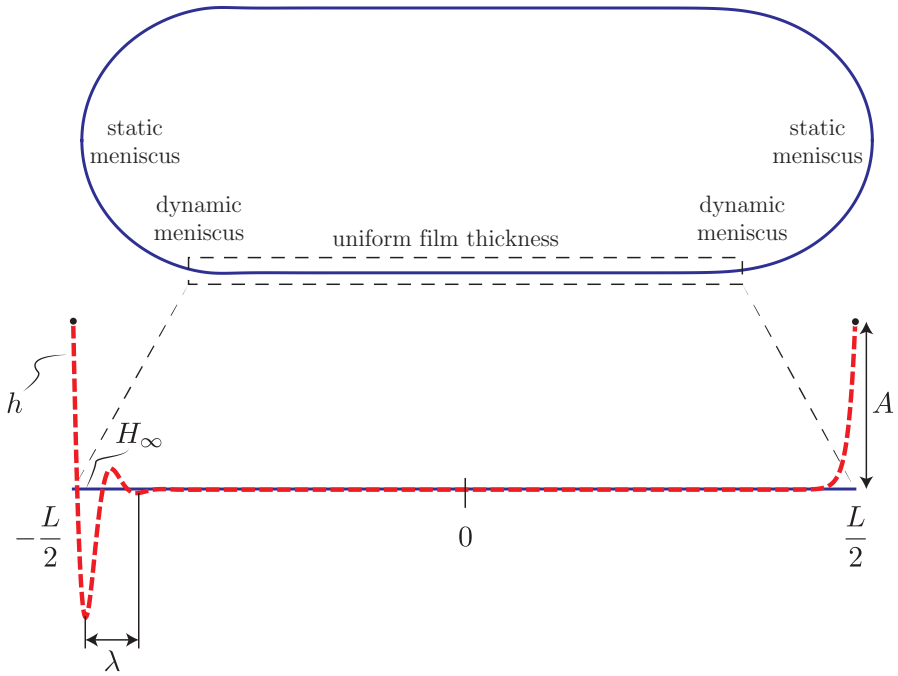

Figure 8.2 – Linear film-thickness perturbation h (red dashed line) around the uniform film thickness H_∞ (blue solid line). Oscillations with characteristic wavelength λ are visible in the rear dynamic meniscus region. The different regions of the bubble are indicated. $Ca = 10^{-3}$, $Bo = 0$, $A = 10^{-3}$, $L = 10$.

Alternatively, one can readily solve Eq. (8.4) as a boundary-value problem by imposing the

values of the film-thickness perturbation and curvature at the extremities of the considered domain. In fact, the film thickness $\bar{H}$ starts deviating from the uniform value H_∞ in the dynamic meniscus, so that one can assume the film-thickness perturbation to be $h(x = \pm L/2) = A$ at a given distance $L/2$ from the center of the bubble (see Fig. 8.2), with A being an arbitrary constant. Assuming that the length of the region where the thickness perturbations vary from 0 to A scales as the perturbation amplitude A, the order of magnitude of the linearized curvature h_{xx} at the boundaries is given by $h_{xx}(x = \pm L/2) = 1/A$. This does not have to be understood as a rigorous matching approach, but rather as a way to find the structure of the film profile in the region where it is close to be uniform when it is forced to be thicker in the surrounding region. The uniform film thickness H_∞ can be well predicted by the law discussed in Chapter 9 (Taylor, 1961; Aussillous & Quéré, 2000)

$$H_\infty = \frac{P(3Ca)^{2/3}}{1 + PQ(3Ca)^{2/3}}, \tag{8.9}$$

where the coefficients for a planar bubble are $P = 0.643$ and $Q = 2.2$. As it is visible in Fig. 8.2, the thickness perturbation presents a monotonous behavior at the front, whereas it is oscillating at the back, as predicted by the solution (8.8). An analogous result could be obtained for a liquid bridge, where the receding and advancing menisci have to be resolved separately. The additional boundary conditions for the film-thickness disturbances in the uniform-film region away from the meniscus are $h = h_{xx} = 0$ (see Fig. 8.5(d)).

The linearized equation for the film-thickness perturbation breaks down as soon as the amplitude of the perturbation reaches the order of the uniform film thickness H_∞. At this point, the nonlinear lubrication equation has to be considered, which is the subject of Section 8.2.2.

8.2.2 Nonlinear solutions

For the sake of simplicity, we consider in this section only the film-thickness profile of a bubble in a planar channel; similar results could be obtained for a liquid bridge in a prewetted tube or for the Landau-Levich-Derjaguin coating problem. As we will see in Chapter 9, the linear solution (8.8) can be employed to integrate the nonlinear lubrication equation (8.3) as an initial value problem starting from the uniform film region to the static cap where the dimensional curvature is constant and is $1/R^*$ for $Ca \ll 1$ (see also Appendix 8.5.1).

Here we show that it is also possible to solve Eq. (8.3) as a boundary-value problem for the entire geometry, including the static meniscus regions. This is easily done with COMSOL Multiphysics using $\bar{H}$ and $\bar{\kappa} = \left(\bar{H}_x/\sqrt{1+\bar{H}_x^2}\right)_x$ as variables and by imposing $\bar{H}(x = \pm L/2) = 1$ and $\bar{\kappa}(x = \pm L/2) = \kappa_{f,r}$ at the bubble front and rear ends, with $\kappa_{f,r}$ being the curvature of the static cap. Anticipating the result of Chapter 9, the front and rear static cap curvatures are well

described by the law

$$\kappa_{f,r} = \frac{1 + T_{f,r}(3Ca)^{2/3}}{1 + Z_{f,r}(3Ca)^{2/3}}, \tag{8.10}$$

where the coefficients are $T_f = 2.29$, $Z_f = 0.41$, $T_r = -0.51$ and $Z_r = -0.11$ for the case of a bubble in a planar channel. As previously anticipated, we do not intend here to perform a rigorous matching, which, for the limit $Ca \ll 1$, can be found in Park & Homsy (1984). Reinelt (1987) pointed out that higher-order corrections to the asymptotic expansion for lager Ca require the computation of both the velocity field and pressure in the outer region, making such an asymptotic approach not very efficient. For $Ca \sim 1$, it is more convenient to directly solve the problem numerically, as performed hereafter.

Furthermore, it is possible to avoid a boundary condition on the static curvature by imposing that the film-thickness profile at the bubble ends has to be symmetric with respect to the channel mid-plane. Since such a condition implies $\bar{H}_x \to \pm\infty$ at $x = \pm L/2$, one has to rewrite the lubrication equation using a curvilinear-coordinate system. The interface is then described by $x = x(s)$, $y = y(s)$ and $\theta = \theta(s)$, for $s \in [0,1]$, where θ is the angle between the interface and the horizontal. The symmetry of the profile at the bubble front and rear ends simply reads $\theta(s = 0,1) = \pm\pi/2$ and the boundary conditions for x and y are: $x(s = 0,1) = \pm L/2$ and $y(s = 0,1) = 1$. For the derivation of the lubrication equation in the curvilinear-coordinate system see the Appendix 8.5.2.

The bubble profiles obtained by the resolution of the lubrication equation in Cartesian coordinates with the imposition of the front/rear static cap curvatures predicted by the model (8.10) and the one obtained by the resolution of the lubrication equation in curvilinear coordinates with the imposition of the verticality condition at the droplet ends are compared to the bubble profile obtained with a two-dimensional Stokes equation, as the ones of Chapter 9, in Fig. 8.3. First, it can be noted that the nonlinear profile also presents oscillations at the back of the bubble, like the ones of the linear solution (see Fig. 8.2), yet of smaller amplitude. Secondly, the nonlinear bubble profiles obtained by the lubrication approaches compare very well with the Stokes result at low capillary numbers, as expected (see Fig. 8.3(a)). At higher capillary numbers, the agreement remains satisfactory, especially in the thin film region, but one has to impose the correct curvature of the front and rear static caps prescribed by the law (8.10). If the front and rear curvature corrections due to the large capillary number are not considered, *i.e.* $T_{f,r} = Z_{f,r} = 0$ in Eq. (8.10), the bubble profile differs more from the one of the 2D-Stokes simulations (see green dash-dotted line and black solid line in Fig. 8.3(b)). As will become clear in Chapter 9, the curvature of the static cap at higher capillary numbers is no longer constant in space. Hence, the film thickness is solely dictated by the solution of the lubrication equation up to the droplet extremities, where it is known that the validity of such an approach is questionable.

The film-thickness profile for a liquid bridge could be also obtained by solving Eq. (8.3) as a boundary value problem. In this case, one has to add the boundary condition $\bar{H} = H_\infty$ and

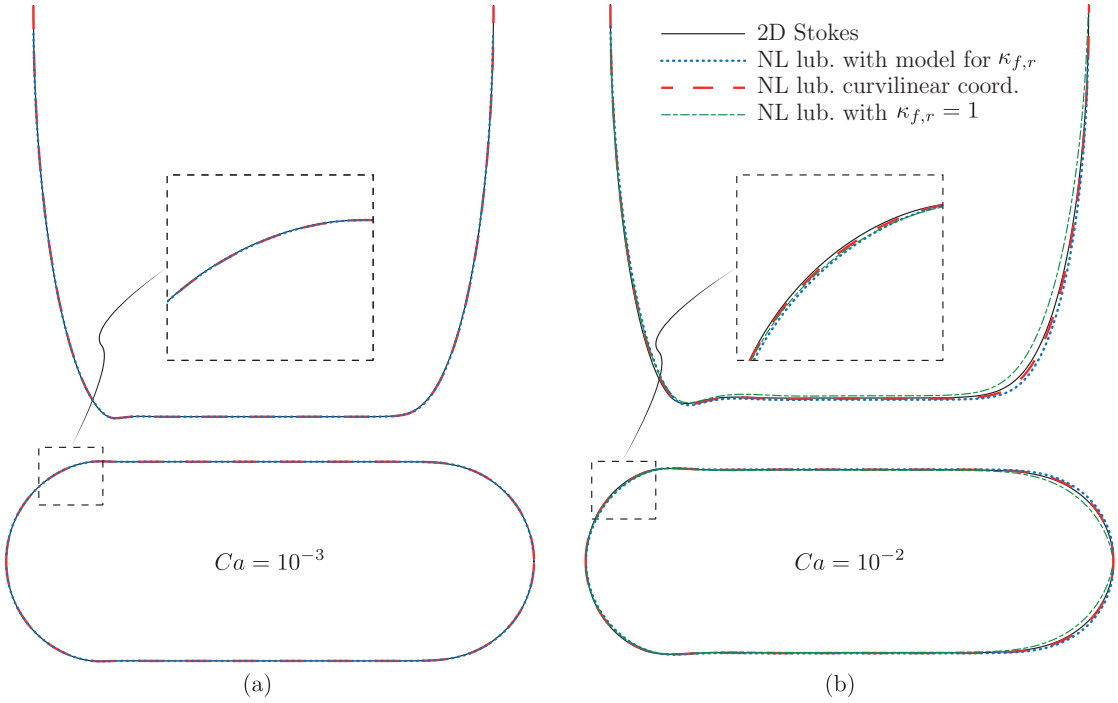

Figure 8.3 – Comparison of the bubble profiles obtained from 2D planar Stokes equations (black solid line), from the nonlinear lubrication equation with the model (8.10) for $\kappa_{f,r}$ (blue dotted line) and from the nonlinear lubrication equation in curvilinear coordinates (red dashed line) for (a) $Ca = 10^{-3}$ and (b) $Ca = 10^{-2}$. The bubble profile obtained using the lubrication equation without corrections, *i.e.* assuming $\kappa_{f,r} = 1$, is indicated by the green dash-dotted line in panel (b). The upper profiles are not scaled, whereas the lower ones are in scale.

$\bar{\kappa} = 0$ downstream, far away from the advancing meniscus, where the film thickness has to match the one of the precursor film. The boundary condition upstream, far away from the receding meniscus, is given by $\bar{H}_x = 0$ and $\bar{\kappa} = 0$, since the film deposited by the receding meniscus is uniform, but its thickness is unknown a priori. The obtained film profiles for the receding and advancing menisci would be very similar to the one shown in Fig. 8.3 for a bubble (see Fig. 8.8(d)).

Hence, we have seen that an advancing meniscus induces oscillations in the film thickness, as if it was 'buckling' (Maleki et al., 2011), whereas a receding meniscus deposits a uniform film. The different film-thickness profiles can be also understood by looking at the flux components in the dynamic meniscus region and remembering that the flux in the one-dimensional film is conserved. In the case of an advancing meniscus, a thicker film advances on a very thin film and the interfacial curvature gradient induces a capillary flow pulling the fluid from the thin film into the thick one. This capillary flux adds to the one induced by the motion of the bubble and mass conservation implies that the film thickness is reduced and oscillates. In the case of a receding meniscus, a thin film is deposited by a thicker film and the capillary

pressure gradient induces a flow which is in the direction opposite to the motion. To satisfy mass conservation, the film thickness has to increase and no oscillations occur.

As a conclusion, the linear lubrication equation is able to capture the main characteristics of a bubble profile, while its exact profile is well predicted by a nonlinear lubrication approach, provided that the boundary conditions are correct.

8.3 Two-dimensional lubrication problem

We consider now the three-dimensional extensions of the previously discussed two-dimensional confined bubble and liquid bridge. A pancake-shaped bubble of dynamic viscosity $\mu_i = 0$, density ρ_i and characteristic size L^* is flowing in a Hele-Shaw cell of height $2R^*$ filled with a liquid of dynamic viscosity μ_o and density ρ_o (see Fig. 8.4(a)), driven by a pressure gradient or by gravity. Similarly, a three-dimensional liquid bridge of dynamic viscosity μ_o and density ρ_o is moving with velocity U_d^* on previously wetted parallel plates (see Fig. 8.4(b)).

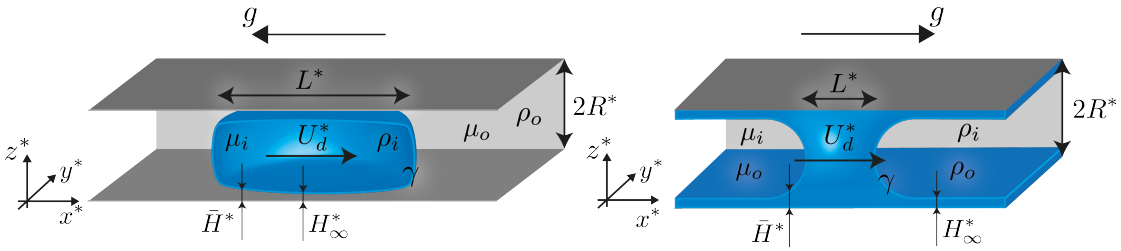

Figure 8.4 – Sketch of the considered problem geometries: bubble (a) and liquid bridge (b) moving at velocity U_d^* in a channel of height $2R^*$. $\rho_o \gg \rho_i$, $\mu_o \gg \mu_i$. H_∞^* is the thickness of the uniform thin film (a) or the precursor film (b). Only half of the channel width is shown.

Under the same assumptions as in Sec. 8.2.1, the two-dimensional nonlinear lubrication equation reads

$$\frac{\partial \bar{H}^*}{\partial t^*} + \frac{\partial}{\partial x^*}\left[\frac{\bar{H}^{*3}}{3\mu_o}\left(\gamma\bar{\kappa}^*_{x^*} - \Delta\rho g\right) - U_d^*\bar{H}^*\right] + \frac{\partial}{\partial y^*}\left(\frac{\bar{H}^{*3}}{3\mu_o}\gamma\bar{\kappa}^*_{y^*}\right) = 0, \tag{8.11}$$

where $\Delta\rho = \rho_o - \rho_i$ is the density difference between the two fluids and $\bar{\kappa}^*$ the mean curvature of the interface. Note the anisotropy of the fluxes: both the buoyancy and the motion in the x^* direction do not affect the flux in the y^* direction, breaking the isotropy induced by the capillary pressure gradient. Using the half-channel height R^* as characteristic length and R^*/U_d^* as characteristic time, the dimensionless lubrication equation for the steady profile is

$$\frac{\partial}{\partial x}\left[\bar{H}^3\left(\frac{1}{3Ca}\bar{\kappa}_x - \frac{Bo}{3Ca}\right) - \bar{H}\right] + \frac{\partial}{\partial y}\left(\bar{H}^3\frac{1}{3Ca}\bar{\kappa}_y\right) = 0. \tag{8.12}$$

where $Ca = \mu_o U_d^* / \gamma$ is the capillary number and $Bo = \Delta\rho g R^{*2} / \gamma$ is the Bond number.

8.3.1 Linear solution of the lubrication equation

With the use of the film-thickness decomposition $\bar{H} = H_\infty + \varepsilon h$, the linear equation for the film-thickness disturbances reads:

$$\frac{H_\infty^3}{3Ca} \underbrace{(h_{xxxx} + 2h_{xxyy} + h_{yyyy})}_{\Delta^2 h} - \left(1 + \frac{H_\infty^2 Bo}{Ca}\right) h_x = 0, \tag{8.13}$$

which is nothing else than Eq. (8.4) where the term h_{xxxx} is replaced by the bi-Laplacian operator $\Delta^2 h$.

In the same spirit as in Section 8.2.1, we can solve the linear lubrication equation (8.13) for the film-thickness perturbations around the uniform film thickness H_∞ as a boundary-value problem. This is equivalent to looking at the perturbations of the uniform thin film region due to the matching of the film thickness in the dynamic meniscus region to a larger value. In the present context, we impose a film-thickness perturbation $h(r = L/2) = A$ and a mean curvature of the order $\Delta h(r = L/2) = 1/A \pm 2/L$ on the perimeter at a radial distance $r = L/2$ from the center of the pancake bubble or liquid bridge. The contribution $2/L$ results from the curvature of the boundary in the (x, y)-plane and is positive in the former case and negative in the latter. For the case of a liquid bridge, the perturbations are outside of the circle of radius $L/2$ and are therefore forced to vanish far away from the liquid bridge, except in the region upstream. The maps of the film-thickness perturbation h for both problems, together with some profiles along the streamwise and spanwise directions, are shown in Fig. 8.5.

At this point, several important observations can be done. First, one can clearly observe that the linear lubrication equation with a perturbed film thickness and curvature along the domain boundary is able to reproduce the catamaran-like pattern observed in pancake bubbles and droplets (Burgess & Foster, 1990; Huerre et al., 2015; Zhu & Gallaire, 2016), in the same way as the corresponding one-dimensional linear lubrication equation is able to reproduce the oscillating behavior of the film thickness at the advancing meniscus. The film thickness is the smallest in the lateral part of the pancake (see Fig. 8.5(a)), so that its three-dimensional shape resembles to the hull of a catamaran. Therefore, we can conjecture that this pattern is the generalization of the one-dimensional oscillations for a two-dimensional concave structure, like a pancake bubble, and is intrinsically related to the anisotropy of the equation. For a convex two-dimensional structure, like the liquid bridge, the film-thickness perturbation profile presents a wake-like decrease in film thickness behind the liquid bridge, with minima again located at the lateral sides (see Fig. 8.5(b)). These valleys of minimal thickness are the corresponding of the catamarans of pancake bubbles.

Secondly, the film-thickness perturbations along the streamwise direction x (see Fig. 8.5(c,d)) deviate from a uniform profile as expected from an advancing and a receding meniscus (see

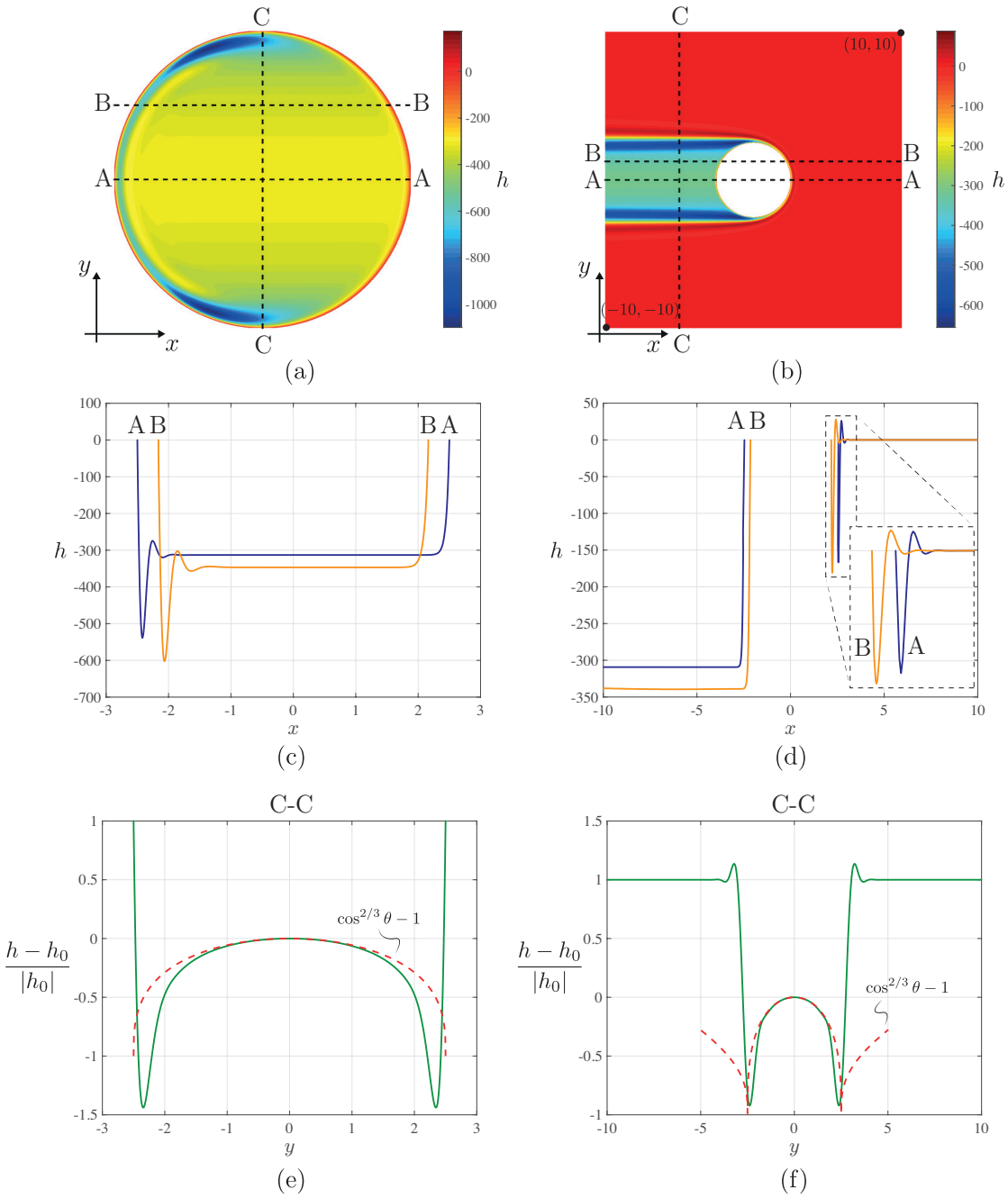

Figure 8.5 – Linear film-thickness perturbation h around the uniform film thickness H_∞ for a pancake bubble (a,c,e) and for a liquid bridge (b,d,f). The film-thickness perturbation map are shown in panels (a,b), the cuts along the streamwise direction at two different y-locations are plotted in panels (c,d) and the normalized difference of the film-thickness perturbation along the spanwise cut C-C with respect to $h_0 = h(y = 0)$ along this cut is shown in panels (e,f), where the analytical prediction is given by the red dashed line. $L = 5$, $A = 10^{-3} \times H_\infty$, $Ca = 10^{-3}$ and $Bo = 0$.

Fig. 8.1). The film thickness oscillates at the advancing meniscus and increases monotonically at the receding meniscus. Note that the perturbations of the film thickness in the uniform film region of a pancake are not vanishing as the base film thickness H_∞ is given by Eq. (8.9), which is an asymptotic estimate but not an exact solution of the lubrication equation. Furthermore, it can be observed that the more one moves away from $y = 0$, the more the thickness of the film is reduced. Therefore, the thickness of the film left by the receding meniscus is not uniform.

To better highlight this crucial point, we show in Fig. 8.5(e,f) the normalized difference between the film-thickness perturbation and its value at $y = 0$. The film thickness decreases as $|y|$ increases, before increasing again close to $|y| = L/2$ to match the boundary condition for the case of a pancake bubble or the precursor film thickness for the case of a liquid bridge.

These qualitative observations can be rationalized by simplifying the linear lubrication equation (8.13) for the different regions of the domain (see Fig. 8.6). The lubrication equation (8.13) in polar coordinates can be simplified to

$$\frac{H_\infty^3}{3Ca} h_{rrrr} - \left(1 + \frac{H_\infty^2 Bo}{Ca}\right)\left(\cos\theta h_r - \frac{\sin\theta}{r} h_\theta\right) = 0. \tag{8.14}$$

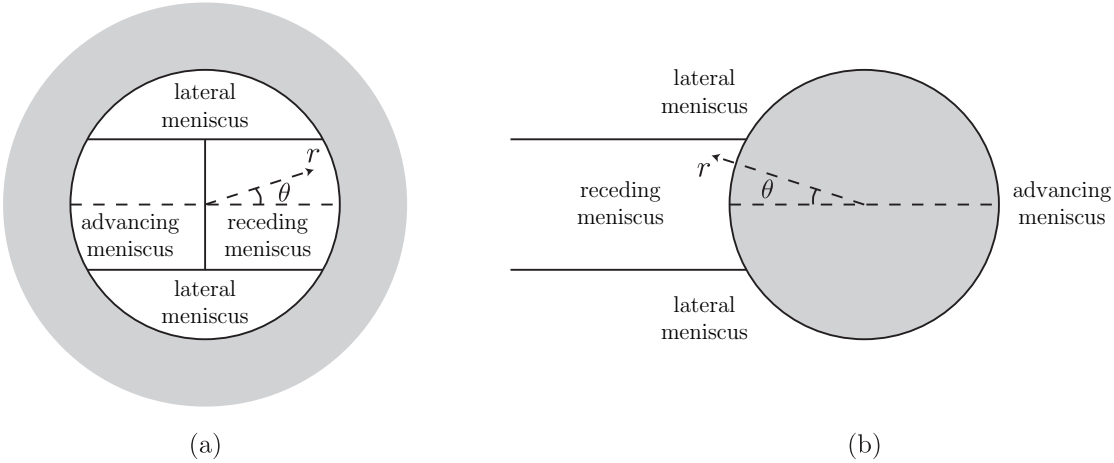

Figure 8.6 – Regions in the thin film of a pancake bubble (a) and in the thin film surrounding a liquid bridge (b). The polar coordinates (r,θ) are introduced and the boundaries are highlighted by the gray area.

For small polar angles θ, the contribution $\sin\theta h_\theta / r$, which corresponds to the flux in the tangential direction, can be neglected so that the linear lubrication equation becomes, after integration along r as in Sec. 8.2.1:

$$h_{rrr} = K_p h, \tag{8.15}$$

with

$$K_p = \left(\frac{3Ca}{H_\infty^3} + \frac{3Bo}{H_\infty}\right)\cos\theta \tag{8.16}$$

which is nothing else that Eq. (8.6) in the radial direction r projected on the streamwise direction. Therefore, we know from Eq. (8.8) that the solution is oscillating at the advancing meniscus and monotonic at the receding one. Focusing for now on $Bo = 0$, we know from the theory of Bretherton (1961) for a pressure driven bubble, or from the theory for the coating of a plate (see Chapter 1), that the thickness deposited by a receding meniscus depends on the velocity normal to the interface. In this case, one has therefore $H_\infty \sim Ca_p^{2/3}$ with $Ca_p = Ca\cos\theta$ as the local capillary number at a given polar angle θ. Hence, the film thickness in the central region of the pancake or liquid bridge varies like $(Ca\cos\theta)^{2/3}$. Once a given film thickness is set by the receding meniscus, the same thickness will be present over the entire thin film region at the corresponding spanwise location y. The good agreement between the theoretical dependence in $\cos^{2/3}\theta$ of the film thickness and the profile along the spanwise direction obtained by resolving the two-dimensional lubrication equation is shown in Fig. 8.5(e,f).

Similarly, the oscillations at the advancing meniscus depend on the polar angle since $K_p = K\cos\theta$. For a pancake bubble, due to the film-thickness nonuniformity resulting from the nonuniform deposition at the front, the wavelength of the oscillations at the back scales as $\lambda \sim (Ca\cos\theta)^{1/3}$. Given the 1/3 power-law dependence, the wavelength is almost unchanged, before rapidly reducing to 0 when $\theta \to \pm\pi/2$ (see Fig. 8.5(a)). On the other hand, the imposed precursor-film thickness H_∞ results in an oscillation wavelength downstream of a liquid bridge scaling as $\lambda \sim H_\infty/(Ca\cos\theta)^{1/3}$. As it is visible in Fig. 8.5(b,d), the wavelength of the oscillations increases as $\theta \to \pm\pi/2$.

It is important to note that a plane cut of the film thickness at a given angle θ does not present a region of constant film thickness. A pancake bubble or a liquid bridge cannot be seen just as the collection of different one-dimensional profiles obtained by the solution to Eq. (8.15) for different polar angles θ. In fact, the film thickness at any spanwise location y is set by the receding meniscus at the corresponding polar angle θ and Eq. (8.15) only indicates the scaling of this film thickness as well as the oscillations at the back.

For $\theta \to \pm\pi/2$, which corresponds to the lateral meniscus region (see Fig. 8.6), the tangential flux term $\sin\theta h_\theta/r$ in Eq. (8.14) can no longer be neglected. Burgess & Foster (1990) performed an involved analysis of the lubrication equation in this region for a pancake bubble and find that the local film thickness in the so-called lateral transition regions scales as $Ca^{4/5}$ rather than as $Ca^{2/3}$. Therefore, for $Ca \ll 1$, the film thickness in these lateral regions is much smaller than the one in the other regions. This explains why one observes catamaran-like structures in the lateral regions of pancake bubbles. Furthermore, Burgess & Foster (1990) have also shown that the polar extent of these lateral regions scales as $Ca^{1/5}$, whereas their radial extent scales as $Ca^{2/5}$ instead of as $Ca^{1/3}$ that one has for the length of advancing and receding dynamic menisci (see also Hodges, Jensen & Rallison (2004*b*)), as we have seen in Chapter

1. Physically speaking, the change in sign of the spanwise curvature h_{yy} close to the lateral transition regions induces a capillary flow pulling out liquid from the region of smaller $|y|$ to the larger $|y|$ region, reducing the local film thickness. For the case of a liquid bridge, we have found that the lateral meniscus region, where the thickness is much smaller, is responsible for 'engraving' deep valleys on the sides of the wake left by the moving liquid bridge. However, the nonuniformity of the thickness in the wake region of a liquid bridge decreases as the distance from the liquid bridge increases due to surface tension effects (see Fig. 8.5(d)). This process is similar to the capillary drainage between rivulets that we have seen in Chapter 4.

Similarity to the film-thickness perturbations induced by a substrate perturbation

The aim of this short digression is to show an interesting parallelism between the linear perturbation field induced by the presence of a liquid bridge and the one induced by a localized perturbation in the substrate. When considering substrate perturbations h^o, the lubrication becomes (see Chapter 6 for more details)

$$\frac{H_\infty^3}{3Ca}\Delta^2 h - \left(1+\frac{H_\infty^2 Bo}{Ca}\right)h_x = -\frac{H_\infty^3}{3Ca}\Delta^2 h^o, \tag{8.17}$$

which is nothing else that Eq. (8.13) with a forcing term on the right hand side due to the substrate topography. Hayes, O'Brien & Lammers (2000) have derived the Green's function for a Dirac perturbation in the substrate gradient and have shown that the induced film-thickness-perturbation field can be obtained by the convolution of the topography shape h^o with the gradient of the Green's function. For instance, a Dirac delta topography perturbation induces a 'halo'-shaped perturbation of the film thickness. The successive works of Decré & Baret (2003) and Blyth & Pozrikidis (2006) have confirmed experimentally and numerically the occurrence of such a pattern, showing that the film thickness is larger ahead of the perturbation and smaller behind. This is reminiscent of the perturbation field around a liquid bridge observed in Fig. 8.5(b).

To better illustrate the similarity between the two different types of film perturbations, we compare in Fig. 8.7 the film-thickness perturbation profile obtained by a small liquid bridge of characteristic size $L = 0.4$ and amplitude $A = 10^{-3}$ to a Gaussian substrate perturbation

$$h^o(x,y) = A^o H_\infty \exp\left[-\frac{x^2+y^2}{2\sigma}\right], \tag{8.18}$$

where we have chosen $\sigma = 0.04$ and $A^o = 10^5$ to have a perturbation close to a Dirac delta. Note that, strictly speaking, the used lubrication approach should fail for a localized topography. However, as pointed out by Hayes et al. (2000) and Kalliadasis et al. (2000), the lubrication theory is found to be a very good approximation also for these extreme cases.

From Fig. 8.7(a-d) it can be noted that the fluid thickness perturbations induced by a liquid bridge or a substrate topography are similar. The reason is that in both cases the thickness of

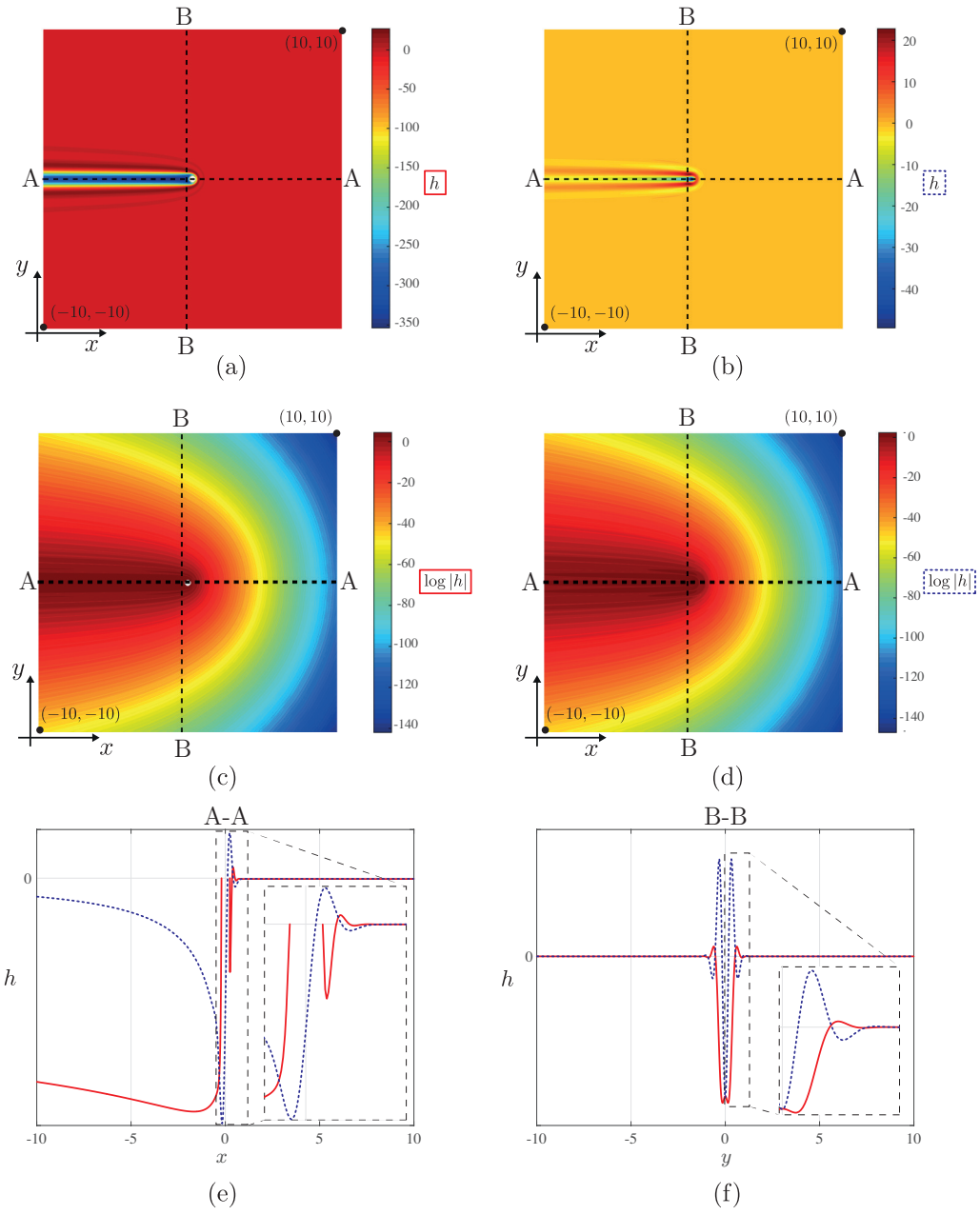

Figure 8.7 – Linear film-thickness perturbation h (a,b) and $\log|h|$ (c,d) around the uniform film thickness H_∞ for a liquid bridge (a,c,e) and a substrate perturbation (b,d,f). Given the exponential decay of h, see solution (8.8), the logarithm of the perturbations is shown in panels (c,d). The film-thickness profiles along the cuts in the streamwise and spanwise directions are shown in panels (e) and (f), respectively, where the vertical axis is rescaled differently for the liquid bridge perturbation (red solid line) than for the substate topography perturbation (blue dotted line) for visualization purposes. $L = 0.4$, $A = 10^{-3} \times H_\infty$, $A^o = 10^5 \times H_\infty$, $\sigma = 0.04$, $Ca = 10^{-3}$ and $Bo = 0$. The amplitudes A and A^o are chosen such as to generate a film perturbation of comparable amplitude.

the film is forced to be larger, either by the imposition of a boundary condition representing the dynamic meniscus of the liquid bridge or by the response to the forcing induced by the substrate topography. From the comparison of the film-thickness profiles along the streamwise direction shown in Fig. 8.7(e) one can observe that the Gaussian substrate topography induces a bump in the film thickness ahead of it. More downstream of the bump, the film thickness presents an oscillation, like for the advancing meniscus of the liquid bridge, whereas at its back the film thickness decreases like for the receding meniscus. However, the thickness of the perturbation at the back presents a very localized thin film region, which is due to the particular forcing of the topography. By looking at the thickness profile in the wake region, along the spanwise direction, one observes that in both cases the film thickness presents an oscillation (see Fig. 8.7(f)). Nevertheless, for the perturbation induced by a substrate topography, there is no spatial variation of the film thickness in $\cos^{2/3}\theta$ as for the film thickness deposited by the receding meniscus of a liquid bridge. The reason is that in the case of a substrate forcing, the film thickness is not uniform over the entire region, like for the liquid bridge, where it is imposed by the boundary condition $h(r = L/2) = A$.

We can conclude that the oscillating film-thickness perturbation induced by a liquid bridge is very similar to the one obtained by a localized substrate perturbation. Furthermore, it is important to stress that this is a very general pattern of the two-dimensional thin film lubrication equation (8.13) when perturbed locally, and results from the anisotropic term h_x induced by the flow motion in one direction. The latter breaks the symmetry that one would have by considering the isotropic surface tension term $\Delta^2 h$ alone. Note that this is the reason for the formation of the wake structure behind the sliding drops on thin films, as we have seen in Chapter 5. Lister et al. (2010) have shown that the presence of these capillary perturbations in the thin film surrounding a sliding drop affects its dynamics. In particular, the wave field induced by a drop interacts with the ones induced by the others, or by a meniscus at the boundaries of the domain, so that repulsive and attractive movements can be observed. Given the fast decay in amplitude of the oscillations, the interaction length is proportional to the width of the first capillary oscillation. Furthermore, it can be pointed out that these drop-drop interactions on a thin film are somewhat reminiscent of the attractive-repelling interactions observed with two-component droplets on a solid substrate, where the interactions are induced by the evaporation of one component (Cira, Benusiglio & Prakash, 2015). These interactions are also similar to the ones found in the Cheerios' effect, where the interface deformation induced by both the wetting properties and the buoyancy of the object deposited at the interface are the key factors (Vella & Mahadevan, 2004; Vella, Metcalfe & Whittaker, 2006). Similar interactions have been found for droplets on immiscible fluids (Keiser, Bense, Colinet, Bico & Reyssat, 2017) or on soft substrates (Karpitschka, Pandey, Lubbers, Weijs, Botto, Das, Andreotti & Snoeijer, 2016). One could therefore think of inducing the motion of pendent drops or liquid bridges by locally generating capillary waves, for instance by a substrate perturbation. The motion of these drops or liquid bridges will then induce an anisotropic capillary wave field resulting in anisotropic interaction forces with neighboring drops and liquid bridges. Note that the crystalline-like arrangement of pendent

droplets observed in Chapters 4 and 5 might be a result of these capillary interactions. It is likely that other arrangements are theoretically possible, but are unstable and thus difficult to observe (Lister et al., 2010).

Finally, we have found that both the catamaran pattern and the valleys observed in Fig. 8.5 for larger L values can be well reproduced by solving Eq. (8.17) with a topography $h^o = \mathrm{H}(r - L/2)$, where H is the Heaviside function centered at $r = L/2$, which corresponds to the boundary of the pancake or liquid bridge. This is equivalent to perturbing the film thickness by a Dirac in the gradient of the topography all along the boundary.

8.3.2 Nonlinear solutions

In the same way as for the one-dimensional case of Sec. 8.2.2, we proceed now to the presentation of the results for the nonlinear film-thickness profiles obtained by the solution of Eq. (8.12). As boundary conditions we impose the film thickness $\bar{H}(r = L/2) = 1$ and the mean curvature $\bar{\kappa}(r = L/2) = \kappa_{f,r}$ at the droplet or liquid-bridge edges. The mean curvature is composed by a component in the (x, y)-plane, which is positive for a pancake bubble and negative for a liquid bridge, and a component in the (x, z)-plane, like the one for the one-dimensional problem, see Eq. (8.10). In view of the discussion of Sec. 8.3.1, and in the spirit of Nagel (2014) and Meiburg (1989), we consider the local capillary number defined with the normal velocity to the static cap for the mean curvature model:

$$\kappa_{f,r}(r,\theta) = \underbrace{\frac{1 + T_{f,r}(3Ca|\cos\theta|)^{2/3}}{1 + Z_{f,r}(3Ca|\cos\theta|)^{2/3}}}_{(x,z)\text{-plane}} \pm \underbrace{\frac{\pi}{4}\frac{1}{r}}_{(x,y)\text{-plane}} , \tag{8.19}$$

where the coefficients with subscript f have to be used for $\theta \in [-\pi/2, \pi/2]$ and the ones with subscript r for $\theta \in [\pi/2, 3\pi/2]$. The correction $\pi/4$ for the curvature $1/r$ in the (x, y)-plane, where $r = L/2$ for a circular geometry, has been derived asymptotically by Park & Homsy (1984). Note that a more involved model could be used to describe the curvature in the (x, z)-plane in the lateral transition regions (Burgess & Foster, 1990).

For the two-dimensional problem, the (x, y)-shape of the pancake or liquid bridge is not defined a priori. However, one can assume that in the limit of small capillary number, the shape $r = r(\theta)$ can be well approximated by a circle.

The nonlinear film-thickness profiles for a pancake and a liquid bridge for a small capillary number are shown in Fig. 8.8. Very similar observations as the ones for the linear results of Fig. 8.5 can be done. Note that the amplitude of the catamarans for the pancake bubble or the valleys left by the moving liquid bridge are weak, yet they present the same trends as their linear counterparts.

An important observation has to be done. Thus far, the thickness of the precursor film for the moving liquid bridge was assumed to be H_∞, given by Eq. (8.9), which is the asymptotic

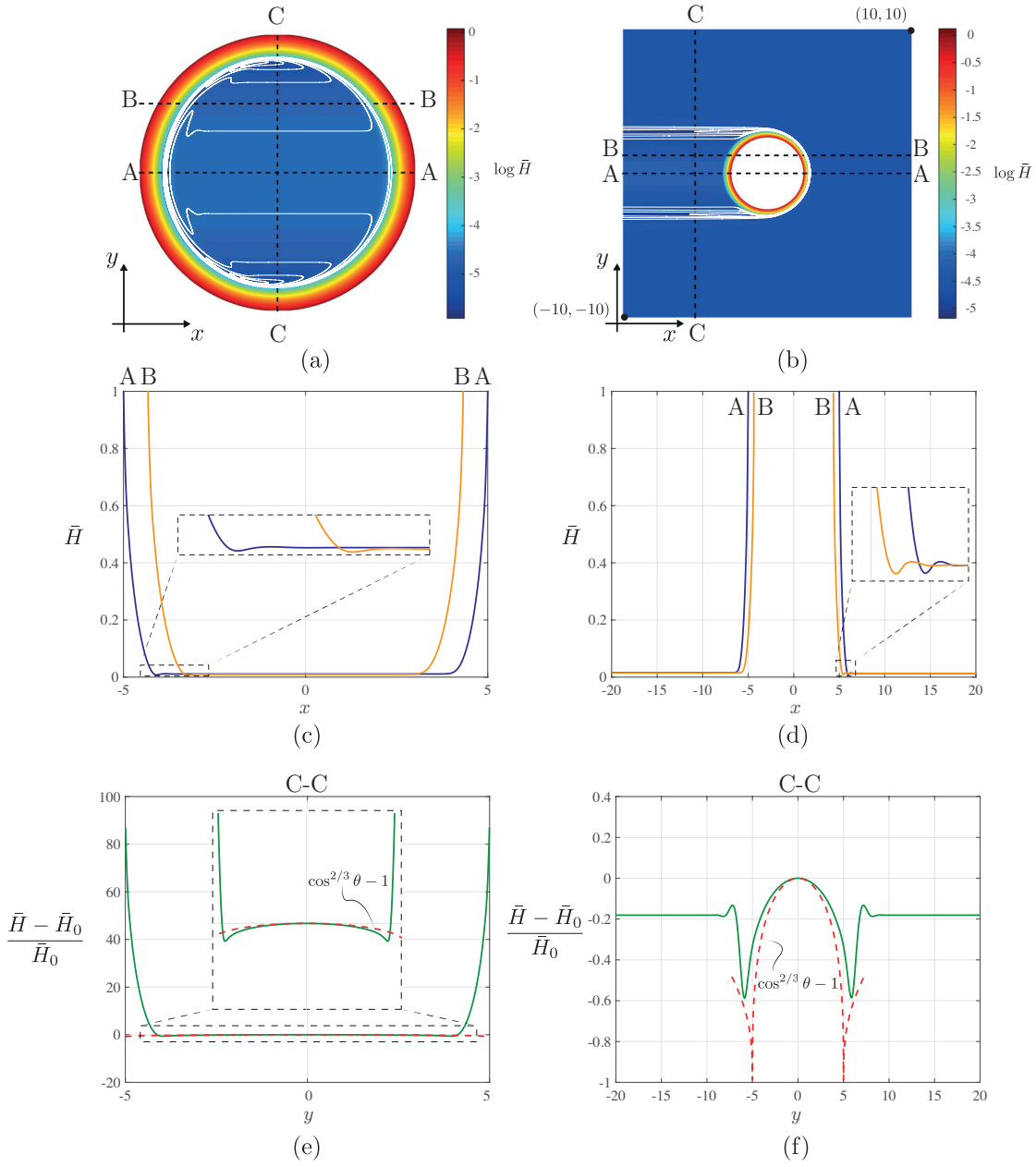

Figure 8.8 – Nonlinear film thickness $\bar{H}$ for a pancake bubble (a,c,e) and for a liquid bridge (b,d,f). The film-thickness map $\log \bar{H}$ is shown in panels (a,b), where isolines have been added for visualization purposes. The cuts along the streamwise direction at two different y-locations are plotted in panels (c,d) and the normalized difference of the film thickness along the spanwise cut C-C with respect to $\bar{H}_0 = \bar{H}(y = 0)$ along this cut is shown in panels (e,f), where the analytical prediction is given by the red dashed line. $L = 10$, $A = 10^{-3} \times H_\infty$, $Ca = 10^{-3}$ and $Bo = 0$.

prediction of the film thickness deposited by a receding meniscus with a capillary number Ca. As we can see in Fig. 8.8(b) the thickness left by the receding meniscus of the liquid bridge is

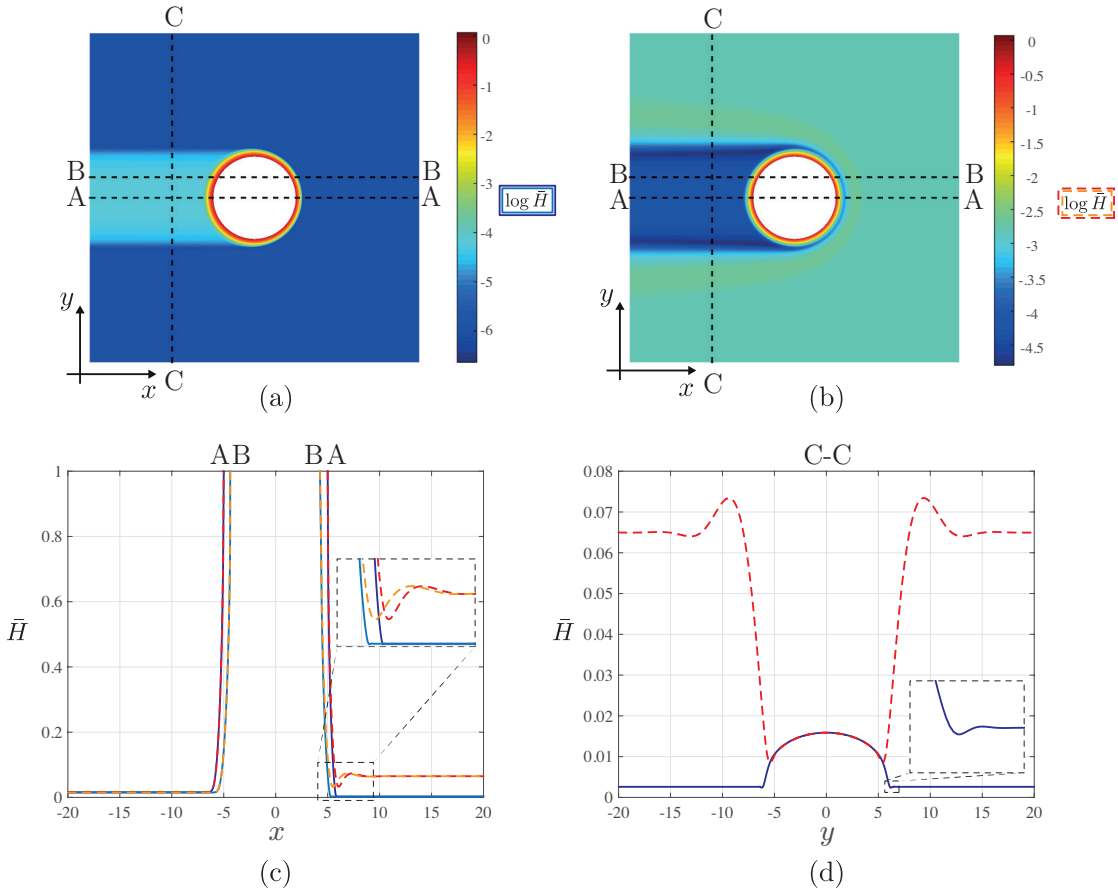

Figure 8.9 – Effect of the thickness b of the precursor film surrounding the liquid bridge. Film-thickness maps for (a) $b = H_\infty/5$, (b) $b = 5 \times H_\infty$ and film-thickness profiles in the streamwise (c) and spanwise (d) directions. $L = 10$, $A = 10^{-3} \times H_\infty$, $Ca = 10^{-3}$ and $Bo = 0$. See Fig. 8.8 for the case $b = H_\infty$.

indeed very close to H_∞. However, the thickness of the precursor film b can be changed as desired. Therefore, if the plates are initially coated with a thickness larger than H_∞, the wake left by liquid bridge with a capillary number Ca will correspond to a region of smaller film thickness (see Fig. 8.9(b)). On the contrary, if the precursor film thickness is smaller than H_∞, the wake will correspond to a region of larger film thickness (see Fig. 8.9(a)). Note that this is precisely the reason why in Chapter 5 the sliding drops generate a wake with strong thin film valleys at the beginning, when the surrounding film is thick, whereas they generate a thicker film at later times, when the surrounding thickness is reduced. The thickness deposited by the receding meniscus is independent of the thickness of the precursor film b and is solely dictated by the capillary number (see Fig. 8.9(c,d)), which still might be a function of b, as we have seen being the case for the Rayleigh-Taylor-induced sliding drops of Chapter 5.

At higher Ca, the precise shape of a pancake is no longer a circle, but it is closer to an oval. The shape could in principle be found by imposing the force and torque-free conditions (see

Chapter 10). In the present work, however, we extract the pancake shape from the results of the three-dimensional boundary element simulations performed by Lailai Zhu (see Zhu & Gallaire (2016) for more details) for an isoviscosity droplet ($\mu_i = \mu_o$). We have found that the boundaries of the deformed pancake in the (x, y)-plane can be well described by the equation

$$\frac{x^2}{c_1^2} + \frac{y^2 \exp(c_3 x)}{c_2^2} = 0, \tag{8.20}$$

where c_1, c_2 and c_3 are fitting coefficients.

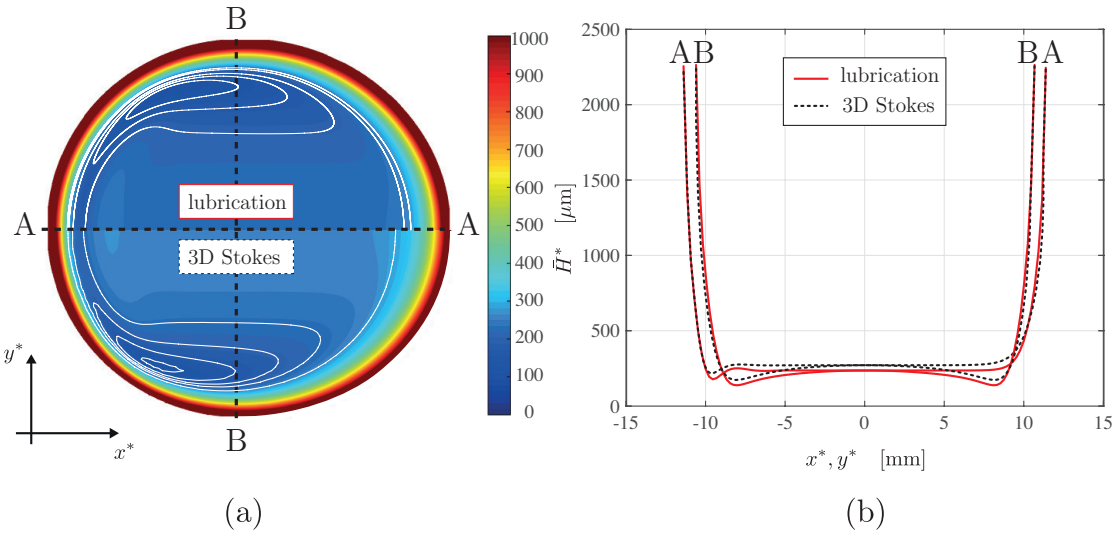

Figure 8.10 – Comparison between the dimensional film thickness $\bar{H}^*$ obtained by the solution of the nonlinear lubrication equation (which assumes $\mu_i = 0$) and the three-dimensional Stokes equations (which assumes $\mu_i = \mu_o$) for $Ca = 4 \times 10^{-2}$ and $Bo = 0.3$.

The comparison between the film-thickness profile obtained by the solution of the nonlinear lubrication equation, with the model (8.19) for the static cap mean curvature $\kappa_{f,r}(r,\theta)$, and the one obtained by the boundary element simulations is shown in Fig. 8.10. One can observe that both methods predict the formation of catamarans at the lateral transition regions, a uniform film thickness in the center and oscillations at the back, as we have seen for the linear results. The agreement is not only qualitative, but almost quantitative. The relative error in the uniform film thickness is of 10% and its absolute value is 30 μm. However, it has to be stressed that for the 3D-Stokes simulations we assumed the same viscosity for both inner and outer phases, $\mu_i = \mu_o$, and not $\mu_i = 0$ as for the lubrication approach. As we will see in Chapter 9, the larger the inner viscosity, the thicker the film. This could explain the thicker film obtained by the boundary element simulations. Furthermore, we have already seen for the one-dimensional case of Fig. 8.3(b) that the lubrication equation slightly underestimates the thickness of the thin film compared to the 2D-Stokes result at large Ca. In light of these differences, the agreement is satisfactory. It has to be mentioned that experiments performed by the colleagues Isha Shukla and Nicolas Kofman nicely agree with the 3D-Stokes results.

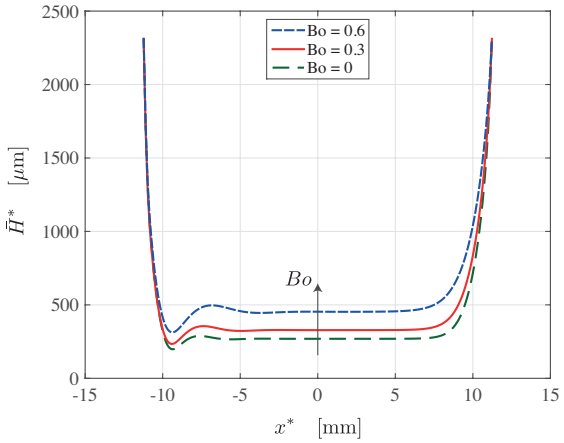

Figure 8.11 – Effect of the Bond number on the dimensional film thickness $\bar{H}^*$ along the centerline $y^* = 0$ obtained by the solution of the nonlinear lubrication equation for $Ca = 4 \times 10^{-2}$ and $Bo = 0$, 0.3 and 0.6.

Finally, it is worth noting that we also performed a computation for the same capillary number but with different Bond numbers and found that the thickness of the uniform film region increases with increasing Bo (see Fig. 8.11). In fact, since the curvature of the static cap has to vary in space in order to balance the variation of hydrostatic pressure in the outer fluid, the stronger the gravitational forces, the larger the curvature variations and thus the thicker the film left by the receding meniscus. The gravitational field induces an additional half-Poiseuille flow in the thin film, which is opposed to the capillary flow induced by the curvature variations in the front dynamic meniscus. Note that in reality, however, the velocity of a pancake bubble, and thus the capillary number, is also affected by the Bond number. Yet, the employed framework allows for the separate investigation of the capillary and the Bond number effects.

8.4 Conclusions and perspectives

The aim of this chapter was to present in a unified way the thickness-profile pattern of the liquid film surrounding one- and two-dimensional advancing and receding menisci. This general problem is closely related to the motion of pendent drops and fingers on thin films (see Chapters 3, 4, 5 and 6), as well as to the thin films surrounding confined bubbles and droplets in microchannels (see Chapters 9 and 10). The obtained lubrication equations have been solved as a boundary value problem, rather than as an initial value problem as usually done in the literature. In order to unravel the structure of the film-thickness profile, we have first considered the linear perturbations around a uniformly-thick film. The perturbations in the boundary conditions mimic the presence of a meniscus of greater film thickness.

For the one-dimensional lubrication equation, we have recovered the oscillating film-thickness profile close to the advancing meniscus and the monotonically increasing film thickness close

to the receding meniscus. The nonlinear solution of the lubrication equation presents the same pattern, yet with smaller amplitude variations.

The advantage of the proposed technique is that the two-dimensional lubrication equation can be easily treated in the same manner. We have been able to show that not only the oscillations at the advancing meniscus, but also the catamaran-like pattern observed in the thin film separating a pancake bubble or droplet from the Hele-Shaw walls can be directly found by solving the linear two-dimensional lubrication equation when perturbing the film thickness at the boundaries. In particular, the catamaran-like structure results from the anisotropic flux induced by the motion of the walls with respect to the pancake and the need to match the film thickness to larger values in the dynamic meniscus region surrounding the region where the thin film is rather uniform. In the central part, the thickness left by the receding meniscus scales as $(Ca\cos\theta)^{2/3}$, and depends therefore on the velocity normal to the interface. This scaling no longer holds in the lateral transition region, where the component of the flux tangential to the interface becomes important and the thickness of the film scales as $Ca^{4/5}$ (Burgess & Foster, 1990). The nonlinear solutions for the film-thickness profile of a pancake bubble compare very well with the results of three-dimensional Stokes equations, evidencing the strength of the used lubrication approach.

Similarly, a liquid bridge moving on a thin precursor film deposits a film at its rear which is not uniform in thickness. In particular, the thickness of the film in the lateral transition region is found to be much smaller than in the central region, as for the catamarans regions of the pancake bubble. Hence, the deposited film presents two valleys corresponding to the lateral ends of the liquid bridge. Furthermore, we have found that since the receding meniscus always deposits the same amount of fluid for a given capillary number, a liquid bridge advancing on a thin or a thick precursor film can leave a region of either larger or smaller film thickness in its wake compared to the surrounding film. However, it has to be stressed that we did not considered here the question of the velocity of such a liquid bridge, which is in fact related to the thickness of the precursor film (see Chapter 5).

We have also shown that a liquid bridge induces a perturbation field in the surrounding thin film which is very similar to the one induced in a thin film flowing over a localized perturbation in the substrate topography. We believe that the so-induced anisotropic field of capillary waves could be exploited to move pendent drops and to modify their two-dimensional arrangement.

It has to be noted that the nonuniform film thickness left by the motion of a liquid bridge would induce coating irregularities. Similarly, if one would like to use pancake bubbles to remove impurities from the channel walls (Khodaparast, Kim, Silpe & Stone, 2017), the result will not be homogeneous either.

As a possible follow-up of this work, it would be interesting to assess if these nonuniformity in the film-thickness distribution might be the reason for the mismatch between the experimentally measured and the theoretically predicted velocities of pancake bubbles and liquid bridges in Hele-Shaw cells (Kopf-Sill & Homsy, 1988; Saffman & Tanveer, 1989; Meiburg, 1989;

Gallaire et al., 2014). A crucial point to consider when developing such a velocity model is the pressure correction induced by the mean curvature of the static cap (Burgess & Foster, 1990; Nagel, 2014). Present models fail already at moderate capillary numbers. We believe that the increased computational capabilities should allow for a better understanding of the precise shape of the static cap at larger capillary numbers, resulting therefore in more accurate models.

In the following Chapter 9 we extend the theory to a confined droplet of nonvanishing viscosity in a two-dimensional capillary, where its velocity can be found by applying mass conservation, whereas in Chapter 10 we will discuss the case of a nonconfined bubble in a microchannel, where the bubble velocity is solely given by the force and torque-free conditions.

8.5 Appendix

8.5.1 Classical derivation of the linearized Landau-Levich-Derjaguin equation (Bretherton, 1961)

One can integrate Eq. (8.3) to obtain

$$\bar{H}^3\left(\frac{1}{3Ca}\bar{\kappa}_x - \frac{Bo}{3Ca}\right) - \bar{H} = Q_\infty, \tag{8.21}$$

where Q_∞ is the integration constant. Mass conservation implies that Q_∞ is equal to the flux in the region of uniform thickness H_∞:

$$Q_\infty = -H_\infty^3\frac{Bo}{3Ca} - H_\infty. \tag{8.22}$$

By combining Eqs. (8.21) and (8.22), and assuming small variations of film thickness resulting in $\bar{\kappa} = \bar{H}_{xx}$, one obtains the equation

$$\bar{H}_{xxx} = 3Ca\frac{\bar{H} - H_\infty}{\bar{H}^3} - \left[\left(\frac{H_\infty}{\bar{H}}\right)^3 - 1\right]Bo. \tag{8.23}$$

Two cases deserve now to be distinguished: the pressure driven bubble and the buoyancy rising bubble. We assume that in the former case gravity can be neglected while it is the dominant term in latter. Furthermore, for the case of a rising bubble in a closed tube, conservation of mass indicates that the flux through the thin uniform film in the laboratory frame has to be equal to the flux displaced by the advancing cap:

$$-H_\infty^3\frac{Bo}{3Ca} = -2(1 - H_\infty) \tag{8.24}$$

so that $Bo/(3Ca) \sim 1/H_\infty^2 \gg 1$ and the buoyancy term in Eq. (8.23) dominates over the pressure one.

Using the change of variable of Bretherton (1961), namely $\bar{H} = H_\infty \bar{\eta}$ and $x = H_\infty/(3Ca)^{1/3}\xi$, the pressure-driven limit of Eq. (8.23) becomes

$$\bar{\eta}_{\xi\xi\xi} = \frac{\bar{\eta}-1}{\bar{\eta}^3}. \tag{8.25}$$

As we will see in Chapter 9, this equation can be linearized around the uniform film thickness: $\bar{\eta} = 1 + \varepsilon\eta$, resulting in the equation

$$\eta_{\xi\xi\xi} = \eta, \tag{8.26}$$

On the other hand, for the buoyancy driven bubble, Bretherton (1961) suggests the change of variable $\bar{H} = H_\infty \bar{\eta}$ and $x = H_\infty/(Bo)^{1/3}\xi$ for Eq. (8.23):

$$\bar{\eta}_{\xi\xi\xi} = 1 - \frac{1}{\bar{\eta}^3}. \tag{8.27}$$

Equation (8.27) can be linearized using $\bar{\eta} = 1 + \varepsilon\eta$ to give

$$\eta_{\xi\xi\xi} = 3\eta \tag{8.28}$$

Therefore, in both cases, the linearized equation reads $\eta_{\xi\xi\xi} = \tilde{K}\eta$, with $\tilde{K} = 1$ or $\tilde{K} = 3$ for the first and second case, respectively. The solution of this linear equation is

$$\eta(\xi) = \alpha \exp(\tilde{K}^{1/3}\xi) + \beta \exp\left(-\frac{\tilde{K}^{1/3}\xi}{2}\right)\cos\left(\frac{\sqrt{3}\tilde{K}^{1/3}\xi}{2} + \phi\right) \tag{8.29}$$

where α and β are real coefficients and ϕ a parameter taken such that the curvatures at the front and rear extremities of the bubble coincide (Cantat, 2013). The same discussion as for Eq. (8.8) holds.

However, the film-thickness profiles in the static region of a pressure and a gravity-driven bubble are different. In fact, away from the uniform thin film one has $\bar{\eta} \gg 1$, so that Eq. (8.25) becomes $\bar{\eta}_{\xi\xi\xi} = 0$, whereas Eq. (8.27) simplifies to $\bar{\eta}_{\xi\xi\xi} = 1$. Therefore, the film thickness reaches a constant curvature in the static cap of a pressure-driven bubble, where the curvature of the film of a gravity-driven bubble increases linearly. In fact, the variation of the hydrostatic pressure gradient has to be balanced by a capillary-pressure gradient. The dimensional constant curvature in the static cap of a pressure-driven bubble can be matched to $1/R^*$ to find the uniform film thickness H_∞. Bretherton (1961) showed in the second part of his paper that a bubble rising with a constant velocity does not exist if the radius of the sealed tube is smaller than $0.918\sqrt{\gamma/(\rho_o g)}$. This problem has been recently revisited by Lamstaes & Eggers (2017). For completeness, we mention that the disjoining pressure effect on the film-thickness profile, due for instance to van der Waals forces, has been investigated by Chaudhury, Acharya & Chakraborty (2014) and Hammoud, Trinh, Howell & Stone (2017).

8.5.2 Lubrication equation for a pressure-driven bubble in a curvilinear-coordinate system

The interface in the curvilinear-coordinate system is described by:

$$x = x(s)\,, \tag{8.30}$$

$$y = y(s)\,, \tag{8.31}$$

$$\theta = \theta(s)\,, \tag{8.32}$$

for $s \in [0,1]$, where θ is the angle between the interface and the horizontal. The symmetry of the profile at the bubble front and rear ends simply reads $\theta = \pm\pi/2$. The metric reads

$$\frac{dx}{ds} = l\cos\theta\,, \tag{8.33}$$

$$\frac{dy}{ds} = l\sin\theta \tag{8.34}$$

with l the length of the interface. The curvature is then simply expressed by $\bar{\kappa} = d\theta/(l\,ds)$. In this framework, the lubrication equation for a pressure-driven bubble can be rewritten as:

$$\frac{1}{3Ca}\frac{y^3}{l^3}\frac{1}{\cos^2\theta}\left(\tan\theta\frac{d\theta}{ds}\frac{d^2\theta}{ds^2}+\frac{d^3\theta}{ds^3}\right)+\frac{1}{Ca}\frac{y^2}{l^3}\frac{1}{\cos^2\theta}\frac{dy}{ds}\frac{d^2\theta}{ds^2}-\frac{1}{\cos\theta}\frac{1}{l}\frac{dy}{ds}=0\,. \tag{8.35}$$

Note that this equation diverges as $\theta \to \pm\pi/2$, but there the boundary conditions are applied. We can therefore multiply by $\cos^2\theta$ which is not vanishing for $\theta \in]-\pi/2,\pi/2[$ and obtain:

$$\frac{1}{3Ca}\frac{y^3}{l^3}\left(\tan\theta\frac{d\theta}{ds}\frac{d^2\theta}{ds^2}+\frac{d^3\theta}{ds^3}\right)+\frac{1}{Ca}\frac{y^2}{l^3}\frac{dy}{ds}\frac{d^2\theta}{ds^2}-\frac{\cos\theta}{l}\frac{dy}{ds}=0\,. \tag{8.36}$$

To solve Eq. (8.36) we employ the Newton method. The unknowns are x, y, θ and l. The system is composed by two first order ordinary differential equations related to the metric, Eqs. (8.33) and (8.34), and a third order differential equation governing the interface location, Eq. (8.36). For the Newton iteration, we still have to define the Jacobian matrix. This is easily found by perturbing the system and considering the resulting linear operator. The Jacobian matrix for y is:

$$\frac{1}{Ca}\frac{y^2}{l^3}\left(\tan\theta\frac{d\theta}{ds}\frac{d^2\theta}{ds^2}+\frac{d^3\theta}{ds^3}\right)\mathrm{I}+\frac{1}{Ca}\frac{2y}{l^3}\frac{dy}{ds}\frac{d^2\theta}{ds^2}\mathrm{I}+\frac{1}{Ca}\frac{y^2}{l^3}\frac{d^2\theta}{ds^2}\mathrm{D}_1-\frac{\cos\theta}{l}\mathrm{D}_1\,, \tag{8.37}$$

where I is the identity matrix and D_i is the i^{th}-oder differential operator. For the θ-component, the Jacobian is:

$$\frac{1}{3Ca}\frac{y^3}{l^3}\left[\left(1+\tan^2\theta\right)\frac{d\theta}{ds}\frac{d^2\theta}{ds^2}\mathrm{I}+\tan\theta\frac{d^2\theta}{ds^2}\mathrm{D}_1+\tan\theta\frac{d\theta}{ds}\mathrm{D}_2+\mathrm{D}_3\right]+\frac{1}{Ca}\frac{y^2}{l^3}\frac{dy}{ds}\mathrm{D}_2+\frac{\sin\theta}{l}\frac{dy}{ds}\mathrm{I}, \tag{8.38}$$

and the one for the length of the bubble interface l the Jacobian is:

$$-\frac{1}{Ca}\frac{y^3}{l^4}\left(\tan\theta\frac{d\theta}{ds}\frac{d^2\theta}{ds^2}+\frac{d^3\theta}{ds^3}\right)-\frac{1}{Ca}\frac{3y^2}{l^4}\frac{dy}{ds}\frac{d^2\theta}{ds^2}+\frac{\cos\theta}{l^2}\frac{dy}{ds}. \tag{8.39}$$

As initial condition, we employ a half circle, which is defined by:

$$x(s) = -\frac{L}{2}\cos(s\pi), \tag{8.40}$$

$$y(s) = 1-\frac{L}{2}\sin(s\pi), \tag{8.41}$$

$$\theta(s) = s\pi-\frac{\pi}{2}, \tag{8.42}$$

$$l = \frac{L}{2}\pi. \tag{8.43}$$

The Newton iteration reads:

$$\mathrm{u} = \mathrm{u}-\mathrm{J}^{-1}\mathrm{f}(\mathrm{u}), \tag{8.44}$$

where u is the solution vector containing x, y, θ and l, J is the matrix containing all the Jacobian matrices and f is the vector with the equations. The boundary conditions $x = -L/2$, $x = L/2$, $y = 1$ and $\theta = \pm\pi/2$ are substituted into some lines of the vector f and the Jacobian matrix is modified correspondingly.

In order to obtain the bubble profile for a given Ca and bubble length, we employ Keller's arclength continuation method (see Doedel (2007) for a comprehensive description). The advantage of such a method is that the next value for the control parameter is not set a priory, but is intrinsically found by the Newton iteration. The value of the control parameter is left as an unknown and an additional equation defining its magnitude is added to the system; it will depend on how the solution is evolving. The Jacobian matrix is modified accordingly. Starting from a bubble having an initial shape corresponding to a half circle, one has first to increase its length so as to have a region with uniform-film thickness close to the wall. Therefore, we first loop over L until a uniform film appears. The capillary number, is subsequentially decreased. To accurately conserve the flow rate at every x-location, it is necessary to refine the grid when increasing the length of the bubble and decreasing the capillary number.

9 Viscous Taylor droplets in axisymmetric and planar tubes: from Bretherton's theory to empirical models

Remark This chapter is largely inspired by the publication of the same name

G. Balestra[1], L. Zhu[1,2,3] and F. Gallaire[1]

[1]Laboratory of Fluid Mechanics and Instabilities, EPFL, CH1015 Lausanne, Switzerland
[2]Linné Flow Centre and Swedish e-Science Research Centre (SeRC), KTH Mechanics, SE 10044 Stockholm, Sweden
[3]Department of Mechanical and Aerospace Engineering, Princeton University, NJ 08544, USA

Microfluidics and Nanofluidics **22**: 67 (2018)

The aim of this study is to derive accurate models for quantities characterizing the dynamics of droplets of nonvanishing viscosity in capillaries. In particular, we propose models for the uniform-film thickness separating the droplet from the tube walls, for the droplet front and rear curvatures and pressure jumps, and for the droplet velocity in a range of capillary numbers, Ca, from 10^{-4} to 1 and inner-to-outer viscosity ratios, λ, from 0, *i.e.* a bubble, to high viscosity droplets. Theoretical asymptotic results obtained in the limit of small capillary number are combined with accurate numerical simulations at larger Ca. With these models at hand, we can compute the pressure drop induced by the droplet. The film thickness at low capillary numbers ($Ca < 10^{-3}$) agrees well with Bretherton's scaling for bubbles as long as $\lambda < 1$. For larger viscosity ratios, the film thickness increases monotonically, before saturating for $\lambda > 10^3$ to a value $2^{2/3}$ times larger than the film thickness of a bubble. At larger capillary numbers, the film thickness follows the rational function proposed by Aussillous & Quéré (2000) for bubbles, with a fitting coefficient which is viscosity-ratio dependent. This coefficient modifies the value to which the film thickness saturates at large capillary numbers. The velocity of the droplet is found to be strongly dependent on the capillary number and viscosity ratio. We also show that the normal viscous stresses at the front and rear caps of the droplets cannot be neglected when calculating the pressure drop for $Ca > 10^{-3}$.

List of symbols[1]

A	coefficient for flow profile
B	coefficient for flow profile
C	coefficient for interface profile of static meniscus
$\mathscr{C}$	mean curvature of droplet interface
D	coefficient for interface profile of static meniscus
c_1, c_2	coefficient for fitting law of P, $\bar{P}$
Ca	capillary number based on droplet velocity
Ca_∞	capillary number based on mean outer velocity
F	coefficient for minimum film thickness
$\bar{F}$	averaged F coefficient
G	coefficient for minimum film thickness
H	thickness of film between wall and droplet
H_{min}	minimum film thickness
H_∞	uniform film thickness
$H_\infty^\star$	critical uniform film thickness for recirculations
K	coefficient for linearized lubrication equation
$\mathbf{I}$	identity tensor
L_d	droplet length
M	coefficient for pressure model
m	rescaled viscosity ratio
N	coefficient for pressure model
$\mathbf{n}$	unit vector normal to the droplet interface
O	coefficient for pressure model
P	coefficient for interface profile of static meniscus
$\bar{P}$	averaged P coefficient
p	pressure
p_{linear}	pressure if constant gradient
Q	coefficient for uniform film-thickness model
q	volume flux
R	capillary tube radius or half width
Re	Reynolds number
r	radial direction (axisymmetric geometry)
$\tilde{r}$	half width of droplet
S	coefficient for classical pressure model
t	time
T	coefficient for plane curvature model
U_d	droplet velocity
U_∞	average outer flow velocity
u_∞	outer far-field velocity profile

[1] Since dimensional variables are considered in this chapter, the asterisk $\blacksquare^*$ is omitted.

$\mathbf{u}$	velocity field
u	streamwise velocity
v	spanwise velocity
x	streamwise direction (planar geometry)
y	spanwise direction (planar geometry)
z	axial direction (axisymmetric geometry)
Z	coefficient for plane curvature model

Greek symbols

α	parameter for solution of linear lubrication equation
β	coefficient for plane curvature model
Δ	difference between inner and outer quantities
Δp^{NP}	pressure correction due to nonparallel flow effects
Δp_{tot}	total pressure drop
γ	surface tension
η	rescaled film thickness
κ	plane curvature of droplet interface in (z,r) or (x,y)
$\kappa_{f,r}$	plane curvature at the front/rear droplet extremities
λ	inner-to-outer dynamic viscosity ratio
μ	dynamic viscosity
ξ	rescaled axial direction
$\boldsymbol{\sigma}$	total stress tensor
τ	viscous stress tensor
ϕ	phase of solution of linear lubrication equation
χ	geometric coefficient
Ω	droplet volume or area

Subscripts and superscripts

f	front cap
i	inner
o	outer
r	rear cap
zz	normal tensor component in the axial direction

Abbreviations

2D	two-dimensional
3D	three-dimensional
ALE	arbitrary Lagrangian-Eulerian
BIM	boundary integral method
FEM	finite element method

9.1 Introduction

The dynamics of a bubble in a microchannel has been the subjects of several studies, since the seminal works of Fairbrother & Stubbs (1935), Taylor (1961) and Bretherton (1961). These long bubbles, also referred to as *Taylor bubbles*, flowing in a tube of radius R, have been characterized by the thickness H_∞ of the uniform film separating them from the tube walls, the minimum thickness H_{min} of the film, the plane curvature of the front and rear caps in the (z,r) or (x,y) plane, κ_f and κ_r, as well as by their velocity U_d. Bretherton (1961) used a lubrication approach to derive the asymptotic scalings in the limit of small capillary numbers, $Ca = \mu_o U_d/\gamma$, where μ_o is the dynamic viscosity of the outer fluid and γ the surface tension. In particular, Bretherton (1961) showed that in the limit of $Ca \to 0$ the film thickness scales as $H_\infty/R \sim 0.643(3Ca)^{2/3}$ and that the plane curvature of the front and rear caps scales as $\kappa_{f,r}R \sim 1+\beta_{f,r}(3Ca)^{2/3}$, with $\beta_{f,r}$ a different coefficient for front and rear caps. The uniform thin-film region is connected to the static cap of constant curvature at the extremities of the bubble through a dynamic meniscus (Cantat, 2013) (see Fig. 9.1). The counterpart theory for

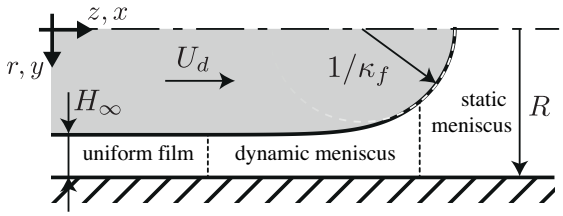

Figure 9.1 – Sketch of the front meniscus of the bubble advancing at velocity U_d in a capillary of radius R with indication of the uniform thin-film region of thickness H_∞, the dynamic meniscus region and the static meniscus region. The plane curvature κ_f of the front static cap in the (z,r) or (x,y) plane is also highlighted.

a bubble in a square duct was derived by Wong, Radke & Morris (1995*a*,*b*) (see also Chapter 10). However, these scalings agree with Taylor's experimental results (Taylor, 1961) only in the small Ca limit, namely when $Ca \lessapprox 10^{-3}$. To understand the dynamics of confined bubbles in a broader parameter range, researchers have performed experiments (Chen, 1986; Aussillous & Quéré, 2000; Fuerstman, Lai, Thurlow, Shevkoplyas, Stone & Whitesides, 2007; Han & Shikazono, 2009; Boden, dos Santos Rolo, Baumbach & Hampel, 2014) as well as numerical simulations (Shen & Udell, 1985; Reinelt & Saffman, 1985; Ratulowski & Chang, 1989; Giavedoni

& Saita, 1997, 1999; Heil, 2001; Kreutzer et al., 2005; Lac & Sherwood, 2009; Gupta, Leung, Manica, Fletcher & Haynes, 2013; Anjos, Borhani, Mangiavacchi & Thome, 2014*a*; Anjos, Mangiavacchi, Borhani & Thome, 2014*b*; Langewisch & Buongiorno, 2015). As an outcome, several correlations have been proposed for the evolutions of the relevant quantities as a function of the different parameters (see for example Han & Shikazono (2009) and Langewisch & Buongiorno (2015)). Among them, Aussillous & Quéré (2000) proposed an ad-hoc rational function with a fitting parameter for the film thickness which is in good agreement with the experimental results of Taylor (1961) for capillary numbers up to 1. The two recent works of Klaseboer et al. (2014) and Cherukumudi et al. (2015) tried to put a theoretical basis to this extended Bretherton's theory for larger Ca.

In contrast to bubbles, which have experienced a vast interest of the scientific community, little amount of effort has been made for droplets whose viscosities are comparable to or much larger than that of the outer fluid. Yet, droplets of arbitrary viscosities are crucial for Lab-on-a-Chip applications (Anna, 2016). A first theoretical investigation of the effect of the inner phase viscosity was conducted by Schwartz et al. (1986), motivated by the discrepancy in the predicted and the measured film thicknesses of long bubbles in capillaries. They demonstrated that the nonvanishing inner-to-outer viscosity ratio could thicken the film. Hodges, Jensen & Rallison (2004*a*) further extended the theory and showed that the film becomes even thicker at intermediate viscosity ratios. Numerical simulations have been performed to investigate the droplets in capillaries (Martinez & Udell, 1990; Tsai & Miksis, 1994; Lac & Sherwood, 2009).

Models predicting the characteristic quantities such as the uniform film thickness and the meniscus curvatures of droplets in capillaries over a wide range of capillary numbers are still missing. For example, the velocity of a droplet of finite viscosity flowing in a channel still remains a simple question yet an open challenge. Such a prediction is, however, of paramount importance for the correct design of droplet microfluidic devices. As an example, Jakiela et al. (2011) performed extensive experiments for droplets in square ducts, showing complex dependencies of the droplet velocity on the capillary number, viscosity ratio and droplet length. Also, what is the pressure drop induced by the presence of a drop in a channel? This question is crucial and has been the subjects of recent works, for example the ones Warnier et al. (2010) and Ładosz, Rigger & von Rohr (2016). Other quantities, such as the minimum film thickness H_{min}, have to be accurately predicted as well. H_{min} becomes essential for heat transfer or cleaning of microchannels applications (Magnini, Ferrari, Thome & Stone, 2017; Khodaparast et al., 2017). Furthermore, being able to predict the flow field inside and outside of the droplet is crucial if one is interested in the mixing capabilities of the system.

Here, we aim at bridging this gap by combining asymptotic derivations with accurate numerical simulations to propose physically inspired empirical models, for the characteristic quantities of a droplet of arbitrary viscosity ratio flowing in an axisymmetric or planar capillary with a constant velocity. The model coefficients are specified by fitting laws. The present work provides the reader with a rigorous theoretical basis, which can be exploited to understand the dynamics of viscous droplets. The considered capillary numbers vary from 10^{-4} to 1

and the inner-to-outer viscosity ratio from 0 to 10^5. Following the work of Schwartz et al. (1986), we extend the low-capillary-number asymptotical results obtained with the lubrication approach of Bretherton (1961) for bubbles to viscous droplets. Numerical simulations based on finite element method (FEM) employing the arbitrary Lagrangian-Eulerian (ALE) formulation are performed to validate the theoretical models and then extend them to the large-capillary-number range, $Ca \sim O(1)$, where the lubrication analysis fails.

The chapter is structured in a way to build, step by step, the models for the uniform film thickness, the front and rear droplet's interface plane curvatures as well as those for the front and rear pressure drops required to compute the total pressure drop along a droplet in a channel. We present the problem setup, governing equations, numerical methods and the validations in Sec. 9.2. The flow fields inside and outside of the droplets as a function of the capillary numbers and viscosity ratios are shown in Sec. 9.3. In particular, the flow profiles in the uniform-film region are derived in Sec. 9.3.1 and the flow patterns are presented in Sec. 9.3.2. The theoretical part starts with the asymptotic derivation of the model for the uniform film thickness in Sec. 9.4. The derivation of the lubrication equation is detailed in Sec. 9.4.1, followed by the film thickness model in Sec. 9.4.2 and its extension to larger capillary numbers in Sec. 9.4.3. With the knowledge of the film thickness, the droplet velocity can be computed analytically (see Sec. 9.5). The minimum film thickness separating the droplet form the channel walls is discussed in Sec. 9.6. To build a total pressure drop model, one still needs the knowledge of the front and rear caps mean curvatures (see Sec. 9.7.1), the front and rear pressure jumps (see Sec. 9.7.2 and 9.7.4) and the front and rear normal viscous stress jumps (see Sec. 9.7.3). The stresses evolutions at the channel centerline and at the wall are presented in Sec. 9.8.1 and Sec. 9.8.2, respectively. Eventually, one can sum up all these contributions to build the total pressure drop, which is described in Sec. 9.8.3. We summarize our results in Sec. 9.9.

9.2 Governing equations and numerical methods

9.2.1 Problem setup

We consider an immiscible droplet of volume Ω and dynamic viscosity μ_i translating at a steady velocity U_d in a planar channel/axisymmetric tube of width/diameter $2R$ filled with an outer fluid of dynamic viscosity μ_o. The volume flux of the outer fluid is q_o, resulting in an average velocity $U_\infty = q_o/(2R)$ and $U_\infty = q_o/(\pi R^2)$ for the planar and axisymmetric configuration, respectively (see Fig. 9.2). Given the small droplet velocity and size, the Reynolds number Re is small and inertial effects can be neglected. Buoyancy is also neglected. The relevant dimensionless numbers include the droplet capillary number $Ca = \mu_o U_d/\gamma$ with γ being the surface tension of the droplet interface and the dynamic viscosity ratio $\lambda = \mu_i/\mu_o$ between the droplet and the outer fluid. The capillary number based on the mean flow velocity is $Ca_\infty = \mu_o U_\infty/\gamma$. For the numerical simulations, the droplet capillary number has been varied within $10^{-4} \lessapprox Ca \lessapprox 1$ to guarantee that the lubrication film is only influenced

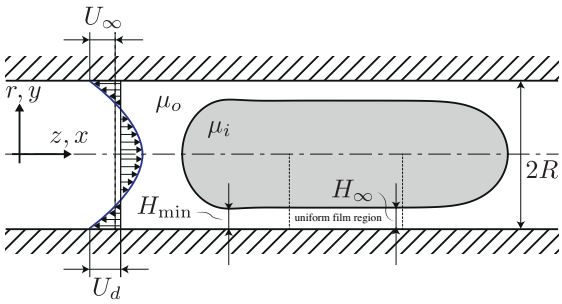

Figure 9.2 – Sketch of the axisymmetric (z, r) and planar (x, y) configurations in the frame of reference moving with the droplet. The flow profiles in the uniform film region are shown in Fig. 9.7.

by the hydrodynamic forces and the dynamics is steady. For smaller capillary numbers, nonhydrodynamic forces such as disjoining pressures due to intermolecular forces might come into play as reported by the recent experiments of Huerre et al. (2015); while for larger capillary numbers, instability and unsteadiness might arise, where the droplet might form a re-entrant cavity at its rear (Tsai & Miksis, 1994), which eventually breaks up into satellite droplets. The viscosity ratios investigated numerically are from the well-known bubble limit of $\lambda = 0$ (Bretherton, 1961) to highly-viscous droplets of $\lambda = 100$ that have been scarcely investigated.

We consider both a three-dimensional axisymmetric tube, and a two-dimensional planar channel featured by the spanwise invariance. Note that the latter configuration does not correspond to the Hele-Shaw-cell-like microfluidic chips, where Darcy or Brinkman equations are more appropriate to describe the flow (Boos & Thess, 1997; Nagel & Gallaire, 2015).

It is worth noting that the confined droplet has to be long enough to develop a region of uniformly thick film at its center (Cantat, 2013) (see Fig. 9.2). However, a long axisymmetric droplet is likely to become unstable to the Rayleigh-Plateau instability. The uniform film region would resemble to a coaxial jet, which is known to be unstable to perturbations with a wavelength longer than $2\pi(R - H_\infty)$ (Eggers & Villermaux, 2008), see also Sec. 1.2.5 of the introductory Chapter 1. Within this range of droplet lengths, we found that the effect of droplet volume Ω is insignificant and hence it is fixed to $\Omega/R^3 = 12.9$ for the axisymmetric geometry and $\Omega/R^2 = 9.3$ for the planar case.

9.2.2 Governing equations

The governing equations are the incompressible Stokes equations for the velocity $\mathbf{u} = (u, v)$ and pressure p:

$$\nabla \cdot \mathbf{u} = 0 \tag{9.1}$$

$$\mathbf{0} = \nabla \cdot \boldsymbol{\sigma}, \tag{9.2}$$

where $\boldsymbol{\sigma} = -p\mathbf{I} + \mu\left[(\nabla\mathbf{u}) + (\nabla\mathbf{u})^T\right]$ denotes the total stress tensor and μ the dynamic viscosity as μ_i (resp. μ_o) inside (resp. outside) the droplet.

The imposed dynamic boundary conditions at the interface are the continuity of tangential stresses

$$\Delta\left[(\mathbf{I}-\mathbf{nn})\boldsymbol{\sigma}\mathbf{n}\right] = \mathbf{0}, \tag{9.3}$$

and the discontinuity of normal stresses due to the Laplace pressure jump

$$\Delta\left(\boldsymbol{\sigma}\mathbf{n}\right) = -\gamma\mathscr{C}\mathbf{n}. \tag{9.4}$$

Δ denotes the difference between the inner and outer quantities, $\mathbf{n}$ the unit normal vector on the interface towards the outer fluid, and $\mathscr{C} = \nabla_S \cdot \mathbf{n}$ the interfacial mean curvature (∇_S is the surface gradient). The plane curvature of interface in the (z,r) or (x,y) plane is denoted as κ and its value at the front and rear droplet extremities is given by κ_f and κ_r, respectively. The mean curvature at the front and rear droplet extremities, which lie on the symmetry axis, is, therefore, given by $\mathscr{C}_{f,r} = \chi\kappa_{f,r}$, where $\chi = 1$ or 2 for a planar or axisymmetric configuration, respectively. At any other point on the droplet interface, the mean curvature is given by the sum of the two principal curvatures.

9.2.3 Numerical methods and implementations

Equations (9.1)-(9.2) with boundary conditions (9.3)-(9.4) are solved by the commercial FEM package COMSOL Multiphysics and the interface is well represented by the arbitrary Lagrangian-Eulerian (ALE) technique. Compared to the commonly known diffuse interface methods such as volume-of-fluid, phase-field, level-set and front-tracking all relying on a fixed Eulerian grid, the ALE approach captures the interface more accurately. Since the interface is always explicitly represented by the discretization points (see Fig. 9.3), the fluid quantities (viscosity, density, etc.), pressure and normal viscous stresses, are discontinuous across the interface. This technique has been used to simulate three-dimensional bubbles in complex microchannels (Anjos et al., 2014*a*), liquid films coating the interior of cylinders (Hazel, Heil, Waters & Oliver, 2012), two-phase flows with surfactants (Ganesan, Hahn, Simon & Tobiska, 2017; Ganesan & Tobiska, 2012) and head-on binary droplet collisions (Li, 2016), to name a few. The *Moving Mesh* module of COMSOL Multiphysics has been recently employed by Rivero-Rodriguez & Scheid (2018) and Hadikhani, Hashemi, Balestra, Zhu, Modestino, Gallaire & Psaltis (2018), see Chapter 10, to investigate the inertial and capillary migration of bubbles in round and rectangular microchannels.

Despite the high fidelity in interface capturing, it is commonly more challenging to develop in-house ALE implementations compared to the diffuse interface counterparts. Additional difficulty arises in the case of large interfacial deformations, when the computational mesh might become highly nonuniform and skewed. It is therefore necessary to remesh the computational

domain and to obtain all the quantities on the new mesh via interpolation. Hence, special expertise in scientific computing and tremendous amount of development effort are required to implement an in-house ALE-based multi-phase flow solvers, which have prevented large portion of the research community from enjoying the high fidelity and elegance of the ALE methods.

Hereby, large mesh deformations can be avoided not only thanks to the convenient moving mesh module of COMSOL, but also by solving the problem in the moving frame of droplet. To achieve so, we impose a laminar Poiseuille inflow of mean velocity $U_\infty - U_d$ at the inlet of the channel and the velocity $-U_d$ at the walls, where the unknown droplet velocity U_d is obtained as part of the solution together with that of the flow field, at each time step, by applying an extra constraint of zero volume-integrated velocity inside the droplet. Such constraints with additional unknowns are imposed in COMSOL Multiphysics by utilizing its so-called 'Global Equations'. This strategy ensures that the deforming droplet barely translates in the streamwise direction, staying approximately at its initial position (say in the center of the domain). Hence, the mesh quality and the robustness of the ALE formulation are appropriately guaranteed.

In this work, we are only concerned with the steady dynamics of the droplet reaching its equilibrium shape. We do not solve the steady Stokes Eq. (9.2) strictly but maintain a negligible time-derivative term $Re\frac{\partial \mathbf{u}}{\partial t}$ for time marching. This procedure can be seen as an iterative scheme to find steady solutions of the Stokes equations. Since, indeed, the time-derivative term vanishes when the equilibrium state is reached, the solutions to the steady Stokes equations are eventually obtained.

It has to be stressed that the computed transient dynamics is not physical and only the final steady solution should be considered. Theoretically, the stability of the latter might be affected by the time-derivative term. However, in practice, no unstable phenomena or multiple-branch solutions were observed in our study. We monitored, during each simulation, the temporal evolution of the velocity, the mean and minimum film thickness as well as the front and rear plane curvatures of the droplet, which exhibited precise time-invariance without exception when the equilibrium state was reached. Our method, therefore, converges to valid stationary solutions, which will be seen in Sec. 9.2.4 to compare well with asymptotic estimates and numerical solutions from the literature.

To reduce the computational cost, half of the channel is considered and axisymmetric or symmetric boundary conditions are imposed at the channel centerline for the axisymmetric and planar configurations, respectively. The setup in COMSOL Multiphysics is intrinsically parallel and the computing time required for an individual case needs no more than one hour based on a standard desktop computer.

A typical mesh is shown in Fig. 9.3. Triangular/quadrilateral elements are used to discretize the domain inside/outside the droplet. Furthermore, a mesh refinement is performed to best resolve the thin lubrication film (see inset of Fig. 9.3). It is worth noting that quadrilateral elements have to be used to discretize the thin film because this region might undergo large

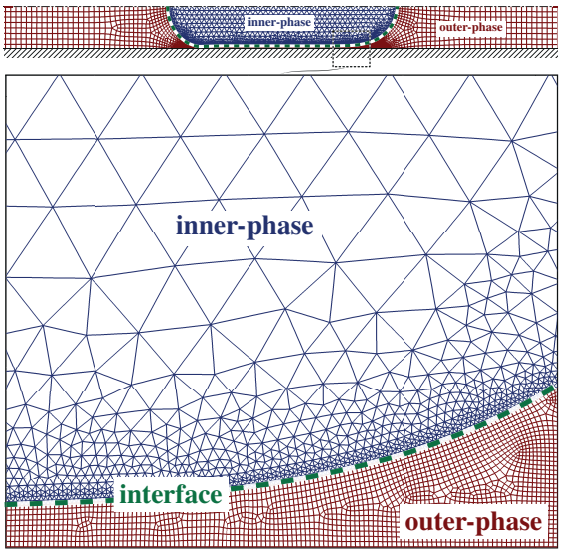

Figure 9.3 – Computational mesh. Inset: mesh refinement in the thin-film region. The triangular inner phase (blue) and quadrilateral outer phase meshes (red) are separated by the explicitly discretized interface (dashed green).

radial deformation resulting in highly distorted and skewed triangular elements if used.

9.2.4 Validation

Our numerical results are first validated for a bubble ($\lambda = 0$) comparing the film thickness with the classical asymptotic theory $H_\infty/R \sim 0.643(3Ca)^{2/3}$ of Bretherton (1961) in the low-Ca limit (see Fig. 9.4). Excellent agreement is revealed even when the capillary number is 10^{-4};

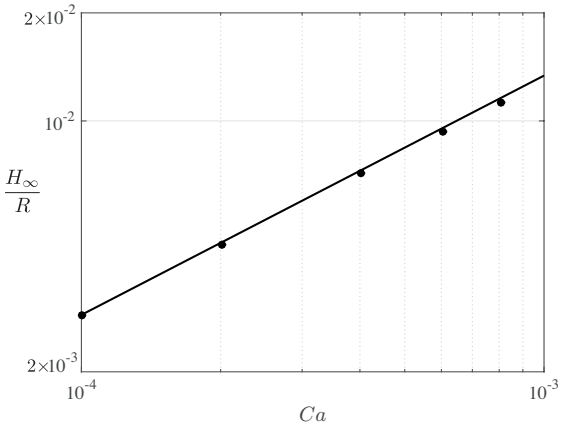

Figure 9.4 – Comparison between the uniform film thickness between the wall and a bubble obtained by the FEM-ALE simulations (symbols) and that predicted by Bretherton (1961) (solid line) for the planar channel.

the discrepancy at larger Ca is mostly because of the asymptotic nature of the model that

becomes less accurate for increasing Ca. At larger capillary numbers, we compare the uniform film thickness with the FEM-based numerical results of Giavedoni & Saita (1997) for a bubble, showing perfect agreement in Fig. 9.5; agreements for the front and rear plane curvatures are also observed and are not reported here.

For viscosity ratios $\lambda > 0$, we have validated our setup against the results from an axisymmetric boundary integral method (BIM) solver (Lac & Sherwood, 2009) for a droplet with $Ca_\infty = 0.05$ of viscosity ratios $\lambda = 0.1$ and 10, again exhibiting perfect agreement as displayed in Fig. 9.6.

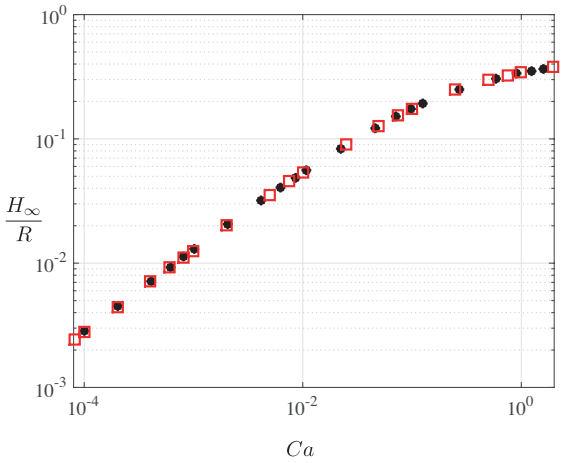

Figure 9.5 – Comparison between the uniform film thickness between the wall and a bubble obtained by the FEM-ALE simulations (full black circles) and that of Giavedoni & Saita (1997) (empty red squares) for the planar channel.

Based on the carefully performed validations against the theory, numerical results from FEM and BIM solvers, we are confident that the developed COMSOL implementation can be used to carry out high-fidelity two-phase simulations efficiently, at least for the 2D and 3D-axisymmetric configurations.

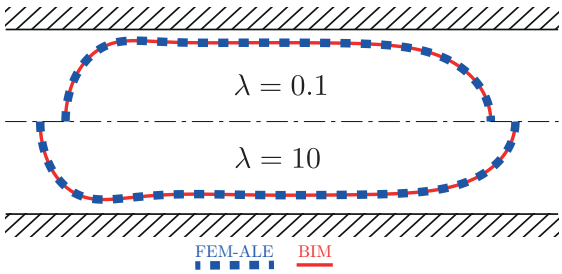

Figure 9.6 – Comparison between the droplet profiles obtained by the FEM-ALE computations (blue dashed) and the BIM (red solid) computations of Lac & Sherwood (2009) for an axisymmetric droplet in a tube with $Ca_\infty = 0.05$ of viscosity ratios $\lambda = 0.1$ (upper half domain) and $\lambda = 10$ (lower half domain).

9.3 Flow field

9.3.1 Velocity profiles in the thin-film region

For a sufficiently long droplet/bubble, a certain portion of the lubrication film is of uniform thickness H_∞ (Bretherton, 1961) (see Fig. 9.2 and Fig. 9.8). Within this portion, the velocity field both inside and outside the droplet is invariant in the streamwise direction and resembles the well known bi-Poiseuille profile that typically arises in several interfacial flows, for example a coaxial jet (Herrada, Ganan-Calvo & Guillot, 2008) (see Fig. 9.7). For $\lambda \ll 1$, the velocity profile in the film is almost linear, whereas for $\lambda \gg 1$, the velocity inside of the droplet is almost constant (plug-like profile). Nevertheless, the parabolic component of these profiles is crucial for the accurate prediction of the droplet velocity (see Sec. 9.5).

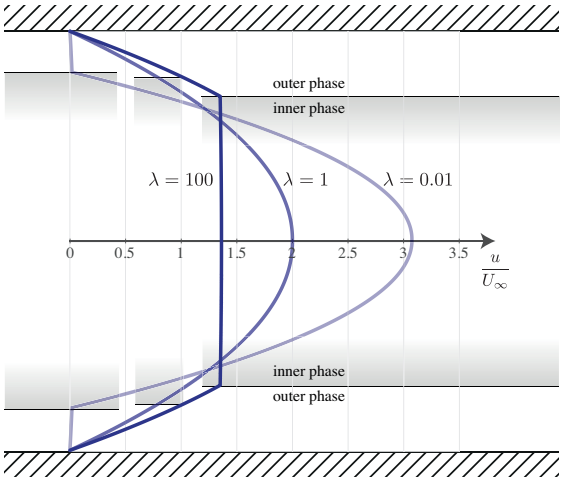

Figure 9.7 – Inner and outer phase velocity profiles in the uniform film region of an axisymmetric droplet with $Ca_\infty = 0.1$ and viscosity ratios $\lambda = 0.01$, 1 and 100, represented in the laboratory frame.

Assuming the bi-Poiseuille velocity profile, we describe the streamwise velocity $u_i(r)$ inside and $u_o(r)$ outside the droplet as a function of the off-centerline distance r as:

$$u_i(r) = \frac{1}{4\mu_i}\frac{dp_i}{dz}r^2 + A_i \ln r + B_i, \tag{9.5}$$

$$u_o(r) = \frac{1}{4\mu_o}\frac{dp_o}{dz}r^2 + A_o \ln r + B_o, \tag{9.6}$$

where p_i and p_o are the inner, respectively outer, pressures, and A_i, B_i, A_o and B_o are undetermined constants. Given the finiteness of $u_i(r)$ at $r = 0$, we have $A_i = 0$. By satisfying the no-slip boundary condition on the channel walls $u_o(R) = -U_d$, the continuity of velocities and tangential stresses on the interface $r = \tilde{r} = R - H$, namely, $u_i(\tilde{r}) = u_o(\tilde{r})$ and

$$\mu_i \frac{du_i}{dz}\Big|_{r=\tilde{r}} = \mu_o \frac{du_o}{dz}\Big|_{r=\tilde{r}}, \tag{9.7}$$

we obtain the remaining constants

$$A_o = \frac{1}{2\mu_o}\left(\frac{dp_i}{dz} - \frac{dp_o}{dz}\right)\tilde{r}^2, \tag{9.8}$$

$$B_i = -\frac{1}{4\mu_i\mu_o}\left[\frac{dp_o}{dz}(R^2-\tilde{r}^2)\mu_i + \frac{dp_i}{dz}\tilde{r}^2\mu_o + 2\left(\frac{dp_i}{dz} - \frac{dp_o}{dz}\right)\tilde{r}^2\mu_i \ln\left(\frac{R}{\tilde{r}}\right)\right] - U_d, \tag{9.9}$$

$$B_o = -\frac{1}{4\mu_o}\left[\frac{dp_o}{dz}R^2 + 2\left(\frac{dp_i}{dz} - \frac{dp_o}{dz}\right)\tilde{r}^2 \ln R\right] - U_d. \tag{9.10}$$

Under the assumption of a slowly evolving film thickness, this velocity profile also holds in the nearby regions, where the thickness is H rather than H_∞. The derivation for the planar geometry is given in Appendix 9.10.1.

9.3.2 Recirculating flow patterns

The axisymmetric velocity profile in the channel away from the droplet, in its moving reference frame, is given by

$$u_\infty(r) = 2U_\infty\left[1 - \left(\frac{r}{R}\right)^2\right] - U_d. \tag{9.11}$$

As will become clear in Sec. 9.5, the droplet velocity can be obtained by imposing mass conservation. For the particular case of a bubble with $\lambda = 0$, mass conservation reads $(U_\infty - U_d)\pi R^2 = -\pi[R^2 - (R - H_\infty)^2]U_d$ (Stone, 2010), yielding $U_\infty/U_d = (1 - H_\infty/R)^2$. The velocity profile (9.11) can therefore be expressed as a function of H_∞/R. As pointed out by Giavedoni & Saita (1997), when $\lambda = 0$, the velocity at the centerline $u_\infty(r = 0)$ in the bubble frame changes sign when $H_\infty = H_\infty^\star = (1 - 1/\sqrt{2})R$. As a consequence, when the uniform film thicknesses is below $H_\infty^\star$, $u_\infty(0) > 0$, an external recirculating flow pattern forms ahead of and behind the bubble. For the planar configuration, the critical film thickness for the appearance of the flow recirculation is $H_\infty^\star = R/3$.

Based on the flow profiles derived in Sec. 9.3 and mass conservation (see Sec. 9.5), we can generalize the critical thickness $H_\infty^\star$ to nonvanishing viscosity ratios ($\lambda > 0$) as (see Appendix 9.10.4 for the derivations):

$$\frac{H_\infty^\star}{R} = 1 - \sqrt{\frac{(\lambda-1)(2\lambda-1)}{2}}\frac{1}{\lambda-1} \tag{9.12}$$

for the axisymmetric case and

$$\frac{H_\infty^\star}{R} = \frac{1}{3}\frac{1}{1-\lambda} \tag{9.13}$$

for the planar case. $H_\infty^\star/R$ reaches the value of 1 when $\lambda = 1/2$ or $\lambda = 2/3$, for the axisymmetric and planar configuration, respectively. Nevertheless, the uniform film thickness is always much smaller than the channel half-width, $H_\infty \ll R$. For a fixed volume of fluid, large film

thicknesses would correspond to long droplets, which might be unstable to the Rayleigh-Plateau instability as discussed in Sec. 9.2.1.

For viscosity ratios $\lambda \geq 1/2$ ($\lambda \geq 2/3$) for the axisymmetric (planar) configuration, there is no critical film thickness above which the recirculation zones disappear, meaning that a recirculation region always exists for any capillary number.

At low capillary numbers, when the film thickness is below $H_\infty^\star$, the external recirculating flows are strong enough to induce the recirculation inside the droplet as well. Consequently, besides the two droplet vertices as permanent stagnation points (blue circles in Fig. 9.8), two stagnation rings emerge on the front and rear part of the axisymmetric interface (red stars in Fig. 9.8); likewise, four stagnation points arise in the planar case. The stagnation rings/points on the dynamic meniscus (red stars in Fig. 9.8) move outwards to the droplet vertices when Ca increases. When $H_\infty > H_\infty^\star$, these stagnation rings/points disappear, taking away with the recirculation regions accordingly (see Fig. 9.8(b)). Only the stagnation points at the droplet vertices remain.

However, since the stagnation rings/points at the droplet interface move outwards to the front and rear extremities when the film thickness increases with the capillary number, the recirculation regions might eventually detach from the interface before the critical film thickness $H_\infty^\star$ is reached. Nevertheless, since recirculation regions exist far away from the droplet as long as $H_\infty < H_\infty^\star$, another flow pattern must exist close to the droplet interface. The detached stagnation points are located on the centerline outside the droplet, and no recirculating flow is present in the region between the detached stagnation point and the one at the droplet vertex (see rear of droplet in Fig. 9.8(d)). Contrasting with the case of Fig. 9.8(c), where the stagnation points on the dynamic meniscus induce recirculating flow inside the droplet at both front and rear parts, the inner rear recirculation zone disappears when the capillary number increases, as shown in Fig. 9.8(d). This indicates that the detachment of the recirculation region is not fore-aft symmetric. There is a large range of parameters for which a rear stagnation point is not at the droplet interface anymore and thus there is no recirculation inside the rear part of the droplet. We have found that the critical film thickness for which the stagnation ring/point at the rear detaches from the droplet interface corresponds to when the rear plane curvature of the droplet changes the sign (see also Sec. 9.7.1). For both the flow patterns as well as for the plane curvatures, the fore-aft asymmetry increases with the capillary number.

The phase diagram with the main different types of flow patterns as a function of the viscosity ratio λ and film thickness H_∞/R is shown in Fig. 9.9. Note that for viscosity ratios $\lambda \geq 1/2$ ($\lambda \geq 2/3$), the recirculation regions will be attached or detached from or to the droplet interface depending on the uniform film thickness. Other very peculiar flow fields, as a detached finite recirculation region at the rear or a detached recirculation region at the front as observed by Giavedoni & Saita (1997, 1999) can be obtained for some parameter combinations. However, since the flow field structures are not the main aim of this work, an extended parametric study to detect all possible patterns has not been performed. Nevertheless, our current results

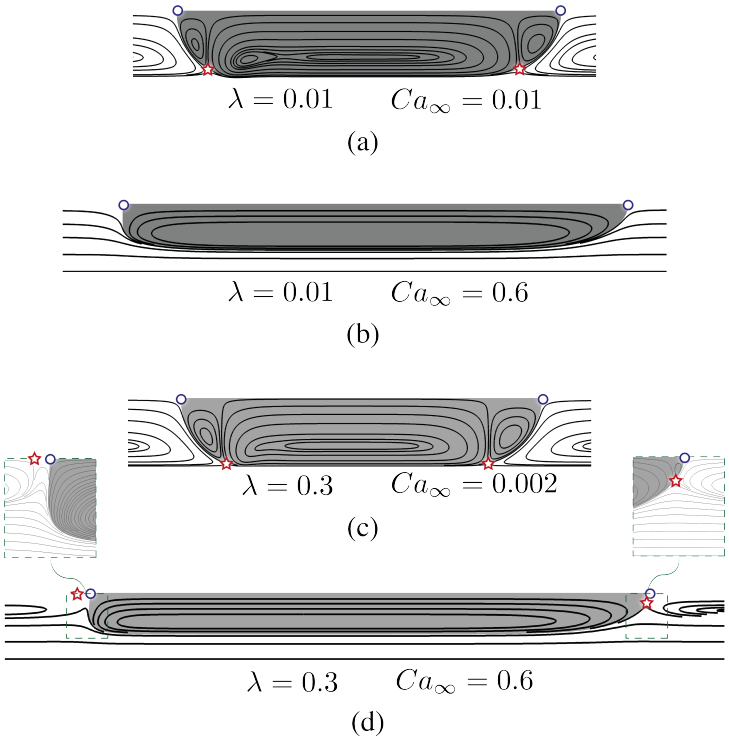

Figure 9.8 – Streamlines and recirculation patterns for an axisymmetric droplet with different capillary numbers Ca_∞ and viscosity ratios λ in a frame of reference moving with the droplet. The results are obtained from FEM-ALE numerical simulations. The permanent stagnation points at the droplet vertices are highlighted by blue circles, whereas the (Ca,λ)-dependent stagnation rings/points are highlighted by red stars. Insets: detailed flow pattern at the droplet front and rear for $\lambda = 0.3$ and $Ca_\infty = 0.6$.

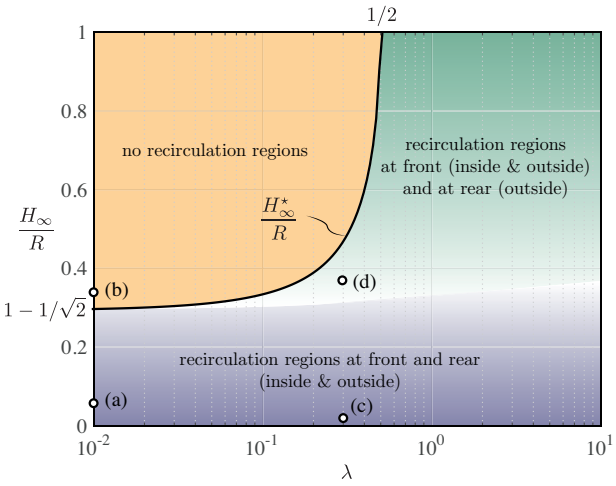

Figure 9.9 – Diagram of the main possible flow patterns for the axisymmetric configuration. The streamlines corresponding to the points (a)-(d) are shown in Fig. 9.8.

do not validate all the flow patterns predicted in Hodges et al. (2004*a*) based on asymptotic arguments, which indeed have not been verified neither experimentally nor numerically.

The flow fields for the planar configuration are not presented here as they are similar to those for the axisymmetric configuration.

9.4 Film thickness

9.4.1 Asymptotic result in the *low-*Ca limit

By following the work of Schwartz et al. (1986), we derive an implicit expression predicting the thickness H_∞ of the uniformly-thick lubrication film in the low-Ca limit when $H/R \ll 1$ satisfies. The derivation of the axisymmetric case is presented below, see Appendix 9.10.2 for the planar case.

The flow rates at any axial location where the external film thickness is H are:

$$\begin{aligned} q_i =& 2\pi \int_0^{R-H} u_i(r) r dr \qquad (9.14)\\ =& -\pi(R-H)^2 \left\{ U_d + \frac{1}{8\mu_i\mu_o} \left[2\frac{dp_o}{dz} H(2R-H)\mu_i + \frac{dp_i}{dz}(R-H)^2\mu_o \right.\right.\\ &\left.\left. + 4\left(\frac{dp_i}{dz} - \frac{dp_o}{dz}\right)(R-H)^2\mu_i \ln\left(\frac{R}{R-H}\right)\right]\right\},\\ q_o =& 2\pi \int_{R-H}^{R} u_o(r) r dr \qquad (9.15)\\ =& -\frac{\pi}{8\mu_o}\left\{ H(2R-H)\left[H^2\left(2\frac{dp_i}{dz} - 3\frac{dp_o}{dz}\right) + 2\left(\frac{dp_i}{dz} - \frac{dp_o}{dz}\right)R^2 - H\left(4\frac{dp_i}{dz} - 6\frac{dp_o}{dz}\right)R\right]\right.\\ &\left. + 4\left(\frac{dp_i}{dz} - \frac{dp_o}{dz}\right)(R-H)^4 \ln\left(\frac{R}{R-H}\right)\right\} - \pi H(2R-H)U_d. \end{aligned}$$

Assuming that $H/R \ll 1$, the volumetric fluxes up to the second order are

$$q_i \approx -\pi R^2 \left(U_d + \frac{1}{8\mu_i}\frac{dp_i}{dz}R^2 + \frac{1}{2\mu_o}\frac{dp_i}{dz}RH + \frac{1}{2\mu_o}\frac{dp_o}{dz}H^2 \right), \qquad (9.16)$$

$$q_o \approx -2\pi RH \left(U_d + \frac{1}{4\mu_o}\frac{dp_i}{dz}HR + \frac{1}{3\mu_o}\frac{dp_o}{dz}H^2 \right). \qquad (9.17)$$

In the droplet frame, the inner flow rate is $q_i = 0$. Furthermore, in the region with a uniformly-thick film, $H = H_\infty$; the inner and outer pressure gradient balances, $\frac{dp_i}{dz} = \frac{dp_o}{dz}$. Using these two conditions one can obtain the pressure gradient in the uniform film region

$$\left.\frac{dp}{dz}\right|_{r=R-H_\infty} \approx -\frac{8\mu_i U_d}{R^2 + 4\lambda H_\infty R + 4\lambda H_\infty^2} \qquad (9.18)$$

and the outer flow rate in the $H_\infty/R \ll 1$ limit is

$$q_o \approx -2\pi R H_\infty \left[\frac{3R^2+6\lambda H_\infty R+4\lambda H_\infty^2}{3(R^2+4\lambda H_\infty R+4\lambda H_\infty^2)}\right] U_d \approx -2\pi R H_\infty \left(\frac{R+2\lambda H_\infty}{R+4\lambda H_\infty}\right) U_d. \tag{9.19}$$

In the dynamic meniscus regions, the inner and outer pressure gradients are not equal and their difference is proportional to the mean curvature of the interface at $r = R-H$, through Laplace's law. By assuming a quasi-parallel flow whose radial velocity is weaker than the axial velocity by one order of magnitude and a small capillary number, the normal stress condition at the interface is not affected by viscous stresses. Hence, the axial gradient of the normal stress condition reads

$$\frac{dp_i}{dz} - \frac{dp_o}{dz} = \gamma \frac{d^3H}{dz^3}, \tag{9.20}$$

where the axial gradient of the curvature in the azimuthal direction is neglected as it is an order smaller. The pressure gradients dp_i/dz and dp_o/dz as functions of H can be obtained from Eqs. (9.16), (9.17) imposing mass conservation, *i.e.* imposing $q_i = 0$ and q_o given by Eq. (9.19):

$$\frac{dp_i}{dz} \approx \frac{4\lambda(-6H_\infty^2\lambda+4H_\infty H\lambda-3H_\infty R+HR)\mu_o U_d}{HR(4H_\infty\lambda+R)(H\lambda+R)}, \tag{9.21}$$

$$\frac{dp_o}{dz} \approx \frac{3(H_\infty-H)[8H_\infty H\lambda^2+2(H_\infty+H)\lambda R+R^2]\mu_o U_d}{H^3(4H_\infty\lambda+R)(H\lambda+R)}. \tag{9.22}$$

By plugging Eqs. (9.21), (9.22) into Eq. (9.20) and adopting the change of variables $H = H_\infty\eta$ and $z = H_\infty(3Ca)^{-1/3}\xi$ in the spirit of Bretherton (1961), we obtain an universal governing equation for the scaled film thickness η when taking the limit $H_\infty/R \to 0$:

$$\frac{d^3\eta}{d\xi^3} = \frac{\eta-1}{\eta^3}\left[\frac{1+2m(1+\eta+4m\eta)}{(1+4m)(1+m\eta)}\right], \tag{9.23}$$

where

$$m = \lambda\frac{H_\infty}{R}$$

denotes the rescaled viscosity ratio. The corresponding planar counterpart reads (see derivation in Appendix 9.10.2)

$$\frac{d^3\eta}{d\xi^3} = 2\frac{\eta-1}{\eta^3}\left[\frac{2+3m(1+\eta+3m\eta)}{(1+3m)(4+3m\eta)}\right]. \tag{9.24}$$

If the limit of vanishing uniform film thickness is not considered, the resulting equations for η would depend on H_∞/R (de Ryck, 2002). In the limit of $m \to 0$, the classical Landau-Levich-Derjaguin equation (Derjaguin, 1943; Landau & Levich, 1942) is retrieved for both configurations (see Chapter 8). Following Bretherton (1961), Eqs. (9.23) and (9.24) can be integrated to find the uniform film thickness H_∞/R (see also Cantat (2013) for more details).

First, the equations can be linearized in the uniform film region around $\eta \approx 1$, giving

$$\frac{d^3\eta}{d\xi^3} = K(\eta - 1), \tag{9.25}$$

where K is a constant depending on the geometrical configurations and the viscosity ratio m. Equation (9.25) has a monotonically increasing solution with respect to ξ for the front dynamic meniscus, $\xi \to \infty$, and an oscillatorily increasing solution for the rear, $\xi \to -\infty$, as derived in Sec. 9.6. The solution of the front meniscus is $\eta(\xi) = 1 + \alpha \exp(K^{1/3}\xi)$, where α is a small parameter, typically 10^{-6}. Second, the nonlinear equations (9.23) and (9.24) can be integrated numerically as an initial value problem with a fourth-order Runge-Kutta scheme, starting from the linear solution until the plane curvature of the interface profile becomes constant. A region of constant plane curvature, called static meniscus region (see Fig. 9.1) exists as $d^3\eta/d\xi^3 \approx 0$ for $\eta \gg 1$ (see red line on Fig. 9.11). In the static meniscus region, the interface profile is a parabola: $\eta = P\xi^2/2 + C\xi + D$, or, in terms of film thickness, $H = P(3Ca)^{2/3}z^2/(2H_\infty) + C(3Ca)^{1/3}z + DH_\infty$, where P, C and D are real-valued constants. Thus, P is set by the constant plane curvature obtained by the integration of the nonlinear equation.

The procedure can be repeated for any rescaled viscosity ratio m and the obtained results for the coefficient P can well described by the fitting law (Schwartz et al., 1986):

$$P(m) = \frac{0.643}{2}\left\{1 + 2^{2/3} + (2^{2/3} - 1)\tanh\left[1.2\log_{10} m + c_1\right]\right\} \tag{9.26}$$

where the constant $c_1 = 0.1657$ for the axisymmetric configuration and $c_1 = 0.0159$ for the planar configuration (see Fig. 9.10). The well known limits for a bubble $P(0) = 0.643$ (Bretherton,

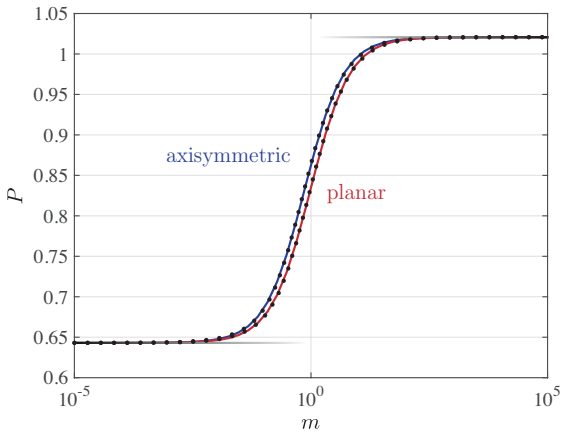

Figure 9.10 – Film-thickness coefficient P obtained for discrete m values (symbols) and fitting law (9.26) (solid lines) as a function of the rescaled viscosity ratio m.

1961) and a very viscous droplet $P(m \to \infty) = 2^{2/3}P(0)$ (Cantat, 2013) are recovered.

To obtain the uniform film thickness, the matching principle proposed by Bretherton (1961)

is employed. The plane curvature $\kappa = d^2H/dz^2 = P(3Ca)^{2/3}/H_\infty$ in the static region has to match that of the front hemispherical cap of radius R, which exists for small capillary numbers (see red dashed line in Fig. 9.11). A rigorous asymptotic matching can be found in Park &

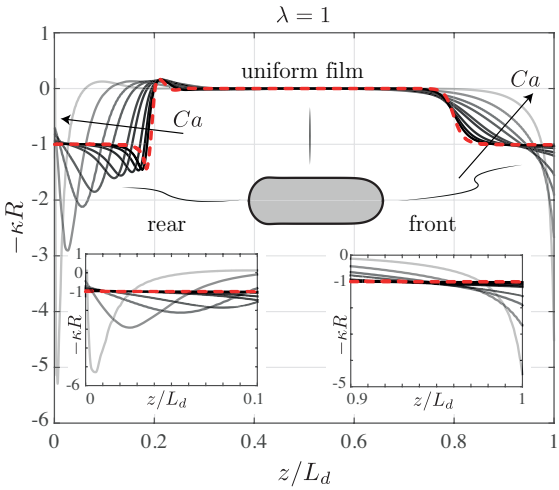

Figure 9.11 – Plane curvature of the droplet interface for exponentially increasing capillary numbers in the range $10^{-4} < Ca < 1$, obtained from FEM-ALE numerical simulations where $\lambda = 1$. The dashed red line is for the smallest Ca. The z axis is rescaled by the droplet length to facilitate the comparison. Insets: zoom-in on the front and rear menisci. Similar profiles are obtained for other viscosity ratios.

Homsy (1984) for a bubble with $m = 0$. When $m \neq 0$, the coefficient $P(m)$ depends implicitly on H_∞, and thus on Ca, through m, leading to an implicit asymptotic relation for H_∞/R as:

$$\frac{H_\infty}{R} = P(m)(3Ca)^{2/3}. \tag{9.27}$$

Strictly speaking, the uniform film thickness of viscous droplets ($\lambda \neq 0$) in the low Ca limit does not scale with $Ca^{2/3}$ as for a bubble ($\lambda = 0$).

9.4.2 Empirical model in the *low*-Ca limit

Equation (9.27) holds for capillary numbers as low as below 10^{-3} (Bretherton, 1961). We solve Eq. (9.27) numerically and present the coefficient P and the uniform film thickness H_∞/R versus Ca in Fig. 9.12 for the axisymmetric case. In order to derive an explicit formulation to predict the film thickness in this Ca regime, we define $\bar{P}$ as a Ca-averaged value of P and define the empirical model

$$\frac{H_\infty}{R} = \bar{P}(\lambda)(3Ca)^{2/3}, \tag{9.28}$$

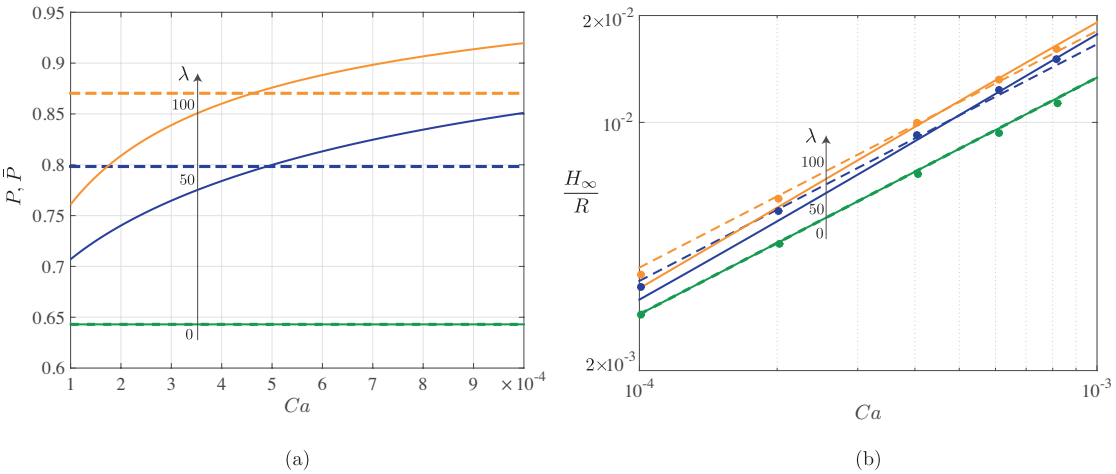

Figure 9.12 – (a) Coefficient P (solid lines) obtained by solving Eq. (9.27) and the mean coefficient $\bar{P}$ (dashed lines) for the axisymmetric configuration. The viscosity ratios are $\lambda = 0$, 50 and 100. (b) The uniform film thickness H_∞/R from Eq. (9.27) (solid lines) and Eq. (9.28) (dashed lines), compared to the FEM-ALE simulation results (symbols).

where $\bar{P}(\lambda)$ is independent of Ca (see dashed lines in Fig. 9.12(a)) and can be approximated by the fitting law (see Fig. 9.13):

$$\bar{P}(\lambda) = \frac{0.643}{2}\left\{1 + 2^{2/3} + (2^{2/3} - 1)\tanh\left[1.28\log_{10}\lambda + c_2\right]\right\}. \tag{9.29}$$

where the constant $c_2 = -2.36$ for the axisymmetric case and $c_2 = -2.52$ for the planar case are obtained by fitting. For $\lambda = 0$, $\bar{P} = 0.643$ is recovered and H_∞/R indeed scales with $Ca^{2/3}$, at

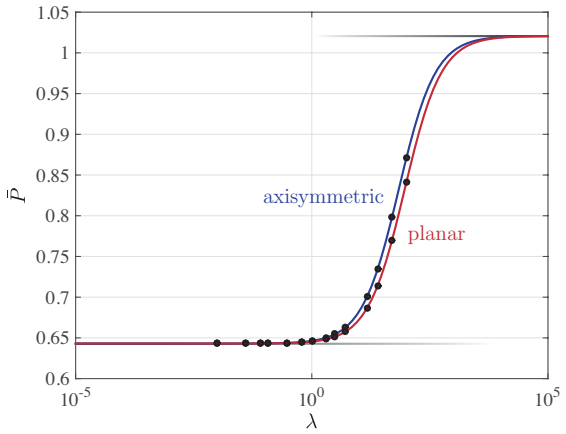

Figure 9.13 – Mean coefficient $\bar{P}$ (symbols) obtained by Ca-averaging the results of the implicit relation Eq. (9.27) and fitting law (solid lines) Eq. (9.29) versus the viscosity ratio λ.

least when $Ca < 10^{-3}$. Figure 9.12(b) also shows that the empirically obtained film thickness (dashed lines) Eq. (9.28) agrees reasonably well with the FEM-ALE simulation results (symbols), whereas the implicit law (solid lines) Eq. (9.27) slightly underestimates them at very low Ca.

To cure this mismatch, Hodges et al. (2004*a*) proposed a modified interface condition, which however is found to overestimate the thickness more than that underestimated by the original implicit law.

9.4.3 Model for $10^{-3} \lessapprox Ca \lessapprox 1$

Despite the explicit law for the uniform-film thickness prediction with $\bar{P}$ proved to be satisfactory, its validity range is restricted to low capillary numbers. As known since the experiments of Taylor (1961), the film thickness of a bubble saturates for increasing Ca. Aussillous & Quéré (2000) proposed a model for $\lambda = 0$, which agrees well with the experimental data of (Taylor, 1961), further inspiring the two very recent works of Klaseboer et al. (2014) and Cherukumudi et al. (2015). In the same vain, we propose an empirical model for the film thickness H_∞ as a function of both Ca and λ

$$\frac{H_\infty}{R} = \frac{\bar{P}(\lambda)(3Ca)^{2/3}}{1+\bar{P}(\lambda)Q(\lambda)(3Ca)^{2/3}}, \tag{9.30}$$

where the coefficient Q is obtained by fitting Eq. (9.30) to the database constructed from our extensive FEM-ALE simulations over a broad range of Ca for different λ. The proposed function of $Q(\lambda)$ is given in Appendix 9.10.5 and plotted in Fig. 9.14. For an axisymmetric bubble,

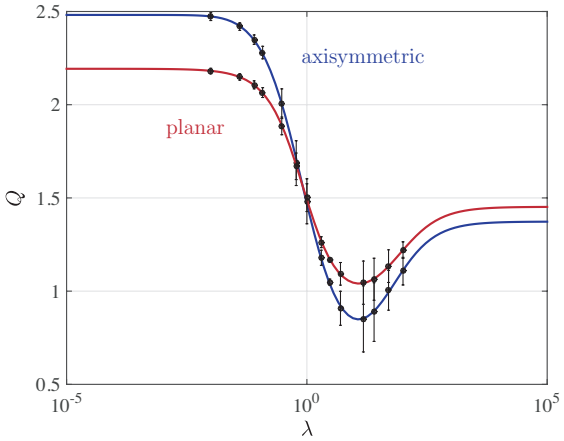

Figure 9.14 – Coefficient Q obtained for the simulated viscosity ratios (symbols) and proposed fitting law (see Appendix 9.10.5) as a function of the viscosity ratio λ.

we find $Q = 2.48$, in accordance with the estimation $Q = 2.5$ of Aussillous & Quéré (2000). We now present in Fig. 9.15 the numerical film thickness (symbols) and the empirical model (lines) for $\lambda = 1$. For the sake of clarity, the results for $\lambda = 0$ and 100 are shown in the Appendix 9.10.6 in Fig. 9.23. For $\lambda = 1$, the thickness of the two configurations coincides. However, when $Ca \sim O(1)$, the film is thicker in the planar configuration than in the axisymmetric one for a bubble ($\lambda = 0$); the trend reverses for a highly-viscous droplet ($\lambda = 100$). This λ-dependence of the film thickness is indeed implied by the crossover of the two fitting functions $Q(\lambda)$ at $\lambda = 1$ shown in Fig. 9.14.

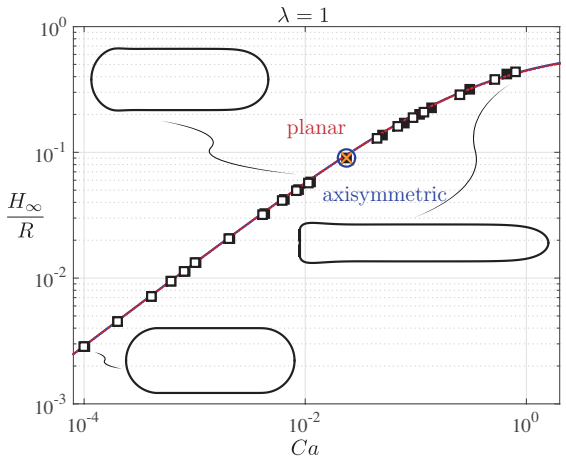

Figure 9.15 – Uniform film thickness given by Eq. (9.30) (lines) and FEM-ALE numerical results (symbols) as a function of the droplet capillary number for $\lambda = 1$ and both axisymmetric (blue solid line, full symbols) and planar (dashed red line, empty symbols) geometries. Cross and circle correspond to a droplet with 37% and 82%, respectively, larger volume than the standard one used for the axisymmetric geometry.

It has to be noted that when the capillary number is increased, the regions of constant plane curvature in the static front and rear caps reduce in size and eventually disappear (see Fig. 9.11), and this for all viscosity ratios. The matching to a region of constant plane curvature for large capillary numbers as proposed by Klaseboer et al. (2014) and Cherukumudi et al. (2015) might be questionable for this Ca-range.

The uniform film thickness of droplets with 37% and 82% larger volume, resulting in longer droplets, are compared in Fig. 9.15, showing that as long as such a uniform region exists, the results are independent of the droplet length.

9.5 Droplet velocity

Equipped with the model of the uniform-film thickness H_∞, we derive the droplet velocity based on the velocity profiles in the uniform-film region given in Sec. 9.3.1. At the location $H = H_\infty$ where the interface is flat, the pressure gradients are equal, $dp_i/dz = dp_o/dz = dp/dz$. We further use $q_o = \pi R^2(U_\infty - U_d)$ imposed by mass conservation and $q_i = 0$ (in the moving frame of the droplet) to obtain the analytical expressions for the pressure gradient

$$\left.\frac{dp}{dz}\right|_{r=R-H_\infty} = \frac{-8R^2 U_\infty \mu_i}{(R-H_\infty)^4 + H_\infty(2R-H_\infty)(2R^2-2H_\infty R+H_\infty^2)\lambda}, \tag{9.31}$$

and the droplet velocity

$$U_d = \frac{R^2[(R-H_\infty)^2 + 2H_\infty(2R-H_\infty)\lambda]}{(R-H_\infty)^4 + H_\infty(2R-H_\infty)(2R^2-2H_\infty R+H_\infty^2)\lambda} U_\infty. \tag{9.32}$$

The relative velocity of the axisymmetric droplet with respect to the underlying velocity reads

$$\frac{U_d - U_\infty}{U_d} = \frac{\left(2 - \frac{H_\infty}{R}\right)\frac{H_\infty}{R}\left[1 + \left(2 - \frac{H_\infty}{R}\right)\frac{H_\infty}{R}(\lambda - 1)\right]}{1 + \left(2 - \frac{H_\infty}{R}\right)\frac{H_\infty}{R}(2\lambda - 1)}. \tag{9.33}$$

An analogous derivation for the planar configuration yields (see Appendix 9.10.3):

$$\frac{U_d - U_\infty}{U_d} = \frac{\frac{H_\infty}{R}\left\{2 - \frac{H_\infty}{R}\left[4 + 2\frac{H_\infty}{R}(\lambda - 1) - 3\lambda\right]\right\}}{2 + \left(2 - \frac{H_\infty}{R}\right)\frac{H_\infty}{R}(3\lambda - 2)}. \tag{9.34}$$

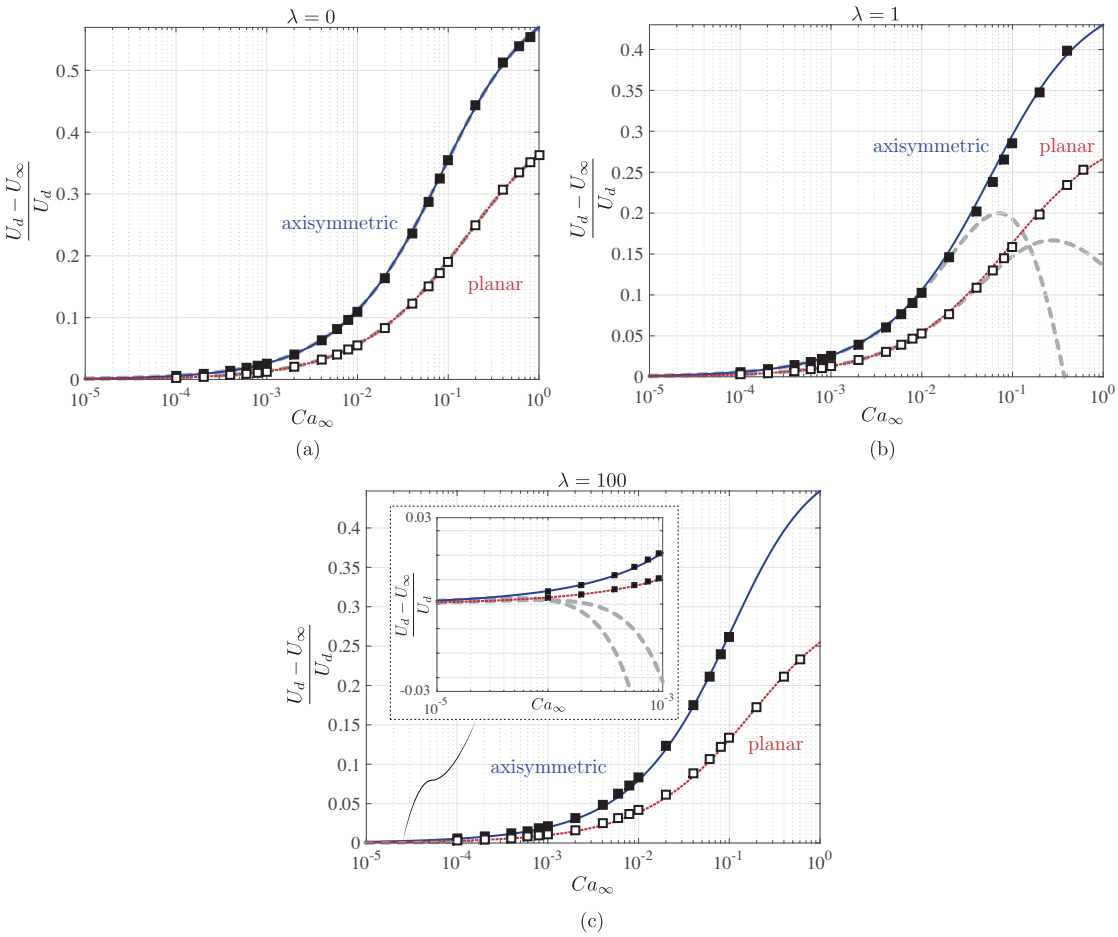

Figure 9.16 – Relative droplet velocity (lines) predicted by Eqs. (9.33) and (9.34) together with the proposed empirical model for the uniform film thickness (9.30) and the results of the FEM-ALE numerical simulations (symbols) as a function of capillary number Ca_∞ for $\lambda = 0$ (a), 1 (b) and 100 (c) and both axisymmetric (blue solid line, full symbols) and planar (dashed red line, empty symbols) geometries. Long dashed gray lines correspond to the asymptotic estimates of Eqs. (9.35) and (9.36).

Equations (9.30) and (9.32) form a system of the two unknowns, namely the droplet capillary

number Ca and the uniform film thickness H_∞/R. It is important to remind that the former is related to the droplet velocity via $Ca = Ca_\infty U_d/U_\infty$. For a given combination of inflow capillary number Ca_∞ and viscosity ratio λ as the input, the system can be solved numerically (see Matlab file `filmThicknessAndVelocity.m` in the Supplementary Material) outputting Ca and H_∞/R. The predicted relative velocity $(U_d - U_\infty)/U_d$ (lines) agrees well the FEM-ALE simulation results (symbols) as shown in Fig. 9.16.

In the limit of $H_\infty/R \to 0$, the relative velocity can be approximated asymptotically as

$$\frac{U_d - U_\infty}{U_d} = 2\left(\frac{H_\infty}{R}\right) - (1+4\lambda)\left(\frac{H_\infty}{R}\right)^2 + O\left(\frac{H_\infty}{R}\right)^3 \tag{9.35}$$

for the axisymmetric case, and

$$\frac{U_d - U_\infty}{U_d} = \left(\frac{H_\infty}{R}\right) - \frac{3\lambda}{2}\left(\frac{H_\infty}{R}\right)^2 + O\left(\frac{H_\infty}{R}\right)^3 \tag{9.36}$$

for the planar geometry. For very low capillary numbers, the asymptotic estimates predict that the relative droplet velocity scales with H_∞/R, and hence with $Ca^{2/3}$ (Stone, 2010). The viscosity ratio λ only enters at second order of H_∞/R, which however influences the validity range of the asymptotic estimates (9.35) and (9.36) considerably. The asymptotic estimates are exact for $\lambda = 0$. In this case, Eqs. (9.35) and (9.36) reduce to the well known predictions for bubbles $(2 - H_\infty/R)H_\infty/R$ and H_∞/R (Bretherton, 1961; Stone, 2010; Langewisch & Buongiorno, 2015), respectively (see Fig. 9.16(a)). For nonvanishing λ, the complete expressions (9.33) and (9.34) should be employed (see Fig. 9.16(b)). For example, the asymptotic estimate for $\lambda = 100$ is only valid when $Ca_\infty < 10^{-4}$ (see Fig. 9.16(c)).

9.6 Minimum film thickness

At low capillary numbers Ca, the droplet interface exhibits an oscillatory profile between the uniform thin film and the rear static cap (see Fig. 9.11). The minimum film thickness in the low Ca limit can be computed by integrating the lubrication equation (9.23) or (9.24) for $\xi = 0$ to $\xi \to -\infty$. The initial condition for this initial value problem is given by the solution of the linear equation (9.25) for negative ξ: $\eta = 1 + \alpha\exp(-K^{1/3}\xi/2)\cos(\sqrt{3}K^{1/3}\xi/2 + \phi)$, where α is a small parameter of order 10^{-6} and ϕ is a parameter taken such that the constant plane curvature of the nonlinear integrated solution at $\xi \to -\infty$ is equal to the one of the front static cap (Bretherton, 1961; Cantat, 2013) as discussed in Sec. 9.4.1. Note that the linear solution for the rear dynamic meniscus presents oscillations. The minimum film thickness of the obtained profile is found to follow the empirical model (Bretherton, 1961)

$$\frac{H_{\min}}{R} = F(m)P(m)(3Ca)^{2/3} \quad \text{with} \quad m = \lambda\frac{H_\infty}{R}, \tag{9.37}$$

where $F(m)$ is a coefficient obtained through fitting Eq. (9.37) to our numerical database (see Fig. 9.17(a)). Similar to the mean coefficient $\bar{P}$ adopted in Sec. 9.4, a Ca-averaged $F(m)$ can be

introduced as $\bar{F}$, which is further assumed as 0.716 in view of its very weak dependence on λ shown in Fig. 9.17(b).

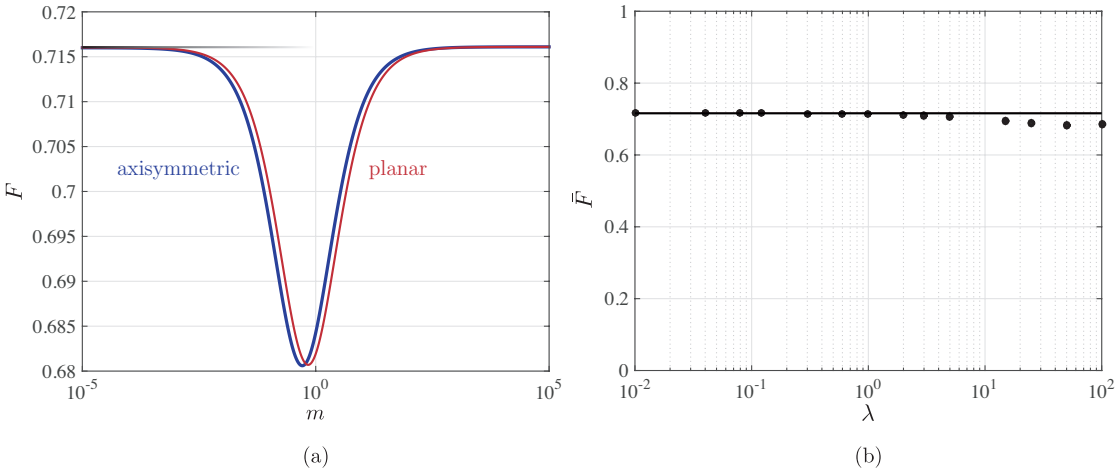

Figure 9.17 – (a) Minimum film-thickness coefficient F as a function of the rescaled viscosity ratio m. (b) Mean coefficient $\bar{F}$ (symbols) and fitting law (solid line) as a function of the viscosity ratio λ

The minimum film thickness is bounded by the thickness of the uniform film and hence will saturate at large capillary numbers. Thus, for sufficiently large Ca values, the oscillations at the rear interface would disappear and $H_{\min} = H_{\infty}$. It is therefore natural to propose a rational function model of $H_{\min}$ for a broader Ca-range as the one for H_{∞}:

$$\frac{H_{\min}}{R} = \frac{\bar{P}(\lambda)\bar{F}(3Ca)^{2/3}}{1+\bar{P}(\lambda)\bar{F}G(\lambda)(3Ca)^{2/3}}. \tag{9.38}$$

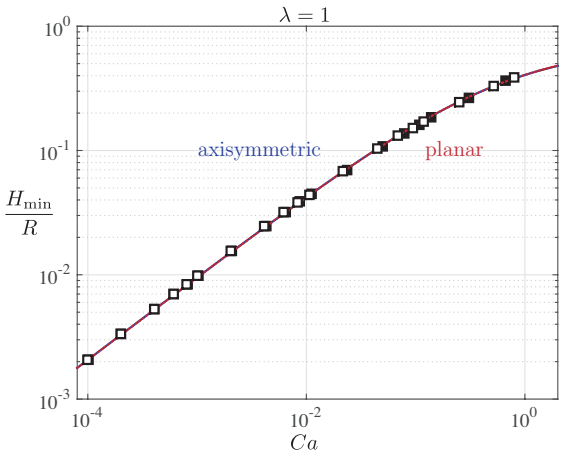

Figure 9.18 – Minimum film thickness given by Eq. (9.38) (lines) and FEM-ALE numerical results (symbols) as a function of the droplet capillary number for $\lambda = 1$ and both axisymmetric (blue solid line, full symbols) and planar (dashed red line, empty symbols) geometries.

The above minimum film-thickness model (9.38) together with the coefficient G is in good agreement with the results of the numerical simulations (see Fig. 9.18 and Fig. 9.24). The

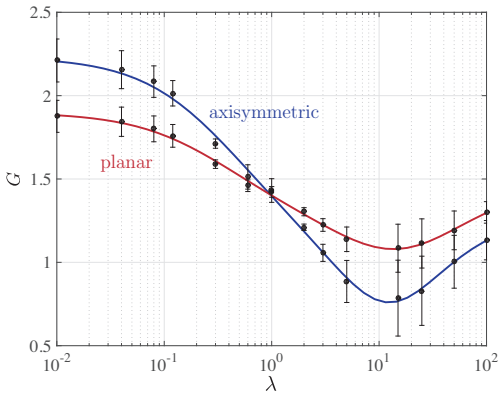

Figure 9.19 – Coefficient G obtained for the simulated viscosity ratios (symbols) and proposed fitting law (9.71) (solid lines) as a function of the viscosity ratio λ.

proposed fitting of the coefficient G as a function of the viscosity ratio (see Fig. 9.19) is given in Appendix 9.10.5.

9.7 Front and rear total stress jumps

The dynamics of a translating bubble in a capillary tube has been characterized since the seminal work of Bretherton (1961) not only by the mean and minimum film thickness, the relative velocity compared to the mean velocity, but also by the mean curvature of the front and rear static menisci. In fact, for $Ca \to 0$, the pressure drop across the interface is directly related to the expression of its mean curvature via the Laplace law. Having generalized the film thickness and droplet velocity models for nonvanishing viscosity ratios, we are hereby focusing on the evolution of the plane curvature of the front and rear static caps versus the capillary number and viscosity ratio. The mean curvature at the droplet extremities is equivalent to the corresponding plane curvature for the planar configuration or to its double for the axisymmetric configuration: $\mathscr{C}_{f,r} = \chi\kappa_{f,r}$, with $\chi = 2$ (resp. $\chi = 1$) for the axisymmetric (resp. planar) configuration (see Sec. 9.2.2). As it will be shown, given the rather broad range of capillary numbers considered (approaching $O(1)$), it is insufficient to consider the interface mean curvature alone to provide an accurate prediction of the pressure drop, but the jump in the normal viscous stress has to be accounted for.

For the incompressible Newtonian fluids considered, the viscous stress tensor is $\boldsymbol{\tau} = \mu\left[(\nabla\mathbf{u}) + (\nabla\mathbf{u})^T\right]$, and hence the z-direction normal total stress σ_{zz} is given by

$$\sigma_{zz} = -p + \tau_{zz} = -p + 2\mu\frac{\partial u}{\partial z}. \tag{9.39}$$

Applying the difference (between inner and outer phases) operator Δ to Eq. (9.39) and based

on the dynamic boundary condition in the normal direction (9.4) at the droplet front and rear extremities, we get

$$\Delta\sigma_{zz_{f,r}} = -\Delta p_{f,r} + \Delta\tau_{zz_{f,r}} = -\gamma\chi\kappa_{f,r}, \tag{9.40}$$

which indicates that the total stress jump at the front/rear extremities scales with the local interface mean curvature and is the sum of the pressure jump and the normal viscous stress jump. These quantities will be modeled separately in the following sections.

9.7.1 Front and rear plane curvatures

In the spirit of the empirical film-thickness model, the plane curvature κ_f of the front meniscus and that of the rear, κ_r, are approximated by the rational function model

$$\kappa_{f,r}R = \frac{1 + T_{f,r}(\lambda)(3Ca)^{2/3}}{1 + Z_{f,r}(\lambda)(3Ca)^{2/3}}, \tag{9.41}$$

where $T_{f,r}$ and $Z_{f,r}$ as λ-dependent constants are obtained by fitting Eq. (9.41) to the FEM-ALE data (see Appendix 9.10.5). It is worth-noting that the asymptotic series of the proposed expression,

$$\kappa_{f,r}R \sim 1 + (T_{f,r} - Z_{f,r})(3Ca)^{2/3} + O(Ca^{4/3}), \tag{9.42}$$

is in line with the law proposed by Bretherton (1961), namely $1 + \beta_{f,r}(3Ca)^{2/3} + O(Ca^{4/3})$. Thus, the empirical model (9.41), which is in excellent agreement with the numerical results

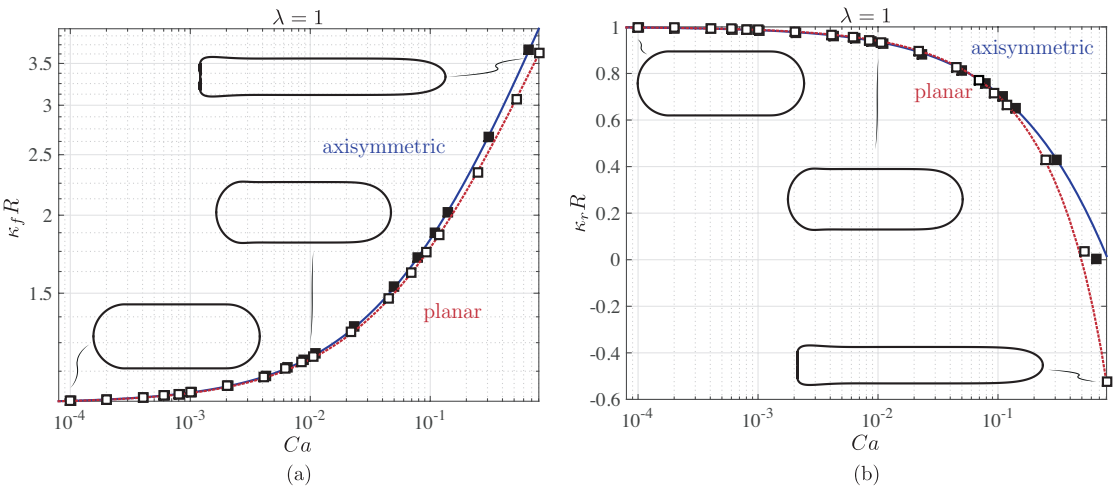

Figure 9.20 – Curvature κ_f of the front (a) and κ_r of the rear (b) meniscus predicted by the model Eq. (9.41) (lines) and FEM-ALE data (symbols) versus Ca for both axisymmetric (blue line, full symbols) and planar (red dashed line, empty symbols) geometries, where the viscosity ratio $\lambda = 1$.

(see Fig. 9.20 as well as Fig. 9.25 and 9.26), can be regarded as an empirical extension of Bretherton's law to a broader capillary numbers range up to 1. The mean curvature at the droplet extremities is given by $\mathscr{C}_{f,r} = \chi\kappa_{f,r}$.

9.7.2 Front and rear pressure jumps – classical model

Following the literature (Bretherton, 1961; Cherukumudi et al., 2015), the dimensionless pressure jump $\Delta p_{f,r}R/\gamma = (p^i_{f,r} - p^o_{f,r})R/\gamma$ at the front and rear of the droplet is described by the empirical model

$$\frac{\Delta p_{f,r}R}{\gamma} = \chi\left[1 + S_{f,r}(\lambda)(3Ca)^{2/3}\right], \tag{9.43}$$

where $\chi = 2$ (resp. $\chi = 1$) for the axisymmetric (resp. planar), and $S_{f,r}$ is a λ-dependent coefficient. Equation (9.43) is in fact inspired by the curvature model proposed by Bretherton (1961) exploiting the Laplace law (Cherukumudi et al., 2015), reason why we call it classical model. The coefficient $S_{f,r}$ could be derived from the integration of the lubrication equation (9.23) or (9.24), which is valid in the low-Ca limit when the viscous stresses and their jumps are negligible. To broaden the Ca range of the model, we obtain $S_{f,r}$ through fitting to the FEM-ALE data. Nevertheless, as visible in Fig. 9.21, the model fails to precisely describe the numerical data, particularly for the rear pressure jump at high Ca values (see Fig. 9.21(b)).

After explaining our model for the normal viscous stress jump in Sec. 9.7.3, we will show in Sec. 9.7.4 that the pressure jump can be better approximated by summing up the two contributions from the interface mean curvature and the normal viscous stress jump, which are modeled separately. The importance of the normal viscous stress jump for the pressure jump is already noticeable when comparing the evolutions of the plane curvature $\kappa_{f,r}$ and the one of the pressure jump $\Delta p_{f,r}/\gamma$ in Figs. 9.20(a) and 9.21(a) or in Figs. 9.20(b) and 9.21(b).

9.7.3 Front and rear normal viscous stress jumps

The dimensionless normal viscous stress jump $\Delta\tau_{zz}R/\gamma = (\tau^i_{zz_{f,r}} - \tau^o_{zz_{f,r}})R/\gamma$ at the front and rear of the droplet is approximated by the following model

$$\frac{\Delta\tau_{zz_{f,r}}R}{\gamma} = \frac{M_{f,r}(\lambda)(3Ca) + N_{f,r}(\lambda)(3Ca)^{4/3}}{1 + O_{f,r}(\lambda)(3Ca)}, \tag{9.44}$$

where $M_{f,r}$, $N_{f,r}$ and $O_{f,r}$ are viscosity ratio dependent coefficients found by fitting Eq. (9.44) to the FEM-ALE data. The normal viscous stress jumps indeed scale with Ca for small capillary numbers, as found by Bretherton (1961). The comparison between the model and the numerical results is shown in the insets of Fig. 9.21, where the results for $\lambda = 0$ are shown. The results for $\lambda = 1$ and 100 can be found in Figs. 9.27 and 9.28. The stress jump $\Delta\tau_{zz}$ is found to be small in the case of $\lambda = 1$ and it varies with Ca nonmonotonically for the other viscosities.

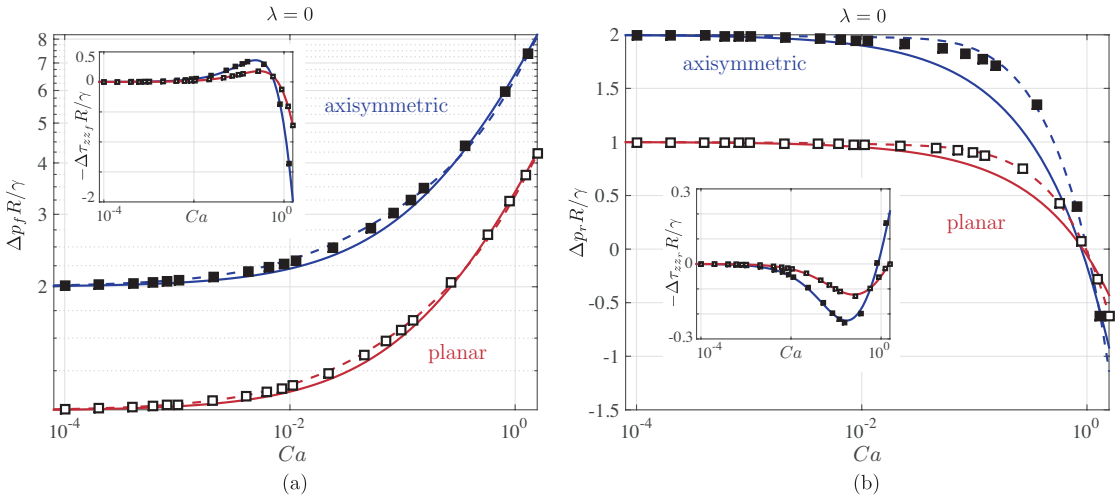

Figure 9.21 – Front (a) and rear (b) pressure jump $\Delta p_{f,r}$ given by Eq. (9.43) (solid lines); front (a) and (b) rear normal viscous stress jump $\Delta\tau_{zz_{f,r}}$ by Eq. (9.44) (inset, solid lines) and FEM-ALE data (symbols) versus Ca for both axisymmetric (blue line, full symbols) and planar (red line, empty symbols) geometries, where the viscosity ratio $\lambda = 0$. The dashed lines correspond to the improved pressure jump model Eq. (9.46). Note the different scale in the insets.

9.7.4 Front and rear pressure jumps – improved model

Using the dynamic boundary condition in the normal direction evaluated at the front and rear caps of the droplet, Eq. (9.40), the pressure jump at the front and rear caps can also be computed as

$$\Delta p_{f,r} = \gamma\chi\kappa_{f,r} + \Delta\tau_{zz_{f,r}}. \tag{9.45}$$

Thus, with the proposed models (9.41) and (9.44) for the interface curvatures and normal viscous stress jumps at hand, the pressure jump model reads

$$\frac{\Delta p_{f,r}R}{\gamma} = \frac{M_{f,r}(\lambda)(3Ca) + N_{f,r}(\lambda)(3Ca)^{4/3}}{1 + O_{f,r}(\lambda)(3Ca)} + \chi\frac{1 + T_{f,r}(\lambda)(3Ca)^{2/3}}{1 + Z_{f,r}(\lambda)(3Ca)^{2/3}}, \tag{9.46}$$

which agrees with the FEM-ALE data better than Eq. (9.43) does (see dashed lines in Fig. 9.21 or Figs. 9.27 and 9.28). Therefore, the jump in normal viscous stresses has to be taken into account for $Ca > 10^{-3}$.

9.8 Stress distribution and total pressure drop

9.8.1 Stress distribution along the channel centerline

The flow field can be classified into parallel and nonparallel regions (see Fig. 9.8). The parallel regions are composed of the region sufficiently far away from the droplet and that encompass-

ing the uniform lubrication film of constant thickness, where the flow is streamwise invariant. The profile of the streamwise velocity $u(r)$ is parabolic and the radial velocity $v \approx 0$. On the contrary, the flow is not parallel near the droplet extremities (see Fig. 9.8) where the flow stagnates. Therefore, the nearby streamwise velocity vary significantly, leading to a nonzero radial velocity v owing to the divergence-free condition.

We show in Fig. 9.22 the distribution of the total stress component $\sigma_{zz} = -p + \tau_{zz}$, of the pressure p and of the viscous stress component $\tau_{zz} = 2\mu\partial u/\partial z$ along the centerline of the channel. τ_{zz} vanishes where the flow is approximately parallel. As seen in Sec. 9.7.3, τ_{zz} is negligible at small Ca, typically below 10^{-3}.

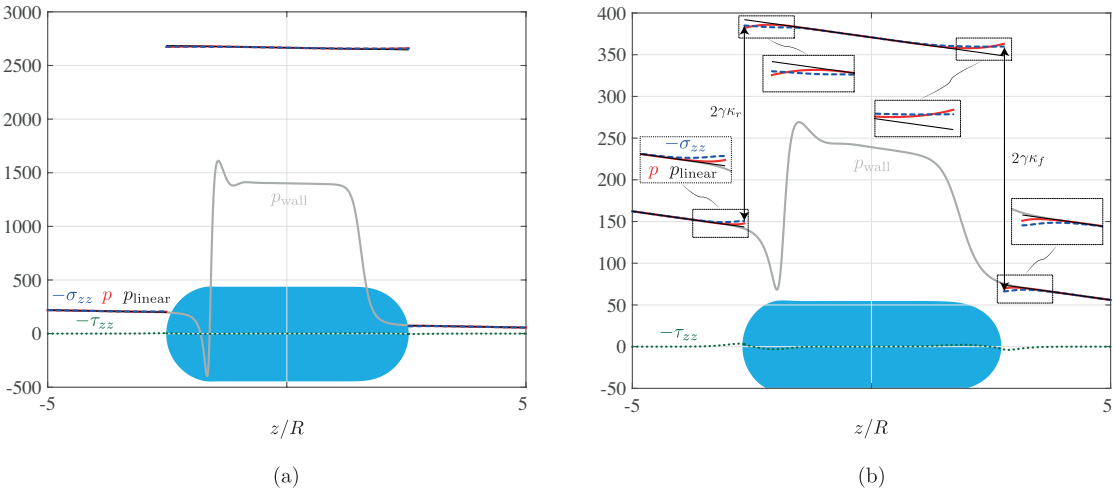

Figure 9.22 – Spatial evolution of the pressure p (red solid line), normal viscous stresses $-\tau_{zz}$ (green dotted line) and total stresses $-\sigma_{zz}$ (blue dashed line) along the centerline for $Ca = 8.2 \times 10^{-4}$ (a) and $Ca = 8.8 \times 10^{-3}$ (b), $\lambda = 1$ and an axisymmetric configuration, obtained from the FEM-ALE numerical simulations. The linear pressure evolution without considering nonparallel flow effects is shown by the thin black lines. The total stresses jumps induced by the mean curvature at the interfaces are indicated by arrows. The droplet shape is indicated in blue. The pressure at the channel wall is indicated by the grey line.

Furthermore, for a larger but still moderate Ca number, it is observed in Fig. 9.22(b) that the pressure (red line) deviates from the linearly varying pressure, p_{linear} (black line), of the unperturbed flow (without droplet) featured with a constant pressure gradient. The deviation is attributed to the nonparallel flow structure near the front and rear caps of the droplet (see Fig. 9.8), hence the pressure based on p_{linear} needs to be corrected by $\Delta p^{\text{NP}} = p - p_{\text{linear}}$. Typical values for the pressure corrections can be found in the Appendix 9.10.7. These corrections are particularly large at large viscosity ratios for the region inside of the droplet. We did not succeed in providing a model to quantify this pressure correction.

Finally, in agreement with the results of Section 9.7, the jump in total stress or pressure at the rear of the droplet is smaller than the one at the front.

9.8.2 Pressure distribution along the channel wall

The pressure distribution on the channel wall is presented on Fig. 9.22 as well (continuous grey line). The influence of the interface mean curvature is clearly visible. The nonmonotonic pressure at the wall close to the droplet rear results from the variation of the plane curvature in the dynamic meniscus region, where the interface oscillates (see also Fig. 9.11).

9.8.3 Droplet-induced total pressure drop along a channel

The prediction of the total pressure drop along a channel induced by the presence of a droplet flowing with a velocity U_d is of paramount importance for the design of two-phase flow pipe networks (Baroud et al., 2010; Ładosz et al., 2016). This allows for a coarse-grained quantification of the complicated local effects induced by the droplet. Droplets can thus be seen as punctual perturbations in the otherwise linear pressure evolution. In this section, we will show that it is possible to predict the total pressure drop induced by a droplet with the models proposed so far.

The total pressure drop can be defined as the difference between the pressure in the outer phase ahead and behind the droplet, namely $\Delta p_{\text{tot}} = p_f^o - p_r^o$ (Kreutzer et al., 2005). It is given by

$$\Delta p_{\text{tot}} = \Delta p_{o,r}^{\text{NP}} + \Delta p_r - \Delta p_{i,r}^{\text{NP}} + \frac{dp_i}{dz} L_d + \Delta p_{i,f}^{\text{NP}} - \Delta p_f - \Delta p_{o,f}^{\text{NP}}, \tag{9.47}$$

where $\Delta p_{f,r}$ are given by the model for the pressure jumps at interfaces, Eq. (9.46). The pressure gradient dp_i/dz in the parallel region inside the droplet is given by Eq. (9.31) and Eq. (9.67) for the axisymmetric and planar geometries, respectively. Assuming the droplet of volume/area Ω (axisymmetric/planar geometry) as a composition of two hemispherical caps of radius $R - H_\infty$, with H_∞ given by Eq. (9.30), connected by a cylinder of the same radius, the droplet length L_d can be approximated at first order for low Ca, *i.e.* for $H_\infty/R \ll 1$, as

$$L_d = \frac{(R + 2H_\infty)}{\pi} \frac{\Omega}{R^3} + \frac{2}{3}(R - H_\infty) \tag{9.48}$$

for the axisymmetric case and

$$L_d = \frac{(R + H_\infty)}{2} \frac{\Omega}{R^2} + \frac{4 - \pi}{2}(R - H_\infty) \tag{9.49}$$

for the planar case.

Equivalently, the total pressure drop can also be calculated using the models for the normal viscous stress jump, Eq. (9.44), and the front and rear plane curvatures, Eq. (9.41), yielding:

$$\Delta p_{\text{tot}} = \Delta p_{o,r}^{\text{NP}} + \Delta \tau_{zz_r} + \chi\gamma\kappa_r - \Delta p_{i,r}^{\text{NP}} + \frac{dp_i}{dz} L_d + \Delta p_{i,f}^{\text{NP}} - \Delta \tau_{zz_f} - \chi\gamma\kappa_f - \Delta p_{o,f}^{\text{NP}}, \tag{9.50}$$

where $\chi = 2$ for the axisymmetric configuration and $\chi = 1$ for the planar one.

If we neglect the nonparallel flows effects on the pressure, Δp^{NP}, the total pressure drop would then be:

$$\Delta p_{\mathrm{tot}} = \Delta p_r + \frac{dp_i}{dz} L_d - \Delta p_f. \tag{9.51}$$

Neglecting the effects of the nonparallel flows would induce an error on the pressure drop, increasing with Ca. For a single droplet of volume $\Omega = 12.9$, the error of Eq. (9.51) compared to the numerical results is less than 3% for $\lambda = 0$, but reaches 15% for $\lambda = 1$ and even 48% for $\lambda = 100$. It is thus important to include the corrections accounting for the nonparallel flow effects to predict the pressure drop accurately, especially when the viscosity ratios $\lambda \gtrapprox 1$. Numerical simulations are therefore crucial to achieve so.

9.9 Conclusions

This chapter generalizes the theory of a confined bubble flowing in an axisymmetric or planar channel that we have discussed in Chapter 8 to droplets of nonvanishing viscosity ratios. Empirical models for the relevant quantities such as the uniform and minimal film thicknesses separating the wall and the droplet, the front and rear droplet plane curvatures, the total pressure drop in the channel and the droplet velocity are derived for the range of capillary numbers from 10^{-4} to 1, and viscosity ratios ranging from the value $\lambda = 0$ for bubbles to highly-viscous droplets. Following the work of Schwartz et al. (1986), we extend the low-capillary-number predictions obtained by the lubrication approach of Bretherton (1961) for bubbles to viscous droplets. Extensive accurate moving-mesh arbitrary Lagrangian-Eulerian (ALE) finite-element numerical simulations are performed for the viscosity-ratio range $\lambda \in [0-100]$ to build a numerical database, based on which we propose empirical models for the relevant quantities. The models are inspired by the low-Ca theoretical asymptotes, but their validity range reaches large capillary numbers ($Ca > 10^{-3}$), where the lubrication approach no longer holds (see Chapter 8).

We have found that the uniform film thickness for $Ca < 10^{-3}$ does not differ significantly with that of a bubble as long as $\lambda < 1$. For larger viscosity ratios, instead, the film thickness increases monotonically and saturates to a value $2^{2/3}$ times the Bretherton's scaling for bubbles when $\lambda > 10^3$. The film thickness can be modeled by a rational function similar to that proposed by Aussillous & Quéré (2000) for bubbles, where the fitting coefficient Q depends on the viscosity ratio. Furthermore, the uniform film thickness saturates at large capillary numbers to a value depending on Q. The minimum film thickness can be predicted analogously. The velocity of a droplet can be unambiguously derived once the uniform film thickness is known. We have shown that considering the full expression of the droplet velocity is crucial as the asymptotic series for low Ca has a very restricted range of validity for nonvanishing viscosity ratios.

Furthermore, we have found that the evolution of the front and rear cap curvatures as a function of the capillary number differs from the one of the pressure jumps at the front and rear droplet interfaces. This is due to the normal viscous stress jumps. The contribution of the jumps has been overlooked in the literature, though it has to be considered for $Ca > 10^{-3}$. With all these models at hand, the pressure drop across a droplet can be computed, which will be valuable for engineering practices.

We also have shown that the flow patterns inside and outside of the droplet strongly depend on the capillary number and viscosity ratio. In particular, for $\lambda < 1/2$ ($\lambda < 2/3$) for the axisymmetric (planar) configuration, when the film thickness is larger than a critical value $H_\infty^\star/R$, recirculating regions at the front and rear of the droplet disappear. Furthermore, the recirculation region in the outer phase detaches from the droplet's rear interface for large film thickness yet smaller than $H_\infty^\star/R$, implying the disappearance of the inner recirculating region at the rear.

The considered problem in a planar configuration could be relevant for the study of a front propagation in a Hele-Shaw cell (Park & Homsy, 1984; Reinelt & Saffman, 1985), as we have seen in Chapter 8, but where the second-phase viscosity is nonvanishing. For instance, one could compute the amount of fluid left on the walls when a finger of immiscible fluid penetrates (Saffman & Taylor, 1958). Furthermore, the problem in the planar configuration can be seen as a first step towards understanding the dynamics of pancake droplets in a Hele-Shaw cell (Huerre et al., 2015; Zhu & Gallaire, 2016). Another possible outlook is the extension of the present theory to capillaries with polygonal cross sections, where the film between the droplet and the walls is not axisymmetric, but thick films known as *gutters* develop in the capillary corners (see Chapter 10). Three-dimensional numerical simulations are then necessary to resolve this asymmetry. A force balance will determine the droplet velocity and an equivalent pressure drop model could be proposed for these geometries.

Despite the fact that this work was motivated by the vast number of droplet-based microfluidic applications, the analytically derived equation (9.24) serves as a generalization of the well known Landau-Levich-Derjaguin-Bretherton equation (Landau & Levich, 1942; Derjaguin, 1943; Bretherton, 1961), see Chapter 8, when the second fluid has a non-negligible viscosity. This equation could therefore be adapted to predict the film thickness in coating problems with two immiscible liquids.

Acknowledgements This work was funded by ERC Grant No. 'SIMCOMICS 280117'. L.Z. gratefully acknowledges the VR International Postdoc Grant from Swedish Research Council '2015-06334' for financial support. The authors would like to acknowledge the valuable comments from the anonymous referees that helped to improve the manuscript.

9.10 Appendix

9.10.1 Derivation of the flow profiles in the thin-film region for the planar configuration

Consider an axial location in the thin-film region. The velocity profiles inside, u_i, and outside, u_o, of the droplet can be described by:

$$u_i(r) = \frac{1}{2\mu_i}\frac{dp_i}{dz}r^2 + A_i r + B_i, \tag{9.52}$$

$$u_o(r) = \frac{1}{2\mu_o}\frac{dp_o}{dz}r^2 + A_o r + B_o, \tag{9.53}$$

where p_i and p_o are the inner, respectively outer, pressures, and A_i, B_i, A_o and B_o are real constants to be determined. Given the symmetry at $r = 0$ of the inner velocity, $A_i = 0$. The other constants are found by imposing the no-slip boundary condition at the channel walls $u(R) = -U_d$ in the droplet reference frame, the continuity of velocities at the interface located at $r = R - H$, $u_i(R-H) = u_o(R-H)$, and the continuity of tangential stresses at the interface

$$\mu_i \frac{du_i}{dz}\Big|_{r=R-H} = \mu_o \frac{du_o}{dz}\Big|_{r=R-H}. \tag{9.54}$$

Eventually one obtains:

$$A_o = \frac{1}{\mu_o}\left(\frac{dp_i}{dz} - \frac{dp_o}{dz}\right)(R-H), \tag{9.55}$$

$$B_i = \frac{1}{2\mu_i\mu_o}\left[-(R-H)^2\frac{dp_i}{dz}\mu_o + H\left(2H\frac{dp_i}{dz} - H\frac{dp_o}{dz} \ -2R\frac{dp_i}{dz}\right)\mu_i\right] - U_d, \tag{9.56}$$

$$B_o = \frac{1}{2\mu_o}\left[\left(\frac{dp_o}{dz} - 2\frac{dp_i}{dz}\right)R^2 - 2HR\left(\frac{dp_o}{dz} - \frac{dp_i}{dz}\right)\right] - U_d. \tag{9.57}$$

9.10.2 Derivation of the interface profile equation for the planar configuration

The flow rates at any axial location where the external film thickness is H are:

$$\begin{aligned} q_i &= 2\int_0^{R-H} u_i(r)dr \\ &= \frac{1}{3\mu_i\mu_o}\left\{-(R-H)\left[3H\left(H\left(\frac{dp_o}{dz} - 2\frac{dp_i}{dz}\right) + 2\frac{dp_i}{dz}R\right)\mu_i \ + \ 2\frac{dp_i}{dz}(R-H)^2\mu_o\right]\right\} - 2U_d(R-H), \end{aligned} \tag{9.58}$$

$$q_o = 2\int_{R-H}^{R} u_o(r)dr = \frac{H^2}{3\mu_o}\left[H\left(3\frac{dp_i}{dz} - 2\frac{dp_o}{dz}\right) - 3\frac{dp_i}{dz}R\right] - 2U_d H. \tag{9.59}$$

In the droplet reference frame, the flow rate of the inner phase has to vanish, $q_i = 0$. Furthermore, in the region where the film is uniform (see Fig. 9.11), $H = H_\infty$, the inner and outer pressure gradients have to be equal. Using these two conditions one can solve for the pressure

gradient in the uniform film region

$$\left.\frac{dp}{dz}\right|_{r=R-H_\infty} \approx -\frac{6\mu_i U_d}{2R^2-(4-6\lambda)H_\infty R+(2-3\lambda)H_\infty^2} \tag{9.60}$$

and for the outer flow rate, where the limit $H_\infty/R \ll 1$ is considered:

$$q_o \approx -2H_\infty\left[\frac{2R^2-(4-3\lambda)H_\infty R+2(1-\lambda)H_\infty^2}{2R^2-(4-6\lambda)H_\infty R+(2-3\lambda)H_\infty^2}\right]U_d \approx -H_\infty\left[\frac{2R-(4-3\lambda)H_\infty}{R-(2-3\lambda)H_\infty}\right]U_d \tag{9.61}$$

The pressure gradients in the dynamic meniscus regions are no longer equal and their difference is proportional to the deformation of the interface $r = R - H$. Under the assumption of a quasi-parallel flow, and neglecting the viscous contribution in view of the lubrication assumption, the Laplace law imposes:

$$\frac{dp_i}{dz}-\frac{dp_o}{dz}=\gamma\frac{d^3H}{dz^3}. \tag{9.62}$$

Knowing q_i and q_o, Eqs. (9.58), (9.59) can be solved for the unknown pressure gradients dp_i/dz, dp_o/dz as a function of H:

$$\frac{dp_i}{dz} \approx \frac{3\lambda\{2H[H_\infty(3\lambda-2)+R]-3H_\infty[H_\infty(3\lambda-4)+2R]\}\mu_o U_d}{H(R-H)[H(3\lambda-4)+4R][H_\infty(3\lambda-2)+R]}, \tag{9.63}$$

$$\begin{aligned}\frac{dp_o}{dz} \approx -6\Bigg\{&\frac{R(H-H_\infty)[3\lambda(H+H_\infty)-2(H+2H_\infty)]}{H^3[H(3\lambda-4)+4R][H_\infty(3\lambda-2)+R]}\\ &+\frac{HH_\infty[H(2-3\lambda)^2+H_\infty(3(5-3\lambda)\lambda-4)]+2R^2(H-H_\infty)}{H^3[H(3\lambda-4)+4R][H_\infty(3\lambda-2)+R]}\Bigg\}\mu_o U_d\end{aligned} \tag{9.64}$$

and substituted into Eq. (9.62). Following Bretherton (1961), the resulting equation can be put in an universal form by the substitutions $H = H_\infty\eta$ and $z = H_\infty(3Ca)^{-1/3}\xi$. In the limit of $H_\infty/R \to 0$, the governing equation for the interface profile reads:

$$\frac{d^3\eta}{d\xi^3}=2\frac{\eta-1}{\eta^3}\left[\frac{2+3m(1+\eta+3m\eta)}{(1+3m)(4+3m\eta)}\right]. \tag{9.65}$$

where

$$m=\lambda\frac{H_\infty}{R} \tag{9.66}$$

is the rescaled viscosity ratio.

9.10.3 Derivation of the droplet velocity model for the planar configuration

The velocity profiles in the uniform film region have been derived in Appendix 9.10.1. In particular, the inner and outer volumetric fluxes are given by Eqs. (9.58) and (9.59), respectively. At the location where $H = H_\infty$ the interface is flat and the pressure gradients are equal,

$dp_i/dz = dp_o/dz = dp/dz$. Furthermore, mass conservation imposes that $q_o = 2R(U_\infty - U_d)$ and since we are in the reference frame of the droplet, $q_i = 0$. The system of two equations can be solved for the pressure gradient

$$\left.\frac{dp}{dz}\right|_{r=R-H_\infty} = \frac{-3RU_\infty\mu_i}{(R-H_\infty)^3 + H_\infty(3R^2 - 3H_\infty R + H_\infty^2)\lambda} \tag{9.67}$$

and the droplet velocity

$$U_d = \frac{R[2(R-H_\infty)^2 + 3H_\infty(2R-H_\infty)\lambda]}{2(R-H_\infty)^3 + 2H_\infty(3R^2 - 3H_\infty R + H_\infty^2)\lambda}U_\infty. \tag{9.68}$$

The relative velocity of the planar droplet reads

$$\frac{U_d - U_\infty}{U_d} = \frac{\frac{H_\infty}{R}\left\{2 - \frac{H_\infty}{R}\left[4 + 2\frac{H_\infty}{R}(\lambda - 1) - 3\lambda\right]\right\}}{2 + \left(2 - \frac{H_\infty}{R}\right)\frac{H_\infty}{R}(3\lambda - 2)}. \tag{9.69}$$

9.10.4 Derivation of the critical uniform film thickness for the appearance of the recirculation regions

The velocity profile in the channel away from the droplet is given by Eq. (9.11) for the axisymmetric configuration and by

$$u_\infty(y) = \frac{3}{2}U_\infty\left[1 - \left(\frac{y}{R}\right)^2\right] - U_d \tag{9.70}$$

for the planar one. The droplet velocity for the former case is given by Eq. (9.32), whereas for the latter it is given by Eq. (9.68). With the use of Eqs. (9.32) and (9.68), the velocity u_∞ can be expressed as a function of H_∞/R. The critical uniform film thickness for the appearance of recirculation regions, $H_\infty^\star$, is obtained by solving $u_\infty(0) = 0$, resulting in Eqs. (9.12) and (9.13) for the axisymmetric and planar configurations, respectively.

9.10.5 Fitting laws for the model coefficients

The model coefficients Q in Eq. (9.30), G in Eq. (9.38), $T_{f,r}$ and $Z_{f,r}$ in Eq. (9.41) and $M_{f,r}$, $N_{f,r}$ and $O_{f,r}$ in Eq. (9.44) can be well approximated by the rational function

$$\frac{a_3\lambda^3 + a_2\lambda^2 + a_1\lambda + a_0}{\lambda^3 + b_2\lambda^2 + b_1\lambda + b_0}, \tag{9.71}$$

where the constants a_i with $i = 0,..,3$ and b_j with $j = 0,..,2$ are given in Tables 9.1 and 9.2 for the axisymmetric and planar geometries, respectively.

	a_0	a_1	a_2	a_3	b_0	b_1	b_2
Q	2.21	111.25	33.84	1.37	0.89	44.86	54.50
G	130.37	186.67	−4.82	1.30	58.41	154.37	10.56
T_f	3262.57	1573.07	7222.70	9.90	1197.26	2006.27	2855.96
T_r	−12031.57	−21476.98	2820.73	77.21	25461.62	11675.00	16374.62
Z_f	3392.32	−1773.73	2984.79	39.56	5249.41	12649.53	32757.19
Z_r	−1842.14	−14129.53	26169.48	160.45	19514.41	14458.49	33771.45
M_f	−4850.40	5797.90	−507.02	1.22	2412.12	2134.95	−222.42
M_r	−6.38	18.59	−10.85	−0.82	−2.68	4.97	2.93
N_f	−5293.51	14808.02	−9344.15	−126.15	−3171.89	−3079.05	8185.38
N_r	−2.93	−17.28	18.94	1.08	1.68	10.76	5.71
O_f	0.01	−0.02	0.08	−0.11	0.06	−0.06	−0.64
O_r	32.38	−429.86	638.07	−5.84	11.85	−155.00	338.88

Table 9.1 – Coefficients of the fitting law for the axisymmetric configuration.

	a_0	a_1	a_2	a_3	b_0	b_1	b_2
Q	98.76	146.42	70.42	1.45	45.04	89.61	77.03
G	168.27	348.60	26.76	1.48	88.60	264.97	34.41
T_f	0.35	1.17	5.41	2.43	0.16	0.57	3.02
T_r	−130.18	−298.84	−55.49	−0.66	256.91	292.80	83.68
Z_f	1096.45	191.51	395.61	−0.08	2690.72	6726.39	2249.29
Z_r	−0.62	−0.66	0.08	−0.21	5.80	−0.74	3.08
M_f	−6.41	17.26	−11.54	0.80	7.40	−2.88	−12.76
M_r	4.10	−3.52	0.17	0.04	4.55	7.67	−5.25
N_f	−6.12	17.95	−11.90	0.19	−9.06	−6.06	30.83
N_r	−50.40	61.95	−14.79	0.51	84.57	41.55	−24.20
O_f	4.52	−2.80	−1.73	0.89	27.19	−57.38	21.87
O_r	2.10	−6.97	2.79	−0.01	1.14	−1.38	−1.96

Table 9.2 – Coefficients of the fitting law for the planar configuration.

9.10.6 Additional results

For seek of clarity, the results for $\lambda = 0$ and 100 are shown in the appendix rather than in the main text, except for the normal viscous stresses jump, whose results for $\lambda = 0$ are presented in the main text as for $\lambda = 1$ the normal viscous stress jumps are small.

9.10.7 Pressure corrections due to nonparallel flow

Some typical total stresses corrections at the outer and inner sides of the droplet interface as a function of Ca and for different viscosity ratios λ are shown in Fig. 9.29 and Fig. 9.30, respectively.

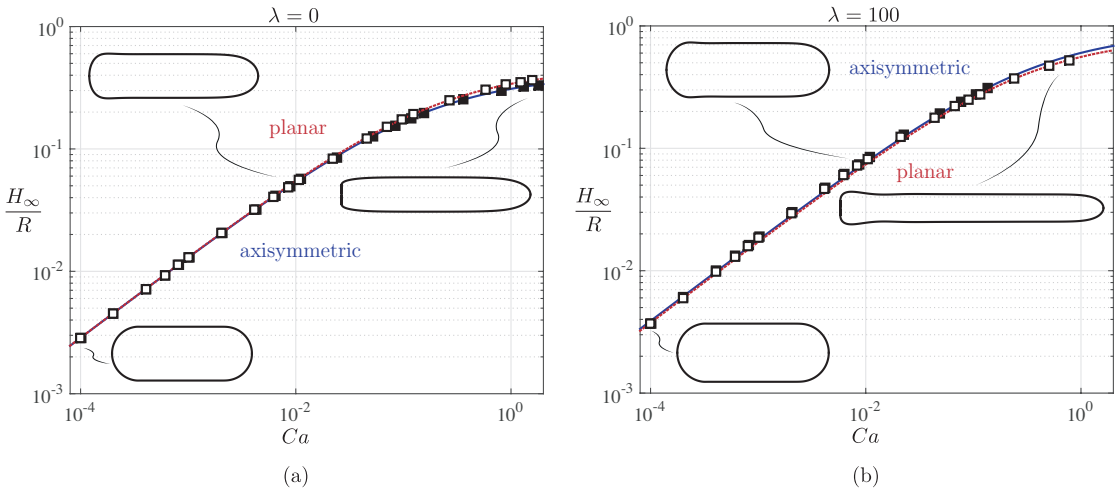

Figure 9.23 – Uniform film thickness given by Eq. (9.30) (lines) and FEM-ALE numerical results (symbols) as a function of the droplet capillary number for $\lambda = 0$ (a) and 100 (b) and both axisymmetric (blue solid line, full symbols) and planar (dashed red line, empty symbols) geometries.

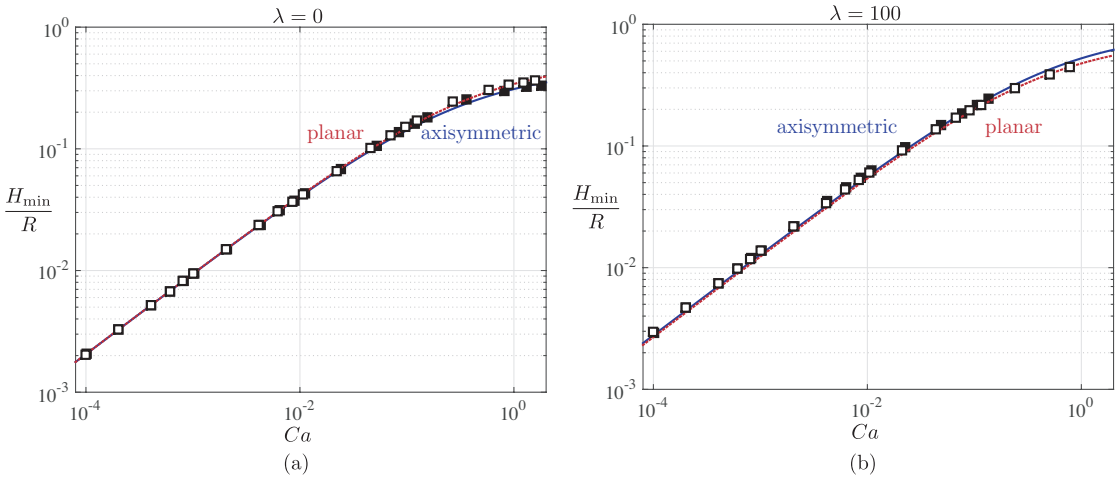

Figure 9.24 – Minimum film thickness given by Eq. (9.38) (lines) and FEM-ALE numerical results (symbols) as a function of the droplet capillary number for $\lambda = 0$ (a) and 100 (b) and both axisymmetric (blue solid line, full symbols) and planar (dashed red line, empty symbols) geometries.

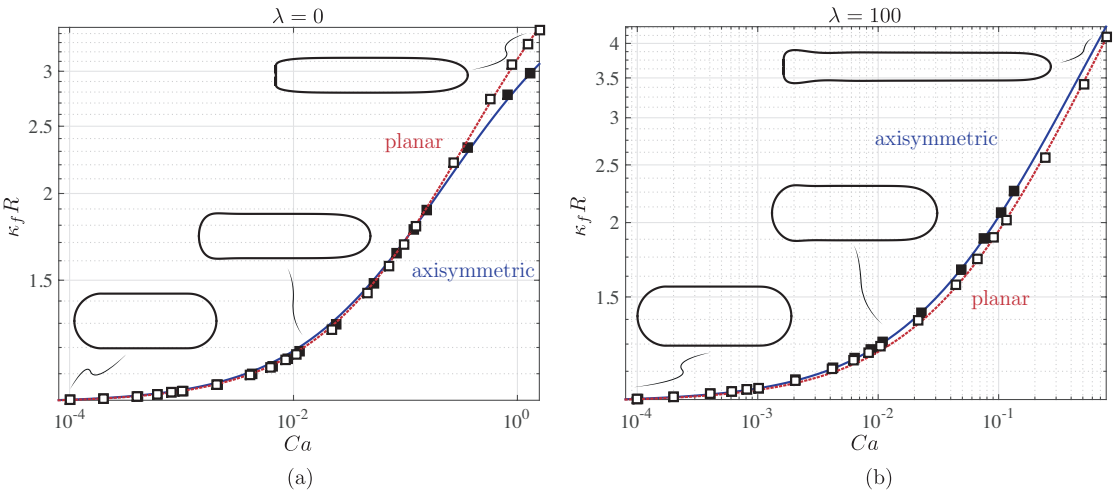

Figure 9.25 – Curvature κ_f of the front meniscus predicted by the model Eq. (9.41) (lines) and FEM-ALE data (symbols) versus Ca for both axisymmetric (blue line, full symbols) and planar (red dashed line, empty symbols) geometries, where the viscosity ratio $\lambda = 0$ (a) and 100 (b).

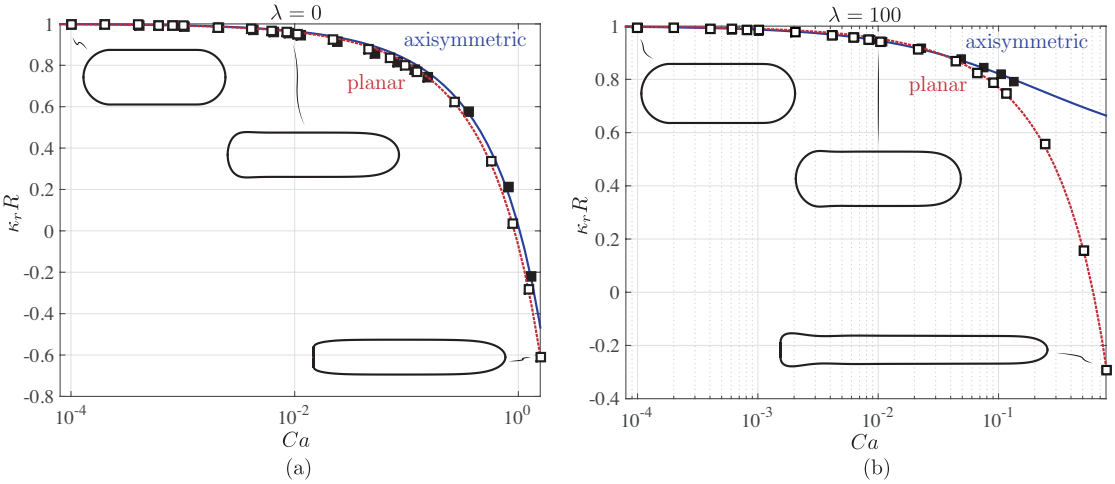

Figure 9.26 – The rear counterpart κ_r of Fig. 9.25.

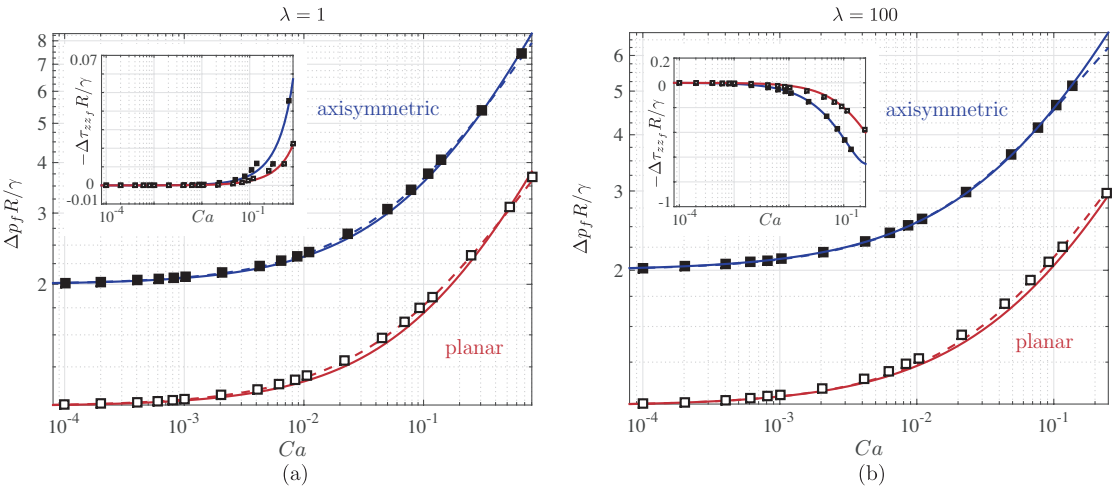

Figure 9.27 – Front pressure jump Δp_f given by Eq. (9.43) (solid lines) and front normal viscous stress jump $\Delta\tau_{zz_f}$ by Eq. (9.44) (inset, solid lines) and FEM-ALE data (symbols) versus Ca for both axisymmetric (blue line, full symbols) and planar (red line, empty symbols) geometries, where the viscosity ratio $\lambda = 1$ (a) and 100 (b). The dashed lines correspond to the improved pressure jump model Eq. (9.46). Note the different scale in the insets.

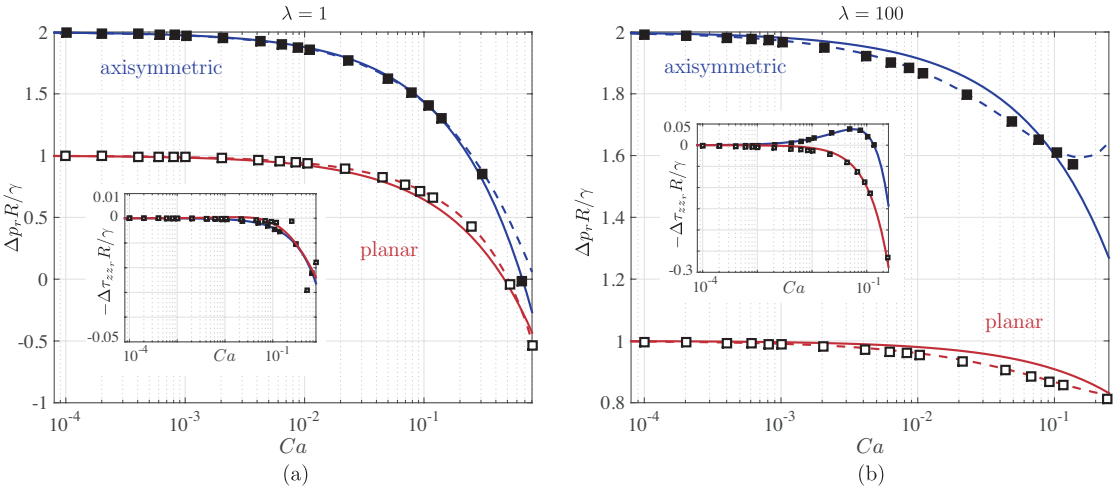

Figure 9.28 – The rear counterpart, pressure jump Δp_r and normal viscous stress jump $\Delta\tau_{zz_r}$, of Fig. 9.27.

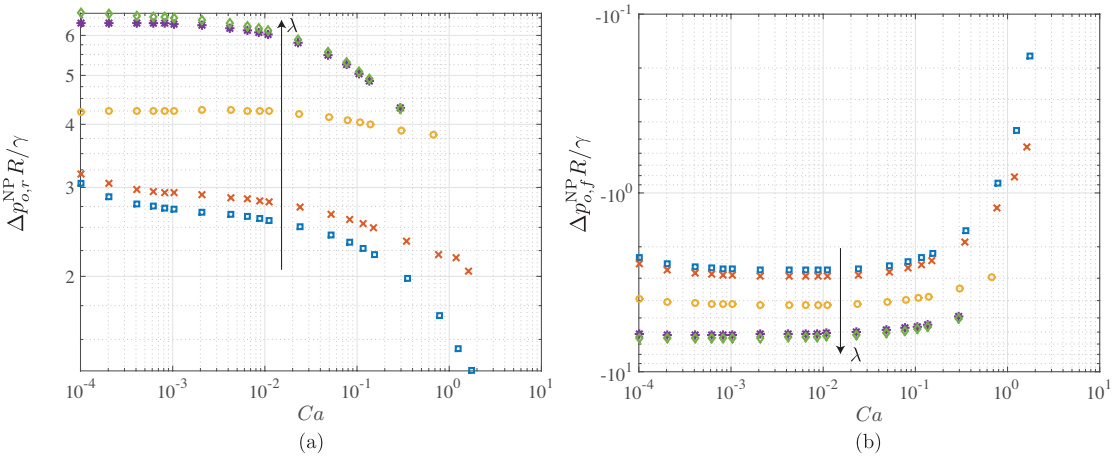

Figure 9.29 – Pressure correction due to nonparallel flow effects at the rear (a) and front (b) outer sides of the interface for $\lambda = 0.04$ (blue squares), 0.12 (red crosses), 1 (yellow circles), 15 (purple stars) and 50 (green diamonds) for the axisymmetric configuration. The results are obtained from FEM-ALE numerical simulations.

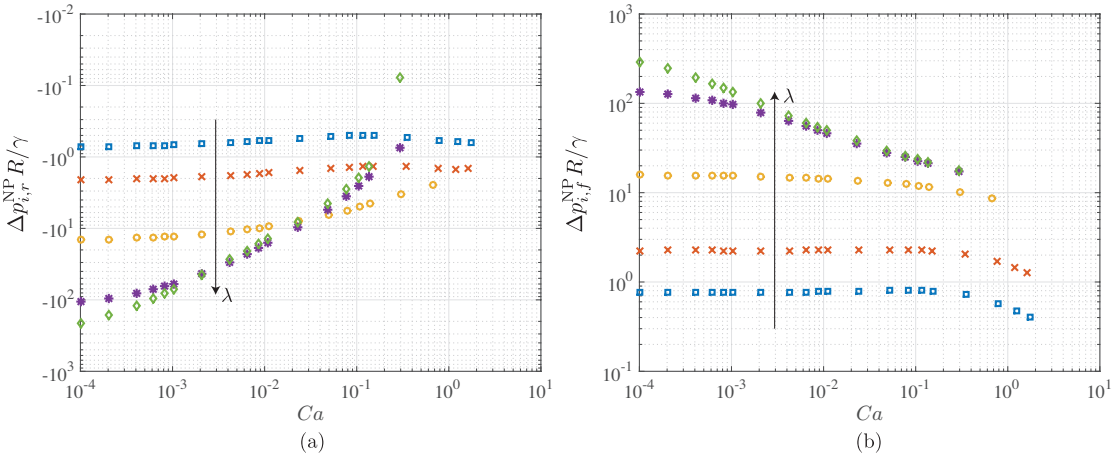

Figure 9.30 – Pressure correction due to nonparallel flow effects at the rear (a) and front (b) inner sides of the interface for $\lambda = 0.04$ (blue squares), 0.12 (red crosses), 1 (yellow circles), 15 (purple stars) and 50 (green diamonds) for the axisymmetric configuration. The results are obtained from FEM-ALE numerical simulations.

10 Bubbles and droplets in polygonal microchannels

10.1 Introduction

The aim of this short chapter is to present a brief overview on the extensions of the previously considered bubbles and droplets in microchannels. In Chapter 9 we have considered droplets flowing in a circular capillary as well as in a planar two-dimensional channel. The latter configuration can be seen as a plane cut in the streamwise direction through a pancake droplet flowing in a Hele-Shaw cell, as the one described in Chapter 8. Here we focus on droplets flowing in polygonal microchannels of square or rectangular cross-section $W^* \times 2R^*$, where the three-dimensionality of the flow is crucial (Anna, 2016). In Section 10.2 we discuss the lubricating-film structure separating such a confined droplet from the channel walls (see Fig. 10.1(a)) and we highlight how this affects the droplet velocity, whereas in Section 10.3 we focus on an unconfined bubble of characteristic size $L^* < W^*$ and $L^* < 2R^*$ (see Fig. 10.1(b)). For the study of Sec. 10.3 we also consider the influence of inertial forces, that have been neglected in the rest of this thesis. The dimensionless number defining the ratio between inertial and viscous forces is the Reynolds number, *Re*. We have found that when the size of a bubble is smaller than the shortest side of the channel, its equilibrium position strongly depends on the flow parameters, namely the Reynolds number, the capillary number, the size of the bubble and the aspect ratio of the channel (Hadikhani et al., 2018).

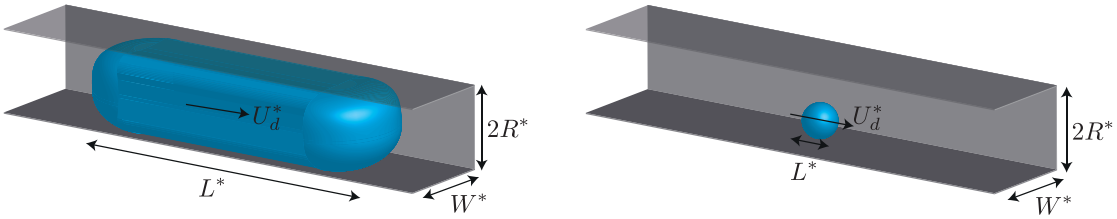

Figure 10.1 – Sketch of the considered geometries. Confined (a) and unconfined (b) bubble or droplet.

10.2 Confined droplets

Let us consider a droplet of viscosity μ_i and length L^* flowing with velocity U_d^* in a microchannel whose width is W^* and height is $2R^*$, filled by a fluid of viscosity μ_o (see Fig. 10.2(a)). The surface tension between the fluids is γ. If we consider $L^* \gg W^*$ and $L^* \gg 2R^*$, the droplet is confined by the lateral walls so that a thin-film region forms close to the sidewalls (see Fig. 10.2(b)), like for the droplets in round capillaries investigated in Chapter 9, or for the pancake bubbles of Chapter 8. However, the polygonal cross-section of the present channels induces additional regions in the flow surrounding the droplet. In fact, the droplet interface does not get close to the channel corners due to surface tension that minimizes the deformation of the interface. Hence, a thick region of outer fluid, usually called *gutter* (Fuerstman et al., 2007), is present at the corners of the polygonal channel. Therefore, the outer phase can flow around the droplet in a much easier way than for a droplet in a round capillary, where the film is thin everywhere. A droplet in a polygonal channel acts as a leaky 'piston' (Wong et al., 1995*a*).

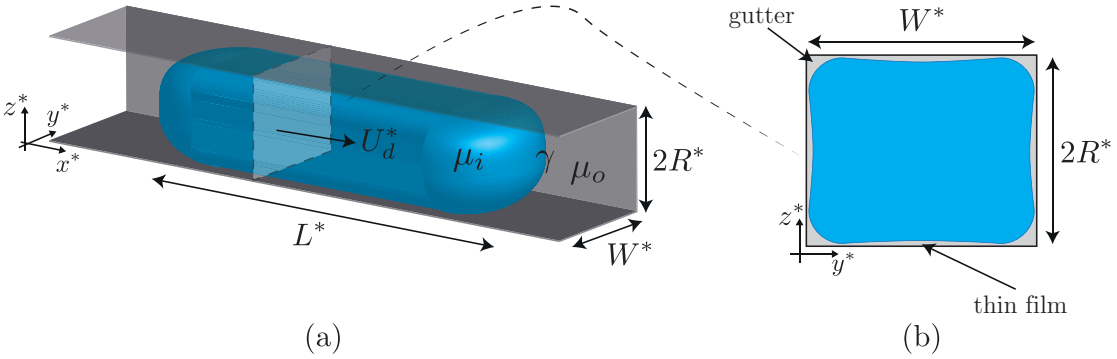

Figure 10.2 – Droplet of length L^* flowing in a rectangular microchannel of width W^* and height $2R^*$. (a) Three-dimensional view of the problem and (b) cross-section of channel occupied by the droplet to highlight the typical film-thickness profile surrounding it. The thickness of the thin-film region is exaggerated for visualization purposes.

The detailed film-thickness profile surrounding a bubble in polygonal channel has been described by Wong et al. (1995*a*), who showed that the thin-film follows a parabolic profile in the directions orthogonal to the flow, similarly to what we have seen for a pancake bubble in Sec. 8.3. Several regions have been identified depending on the streamwise location along the bubble. Furthermore, Wong et al. (1995*b*) found that the pressure drop induced by a bubble in a polygonal capillary scales as $Ca = \mu_o U_d^*/\gamma$ for small Ca, typically of the order of 10^{-6} (Jakiela et al., 2011), whereas it scales as $Ca^{2/3}$ for larger values. Note that the critical capillary number for the transition depends on the geometry of the channel and the length of the bubble. The linear regime is a result of the flow in the gutters and is therefore absent in circular channels. When the capillary number is very small, surface tension effects dominate over viscous effects and the flow in the thin-film regions is much less important than the flow in the gutters. Hence, dissipation mainly occurs due the flow through the gutters and not because of the motion of

the bubble. For both regimes, in addition to the pressure drop induced by the flow in the thin films and in the gutters, the latter depending on the length of the bubble, one has to consider the pressure drop induced by the curved caps, as we have seen in Chapter 9.

The picture is much more complex when the inner-phase viscosity μ_i is nonzero and in the presence of surfactants. Wong & Rao (2015) extended the theory of a bubble in a polygonal channel to viscous droplets, but the work is still unpublished. Fuerstman et al. (2007) have found that intermediate concentrations of surfactants increase the flow through the gutters and thus their relative importance in the pressure drop compared to the pressure drop induced by the front and rear static caps, that dominates at low and high concentration of surfactants. The disagreement of the droplet velocities between the works of Vanapalli, Banpurkar, van den Ende, Duits & Mugele (2009), Labrot, Schindler, Guillot, Colin & Joanicot (2009) and Sessoms, Belloul, Engl, Roche, Courbin & Panizza (2009) further evidences the complexity of the droplet dynamic in polygonal capillaries. By performing a large amount of experiments, Jakiela et al. (2011) have found that the droplet velocity depends in a complicated and nonmonotonic way on the capillary number, on the viscosity ratio between the two phases and on the length L^*, especially when the viscosity of the inner phase is larger than the one of the surrounding fluid. Furthermore, their experimental results show a similar dependence on the viscosity ratio $\lambda = \mu_i/\mu_o$ as the one we derived theoretically in Chapter 9 for a circular capillary. More precisely, the droplet velocity is only weakly dependent on Ca for $\lambda \leq 1$ and $\lambda \gg 1$, whereas it varies strongly with the capillary number for λ slightly larger than unity (see Fig. 9.13 and Sec. 9.5 of Chapter 9). For $\lambda \leq 1$, Jakiela et al. (2011) have found that the velocity of a droplet with $L^* \gtrapprox 2W^* = 4R^*$ is approximatively the average velocity of the outer phase. However, for $\lambda > 1$, which is the case for droplets containing physiological liquids, the velocity strongly depends on the length L^*.

Note that the flow pattern observed in droplets flowing in polygonal channels differs from the one we have found in circular capillaries (Jakiela, Korczyk, Makulska, Cybulski & Garstecki, 2012). The difference is very likely due to the presence of the gutters, where the large velocities induce different recirculation regions inside of the droplet. In fact, Jakiela et al. (2012) have found that – in contrast to the case of droplets in round capillaries – no recirculation regions are present at the droplet extremities when the capillary number is very small, and thus, when the effect of the gutters dominates. For relatively larger Ca, however, when the effect of the gutter is less pronounced, recirculation regions close to the droplet caps appear and the flow field is similar to the one we have found for the axisymmetric droplets in Chapter 9. Hein, Moskopp & Seemann (2015) have shown that the flow field inside of droplets flowing in rectangular microchannels is responsible for a nonuniform accumulation of particles.

To conclude, we believe that the arbitrary Lagrangian-Eulerian (ALE) numerical technique we employed in Chapter 9 could be used here to shed light on the droplet dynamics in polygonal microchannels. In particular, and in a similar fashion to what we have done in the previous chapter, one could extend the low capillary theoretical asymptotes to a larger Ca-range, which is relevant for practical applications. In the following Section 10.3 we present some results

obtained by pursuing this numerical path, for a problem where theoretical results are not yet available and where the confinement is less.

10.3 Unconfined bubbles

Remark This section is largely inspired by the publication

Inertial manipulation of bubbles in rectangular microfluidic channels

P. Hadikhani[1], S. M. H. Hashemi[1], G. Balestra[2], L. Zhu[3,4], M. A. Modestino[5], F. Gallaire[2] and D. Psaltis[1]

[1]Optics Laboratory, EPFL, CH1015 Lausanne, Switzerland
[2]Laboratory of Fluid Mechanics and Instabilities, EPFL, CH1015 Lausanne, Switzerland
[3]Linné Flow Centre and Swedish e-Science Research Centre (SeRC), KTH Mechanics, SE 10044 Stockholm, Sweden
[4]Department of Mechanical and Aerospace Engineering, Princeton University, NJ 08544, USA
[5]Department of Chemical and Biomolecular Engineering, Tandon School of Engineering, New York University, Brooklyn, NY 11201, USA

Lab on a Chip **18**, 1035 (2018)

Author contributions G.B. prepared the numerical setup together with L.Z., performed some simulations, analyzed the results and contributed to the writing of the paper.

When the characteristic size of the bubble L^* is smaller than the width W^* and the height $2R^*$ of the rectangular microchannel, the bubble is no longer confined (see Fig. 10.3(a)). Such small gaseous bubbles form, for instance, close to the electrodes of microchannels where electrolysis is performed (Carmo, Fritz, Mergel & Stolten, 2013). Hashemi, Modestino & Psaltis (2015) have shown that by controlling the trajectory of the generated bubbles one can remove the solid membrane, which decreases the ohmic losses and provides more flexibility in the selection of the catalysts and a simplified cell design (Modestino, Rivas, Hashemi, Gardeniers & Psaltis, 2016). In the absence of surfactants and van der Waals forces, the steady state velocity of such a bubble is solely dictated by the force and torque-free conditions. The velocity of small undeformable bubbles can be easily obtained once their location in the cross-section of the channel is known. For example, when the small bubble is close to the center of the channel, its velocity will approximatively be the centerline velocity. However, when the bubble occupies the majority of the channel cross-section, the determination of its velocity is a more complex problem, similar to the one of confined bubbles discussed in Sec. 10.2.

In the following, we show that the position of a bubble in the cross-section of the channel

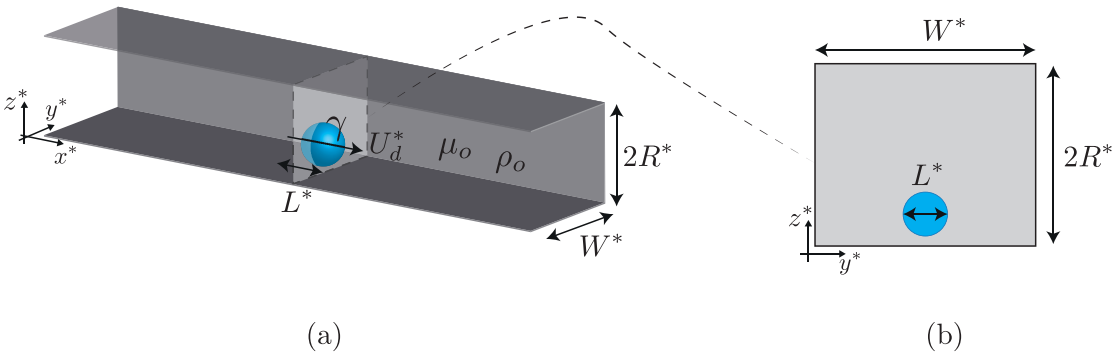

Figure 10.3 – Bubble of characteristic size L^* flowing in a rectangular microchannel of width W^* and height $2R^*$. (a) Three-dimensional view of the problem and (b) cross-section of channel occupied by the bubble.

can be modified by varying the capillary number of the flow, $Ca = \mu_o U_c^* / \gamma$, where U_c^* is the centerline velocity, the Reynolds number $Re = \rho_o U_c^* L^* / (2\mu_o)$, the size of the bubble L^* as well as the aspect ratio of the channel $W^*/2R^*$. Several theoretical (Ho & Leal, 1974), experimental (Di Carlo, Irimia, Tompkins & Toner, 2007; Di Carlo, Edd, Humphry, Stone & Toner, 2009) and numerical (Chen, Xue, Zhang, Hu, Jiang & Sun, 2014) works have been focused on the crossflow positioning of rigid particles since the seminal work of Segré (1961) and Segré & Silberberg (1962); see Amini, Lee & Di Carlo (2014) for a review. However, the deformability of the bubble considered in the present work allows for new interesting dynamics. Similar effects have been recently found for the dynamics of deformable capsules in square microchannels (Schaaf & Stark, 2017).

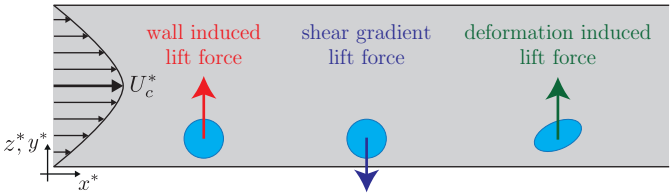

Figure 10.4 – Forces acting on the bubble in the presence of inertia: a wall-induced lift directing towards the centerline which diminishes as the bubble moves away from the wall, a shear-gradient lift that pushes the bubble towards the wall, and a deformation-induced lift pointing towards the centerline which becomes stronger as the bubble deformation increases.

At moderate Reynolds number, typically $1 < Re < 100$, the equilibrium position of the bubble is given by the balance of the wall-induced lift force, the shear gradient lift force and the deformation-induced lift force (see Fig. 10.4). Note that in the case of $Re = 0$, symmetry arguments based on the form of the linear Stokes equations preclude any cross-stream migration (Leal, 1980; Di Carlo et al., 2009). The wall-induced lift force originates from the asymmetry in the flow field around the bubble due to the presence of the wall (Zhang, Yan, Yuan, Alici, Nguyen, Warkiani & Li, 2016). Cox & Hsu (1977), Vasseur & Cox (1977) and Kennedy, Pozrikidis & Skalak (1994) have shown that a particle moving parallel to a wall experiences a force away

from it, which decreases with increasing distance from the wall. On the other hand, the shear-gradient lift force induced by the curvature of the velocity profile acts toward the wall (Vasseur & Cox, 1976; McLaughlin, 1991; Zhang et al., 2016). In addition to these two forces, which are also present for rigid particles, the deformability of the bubble interface induces a lift force acting towards the center of the channel (Chan & Leal, 1979; Mortazavi & Tryggvason, 2000; Zhang et al., 2016). Stan, Guglielmini, Ellerbee, Caviezel, Stone & Whitesides (2011) and Stan, Ellerbee, Guglielmini, Stone & Whitesides (2013) found that the analytical predictions of the deformation and inertial induced lift forces, derived for very small bubbles, do not provide a satisfactory quantitative prediction of these forces on bubbles of larger size, which are found to be enhanced due to the proximity of the bubble interface to the walls.

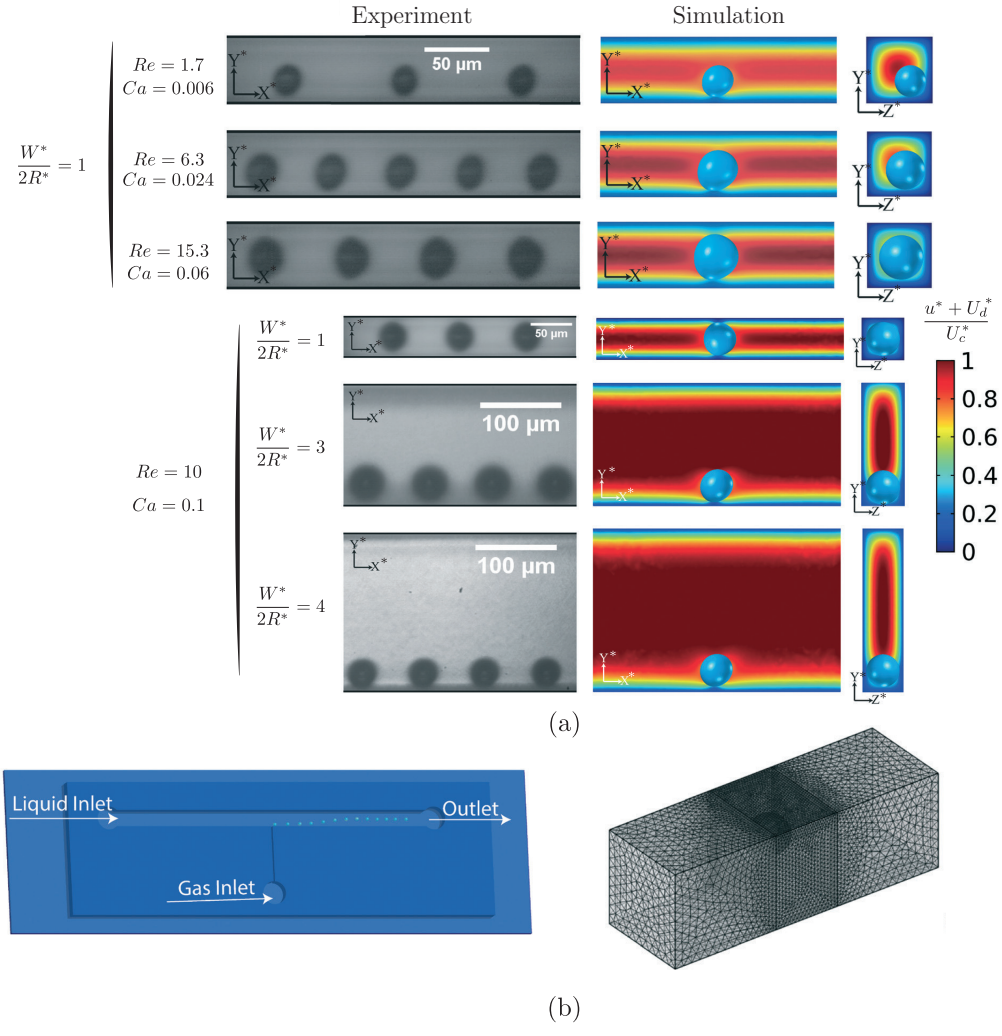

Figure 10.5 – Comparison between experimental and numerical results for both square and rectangular channel geometries (a). A sketch of the experimental channel and the computational mesh are also shown (b).

Recently, Rivero-Rodriguez & Scheid (2018) performed a complete analysis of the equilibrium

positions of a train of bubbles in a circular channel by developing an asymptotic expansion for small Reynolds or/and small capillary numbers, together with nonlinear numerical simulations. They considered the effect of stress-free, rigid and deformable bubbles, as well as the effect of body forces and the size of the bubble on the equilibrium position. The bubble deformability was shown to promote equilibrium positions at the channel's center, whereas inertial effects shift the equilibrium position closer to the wall. The latter effect is enhanced when the bubble is assumed undeformable but stress free.

Here we investigate the equilibrium positions of a bubble flowing in a polygonal capillary by performing numerical simulations using the numerical framework of Chapter 9 extended to the third dimension as well as by performing experiments. The considered range of Reynolds and capillary number is $1 < Re < 40$ and $0.1 < Ca < 1$. Throughout this work, we found that the numerical results obtained by the arbitrary Lagrangian-Eulerian (ALE) technique are in very good agreement with the experimental results, evidencing the strength of the computational approach (see for example Fig. 10.5). A summary of the different equilibrium positions that we have found is sketched in Fig. 10.6, where the results for both square and rectangular channels are illustrated together [1].

Let us assume first that the channel is square, $2R^* = W^* = S^*$. If inertial effects are negligible, or if the deformability of the bubble is important, or if the bubble is very large, the bubble moves to the channel's center due to the absence of inertia-driven lateral migration or due to deformation-induced lift forces (see green arrow and position 1 in Fig. 10.6). However, when the Reynolds number is increased, the equilibrium position of bubbles shifts toward the walls of the channel (see red arrow and positions 3, 4 and 5 in Fig. 10.6). This is known to be also the case for stress-free undeformable and rigid particles (Zhang et al., 2016), see position 2 in Fig. 10.6. Such an inertial migration results from the increased difference in the relative velocity at the two sides of the bubble/particle when the Reynolds number increases, which yields a stronger shear gradient lift force. Note that deformable bubbles differ from solid particles as the result of both the free-shear condition at the interface and their deformability. As a result, despite inertial effects shift both objects towards the wall, their respective equilibrium positions might differ in a polygonal channel, where there is no polar symmetry. The equilibrium position of solid particles is known to be close to the center of the longest side (position 2 in Fig. 10.6), see Zhou & Papautsky (2013) for instance.

We have found that large bubbles, typically larger than half of the channel width, have an equilibrium position which is along the channel's diagonal (position 4 in Fig. 10.6). In fact, the shear experienced along the diagonals is the smallest. However, when the size of a bubble decreases, typically below half the channel width, their deformability becomes less relevant and these bubbles start behaving like rigid particles, reason why their equilibrium position is between the diagonal and center of the side (position 5 in Fig. 10.6). On the one hand, the deformation-induced lift force pushes the bubble towards the diagonal line where the shear

[1] Note that one could combine inertial and capillary forces through the Ohnesorge number, but here we prefer to keep Re and Ca effects separate for the sake of clarity.

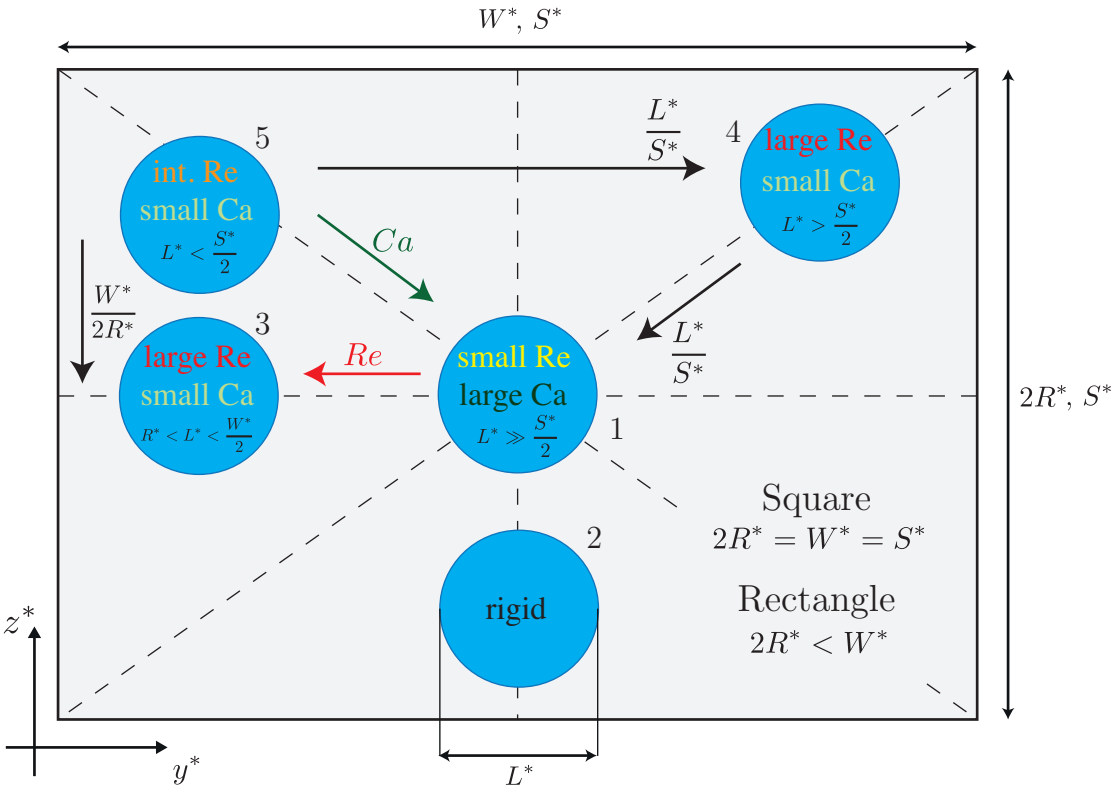

Figure 10.6 – Different kind of possible bubble equilibrium positions: centerline of the channel (1), close to the wide side (2), close to the narrow side (3), on the diagonal (4) and between the diagonal and the narrow side (5). Arrows indicate the effect of an increase in the specified quantity, when keeping the others fixed; square channel $2R^* = W^* = S^*$ and rectangular channel $2R^* \leq W^*$; $L^* < 2R^*$.

stress is smaller, but on the other hand, such a small bubble moves towards the center of the sidewall similar to a small solid particle (Prohm & Stark, 2014). Therefore, as the diameter of the bubble decreases, the deformability of the bubble decreases and the equilibrium position of the bubble moves closer to the center of the sidewall.

In the case of a rectangular channel, if the half length of the shortest side is smaller than the bubble diameter, the latter will tend to an equilibrium position corresponding to the shortest side (position 3 in Fig. 10.6 and Fig. 10.5). In fact, in a channel with $W^* > 2R^*$, the bubble diameter L^* can be larger than half of the height in the z^* direction, R^*, and smaller than half of the width in the y^* direction, $W^*/2$. Therefore, the bubble moves towards the center in the z^* direction and towards the wall in the y^* direction. An equivalent reasoning can be done if $W^*/2 < L^* < R^*$. Strikingly, this is in stark contrast to the equilibrium of solid particles, which is along the longest channel's side (position 2 in Fig. 10.6). We verified that this difference in equilibrium positions is intrinsically related to the stress-free or rigid boundary condition at the interface by performing the same experiment with a solid particle as well as by adding surfactants to the flow. In both latter cases, the bubble moves to the wider side of the channel.

For more details we refer the reader to Hadikhani et al. (2018).

10.4 Conclusions and perspectives

In this chapter we have considered both confined and unconfined bubbles and droplets in polygonal capillaries. We have seen that confined droplets not only present a thin-film region separating their interface from the channel sidewalls, like the thin-film region separating the pancake bubbles and droplets investigated in Chapter 8, but they give also rise to gutters in the channel's corners. The flow in the gutters drastically modifies the dynamics of these bubbles or droplets, resulting in nonmonotonic dependencies on the capillary number, on the viscosity ratio between the inner and the outer phases and on their length.

When the length of the bubble is smaller than the shortest side of the channel, the bubble is no longer confined and both thin-film regions and gutters disappear. In the absence of inertia, the bubble remains at the center of the channel. However, as soon as inertia is no longer negligible, the bubble moves in the cross-section of the channel as a result of the wall-induced, shear-induced and deformation-induced lift forces. We have found that at high Reynolds numbers the flow pushes the bubble towards the wall, while a large capillary number or a large bubble size shifts the equilibrium position towards the center. Furthermore, if the aspect ratio of the channel is larger than unity, the bubble moves towards the narrow sidewall. This equilibrium position differs from the one of solid particles, whose equilibrium position is located close to the wider sidewall, as for bubbles contaminated by surfactants. Therefore, separating uncontaminated bubbles from contaminated bubbles or rigid particles can be done by employing a channel of large aspect ratio.

As a possible follow-up of this work, it would be interesting to investigate the effect of the interactions between the bubbles (see for instance Fig. 10.5). This can be readily done numerically by imposing periodic boundary conditions at the channel ends. Bubbles of different sizes flowing in the same microchannel should also be investigated. Their different velocities might give rise to very interesting dynamics. Furthermore, by considering the nonvanishing viscosity of the inner phase, one could generalize this study to droplets in rectangular microchannels. Such an extension is of practical relevance since most Lab-on-a-Chip applications deal with the motion of droplets of a viscous fluid in a microchannel. Being able to sort droplets depending on their size, viscosity ratio, velocity and deformability without any membrane or pattern on the channel walls would be very effective. In addition to these numerical and experimental studies, it would be very enlightening to perform a rigorous theoretical stability analysis to investigate the bifurcations yielding the different equilibrium positions, along the lines of Rivero-Rodriguez & Scheid (2018).

11 Conclusions and perspectives

Detailed conclusions can be found at the end of each chapter, reason why only general conclusions are drawn here, together with some opening perspectives.

The aim of **Part I** was the investigation of the substrate-curvature effect on both Rayleigh-Taylor and fingering instabilities of thin liquid films. A summary of the main results for the Rayleigh-Taylor instability is shown in Fig. 11.1. In **Chapter 3** we have found that when a finite quantity of fluid coats the underneath of a cylindrical or spherical substrate, the curvature of the latter induces a twofold stabilizing effect.

First, the component of gravity parallel to the substrate induces a flow from top to bottom which reduces the thickness of the film in the upper region and is responsible for the asymptotic stability of the system with respect to infinitesimal perturbations. We have shown that an initial growth of the perturbations at the upper pole is only possible if the modified Bond number $Bo = \rho g H_i^* R^* / \gamma$, prescribing the ratio between gravity and capillary forces, is larger than 12 for a cylindrical geometry and larger than 24 for a spherical geometry. Note that the Bond number is modified such that it contains both the effect of the initial film thickness H_i^* and the effect of the substrate curvature radius R^*. Therefore, large Bond numbers indicate large film thicknesses or large curvature radii. As discussed in **Chapter 5**, the two-times larger critical Bond number for a spherical geometry is due to the two-times faster drainage induced by the two-times larger mean curvature of a sphere compared to the one of a cylinder (see Fig. 11.1(a)).

Second, the spatially increasing gravity-induced drainage stretches the perturbations in the polar direction, enhancing their stabilization along this direction (see red terms in Table 11.1). In **Chapter 4** we have shown that the linearly most amplified pattern in a cylinder corresponds therefore to rivulets, perturbations with a wavevector aligned with the cylinder's axis, since they only experience the film thinning but not the stretching effect. When the Bond number is further increased, typically above a value of 100 for our experimental settings, the nonlinear effects start to matter before the linear growth selects the formation of rivulets. By numerically solving the two-dimensional nonlinear lubrication equation we have found that the most

amplified pattern at sufficiently large Bond numbers corresponds to a two-dimensional pattern of droplets, in agreement with the performed experiments. In a spherical geometry, rivulets cannot form due to the singularity of the geometry at the pole. We have found in **Chapter 5** that the most amplified azimuthal wavenumber is only selected by nonlinear effects. At low Bond numbers, yet larger than 24, the initially most amplified pattern corresponds to a single droplet close to the north pole, which eventually slides along the sides and generates other droplets through nonlinear interactions if the Bond number is sufficiently large. On the other hand, at high Bond numbers, several droplets directly form close to the pole (see Fig. 11.1(a)).

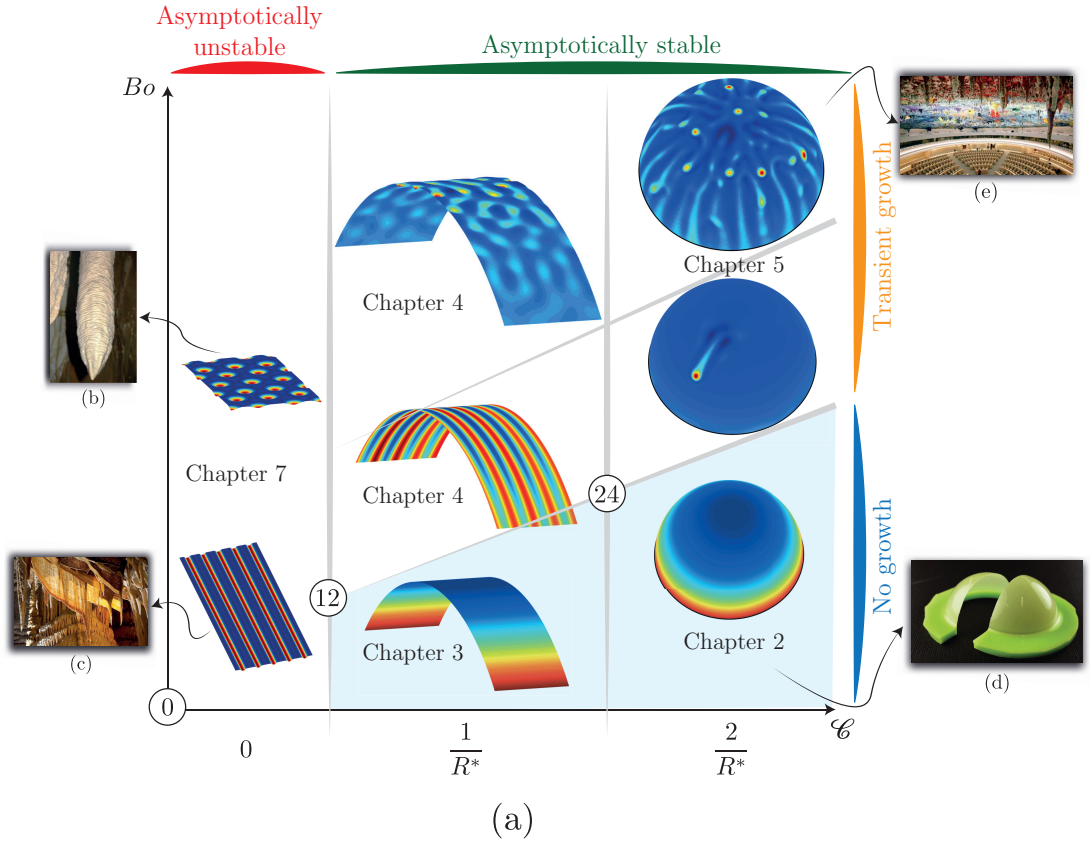

Figure 11.1 – The stabilizing effect of the substrate mean curvature $\mathscr{C}$ and the destabilizing effect of the Bond number $Bo = \rho g H_i^* R^* / \gamma$ on the Rayleigh-Taylor instability (a) and examples of applications (b-e): (b) stalactite forming under a roughly horizontal cave ceiling (taken from Camporeale (2015)), (c) drapery forming under an inclined cave ceiling (taken from http://www.geologyfortoday.com), (d) hemispherical elastic shell obtained by the gravity-driven coating of a sphere (Lee et al., 2016*a*) and (e) stalactites on the UN Room of *Human Rights and the Alliance of Civilisations* in Geneva created by the Spanish artist Miquel Barceló. The colorcode in panel (a) indicates the film thickness.

Hence, for both cylindrical and spherical geometries, one observes no growth of perturbations for Bond number smaller than a critical value and a two-dimensional pattern of droplets similar to the one observed for the planar substrate (Fermigier et al., 1992) for high Bond

numbers. The latter pattern can be rationalized by noting that when the Bond number is sufficiently large, the substrate close to the pole can be considered again as locally quasi-planar on the length scale of the most amplified Rayleigh-Taylor instability wavelength.

For what concerns the fingering instability on a cylinder, we have shown in **Chapter 6** that the most amplified spanwise wavenumber of the fluid's initial perturbations is related to the length of the base-flow capillary ridge and depends therefore on the polar location. Small spanwise wavelengths dominate at short times, when the liquid is localized close to the uppermost cylinder generatrix, but they require a large disturbance amplitude to appear. On the other hand, large fingering wavelengths arise when the liquid front reaches larger angles. In this case the transient growth is much stronger and might trigger the fingers' formation also when disturbances of small amplitude are initially present. The larger the local substrate inclination, the stronger the advection and thus the sharper the capillary ridge, which results in a larger growth of the fingering instability. Hence, in contrast to what we have found for the Rayleigh-Taylor instability, the substrate curvature has a destabilizing effect on the fingering instability. Furthermore, we have found that a general optimal-substrate-topography perturbation promoting the fingers' formation exists and corresponds to the most time-independent perturbation.

When the Bond number is sufficiently small, *i.e.* the film thickness or the curvature radius are sufficiently small, or when the capillary ridge is absent, the thin-film flow on the inside or on the outside of a spherical substrate, respectively, can be employed to produce thin-shell structures of nearly uniform thickness upon the cross-linking of the polymer solution (see Fig. 11.1(d)). For the sake of completeness, it has to be mentioned that if one pours some liquid onto a dry substrate, a capillary ridge will always form, but, if the film thickness is sufficiently large, surface tension effects are negligible and the advancing front is stable so that no fingers form (Ancey et al., 2009). When both Rayleigh-Taylor and fingering instabilities are absent, the thin-film flow is stable and the dynamics on the interior or on the exterior of the substrate are identical. Combining the base-state drainage dynamics with the rheology of the considered polymer solution one can predict the precise final shell profile. As we have demonstrated in **Chapters 2** and **6**, these stable draining flows possess the salutary feature of forgetting the initial condition after a time proportional to the drainage time. As a result, the proposed fabrication technique is very robust if the curing time τ_c is much larger than the drainage time. The final shell thickness depends only on the mold-curvature radius and on the physical properties through the relation $H_f^* \sim \sqrt{\mu_0 R^*/(\rho g \tau_c)}$. Despite the fact that in **Chapter 2** we focused on the spherical geometry, the same fabrication technique can be directly employed for cylindrical substrates, yet with the stronger restriction of a smaller Bond number if the polymer solution is poured inside a cylinder. Other curved substrates could also be employed; the larger the mean curvature, the more stable the flow underneath the substrate, but the more unstable the flow on the outside. *Strongly curved shells should be fabricated by coating the inside of the mold, whereas weakly curved shells should be fabricated by coating the outside of the mold.* This fabrication process is analogous to spin-coating, albeit with gravity forces in lieu of centrifugal forces. In contrast to other manufacturing techniques,

the proposed process is versatile and inexpensive, which makes it suitable for fast prototyping.

In **Part II** we have seen that some karst formations encountered in limestone caves are directly related to the hydrodynamic instabilities of thin-film flows. We have found that both the linear deposition process of calcium carbonate on the substrate and the nonlinear hydrodynamic effects promote the formation of rivulets under a strongly inclined substrate, similar to the ones observed for the cylindrical substrate (see Fig. 11.1(a)). However, due to the constant liquid flux imposed, these patterns persist over time and it is very likely that they are related to the origin of draperies, as shown in Fig. 11.1(c). On the other hand, when the substrate is close to the horizontal, stalactites would be initiated as a result of the two-dimensional pattern of dripping droplets (see Fig. 11.1(a,b)). This is also the case when the substrate is curved as seen in **Part I**, but with a very large curvature radius so that the Rayleigh-Taylor instability results in the formation of isolated dripping droplets (see Fig. 11.1(e)). In view of the large time-scale separation between the deposition process and the hydrodynamic instability, it can be assumed that the initial pattern formation is solely dictated by the fluid-flow instability and the substrate growth is then only proportional to the film thickness. At the end of **Chapter 7** we have shown that the dependence of the most amplified rivulet wavelength on the inclination angle is responsible for the formation of flutings and nonequidistant draperies on curved/inclined cave walls. By performing a spatio-temporal analysis we have also shown that the flow under a concave curved substrate is indeed absolutely unstable where the substrate is locally almost horizontal, rationalizing the success of the analyses of **Chapters 3, 4** and **5**, focused on the uppermost region close to the cylinder's or sphere's pole. As it is known for spatially developing flows, the absolutely unstable region at the inlet of the domain, here the pole, where the draining velocity is zero, selects the global stability properties of the system (Chomaz, 2005). On the other hand, when the substrate at the inlet is closer to the verticality, as for a convex substrate, the thin film is initially convectively unstable. In this case, the flow amplifies inlet perturbations, but it does not display an intrinsic wavelength selection.

In **Part III** the focus was laid on the stable thin-film patterns arising in microchannels of different geometries. In **Chapter 8** we have generalized the one- and two-dimensional thin-film patterns induced by advancing and receding menisci – typically observed for bubbles in channels or in Hele-Shaw cells – to liquid bridges moving on parallel prewetted plates. In these cases the film thickness nonuniformity does not result from an instability, but from the solution of the linear lubrication equation to specific boundary conditions. We have shown that regions of very small film thicknesses arise at the lateral parts of the two-dimensional menisci, which have two nonzero principal curvatures. These patterns can be seen as the two-dimensional generalization of the oscillations close to the advancing meniscus observed in the one-dimensional configuration. Catamaran-like patterns arise for pancake bubbles in Hele-Shaw cells, whereas valleys of reduced film thickness are left by the sides of the moving liquid bridges. The nonlinear lubrication results are in good agreement with the ones obtained by solving the Stokes equations. As for the thin-film flows discussed in the two previous parts of this thesis, the patterns induced by the motion of bubbles and liquid bridges in microchannels might impact the final application. For example, if ones would like to use confined bubbles to

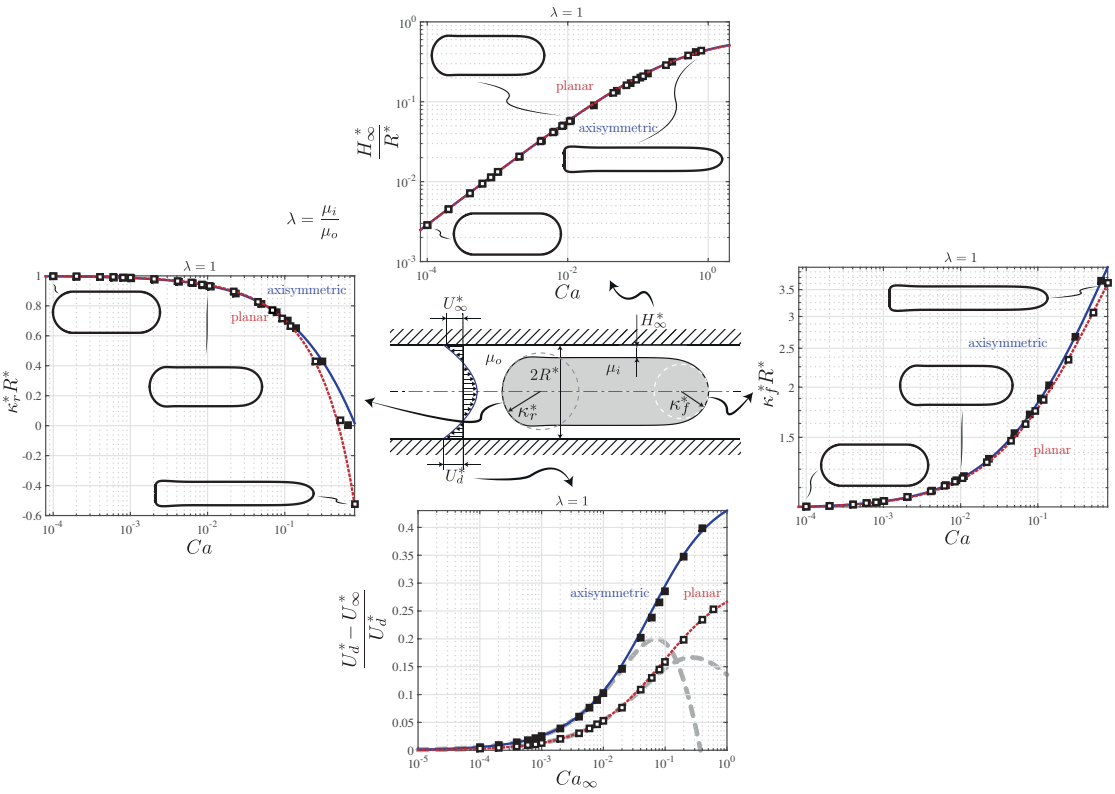

Figure 11.2 – Summary of the capillary-number dependences of some relevant quantities for an isoviscosity confined droplet in a planar or axisymmetric channel. H^*_∞ is the uniform film thickness, $\kappa^*_{f,r}$ is the front/rear static cap curvatures and $(U^*_d - U^*_\infty)/U^*_d$ is the relative droplet velocity with respect to the outer fluid average velocity. See Chapter 9 for more details.

remove impurities from the channel walls, or to remove heat from a microchip, the result will not be uniform in space. Similarly, if drops move on thin-coating films, they will leave a trace of their motion (see Fig. 11.3).

Bretherton's theory for confined Taylor bubbles at low capillary numbers in circular channels has been extended to droplets of nonvanishing inner viscosities and to large capillary numbers in **Chapter 9**, where asymptotic results of the lubrication equation are combined with moving mesh numerical simulations (see Fig. 11.2). The film thickness, which is rather unaffected by the viscosity of the inner phase when the latter is smaller than the one of the outer phase, is found to directly determinate the droplet velocity. The proposed empirical models for relevant quantities as the front/rear static curvatures and the total pressure drop induced by a droplet are of practical relevance for the accurate design of circular-microchannels circuits. We have shown that including viscous effects is crucial for capillary numbers larger than $Ca > 10^{-3}$.

Finally, we considered confined and unconfined bubbles in polygonal capillaries in **Chapter 10**. In contrary to confined bubbles in round capillaries, regions of thicker films arise in the corners of polygonal capillaries, which significantly affect the bubble velocity. As soon as

the bubble is no longer confined by the channel walls, its equilibrium position is found to depend on the bubble deformability, on its size compared to the channel dimensions and on the aspect ratio of the channel when inertial effects are considered. At large capillary numbers or small Reynolds numbers the bubble remains at the center of the channel, but when the Reynolds number is increased the bubble moves away from the channel's center. The equilibrium position is along the channel's diagonal when the bubble characteristic diameter overcomes the half-channel-side length; otherwise the bubble position is off the diagonal. Interestingly, we have found that for rectangular channels with one side whose half length is smaller than the bubble diameter, the latter moves close to the shortest side. This is in contrast to what is known for solid or rigid particles, which always move close to the longer side of a rectangular channel when inertial effects matter. The different equilibrium positions depending on the flow parameters can be employed for bubbles and particles sorting, as well as for the indirect measurement of the rheological properties of the liquids.

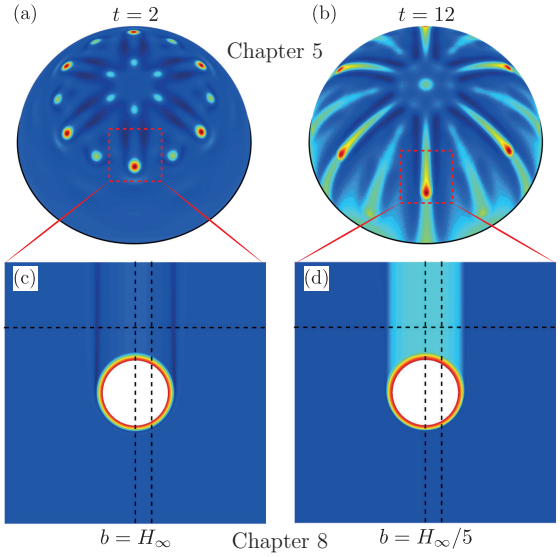

Figure 11.3 – Thin-film patterns induced by sliding drops (a,b) and by moving liquid bridges on prewetted plates (c,d). (a,b) $Bo = 150$, $m_0 = 6$, $\varepsilon = 10^{-2}$; (c,d) $Ca = 10^{-3}$. The time of the snapshots are indicated in panels (a,b) whereas the precursor film thickness is specified in panels (c,d).

All along this thesis we encountered moving menisci where a thicker fluid region advances on a thinner film. Despite the fact that the forces at play and the origin of the motion might differ, the thin-film patterns induced by these moving menisci are extremely similar. We have shown in **Chapter 8** that such patterns are very general and they also arise when the thin film flows over a localized substrate-topography perturbation. It has to be mentioned that these patterns are directly related to the Green's function of the underlying lubrication equations.

In Fig. 11.3 we illustrate the similarity in the film-thickness profile obtained by a Rayleigh-Taylor-induced droplet sliding under a spherical substrate and by the motion of a liquid bridge between two prewetted plates. For the flow under a spherical substrate, when the

thickness of the surrounding film is still large at short times, the sliding-drop motion induces thin-film valleys at its sides (see Fig. 11.3(a)), in exactly the same way as a liquid bridge does when moving on a precursor film of thickness comparable to the one left behind by the receding meniscus (see Fig. 11.3(c)). Furthermore, one can observe that in both cases the film thickness presents an oscillation just ahead of the sliding drop, or liquid bridge, induced by the advancing meniscus at the front. On the other hand, a drop sliding on the thinner film under the sphere at later times leaves a thicker film region in its wake (see Fig. 11.3(b)), as a liquid bridge does when it moves on a precursor film whose thickness is smaller than the one left by the receding meniscus at this capillary number. We have found that the thickness of the precursor film on which droplets slide strongly affects their velocity, which we modelled using the shock speed theory in **Chapter 5** .

In this thesis we did not only encountered two-dimensional moving menisci as the ones described in Fig. 11.3, but we have also often observed one-dimensional moving menisci. Some examples of advancing menisci are shown in Fig. 11.4. An oscillating film-thickness pattern induced by the advancing meniscus arises for example in the problem of a prewetted plate plunged into a liquid bath (see Fig. 11.4(a)), at the front of a liquid bridge moving between two prewetted plates or at the front of a sliding drop as seen in Fig. 11.3 and Fig. 11.4(c), at the rear of a Taylor bubble moving in a channel (see Fig. 11.4(b)), in the region where the thin draining flow in a cylinder or sphere enters the liquid pool at its bottom (see Fig. 11.4(c)) and at the front of a capillary ridge advancing on a precursor film (see Fig. 11.4(d)). *It is interesting to note that the stable thin-film drainage in a cylindrical or a spherical substrate can be also seen as the rising motion of a bubble in a cylinder or a sphere.* Therefore, oscillations at this 'rear meniscus' are naturally expected (Bretherton, 1961). The film thickness at the receding menisci, *e.g.* at the 'front meniscus' of a Taylor bubble, that also arise in the aforementioned configurations varies, on the other hand, monotonically. Furthermore, it has to be mentioned that the velocity profile in the thin film can be either a portion of a Poiseuille profile or a plug profile depending on the forces at play and on the viscosity of the outer fluid, but this is found not to play a major role in the formation of these oscillating or monotonic thin-film patterns.

Many of the thin-film patterns encountered throughout this thesis are anisotropic. Some examples are shown in Fig. 11.5. The rivulets of **Chapters 4** and **7**, the fingers of **Chapter 6** and the catamarans or valleys of **Chapter 8** all present structures aligned with the direction of the flow.

The formation of these patterns can be rationalized by considering the lubrication equation whose main 'ingredients' have been described in the introductory **Chapter 1**. For the sake of clarity, we report the nonlinear and the linear lubrication equations used for the different parts of this thesis in Table 11.1. It is remarkable to note that the governing equations for all the considered problems present an isotropic and an anisotropic part. The isotropic part is composed by the capillary pressure gradient and by the variation of the hydrostatic pressure distribution, if present, whereas the anisotropic part solely results from the advection term. *Strikingly, the advection term in the lubrication equation is responsible for the selection of*

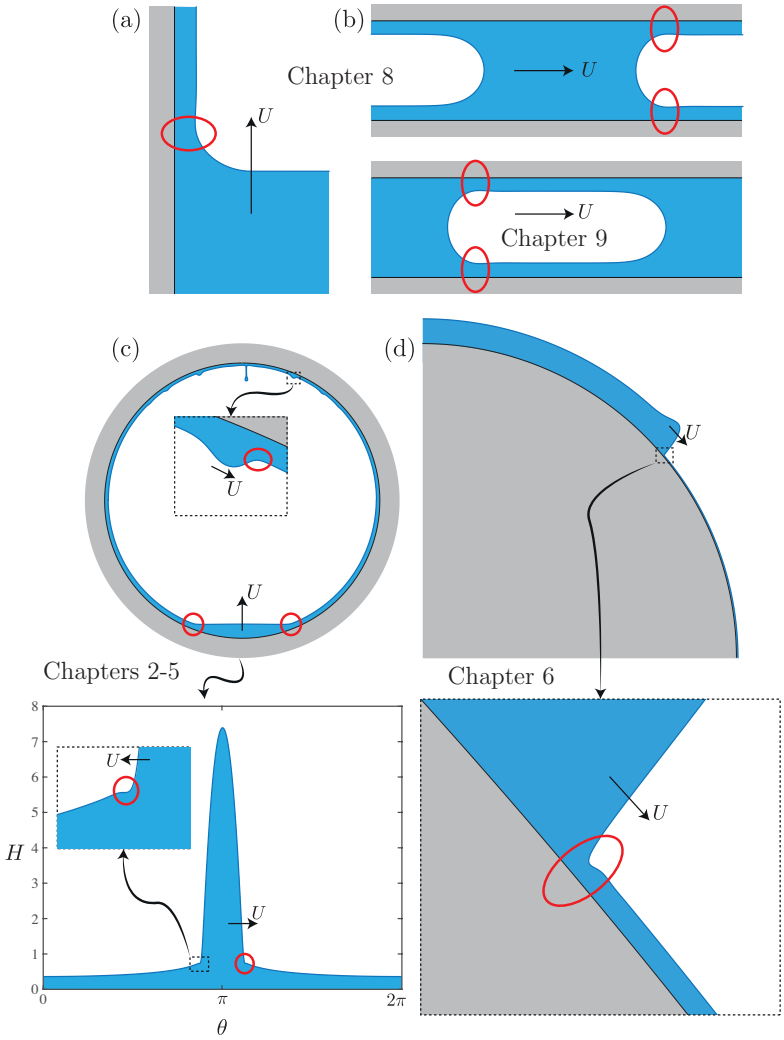

Figure 11.4 – Thin-film patterns induced by advancing menisci: (a) prewetted plate plunged into a liquid bath, (b) Taylor bubble and liquid bridge in a channel, (c) thin-film flow in a cylinder or sphere and (d) capillary-ridge motion on a curved prewetted substrate. U denotes the relative motion of the meniscus with respect to the thin film; the oscillation in the film thickness is highlighted by a red circle.

the anisotropic patterns aligned with the flow. For the thin-film flow on a curved substrate discussed in **Part I**, whose lubrication equation at the pole can be written in a general form using the operators in the proper coordinate system, the advection term depends linearly on the distance from the pole due to the increasing inclination (see red terms in Table 11.1). We have found that the increasing advection for the curved geometry of **Part I** is responsible for a *linear* selection of the rivulets pattern. Waves are further stabilized by the wavenumber-stretching mechanism. On the other hand, for the flow under an inclined plane considered in **Part II**, the advection term resulting from the gravity component parallel to the substrate is constant due to the constant inclination angle ϕ (see orange terms in Table 11.1). Hence, the

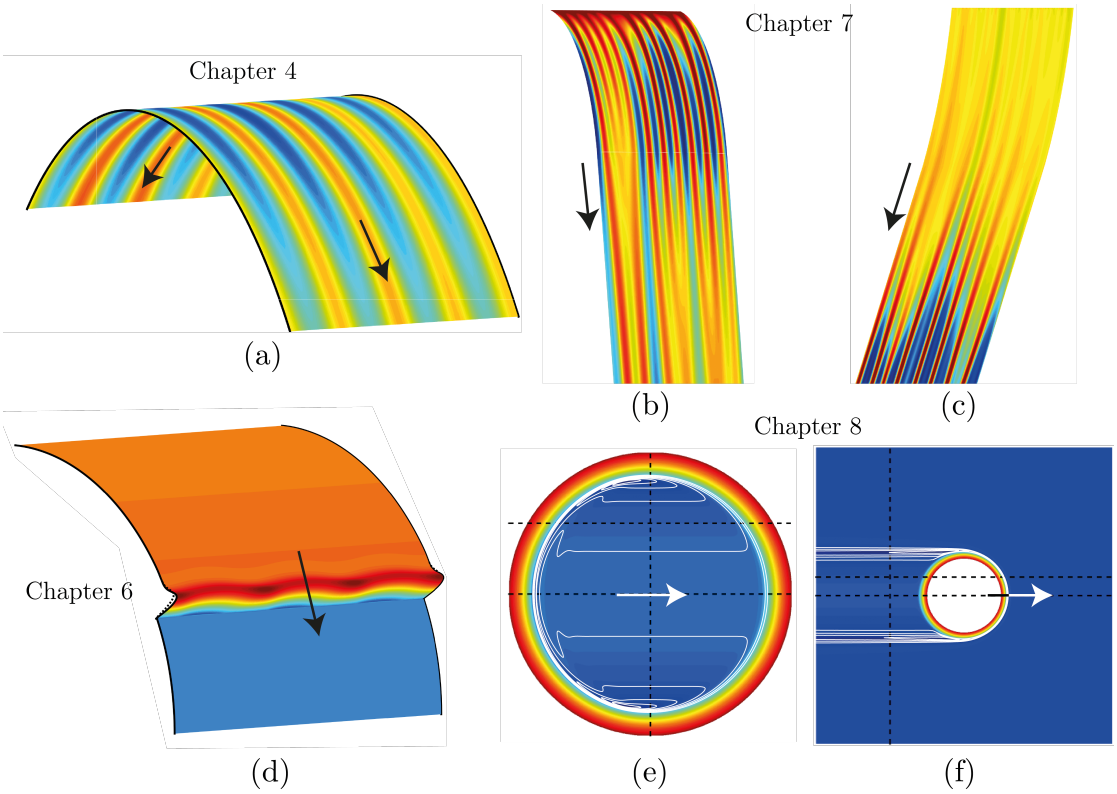

Figure 11.5 – Examples of anisotropic thin-film patterns discussed in this thesis: (a,b,c) rivulets under a cylindrical and inclined substrates induced by the Rayleigh-Taylor instability, (d) spanwise perturbations of a capillary ridge flowing on a cylinder eventually resulting in the formation of fingers, (e) film-thickness profile between a pancake bubble and the Hele-Shaw walls and (f) film-thickness profile around a moving liquid bridge between two prewetted plates. The direction of motion is indicated by an arrow.

rivulets pattern in **Part II** is solely selected by *nonlinear* effects. Waves are further stabilized by the additional capillary flow due to the advection-induced steepening mechanism.

The only difference between the lubrication equations employed in **Parts I** and **II** and the classical lubrication equation for the thin-film dynamics under a horizontal planar substrate is the advection term, which is key in breaking the symmetry of the problem and promotes the formation of rivulets. Fermigier et al. (1992) have shown that for a thin film under a horizontal planar substrate there is no linear selection of a specific pattern, which only results from nonlinear interactions. Although this is also true for the flow under an inclined plane, the patterns for the horizontal and inclined plane differ due to the advection term.

Note that, for the fingering instability, the increasing advection due to the variation of the local inclination enhances the capillary ridge in the base-flow profile, which is invariant in the spanwise direction, and promotes therefore the formation of fingers.

For the thin films investigated in **Part III**, if one neglects the possible gravitational term, the

Geometry	Nonlinear	Linear
Part I – curved	$\bar{H}_t + \nabla\cdot\left[\frac{\bar{H}^3}{3}\nabla\left(\frac{\bar{\kappa}}{Bo} \pm \bar{H} + \frac{x^2}{2}\right)\right] = 0$	$h_t + \frac{H^3}{3}\left(\frac{\Delta^2 h}{Bo} \pm \nabla^2 h\right) + H^2\,(x h_x + h) = 0$
Part II – inclined	$\bar{H}_t + \nabla\cdot\left[\frac{\bar{H}^3}{3}\nabla\left(\bar{\kappa} + \bar{H} + x\tilde{\ell}_c\cot\phi\right)\right] = 0$	$h_t + \frac{H^3}{3}\left(\Delta^2 h + \nabla^2 h\right) + H^2 h_x \tilde{\ell}_c \cot\phi = 0$
Part III – meniscus	$\nabla\cdot\left[\frac{\bar{H}^3}{3}\frac{\nabla\bar{\kappa}}{Ca} - \bar{H}\mathbf{e}_x\right] = 0$	$\frac{H^3}{3}\frac{\Delta^2 h}{Ca} - h_x = 0$

Table 11.1 – Lubrication equations for the film thickness considered in the different parts of the thesis. Nonlinear equations for the total film thickness $\bar{H}$ and curvature $\bar{\kappa}$ and linear equations for the small perturbations h around the base state H, with $\bar{H} = H + \varepsilon h$ and $\varepsilon \ll 1$. Part I: dynamics of the thin film above ($-$ sign in the variation of the hydrostatic pressure) and below ($+$ sign in the variation of the hydrostatic pressure) a curved substrate close to the pole. For the cylindrical geometry, the gradient ∇, divergence $\nabla\cdot$, Laplacian ∇^2 and bi-Laplacian Δ^2 operators are expressed in a Cartesian coordinate system (x, y), whereas for the spherical geometry they are expressed in a polar coordinate system (x, ϕ), where x is now the radial coordinate. $Bo = \rho g H_i^* R^*/\gamma$ is the modified Bond number. Part II: the thin film flows under a planar substrate inclined with an angle ϕ with respect to the vertical. The operators are expressed in the Cartesian coordinate system (x, y). $\tilde{\ell}_c = \sqrt{\gamma/(\rho g \sin\phi)}/H_i^*$ is the dimensionless capillary length based on the gravity component normal to the substrate. Part III: steady lubrication equation for the thin film separating a bubble/droplet/liquid bridge from the channel walls or resulting from a dip coating process, in the reference frame moving with the meniscus (gravitational effects are here neglected for the sake of simplicity). The operators are expressed in the Cartesian coordinate system (x, y). $Ca = \mu_o U_d^*/\gamma$ is the capillary number. The anisotropic terms are highlighted in colors.

steady lubrication equation solely reduces to the capillary flux and to a flux proportional to the film thickness, which results from the reference frame moving with the bubble/droplet/liquid bridge or, more generally, with a meniscus. For these steady problems, the boundary conditions are crucial. Yet, even if one considers isotropic boundary conditions, the resulting thin-film pattern is anisotropic. In the same way as for the gravity-driven thin-film flows of the two previous parts, the advection term highlighted in blue in Table 11.1 is responsible for the selection of a pattern whose structures are aligned with the direction of motion. More precisely, this pattern is directly obtained by the *linear* solution of the lubrication equation.

In this thesis great importance was given to the linear mechanisms governing instabilities on curved substrates; nonlinear effects have been investigated only through numerical simulations and simplified theoretical models. Inspired by the work of Fermigier et al. (1992), we attempted to perform a weakly nonlinear analysis for the Rayleigh-Taylor instability under a curved substrate in order to investigate the most amplified two-dimensional pattern observed at large Bond numbers. Unfortunately, the transient nature of the flow and its space dependence made this approach very involved. Yet, we still believe that the formalism of amplitude equations could be of use in the study of the pattern selection in these thin-film flows. Such

an approach has, for instance, proven to be successful in the case of the Rayleigh-Bénard-Poiseuille instability, which shares quite some analogies with the flow down an inclined plane. Furthermore, theoretical linear and nonlinear two-dimensional spatio-temporal analyses could also shed light on the pattern formation in thin-film flows.

In the same way as we applied here nonmodal hydrodynamic stability concepts to thin-film flows, it would be very interesting to employ optimal control concepts, that are widely used for the control of open shear flow (Boujo, 2014), for the control of these interfacial flows. As we have mentioned at the end of **Chapter 6**, the optimal control could be for instance performed by modifying the substrate topography and would annihilate the formation of fingers or other instabilities. With the increased number of applications where these thin-film flows are crucial, we believe that there is a large potential in the use of classic hydrodynamic concepts that have been proven to be successful in the past years in the context of flows at high Reynolds numbers to these low-Reynolds-number interfacial flows.

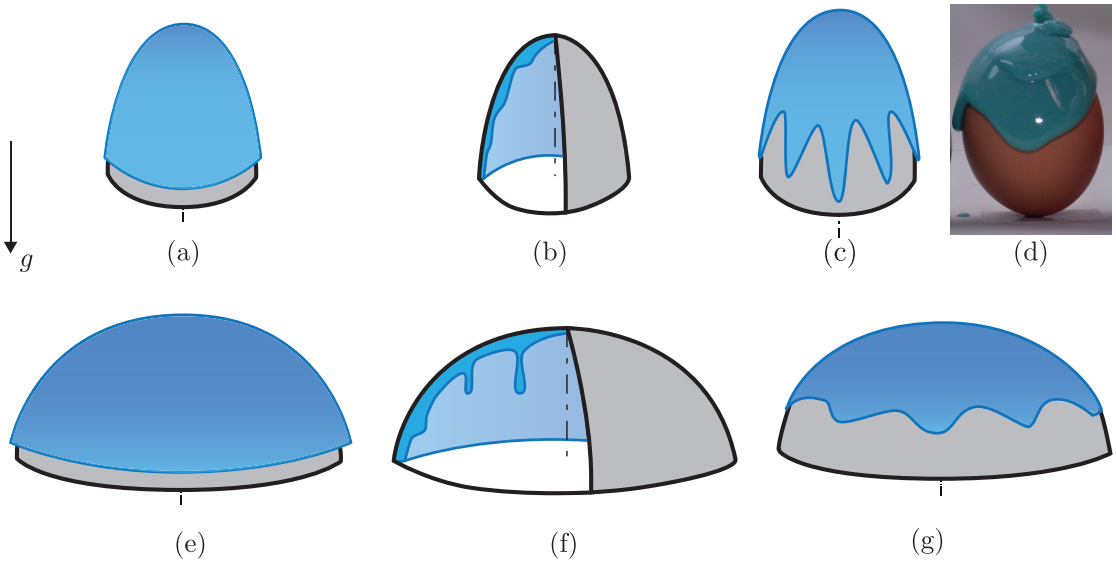

Figure 11.6 – Possible thin-film patterns on ellipsoids with (a-d) the major axis longer than the minor axis and (e-g) the major axis shorter than the minor axis. The major axis is always aligned with gravity.

In order to complete the picture of the different instabilities investigated during this thesis, the fingering instability on a spherical substrate should be considered, thereby providing a detailed theoretical interpretation of the results of Takagi & Huppert (2010). As we have seen for the Rayleigh-Taylor instability, the spherical geometry imposes further constraints on the pattern selection. The same could be done also for the fingering instability driven by centrifugal forces in spin-coating devices (see Melo et al. (1989) and Fraysse & Homsy (1994) for the experimental investigations), where the flow is also transient and space dependent.

As a follow-up question to these studies, it would be natural to investigate the stable and

unstable thin-film flow inside and outside of an ellipsoidal substrate with different principal semi-axes lengths (see Fig. 11.6). This flow configuration could be employed to fabricate ellipsoidal shells in order to study their buckling behavior (Ebrahimi et al., 2014). The major axis can be aligned with the direction of gravity or orthogonal to it, and it can be longer or shorter than the minor axis. We speculate that when the major axis is aligned with the direction of gravity and it is longer than the minor axis, the film-thickness variations should be larger due to the increased drainage, whereas a more uniform film is expected when the major axis is shorter than the minor axis. Furthermore, it is likely that the local film thickness also depends on the local mean curvature of the substrate, which we have seen to play a role in the film-thickness selection for a spherical substrate. Depending on the ratio between major an minor axes, as well as on the direction of the major axis compared to gravity, the ellipsoidal substrate might further stabilize/enhance the Rayleigh-Taylor/fingering instability if the substrate curvature increases in the direction of the flow (see Fig. 11.6 for possible scenarios).

In the same spirit, it would be of significant practical relevance to consider the inverse-engineering problem of designing particular substrate geometries in order to obtain the desired thin-film profile, as, for instance, a profile of perfectly uniform thickness or a profile presenting a controlled defect.

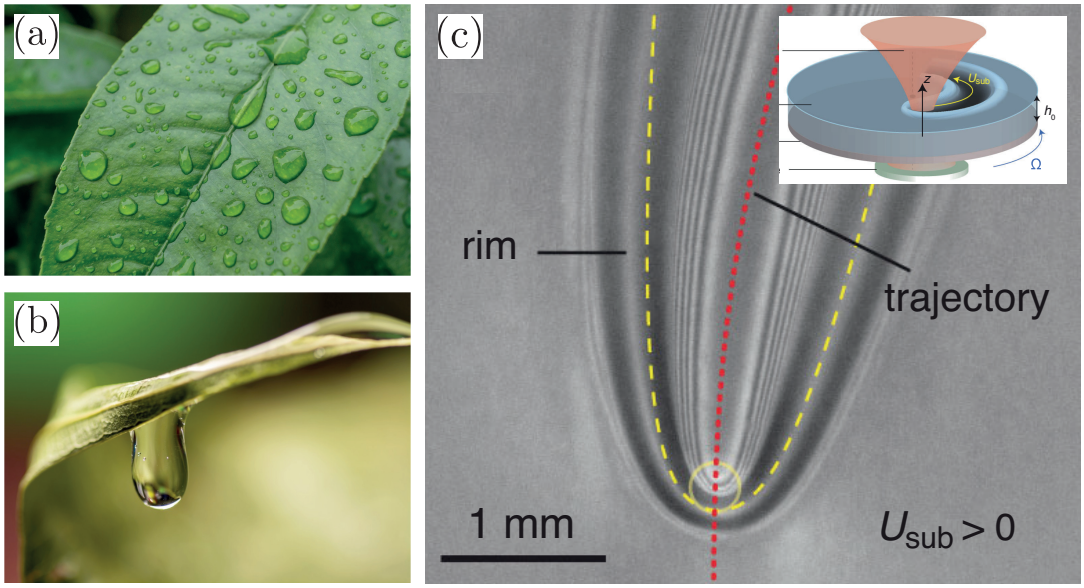

Figure 11.7 – Thin-film flow on a leaf (a) and under a leaf (b); images taken from (a) https://www.maxpixel.net and (b) https://pxhere.com. (c) Infrared-laser-induced thermo-capillary deformation and destabilization of thin liquid films on moving substrates (taken from Wedershoven et al. (2015)); note the very strong similarity with the pattern induced by a moving liquid bridge of Fig. 11.3.

With the knowledge gained through all the stability analyses of the thin-film flows over these simple geometric primitives, which can all be treated by a lubrication equation written in a

cylindrical, spherical or ellipsoidal coordinate systems, one could consider more complex geometries, where the lubrication equation has to be written in a two-dimensional curvilinear coordinate system. This would allow one to address more involved problems, as the long-time morphogenesis of karst formations like the secondary instability of draperies that we have mentioned in **Chapter 7**, or the flow of rain water on a leaf (Mayo, McCue, Moroney, Forster, Kempthorne, Belward & Turner, 2015), as shown in Fig. 11.7(a,b). Nature abounds with examples of thin-film flows on complex geometries and their study might be beneficial for the society. For example, studying how raindrops are ejected from leaves is crucial for the study of how pathogens spread in nature (Gilet & Bourouiba, 2014).

In addition to that, considering other boundary conditions at both the solid and the liquid surfaces would open the door to many more applications of thin-film flows. One could investigate evaporation processes, surface-stress flows induced by thermal gradients, surface-tension gradients or external flows, flows on hydrophobic patterned surfaces, etc. It has been shown that thin films can be controlled by applying light or, more in general, electrical and magnetic fields (Darhuber & Troian, 2005; Muller, Wedershoven & Darhuber, 2017), see also Fig. 11.7(c). The different boundary conditions will affect the flow dynamics and its stability. The desired thin-film profile could therefore also be achieved by imposing particular boundary conditions for the flow on a substrate. As an example, one could think of using slip boundary conditions on the substrate or outer pressure gradients in order to influence the film-thickness profile. We believe in the strong potential of collaborations with material scientists for the development of new processes where thin films play a crucial role. For instance, how a film dries might impact the final result of soft-lithography processes and one has to consider the strong capillary effects at these scales.

For what concerns the microfluidic applications of thin films, the next crucial step would be the modeling of the velocity of confined droplets and bubbles in polygonal capillaries. Numerical simulations should shed light on the shape of the dynamic and static menisci at large capillary numbers. In a similar way to what we did in **Chapter 9** for droplets in round capillaries, one could then develop a model for the pressure drop induced by the curved menisci. For the pancake bubbles or droplets in Hele-Shaw cells, one should also consider the force induced by the flow around the pancake and the one induced by the motion of the latter in the channel. Note that at large capillary numbers the pancake is no longer circular and the in-plane curvature modifies these forces. We tried to tackle this problem, but the pancake velocity predicted by our model was found to be incorrect by $10-20\,\%$. Additional numerical simulations should be performed to improve the accuracy of the model. The development of such models should also be undertaken for doubly-confined bubbles and droplets in polygonal microchannels where gutters arise. Similarly, one should address the question of the velocity of liquid bridges as a function of the precursor-film thickness. Present models fail in this task. Yet, we believe that one could solve this issue by building upon the model proposed in **Chapter 5**. Note that in addition to the steady regime, one should extend the study to the transient regime, which is for instance crucial for the flow onset in a microfluidic device.

Once the dynamic meniscus region of pancake droplets is well understood, it would be very beneficial to couple the pressure drop induced in these regions to the Brinkman models for the multiphase flow in microchannels with a large width-to-height aspect ratios (Nagel & Gallaire, 2015). Such an approach has been recently shown to very well capture the dynamics of fibers in microchannels (Nagel, Brun, Berthet, Lindner, Gallaire & Duprat, 2018).

When bubbles or droplets are no longer confined, we have seen in **Chapter 10** that the equilibrium position in the cross-stream direction can be modified by changing the parameters. However, the reason for the stability of some positions compared to others remains unclear. Further studies as done in Rivero-Rodriguez & Scheid (2018) should be performed and extended to the case of nonvanishing viscosity ratios.

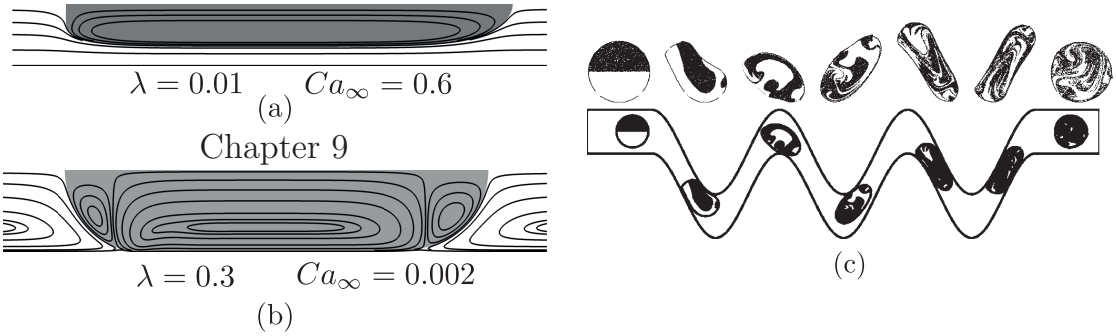

Figure 11.8 – (a,b) Flow field inside a droplet at different outer flow capillary numbers Ca_∞ and viscosity ratios $\lambda = \mu_i/\mu_o$. (b) Snapshots of mixing patterns inside a droplet flowing in a serpentine channel (take from Muradoglu & Stone (2005)).

Finally, as we have seen in **Chapter 9**, the flow field inside droplets strongly depends on the flow conditions. At low Reynolds numbers, the nonlinear advective term in the Navier-Stokes equations is dropped so that turbulence does not emerge. Since molecular diffusion is a relatively slow process, chaotic advection is essential to obtain a rapid mixing in microfluidic devices. Several techniques have been employed in the past and we refer to Song, Chen & Ismagilov (2006) for some examples. For instance, one should avoid separate recirculation regions as the ones of Fig. 11.8(b) since the contained fluid would remain isolated from the rest of the droplet, resulting in an ineffective mixing. Chaotic advection relies on stretching, folding and reorienting events between two fluid regions so as to achieve layers of fluids which become thinner and thinner until diffusion finalizes the mixing (see Fig. 11.8(c)). Therefore, investigating the time-dependent flow filed inside droplets in order to maximize the chaotic advection could be of great help for the improvement of the mixing capabilities of Lab-on-a-Chip devices. This can be for instance done by using the formalism of Lagrangian Coherent Structures (Haller, 2015; Allshouse & Peacock, 2015).

Under normal conditions the research scientist is not an innovator but a solver of puzzles, and the puzzles upon which he concentrates are just those which he believes can be both stated and solved within the existing scientific tradition.
— Thomas S. Kuhn *The Structure of Scientific Revolutions*, 1962

Science sans conscience n'est que ruine de l'homme.
— Edgar Morin *Science avec conscience*, 1990

Bibliography

ABADIE, T., AUBIN, J., LEGENDRE, D. & XUEREB, C. 2012 Hydrodynamics of gas-liquid Taylor flow in rectangular microchannels. *Microfluidics and Nanofluidics* **12** (1-4), 355–369.

ABBYAD, P., DANGLA, R., ALEXANDROU, A. & BAROUD, C. N. 2011 Rails and anchors: guiding and trapping droplet microreactors in two dimensions. *Lab on a Chip* **11** (5), 813–821.

ABDELALL, F. F., ABDEL-KHALIK, S. I., SADOWSKI, D. L., SHIN, S. & YODA, M. 2006 On the Rayleigh-Taylor instability for confined liquid films with injection through the bounding surfaces. *International Journal of Heat and Mass Transfer* **49** (7), 1529–1546.

ADOU, A.-H. E. & TUCKERMAN, L. S. 2016 Faraday instability on a sphere: Floquet analysis. *Journal of Fluid Mechanics* **805**, 591–610.

ALEKSEENKO, S. V., AKTERSHEV, S. P., BOBYLEV, A. V., KHARLAMOV, S. M. & MARKOVICH, D. M. 2015 Nonlinear forced waves in a vertical rivulet flow. *Journal of Fluid Mechanics* **770**, 350–373.

ALEXEEV, A. & ORON, A. 2007 Suppression of the Rayleigh-Taylor instability of thin liquid films by the Marangoni effect. *Physics of Fluids* **19** (8), 082101.

ALLSHOUSE, M. R. & PEACOCK, T. 2015 Lagrangian based methods for coherent structure detection. *Chaos: An Interdisciplinary Journal of Nonlinear Science* **25** (9), 097617.

AMINI, H., LEE, W. & DI CARLO, D. 2014 Inertial microfluidic physics. *Lab on a Chip* **14** (15), 2739–2761.

ANCEY, C. 2001*a* 21 Debris Flows and Related Phenomena. In *Geomorphological Fluid Mechanics*, pp. 528–547. Springer.

ANCEY, C. 2001*b* Snow avalanches. In *Geomorphological Fluid Mechanics*, pp. 319–338. Springer.

ANCEY, C. 2007 Plasticity and geophysical flows: a review. *Journal of Non-Newtonian Fluid Mechanics* **142** (1-3), 4–35.

ANCEY, C., COCHARD, S. & ANDREINI, N. 2009 The dam-break problem for viscous fluids in the high-capillary-number limit. *Journal of Fluid Mechanics* **624**, 1–22.

ANJOS, G., BORHANI, N., MANGIAVACCHI, N. & THOME, J. R. 2014*a* A 3D moving mesh finite element method for two-phase flows. *Journal of Computational Physics* **270**, 366–377.

ANJOS, G., MANGIAVACCHI, N., BORHANI, N. & THOME, J. R. 2014*b* 3D ALE finite-element method for two-phase flows with phase change. *Heat Transfer Engineering* **35** (5), 537–547.

ANNA, S. L. 2016 Droplets and bubbles in microfluidic devices. *Annual Review of Fluid Mechanics* **48**, 285–309.

AUDOLY, B. & POMEAU, Y. 2010 *Elasticity and geometry: from hair curls to the non-linear response of shells*. Oxford University Press.

AUSSILLOUS, P. & QUÉRÉ, D. 2000 Quick deposition of a fluid on the wall of a tube. *Physics of Fluids* **12** (10), 2367–2371.

BABCHIN, A. J., FRENKEL, A. L., LEVICH, B. G. & SIVASHINSKY, G. I. 1983 Nonlinear saturation of Rayleigh-Taylor instability in thin films. *Physics of Fluids* **26** (11), 3159–3161.

BACKHOLM, M., BENZAQUEN, M., SALEZ, T., RAPHAËL, E. & DALNOKI-VERESS, K. 2014 Capillary levelling of a cylindrical hole in a viscous film. *Soft Matter* **10** (15), 2550–2558.

BALMFORTH, N., GHADGE, S. & MYERS, T. 2007 Surface tension driven fingering of a viscoplastic film. *Journal of Non-Newtonian Fluid Mechanics* **142** (1-3), 143–149.

BALMFORTH, N. J., CRASTER, R. V., RUST, A. C. & SASSI, R. 2006 Viscoplastic flow over an inclined surface. *Journal of Non-Newtonian Fluid Mechanics* **139** (1-2), 103–127.

BARENBLATT, G. I. 1996 *Scaling, self-similarity, and intermediate asymptotics: dimensional analysis and intermediate asymptotics*, vol. 14. Cambridge University Press.

BARKLEY, D., BLACKBURN, H. M. & SHERWIN, S. J. 2008 Direct optimal growth analysis for timesteppers. *International Journal for Numerical Methods in Fluids* **57** (9), 1435–1458.

BAROUD, C. N., GALLAIRE, F. & DANGLA, R. 2010 Dynamics of microfluidic droplets. *Lab on a Chip* **10** (16), 2032–2045.

BEALL, G. L. 1998 Rotational Molding Design, Materials, Tooling and Processing. *Hanser/Gardner Publications* pp. 80–85.

BENDE, N. P., EVANS, A. A., INNES-GOLD, S., MARIN, L. A., COHEN, I., HAYWARD, R. C. & SANTANGELO, C. D. 2015 Geometrically controlled snapping transitions in shells with curved creases. *Proceedings of the National Academy of Sciences* **112** (36), 11175–11180.

BENDER, C. M. & ORSZAG, S. A. 2013 *Advanced mathematical methods for scientists and engineers I: Asymptotic methods and perturbation theory*. Springer Science & Business Media.

BENILOV, E. S. & LAPIN, V. N. 2013 Inertial instability of flows on the inside or outside of a rotating horizontal cylinder. *Journal of Fluid Mechanics* **736**, 107–129.

BENZAQUEN, M., FOWLER, P., JUBIN, L., SALEZ, T., DALNOKI-VERESS, K. & RAPHAËL, E. 2014 Approach to universal self-similar attractor for the levelling of thin liquid films. *Soft Matter* **10** (43), 8608–8614.

BENZAQUEN, M., SALEZ, T. & RAPHAËL, E. 2013 Intermediate asymptotics of the capillary-driven thin-film equation. *The European Physical Journal E* **36** (8), 82.

BERGEMANN, N., JUEL, A. & HEIL, M. 2018 Viscous drops on a layer of the same fluid: from sinking, wedging and spreading to their long-time evolution. *Journal of Fluid Mechanics* **843**, 1–28.

BERS, A. 1983 *Space-time evolution of plasma instabilities – absolute and convective*. North-Holland, Amsterdam.

BERTAGNI, M. B. & CAMPOREALE, C. 2017 Nonlinear and subharmonic stability analysis in film-driven morphological patterns. *Physical Review E* **96** (5), 053115.

BERTOZZI, A. L. 1996 Symmetric singularity formation in lubrication-type equations for interface motion. *SIAM Journal on Applied Mathematics* **56** (3), 681–714.

BERTOZZI, A. L. 1998 The mathematics of moving contact lines in thin liquid films. *Notices AMS* **45** (6/7), 689–697.

BERTOZZI, A. L. & BRENNER, M. P. 1997 Linear stability and transient growth in driven contact lines. *Physics of Fluids* **9** (3), 530–539.

BEWLEY, T. R., TEMAM, R. & ZIANE, M. 2000 A general framework for robust control in fluid mechanics. *Physica D: Nonlinear Phenomena* **138** (3-4), 360–392.

BHAMLA, M. S., GIACOMIN, C. E., BALEMANS, C. & FULLER, G. G. 2014 Influence of interfacial rheology on drainage from curved surfaces. *Soft Matter* **10** (36), 6917–6925.

BICO, J. & QUÉRÉ, D. 2002 Self-propelling slugs. *Journal of Fluid Mechanics* **467**, 101–127.

BIELARZ, C. & KALLIADASIS, S. 2003 Time-dependent free-surface thin film flows over topography. *Physics of Fluids* **15** (9), 2512–2524.

BLYTH, M. G. & POZRIKIDIS, C. 2006 Film flow down an inclined plane over a three-dimensional obstacle. *Physics of Fluids* **18** (5), 052104.

BODEN, S., DOS SANTOS ROLO, T., BAUMBACH, T. & HAMPEL, U. 2014 Synchrotron radiation microtomography of Taylor bubbles in capillary two-phase flow. *Experiments in Fluids* **55** (7), 1768.

BOOS, W. & THESS, A. 1997 Thermocapillary flow in a Hele–Shaw cell. *Journal of Fluid Mechanics* **352**, 305–330.

BOOS, W. & THESS, A. 1999 Cascade of structures in long-wavelength Marangoni instability. *Physics of Fluids* **11** (6), 1484–1494.

BOUJO, E. 2014 An adjoint-based approach to the optimal control of separated flows. PhD thesis, EPFL.

BOWEN, M. & WITELSKI, T. P. 2006 The linear limit of the dipole problem for the thin film equation. *SIAM Journal on Applied Mathematics* **66** (5), 1727–1748.

BRAUN, R. J., USHA, R., MCFADDEN, G. B., DRISCOLL, T. A., COOK, L. P. & KING-SMITH, P. E. 2012 Thin film dynamics on a prolate spheroid with application to the cornea. *Journal of Engineering Mathematics* **73** (1), 121–138.

BRENNER, M. P. 1993 Instability mechanism at driven contact lines. *Physical Review E* **47** (6), 4597.

BRETHERTON, F. P. 1961 The motion of long bubbles in tubes. *Journal of Fluid Mechanics* **10** (02), 166–188.

BRIGGS, R. J. 1964 *Electron-stream interaction with plasmas*, vol. 121. MIT press Cambridge, MA.

BRUN, P.-T. 2016 Private communication.

BRUN, P.-T. 2017 A sticky situation. *Journal of Fluid Mechanics* **820**, 1–4.

BRUN, P.-T., DAMIANO, A., RIEU, P., BALESTRA, G. & GALLAIRE, F. 2015 Rayleigh-Taylor instability under an inclined plane. *Physics of Fluids* **27** (8), 084107.

DE BRUYN, J. R. 1997 Crossover between surface tension and gravity-driven instabilities of a thin fluid layer on a horizontal cylinder. *Physics of Fluids* **9** (6), 1599–1605.

DE BRUYN, J. R., HABDAS, P. & KIM, S. 2002 Fingering instability of a sheet of yield-stress fluid. *Physical Review E* **66** (3), 031504.

BRZOSKA, J. B., BROCHARD-WYART, F. & RONDELEZ, F. 1992 Exponential growth of fingering instabilities of spreading films under horizontal thermal gradients. *EPL (Europhysics Letters)* **19** (2), 97.

BUHMANN, D. & DREYBRODT, W. 1985 The kinetics of calcite dissolution and precipitation in geologically relevant situations of karst areas: 1. Open system. *Chemical Geology* **48** (1-4), 189–211.

BURGESS, D. & FOSTER, M. R. 1990 Analysis of the boundary conditions for a Hele–Shaw bubble. *Physics of Fluids A: Fluid Dynamics* **2** (7), 1105–1117.

BURGESS, J. M., JUEL, A., MCCORMICK, W. D., SWIFT, J. B. & SWINNEY, H. L. 2001 Suppression of dripping from a ceiling. *Physical Review Letters* **86** (7), 1203–1206.

BUSH, J. W. M. 1997 The anomalous wake accompanying bubbles rising in a thin gap: a mechanically forced Marangoni flow. *Journal of Fluid Mechanics* **352**, 283–303.

CAMPOREALE, C. 2015 Hydrodynamically locked morphogenesis in karst and ice flutings. *Journal of Fluid Mechanics* **778**, 89–119.

CAMPOREALE, C. 2017 An asymptotic approach to the crenulation instability. *Journal of Fluid Mechanics* **826**, 636–652.

CAMPOREALE, C. & RIDOLFI, L. 2012*a* Hydrodynamic-driven stability analysis of morphological patterns on stalactites and implications for cave paleoflow reconstructions. *Physical Review Letters* **108** (23), 238501.

CAMPOREALE, C. & RIDOLFI, L. 2012*b* Ice ripple formation at large Reynolds numbers. *Journal of Fluid Mechanics* **694**, 225–251.

CANTAT, I. 2013 Liquid meniscus friction on a wet plate: Bubbles, lamellae, and foams. *Physics of Fluids* **25** (3), 031303.

CARMO, M., FRITZ, D. L., MERGEL, J. & STOLTEN, D. 2013 A comprehensive review on PEM water electrolysis. *International Journal of Hydrogen Energy* **38** (12), 4901–4934.

CARRIERE, P. & MONKEWITZ, P. A. 1999 Convective versus absolute instability in mixed Rayleigh–Bénard–Poiseuille convection. *Journal of Fluid Mechanics* **384**, 243–262.

CARROLL, B. J. 1976 The accurate measurement of contact angle, phase contact areas, drop volume, and Laplace excess pressure in drop-on-fiber systems. *Journal of Colloid and Interface Science* **57** (3), 488–495.

CAZABAT, A. M., HESLOT, F., TROIAN, S. M. & CARLES, P. 1990 Fingering instability of thin spreading films driven by temperature gradients. *Nature* **346** (6287), 824.

CHAMPOUGNY, L., RIO, E., RESTAGNO, F. & SCHEID, B. 2017 The break-up of free films pulled out of a pure liquid bath. *Journal of Fluid Mechanics* **811**, 499–524.

CHAN, P. C.-H. & LEAL, L. G. 1979 The motion of a deformable drop in a second-order fluid. *Journal of Fluid Mechanics* **92** (1), 131–170.

CHAN, P. Y. & GOLDENFELD, N. 2007 Steady states and linear stability analysis of precipitation pattern formation at geothermal hot springs. *Physical Review E* **76** (4), 046104.

CHANDRASEKHAR, S. 1981 *Hydrodynamic and Hydromagnetic Stability*. New York: Dover.

CHAROGIANNIS, A., DENNER, F., VAN WACHEM, B. G. M., KALLIADASIS, S., SCHEID, B. & MARKIDES, C. N. 2018 Experimental investigations of liquid falling films flowing under an inclined planar substrate. *Submitted to Physical Review Fluids* .

CHARRU, F. 2012 *Instabilités hydrodynamiques*. EDP Sciences.

CHAUDHURY, K., ACHARYA, P. V. & CHAKRABORTY, S. 2014 Influence of disjoining pressure on the dynamics of steadily moving long bubbles inside narrow cylindrical capillaries. *Physical Review E* **89** (5), 053002.

CHEN, A. S.-H. & MORRIS, S. W. 2011 Experiments on the morphology of icicles. *Physical Review E* **83** (2), 026307.

CHEN, A. S.-H. & MORRIS, S. W. 2013 On the origin and evolution of icicle ripples. *New Journal of Physics* **15** (10), 103012.

CHEN, J.-D. 1986 Measuring the film thickness surrounding a bubble inside a capillary. *Journal of Colloid and Interface Science* **109** (2), 341–349.

CHEN, X., XUE, C., ZHANG, L., HU, G., JIANG, X. & SUN, J. 2014 Inertial migration of deformable droplets in a microchannel. *Physics of Fluids* **26** (11), 112003.

CHERUKUMUDI, A., KLASEBOER, E., KHAN, S. A. & MANICA, R. 2015 Prediction of the shape and pressure drop of Taylor bubbles in circular tubes. *Microfluidics and Nanofluidics* **19** (5), 1221–1233.

CHOMAZ, J.-M. 2003 Fully nonlinear dynamics of parallel wakes. *Journal of Fluid Mechanics* **495**, 57–75.

CHOMAZ, J.-M. 2005 Global instabilities in spatially developing flows: non-normality and nonlinearity. *Annual Review of Fluid Mechanics* **37**, 357–392.

CHOMAZ, J.-M., HUERRE, P. & REDEKOPP, L. G. 1991 A frequency selection criterion in spatially developing flows. *Studies in Applied Mathematics* **84** (2), 119–144.

CIMPEANU, R., PAPAGEORGIOU, D. T. & PETROPOULOS, P. G. 2014 On the control and suppression of the Rayleigh-Taylor instability using electric fields. *Physics of Fluids* **26** (2), 022105.

CIRA, N. J., BENUSIGLIO, A. & PRAKASH, M. 2015 Vapour-mediated sensing and motility in two-component droplets. *Nature* **519** (7544), 446.

CLAUDIN, P., DURÁN, O. & ANDREOTTI, B. 2017 Dissolution instability and roughening transition. *Journal of Fluid Mechanics* **832**, R2.

COSSU, C. 2014 An Introduction to Optimal Control - Lecture notes from the FLOW-NORDITA Summer School on Advanced Instability Methods for Complex Flows, Stockholm, Sweden, 2013. *Applied Mechanics Reviews* **66** (2), 024801.

COUAIRON, A. & CHOMAZ, J.-M. 1997 Absolute and convective instabilities, front velocities and global modes in nonlinear systems. *Physica D: Nonlinear Phenomena* **108** (3), 236–276.

COUDER, Y., FORT, E., GAUTIER, C.-H. & BOUDAOUD, A. 2005 From bouncing to floating: Noncoalescence of drops on a fluid bath. *Physical Review Letters* **94** (17), 177801.

COUVREUR, S. & DAERR, A. 2012 The role of wetting heterogeneities in the meandering instability of a partial wetting rivulet. *EPL (Europhysics Letters)* **99** (2), 24004.

COX, R. G. & HSU, S. K. 1977 The lateral migration of solid particles in a laminar flow near a plane. *International Journal of Multiphase Flow* **3** (3), 201–222.

CRASTER, R. V. & MATAR, O. K. 2009 Dynamics and stability of thin liquid films. *Reviews of Modern Physics* **81** (3), 1131.

CRAWFORD, R. J. & KEARNS, M. P. 2012 *Practical guide to rotational moulding*, 2nd edn. Smithers Rapra Technology.

DAERR, A., EGGERS, J., LIMAT, L. & VALADE, N. 2011 General mechanism for the meandering instability of rivulets of Newtonian fluids. *Physical Review Letters* **106** (18), 184501.

DALLASTON, M. C., TSELUIKO, D., ZHENG, Z., FONTELOS, M. A. & KALLIADASIS, S. 2017 Self-similar finite-time singularity formation in degenerate parabolic equations arising in thin-film flows. *Nonlinearity* **30** (7), 2647.

DANGLA, R., GALLAIRE, F. & BAROUD, C. N. 2010 Microchannel deformations due to solvent-induced PDMS swelling. *Lab on a Chip* **10** (21), 2972–2978.

DARHUBER, A. A. & TROIAN, S. M. 2005 Principles of microfluidic actuation by modulation of surface stresses. *Annual Review of Fluid Mechanics* **37**, 425–455.

DECRÉ, M. M. J. & BARET, J.-C. 2003 Gravity-driven flows of viscous liquids over two-dimensional topographies. *Journal of Fluid Mechanics* **487**, 147–166.

DELAINE, J. 1983 Roman Baths. *Journal of the Anthropological Society of South Australia* **21** (7), 4–11.

DELBENDE, I. & CHOMAZ, J.-M. 1998 Nonlinear convective/absolute instabilities in parallel two-dimensional wakes. *Physics of Fluids* **10** (11), 2724–2736.

DELON, G., FERMIGIER, M., SNOEIJER, J. H. & ANDREOTTI, B. 2008 Relaxation of a dewetting contact line. Part 2. Experiments. *Journal of Fluid Mechanics* **604**, 55–75.

DERJAGUIN, B. 1943 On the thickness of the liquid film adhering to the walls of a vessel after emptying. *Acta Physicochimica URSS* **20** (43), 349–352.

DI CARLO, D., EDD, J. F., HUMPHRY, K. J., STONE, H. A. & TONER, M. 2009 Particle segregation and dynamics in confined flows. *Physical Review Letters* **102** (9), 094503.

DI CARLO, D., IRIMIA, D., TOMPKINS, R. G. & TONER, M. 2007 Continuous inertial focusing, ordering, and separation of particles in microchannels. *Proceedings of the National Academy of Sciences* **104** (48), 18892–18897.

DOEDEL, E. J. 2007 Lecture notes on numerical analysis of nonlinear equations. In *Numerical Continuation Methods for dynamical systems*, pp. 1–49. Springer.

DOUADY, S. & COUDER, Y. 1996 Phyllotaxis as a dynamical self organizing process. Part I: the spiral modes resulting from time-periodic iterations. *Journal of Theoretical Biology* **178** (3), 255–273.

DREYBRODT, W. 1999 Chemical kinetics, speleothem growth and climate. *Boreas* **28** (3), 347–356.

DUCLAUX, V., CLANET, C. & QUÉRÉ, D. 2006 The effects of gravity on the capillary instability in tubes. *Journal of Fluid Mechanics* **556**, 217–226.

DUFFY, B. R. & MOFFATT, H. K. 1995 Flow of a viscous trickle on a slowly varying incline. *The Chemical Engineering Journal and The Biochemical Engineering Journal* **60** (1-3), 141–146.

DUPRAT, C., RUYER-QUIL, C. & GIORGIUTTI-DAUPHINÉ, F. 2009 Spatial evolution of a film flowing down a fiber. *Physics of Fluids* **21** (4), 042109.

DUPRAT, C., RUYER-QUIL, C., KALLIADASIS, S. & GIORGIUTTI-DAUPHINÉ, F. 2007 Absolute and convective instabilities of a viscous film flowing down a vertical fiber. *Physical Review Letters* **98** (24), 244502.

EBRAHIMI, H., AJDARI, A., VELLA, D., BOUDAOUD, A. & VAZIRI, A. 2014 Anisotropic Blistering Instability of Highly Ellipsoidal Shells. *Physical Review Letters* **112** (9), 094302.

EGGERS, J. & VILLERMAUX, E. 2008 Physics of liquid jets. *Reports on Progress in Physics* **71** (3), 036601.

ELISHAKOFF, I. 2014 *Resolution of the twentieth century conundrum in elastic stability*. World Scientific.

EMSLIE, A. G., BONNER, F. T. & PECK, L. G. 1958 Flow of a viscous liquid on a rotating disk. *Journal of Applied Physics* **29** (5), 858–862.

ERES, M. H., SCHWARTZ, L. W. & ROY, R. V. 2000 Fingering phenomena for driven coating films. *Physics of Fluids* **12** (6), 1278–1295.

FAIRBROTHER, F. & STUBBS, A. E. 1935 119. Studies in electro-endosmosis. Part VI. The 'bubble-tube' method of measurement. *Journal of the Chemical Society (Resumed)* pp. 527–529.

FALCON, C., FALCON, E., BORTOLOZZO, U. & FAUVE, S. 2009 Capillary wave turbulence on a spherical fluid surface in low gravity. *EPL (Europhysics Letters)* **86** (1), 14002.

FAUVE, S. 2005 Pattern forming instabilities. In *Hydrodynamics and Nonlinear Instabilities* (ed. C. Godrèche & P. Manneville), chap. 4, pp. 387-491. Cambridge University Press.

FERMIGIER, M., LIMAT, L., WESFREID, J. E., BOUDINET, P. & QUILLIET, C. 1992 Two-dimensional patterns in Rayleigh-Taylor instability of a thin layer. *Journal of Fluid Mechanics* **236**, 349–383.

FRAYSSE, N. & HOMSY, G. M. 1994 An experimental study of rivulet instabilities in centrifugal spin coating of viscous Newtonian and non-Newtonian fluids. *Physics of Fluids* **6** (4), 1491–1504.

FUERSTMAN, M. J., LAI, A., THURLOW, M. E., SHEVKOPLYAS, S. S., STONE, H. A. & WHITESIDES, G. M. 2007 The pressure drop along rectangular microchannels containing bubbles. *Lab on a Chip* **7** (11), 1479–1489.

GALLAIRE, F. & BRUN, P.-T. 2017 Fluid dynamic instabilities: theory and application to pattern forming in complex media. *Philosophical Transactions of the Royal Society of London A* **375** (2093), 20160155.

GALLAIRE, F., MELIGA, P., LAURE, P. & BAROUD, C. N. 2014 Marangoni induced force on a drop in a Hele–Shaw cell. *Physics of Fluids* **26** (6), 062105.

GALLINO, G., ZHU, L. & GALLAIRE, F. 2016 The stability of a rising droplet: an inertialess non-modal growth mechanism. *Journal of Fluid Mechanics* **786**, R2.

GAÑÁN-CALVO, A. M. & GORDILLO, J. M. 2001 Perfectly monodisperse microbubbling by capillary flow focusing. *Physical Review Letters* **87** (27), 274501.

GANESAN, S., HAHN, A., SIMON, K. & TOBISKA, L. 2017 ALE-FEM for Two-Phase and Free Surface Flows with Surfactants. In *Transport Processes at Fluidic Interfaces* (ed. D. Bothe & A. Reusken), pp. 5–31. Cham: Springer.

GANESAN, S. & TOBISKA, L. 2012 Arbitrary Lagrangian–Eulerian finite-element method for computation of two-phase flows with soluble surfactants. *Journal of Computational Physics* **231** (9), 3685–3702.

DE GENNES, P.-G., BROCHARD-WYART, F. & QUÉRÉ, D. 2004 *Capillarity and Wetting Phenomena: Drops, Bubbles, Pearls, Waves*. Springer New York.

GIAVEDONI, M. D. & SAITA, F. A. 1997 The axisymmetric and plane cases of a gas phase steadily displacing a Newtonian liquid – A simultaneous solution of the governing equations. *Physics of Fluids* **9** (8), 2420–2428.

GIAVEDONI, M. D. & SAITA, F. A. 1999 The rear meniscus of a long bubble steadily displacing a Newtonian liquid in a capillary tube. *Physics of Fluids* **11** (4), 786–794.

GILET, T. & BOUROUIBA, L. 2014 Rain-induced Ejection of Pathogens from Leaves: Revisiting the Hypothesis of Splash-on-Film using High-speed Visualization. *Integrative and Comparative Biology* **54** (6), 974–984.

GOLDENFELD, N., CHAN, P. Y. & VEYSEY II, J. 2006 Dynamics of precipitation pattern formation at geothermal hot springs. *Physical Review Letters* **96** (25), 254501.

GOODWIN, R. & HOMSY, G. M. 1991 Viscous flow down a slope in the vicinity of a contact line. *Physics of Fluids A: Fluid Dynamics* **3** (4), 515–528.

GORDILLO, J. M., GAÑÁN-CALVO, A. M. & PÉREZ-SABORID, M. 2001 Monodisperse microbubbling: Absolute instabilities in coflowing gas–liquid jets. *Physics of Fluids* **13** (12), 3839–3842.

GREER, J. B., BERTOZZI, A. L. & SAPIRO, G. 2006 Fourth order partial differential equations on general geometries. *Journal of Computational Physics* **216** (1), 216–246.

GROTBERG, J. B. 1994 Pulmonary flow and transport phenomena. *Annual Review of Fluid Mechanics* **26** (1), 529–571.

GUILLOT, P., COLIN, A., UTADA, A. S. & AJDARI, A. 2007 Stability of a jet in confined pressure-driven biphasic flows at low Reynolds numbers. *Physical Review Letters* **99** (10), 104502.

GÜNTHER, A. & JENSEN, K. F. 2006 Multiphase microfluidics: from flow characteristics to chemical and materials synthesis. *Lab on a Chip* **6** (12), 1487–1503.

GUPTA, R., LEUNG, S. S. Y., MANICA, R., FLETCHER, D. F. & HAYNES, B. S. 2013 Three Dimensional Effects in Taylor Flow in Circular Microchannels. *La Houille Blanche* (2), 60–67.

HADIKHANI, P., HASHEMI, S. M. H., BALESTRA, G., ZHU, L., MODESTINO, M. A., GALLAIRE, F. & PSALTIS, D. 2018 Inertial manipulation of bubbles in rectangular microfluidic channels. *Lab on a Chip* **18** (7), 1035–1046.

HALLER, G. 2015 Lagrangian Coherent Structures. *Annual Review of Fluid Mechanics* **47**, 137–162.

HAMMER, Ø., DYSTHE, D., LELU, B., LUND, H., MEAKIN, P. & JAMTVEIT, B. 2008 Calcite precipitation instability under laminar, open-channel flow. *Geochimica et Cosmochimica Acta* **72** (20), 5009–5021.

HAMMOND, P. S. 1983 Nonlinear adjustment of a thin annular film of viscous fluid surrounding a thread of another within a circular cylindrical pipe. *Journal of Fluid Mechanics* **137**, 363–384.

HAMMOUD, N. 2016 On Instabilities in Thin-Film Flows. PhD thesis, Princeton University.

HAMMOUD, N. H., TRINH, P. H., HOWELL, P. D. & STONE, H. A. 2017 Influence of van der Waals forces on a bubble moving in a tube. *Physical Review Fluids* **2** (6), 063601.

HAN, Y. & SHIKAZONO, N. 2009 Measurement of liquid film thickness in micro square channel. *International Journal of Multiphase Flow* **35** (10), 896–903.

HASHEMI, S. M. H., MODESTINO, M. A. & PSALTIS, D. 2015 A membrane-less electrolyzer for hydrogen production across the ph scale. *Energy & Environmental Science* **8** (7), 2003–2009.

HAYES, M., O'BRIEN, S. B. G. & LAMMERS, J. H. 2000 Green's function for steady flow over a small two-dimensional topography. *Physics of Fluids* **12** (11), 2845–2858.

HAZEL, A. L., HEIL, M., WATERS, S. L. & OLIVER, J. M. 2012 On the liquid lining in fluid-conveying curved tubes. *Journal of Fluid Mechanics* **705**, 213–233.

HEIL, M. 2001 Finite Reynolds number effects in the Bretherton problem. *Physics of Fluids* **13** (9), 2517–2521.

HEIN, M., MOSKOPP, M. & SEEMANN, R. 2015 Flow field induced particle accumulation inside droplets in rectangular channels. *Lab on a Chip* **15** (13), 2879–2886.

HERRADA, M. A., GANAN-CALVO, A. M. & GUILLOT, P. 2008 Spatiotemporal instability of a confined capillary jet. *Physical Review E* **78** (4), 046312.

HILL, C. A. & FORTI, P. 1997 *Cave minerals of the world*, vol. 2. National Speleological Society.

HO, B. P. & LEAL, L. G. 1974 Inertial migration of rigid spheres in two-dimensional unidirectional flows. *Journal of Fluid Mechanics* **65** (2), 365–400.

HOCKING, L. M. 1990 Spreading and instability of a viscous fluid sheet. *Journal of Fluid Mechanics* **211**, 373–392.

HOCKING, L. M. & MIKSIS, M. J. 1993 Stability of a ridge of fluid. *Journal of Fluid Mechanics* **247**, 157–177.

HODGES, S. R., JENSEN, O. E. & RALLISON, J. M. 2004*a* The motion of a viscous drop through a cylindrical tube. *Journal of Fluid Mechanics* **501**, 279–301.

HODGES, S. R., JENSEN, O. E. & RALLISON, J. M. 2004*b* Sliding, slipping and rolling: the sedimentation of a viscous drop down a gently inclined plane. *Journal of Fluid Mechanics* **512**, 95–131.

HÖGBERG, M. & HENNINGSON, D. 1998 Secondary instability of cross-flow vortices in Falkner–Skan–Cooke boundary layers. *Journal of Fluid Mechanics* **368**, 339–357.

HOLLOWAY, K. E., HABDAS, P., SEMSARILLAR, N., BURFITT, K. & DE BRUYN, J. R. 2007 Spreading and fingering in spin coating. *Physical Review E* **75** (4), 046308.

HOSOI, A. E. & MAHADEVAN, L. 1999 Axial instability of a free-surface front in a partially filled horizontal rotating cylinder. *Physics of Fluids* **11** (1), 97–106.

HOWELL, P. D. 2003 Surface-tension-driven flow on a moving curved surface. *Journal of Engineering Mathematics* **45** (3-4), 283–308.

HUERRE, A., THEODOLY, O., LESHANSKY, A. M., VALIGNAT, M.-P., CANTAT, I. & JULLIEN, M.-C. 2015 Droplets in microchannels: dynamical properties of the lubrication film. *Physical Review Letters* **115** (6), 064501.

HUERRE, P. 2000 Open shear flow instabilities. In *Perspectives in Fluid Dynamics* (ed. G. Batchelor, H. Moffatt & G. Worster), pp. 159–229. Cambridge University Press.

HUERRE, P. & MONKEWITZ, P. A. 1985 Absolute and convective instabilities in free shear layers. *Journal of Fluid Mechanics* **159**, 151–168.

HUERRE, P. & MONKEWITZ, P. A. 1990 Local and global instabilities in spatially developing flows. *Annual Review of Fluid Mechanics* **22** (1), 473–537.

HUERRE, P. & ROSSI, M. 1998 Hydrodynamic instabilities in open flows. *Collection Alea-Saclay: Monographs and Texts in Statistical Physics* **1** (3), 81–294.

HUPPERT, H. E. 1982*a* Flow and instability of a viscous current down a slope. *Nature* **300** (5891), 427.

HUPPERT, H. E. 1982*b* The propagation of two-dimensional and axisymmetric viscous gravity currents over a rigid horizontal surface. *Journal of Fluid Mechanics* **121**, 43–58.

HUPPERT, H. E., SHEPHERD, J. B., SIGURDSSON, R. H. & SPARKS, S. J. 1982 On lava dome growth, with application to the 1979 lava extrusion of the Soufriere of St. Vincent. *Journal of Volcanology and Geothermal Research* **14** (3-4), 199–222.

INDEIKINA, A., VERETENNIKOV, I. & CHANG, H.-C. 1997 Drop fall-off from pendent rivulets. *Journal of Fluid Mechanics* **338**, 173–201.

JAKIELA, S., KORCZYK, P. M., MAKULSKA, S., CYBULSKI, O. & GARSTECKI, P. 2012 Discontinuous transition in a laminar fluid flow: a change of flow topology inside a droplet moving in a micron-size channel. *Physical Review Letters* **108** (13), 134501.

JAKIELA, S., MAKULSKA, S., KORCZYK, P. M. & GARSTECKI, P. 2011 Speed of flow of individual droplets in microfluidic channels as a function of the capillary number, volume of droplets and contrast of viscosities. *Lab on a Chip* **11** (21), 3603–3608.

JENSEN, O. E. 1997 The thin liquid lining of a weakly curved cylindrical tube. *Journal of Fluid Mechanics* **331**, 373–403.

JIMÉNEZ, F. L., MARTHELOT, J., LEE, A., HUTCHINSON, J. W. & REIS, P. M. 2017 Technical brief: knockdown factor for the buckling of spherical shells containing large-amplitude geometric defects. *Journal of Applied Mechanics* **84** (3), 034501.

KAITA, R., BERZAK, L., BOYLE, D., GRAY, T., GRANSTEDT, E., HAMMETT, G., JACOBSON, C. M., JONES, A., KOZUB, T., KUGEL, H. ET AL. 2010 Experiments with liquid metal walls: Status of the lithium tokamak experiment. *Fusion Engineering and Design* **85** (6), 874–881.

KALLIADASIS, S., BIELARZ, C. & HOMSY, G. M. 2000 Steady free-surface thin film flows over topography. *Physics of Fluids* **12** (8), 1889–1898.

KALLIADASIS, S. & CHANG, H.-C. 1994 Drop formation during coating of vertical fibres. *Journal of Fluid Mechanics* **261**, 135–168.

KALLIADASIS, S., RUYER-QUIL, C., SCHEID, B. & VELARDE, M. G. 2011 *Falling liquid films*, vol. 176. Springer Science & Business Media.

KALPAKJIAN, S. & SCHMID, S. R. 2014 *Manufacturing engineering and technology*. Pearson.

KAPITZA, P. L. & KAPITZA, S. P. 1949 Wave flow of thin viscous liquid films. *Zh. Exper. i Teor. Fiz* **19**, 105–120.

KARPITSCHKA, S., PANDEY, A., LUBBERS, L. A., WEIJS, J. H., BOTTO, L., DAS, S., ANDREOTTI, B. & SNOEIJER, J. H. 2016 Liquid drops attract or repel by the inverted Cheerios effect. *Proceedings of the National Academy of Sciences* **113** (27), 7403–7407.

KATAOKA, D. E. & TROIAN, S. M. 1997 A theoretical study of instabilities at the advancing front of thermally driven coating films. *Journal of Colloid and Interface Science* **192** (2), 350–362.

KATIFORI, E., ALBEN, S., CERDA, E., NELSON, D. R. & DUMAIS, J. 2010 Foldable structures and the natural design of pollen grains. *Proceedings of the National Academy of Sciences* **107** (17), 7635–7639.

KAUFMANN, G. 2003 Stalagmite growth and palaeo-climate: the numerical perspective. *Earth and Planetary Science Letters* **214** (1-2), 251–266.

KAUFMANN, G. & DREYBRODT, W. 2007 Calcite dissolution kinetics in the system CaCO3–H2O–CO2 at high undersaturation. *Geochimica et Cosmochimica Acta* **71** (6), 1398–1410.

KEISER, L., BENSE, H., COLINET, P., BICO, J. & REYSSAT, E. 2017 Marangoni Bursting: Evaporation-Induced Emulsification of Binary Mixtures on a Liquid Layer. *Physical Review Letters* **118** (7), 074504.

KENNEDY, M. R., POZRIKIDIS, C. & SKALAK, R. 1994 Motion and deformation of liquid drops, and the rheology of dilute emulsions in simple shear flow. *Computers & Fluids* **23** (2), 251–278.

KERSWELL, R. R., PRINGLE, C. C. T. & WILLIS, A. P. 2014 An optimization approach for analysing nonlinear stability with transition to turbulence in fluids as an exemplar. *Reports on Progress in Physics* **77** (8), 085901.

KHODAPARAST, S. 2014 Micro Particle Shadow Velocimetry (μPSV) of Single-and Two-phase Flows through Microchannels. PhD thesis, EPFL.

KHODAPARAST, S., KIM, M. K., SILPE, J. E. & STONE, H. A. 2017 Bubble-driven detachment of bacteria from confined microgeometries. *Environmental Science & Technology* **51** (3), 1340–1347.

KHODAPARAST, S., MAGNINI, M., BORHANI, N. & THOME, J. R. 2015 Dynamics of isolated confined air bubbles in liquid flows through circular microchannels: an experimental and numerical study. *Microfluidics and Nanofluidics* **19** (1), 209–234.

KIETZIG, A.-M., HATZIKIRIAKOS, S. G. & ENGLEZOS, P. 2010 Physics of ice friction. *Journal of Applied Physics* **107** (8), 4.

KIM, H.-Y., KIM, J.-H. & KANG, B. H. 2004 Meandering instability of a rivulet. *Journal of Fluid Mechanics* **498**, 245–256.

KING, A. A., CUMMINGS, L. J., NAIRE, S. & JENSEN, O. E. 2007 Liquid film dynamics in horizontal and tilted tubes: Dry spots and sliding drops. *Physics of Fluids* **19** (4), 042102.

KISTLER, S. F., SCHWEIZER, P. M. ET AL. 1997 *Liquid film coating*. Springer.

KLASEBOER, E., GUPTA, R. & MANICA, R. 2014 An extended Bretherton model for long Taylor bubbles at moderate capillary numbers. *Physics of Fluids* **26** (3), 032107.

KOFMAN, N., MERGUI, S. & RUYER-QUIL, C. 2014 Three-dimensional instabilities of quasi-solitary waves in a falling liquid film. *Journal of Fluid Mechanics* **757**, 854–887.

KOFMAN, N., RUYER-QUIL, C. & MERGUI, S. 2016 Selection of solitary waves in vertically falling liquid films. *International Journal of Multiphase Flow* **84**, 75–85.

KÖHLER, J. M. & CAHILL, B. P. 2014 *Micro-Segmented Flow: Applications in Chemistry and Biology. Biological and Medical Physics, Biomedical Engineering* . Springer Berlin Heidelberg.

KONDIC, L. 2003 Instabilities in gravity driven flow of thin fluid films. *SIAM Review* **45** (1), 95–115.

KONDIC, L. & DIEZ, J. 2001 Pattern formation in the flow of thin films down an incline: Constant flux configuration. *Physics of Fluids* **13** (11), 3168–3184.

KOPF-SILL, A. R. & HOMSY, G. M. 1988 Bubble motion in a Hele–Shaw cell. *The Physics of Fluids* **31** (1), 18–26.

KRECHETNIKOV, R. 2009 Rayleigh-Taylor and Richtmyer-Meshkov instabilities of flat and curved interfaces. *Journal of Fluid Mechanics* **625**, 387–410.

KRECHETNIKOV, R. 2010 On application of lubrication approximations to nonunidirectional coating flows with clean and surfactant interfaces. *Physics of Fluids* **22** (9), 092102.

KREUTZER, M. T., KAPTEIJN, F., MOULIJN, J. A., KLEIJN, C. R. & HEISZWOLF, J. J. 2005 Inertial and interfacial effects on pressure drop of Taylor flow in capillaries. *AIChE Journal* **51** (9), 2428–2440.

LABROT, V., SCHINDLER, M., GUILLOT, P., COLIN, A. & JOANICOT, M. 2009 Extracting the hydrodynamic resistance of droplets from their behavior in microchannel networks. *Biomicrofluidics* **3** (1), 012804.

LAC, E. & SHERWOOD, J. 2009 Motion of a drop along the centreline of a capillary in a pressure-driven flow. *Journal of Fluid Mechanics* **640**, 27–54.

ŁADOSZ, A., RIGGER, E. & VON ROHR, P. R. 2016 Pressure drop of three-phase liquid-liquid-gas slug flow in round microchannels. *Microfluidics and Nanofluidics* **20** (3), 49.

LAMSTAES, C. & EGGERS, J. 2017 Arrested bubble rise in a narrow tube. *Journal of Statistical Physics* **167** (3-4), 656–682.

LANDAU, L. & LEVICH, B. 1942 Dragging of a liquid by a moving plate. *Acta Physicochimica URSS* **17** (42), 42–54.

LANGEWISCH, D. R. & BUONGIORNO, J. 2015 Prediction of film thickness, bubble velocity, and pressure drop for capillary slug flow using a CFD-generated database. *International Journal of Heat and Fluid Flow* **54**, 250–257.

LAPUERTA, V., MANCEBO, F. J. & VEGA, J. M. 2001 Control of Rayleigh-Taylor instability by vertical vibration in large aspect ratio containers. *Physical Review E* **64** (1), 016318.

LAZARUS, A., FLORIJN, H. C. B. & REIS, P. M. 2012 Geometry-induced rigidity in nonspherical pressurized elastic shells. *Physical Review Letters* **109** (14), 144301.

LE GRAND-PITEIRA, N., DAERR, A. & LIMAT, L. 2006 Meandering rivulets on a plane: A simple balance between inertia and capillarity. *Physical Review Letters* **96** (25), 254503.

LEAL, L. G. 1980 Particle motions in a viscous fluid. *Annual Review of Fluid Mechanics* **12** (1), 435–476.

LEAL, L. G. 2007 *Advanced transport phenomena: fluid mechanics and convective transport processes*, vol. 7. Cambridge University Press.

LEE, A., BRUN, P.-T., MARTHELOT, J., BALESTRA, G., GALLAIRE, F. & REIS, P. M. 2016*a* Fabrication of slender elastic shells by the coating of curved surfaces. *Nature Communications* **7**, 11155.

LEE, A., JIMÉNEZ, F. L., MARTHELOT, J., HUTCHINSON, J. W. & REIS, P. M. 2016*b* The geometric role of precisely engineered imperfections on the critical buckling load of spherical elastic shells. *Journal of Applied Mechanics* **83** (11), 111005.

LEE, N. C. 2006 *Practical Guide to Blow Moulding*. Smithers Rapra Techonology.

LENSCHEN, M., CALVO, A. & CACHILE, M. 2010 Rayleigh-Taylor instability under a flat beam. *Physical Review E* **81** (1), 017302.

LESLIE, G. A., WILSON, S. K. & DUFFY, B. R. 2013 Three-dimensional coating and rimming flow: a ring of fluid on a rotating horizontal cylinder. *Journal of Fluid Mechanics* **716**, 51–82.

LEUNG, S. S. Y., GUPTA, R., FLETCHER, D. F. & HAYNES, B. S. 2011 Effect of flow characteristics on Taylor flow heat transfer. *Industrial & Engineering Chemistry Research* **51** (4), 2010–2020.

LEVEQUE, R. J. 1990 *Conservative Methods for Nonlinear Problems*, pp. 122–135. Basel: Birkhäuser Basel.

LHUISSIER, H. & VILLERMAUX, E. 2012 Bursting bubble aerosols. *Journal of Fluid Mechanics* **696**, 5–44.

LI, J. 2016 Macroscopic Model for Head-On Binary Droplet Collisions in a Gaseous Medium. *Physical Review Letters* **117** (21), 214502.

LIMAT, L. 1993 Instabilité d'un liquide suspendu sous un surplomb solide: Influence de l'épaisseur de la couche. *Comptes rendus de l'Académie des sciences. Série 2, Mécanique, Physique, Chimie, Sciences de l'univers, Sciences de la Terre* **317** (5), 563–568.

LIMAT, L., JENFFER, P., DAGENS, B., TOURON, E., FERMIGIER, M. & WESFREID, J. E. 1992 Gravitational instabilities of thin liquid layers: dynamics of pattern selection. *Physica D* **61** (1), 166–182.

LIN, T.-S., KONDIC, L. & FILIPPOV, A. 2012 Thin films flowing down inverted substrates: Three-dimensional flow. *Physics of Fluids* **24** (2), 022105.

LING, Y., FULLANA, J.-M., POPINET, S. & JOSSERAND, C. 2016 Droplet migration in a Hele–Shaw cell: Effect of the lubrication film on the droplet dynamics. *Physics of Fluids* **28** (6), 062001.

LISTER, J. R., RALLISON, J. M., KING, A. A., CUMMINGS, L. J. & JENSEN, O. E. 2006 Capillary drainage of an annular film: the dynamics of collars and lobes. *Journal of Fluid Mechanics* **552**, 311–343.

LISTER, J. R., RALLISON, J. M. & REES, S. J. 2010 The nonlinear dynamics of pendent drops on a thin film coating the underside of a ceiling. *Journal of Fluid Mechanics* **647**, 239–264.

LUCHINI, P. & BOTTARO, A. 2014 Adjoint equations in stability analysis. *Annual Review of Fluid Mechanics* **46** (1), 493.

MAGNINI, M., FERRARI, A., THOME, J. R. & STONE, H. A. 2017 Undulations on the surface of elongated bubbles in confined gas-liquid flows. *Physical Review Fluids* **2** (8), 084001.

MAJESKI, R., KUGEL, H., KAITA, R., AVASARALA, S., BELL, M., BELL, R., BERZAK, L., BEIERSDORFER, P., GERHARDT, S., GRANSTEDT, E. ET AL. 2010 The impact of lithium wall coatings on NSTX discharges and the engineering of the Lithium Tokamak eXperiment (LTX). *Fusion Engineering and Design* **85** (7-9), 1283–1289.

MALEKI, M., REYSSAT, M., RESTAGNO, F., QUÉRÉ, D. & CLANET, C. 2011 Landau–Levich menisci. *Journal of Colloid and Interface Science* **354** (1), 359–363.

MANTIČ-LUGO, V., ARRATIA, C. & GALLAIRE, F. 2014 Self-consistent mean flow description of the nonlinear saturation of the vortex shedding in the cylinder wake. *Physical Review Letters* **113** (8), 084501.

MAO, X., BLACKBURN, H. M. & SHERWIN, S. J. 2013 Calculation of global optimal initial and boundary perturbations for the linearised incompressible Navier-Stokes equations. *Journal of Computational Physics* **235**, 258–273.

MARTINEZ, M. J. & UDELL, K. S. 1990 Axisymmetric creeping motion of drops through circular tubes. *Journal of Fluid Mechanics* **210**, 565–591.

MAUREL, A., PAGNEUX, V. & WESFREID, J. E. 1995 Mean-flow correction as non-linear saturation mechanism. *EPL (Europhysics Letters)* **32** (3), 217.

MAYO, L. C., MCCUE, S. W., MORONEY, T. J., FORSTER, W. A., KEMPTHORNE, D. M., BELWARD, J. A. & TURNER, I. W. 2015 Simulating droplet motion on virtual leaf surfaces. *Royal Society Open Science* **2** (5), 140528.

MCGRAW, J. D., SALEZ, T., BÄUMCHEN, O., RAPHAËL, E. & DALNOKI-VERESS, K. 2012 Self-similarity and energy dissipation in stepped polymer films. *Physical Review Letters* **109** (12), 128303.

MCLAUGHLIN, J. B. 1991 Inertial migration of a small sphere in linear shear flows. *Journal of Fluid Mechanics* **224**, 261–274.

MEAKIN, P. & JAMTVEIT, B. 2009 Geological pattern formation by growth and dissolution in aqueous systems. *Proceedings of the Royal Society of London A: Mathematical, Physical and Engineering Sciences* .

MEIBURG, E. 1989 Bubbles in a Hele–Shaw cell: Numerical simulation of three-dimensional effects. *Physics of Fluids A: Fluid Dynamics* **1** (6), 938–946.

MELO, F. 1993 Localized states in a film-dragging experiment. *Physical Review E* **48** (4), 2704.

MELO, F., JOANNY, J. F. & FAUVE, S. 1989 Fingering instability of spinning drops. *Physical Review Letters* **63** (18), 1958.

MEYERHOFER, D. 1978 Characteristics of resist films produced by spinning. *Journal of Applied Physics* **49** (7), 3993–3997.

MIKAELIAN, D., HAUT, B. & SCHEID, B. 2015 Bubbly flow and gas-liquid mass transfer in square and circular microchannels for stress-free and rigid interfaces: dissolution model. *Microfluidics and Nanofluidics* **19** (4), 899–911.

MODESTINO, M. A., RIVAS, D. F., HASHEMI, S. M. H., GARDENIERS, J. G. E. & PSALTIS, D. 2016 The potential for microfluidics in electrochemical energy systems. *Energy & Environmental Science* **9** (11), 3381–3391.

MOFFATT, H.-K. 1998 Microhydrodynamics. École Polytechnique X, Tome 1.

MONKEWITZ, P. A., HUERRE, P. & CHOMAZ, J.-M. 1993 Global linear stability analysis of weakly non-parallel shear flows. *Journal of Fluid Mechanics* **251**, 1–20.

MORIARTY, J. A., SCHWARTZ, L. W. & TUCK, E. O. 1991 Unsteady spreading of thin liquid films with small surface tension. *Physics of Fluids A: Fluid Dynamics* **3** (5), 733–742.

MORTAZAVI, S. & TRYGGVASON, G. 2000 A numerical study of the motion of drops in Poiseuille flow. Part 1. Lateral migration of one drop. *Journal of Fluid Mechanics* **411**, 325–350.

MULLER, J., WEDERSHOVEN, H. M. & DARHUBER, A. A. 2017 Monitoring photochemical reactions using Marangoni flows. *Langmuir* **33** (15), 3647–3658.

MURADOGLU, M. & STONE, H. A. 2005 Mixing in a drop moving through a serpentine channel: A computational study. *Physics of Fluids* **17** (7), 073305.

MUTABAZI, I., WESFREID, J. E. & GUYON, E. 2010 *Dynamics of spatio-temporal cellular structures: Henri Bénard centenary review*, vol. 207. Springer.

MYERS, T. G. 1998 Thin films with high surface tension. *SIAM Review* **40** (3), 441–462.

MYERS, T. G., CHARPIN, J. P. F. & CHAPMAN, S. J. 2002 The flow and solidification of a thin fluid film on an arbitrary three-dimensional surface. *Physics of Fluids* **14** (8), 2788–2803.

NAGEL, M. 2014 Modeling droplets flowing in microchannels. PhD thesis, EPFL, Lausanne.

NAGEL, M., BRUN, P.-T., BERTHET, H., LINDNER, A., GALLAIRE, F. & DUPRAT, C. 2018 Oscillations of confined fibres transported in microchannels. *Journal of Fluid Mechanics* **835**, 444–470.

NAGEL, M., BRUN, P.-T. & GALLAIRE, F. 2014 A numerical study of droplet trapping in microfluidic devices. *Physics of Fluids* **26** (3), 032002.

NAGEL, M. & GALLAIRE, F. 2015 Boundary elements method for microfluidic two-phase flows in shallow channels. *Computers & Fluids* **107**, 272–284.

NASTO, A. & REIS, P. M. 2014 Localized structures in indented shells: A numerical investigation. *Journal of Applied Mechanics* **81** (12), 121008.

OCKENDON, H. & OCKENDON, J. R. 1995 *Viscous flow*, vol. 13. Cambridge University Press.

OLSSON, P. J. & HENNINGSON, D. S. 1995 Optimal disturbance growth in watertable flow. *Studies in Applied Mathematics* **94** (2), 183–210.

ORON, A., DAVIS, S. H. & BANKOFF, S. G. 1997 Long-scale evolution of thin liquid films. *Reviews of Modern Physics* **69** (3), 931.

ORON, A. & ROSENAU, P. 1989 Nonlinear evolution and breaking of interfacial Rayleigh-Taylor waves. *Physics of Fluids A: Fluid Dynamics* **1** (7), 1155–1165.

PARK, C. D. & NOSOKO, T. 2003 Three-dimensional wave dynamics on a falling film and associated mass transfer. *AIChE Journal* **49** (11), 2715–2727.

PARK, C.-W. & HOMSY, G. M. 1984 Two-phase displacement in Hele–Shaw cells: theory. *Journal of Fluid Mechanics* **139**, 291–308.

PATERSON, C., WILSON, S. K. & DUFFY, B. R. 2014 Rivulet flow round a horizontal cylinder subject to a uniform surface shear stress. *The Quarterly Journal of Mechanics and Applied Mathematics* **67** (4), 567–597.

PITTS, E. 1973 The stability of pendent liquid drops. Part 1. Drops formed in a narrow gap. *Journal of Fluid Mechanics* **59** (4), 753–767.

PLATEAU, J. A. F. 1873 *Statique expérimentale et théorique des liquides soumis aux seules forces moléculaires*, vol. 2. Gauthier-Villars.

POUGATCH, K. & FRIGAARD, I. 2011 Thin film flow on the inside surface of a horizontally rotating cylinder: Steady state solutions and their stability. *Physics of Fluids* **23** (2), 022102.

PROBSTEIN, R. F. 1989 *Physicochemical Hydrodynamics: An Introduction*. Butterworth.

PROHM, C. & STARK, H. 2014 Feedback control of inertial microfluidics using axial control forces. *Lab on a Chip* **14** (12), 2115–2123.

QUÉRÉ, D. 1999 Fluid coating on a fiber. *Annual Review of Fluid Mechanics* **31** (1), 347–384.

RATULOWSKI, J. & CHANG, H.-C. 1989 Transport of gas bubbles in capillaries. *Physics of Fluids A: Fluid Dynamics* **1** (10), 1642–1655.

RAYLEIGH, L. 1878 On the instability of jets. *Proceedings of the London mathematical society* **1** (1), 4–13.

RAYLEIGH, L. 1882 Investigation of the Character of the Equilibrium of an Incompressible Heavy Fluid of Variable Density. *Proceedings of the London Mathematical Society* **s1-14** (1), 170-177.

REES, H. & CATOEN, B. 2006 *Selecting injection molds: weighing cost versus productivity*. Hanser Gardner Publications.

REINELT, D. A. 1987 Interface conditions for two-phase displacement in Hele–Shaw cells. *Journal of Fluid Mechanics* **183**, 219–234.

REINELT, D. A. & SAFFMAN, P. G. 1985 The penetration of a finger into a viscous fluid in a channel and tube. *SIAM Journal on Scientific and Statistical Computing* **6** (3), 542–561.

REIS, P. M. 2015 A Perspective on the Revival of Structural (In)Stability With Novel Opportunities for Function: From Buckliphobia to Buckliphilia. *Journal of Applied Mechanics* **82** (11), 111001.

REISFELD, B. & BANKOFF, S. G. 1992 Non-isothermal flow of a liquid film on a horizontal cylinder. *Journal of Fluid Mechanics* **236**, 167–196.

REYNOLDS, O. 1886 IV. On the theory of lubrication and its application to Mr. Beauchamp tower's experiments, including an experimental determination of the viscosity of olive oil. *Philosophical Transactions of the Royal Society of London* **177**, 157–234.

REYSSAT, E. 2014 Drops and bubbles in wedges. *Journal of Fluid Mechanics* **748**, 641–662.

RIBOUX, G. & GORDILLO, J. M. 2014 Experiments of drops impacting a smooth solid surface: A model of the critical impact speed for drop splashing. *Physical Review Letters* **113** (2), 024507.

RIBOUX, G. & GORDILLO, J. M. 2015 The diameters and velocities of the droplets ejected after splashing. *Journal of Fluid Mechanics* **772**, 630–648.

RIETZ, M., SCHEID, B., GALLAIRE, F., KOFMAN, N., KNEER, R. & ROHLFS, W. 2017 Dynamics of falling films on the outside of a vertical rotating cylinder: waves, rivulets and dripping transitions. *Journal of Fluid Mechanics* **832**, 189–211.

RIO, E. & BOULOGNE, F. 2017 Withdrawing a solid from a bath: How much liquid is coated? *Advances in Colloid and Interface Science* **247**, 100–114.

RISTROPH, L. 2018 Sculpting with flow. *Journal of Fluid Mechanics* **838**, 1–4.

RIVERO-RODRIGUEZ, J. & SCHEID, B. 2018 Bubble dynamics in microchannels: inertial and capillary migration forces. *Journal of Fluid Mechanics* **842**, 215–247.

RIVETTI, M., SALEZ, T., BENZAQUEN, M., RAPHAËL, E. & BÄUMCHEN, O. 2015 Universal contact-line dynamics at the nanoscale. *Soft Matter* **11** (48), 9247–9253.

RODRÍGUEZ-RODRÍGUEZ, J., SEVILLA, A., MARTÍNEZ-BAZÁN, C. & GORDILLO, J. M. 2015 Generation of microbubbles with applications to industry and medicine. *Annual Review of Fluid Mechanics* **47**, 405–429.

ROHLFS, W., PISCHKE, P. & SCHEID, B. 2017 Hydrodynamic waves in films flowing under an inclined plane. *Physical Review Fluids* **2** (4), 044003.

ROLLER, M. B. 1986 Rheology of curing thermosets: A review. *Polymer Engineering & Science* **26** (6), 432–440.

ROMANOV, D., KAUFMANN, G. & DREYBRODT, W. 2008 Modeling stalagmite growth by first principles of chemistry and physics of calcite precipitation. *Geochimica et Cosmochimica Acta* **72** (2), 423–437.

ROST, M. & KRUG, J. 1995 Anisotropic Kuramoto-Sivashinsky equation for surface growth and erosion. *Physical Review Letters* **75** (21), 3894.

ROY, R. V., ROBERTS, A. J. & SIMPSON, M. E. 2002 A lubrication model of coating flows over a curved substrate in space. *Journal of Fluid Mechanics* **454**, 235–261.

DE RYCK, A. 2002 The effect of weak inertia on the emptying of a tube. *Physics of Fluids* **14** (7), 2102–2108.

SAFFMAN, P. F. & TANVEER, S. 1989 Prediction of bubble velocity in a Hele–Shaw cell: Thin film and contact angle effects. *Physics of Fluids A: Fluid Dynamics* **1** (2), 219–223.

SAFFMAN, P. G. & TAYLOR, G. 1958 The penetration of a fluid into a porous medium or Hele–Shaw cell containing a more viscous liquid. *Proceedings of the Royal Society of London. Series A. Mathematical and Physical Sciences* **245** (1242), 312–329.

SANTOS, I. F. 2011 On the future of controllable fluid film bearings. *Mechanics & Industry* **12** (4), 275–281.

SAPRYKIN, S., KOOPMANS, R. J. & KALLIADASIS, S. 2007 Free-surface thin-film flows over topography: influence of inertia and viscoelasticity. *Journal of Fluid Mechanics* **578**, 271–293.

SAVART, F. 1833 Mémoire sur la constitution des veines liquids lancées par des orifices circulaires en mince paroi. *Ann. Chim.* **53**, 337–386.

SCHAAF, C. & STARK, H. 2017 Inertial migration and axial control of deformable capsules. *Soft Matter* **13** (19), 3544–3555.

SCHEID, B., KALLIADASIS, S., RUYER-QUIL, C. & COLINET, P. 2008 Interaction of three-dimensional hydrodynamic and thermocapillary instabilities in film flows. *Physical Review E* **78** (6), 066311.

SCHEID, B., KOFMAN, N. & ROHLFS, W. 2016 Critical inclination for absolute/convective instability transition in inverted falling films. *Physics of Fluids* **28** (4), 044107.

SCHMID, P. J. 2007 Nonmodal stability theory. *Annual Review of Fluid Mechanics* **39**, 129–162.

SCHMID, P. J. & HENNINGSON, D. S. 2001 *Stability and Transition in Shear Flows, Applied Mathematical Sciences*. Springer-Verlag New York.

SCHMIDKONZ, B. 1998 Die Geochemie von Calciumcarbonat. *Teil 1), Chem. Sch* (1), 21.

SCHMIDKONZ, B. & WITTKE, G. 2006 Tropfsteine im Zeitraffer. Geochemie und Betonkorrosion. *Chemie in unserer Zeit* **40** (4), 246–251.

SCHWARTZ, L. W. 1989 Viscous flows down an inclined plane: Instability and finger formation. *Physics of Fluids A: Fluid Dynamics* **1** (3), 443–445.

SCHWARTZ, L. W., PRINCEN, H. M. & KISS, A. D. 1986 On the motion of bubbles in capillary tubes. *Journal of Fluid Mechanics* **172**, 259–275.

SCHWARTZ, L. W. & ROY, R. V. 2004 Theoretical and numerical results for spin coating of viscous liquids. *Physics of Fluids* **16** (3), 569–584.

SCHWARTZ, L. W. & WEIDNER, D. E. 1995 Modeling of coating flows on curved surfaces. *Journal of Engineering Mathematics* **29** (1), 91–103.

SCRIVEN, L. E. 1988 Physics and Applications of Dip Coating and Spin Coating. *MRS Proceedings* **121**, 717–729.

SEGRÉ, G. 1961 Radial Particle Displacements in Poseuille Flow of Suspensions. *Nature* **189**, 209–210.

SEGRÉ, G. & SILBERBERG, A. 1962 Behaviour of macroscopic rigid spheres in Poiseuille flow Part 2. Experimental results and interpretation. *Journal of Fluid Mechanics* **14** (1), 136–157.

SEIDEN, G. & THOMAS, P. J. 2011 Complexity, segregation, and pattern formation in rotating-drum flows. *Reviews of Modern Physics* **83**, 1323–1365.

SEIWERT, J. 2010 Entraînements visqueux. PhD thesis, Ecole Polytechnique X.

SELVA, B., CANTAT, I. & JULLIEN, M.-C. 2011 Temperature-induced migration of a bubble in a soft microcavity. *Physics of Fluids* **23** (5), 052002.

SESSOMS, D. A., BELLOUL, M., ENGL, W., ROCHE, M., COURBIN, L. & PANIZZA, P. 2009 Droplet motion in microfluidic networks: Hydrodynamic interactions and pressure-drop measurements. *Physical Review E* **80** (1), 016317.

SHARP, D. H. 1984 An overview of Rayleigh-Taylor instability. *Physica D* **12** (1-3), 3–18.

SHEN, E. I. & UDELL, K. S. 1985 A finite element study of low Reynolds number two-phase flow in cylindrical tubes. *Journal of Applied Mechanics* **52** (2), 253–256.

SHORT, M. B. 2006 Fluids, Form, and Function: The Role of Fluid Dynamics in the Evolution of Stalactites, Icicles, and Aquatic Microorganisms. PhD thesis, The University of Arizona.

SHORT, M. B., BAYGENTS, J. C., BECK, J. W., STONE, D. A., TOOMEY, R. S. & GOLDSTEIN, R. E. 2005*a* Stalactite Growth as a Free-Boundary Problem: A Geometric Law and Its Platonic Ideal. *Physical Review Letters* **94** (1), 018501.

SHORT, M. B., BAYGENTS, J. C. & GOLDSTEIN, R. E. 2005*b* Stalactite growth as a free-boundary problem. *Physics of Fluids* **17** (8), 083101.

SHORT, M. B., BAYGENTS, J. C. & GOLDSTEIN, R. E. 2006 A free-boundary theory for the shape of the ideal dripping icicle. *Physics of Fluids* **18** (8), 083101.

SILVI, N. & DUSSAN V, E. B. 1985 The rewetting of an inclined solid surface by a liquid. *Physics of Fluids* **28** (1), 5–7.

SLADE, D., VEREMIEIEV, S., LEE, Y. C. & GASKELL, P. H. 2013 Gravity-driven thin film flow: The influence of topography and surface tension gradient on rivulet formation. *Chemical Engineering and Processing: Process Intensification* **68**, 7–12.

SNOEIJER, J. H. 2006 Free-surface flows with large slopes: Beyond lubrication theory. *Physics of Fluids* **18** (2), 021701.

SNOEIJER, J. H., ZIEGLER, J., ANDREOTTI, B., FERMIGIER, M. & EGGERS, J. 2008 Thick films of viscous fluid coating a plate withdrawn from a liquid reservoir. *Physical Review Letters* **100** (24), 244502.

SONG, H., CHEN, D. L. & ISMAGILOV, R. F. 2006 Reactions in droplets in microfluidic channels. *Angewandte Chemie International Edition* **45** (44), 7336–7356.

SPAID, M. A. & HOMSY, G. M. 1996 Stability of Newtonian and viscoelastic dynamic contact lines. *Physics of Fluids* **8** (2), 460–478.

STAN, C. A., ELLERBEE, A. K., GUGLIELMINI, L., STONE, H. A. & WHITESIDES, G. M. 2013 The magnitude of lift forces acting on drops and bubbles in liquids flowing inside microchannels. *Lab on a Chip* **13** (3), 365–376.

STAN, C. A., GUGLIELMINI, L., ELLERBEE, A. K., CAVIEZEL, D., STONE, H. A. & WHITESIDES, G. M. 2011 Sheathless hydrodynamic positioning of buoyant drops and bubbles inside microchannels. *Physical Review E* **84** (3), 036302.

STILLWAGON, L. E. & LARSON, R. G. 1988 Fundamentals of topographic substrate leveling. *Journal of Applied Physics* **63** (11), 5251–5258.

STONE, H. A. 2010 Interfaces: in fluid mechanics and across disciplines. *Journal of Fluid Mechanics* **645**, 1–25.

STONE, H. A., STROOCK, A. D. & AJDARI, A. 2004 Engineering flows in small devices: microfluidics toward a lab-on-a-chip. *Annual Review of Fluid Mechanics* **36**, 381–411.

STOOP, N., LAGRANGE, R., TERWAGNE, D., REIS, P. M. & DUNKEL, J. 2015 Curvature-induced symmetry breaking determines elastic surface patterns. *Nature Materials* **14** (3), 337–342.

TAKAGI, D. 2010 Spreading of viscous fluids and granular materials on slopes. PhD thesis, University of Cambridge.

TAKAGI, D. & HUPPERT, H. E. 2010 Flow and instability of thin films on a cylinder and sphere. *Journal of Fluid Mechanics* **647**, 221.

TANNER, L. H. 1986 Les gouttes **17**, 184.

TAYLOR, G. 1950 The instability of liquid surfaces when accelerated in a direction perpendicular to their planes. I. *Proceedings of the Royal Society A* **201** (1065), 192–196.

TAYLOR, G. 1961 Deposition of a viscous fluid on the wall of a tube. *Journal of Fluid Mechanics* **10** (02), 161–165.

TAYLOR, G. & SAFFMAN, P. G. 1959 A note on the motion of bubbles in a Hele–Shaw cell and porous medium. *The Quarterly Journal of Mechanics and Applied Mathematics* **12** (3), 265–279.

TENNYSON, R. C. 1968 The effects of unreinforced circular cutouts on the buckling of circular cylindrical shells under axial compression. *Journal of Engineering for Industry* **90** (4), 541–546.

TERWAGNE, D., BROJAN, M. & REIS, P. M. 2014 Smart morphable surfaces for aerodynamic drag control. *Advanced Materials* **26** (38), 6608–6611.

THIELICKE, W. & STAMHUIS, E. 2014 PIVlab–towards user-friendly, affordable and accurate digital particle image velocimetry in MATLAB. *Journal of Open Research Software* **2** (1).

THOMPSON, D. W. 1917 *On growth and form*. Cambridge University Press, 1942 edition.

THOMSON, J. 1855 XLII. On certain curious motions observable at the surfaces of wine and other alcoholic liquors. *Philosophical Magazine Series 4* **10** (67), 330–333.

THORODDSEN, S. T. & MAHADEVAN, L. 1997 Experimental study of coating flows in partially-filled horizontally rotating cylinder. *Experiments in Fluids* **23**, 1–13.

TREFETHEN, L. N. 2000 *Spectral methods in MATLAB*, vol. 10. Philadelphia: SIAM.

TREFETHEN, L. N. 2018 Backward heat equation. https://people.maths.ox.ac.uk/trefethen/pdectb/backward2.pdf, accessed: 15.05.2018.

TRINH, P. H., KIM, H., HAMMOUD, N., HOWELL, P. D., CHAPMAN, S. J. & STONE, H. A. 2014 Curvature suppresses the Rayleigh-Taylor instability. *Physics of Fluids* **26** (5), 051704.

TROIAN, S. M., HERBOLZHEIMER, E., SAFRAN, S. A. & JOANNY, J. F. 1989 Fingering instabilities of driven spreading films. *EPL (Europhysics Letters)* **10** (1), 25.

TSAI, T. M. & MIKSIS, M. J. 1994 Dynamics of a drop in a constricted capillary tube. *Journal of Fluid Mechanics* **274**, 197–217.

TUCK, E. O. & SCHWARTZ, L. W. 1990 A numerical and asymptotic study of some third-order ordinary differential equations relevant to draining and coating flows. *SIAM review* **32** (3), 453–469.

UTADA, A. S., FERNANDEZ-NIEVES, A., GORDILLO, J. M. & WEITZ, D. A. 2008 Absolute instability of a liquid jet in a coflowing stream. *Physical Review Letters* **100** (1), 014502.

VAN DYKE, M. 1975 Perturbation methods in fluid mechanics/Annotated edition. *NASA STI/Recon Technical Report A* **75**.

VAN SAARLOOS, W. 2003 Front propagation into unstable states. *Physics Reports* **386** (2), 29–222.

VANAPALLI, S. A., BANPURKAR, A. G., VAN DEN ENDE, D., DUITS, M. H. G. & MUGELE, F. 2009 Hydrodynamic resistance of single confined moving drops in rectangular microchannels. *Lab on a Chip* **9** (7), 982–990.

VANDEPARRE, H., PIÑEIRUA, M., BRAU, F., ROMAN, B., BICO, J., GAY, C., BAO, W., LAU, C. N., REIS, P. M. & DAMMAN, P. 2011 Wrinkling hierarchy in constrained thin sheets from suspended graphene to curtains. *Physical Review Letters* **106** (22), 224301.

VASSEUR, P. & COX, R. G. 1976 The lateral migration of a spherical particle in two-dimensional shear flows. *Journal of Fluid Mechanics* **78** (2), 385–413.

VASSEUR, P. & COX, R. G. 1977 The lateral migration of spherical particles sedimenting in a stagnant bounded fluid. *Journal of Fluid Mechanics* **80** (3), 561–591.

VAZIRI, A. & MAHADEVAN, L. 2008 Localized and extended deformations of elastic shells. *Proceedings of the National Academy of Sciences* **105** (23), 7913–7918.

VELLA, D., HUANG, J., MENON, N., RUSSELL, T. P. & DAVIDOVITCH, B. 2015 Indentation of ultrathin elastic films and the emergence of asymptotic isometry. *Physical Review Letters* **114** (1), 014301.

VELLA, D. & MAHADEVAN, L. 2004 The 'Cheerios effect'. *arXiv preprint cond-mat/0411688* .

VELLA, D., METCALFE, P. D. & WHITTAKER, R. J. 2006 Equilibrium conditions for the floating of multiple interfacial objects. *Journal of Fluid Mechanics* **549**, 215–224.

VEREMIEIEV, S., THOMPSON, H. M., LEE, Y. C. & GASKELL, P. H. 2011 Inertial two-and three-dimensional thin film flow over topography. *Chemical Engineering and Processing: Process Intensification* **50** (5-6), 537–542.

VERNEUIL, E., CORDERO, M., GALLAIRE, F. & BAROUD, C. N. 2009 Laser-induced force on a microfluidic drop: origin and magnitude. *Langmuir* **25** (9), 5127–5134.

VESIPA, R., CAMPOREALE, C. & RIDOLFI, L. 2015 Thin-film-induced morphological instabilities over calcite surfaces. *Proceedings of the Royal Society A* **471** (2176), 20150031.

VEYSEY II, J. & GOLDENFELD, N. 2008 Watching rocks grow. *Nature Physics* **4** (4), 310.

VILLERMAUX, E. 2012 The formation of filamentary structures from molten silicates: Pele's hair, angel hair, and blown clinker. *Comptes Rendus Mécanique* **340** (8), 555–564.

WANG, M.-W. & CHOU, F.-C. 2001 Fingering instability and maximum radius at high rotational Bond number. *Journal of the Electrochemical Society* **148** (5), G283–G290.

WARNIER, M. J. F., DE CROON, M. H. J. M., REBROV, E. V. & SCHOUTEN, J. C. 2010 Pressure drop of gas-liquid Taylor flow in round micro-capillaries for low to intermediate Reynolds numbers. *Microfluidics and Nanofluidics* **8** (1), 33.

WEDERSHOVEN, H. M. J. M., BERENDSEN, C. W. J., ZEEGERS, J. C. H. & DARHUBER, A. A. 2015 Infrared-laser-induced thermocapillary deformation and destabilization of thin liquid films on moving substrates. *Physical Review Applied* **3** (2), 024005.

WEIDEMAN, J. A. & REDDY, S. C. 2000 A MATLAB differentiation matrix suite. *ACM Transactions on Mathematical Software (TOMS)* **26** (4), 465–519.

WEIDNER, D. E. 2012 The effect of surfactant convection and diffusion on the evolution of an axisymmetric pendant droplet. *Physics of Fluids* **24** (6), 062104.

WEIDNER, D. E., SCHWARTZ, L. W. & ERES, M. H. 1997 Simulation of coating layer evolution and drop formation on horizontal cylinders. *Journal of Colloid and Interface Science* **187** (1), 243–258.

WEIDNER, D. E., SCHWARTZ, L. W. & ERES, M. H. 2007 Suppression and reversal of drop formation in a model paint film. *Chemical Product and Process Modeling* **2** (3), 19.

WEINSTEIN, S. J. & RUSCHAK, K. J. 2004 Coating flows. *Annual Review of Fluid Mechanics* **36**, 29–53.

WILCZEK, M., TEWES, W., ENGELNKEMPER, S., GUREVICH, S. V. & THIELE, U. 2017 Sliding Drops: Ensemble Statistics from Single Drop Bifurcations. *Physical Review Letters* **119** (20), 204501.

WILSON, S. D. R. 1982 The drag-out problem in film coating theory. *Journal of Engineering Mathematics* **16** (3), 209-221.

WILSON, S. K. & DUFFY, B. R. 1998 On the gravity-driven draining of a rivulet of viscous fluid down a slowly varying substrate with variation transverse to the direction of flow. *Physics of Fluids* **10** (1), 13–22.

WITELSKI, T. P. & BOWEN, M. 2003 ADI schemes for higher-order nonlinear diffusion equations. *Applied Numerical Mathematics* **45** (2), 331–351.

WONG, H., RADKE, C. & MORRIS, S. 1995*a* The motion of long bubbles in polygonal capillaries. Part 1. Thin films. *Journal of Fluid Mechanics* **292**, 71–94.

WONG, H., RADKE, C. & MORRIS, S. 1995*b* The motion of long bubbles in polygonal capillaries. Part 2. Drag, fluid pressure and fluid flow. *Journal of Fluid Mechanics* **292**, 95–110.

WONG, H. & RAO, S. 2015 The motion of long drops in rectangular capillaries at low capillary numbers. In *APS Meeting Abstracts*.

YIANTSIOS, S. G. & HIGGINS, B. G. 1989 Rayleigh-Taylor instability in thin viscous films. *Physics of Fluids A* **1** (9), 1484–1501.

ZHANG, J., YAN, S., YUAN, D., ALICI, G., NGUYEN, N.-T., WARKIANI, M. E. & LI, W. 2016 Fundamentals and applications of inertial microfluidics: a review. *Lab on a Chip* **16** (1), 10–34.

ZHOU, J. & PAPAUTSKY, I. 2013 Fundamentals of inertial focusing in microchannels. *Lab on a Chip* **13** (6), 1121–1132.

ZHU, L. & GALLAIRE, F. 2016 A pancake droplet translating in a Hele-Shaw cell: lubrication film and flow field. *Journal of Fluid Mechanics* **798**, 955–969.

Rue de l'Industrie 3
1005 Lausanne
+ 41 76 419 09 88
gioele88@bluewin.ch

Gioele Balestra

5 September 1988
Sorengo, TI, Switzerland

Swiss and German

EDUCATION

05.2014 – 08.2018	*PhD in Mechanical Engineering*, EPFL, Lausanne, Switzerland Laboratory of Fluid Mechanics and Instabilities Thesis title: "*Pattern formation in thin liquid films: from coating-flow instabilities to microfluidic droplets*" under the supervision of Prof. François Gallaire
09.2011 – 03.2014	*Master* in Mechanical Engineering (focus *Fluid Mechanics*), ETH, Zurich, Switzerland Thesis title: "*Spatio-Temporal Linear Stability Analysis for Heated Coaxial Jet Flows*" Final mark: 5.99/6 *with distinction*
09.2008 – 07.2011	*Bachelor* in Mechanical Engineering, EPFL, Lausanne, Switzerland Final mark: 5.84/6 *with distinction*
02.2008 – 06.2008	*PolyMaths* Preparatory Semester, EPFL, Lausanne, Switzerland
09.2003 – 06.2007	High-School (focus *Mathematics-Physics*), Liceo Lugano 2, Switzerland Final mark: 5.83/6 *with distinction*

PROFESSIONAL EXPERIENCES

02.2013 – 07.2013	Air Flow Consulting AG, Zurich, Switzerland: responsible for *Computational Fluid Dynamics* simulations of fire, contamination control and ventilation systems of rooms and buildings
08.2010 – 09.2010	MATISA Matériel Industriel SA, Crissier, Switzerland: served as apprentice in the area of *milling*, *turning* and *drilling* with both manual and automatic processing

TEACHING EXPERIENCE

Teaching assistant	*Hydrodynamics* (EPFL Master 2016-2017, by F. Gallaire) *Fluid Flow* (EPFL Bachelor 2015-2017, by F. Gallaire) *Flow of Dispersed Media* (EPFL Master 2014-2015, by M. Ramaioli and L. Zhu) *Turbulent Flow* (ETH Master 2012-2013, by L. Kleiser and P. Jenny)
Students supervisor (semester projects)	*Rayleigh-Taylor instability under a spherical substrate* (EPFL Master 2017) *Fingering instability of thin films flowing on curved substrates* (EPFL Master 2017) *Experimental investigation of cave drapery formation* (EPFL Bachelor 2017) *Ice-disk formation in a river* (EPFL Bachelor 2016 and l'X student 2017) *Chaotic mixing in a droplet* (Sherbrooke University student 2015, EPFL Master 2016) *Push-me pull-you: an efficient microswimmer* (EPFL Bachelor 2015)

CONFERENCES AND COURSES

- European Coating Symposium, Fribourg (CH), November 2017
  Balestra, G., Brun, P.-T., Kofman, N., Lee, A., Marthelot, J., Reis, P.M. and Gallaire, F. *Gravity-driven thin-film coatings under curved geometries*
- Complex Motion in Fluids, Cambridge (UK), September 2017
- 11th European Fluid Mechanics Conference, Sevilla (ES), September 2016
  Balestra, G., Kofman, N., Brun, P.-T. and Gallaire, F. *Thin films coating the interior of cylindrical substrates: from rivulets to dripping droplets*

- MicroMAST Spring School on Fundamentals of Surface Tension and Wetting, ULB (BE), May 2016
- 68th Annual Meeting of the APS Division of Fluid Dynamics, Boston (US), November 2015
  Balestra, G., Brun, P.-T., Lee, A., Marthelot, J., Reis, P.M. and Gallaire, F. *Dripping from a curved ceiling: a linear optimal transient growth analysis*
- Interaction of microscopic structures and organisms with fluid flows, Udine (IT), May 2015
- Dynamiques interfaciales en matière molle, Peyresq (FR), June 2014

PUBLICATIONS

- Balestra, G., Scheid, B., Wyart, M. and Gallaire, F., *in preparation*
- Shukla, I., Zhu, L., Kofman, N., Balestra, G. and Gallaire, F., *in preparation*
- Balestra, G., Badaoui, M., Ducimetière, Y.-M. and Gallaire, F. Fingering instability on curved substrates: optimal initial film and substrate perturbations, *submitted to the Journal of Fluid Mechanics*
- Balestra, G., Nguyen, D. and Gallaire, F. Rayleigh-Taylor instability under a spherical substrate, *submitted to Physical Review Fluids*
- Balestra, G., Zhu, L. and Gallaire, F. (2018). Viscous Taylor droplets in axisymmetric and planar tubes: from Bretherton's theory to empirical models. *Microfluid Nanofluid,* 22: 67
- Hadikhani, P., Hashemi, S.M.H., Balestra, G., Zhu, L., Modestino, M.A., Gallaire, F. and Psaltis, D. (2018). Inertial manipulation of bubbles in rectangular microfluidic channels. *Lab Chip*, 18, 1035
- Balestra, G., Kofman, N., Brun, P.-T., Scheid, B. and Gallaire, F. (2017). Three-dimensional Rayleigh-Taylor instability under a unidirectional curved substrate. *J. Fluid Mech.,* 837, 19-47
- Balestra, G., Brun, P.-T. and Gallaire, F. (2016). Rayleigh-Taylor instability under curved substrates: An optimal transient growth analysis. *PRF,* 1, 083902
- Lee, A., Brun, P.-T., Marthelot, J., Balestra, G., Gallaire, F. and Reis, P.M. (2016). Fabrication of slender elastic shells by the coating of curved surfaces. *Nat. Commun.*, 7, 11155
- Brun, P.-T., Damiano, A., Rieu, P., Balestra, G. and Gallaire, F. (2015). Rayleigh-Taylor instability under an inclined plane. *Phys. Fluids*, 27, 084107
- Balestra, G., Gloor, M. and Kleiser, L. (2015). Absolute and convective instabilities of heated coaxial jet flow. *Phys. Fluids,* 27, 054101

AWARDS

- *1st rank* of ETH Master Mechanical Engineering 2015 (*Willi-Studer Prize)*
- *1st rank* of EPFL Bachelor 2011 (all sections together)
- *1st rank* of High-School Lilu2 2007
- *Best* High-School *Project* 2007

LANGUAGES

Italian	*mother tongue*
French	*excellent knowledge*
German	*very good knowledge*
English	*very good knowledge*
Spanish	*basic knowledge*

OTHER ACTIVITIES

Military Service 07.2007 – 11.2007	Office Soldier at the Swiss Air Forces, Payerne Responsible for *administration*, *organization* and *planning* of the officer candidates school
Student Representative 09.2009 – 07.2011	Mechanical Engineering class at EPF Lausanne, Switzerland - Representing students in the *teaching committee* and *section council* - Organization of a one-week *study trip* to Britain for 50 people including *industry* tours
Volunteer 09.2000 – 09.2011	"Derby Casse di Sapone", Porza, Switzerland - Responsible for the race start